Czech Technical University in Prague
Faculty of Electrical Engineering
Department of Electromagnetic Field

Hollow-core optical fibers for sensing and communications

Habilitation thesis

Matěj Komanec

2021

Copyright

Acknowledgement

I would like to thank Professor Stanislav Zvánovec, my former Ph.D. supervisor, research mentor and most of all my friend, for all his support during my work on this habilitation thesis. Then I would like to thank Professor Radan Slavík, my collaborator from the University of Southampton, and also an old friend of mine, for his expertise, new ideas, fruitful discussions, all the fibers and for taking care of me while I was in Southampton.

Then I would like to thank all my Ph.D. students and team members, who did a lot of work in the framework of the presented research fields. Thank you Tomáš Němeček, Dmytro Suslov, Jan Bohata, Tomáš Martan, Daniel Dousek and Ailing Zhong.

Finally, I would like to thank my family, especially my wife Klára who did support me all the time. I thank my daughter Sára as she always gives me so much optimism. Last thanks go to my parents, who gave me both love for technology and teaching.

Abstract

Hollow-core optical fibers represent the state-of-the-art in fiber optics and are on the verge of surpassing the loss performance of standard single-mode fibers in the very near future. Apart from low loss, they bring high-power delivery possibilities, mid-infrared guidance even when made of silica and numerous other advantages. Nevertheless, their incorporation into standard fiber-optic systems is desired. In my habilitation thesis I present the development of a novel type of hollow-core fiber interconnection, based on the fiber array approach which led to record-low insertion loss, negligible back reflections and higher-order mode suppression. Our interconnection technique is then demonstrated in Fabry-Perot interferometer and microwave photonics applications.

Key Words

Photonic crystal fibers, hollow-core optical fibers, coupling methods, fiber interconnections, Fabry-Perot interferometer, microwave photonics

Abstrakt

Optická vlákna s dutým jádrem (hollow-core optical fibers) představují pokročilý typ optických vláken s parametry měrného útlumu téměř překračujícími hodnoty útlumu dosahovaného u klasických jednovidových optických vláken. Kromě jejich nízkých ztrát přinášejí možnosti přenosu vysokých výkonů, přenos ve střední infračervené oblasti, přestože jsou tvořeny křemenným sklem, a mnoho dalších výhod. Nicméně stále není dostupné jejich napojení se standardními vláknově-optickými systémy. Ve své habilitační práci popisuji vývoj nového typu napojení optických vláken s dutým jádrem, který je založen na využití vláknových polí a který vedl k dosažení rekorně nízkých vazebních ztrát, zanedbatelného zpětného odrazu a potlačení vyšších vidů. Naše metoda napojení je pak demonstrována jak v rámci Fabry-Perotova interferometru, tak i v oblasti mikrovlnné fotoniky.

Klíčová Slova

Fotonická vlákna, optická vlákna s dutým jádrem, metody vazby, vláknová propojení, Fabry-Perotův interferometr, mikrovlnná fotonika

Contents

Page

1 Motivation **1**

2 Introduction **3**

2.1 Historical overview . . . 3
2.2 Photonic-bandgap HCFs . . . 5
2.3 Antiresonant HCFs . . . 7
2.4 Negative curvature antiresonant fibers . . . 9
2.5 Nested nodeless antiresonant fibers . . . 11

3 Hollow-core fiber applications **13**

3.1 HCF interconnection techniques . . . 13
3.2 HCF-based applications . . . 15
3.3 Limitations and challenges . . . 21

4 Aims of the thesis **23**

5 Required know-how with specialty optical fibers **25**

5.1 Interfacing chalcogenide fibers to SSMFs . . . 25
5.2 Specialty optical fibers for the detection of liquids . . . 27
5.3 Modeling and characterization of PCFs . . . 28

6 Hollow-core fiber interconnection to conventional fiber-optic systems **31**

6.1 Proposed fiber-array-based HCF interconnection . . . 31
6.2 Long-term stability of the interconnection . . . 36

7 HCF-based applications **39**

7.1 Fiber Fabry-Perot interferometers . . . 39
7.2 Gas filling and sensing . . . 41
7.3 Microwave photonics . . . 42

8 Conclusions **47**

9 Future outlook **49**

10 Author's Publications **51**

References **55**

Appendix - Selected papers **67**

Abbreviations

ARF	Anti-Resonant Fiber
ARROW	Anti-Resonant Reflecting Optical Waveguide
CL	Confinement Loss
CS DSB	Carrier-Suppressed Double-SideBand
DWDM	Dense Wavelength-Division Multiplexing
DSB	Double-SideBand
FDFD	Finite-Difference Frequency-Domain (method)
FDTD	Finite-Difference Time-Domain (method)
FEM	Finite Element Method
FFPI	Fiber Fabry-Perot Interferometer
FSR	Free Spectral Range
FWHM	Full Width at Half Maximum
GRIN	Graded-Index
HCF	Hollow-Core Fiber
HOFGLAS	Hollow-core Optical Fiber Gas LAsers
HOM	Higher-Order Mode
IL	Insertion Loss
LMA	Large-Mode Area
MFA	Mode-Field Adapter
MFD	Mode-Field Diameter
MIR	Mid-InfraRed
MZI	Mach-Zehnder Interferometer
NANF	Nested Antiresonant Nodeless Fiber
NIR	Near-InfraRed
NRZ	Non-Return-to-Zero
OOK	On-Off Keying
PBG	Photonic-Bandgap
PBGF	Photonic-Bandgap Fiber
PCF	Photonic Crystal Fiber
PRISM	Perturbed Resonance for Improved Single Modednes
RL	Return Loss
RoF	Radio-over-Fiber

SC-PCF	Suspended-Core Photonic Crystal Fiber
SSL	Surface Scattering Loss
SSMF	Standard Single-Mode Fiber
TCD	Thermal Coefficient of Delay
VIS	Visible

CHAPTER 1 Motivation

Optical fibers have undergone a significant evolution since their invention in the 20th century finding their use in various application fields such as long-haul data communication, point and distributed sensing, fiber lasers, medicine, chemical analysis, and high-power delivery. Optical fibers thrive on their mechanical and chemical resistance, electromagnetic interference immunity, low weight, small size, and low cost. To unlock their vast potential, optical fiber designs have significantly diverged from the conventional core-cladding silica-glass premise. Numerous fiber materials, apart from silica, have been studied, such as chalcogenide [1, 2] and fluoride glass-based fibers [3, 4]. Various fiber structures have been proposed, such as dispersion-shifted [5], dispersion-compensating [6] or bend-insensitive [7] fibers. Rare-earth doped fibers for amplifiers have been introduced [8]. Finally, microstructured optical fibers emerged at the end of the 20th century [9].

Microstructured optical fibers provide vast options for fiber property tailoring, such as the possibility of chromatic dispersion tailoring and extended single-mode guidance. They offer the possibilities, e.g., of the compensation of accumulated chromatic dispersion [10], of tuning the chromatic dispersion profile and zero-dispersion wavelength [11], of enabling single-mode guidance in the visible (VIS) region [12], and much more.

Furthermore, by combining non-silica glass materials and microstructured design, highly nonlinear fibers with a specifically tailored chromatic dispersion profile can be obtained. This is highly suitable for a more efficient and extremely broadband supercontinuum generation. Supercontinuum sources are nowadays widely used in medicine, analytical chemistry and spectroscopy as they emit in the mid-infrared (MIR) region [13].

Nevertheless, the propagation of an optical signal in a solid-glass fiber core presents certain drawbacks, such as nonlinearity, latency and material losses. Significant efforts have, therefore, been carried out in the field of hollow-core optical fibers (HCFs) which guide light in an air-filled core. Thanks to the invention of HCFs, low latency transmission was achieved [14], negligible nonlinearity was presented [15], and extremely low loss competing with the best silica-based fibers has been recently demonstrated [16]. Hollow-core fibers represent, in 2021, the state-of-the-art in optical fiber development and are of considerable interest as they represent many new opportunities for researchers and application developers.

This habilitation thesis covers my and my research team's path to innovative HCF applications in numerous fiber-optic systems based on a novel approach of HCF interconnection methodology. First, I will introduce the preliminary steps which were focused on solid-core specialty optical fibers, photonic crystal fiber modeling and sensing approaches with specialty optical fibers. These preliminary steps enabled further research of the HCF and led to the proposal of a novel type of interconnection between standard single-mode fiber (SSMF) and HCF using fiber arrays and gluing instead of conventional splicing techniques. This interconnection was developed in close collaboration with the University of Southampton's Optoelectronics Research Centre (ORC) and was tested using the latest HCFs. As a result, we have significantly surpassed previous state-of-the-art results and presented world-record low-loss interconnection of HCFs.

Afterwards, we demonstrated numerous application possibilities enabled by our novel interconnection approach, such as high suppression of back reflections, high-stability Fabry-Perot interferometers and microwave photonics narrow-band filters. The thesis concludes with our current research aims and a brief future outlook.

CHAPTER 2 Introduction

In this chapter, I will first briefly overview the history of hollow-core optical fibers. Then I will present and discuss the key HCF representatives: photonic-bandgap fibers (PBGFs), antiresonant fibers (ARFs) and state-of-the-art nested antiresonant nodeless fibers (NANFs). A short discussion of waveguiding mechanisms for each of these fibers is included. Lastly, I will discuss the current main limiting factors of HCFs, attenuation and higher-order modes.

In general, HCFs can be divided into three categories, according to the HCF design and waveguiding principle:

- Bragg hollow-core fibers with a layered structure of the cladding (1D photonic crystal).
- Hollow-core photonic-bandgap fibers with a large number of periodic air-holes arranged in rings surrounding the central air-core - see examples in Fig. 2.1a) and Fig. 2.1b).
- Antiresonant hollow-core fibers with a Kagome or a tubular cladding structure - examples given in Fig. 2.1c-h).

Bragg HCFs are not in the scope of this thesis and are only mentioned in the historical overview.

2.1 Historical overview

The idea of light guidance in a hollow-core waveguide has existed since the end of the 19th century, when J. Thomson [17] and J. Rayleigh [18] first discussed the possibility of metallic waveguides. Later, in the 1960s, at Bell labs, a dielectric hollow-core metal-coated capillary waveguide was proposed [19] for the short-range transmission of millimeter waves. With the advent of optical fibers later in the 1960s, the focus had shifted to solid-core glass fibers and the development of hollow-core waveguides for light delivery was significantly limited.

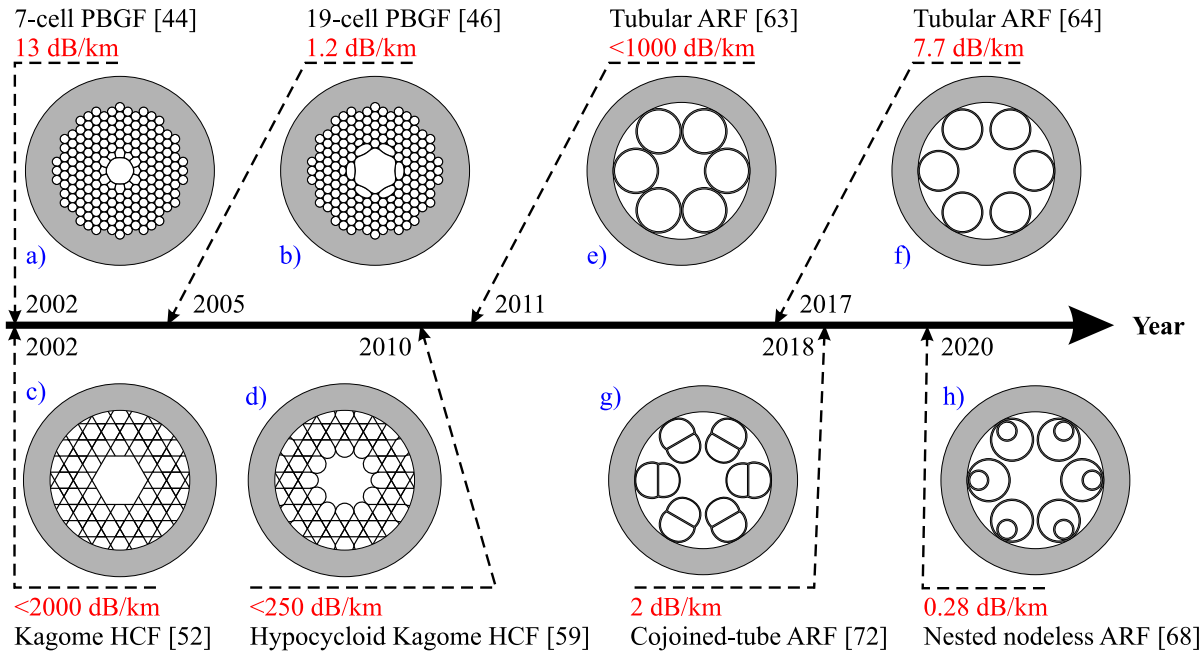

Figure 2.1: Timeline of the hollow-core optical fiber evolution including both fiber design and attenuation milestones; values are given for the wavelength of 1550 nm (with exception for f) which is at 750 nm).

In the early 1980s, hollow-core metal-coated capillary waveguides made from PbO_2 glass were introduced. These capillary waveguides were designed for wavelengths around 10.63 μm to guide light from CO_2 lasers [20] and exhibited attenuation of 7.7 dB/m. In 1991, a silica-glass-based capillary waveguide was developed for CO_2 laser delivery with attenuation below 1 dB/m [21]. It is important to mention that these capillary waveguides typically had core diameters larger than 1 mm.

Later, in 1993, hollow-core capillary waveguides, based on the silica-air design, were used for sensing purposes. First, for gas concentration measurements, a hollow-core capillary waveguide with a 1.5 mm inner core diameter and of 1 m length was used as a gas cell to analyze NH_3 content at a wavelength of 10 μm [22]. Second, an interferometric sensor was demonstrated [23] using a hollow-core capillary glass waveguide with a 70 μm inner diameter and length of 137 μm, therefore having a core dimension similar to what we today know as a hollow-core fiber. In 1995, a simple-glass hollow-core capillary waveguide was used to transport atoms by optical forces [24], with the main limitation being the attenuation of the glass capillary. This limitation showed the need for better light guidance, i.e., lower waveguide attenuation.

As a transition from hollow-core glass capillary waveguides to modern HCFs we can consider the so called Bragg fibers, which were developed as an alternative to the previously mentioned waveguides for wavelengths around 10 µm. The first Bragg HCF, denoted as the Omniguide fiber, was presented in 2002 [25] with an air core surrounded by a high-refractive-index glass and low-refractive-index polymer microstructure. Omniguide fibers exhibited less than 1 dB/m attenuation at 10.6 μm and it was possible to get tens

of meters of Omniguide fiber in a single fiber draw. In 2004, Bragg fibers from pure silica were presented, where the fiber cross-section was formed by concentric glass rings supported by struts [26].

A fundamental breakthrough leading to modern HCFs occurred a few years earlier in 1996 when the very first experimental results of a photonic crystal fiber (PCF) were published [9] revolutionizing the fiber-optic world. Even though PCFs are solid-core fibers their development significantly advanced HCF research and the first modern HCFs became possible soon after. The idea of the PCF originated from P. Russell and was based on two papers by Y. Jablonovitch [27] and S. John [28], who first showed the possibilities of 2D and 3D photonic crystals that trap light in a periodic structure with a varying refractive index. The PCF guidance mechanism allowed unprecedented freedom in the tailoring of the resulting fiber parameters, such as the chromatic dispersion curve, significantly altering the mode-field diameter, shifting the single-mode cut-off wavelength to shorter wavelengths and the ability to move the zero-dispersion wavelength [29]. All these parameters can be easily modified by changing the design of the PCF microstructure. In 1997, endlessly-single mode PCFs appeared [12]. In 1998, group-velocity dispersion management was presented [11] and in 2000, supercontinuum generation was first demonstrated using PCFs with the zero-dispersion wavelength at 800 nm producing broadband radiation from VIS to near-infrared (NIR) wavelengths [30].

2.2 Photonic-bandgap HCFs

Based on the PCF concept, the first photonic-crystal HCF was presented in 1999 [31], having a silica-based honeycomb microstructure with a core diameter of 14.8 μm. This first hollow-core photonic-bandgap fiber (HC-PBGF, or more simply PBGF) led to numerous research and application areas where HCFs were advantageously used afterwards, such as gas sensing [32], gas-filled lasers [33], fiber-optic gyroscopes [34], high-speed data transmission [35], and many more applications [36, 37].

PBGF is formed by introducing a defect in the periodic photonic crystal structure. Light is then trapped in the defect, as it cannot escape through the cladding due to the photonic bandgap (PBG) effect, and is guided along the fiber. The defect can be created by removing several capillaries from the center of the preform (e.g., to form a symmetric low-index core, we can remove 7, 19 or 37 capillaries, thus so-called 7-, 19- and 37-cell PBGFs are drawn). Two examples are given in Fig. 2.1a,b.

The first description of the guidance mechanism, based on the analogy with solid-state physics, appeared in 1999 [31] and described the 2D PBG effect principle, which was denoted as "frustrated tunneling PBG guidance". The cladding structure was considered as a double layer dielectric stack with an air-core in between. Light was confined once the stacks provided PBG for a range of propagation constants at fixed optical frequencies

($\beta = k\,n\cos\phi$), where β is the propagation constant, k stands for the wavenumber, n is the refractive index and ϕ represents the incident mode angle at the air-glass interface.

In the following effort to find the best lattice configuration, numerical approaches from solid-state physics were applied to calculate the PBG supporting the air-guided mode of a unit cell with periodic boundary conditions as a function of the wavevector direction [38, 39]. These first papers brought noteworthy PBGF design optimizations, such as a triangular lattice outperforming a honeycomb lattice [40] and the introduction of bandwidth scaling based on the air-filling factor (amount of air content compared to glass material) [41]. These approaches considered only a perfectly symmetric PBGF microstructure. However, small microstructure deformations were always introduced during the drawing process of the real PBGF, which resulted in different PBGF properties.

With the rapid increase in computational power, methods such as the finite element method (FEM) [42], finite difference time-domain (FDTD) and finite difference frequency-domain (FDFD) methods [43] became more common. These methods allowed for a far more accurate description of mode distribution in PBGFs as they consider the real fiber microstructure, instead of the idealized one which was the case of previously used analytical models. However, these methods did not explain the physical mechanisms, nor did they provide any more-in-depth understanding of light propagation in the PBGF. Nevertheless, since then they have often been applied due to improved computational capacities and satisfactory approximate results.

PBGFs were envisioned to surpass the minimal attenuation of SSMFs, which is limited by intrinsic material absorption and scattering in the glass core of SSMF. This would make PBGFs highly desirable in a number of applications, such as fiber-optic data networks. In 2002, a 7-cell PBGF with attenuation of 13 dB/km was reported [44] (see Fig. 2.1a). In 2004, attenuation improved to 1.7 dB/km [45].

It was the microstructure design of the PBGF that eventually limited the effort of achieving low attenuation as PBGFs exhibit significant surface scattering loss (SSL) which is a result of the mode-field overlap with the glass material - the core glass boundary. This overlap results in light scattering at the air-glass interface, caused by the inner surface roughness and HCF non-uniformity. This roughness is connected to the surface capillary waves that are thermodynamically locked in when the HCF cools down during the drawing process. On the other hand, confinement loss (CL) in PBGFs is negligible. This is thanks to the large number of the air-hole rings that increase the mode confinement in the PBGF core.

Additionally, the microstructure design of PBGFs contains a large number of thick glass nodes. These are formed by the glass material between the cladding air-holes. The glass nodes show strong wavelength dependence of their refractive index. Moreover, the glass refractive index significantly increases the effective refractive index of the cladding region that can then be matched with the effective refractive index of the core guided mode.

In practice this limits the usable bandwidth of PBGF to a range of selected wavelengths (the photonic bandgap), instead of one broader transmission window.

In 2005, a combination of the antiresonant effect and PBG led to a PBGF with attenuation as low as 1.2 dB/km [46] at 1550 nm, which is, until today, the record-low attenuation for PBGFs at 1550 nm (see Fig. 2.1b). The antiresonance was obtained by adding a thicker core glass boundary. Nevertheless, this created a drawback in the form of surface modes. Surface modes are guided at the interface of the core glass boundary and the air core and can be phase-matched with the fundamental mode of the PBGF at certain wavelengths. If phase matching occurs, guided wave is coupled to the core glass boundary which leads to increased losses of the guided mode [45–47].

The path to PBGFs with low attenuation has also led to substantially larger core diameters than that of SSMFs. The enlargement of the core diameter was inevitably tied with an increased number of modes propagating in the PBGF leading to multi-path interference. For PBGFs, the number of modes is given by the PBG - approximately 10-12 modes are present in the case of a 7-cell PBGF, around 40 modes for 19-cell PBGF and approximately 80 modes in the case of 37-cell PBGF [48]. The first few higher-order modes (HOMs) do not have significantly larger attenuation than the fundamental mode, thus they can propagate over long PBGF lengths, i.e., the lowest-order HOM (LP_{11}) propagates with attenuation of only about 2.5 times larger than the fundamental mode (LP_{01}) [49].

To overcome this limitation, an improved PBGF design, the so-called Perturbed Resonance for Improved Single Modedness (PRISM) fiber was presented [50]. PRISM fiber is a 19-cell hollow-core PBGF with attenuation of 7.5 dB/km at 1.59 µm. To reduce HOMs, two additional 7-cell (shunt) cores were included in the PBGF microstructure. These shunt cores were designed so that they were phase-matched with the low-order HOMs leading to strictly fundamental mode propagation. These PRISM fibers have recently been presented commercially in the form of an optical cable by OFS Optics [51].

2.3 Antiresonant HCFs

An alternative to PBGFs appeared in 2002 when a new type of HCF, denoted as a Kagome HCF was presented [52]. Kagome HCFs have an extremely delicate structure of thin triangular-lattice struts with no cladding nodes, see Fig. 2.1c). Due to the absence of cladding nodes, they allow multi-band/broadband transmission windows, therefore having an advantage over PBGFs. Nevertheless, the attenuation of Kagome HCF was still higher than that of PBGFs by more than two orders of magnitude [53] which was denoted to the core mode leakage, i.e., high CL.

The guiding principle of Kagome HCFs is different than that of PBGF, as with the change in the cladding structure, photonic bandgaps no longer existed. The guidance in the core was attributed to inhibited coupling (antiresonance), where a low density of states

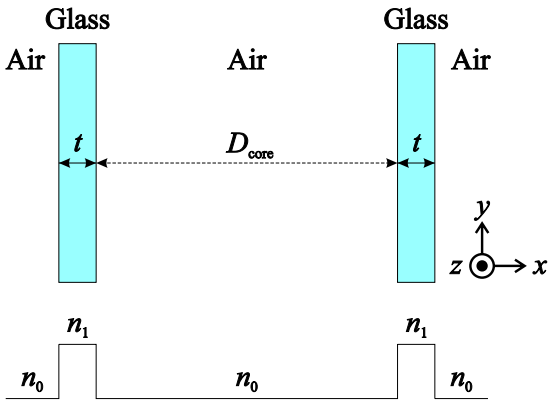

Figure 2.2: 1D slab waveguide structure, glass with refractive index n_1, air with refractive index n_0, t is glass thickness and D_{core} is slab width corresponding to the fiber core diameter.

exists in the cladding and the guided core mode/modes have negligible overlap with the cladding modes.

Antiresonant reflection confines light in the air-core (or generally lower refractive index region) without the need for periodic cladding and the PBG effect. The antiresonant reflecting optical waveguide (ARROW) model has often been used to describe ARFs. The idea first originated in 1986 [54] and was further developed in 2002 and 2006 [55, 56]. The principle of the ARROW model assumed high-index circular layers around the low-index (air) core where each layer acts as a Fabry-Pérot resonator.

To understand the antiresonance principle, the example of a 1D slab waveguide is often given. The situation is depicted in Fig. 2.2 with the core diameter $D_{\text{core}} >> \lambda$, where λ is wavelength. The resonance condition (phase difference is $2m\pi$) for the transversal wave vector k_{T} is described as [57]:

$$k_{\text{T}}\, t = \pi m \tag{2.1}$$

$$k_{\text{T}} = \sqrt{k^2 n_1^2 - \beta^2} = k\sqrt{n_1^2 - 1}, \tag{2.2}$$

where β is the propagation constant (in the direction of propagation). We consider n_1 as the refractive index of the glass material and the refractive index of air is $n_0 = 1$. Parameter m is a real positive integer and t is glass thickness.

We can then find a resonance wavelength λ_{res}, where all the light is transmitted in the transversal direction given as [57]:

$$\lambda_{\text{res}} = \frac{2t\sqrt{n_1^2 - 1}}{m}, \qquad m = 1, 2, 3, \ldots \tag{2.3}$$

For wavelengths other than λ_{res}, light is confined inside the air-core with low leakage loss. The solution of the 1D slab waveguide based on anti-resonance leads to a range of

glass thickness that is based on m which results in high leakage and, therefore, high loss for given wavelengths. Fiber transmission windows are present between them (see example cases given in [57]). Apart from glass thickness t, air-core diameter D_{core} also plays a crucial role in the confinement of the fundamental mode. The transmission windows do not change based on D_{core}, but CL increases as D_{core} gets larger [57].

Moving from the 1D slab waveguide to the simplest case of a fiber structure, we can assume a high-index glass capillary, which forms two reflective surfaces as depicted in Fig. 2.3. For a mode existing in the glass ring, the effective refractive index is between that of glass and air. For a mode propagating in the air-core, the effective refractive index is lower than that of air. Depending on glass thickness t, multiple transmission bands will be present, with losses dependant on t and D_{core}. The modes guided in the capillary can be easily calculated using FEM [57] or mode-matching methods [58]. The next step is a negative-curvature ARF, which is discussed in the following section.

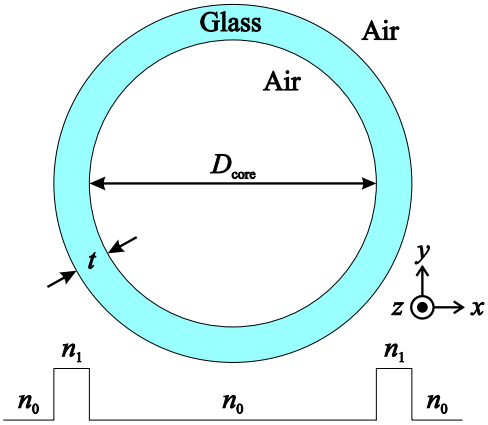

Figure 2.3: Capillary fiber structure, glass with refractive index n_1, air with refractive index n_0, t is glass thickness, D_{core} is the capillary inner diameter and z is the direction of light propagation.

2.4 Negative curvature antiresonant fibers

The next milestone in HCF development occurred in 2010 with the development of negative-curvature Kagome HCFs, also denoted as hypocycloid fibers [59]. The reason behind the negative curvature emanated from the idea of removing the attenuation limit caused by SSL. If the core boundary has a negative radius, the mode-field overlap will be negligible, thus SSL will be suppressed. The negative curvature represents the shape of the first glass ring around the fiber core (see Fig. 2.1d) which led to a decrease of fiber attenuation down to hundreds of dB/km while keeping the bandwidth advantage of Kagome HCF (around 1000 nm, one octave). Although the attenuation of this negative-curvature Kagome HCF was still significantly higher than that of PBGF, the bandwidth

was superior to that of the PBGF. Later, in 2016, a negative-curvature Kagome HCF with attenuation of 12.3 dB/km at 1 μm was presented [60].

In parallel, efforts were focused on exploiting the negative curvature while simultaneously reducing microstructure complexity. In 2010 and 2011, the first ARFs with a low-complexity design appeared, showing a simplified PBGF lattice [61], a simplified hypocycloid Kagome lattice [62] and, finally, a tubular lattice [63]. These tubular ARFs did not require a periodic lattice and worked just on the principle of antiresonance. Among the negative-curvature lattice variants, the tubular ARF showed the best performance while using the simplest design which is why it has been further developed (see Fig. 2.1e,f). The lowest current attenuation of a single-ring tubular ARF is 7.7 dB/km at 750 nm [64].

A simple tubular ARF is shown in Fig. 2.4a with a set of glass capillaries around the central air-core, which are in contact with each other. The core boundary is then formed by the glass capillary walls having a negative curvature with respect to the radial direction. The overall geometry of such a tubular ARF (negative curvature fiber) is described by D_{core}, t, the capillary diameter D_{cap} and the number of capillaries p as [57]:

$$D_{\text{core}} = \frac{D_{\text{cap}} + 2t}{\sin(\pi/p)} - (D_{\text{cap}} + 2t). \tag{2.4}$$

Figure 2.4b shows an example of an advanced type of the negative curvature fiber with non-touching capillaries and parameter g defining the gap - the smallest distance between two adjacent capillaries. This microstructure design eliminates the remaining glass nodes (touching points) which leads to the absence of surface modes and thus improves the bandwidth of the fiber. Furthermore, the addition of the gap leads to better confinement of the core mode, so it reduces CL and, therefore, the overall attenuation of the tubular ARF is lower. The effect of D_{core} on transmission bands and CL is identical to capillary ARFs.

Antiresonance prohibits the air-core mode from overlapping with the glass material (glass capillaries). This leads to low SSL and low material-induced loss required for low attenuation. Nevertheless, to achieve competitive losses to SSMFs greater coupling suppression between the air-core mode and the cladding modes is required. This coupling suppression is denoted as inhibited coupling [64]. Inhibited coupling is achieved by the already mentioned low overlap between the core and cladding modes and, furthermore, by having a mismatch of core and cladding modes effective refractive indices. Reduction of CL was achieved by adding additional resonators in the tubular ARF forming nested and co-joined tube ARFs which are discussed in the following section.

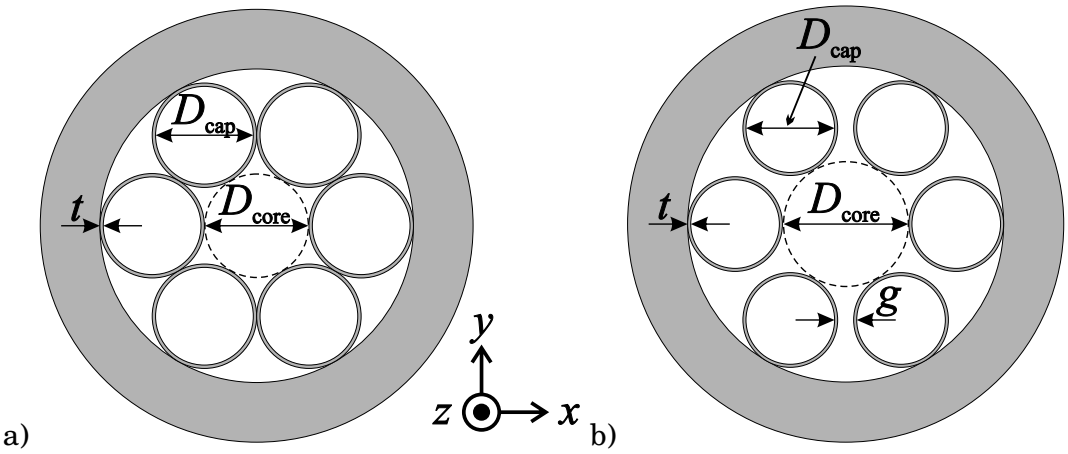

Figure 2.4: Tubular (negative curvature) antiresonant fiber structure with: a) touching and b) non-touching glass capillaries.

2.5 Nested nodeless antiresonant fibers

In 2014, a fundamental study was published [65] showing the potential of tubular (negative curvature) ARFs when including additional (nested) resonators inside of each of the existing capillaries (see Fig. 2.1h). The nested capillaries serve as an additional layer of resonators and significantly improve the CL of the ARF. The resulting design is then called nested antiresonant nodeless fiber - NANF. It was also envisioned that NANFs could eventually surpass the attenuation of other HCF types and that of SSMFs due to their negligible optical field overlap with the glass leading to low SSL and high mode confinement leading to low CL. Figure 2.5 illustrates the difference between the PBGF design and the state-of-the-art NANF design on two samples of HCFs used in our experimental work.

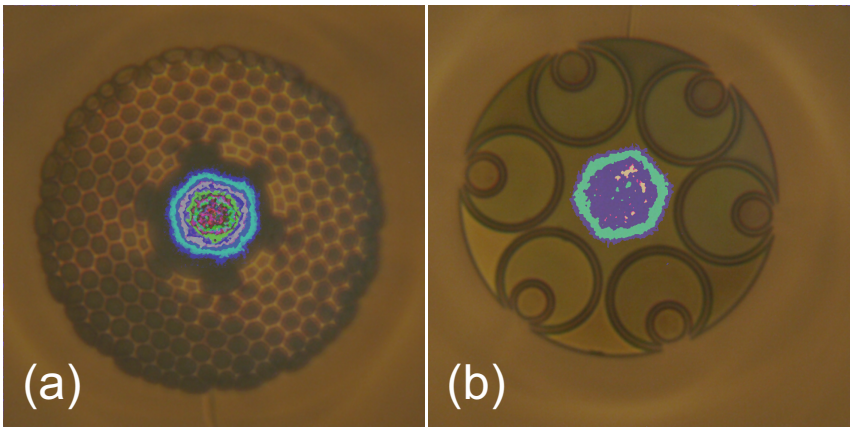

Figure 2.5: Scanning-electron photograph of two real HCFs with their respective mode-field distributions which were measured by the near-field technique, a) 19-cell PBGF, b) 6-tube NANF.

For state-of-the-art NANFs, SSL is lower than 10^{-1} dB/km and CL is only 10^{-8} [65]. In [65] it was also shown that for $D_{\text{core}} = 50\,\mu$m, SSL and CL are equal, with CL scaling with the core radius R_{core} as R_{core}^{-8} and SSL scaling with R_{core}^{-3}.

In [65] it was calculated that for $D_{\text{core}} = 40\,\mu$m the NANF would have attenuation of the 0.1 dB/km level, which would surpass SSMFs in the wavelength region of 1.5 to 2.3μm. Increasing the size of D_{core} would lead to even lower NANF attenuation thanks to the reduction in light overlap with glass. Nevertheless, increasing the core size leads to more guided HOMs, the same as for PBGFs which are unwanted or even detrimental in numerous applications.

The combination of negligible SSL and lowered CL led to practical demonstrations of NANFs with only 1.3 dB/km in 2018 [66] and this attenuation value was significantly decreased just a year later by NANF with attenuation of 0.65 dB/km at 1550 nm [67]. In 2020, a NANF with attenuation of only 0.28 dB/km was presented [68], and, finally, in 2021 record-low attenuation of 0.22 dB/km [16] at 1625 nm was demonstrated challenging the record attenuation of SSMFs with 0.14 dB/km at 1550 nm [69]. This record-low attenuation of NANFs has been supported by using enhanced fiber drawing technology as described in detail in [70]. The mastering of the drawing technology allowed for better control of the fiber structure, which led to the decrease of CL and also allowed for thinner capillary walls and resulted in a shift from the 2nd transmission window to the 1st transmission window (as discussed in simplified version in Section 2.3), subsequently enhancing the low-loss bandwidth of the NANF by a factor of almost 3. Note, that at shorter wavelengths NANFs have already matched or even surpassed the attenuation of solid-core silica fibers [16, 71].

In parallel, in 2018, a different type of a nodeless ARF was presented, a cojoined-tube fiber (CTF) with minimal attenuation of 2 dB/km at 1512 nm [72] (see Fig. 2.1g).

Furthermore, extraordinary polarization purity in ARFs, specifically NANFs operating in the 1st antiresonance window, was presented in 2020 [73], showing cross-coupling between orthogonal polarization modes in the order of 10^{-10}. This result is crucial for high-performance interferometers and other applications requiring high polarization purity.

Research and technology development have also recently focused on non-silica ARFs to cover wavelengths above 5 μm. Chalcogenide ARFs have been successfully drawn, e.g., an arched inner structure ARF made of arsenic-sulfide glass showed attenuation below 0.1 dB/m at 10.6 μm [74]. Tellurite glass tubular ARF has been presented [75] using fiber extrusion with minimum attenuation of 4.8 dB/m in the vicinity of 5 μm, where modeling suggests sub-1dB/m levels can be reached once the drawing technology is perfected. Borosilicate 8-tube ARFs have been reported with sub-dB/m attenuation in the VIS region and around 4 dB/m attenuation around 5 μm with negligible bending losses [76].

CHAPTER 3 Hollow-core fiber applications

This chapter covers recent achievements in HCF development, focusing on HCF applications and HCF incorporation into conventional SSMF-based systems. I summarize the main research and application fields where HCF advantages have enabled breakthrough results.

3.1 HCF interconnection techniques

As progress was made in HCFs, the question of how to incorporate them into conventional SSMF-based optical systems was at hand. The first and most common option was to use fiber fusion splicing. During fusion splicing the fiber ends are heated and then pressed together to form a permanent and low-loss splice. This process had already been automated and perfected when HCFs first appeared. The main concern was the delicate microstructure of the HCF, especially of PBGFs and Kagome HCFs, which collapse easily when heated. Therefore, modified splicing techniques have emerged for HCF-SSMF splicing with the focus on preserving the HCF microstructure [77, 78]. The modification has been mostly in using an offset heating (by arc, filament or CO_2 laser) so that the SSMF is heated more than the HCF, see Fig. 3.1a). Unfortunately, this generally led to low strength splices.

Apart from the splice quality in terms of mechanical strength of HCF-SSMF, two other factors are important. Splice insertion loss (IL) and back-reflection level expressed as return loss (RL). Both these parameters are well known to the fiber-optic community.

For HCFs there are two peculiarities which are not common in the SSMF world. First, RL is critical as the silica (SSMF) - air (HCF) interface has a 4% back reflection (RL of -15 dB). Second, as mentioned above, low attenuation HCFs are inherently multi-moded, thus the interconnection of SSMF-HCF can be viewed as a single-mode to multi-mode coupling (and vice versa at the HCF output). At the input side, SSMF-HCF, the fundamental mode of SSMF is coupled to the fundamental mode of HCF but also into HOMs of HCF which have greater attenuation. This leads to losses caused by input coupling. On the output side, HCF-SSMF, multiple HCF modes are coupled to the SSMF, which acts as a modal filter and again losses are experienced. Additionally, the HOMs propagate with time delay and when coupled back into SSMF, can interfere with the

fundamental mode. This results in a noise, which is especially detrimental in coherent applications.

Initial reports on HCF splicing appeared in 2005 where the effect of an HCF microstructure collapse via an arc-discharge was studied [77]. In the same year, HCFs were spliced for use in gas-cells [78] with insertion loss (IL) of the interconnection of 1.7 dB. In 2006 a more detailed splicing analysis was carried out [79], focusing on 7-cell and 19-cell PBGFs. It was found that the interconnection is not symmetrical. In the case of 7-cell PBGF, for the SSMF-PBGF splice IL of 1.5-2.0 dB was observed, whereas for the PBGF-SSMF splice IL was 2.6-3.0 dB. In the case of 19-cell PBGF, IL was 0.3-0.5 dB and over 2.0 dB for the SSMF-PBGF and PBGF-SSMF splices, respectively.

This unbalanced IL result was extremely important, as it showed a significant effect of HOMs on measured IL, as mentioned above. If the mode-fields of SSMF and HCF are not matched, light is coupled into HOMs which then contribute to the measured IL. For proper IL estimation of any SSMF-HCF/HCF-SSMF interconnection, HOMs must either not be excited at all, or HOM content must be analyzed and accounted for.

Further attempts at HCF-SSMF splicing brought improved IL and were focused on suppressing unwanted back reflections that occur at the glass-air interface. In 2007, splicing of flat and angled-cleaved 7-cell PBGFs was presented [80], with IL of 0.9 dB and 3.0 dB for flat and angled-cleaved PBGFs, respectively, with return loss (RL) of -16 dB and -60 dB. In 2016, splicing of 7-cell and 19-cell angled-cleaved PBGFs [81] brought improved IL of 1-2 dB with slightly lower RL of −50 dB. IL in this work was measured including HOMs which explains the great range of obtained IL values, furthermore, the obtained cleave angle variation was significant, from 7 to 12 °. In the same year, high-strength fusion splicing of 7-cell PBGF was demonstrated with IL of 1.3 dB [82].

To achieve sub-1 dB insertion losses, the move to bridge fibers acting as mode-field adapters (MFAs) was necessary. MFAs are placed between SSMF and HCF and accommodate the mode-field difference so that it matches better with HCF. In 2014, mode-field diameter (MFD) accommodation using a few-mode fiber to a 7-cell PBGF was published [83], showing the potential of bridge fibers. Splice IL of only 0.73 dB was obtained for the interconnection.

An interesting solution has recently appeared using micro-optic collimator technology [84], where IL of 0.53 dB was presented for a single SSMF-HCF interconnection with RL better than -45 dB and good HOM suppression (> 20 dB), see Fig. 3.1b).

A tapered SSMF as a coupling option has been theoretically and experimentally investigated [85]. The SSMF taper was designed to match the MFD of the studied HCFs and was then inserted into the HCF core area (see Fig. 3.1c). The resulting IL was, e.g., approximately 0.8 dB for an SSMF-NANF coupling, well below the theoretically predicted values, which was caused by HOMs being present at the detector due to the short lengths of tested HCFs (tens of centimeters).

For higher optical powers (above 1 W) an approach using nanotapers, i.e., nanospikes was proposed [32, 86] where an ultra-thin fiber tip (having a few hundreds of nanometers diameter) is inserted into the HCF and via opto-mechanical forces is then self-aligned in the HCF core. This coupling provided IL of around 3 dB (depending of optical power) and back reflections suppressed below -33 dB.

Just recently a combined approach of fiber tapering and fusion splicing led to a low-loss fusion splicing of an 8-tube NANF with only IL of 0.88 dB for the whole SMF-HCF-SMF system including the specially designed reverse taper acting as MFA [87]. Back reflections were not mitigated via this approach.

An illustrative comparison of different HCF-SSMF interconnection techniques is given in Fig. 3.1, where the fiber-array based interconnection technique in Fig. 3.1d), which we developed, is discussed in detail in Chapter 6.

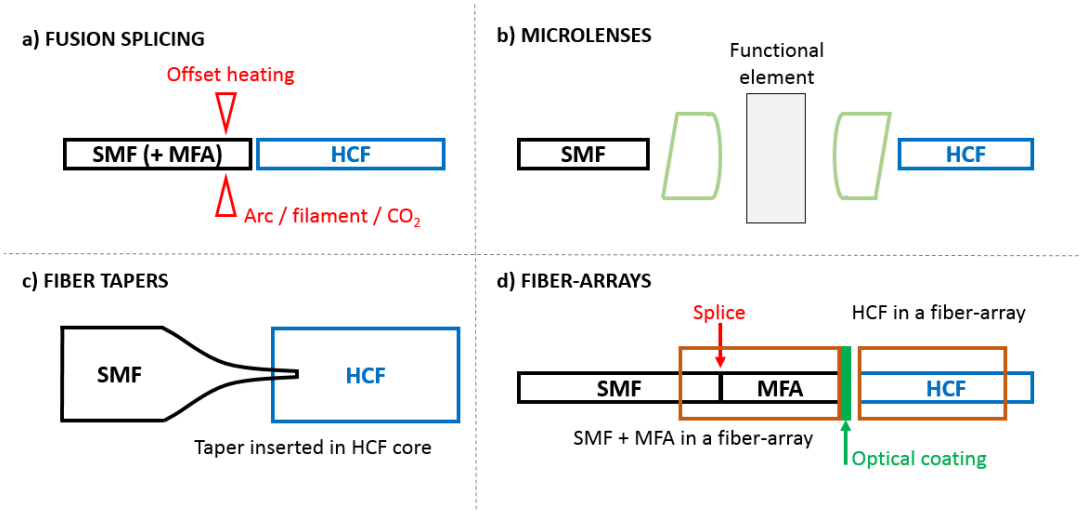

Figure 3.1: Illustrative comparison of the main interconnection techniques of SSMF and HCF.

3.2 HCF-based applications

Here I provide a brief summary of selected research and application fields where HCFs show their potential. At the end I conclude with observed limitations in state-of-the-art achievements which were the primary impulse for my research.

Interferometry

In interferometry, HCFs offer the advantages of low nonlinearity thanks to the negligible light-glass interaction and HCF environmental (temperature) insensitivity [88]. The flagship representative among all fiber-optic interferometric sensors is the Sagnac interferometer acting as a fiber-optic gyroscope (FOG). A proposal of a HCF-based FOG

was presented in [34] in 2012 using a 7-cell PBGF of 20 m length. Seeing rapid progress, HCF-based FOGs have evolved and are now based on NANFs while providing impressive performance in long-term stability of 0.05 deg/h [89] nearing the requirements for civil aircraft navigation. Additionally, HCF-based FOGs build on ultra-low backscaterring and, in 2021, backscaterring four orders lower than of SSMFs was reported with a record value of -118 dB/m [90] presenting a four-order better performance than previously reported for PBGFs [91].

Apart from FOGs, HCF-based Mach-Zehnder interferometers (MZIs) have been predominantly used as gas/pressure sensors, such as the one shown in [92], where the refractive index of gas was measured using two segments of 3.3 mm-long PBGFs in the form of an in-line MZI gas sensor. Alternatively, periodic modifications of the HCF inner structure have been used to form MZIs, e.g., in [93] a strain sensor has been realized showing 1.3-times enhanced performance over an unmodified HCF.

An ARF-based interference sensor for simultaneous strain and temperature measurement working on the principle of multi-path interference and antiresonance was presented [94]. In this work, the interference between the fundamental mode and the first HOM showed a significant response to both strain and temperature, while the antiresonance condition also changed. This double response to strain and temperature was observed as resonance dips in the transmission spectrum and, thus, advantageously used to discriminate between the measured strain and temperature. Only short 8-tube NANF samples with lengths below 0.5 m were used, with the best strain sensitivity of -2.23 pm/$\mu\epsilon$ and temperature sensitivity of -17.45 pm/°C.

Similarly, a dual-core ARF has been proposed and demonstrated acting as a supermodal interferometer [95]. The principle of the sensor was based on a dual-core ARF, where both cores were connected via an air channel so that the evanescent field could interact and form supermodes. Once a broadband optical signal was launched into one core, an interference pattern could be observed at the output given by the coherently interfering transverse modes. If external stress (bending) was applied to the dual-core ARF, the interference pattern shifted in wavelength and this wavelength shift was observed and calibrated to the stress value. Using this approach a high pressure sensitivity of 39.3 nm/MPa with low temperature cross-talk was obtained.

Temperature-insensitivity of HCF-based optical systems has been further studied. The behaviour of coated and uncoated HCFs down to cryogenic temperatures has been investigated using an MZI approach [96] presenting a temperature-insensitive HCF operation at around -70 °C for a bare 19-cell PBGF.

Fiber Fabry-Pérot interferometers (FFPIs) are widely used based on HCFs as the HCF acts as an air cavity with its long length and high level of light confinement. An analysis of a gas refractive index has been shown using a 7-cell PBGF spliced on SSMF on both sides forming a 24.9-mm long cavity with a resolution of 10^{-6} RIU (refractive index

unit) [97]. Vibration sensing using a 18.5-mm long Kagome-ARF cavity spliced on SSMF on both sides has been demonstrated with a broad 1-20 000 Hz measurement range while being temperature insensitive [98]. A thickness measurement using a capillary HCF-based cavity has been presented to analyze graphene-oxide layers down to a thickness of 0.21 nm [99]. An FFPI for high-temperature sensing based on the Vernier effect has been proposed using a simplified HCF with a maximum measurable temperature of 1050 °C [100]. Relative humidity detection has been made possible using graphene-quantum dots in polyvinyl alcohohol injected in the HCF [101]. This FFPI sensor showed good linearity and a broad relative humidity range of 13-81 %.

Data transmission

HCFs are especially suitable for data transmission thanks to their low latency [14], low nonlinearity [15], and, in the case of NANFs, extreme bandwidth and low attenuation. In 2019, data transmission over a 1-km-long NANF (bandwidth of 700 nm, attenuation of 6.6 dB/km at 1550 nm) was demonstrated with 50 Gbit/s On-Off Keying (OOK) and 100 Gbit/s 4-level Pulse Amplitude Modulation (4PAM) signals [102]. The same year, a 4.8-km-long NANF segment with attenuation of 1.18 dB/km at 1550 nm was used in a recirculating loop [103], which allowed for a data transmission over a 341-km-long NANF link with a better pre-forward error correction bit error rate than $3{\cdot}10^{-2}$. Furthermore, in 2019, a nonlinearity-free coherent transmission was presented with a total data rate of 6.8 Tbit/s using a 270-m long 7-tube ARF [104].

To demonstrate ARF broader bandwidth (exceeding 1000 nm, i.e., one octave) compared to PBGFs (maximum hundreds of nanometers), a study using 10 Gbit/s OOK non-return-to-zero (NRZ) transmission parallel at 1065, 1565 and 1963 nm was carried out showing outstanding performance at all selected wavelengths [105].

Furthermore, low latency communication has been shown using this first HCF cable on a dense wavelength-division multiplexing (DWDM) transmission with 35 channels of 10 Gbit/s OOK NRZ data rates. Another important result from 2020 discusses the low thermal sensitivity of HCFs, in this case for optically-switched data centers [106]. Here, HCFs can drastically reduce the optical switching complexity in terms of clock recovery by eliminating the temperature dependent refractive index and length variations of SSMFs, as HCFs have around 20times lower temperature dependence.

For practical use of HFCs in communications, an 11-km long PBGF was drawn in 2016 [107] to show the high uniformity of fiber parameters. In the next step, PBGF with shunt cores to reduce HOMs was presented in 2020 in the form of an optical cable [108]. These results can be treated as the first step to practical HCF data communication. In 2021, Lumenisity launched the field deployment of its state-of-the-art 5-tube NANF, already in a cabled version, for a 48x DWDM system with more than a 1000 km reach [109] with a total C-band throughput of 38.4 Tb/s considering a system at 800 Gb/s (less than 200 km reach).

Gas sensing

As discussed, HCFs are excellent candidates for highly sensitive gas-sensing applications [110] especially due to their almost 100 % mode-field overlap with the studied gas analyte. HCFs also allow the possibility to construct long-length gas cells which substitute the need for conventional multi-path free-space cells [111]. Among HCFs, ARFs provide a homogeneous and low-defect structure with the substantial mitigation of HOMs, thus becoming the most suitable for gas cells. A further advantage of silica ARFs for gas sensing is their MIR transparency. Even though silica is opaque above 2.4 μm, thanks to the negligible overlap of the core mode with the glass material, silica ARFs can work up to 4.0 μm with reasonable attenuation of 1.5 dB/m [112].

The common approach to analyzing gases is to use infra-red (IR) spectroscopy [113]. A recent overview of laser-based sensing is provided in [114] which discusses HCF filling options, measurement configurations and the use of PBGFs, ARFs and capillary fibers. In general, it was observed that capillary fibers suffer from significant background noise caused by HOMs [115]. For HCFs, the filling time is a limiting factor, as was theoretically studied in [116] which compared a 1.1-m long 7-cell PBGF with a core diameter of 10 μm and a Kagome ARF a core diameter of 10 μm. The results of the analysis showed that the filling time should be reduced to 10 s for the Kagome ARF from 19 s for the 7-cell PBGF, however both cases require gas pressure of 4 atm. Drilling using a femtosecond laser or dividing the PBGF into several subsections have been proposed to overcome the filling time limitation [117, 118]. Furthermore, as with capillary fibers, PBGFs suffer from HOM-induced interference noise. ARFs have shorter filling times thanks to their larger core diameter, reducing the time to an order of seconds, whereas the HOM noise limitation is still present.

To overcome noise stemming from HOMs, the photothermal spectroscopy approach has been employed for HCFs, e.g., in [119] acetylene detection down to order of ppt was demonstrated using a 4.67-m long 7-tube ARF. Another complementary detection technique, the Raman spectroscopy, was found to be especially advantageous when studying multi-component gas analytes as it does not require a strict wavelength to match the respective absorption line [120].

Other recent achievements from 2020 using ARFs have shown, e.g., sub-ppm carbon oxide detection at 2.3 μm based on laser absorption and an 8-tube ARF [121], 2.2 ppb acetylene sensing using photothermal spectroscopy in an long-period-grating-assisted ARF [122], or using non-silica ARF for the sensing of nitrous oxide at 5.24 μm with a detection limit at 20 ppb per volume [123].

Gas-based lasers, supercontinuum generation and pulse shaping

The possibility of filling HCFs with specific gases has led to major achievements in the research of supercontinuum generation, pulse self-compression, deep-UV and MIR lasers, and Raman frequency combs. Gases allow for vast tunability in both their linear (dispersion) and nonlinear properties simply by varying gas pressure and the gas composition. Once gas is injected into the HCF core, a maximum interaction between the propagating high-intensity light and the gas can be achieved. Furthermore, ARFs, in particular, are good candidates for the MIR region, even when made of silica, as the fundamental mode overlap to the glass cladding is negligible.

The concept of gas lasers using HCFs builds on the the advantages of a high damage threshold, good heat management and very high quantum efficiency [124]. The possibility of having pressurized gas confined in the small HCF core has been very appealing, leading to the HOFGLAS (Hollow-core Optical Fiber Gas LASers) concept. The results from the first decade of experiments from 2002-2012 are well summarized in [111].

Recently, with ARFs becoming more widespread and mature, MIR gas lasers have been presented, mostly pumped with easily accessible C-band pulsed lasers. A step-tunable laser for a range of 3.09-3.2 μm, based on acetylene-filled 6-tube ARF with CW power of 0.77 W, was demonstrated in 2018 [125] surpassing the result from 2017 [33] using a Kagome ARF also filled with acetylene and lasing at 3.1 μm. Recently in 2019 and 2020, two papers presented gas lasers with an emission above 4 μm. First, a 4.6 μm laser using an N_2O-filled Kagome ARF [126] with quantum efficiency of 9% and second, a Raman laser using hydrogen-filled 7-tube ARF delivering 17.6 μJ pulses at 4.2 μm with 74 % quantum efficiency [127]. The results in [127] are state-of-the-art in terms of quantum efficiency and pulse energy for gas lasers based on HCFs above 3 μm.

Using ARFs, deep-UV (200 nm) up to MIR (4000 nm), multi-octave supercontinuum has been demonstrated for a 7-tube ARF filled with argon at 30 bar [128] in 2019 and later expanded to 5000 nm using helium filling [129] and NANF. Supercontinuum generation is closely tied to soliton dynamics and pulse compression, where, e.g., in [130] sub-femtosecond pulses were obtained, comparing the conventional pulse post compression using gratings with the HCF capability of pulse self-compression inside the fiber.

Apart from lasers and nonlinear optics, other applications worth mentioning are, e.g., the use of acetylene-filled PBGF to form an optical frequency standard discussing 4 types of PBGFs [131] where frequency instability of only $4x10^{-12}$ Hz over 10^4 s was achieved.

High-power beam delivery

For high-power beam delivery, HCFs are extremely interesting due to their high damage threshold [37, 132] which rises from the negligible field overlap with the glass material. From particular power levels (depending on a continuous-wave or pulsed regime and on

particular wavelengths) HCFs, or more specifically ARFs, are the only option, as solid-core fibers are limited by their glass material damage threshold. For silica glass the damage threshold is in order of nano-Joules (e.g., in the order of MW for picosecond pulse regime [133]), for PBGFs then in order of micro-Joules [36]. The other factor is fiber nonlinearity, where air has nonlinearity γ of almost two orders lower than silica ($\sim 6 \cdot 10^{-23}$ m^2/W and $\sim 2 \cdot 10^{-22}$ m^2/W, respectively [134]).

Works focused on femtosecond pulses reported self-compressed pulses down to 50 fs [135] and 44 fs [136] at milli-Joule energy levels. Both these works used hypocycloid Kagome ARFs with a 1030 nm ytterbium laser source. Nanosecond pulse transmission of 45 W average power at a wavelength of 1980 nm has been demonstrated recently [137] showing promising capabilities of ARFs for MIR beam delivery.

A study considering ultra-short pulse propagation in ice-cream cone shaped ARF [138] has confirmed an increase in the power threshold by at least 14 MW once the ARF is filled with argon gas and by 26 MW once ARF is evacuated. Similarly, in [135] helium proved to significantly increase power thresholds. Practical applications in laser machining, its limitations and the advantages of HCFs are discussed in [139], showing an existing commercial tool. New possibilities appear in the UV region with ARFs, as presented in [140] showing the delivery of 17 ns pulses at 266 nm with energy of 0.46 μJ.

Microwave photonics

In microwave photonics, SSMFs substitute lossy coaxial cables at frequencies over 10 GHz for longer distances (tens of meters and more) thanks to their low attenuation (0.18 dB/km compared to >1 dB/m for coaxial cables). Nevertheless, the nonlinear behaviour of SSMFs (e.g., stimulated Brillouin scattering, Kerr nonlinearities) limits their use in radio-over-fiber (RoF) systems in terms of maximum optical power that can be transmitted without signal distortions.

HCFs offer low nonlinearity which is vital for analog signal transmission in microwave photonics and can eventually lead to completely passive remote antenna unit design consisting of just a photodiode and antenna. The key enablers are high-power photodiodes, where significant progress has been reported, e.g., in [141] showing -0.4 dBm, 10 dBm and 14.3 dBm at frequencies of 18 GHz, 12 GHz, and 5 GHz, respectively. On the source side, high-power narrow-line-width lasers have been presented [142] together with high-power handling Mach-Zehnder modulators [143], which are typically used for analog signal modulation on the optical carrier.

A significant advantage of HCFs is their environmental (mainly thermal) insensitivity [88], which may be exploited for stability enhancement in radio-over-fiber (RoF) links. Temperature changes result in two effects, the glass refractive index variation and the change of the fibre length. In SSMF the refractive index change has about 20 times larger magnitude than the fiber length change and thus contributes to approximate

95% of the total fiber thermal sensitivity. SSMFs have a thermal coefficient of delay (TCD) ~40 ps/km/K [144]. Therefore, guiding light in an air-core eliminates the majority of thermal effect contribution as PBGF exhibit TCD of ~2 ps/km/K. This low sensitivity to temperature is especially interesting for delay lines used, e.g., in clock distribution or 5G networks. Zero temperature sensitivity has been shown for PBGFs [145] where TCD was measured to be 0.37 ps/km/K at 1609 nm and -0.28 ps/km/K at 1612 nm. Therefore within a narrow band TCD was almost 100 times lower than that of SSMF.

Another application of HCF-based systems in microwave photonics lies in ultra narrow-band filtering of RF signals, e.g., by using gas-filled HCFs with enhanced Brillouin performance which can be used for filtering and signal processing [146].

3.3 Limitations and challenges

For many of the above-mentioned research fields where HCF excels, there are still limitations which need to be addressed. One of the key challenges is the HCF to SSMF interconnection where more diverse techniques are required to fulfill the various demands on the interconnection properties, e.g.:

- HCFs have already demonstrated extremely low attenuation suitable for long-haul **data transmission**, thus a low-loss interconnection of HCF is appealing.
- 5G networks and **microwave photonics** are on the rise and fiber-optic links represent a substantial segment in combined RF-optical networks. Even though conventional SSMFs bring numerous advantages over metallic (coaxial) cables, they are still limited by nonlinearity and they exhibit non-negligible latency and dispersion.
- **Gas cells** are typically built in a laboratory environment where light is coupled via lens-systems, which is complicated and cumbersome. Alternatively, gas cells can be fusion spliced to solid-core fibers resulting in poor performance with **high IL of the interconnection** and **unwanted back reflections**.
- PBGFs for **gas cells** suffer from slow filling times, where ARFs reduce the filling time thanks to larger core diameter. Nevertheless, it would be highly advantageous to have a multi-path HCF-based gas cell to reduce the filling time. Highly-reflective coatings are necessary for such a multi-path cell.
- HOM-caused interference can be viewed from two perspectives. First, it can be used for sensing, mostly strain (as discussed above). Second, it is a source of noise in many applications which is especially critical in high-power delivery, ultra-sensitive interferometry and sensing (such as fiber-optic gyroscopes) and data communication. To eliminate HOM interference (often denoted as multi-path interference) or to selectively excite them, special **coupling methods need to be developed**.

- **HOMs** are a significant source of noise for high-resolution **gas sensing**, **fiber-optic gyroscopes** and high-finesse **Fabry-Pérot fiber interferometers**. Therefore, strictly **fundamental mode excitation** is required.
- **HCF-based FOGs** require a stable, low-loss and especially low-back-reflection interconnection. E.g., state-of-the-art results [89] presented free-space optics coupling with 0.65 dB insertion loss on the coupling. Still the back reflection at the silica-air interface has not been satisfyingly addressed.
- Compact **gas lasers** require a permanent interconnection with a defined reflection/transmission coefficients, which can be achieved via **optical coatings** at the SSMF-HCF interconnection boundary.
- In low-attenuation state-of-the-art NANFs [67, 68], lowest-order HOM (LP_{11}) propagates with attenuation of only a few dB/km, whereas all other HOMs have attenuation in the order of hundreds or even thousands of dB/km. Therefore, to obtain **single-mode guidance**, HOMs must not be excited, which can be achieved by advanced coupling techniques. However, with the newest NANFs [16] HOMs are attenuated significantly, with LP_{11} mode propagating with attenuation of over a 2000 dB/km. In this case coupling into HOMs would result in increased loss of the fiber-optic link.

Based on the above-mentioned points, it is clear that a low-loss interconnection between HCF and SSMF is desired. Apart from being low-loss, the interconnection should be i) permanent and mechanically strong to enable HCF-based component transportation and practical (not only laboratory) applications; ii) it should be hermetically sealed to prevent humidity (atmospheric) degradation of HCF and allow employment in high-pressure gas cells; iii) it should suppress HOMs to reduce system noise and unwanted interference; iv) it should allow deposition of optical coatings to either reduce back reflections (and reduce transmission loss) or to form high-finesse resonator.

All these points lead to the proposal, design and validation of a new type of HCF-SSMF interconnection and open several new research fields which will both be discussed in the following chapters.

CHAPTER 4 Aims of the thesis

Given the above-mentioned state-of-the-art in Chapter 2 and Chapter 3, it is clear that there is a significant interest in application of HCFs. However, to facilitate the transition from laboratory to practical implementation of HCFs a novel interconnection technique with SSMF is highly desired, as summarized in Section 3.3. For that we first have to address several milestones.

1. Required know-how with specialty optical fibers:
    - To propose an approach of a permanent fiber interconnection between soft-glass (having different refractive index) or microstructured optical fibers (different MFD) and SSMFs, where fusion splicing is not preferred because of high temperatures and damage to optical coatings.
    - To examine various sensing approaches such as refractometry and spectroscopy using specialty optical fibers. Study methods of microstructured fiber filling with particular analytes.
    - To prepare simulation models for efficient coupling to microstructured optical fibers with specific parameters such as mode-field distribution, chromatic dispersion, guided modes, etc. and to experimentally verify those parameters.
2. Innovative interconnection of hollow-core fibers to conventional fiber-optic systems:
    - To identify possible means of HCF interconnection, compare to state-of-the-art approaches.
    - To design, develop and verify a novel approach to HCF interconnection capable of low insertion loss, low back reflection and fundamental mode excitation.
    - To evaluate long-term and thermal stability of our HCF interconnection.

3. HCF-based components with application in interferometry and microwave photonics:

    - To evaluate photonic link performance first using SSMFs; to test high-frequency 5G bands, analyze radio-over-fiber (RoF) performance limits in terms of fiber chromatic dispersion, attenuation and nonlinearity.
    - To study possible HCF applications in upcoming 5G networks; to design Fabry-Pérot fiber interferometers acting as microwave photonics filters with high environmental stability.
    - To design and prepare long-length Fabry-Pérot resonators based on novel HCFs, e.g., antiresonant optical fibers while providing a detailed parameter analysis.

CHAPTER 5 Required know-how with specialty optical fibers

The novel work on HCFs covered in this thesis required specific preliminary steps to be carried out. These preliminary steps were focused on solid-core optical fibers and microstructured optical fibers based on non-silica (soft-glass) materials and/or significantly different MFD compared to SSMFs. The developed methods were then advantageously used for the following HCF research.

First, I will focus on chalcogenide optical fibers on which the idea of the fiber-array based interconnection of dissimilar fibers was experimentally verified for the first time. Next, I will discuss our achievements in microstructured optical fiber filling with liquid analytes and results in the field of refractometric detection of liquids. Last, our outcomes of microstructured optical fiber modeling, which provided a basis for later HCF coupling modeling together with experimental PCF characterization, will be overviewed.

5.1 Interfacing chalcogenide fibers to SSMFs

At first, we focused on step-index arsenic-selenide (As_2Se_3, refractive index (RI) $n = 2.8$ at 1550 nm) and arsenic-sulfide fibers (As_2S_3, $n = 2.4$ at 1550 nm). One aim was to exploit the high nonlinearity of As_2Se_3 (nonlinear coefficient of 1300 $W^{-1}km^{-1}$ at 1550 nm) for all-optical signal processing in the 1550 nm band and for supercontinuum generation. We had at our disposal a single-mode As_2Se_3 fiber with core diameter of 6.3 μm, 0.6 dB/m attenuation at 1550 nm and single-mode mode cut-off at approximately 1300 nm. The critical factor was the interconnection of the As_2Se_3 fiber to standard SSMF (SiO_2, $n = 1.45$ at 1550 nm).

First, for nonlinear processes to be effective, one needs to increase the optical power significantly, thus reflections caused by the refractive index mismatch might be detrimental. For the As_2Se_3-SiO_2 interface, the reflection exceeds 10 %, which also means Fresnel losses of almost 0.5 dB at a single interface. Therefore, we came up with the solution of using optical coatings, more specifically anti-reflective coatings, to smoothen the RI difference.

Second, chalcogenide glasses are soft-glasses with melting point around 200 °C and release highly toxic fumes, if heated. Therefore, fusion splicing was not an option, moreover it would prevent the application of optical coatings because of the high temperature during

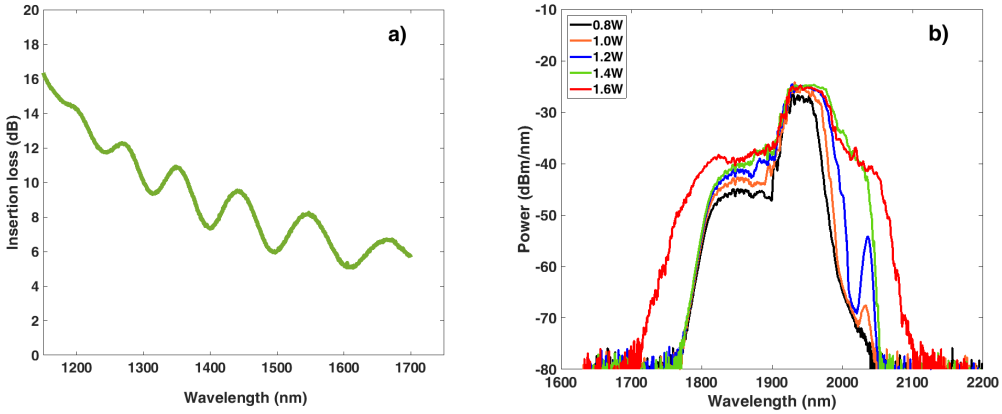

Figure 5.1: Results of interconnected 4.5-m long As_2Se_3 fiber interconnected on both sides to SSMF, a) wavelength dependence of insertion loss [C1], b) supercontinuum generation when pumped with a 2 ps laser at 2000 nm at various average optical power levels.

splicing. We considered the idea of employing a modification of a well-known approach of interconnecting fiber arrays to planar photonic chips, using just two fiber arrays, one featuring the chalcogenide fiber and the other the SSMF. The SSMF fiber-array would have the AR coating deposited on its end-facet. The advantage of the fiber-array approach is that it needs temperatures up to only 100 °C (glue curing temperatures), which optical coatings can withstand.

Third, the As_2Se_3 fiber had a smaller core diameter than SSMF, which led to a MFD mismatch causing additional losses. Therefore, MFA based on a bridge fiber was proposed and spliced on the SSMF. The bridge fiber was a bend-insensitive single mode fiber with 1 μm smaller MFD than SSMF, thus being closer to the As_2Se_3 fiber. The MFA-SSMF component was placed in the fiber-array with the AR coating deposited on the fiber-array end-face.

The final component thus included a designed optical coating for the As_2Se_3-SiO_2 interface which was deposited at the MFA polished end-face and finally assembled using the fiber-array approach [C1]. Results of a 4.5-m long As_2Se_3 fiber interconnected on both sides to SSMF via a short segment of the bridge fiber are presented in Fig. 5.1a. The overall IL at 1600 nm was close to 5 dB, which provided an interconnection IL of less than 1 dB once As_2Se_3 fiber attenuation (<1 dB/m) was excluded. Figure 5.1b shows supercontinuum generation with this interconnected sample when pumped with a 2 ps laser at 2000 nm.

This was a significant step to the state-of-the-art HCF interconnection we later developed as it introduced a new interconnection approach, considered a simple MFD accommodation and included AR coatings. In Fig. 5.1a we can see that the IL spectral profile is not flat, which was due to less than ideal MFD matching and possible HOM excitation, as the interconnection technology was still immature.

5.2 Specialty optical fibers for the detection of liquids

In parallel with the work on single-mode chalcogenide fibers, we also focused on microstructured optical fibers, specifically on silica and lead-silicate suspended-core PCFs (SC-PCFs). Here, the main aim was to design a simple refractometric sensor to measure only changes in detected power and not the spectral profile. The biggest challenges were to efficiently couple light into small 1.4-4.0 μm core diameters of studied SC-PCFs and to obtain the highest possible detection sensitivity in a broad RI range.

To acquire high resolution and sensitivity, it is necessary to maximize propagating field overlap with the measured analyte. In this aspect, we modelled SC-PCFs with small core diameters, high evanescent wave power fraction in the particular analyte and optimal sensing parameters (resolution and sensitivity), which we had subsequently ordered to be drawn.

For the sake of comparison, we also studied tapered SSMFs, which, when tapered to similar diameters as the core diameters of SC-PCFs, should behave similarly (see Fig. 5.2 for an illustrative schematic of the sensor operating principle based on SC-PCF and tapered SSMF). The rationale behind this comparison was that the same sensing performance results in us working with either a low-cost tapered SSMF which is fragile and unprotected, or having to inject the liquid in the SC-PCF where the core is protected by the fiber itself at the cost of the challenging light coupling, fiber cleaving and high fiber price.

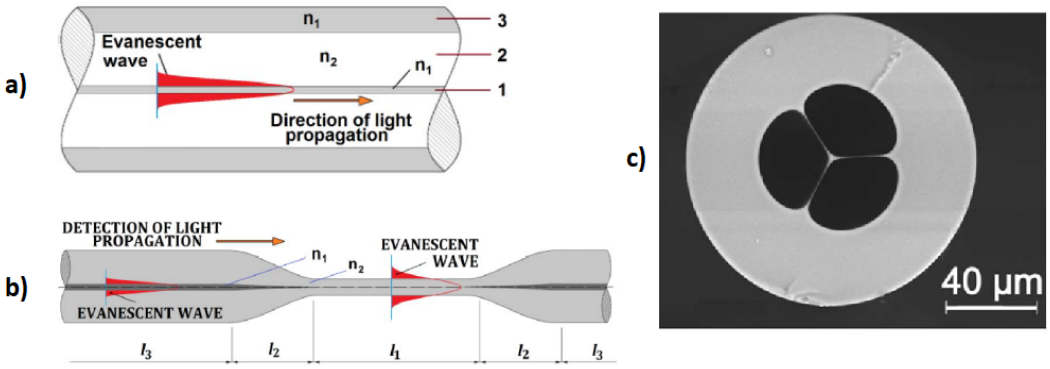

Figure 5.2: Refractometric principle of a) an SC-PCF sensor, 1 = solid pure silica glass core (n_1), 2 = cladding with 3 air-holes (n_2), 3 = pure silica cladding (n_1)„ and b) a tapered SSMF sensor, n_1 is doped silica core, n_2 is pure silica cladding, l_1 is the waist region, l_2 are the transition regions and l_3 is the untapered SSMF, c) an SEM image of one of the tested SC-PCFs with 2.75 µm core diameter [J2],[J4].

Our findings are reported in five journal papers [J1-J5] and showed that SSMF tapers and silica SC-PCFs exhibited similar performance with a resolution in the order of 10^{-4}

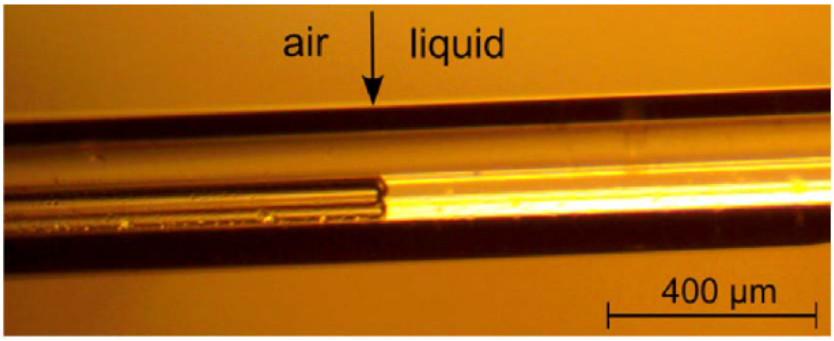

Figure 5.3: Equal filling of 3-hole SC-PCF with a liquid analyte [J2]

RIU for the detection of liquids with RI in the range of 1.318 (RI of water at 1550 nm) to 1.430 (limited by the RI of silica).

Our results achieved in the field of refractometry have generated interesting findings, tremendous experimental know-how and fiber filling expertise (see Fig. 5.3 showing equally-filled SC-PCF holes). Still, new challenges appeared, especially regarding coupling into small core diameters where repeatability and stability has proven to be a critical factor. Using a firmly interconnected fiber with a bigger core would definitely bring enhanced sensing performance.

Furthermore, in cooperation with the team from Saratov State University, we carried out experimental work in the field of MIR evanescent-wave spectroscopy focusing on chalcogenide multimode step-index fibers as chalcogenide fibers are one of the best candidates for MIR transmission thereby opening vast sensing possibilities. In our investigation of light coupling and HOM excitation, we were interested in studying the fundamentals and possible ways of sensitivity enhancement using selective HOM excitation in chalcogenide fibers. These efforts resulted in the study of selective mode sensitivity for the detection of liquids above 2000 nm based on evanescent-wave spectroscopy [J6].

Nevertheless, selective mode excitation proved to be challenging, as the experimental work with chalcogenide fibers required an extremely delicate and cautious approach due to their fragility and toxicity.

Therefore, HCFs were the logical step forward as HCFs can provide almost 100 % mode overlap with the analyte, their mode-field distribution can be well defined, selective HOM excitation is possible, and they guide well into MIR up to approximately 4.5 μm even when made of silica.

5.3 Modeling and characterization of PCFs

As we were working with specialty optical fibers, mainly PCFs, having accurate fiber parameters and close-to-reality models was a must. Both for evanescent-wave estimation or nonlinear response calculation, precise knowledge of the PCF parameters is needed.

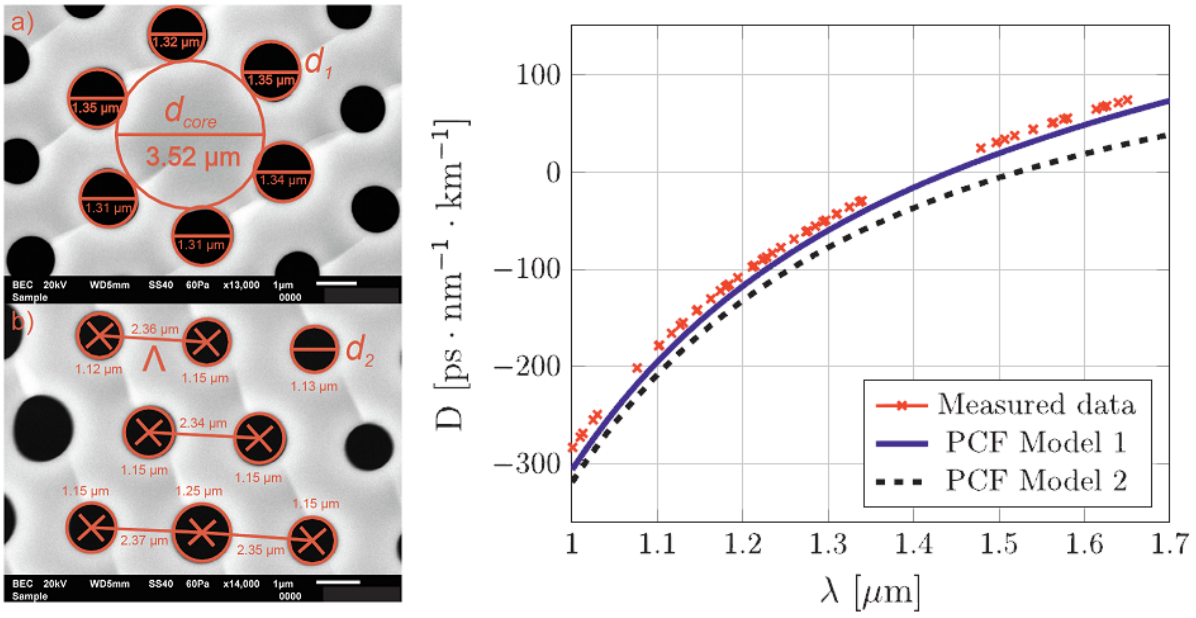

Figure 5.4: Real hexagonal solid-core lead-silicate PCF and its structural parameters, chromatic dispersion curve - measured vs. calculated for an ideal and real (based on an SEM image of the PCF) model [J10].

However, as fibers are drawn, distortions from the ideal design occur and can considerably affect the desired application in various magnitude.

We first modelled solid-core chalcogenide PCFs, with a focus on a hexagonal PCF lattice, where the model incorporated PCF lattice deformation that occurs during the fiber drawing process. These deformations then have impact in practical applications, such as supercontinuum generation [J7]. Afterwards, a flat-chromatic-dispersion PCF for fiber-optic telecommunications was designed [J8].

Parallel studies of SC-PCF modeling for evanescent-wave sensing were carried out resulting in a generalized SC-PCF model for the detection of liquids [J9] as discussed in the previous section. Furthermore, we characterized the chromatic dispersion of lead-silicate PCFs over a broad wavelength range [C2].

As a result of our efforts at precise modeling and fiber characterization, we published an overview of our work in a paper summarizing accurate PCF modeling and relevant characterization techniques [J10]. The paper described the whole process from acquiring an unknown PCF, to PCF model creation and possible experimental techniques to verify the model's accuracy. We have demonstrated how even a slight variation of RI can shift the zero-dispersion wavelength significantly. Figure 5.4 shows the calculated vs. measured chromatic dispersion profile for a hexagonal solid-core lead-silicate PCF.

This work allowed us to acquire the know-how in the field of PCF simulation and characterization and serves now as a basis for HCF interconnection design and HCF characterization, mainly for precise MFD measurement which is critical in determining how to approach the ideal MFD accommodation.

CHAPTER 6 Hollow-core fiber interconnection to conventional fiber-optic systems

So far, the practical implementation of HCFs has been generally limited to laboratory applications where the latest achievements with cabled HCFs [108, 109] pave the way for more widespread use of HCFs. Still, the difficulty in connecting HCFs with existing fiber-optic systems that are mostly based on SSMFs remains as discussed in Section 3.1. This is especially true for 19- and 37-cell PBGFs and state-of-the-art NANFs having core diameters over 30 μm. Additionally, precise MFD matching must be carried out so that HOMs are not excited. Using lenses with precise alignment is not a viable long-term solution due to limited time stability. A solution involving connectors is challenging as well, as the exposed HCF is susceptible to mechanical damage or a humid environment [147]. Therefore, a permanent and hermetic interconnection is required, as with conventional fiber-optic components.

Key requirements of the interconnection, apart from being permanent and hermetic, are:

- Low insertion loss
- Suppressed back reflections on the silica-air interface, i.e., low return loss
- Strict fundamental mode excitation (suppression of HOMs)

6.1 Proposed fiber-array-based HCF interconnection

When we first came up with the idea of an alternative HCF-SSMF interconnection approach, the best interconnection result had not yet been reached by a splice, but by using an HCF connector [148] and a large-mode area (LMA) single-mode fiber acting as a mode-field adapter (afterwards spliced to SSMF) with a benchmark IL of 0.3 dB and RL of -31 dB thanks to a deposited anti-reflective (AR) coating on the LMA fiber.

Prior to HCFs, we used AR coating to accommodate the difference in refractive indices and bridge fibers to accommodate MFD for the interconnection of solid-core chalcogenide fibers to SSMFs. The deposition of AR coating, or generally any optical coating, was

extremely appealing for HCFs. However, fusion splicing prohibits the use of optical coatings due to high temperatures during splicing. Therefore, we have developed a new alternative interconnection technology for HCFs, which was originally envisioned to provide MFD accommodation, low IL and to suppress unwanted back reflections, i.e., low RL.

PBGF interconnection

Based on previous know-how, I have proposed a PBGF-SSMF interconnection method based on a modified fiber-array technology [J11], which solves the issue with back reflections by allowing the deposition of optical coatings. Furthermore, fundamental mode coupling is achieved by using mode-field adapters in the form of commercially-available graded-index multimode (GRIN) fiber-based MFAs.

As a result, in 2019, we published, in collaboration with the Optoelectronics Research Centre, University of Southampton, a low-loss, low-back-reflection reciprocal PBGF-SSMF interconnection [J11]. The interconnection was based on modified fiber-array technology and GRIN MFAs using OM1 type GRIN fibers which provided maximum MFD of around 20 μm once spliced on SSMF (very close to the MFD of our PBGF). This first result showed state-of-the-art IL per a single interconnection of 0.30 dB for fundamental mode coupling and RL of almost -30 dB, which are comparable values to [148], but with a significant advantage of having a permanent and hermetic interconnection, whereas in [148] a connector approach was used which does not protect the HCF end-facet from mechanical damage nor does it protect it from atmospheric effects, dust, etc. Moreover, in [148] an in-house drawn LMA fiber was used, whereas we employed a commercially available multi-mode GRIN fiber acting as the MFA.

The basic principle of the interconnection is depicted in Fig. 6.1 showing the two fiber arrays before gluing. First we use a 1-channel fiber array for the solid-core fiber and mode-field adaptation (Fig. 6.1a)). We fusion splice GRIN fiber to the end of the input SSMF. We cleave the GRIN fiber to a length longer than the target length (calculated in simulation models) and insert the spliced SSMF-GRIN segment into the fiber-array before gluing it in place. Finally, we polish the fiber-array end-face until the desired GRIN length is achieved. This process allows for very precise control of the GRIN fiber length (μm-level), which is essential for low-loss interconnection. Subsequently, we deposit the AR coating on the GRIN end-facet.

HCF cannot be polished in the V-groove in the same way as the solid-core GRIN fiber because of the possible damage to the delicate microstructure and ingression of polishing products. Thus, we modified the FA assembly procedure for HCF, which also takes into account the fact that HCF generally have non-standard outer diameters which can vary from HC-PBGF sample to sample. The fiber array is again a 1-channel type, but includes three V-grooves. The two side V-grooves are used to set the vertical gap between the upper

and lower blocks of the fiber array by using HCF segments made of the same fiber (same diameter) as that to be used in the interconnection. At this stage, we intentionally leave the central V-groove empty. Subsequently, the HCF fiber array is polished and cleaned. After that, we insert a freshly cleaved HCF into the central V-groove and precisely align its end-face with the front edge of the fiber array (see Fig. 6.1b)).

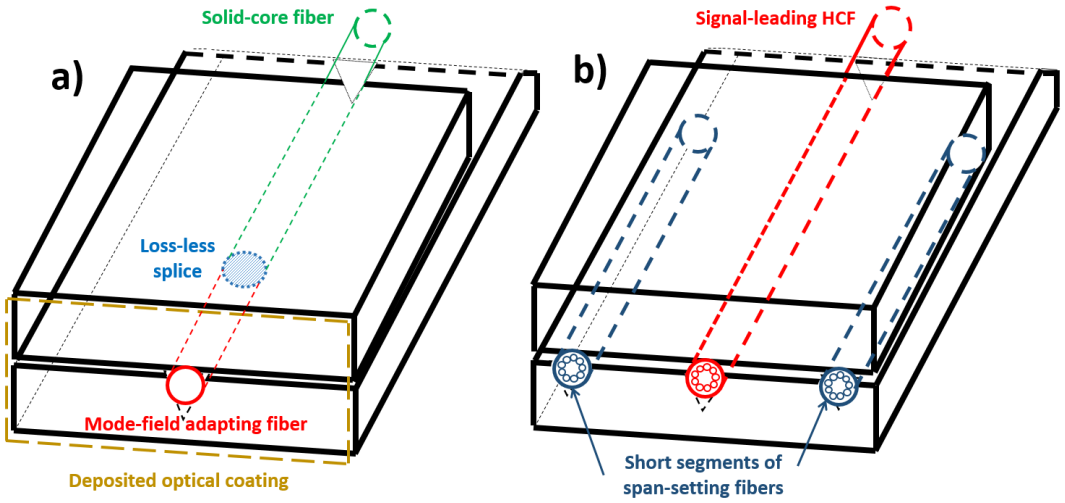

Figure 6.1: Principle of the fiber-array-based interconnection of hollow-core to solid-core fiber, a) solid-core fiber with spliced mode-field adapting fiber segment in a 1-channel fiber-array, b) hollow-core fiber in a 3-channel fiber-array, where the side channels serve for precise gap setting [J11].

Fig. 6.2 then shows both fiber-arrays glued together at temperatures below 80°C (considered a "cold splice" technique). Our interconnection can essentially work for any HCF with any solid-core fiber, while any optical coating can be deposited.

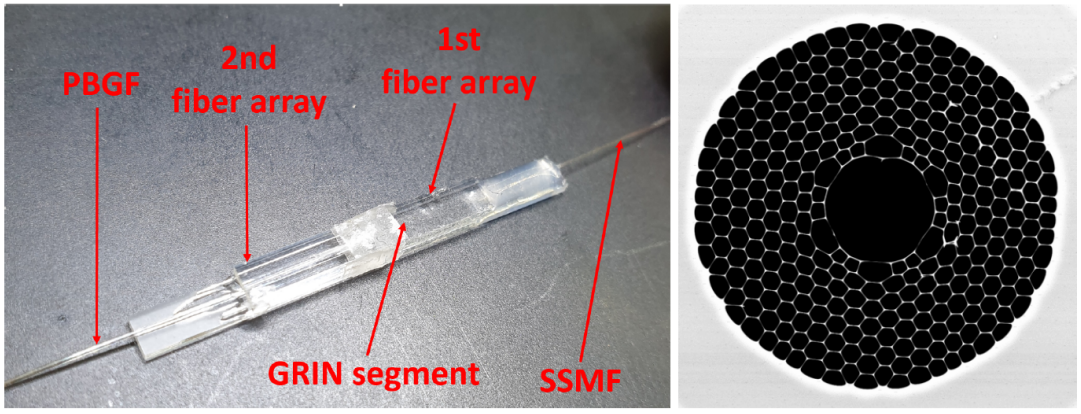

Figure 6.2: a) glued fiber-array interconnection, b) used 19-cell PBGF SEM image [C3].

Furthermore, we were able to suppress HOMs significantly by precise alignment and MFD matching. For monitoring HOM content, we employed a simple, but powerful, method of using the Fourier transform of the measured HOMs and fundamental mode

interference pattern by an optical spectrum analyzer. It was thus possible to calculate the relative amplitude of the propagating HOMs and to know which HOMs propagate in the particular HCF so we can effectively mitigate them by design of the interconnection. This technique is described in detail in [J11]. An example of the interference pattern for a 10-m-long PBGF is shown in Fig. 6.3a). The Fourier transform is shown in Fig. 6.3b) where we can also see greater than 30 dB suppression of all HOMs.

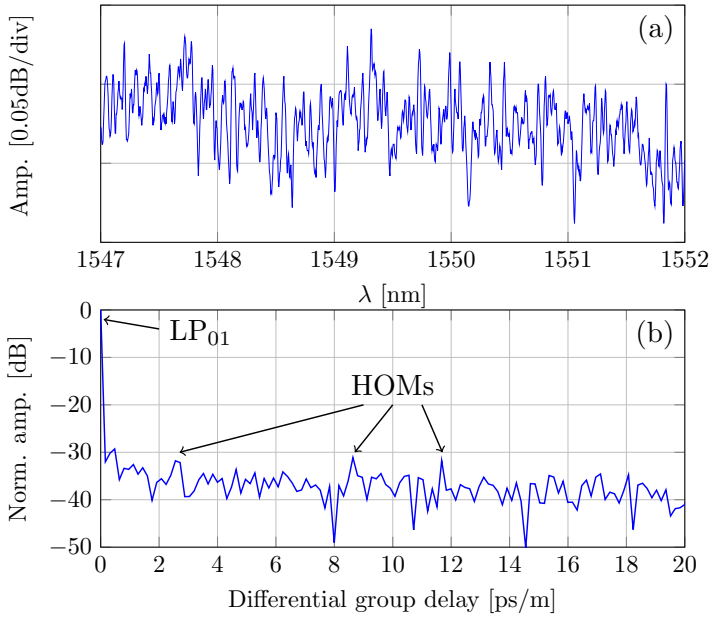

Figure 6.3: Higher-order mode interference pattern in a 10-m-long PBGF. (a) Measured using an optical spectrum analyzer and (b) its Fourier transform [J12].

NANF interconnection

Our first result [J11], showed very low HOM excitation (as shown in Fig. 6.3), which is welcomed in many HCF applications. Nevertheless, PBGFs are inherently multi-modal and HOMs propagate with low attenuation, so, even with high HOM suppression, PBGF still exhibits multi-modal behavior. The next logical step was to move to ARFs, specifically NANFs, which have currently surpassed PBGFs in most aspects. Working with state-of-the-art NANFs provided by the University of Southampton and using our interconnection approach, we modified graded-index MFAs for NANFs and preliminary results showed IL below 0.5 dB with RL of -35 dB using an improved AR coating in 2019 [C4].

Thanks to the fact that the NANF has 6 tubes it has much closer mode-field distribution to a Gaussian distribution than the previously used PBGF which is critical for our low-loss coupling of SSMF to NANF and vice versa. An image of an experimental NANF overlapped with its mode-field distribution can be seen in Fig. 6.4.

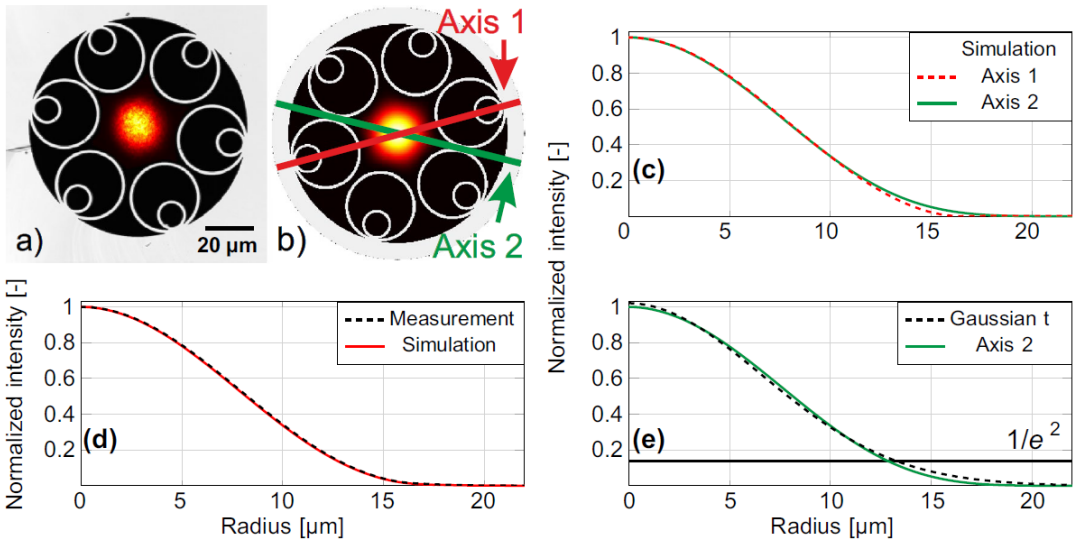

Figure 6.4: (a) Measured mode field distribution at the output of NANF overlaid with the captured image of the NANF core area. (b) Simulated fundamental mode field distribution overlaid with the NANF microstructure acquired by SEM. (c) Mode field profiles from (b) along the two principal axes shown in (b). (d) Averaged axis 1- and 2-mode field profiles from measurement and simulation. (e) Mode field profile from (c) and its Gaussian fit [J13].

Just recently we published a record-low-loss interconnection of SSMF-NANF with only 0.15 dB and RL below -40 dB [J13]. The fundamental coupling limit was calculated to be 0.08 dB, therefore we are just 0.07 dB from the minimum theoretical IL value as shown in Fig. 6.5. The cross-coupling to HOMs was almost negligible with -35 dB cross-coupling into the LP_{11} mode. The key in getting close to the fundamental limits was that we achieved almost perfect mode-field overlap and strictly fundamental mode excitation. This was enabled by calculating the proper GRIN length using our in-house developed models, by precise polishing of the MFA to the desired lengths, by having high-quality AR coatings and by precise alignment and optimized final gluing procedure. We used an OM2 GRIN fiber type instead of OM1, as OM2 based MFA provided slightly larger MFD which was closer to the MFD of NANF ($\sim 24\,\mu$m).

Further progress in achieving lower IL is limited by the mode-field shape and is thus defined mostly by the specific HCF. Better mitigation of HOMs is not necessary for the majority of applications, as commonly cross-coupling below -25 dB into HOMs is considered as single-mode regime.

Lower RL is possible by using better AR coatings or by angled-coupling, as we recently demonstrated with RL better than -60 dB while keeping the IL below 1 dB for the whole SSMF-NANF-SSMF system [C5]. We used an angled MFA polished to the desired length, i.e., MFD. We tested MFAs polished at angles ranging from 0 to 10°. Results for the boundary angles of 0° and 10° and 10 are presented in Fig. 6.6. We can see that the 10° angled MFA suppresses the back-reflections over a broad wavelength range.

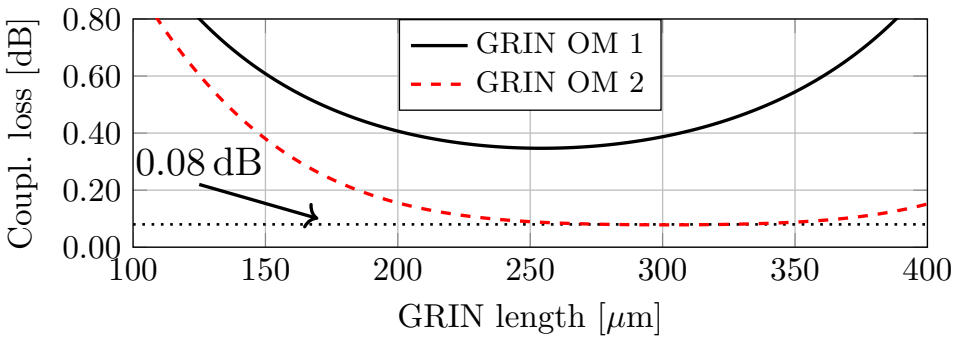

Figure 6.5: Coupling loss between NANF fundamental mode and output of GRIN mode field adapter. Black dotted line show the theoretical minimum loss, red dashed line shows minimum coupling loss of NANF with a GRIN fiber type OM2 based MFA and black line shows minimum coupling loss of NANF with a GRIN fiber type OM1 based MFA [J13].

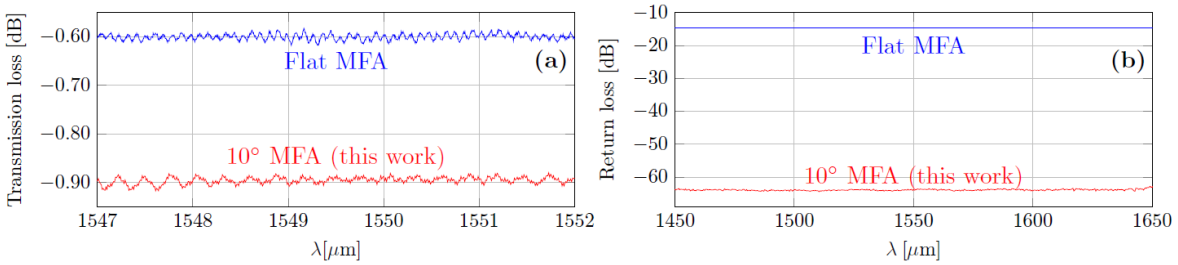

Figure 6.6: Results of a flat and 10° angled MFA interconnection between SSMF and a 6-tube NANF, a) measured HOM interference pattern, b) return loss [C5].

6.2 Long-term stability of the interconnection

Considering the practical application of our interconnections, long-term stability must be ensured, especially with regard to temperature variations and humidity effects. At first, we focused on the thermal behaviour of our interconnection (bearing in mind to test humidity effects in the very near future) and prepared 3 samples of PBGF-SSMF interconnections where the choice of PBGF vs. NANF does not matter in the case of stability tests. One sample had a flat MFA and two samples featured angled MFAs. All samples had the interconnection on one side only and the other side was aligned outside of the climatic chamber to eliminate any discrepancies.

Prior to the temperature cycles, we measured IL of three interconnected HCF samples over a period of 100 days at room temperature, observing a variation in IL of less than 0.02 dB. Then we placed them in the climatic chamber and heated them to +85°C over four cycles. Maximum insertion loss variation of 0.10 dB was observed for HCF samples with angled MFA interconnections and only 0.02 dB for a HCF sample with a flat MFA interconnection (see Fig. 6.7).

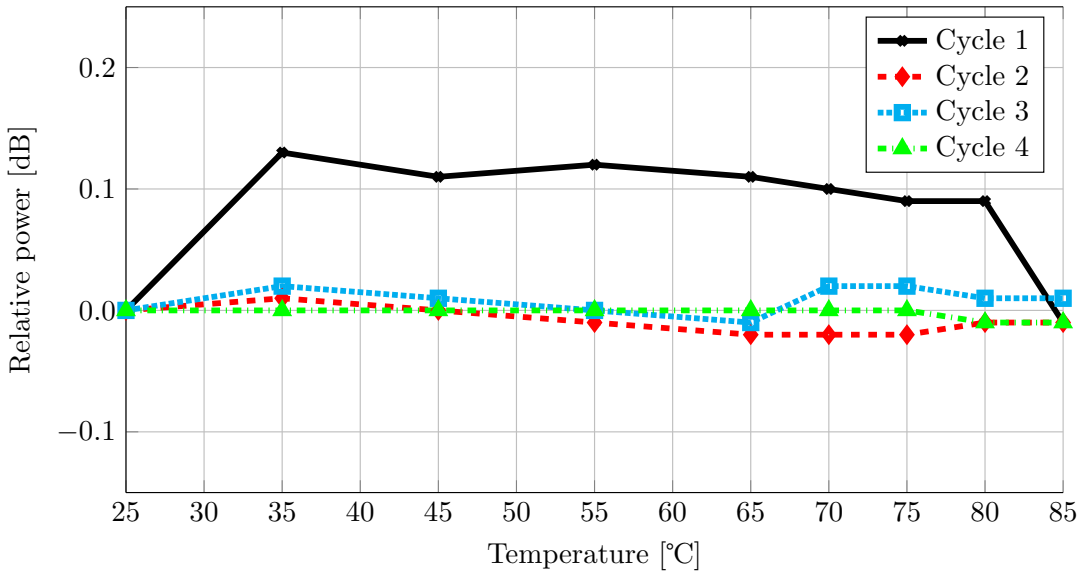

Figure 6.7: Relative power dependence on temperature of Sample 1 (18m PBGF) - with flat mode-field adapters, positive values represent IL improvement (gain) [C3].

It can be observed that the interconnection relaxes during the first cycle and then remains stable. As angled MFAs did fluctuate more (given the larger amount of glue at the interconnection), more research is demanded to reliable and low-loss performance.

CHAPTER 7 HCF-based applications

Our innovative interconnection technology incorporates the advantages of low loss, low back reflections and fundamental mode excitation that are essential for many applications including interferometry, microwave photonics and sensing.

In this chapter I will overview those research fields where we have already been using our interconnection approach, whereas in the following chapters I will provide a future outlook and possible application fields.

7.1 Fiber Fabry-Perot interferometers

Our focus has been on HCF-based FFPIs which can advantageously use the possibility of optical coating deposition thanks to our interconnection technique. In contrast to previous results, to form a HCF-based Fabry-Perot resonator we apply highly-reflective (HR) coatings on a pair of MFAs. The MFAs are then aligned with the HCF, for maximum FFPI finesse, and glued afterwards. Our FFPIs thus have SSMF pigtails for easy integration into conventional fiber-optic systems.

In our first experiment, we used 13-layer Ta_2O_5/SiO_2 dielectric coating optimized for the C-band (1530-1565 nm) and achieved reflectivity $> 98\,\%$. We prepared two long-length FFPIs [J14] with lengths of 5 m and 23 m. Over the entire C-band finesse values ranged from 140 to 160 for the 5-m-long NANF-FFPI and from 120 to 138 for the 23-m-long NANF-FFPI. The lower finesse of the 23-m-long NANF-FFPI was likely caused by NANF attenuation. Measured RF spectra of both FFPIs are given in Fig. 7.1. At 1550 nm the free-spectral range (FSR) was 28.1 MHz for the 5m-long NANF-FFPI and 6.5 MHz for the 23m-long NANF-FFPI, respectively.

Birefringence is present in NANFs as the fabricated NANF structure is not perfectly symmetric and because of fiber bending/coiling. Therefore, transmission peaks occur at two different positions within one FSR period when varying the polarization state of the launched light, e.g., using a polarization controller. The transmitted spectra for the two polarization eigenstates of our NANF-FFPIs are depicted in Fig. 7.2. The polarization peak spectral splitting was 15.1 MHz and 2.42 MHz for the 5-m-long NANF-FFPI and 23-m-long NANF-FFPI, respectively. The polarization dependence of HCF-based FFPIs is one thing to consider for future investigations, as polarization-sensitive drifts might be limiting in some applications.

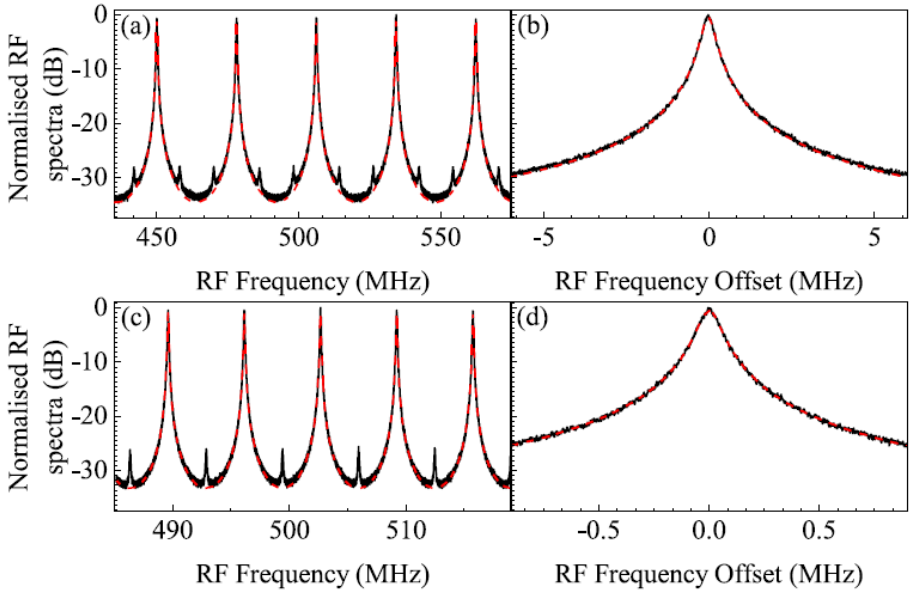

Figure 7.1: Measured results for 5-m-long NANF-FFPI (a, b) and 23-m-long NANF-FFPI (c, d). Normalized RF power spectra around 500 MHz (a,c) and their details around one peak (b, d). Solid black: measured, red dashed: fitted [J14].

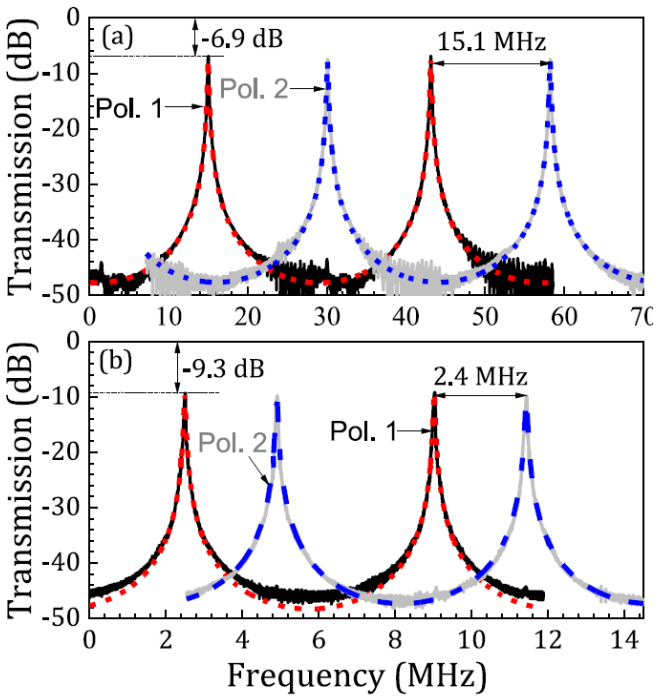

Figure 7.2: (Measured optical transmission spectra along the two principal axes of birefringence (Pol. 1, black and Pol. 2, grey solid) of (a) 5-m-long and (b) 23-m-long NANF-FFPI. The insertion loss and polarization-induced spectral splitting are also shown. The red and blue dashed lines are data fitted by the transmission function of the FFPI [J14].

To conclude, we achieved a FFPI transmission peak width as narrow as 47 kHz meaning an equivalent time delay of 3.2 km. This is only a factor of three broader in FWHM than state-of-the-art bulk Fabry-Perot cavities that are typically 10-cm-long and have a finesse in excess of 10^5. If we thus improve our FFPI finesse by having better HR coatings (higher reflectivity) or more precise angle alignment, we can soon match the results achieved within bulk cavities.

7.2 Gas filling and sensing

The application in gas sensing and related fields is currently being studied by our team and builds upon both our know-how with HCF interconnection and our close cooperation with the University of Southampton where gas filling and sensing experiments will be conducted, similar to the results presented in [149, 150] where, especially in [149], our permanent and hermetic interconnection can bring practical benefits.

First, we focus on gas filling time dependence on fiber length, coupling configuration and gas cell designs. We expect shorter filling times compared to PBGFs thanks to the larger NANF core area. Gas-cell formation is possible by adding gas inlets in the interconnection. The gas cell lengths are expected to be from tens of cm up to 20 m, where gas filling under pressure is expected. For some applications, the above-mentioned FFPI configuration can also be used to create a high-finesse HCF resonator which will allow us to shorten the cavity length by the finesse factor, thus reducing filling time significantly.

The HCF resonator can be advantageously used to significantly increase the interaction length with any analyte present in the HCF. The increase in interaction length depends on HCF attenuation and coating reflectivity. We aim to enhance to the previously achieved reflectivity rate of 98 % to at least 99 %.

In a gas sensing configuration for strong interactions a single-pass gas cell is assumed. In this case the goal is significantly reduced back reflections. The key limiting factor here are back reflections at the SSMF/NANF boundary which forms a parasitic cavity and builds up in energy, thus causing measurement uncertainty. We can use our angled-coupling approach [C5], with RL below -60 dB and IL below 0.5 dB. Angled coupling, in contrast to anti-reflective coatings, has an additional advantage over our previous results, namely the significantly broader bandwidth of low back reflections.

7.3 Microwave photonics

With the onset of 5th generation networks, high-speed data connectivity and the Internet of Things, optical fibers have begun to play an even more important role. Apart from being the data medium in backbone networks, they also represent key advantages for radio-frequency (RF) transmissions in frequency bands over 10 GHz where conventional coaxial cables exhibit extreme attenuation values (e.g., ~3 dB/m above 6 GHz). SSMFs have a typical attenuation of 0.20 dB/km when in the form of a cable. This level of attenuation is absolutely satisfactory for the majority of microwave photonics/radio-over-fiber (RoF) networks as they require mostly tens to hundreds of meters of fiber length.

A limiting factor, however, lies in the chromatic dispersion of SSMFs, which causes dips in the transmission spectrum in dependence on fiber length. We have analyzed the frequency dependence of the signal transmission with regard to the chromatic dispersion of SSMFs in [J15] for the double-sideband (DSB) and carrier-suppressed double-sideband (CS DSB) modulation schemes within RoF systems. Fig. 7.3 shows the results where the chromatic dispersion is not affecting the transmission at all for the CS DSB modulation scheme. On the other hand, the DSB microwave photonics link experiences a significant chromatic dispersion induced power fading. This fading can be compensated by, e.g., using a filter [151] to introduce an optical single-sideband transmission, or by simultaneous intensity and phase modulation [152], but at the cost of increased complexity in the system. Contrary to SSMFs, HCFs would allow significantly more relaxed limits for the modulation techniques as their chromatic dispersion is mostly around 2-3 ps/nm·km in the C-band.

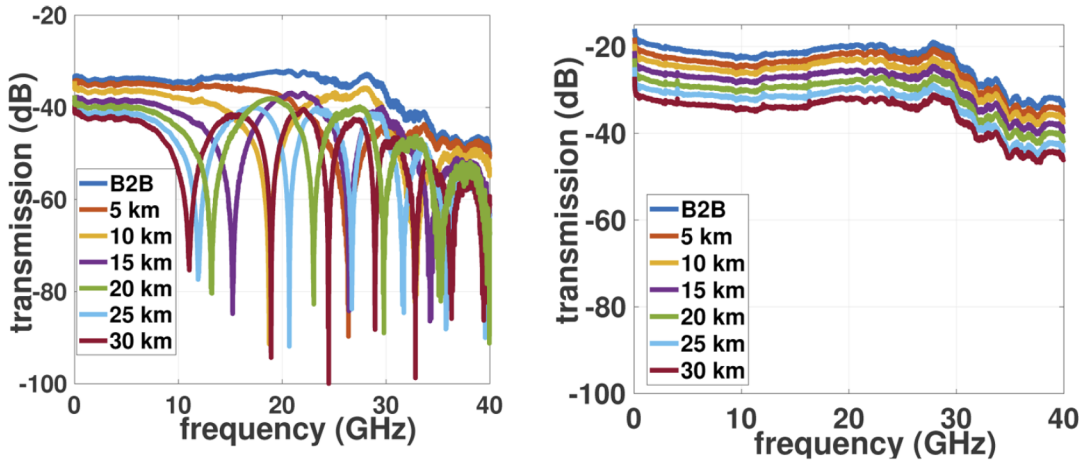

Figure 7.3: RF signal transmission response for different SSMF lengths in DSB (left) and CS DSB (right) modulation schemes [J15].

Furthermore, the nonlinearity of SSMFs can be a limiting factor [104], especially when a high-power optical carrier is used. HCF can provide nonlinearity-free transmission for such high-power RoF systems as light is propagating in the air.

In recent years, we have tested multiple 5G network scenarios for various RF frequency ranges from 3.5 GHz up to 27 and 39 GHz with the scale of the bandwidth up to 400 MHz [J15-J21] where the above-mentioned potential of HCFs can be well exploited. Using HCFs in RoF systems, we can introduce several major advantages over solid-core fibers, such as:

- negligible nonlinearity and a high damage threshold allowing for high-optical powers to be transferred, which are required for completely passive remote radio units
- low chromatic dispersion, thus reducing transmission frequency dips and enabling more modulation techniques to be employed
- thermally insensitive fiber delay lines for signal processing
- possibility of forming ultra narrow-band filters based on Fabry-Perot resonators

In terms of these above-mentioned advantages, we have already developed full RoF and radio over free space optics systems setups where their performance was charaterised and will continue to be tested with HCFs in the following years.

The ability to define controllable time delays is essential for signal processing in microwave photonics. For long time delays or, in the case of tunable delays, optical fibers are often advantageously used. However, time delay stability is vital, especially considering the temperature variations along the fiber-optic link which can be several kilometers long. One of the sample cases for delay line application can be beam-steered antennas based on phase-shifting where a stable phase difference is required. In this field an experimental test of antenna beam steering at 6 and 26 GHz using the properties of fiber chromatic dispersion of SSMFs [J23] was conducted. These results serve as a building block for HCF application in similar scenarios. Furthermore, in [J22] an overview of fiber-optic delay line approaches, their thermal dependencies and overall performance comparison has been provided.

Regarding ultra narrow-band filters, we have recently published two papers, one solely on FFPIs based on NANFs [J14] and the second paper on the use of NANF-FFPI as an RF filter [J22] where we evaluated its temperature stability in detail.

In [J14], we have shown 14.5 times lower thermal sensitivity for an FFPI-based RF filter when made of HCF compared to an SSMF-based FFPI of identical optical length. For the temperature stability evaluation we placed the 5-m-long NANF-FFPI together with a 3.6-m-long SSMF-based FFPI into the same thermal chamber. The results demonstrating temperature stability are presented in Fig. 7.4.

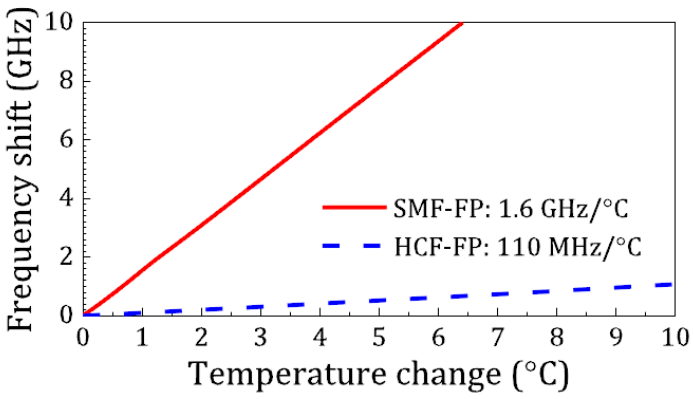

Figure 7.4: Frequency shift of a selected transmission peak in the 5-m-long NANF-FFPI and of the 3.6-m-long SSMF-based FFPI (of equivalent optical length) as the temperature is increased [J14].

From Fig. 7.4 the advantage of HCF, in this case NANF-based FFPI, is clear and its temperature stability can provide a significant advantage for applications not only in microwave photonics. Furthermore, this work introduced the first demonstration of temperature-insensitivity for ARFs.

We further characterized our 5-m-long NANF-FFPI microwave photonics filter [J14], Fig. 7.5 shows filter characteristics at 10, 20 and 40 GHz. The 3 dB bandwidth was 183 kHz.

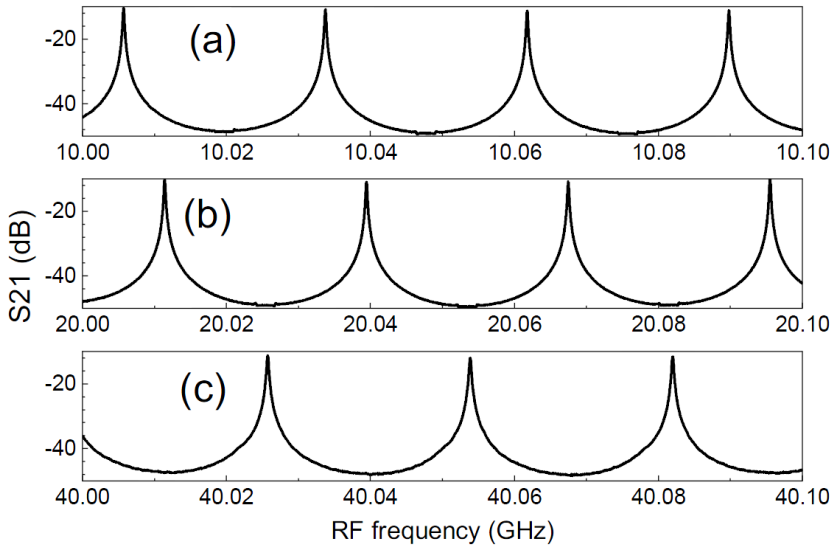

Figure 7.5: Amplitude transfer characteristics of the 5-m-long NANF-FFPI filter at 10 GHz (a), 20 GHz (b), and 40 GHz (c) over spans of 100 MHz [J22].

Temperature sensitivity was then examined using the same three frequencies with a 1 K step and compared to an SSMF-based filter of the same optical length (3.6-m-long), see results in Fig. 7.6. For the SSMF-based filter, the transmission characteristics shift at a rate of 334 kHz/K while for the NANF-based filter the rate is only 21 kHz/K, i.e., a value almost 16 times lower than expected based on [88] and matching the results presented in [J14].

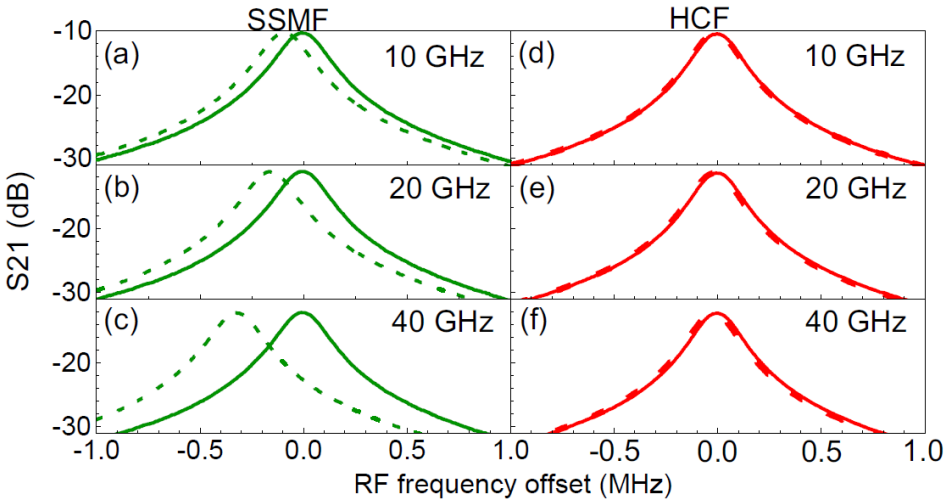

Figure 7.6: Transmission characteristics measured at 25 °C (solid) and 26 °C (dashed) for an SMF-based filter (a-c, red) and an HCF-based filter (d-f, green) measured at 10 GHz (a, d), 20 GHz (b, e), and 40 GHz (c,f) [J22].

CHAPTER 8 Conclusions

In my habilitation thesis I first reviewed the history of hollow-core optical fibers, from the first trials in the second half of the 20th century, the breakthrough invention of photonic crystal fibers, through to the 21st century and very recent achievements showing the possibility of hollow-core fibers to outperform SSMFs in the very near future. Then I discussed the most promising cutting-edge research and application fields of hollow-core fibers.

Based on the state-of-the-art, I outlined the main limitations and challenges for future hollow-core fiber applications in fiber-optic systems and, as a solution, I proposed a new interconnection method of hollow-core fibers to standard solid-core fibers. The pillars of this new interconnection method are built on the expertise and experimental know-how obtained from my work with chalcogenide and suspended-core fibers, as well as photonic crystal fiber modeling.

The proposed interconnection method uses the fiber-array approach based on gluing, rather than fusion splicing, and includes precise mode-field matching. Our interconnection technique allows optical coatings to be used either to eliminate Fresnel losses and back reflections, or to create strong mirrors which can then form HCF-based resonators. Secondly, insertion loss is reduced close to fundamental levels thanks to mode-field adaptation using multi-mode graded-index fibers of a defined length. Finally, higher-order mode excitation is suppressed significantly leading to effectively single-mode operation and reduction in noise caused by multi-path interference.

The main interconnection result represents a record-low insertion loss of only 0.15 dB per interconnection from SSMF to a state-of-the-art 6-tube NANF, with minimal back reflections and negligible cross-coupling to higher-order modes. Afterwards, we have further evolved our interconnection using angled mode-field adapters making the interconnection Fresnel-loss free with return loss below -60 dB while keeping losses below 0.5 dB per interconnection.

Furthermore, we have formed high-finesse fiber Fabry-Perot resonators and demonstrated their excellent thermal stability and, subsequently, provided possible microwave photonics and gas sensing applications.

CHAPTER 9 Future outlook

Innovative results in numerous research fields are expected based on our broad experience with HCFs, their efficient coupling with low loss, low back reflection and strictly fundamental mode excitation. The possibility of optical coatings means not only mitigation of back reflections, but also having excellent performance in resonators, once high-reflectivity coatings are deposited. Additional features of optical coatings, such as wavelength-selective filters, are envisioned.

A deep know-how of the interconnection design allows us to tailor the gap between the MFA and HCF where we can add gas inlets while keeping the ultra-low insertion loss and fundamental mode excitation. Gas lasers or gas sensing are thus possible. By further developing the coupling design, we can work on optical components, such as Faraday rotators embedded directly on HCFs.

To name a few fields of future interest:

- Increasing optical power places higher requirements on the optical coatings, the heat transfer from the interconnection and high HOM suppression. High-power optical coatings must still be investigated, e.g., including nanostructured coating designs.
- The proposed interconnection has recently demonstrated record-low insertion loss for NANF and may serve well in future high-speed optical communication networks. Long-term temperature stability has been already examined, but more environmental tests must be carried out.
- Forming gas cells with a low-loss permanent interconnection with the capability of either gas sealing in the HCF or with gas inlets to enable gas flow in the HCF.
- High-power signal transfer for microwave photonics/radio-over-fiber system exploiting both HCF low nonlinearity and a flat chromatic dispersion profile.
- High-performance interferometers based on HCFs, such as fiber-optic gyroscopes, might thrive using our interconnection technology.

To conclude, the list is long with many interesting research fields to delve into.

CHAPTER 10 Author's Publications

List of author's publications relevant to the habilitation thesis

All authors contributed equally.

Papers in the peer-reviewed journals:

[J1] M. Komanec, T. Martan, T. Nemecek, S. Zvanovec, "Multimode fiber tapers for reproducible refractometric liquid detection," *Optical Engineering*, 54(4), 2015.

[J2] T. Nemecek, M. Komanec, T. Martan, R. Ahmad, S. Zvanovec, "Suspended-core microstructured fiber for refractometric detection of liquids," *Applied Optics*, 54(30), 8899-8903, 2015.

[J3] A.-N. Castro Martinez, M. Komanec, T. Nemecek, S. Zvanovec, S. Khotiaintsev, "Fiber optic refractometric sensors using a semi-ellipsoidal sensing element," *Applied Optics*, 55(10), 2574-2579, 2016.

[J4] T. Martan , T. Nemecek, M. Komanec, R. Ahmad, S. Zvanovec, "Refractometric detection of liquids using tapered optical fiber and suspended core microstructured fiber: a comparison of methods," *Applied Optics*, 56(9), 2388-2396, 2017.

[J5] M. Komanec, T. Nemecek. P.-M. Vidner, T. Martan, F. Lahodny, S. Zvanovec, "Structurally-modified tapered optical fiber sensors for long-term detection of liquids," *Optical Fiber Technology*, 47, 187-191, 2019.

[J6] E. A. Romanova, S. Korsakova, M. Komanec, T. Nemecek, A. Velmuzhov, M. Sukhanov, V. S. Shiryaev, "Multimode Chalcogenide Fibers for Evanescent Wave Sensing in the Mid-IR," *IEEE Journal of Selected Topics in Quantum Electronics*, 23(2), 289-295, 2017.

[J7] R. Ahmad and M. Komanec and S. Zvanovec, "Circular Lattice Photonic Crystal Fiber for Mid-IR Supercontinuum Generation," *IEEE Photonics Technology Letters*, 28(23), 2736-2739, 2016.

[J8] R. Ahmad, M. Komanec, D. Suslov, S. Zvanovec, “Modified Octagonal Photonic Crystal Fiber for Residual Dispersion Compensation over Telecommunication Band,“ *Radioengineering*, 27(1), 2018.

[J9] T. Nemecek, M. Komanec, B. Nelsen, T. Martan, D. Suslov, P. Hartmann, S. Zvanovec, “Experimentally and analytically derived generalized model for the detection of liquids with suspended-core optical fibers,“ *Optical Fiber Technology*, 45, 295-299, 2018.

[J10] D. Suslov, M. Komanec, T. Němeček, J. Bohata, S. Zvánovec, “Exact modeling of photonic crystal fibers for determination of fundamental properties“ *Optical Fiber Technology*, 56, 102177, 2020.

[J11] M. Komanec, D. Suslov, S. Zvánovec, Y. Chen, T. Bradley, S.R. Sandoghchi, E.R. Numkam Fokoua, G.T. Jasion, M.N. Petrovich, F. Poletti, D.J. Richardson, R. Slavík, “Low-Loss and Low-Back-Reflection Hollow-Core to Standard Fiber Interconnection,“ *IEEE Photonics Technology Letters*, 31(10), 723-726, 2019.

[J12] M. Komanec, D. Dousek, D. Suslov, S. Zvánovec, “Hollow-Core Optical Fibers,“ *Radioengineering*, 29(3), 417-430, 2020.

[J13] D. Suslov, M. Komanec, E. R. Numkam Fokoua, D. Dousek, A. Zhong, S. Zvánovec, T. Bradley, F. Poletti, D. J. Richardson, R. Slavík, “Low loss, high-performance interconnection between standard single-mode fiber and antiresonant hollow-core fiber,“ *Scientific Reports*, 11, 8799, 2021.

[J14] M. Ding, M. Komanec, D. Suslov, D. Dousek, S. Zvánovec, E.-R. Numkam Fokoua, T. Bradley, F. Poletti, D.-J. Richardson, R. Slavík, “Long-Length and Thermally Stable High-Finesse Fabry-Perot Interferometers Made of Hollow Core Optical Fiber,“ *Journal of Lightwave Technology*, 38(8), 2423-2427, 2020.

[J15] J. Bohata, D. N. Nguyen, J. Spáčil, M. Komanec, B. Ortega, L. Vallejo, Z. Ghassemlooy, and S. Zvánovec, “Experimental comparison of DSB and CS-DSB mmW formats over a hybrid fiber and FSO fronthaul network for 5G,“ *Opt. Express* 29, 27768-27782, 2021.

[J16] J. Bohata, M. Komanec, J. Spáčil, Z. Ghassemlooy, S. Zvánovec, R. Slavík, “24-26 GHz radio-over-fiber and free-space optics for fifth-generation systems,“ *Optics Letters*, 43(5), 1035-1038, 2018.

[J17] J. Bohata, M. Komanec, J. Spacil, R. Slavik, S. Zvanovec, “Transmitters for Combined Radio Over a Fiber and Outdoor Millimeter-Wave System at 25 GHz,“ *IEEE Photonics Journal*, 12(3), 1-14, 2020.

[J18] D. N. Nguyen, J. Bohata, J. Spacil, M. Komanec, N. Stevens, Z. Ghassemlooy, P.-T. Dat, S. Zvanovec, “Polarization Division Multiplexing-Based Hybrid Microwave Photonic Links for Simultaneous mmW and Sub-6 GHz Wireless Transmissions,“ *IEEE Photonics Journal*, 12(6), 1-14, 2020.

[J19] D. N. Nguyen, J. Bohata, M. Komanec, S. Zvanovec, B. Ortega, Z. Ghassemlooy, "Seamless 25 GHz Transmission of LTE 4/16/64-QAM Signals Over Hybrid SMF/FSO and Wireless Link," *Journal of Lightwave Technology*, 37(24), 6040-6047, 2019.

[J20] D. N. Nguyen, J. Bohata, J. Spacil, D. Dousek, M. Komanec, S. Zvanovec, Z. Ghassemlooy, B. Ortega, "M-QAM transmission over hybrid microwave photonic links at the K-band," *Optics Express*, 27(23), 33745-33756, 2019.

[J21] L. Vallejo, M. Komanec, B. Ortega, J. Bohata, D.-N. Nguyen, S. Zvanovec, V. Almenar, "Impact of Thermal-Induced Turbulent Distribution Along FSO Link on Transmission of Photonically Generated mmW Signals in the Frequency Range 26–40 GHz," *IEEE Photonics Journal*, 12(1), 1-9, 2020.

[J22] M. Ding, Z. Feng, D. Marpaung, X. Zhang, M. Komanec, D. Suslov, D. Dousek, S. Zvánovec, E.-R. Numkam Fokoua, T. Bradley, F. Poletti, D.-J. Richardson, R. Slavík, "Optical Fiber Delay Lines in Microwave Photonics: Sensitivity to Temperature and Means to Reduce it," *Journal of Lightwave Technology*, 39, 2311-2318, 2021.

[J23] J. Bohata, M. Komanec, J. Spáčil, P. Hazdra, T. Lonský, Z. Hradecký, and S. Zvánovec, "Experimental demonstration of a microwave photonic link using an optically phased antenna array for a millimeter wave band," *Applied Optics*, 60(4), 1013-1020, 2021.

Papers presented in international proceedings:

[C1] M. Komanec, T. Nemecek, D. Suslov, R. Ahmad, T. Martan, "Optical switching based on arsenic-selenide and lead-silicate fibers," *10th International Symposium on Communication Systems, Networks and Digital Signal Processing (CSNDSP)*, 2016.

[C2] T. Nemecek, M. Komanec, D. Suslov, P. Peterka, D. Pysz, R. Buczynski, B. Nelsen, S. Zvanovec, "Development and characterization of highly-nonlinear multicomponent glass photonic crystal fibers for mid-infrared applications", *SPIE, Micro-structured and Specialty Optical Fibres V*, 10232, 1-8, 2017.

[C3] D. Dousek, M. Komanec, A. Zhong, D. Suslov, S. Zvánovec, P. Veselý, Y. Chen; T.-D. Bradley, E.-R. Numkam Fokoua, F. Poletti, D.-J. Richardson, R. Slavík, "Long-term stability of hollow core to standard optical fiber interconnection", *SPIE, Micro-structured and Specialty Optical Fibres VII*, 117731B, 1-6, 2021.

[C4] D. Suslov, M. Komanec, S. Zvánovec, T. Bradley, F. Poletti, D.J. Richardson, R. Slavík, "Highly-efficient and low return-loss coupling of standard and antiresonant hollow-core fibers," *Proceedings of Frontiers in Optics*, The Optical Society, 2019. p. 1-2. ISBN 978-1-943580-67-5.

[C5] D. Suslov, D. Dousek, S. Zvánovec, E. R. Numkam Fokoua, F. Poletti, D.J. Richardson, M. Komanec, R. Slavík, "Angled interconnection between standard single-mode fiber and nested nodeless antiresonant fibers", *CLEO*, OSA, STu1Q.5, 2021.

References

[1] J. Sanghera and I. Aggarwal, "Active and passive chalcogenide glass optical fibers for IR applications: a review," *Journal of Non-Crystalline Solids*, vol. 256-257, pp. 6–16, 1999.

[2] P. Lucas, G. J. Coleman, S. Jiang, T. Luo, and Z. Yang, "Chalcogenide glass fibers: Optical window tailoring and suitability for bio-chemical sensing," *Optical Materials*, vol. 47, pp. 530–536, 2015.

[3] D. Tran, G. Sigel, and B. Bendow, "Heavy metal fluoride glasses and fibers: A review," *Journal of Lightwave Technology*, vol. 2, no. 5, pp. 566–586, 1984.

[4] S. Jackson, "Towards high-power mid-infrared emission from a fibre laser," *Nature Photonics*, vol. 6, pp. 423–431, 07 2012.

[5] L. Cohen, C. Lin, and W. French, "Tailoring zero chromatic dispersion into the 1.5–1.6μm low-loss spectral region of single-mode fibres," *Electronics Letters*, vol. 15, pp. 334–335(1), 1979.

[6] L. Grüner-Nielsen, M. Wandel, P. Kristensen, C. Jorgensen, L. V. Jorgensen, B. Edvold, B. Pálsdóttir, and D. Jakobsen, "Dispersion-compensating fibers," *J. Lightwave Technol.*, vol. 23, no. 11, p. 3566, Nov 2005.

[7] D. Boivin, L.-A. de Montmorillon, L. Provost, N. Montaigne, F. Gooijer, E. Aldea, J. Jensma, and P. Sillard, "Recent developments in bend-insensitive and ultra-bend-insensitive fibers," in *Optical Components and Materials VII*, vol. 7598. SPIE, 2010, pp. 139 – 150.

[8] R. Mears, L. Reekie, I. M. Jauncey, and D. Payne, "Low-noise erbium-doped fibre amplifier operating at 1.54μm," *Electronics Letters*, vol. 23, pp. 1026–1028, 1987.

[9] J. C. Knight, T. A. Birks, P. S. J. Russell, and D. M. Atkin, "All-silica single-mode optical fiber with photonic crystal cladding," *Opt. Lett.*, vol. 21, no. 19, pp. 1547–1549, Oct 1996.

[10] T. Birks, D. Mogilevtsev, J. Knight, and P. St. J. Russell, "Dispersion compensation using single-material fibers," *IEEE Photonics Technology Letters*, vol. 11, no. 6, pp. 674–676, 1999.

[11] D. Mogilevtsev, T. A. Birks, and P. S. J. Russell, "Group-velocity dispersion in photonic crystal fibers," *Opt. Lett.*, vol. 23, no. 21, pp. 1662–1664, Nov 1998.

[12] T. A. Birks, J. C. Knight, and P. S. J. Russell, "Endlessly single-mode photonic crystal fiber," *Optics Letters*, vol. 22, no. 13, pp. 961–963, Jul 1997.

[13] Y. Wu, M. Meneghetti, J. Troles, and J.-L. Adam, "Chalcogenide microstructured optical fibers for mid-infrared supercontinuum generation: Interest, fabrication, and applications," *Applied Sciences*, vol. 8, p. 1637, 09 2018.

[14] M. Kuschnerov, B. J. Mangan, K. Gong, V. A. J. M. Sleiffer, M. Herrmann, J. W. Nicholson, J. M. Fini, L. Meng, R. S. Windeler, E. M. Monberg, A. DeSantolo, K. Mukasa, V. Mikhailov, U. Feiste, W. Zhang, and R. Yu, "Transmission of commercial low latency interfaces over hollow-core fiber," *Journal of Lightwave Technology*, vol. 34, no. 2, pp. 314–320, Jan 2016.

[15] P. Roberts, F. Couny, T. Birks, J. Knight, P. St Russell, B. Mangan, H. Sabert, D. Williams, and L. Farr, "Achieving low loss and low nonlinearity in hollow core photonic crystal fibers," in *Lasers and Electro-Optics*, 2005, pp. 1240–1242 Vol. 2.

[16] H. Sakr, T. D. Bradley, G. T. Jasion, E. N. Fokoua, S. R. Sandoghchi, I. A. Davidson, A. Taranta, G. Guerra, W. Shere, Y. Chen, J. R. Hayes, D. J. Richardson, and F. Poletti, "Hollow Core NANFs with Five Nested Tubes and Record Low Loss at 850, 1060, 1300 and 1625nm," in *2021 Optical Fiber Communications Conference and Exhibition (OFC)*, 2021, pp. 1–3.

[17] J. J. Thomson, *Notes on Recent Researches in Electricity and Magnetism: Intended as a Sequel to Professor Clerk-Maxwell's Treatise on Electricity and Magnetism*. The Clarendon press, 1893.

[18] Lord Rayleigh F.R.S., "XVIII. On the passage of electric waves through tubes, or the vibrations of dielectric cylinders," *The London, Edinburgh, and Dublin Philosophical Magazine and Journal of Science*, vol. 43, no. 261, pp. 125–132, 1897.

[19] E. A. J. Marcatili and R. A. Schmeltzer, "Hollow metallic and dielectric waveguides for long distance optical transmission and lasers," *The Bell System Technical Journal*, vol. 43, no. 4, pp. 1783–1809, 1964.

[20] T. Hidaka, T. Morikawa, and J. Shimada, "Hollow-core oxide-glass cladding optical fibers for middle-infrared region," *Journal of Applied Physics*, vol. 52, p. 4467, 1981.

[21] N. Nagano, M. Saito, M. Miyagi, N. Baba, and N. Sawanobori, "TiO2-SiO2 based glasses for infrared hollow waveguides," *Appl. Opt.*, vol. 30, no. 9, pp. 1074–1079, 1991.

[22] Y. Saito, T. Kanaya, A. Nomura, and T. Kano, "Experimental trial of a hollow-core waveguide used as an absorption cell for concentration measurement of NH3 gas with a CO2 laser," *Optics Letters*, vol. 18, no. 24, pp. 2150–2152, 1993.

[23] J. S. Sirkis, D. D. Brennan, M. A. Putman, T. A. Berkoff, A. D. Kersey, and E. J. Friebele, "In-line fiber étalon for strain measurement," *Opt. Lett.*, vol. 18, no. 22, pp. 1973–1975, Nov 1993.

[24] M. J. Renn, D. Montgomery, O. Vdovin, D. Z. Anderson, C. E. Wieman, and E. A. Cornell, "Laser-guided atoms in hollow-core optical fibers," *Phys. Rev. Lett.*, vol. 75, pp. 3253–3256, Oct 1995.

[25] B. Temelkuran, S. D. Hart, G. Benoit, J. D. Joannopoulos, and Y. Fink, "Wavelength-scalable hollow optical fibres with large photonic bandgaps for CO2 laser transmission," *Nature*, vol. 420, pp. 650–653, 2002.

[26] G. Vienne, Y. Xu, C. Jakobsen, H.-J. Deyerl, J. B. Jensen, T. Sørensen, T. P. Hansen, Y. Huang, M. Terrel, R. K. Lee, N. A. Mortensen, J. Broeng, H. Simonsen, A. Bjarklev, and A. Yariv, "Ultra-large bandwidth hollow-core guiding in all-silica Bragg fibers with nano-supports," *Opt. Express*, vol. 12, no. 15, pp. 3500–3508, Jul 2004.

[27] E. Yablonovitch, "Inhibited spontaneous emission in solid-state physics and electronics," *Phys. Rev. Lett.*, vol. 58, pp. 2059–2062, May 1987.

[28] S. John, "Strong localization of photons in certain disordered dielectric superlattices," *Phys. Rev. Lett.*, vol. 58, pp. 2486–2489, Jun 1987.

[29] F. Poli, A. Cucinotta, and S. Selleri, *Photonic Crystal Fibers: Properties and Applications*. Springer, 2007.

[30] J. K. Ranka, R. S. Windeler, and A. J. Stentz, "Visible continuum generation in air–silica microstructure optical fibers with anomalous dispersion at 800 nm," *Opt. Lett.*, vol. 25, no. 1, pp. 25–27, Jan 2000.

[31] R. Cregan, B. Mangan, J. Knight, T. Birks, P. Russell, P. Roberts, and D. Allan, "Single-mode photonic band gap guidance of light in air," *Science*, vol. 285, no. 5433, pp. 1537–1539, 9 1999.

[32] R. Pennetta, S. Xie, F. Lenahan, M. Mridha, D. Novoa, and P. S. J. Russell, "Fresnel-Reflection-Free Self-Aligning Nanospike Interface between a Step-Index Fiber and a Hollow-Core Photonic-Crystal-Fiber Gas Cell," *Physical Review Applied*, vol. 8, no. 1, p. 014014, Jul 2017.

[33] N. Dadashzadeh, M. P. Thirugnanasambandam, H. W. K. Weerasinghe, B. Debord, M. Chafer, F. Gerome, F. Benabid, B. R. Washburn, and K. L. Corwin, "Near diffraction-limited performance of an OPA pumped acetylene-filled hollow-core fiber laser in the mid-IR," *Opt. Express*, vol. 25, no. 12, pp. 13 351–13 358, Jun 2017.

[34] M. A. Terrel, M. J. F. Digonnet, and S. Fan, "Resonant fiber optic gyroscope using an air-core fiber," *J. Lightwave Technol.*, vol. 30, no. 7, pp. 931–937, Apr 2012.

[35] F. Poletti, N. Wheeler, M. Petrovich, N. Baddela, E. Numkam Fokoua, J. Hayes, D. Gray, Z. Li, R. Slavík, and D. Richardson, "Towards high-capacity fibre-optic communications at the speed of light in vacuum," *Nature Photonics*, vol. 7, no. 4, pp. 279–284, 2013.

[36] X. Peng, M. Mielke, and T. Booth, "High average power, high energy 1.55 μm ultra-short pulse laser beam delivery using large mode area hollow core photonic band-gap fiber," *Opt. Express*, vol. 19, no. 2, pp. 923–932, Jan 2011.

[37] J. Shephard, F. Couny, P. Russell, J. Jones, J. Knight, and D. Hand, "Improved hollow-core photonic crystal fiber design for delivery of nanosecond pulses in laser micromachining applications," *Applied Optics*, vol. 44, no. 21, pp. 4582–4588, 2005.

[38] S. E. Barkou, J. Broeng, and A. Bjarklev, "Silica–air photonic crystal fiber design that permits waveguiding by a true photonic bandgap effect," *Opt. Lett.*, vol. 24, no. 1, pp. 46–48, Jan 1999.

[39] A. Maradudin and A. McGurn, "Out of plane propagation of electromagnetic waves in a two-dimensional periodic dielectric medium," *Journal of Modern Optics*, vol. 41, no. 2, pp. 275–284, 1994.

[40] J. Broeng, S. E. Barkou, T. Søndergaard, and A. Bjarklev, "Analysis of air-guiding photonic bandgap fibers," *Opt. Lett.*, vol. 25, no. 2, pp. 96–98, Jan 2000.

[41] N. A. Mortensen and M. D. Nielsen, "Modeling of realistic cladding structures for air-core photonic bandgap fibers," *Opt. Lett.*, vol. 29, no. 4, pp. 349–351, Feb 2004.

[42] J. Jin, *The Finite Element Method in Electromagnetics, 2nd ed.* Wiley, 2002.

[43] K. Zamani Aghaie, S. Fan, and M. J. F. Digonnet, "Birefringence Analysis of Photonic-Bandgap Fibers Using the Hexagonal Yee's Cell," *IEEE Journal of Quantum Electronics*, vol. 46, no. 6, pp. 920–930, 2010.

[44] N. Venkataraman, M. T. Gallagher, C. M. Smith, D. Muller, J. A. West, K. W. Koch, and J. C. Fajardo, "Low Loss (13 dB/km) Air Core Photonic Band-Gap Fibre," in *2002 28TH European Conference on Optical Communication*, vol. 5, 2002, pp. 1–2.

[45] B. J. Mangan, L. Farr, A. Langford, P. J. Roberts, D. P. Williams, F. Couny, M. Lawman, M. Mason, S. Coupland, R. Flea, H. Sabert, T. A. Birks, J. C. Knight, and P. S. J. Russell, "Low loss (1.7 dB/km) hollow core photonic bandgap fiber," in *Optical Fiber Communication Conference*. Optical Society of America, 2004, p. PD24.

[46] P. J. Roberts, F. Couny, H. Sabert, B. J. Mangan, D. P. Williams, L. Farr, M. W. Mason, A. Tomlinson, T. A. Birks, J. C. Knight, and P. S. Russell, "Ultimate low loss of hollow-core photonic crystal fibres," *Opt. Express*, vol. 13, no. 1, pp. 236–244, Jan 2005.

[47] D. V. Skryabin, "Coupled core-surface solitons in photonic crystal fibers," *Opt. Express*, vol. 12, no. 20, pp. 4841–4846, Oct 2004.

[48] F. Poletti, M. N. Petrovich, and D. J. Richardson, "Hollow-core photonic bandgap fibers: technology and applications," *Nanophotonics*, vol. 2, no. 5-6, pp. 315 – 340, 2013.

[49] Y. Jung, V. A. J. M. Sleiffer, N. Baddela, M. N. Petrovich, J. R. Hayes, N. V. Wheeler, D. R. Gray, E. Numkam Fokoua, J. P. Wooler, N. H. . Wong, F. Parmigiani, S. U. Alam, J. Surof, M. Kuschnerov, V. Veljanovski, H. de Waardt, F. Poletti, and D. J. Richardson, "First demonstration of a broadband 37-cell hollow core photonic bandgap fiber and its application to high capacity mode division multiplexing," in *2013 Optical Fiber Communication Conference and Exposition and the National Fiber Optic Engineers Conference (OFC/NFOEC)*, 2013, pp. 1–3.

[50] J. M. Fini, J. W. Nicholson, R. S. Windeler, E. M. Monberg, L. Meng, B. Mangan, A. DeSantolo, and F. V. DiMarcello, "Low-loss hollow-core fibers with improved single-modedness," *Opt. Express*, vol. 21, no. 5, pp. 6233–6242, Mar 2013.

[51] OFC. AccuCore HCF. [Online]. Available: http://www2.ofsoptics.com/accucore-hcf

[52] F. Benabid, J. C. Knight, G. Antonopoulos, and P. S. J. Russell, "Stimulated raman scattering in hydrogen-filled hollow-core photonic crystal fiber," *Science*, vol. 298, no. 5592, pp. 399–402, 2002.

[53] G. J. Pearce, G. S. Wiederhecker, C. G. Poulton, S. Burger, and P. S. J. Russell, "Models for guidance in kagome-structured hollow-core photonic crystal fibres," *Opt. Express*, vol. 15, no. 20, pp. 12 680–12 685, Oct 2007.

[54] M. A. Duguay, Y. Kokubun, and T. L. Koch, "Antiresonant reflecting optical waveguides in SiO2-Si multilayer structures," *Applied Physics Letters*, vol. 49, no. 13, 1986.

[55] N. M. Litchinitser, A. K. Abeeluck, C. Headley, and B. J. Eggleton, "Antiresonant reflecting photonic crystal optical waveguides," *Opt. Lett.*, vol. 27, no. 18, pp. 1592–1594, Sep 2002.

[56] G. Renversez, P. Boyer, and A. Sagrini, "Antiresonant reflecting optical waveguide microstructured fibers revisited: a new analysis based on leaky mode coupling," *Opt. Express*, vol. 14, no. 12, pp. 5682–5687, Jun 2006.

[57] C. Wei, R. J. Weiblen, C. R. Menyuk, and J. Hu, "Negative curvature fibers," *Adv. Opt. Photon.*, vol. 9, no. 3, pp. 504–561, Sep 2017.

[58] P. Choudhury and T. Yoshino, "A rigorous analysis of the power distribution in plastic clad annular core optical fibers," *Optik*, vol. 113, no. 11, pp. 481 – 488, 2002.

[59] Y. Y. Wang, F. Couny, P. J. Roberts, and F. Benabid, "Low loss broadband transmission in optimized core-shape Kagome Hollow-Core PCF," in *Conference on Lasers and Electro-Optics 2010*. Optical Society of America, 2010, p. CPDB4.

[60] N. Wheeler, T. Bradley, J. Hayes, M. Gouveia, Y. Chen, S. Sandoghchi, F. Poletti, M. Petrovich, and D. Richardson, "Low loss kagome fiber in the 1 μm wavelength region," in *Advanced Photonics 2016 (IPR, NOMA, Sensors, Networks, SPPCom, SOF)*. Optical Society of America, 2016, p. SoM3F.2.

[61] S. Février, B. Beaudou, and P. Viale, "Understanding origin of loss in large pitch hollow-core photonic crystal fibers and their design simplification," *Opt. Express*, vol. 18, no. 5, pp. 5142–5150, Mar 2010.

[62] F. Yu, W. J. Wadsworth, and J. C. Knight, "Low loss silica hollow core fibers for 3–4 μm spectral region," *Opt. Express*, vol. 20, no. 10, pp. 11 153–11 158, May 2012.

[63] A. D. Pryamikov, A. S. Biriukov, A. F. Kosolapov, V. G. Plotnichenko, S. L. Semjonov, and E. M. Dianov, "Demonstration of a waveguide regime for a silica hollow - core microstructured optical fiber with a negative curvature of the core boundary in the spectral region > 3.5 μm," *Opt. Express*, vol. 19, no. 2, pp. 1441–1448, Jan 2011.

[64] B. Debord, A. Amsanpally, M. Chafer, A. Baz, M. Maurel, J. M. Blondy, E. Hugonnot, F. Scol, L. Vincetti, F. Gérôme, and F. Benabid, "Ultralow transmission loss in inhibited-coupling guiding hollow fibers," *Optica*, vol. 4, no. 2, pp. 209–217, Feb 2017.

[65] F. Poletti, "Nested antiresonant nodeless hollow core fiber," *Opt. Express*, vol. 22, no. 20, pp. 23 807–23 828, Oct 2014.

[66] T. D. Bradley, J. R. Hayes, Y. Chen, G. T. Jasion, S. R. Sandoghchi, R. Slavík, E. N. Fokoua, S. Bawn, H. Sakr, I. A. Davidson, A. Taranta, J. P. Thomas, M. N. Petrovich, D. J. Richardson, and F. Poletti, "Record Low-Loss 1.3dB/km Data Transmitting Antiresonant Hollow Core Fibre," in *2018 European Conference on Optical Communication (ECOC)*, 2018, pp. 1–3.

[67] T. D. Bradley, G. T. Jasion, J. R. Hayes, Y. Chen, L. Hooper, H. Sakr, M. Alonso, A. Taranta, A. Saljoghei, H. C. Mulvad, M. Fake, I. A. K. Davidson, N. V. Wheeler, E. N. Fokoua, W. Wang, S. R. Sandoghchi, D. J. Richardson, and F. Poletti, "Antiresonant hollow core fibre with 0.65 dB/km attenuation across the C and L telecommunication bands," in *45th European Conference on Optical Communication (ECOC 2019)*, 2019, pp. 1–4.

[68] G. T. Jasion, T. D. Bradley, K. Harrington, H. Sakr, Y. Chen, E. N. Fokoua, I. A. Davidson, A. Taranta, J. R. Hayes, D. J. Richardson, and F. Poletti, "Hollow Core NANF with 0.28 dB/km Attenuation in the C and L Bands," in *Optical Fiber Communication Conference Postdeadline Papers 2020*. Optical Society of America, 2020, p. Th4B.4.

[69] Y. Tamura, H. Sakuma, K. Morita, M. Suzuki, Y. Yamamoto, K. Shimada, Y. Honma, K. Sohma, T. Fujii, and T. Hasegawa, "The First 0.14-dB/km Loss Optical Fiber and its Impact on Submarine Transmission," *Journal of Lightwave Technology*, vol. 36, no. 1, pp. 44–49, 2018.

[70] G. T. Jasion, T. Bradley, H. Sakr, J. R. Hayes, Y. Chen, A. Taranta, H. C. Mulvad, I. A. Davidson, N. V. Wheeler, E. N. Fokoua, W. Wang, D. J. Richardson, and F. Poletti, "Recent breakthroughs in hollow core fiber technology," in *Next-Generation Optical Communication: Components, Sub-Systems, and Systems IX*, G. Li and X. Zhou, Eds., vol. 11309, International Society for Optics and Photonics. SPIE, 2020, pp. 1 – 8.

[71] H. Sakr, Y. Chen, G. Jasion, T. Bradley, J. Hayes, H. C. Mulvad, I. Davidson, E. Numkam Fokoua, and F. Poletti, "Hollow core optical fibres with comparable attenuation to silica fibres

between 600 and 1100 nm," *Nature Communications*, vol. 11, 11 2020.

[72] S.-F. Gao, Y.-Y. Wang, W. Ding, D.-L. Jiang, S. Gu, X. Zhang, and P. Wang, "Hollow-core conjoined-tube negative-curvature fibre with ultralow loss," *Nature Communications*, vol. 9, p. 2828, 2018.

[73] A. Taranta, E. N. Fokoua, S. A. Mousavi, J. R. Hayes, T. D. Bradley, G. T. Jasion, and F. Poletti, "Exceptional polarization purity in antiresonant hollow-core optical fibresr," *Nature Photonics*, vol. 14, pp. 504–510, 2020.

[74] F. Chenard, O. Alvarez, and A. Buff, "Novel hollow-core chalcogenide fiber with anti-resonant arches for high-power infrared laser transmission," in *Components and Packaging for Laser Systems VI*, A. L. Glebov and P. O. Leisher, Eds., vol. 11261, International Society for Optics and Photonics. SPIE, 2020, pp. 129 – 138.

[75] A. Ventura, J. G. Hayashi, J. Cimek, G. Jasion, P. Janicek, F. B. Slimen, N. White, Q. Fu, L. Xu, H. Sakr, N. V. Wheeler, D. J. Richardson, and F. Poletti, "Extruded tellurite antiresonant hollow core fiber for Mid-IR operation," *Opt. Express*, vol. 28, no. 11, pp. 16 542–16 553, May 2020.

[76] W. Belardi and P. J. Sazio, "Borosilicate based hollow-core optical fibers," *Fibers*, vol. 7, no. 8, 2019.

[77] L. Xiao, W. Jin, M. S. Demokan, H. L. Ho, Y. L. Hoo, and C. Zhao, "Fabrication of selective injection microstructured optical fibers with a conventional fusion splicer," *Opt. Express*, vol. 13, no. 22, pp. 9014–9022, Oct 2005.

[78] F. Benabid, F. Couny, J. C. Knight, T. A. Birks, and P. S. J. Russell, "Compact, stable and efficient all-fibre gas cells using hollow-core photonic crystal fibres," *Nature*, vol. 434, pp. 488–491, 2005.

[79] R. Thapa, K. Knabe, K. L. Corwin, and B. R. Washburn, "Arc fusion splicing of hollow-core photonic bandgap fibers for gas-filled fiber cells," *Opt. Express*, vol. 14, no. 21, pp. 9576–9583, 2006.

[80] F. Couny, F. Benabid, and P. S. Light, "Reduction of Fresnel Back-Reflection at Splice Interface Between Hollow Core PCF and Single-Mode Fiber," *IEEE Photonics Technology Letters*, vol. 19, no. 13, pp. 1020–1022, 2007.

[81] G. A. Miller and G. A. Cranch, "Reduction of intensity noise in hollow core optical fiber using angle-cleaved splices," *IEEE Photonics Technology Letters*, vol. 28, no. 4, pp. 414–417, 2016.

[82] C. Wu, J. Song, Z. Zhang, and N. Song, "High strength fusion splicing of hollow-core photonic bandgap fiber and single-mode fiber," in *Photonics and Fiber Technology 2016 (ACOFT, BGPP, NP)*. Optical Society of America, 2016, p. AW4C.7.

[83] S. Gao, Y. Wang, C. Tian, and P. Wang, "Splice Loss Optimization of a Photonic Bandgap Fiber via a High V-Number Fiber," *IEEE Photonics Technology Letters*, vol. 26, no. 21, pp. 2134–2137, 2014.

[84] Y. Jung, H. Kim, Y. Chen, T. D. Bradley, I. A. Davidson, J. R. Hayes, G. Jasion, H. Sakr, S. Rikimi, F. Poletti, and D. J. Richardson, "Compact micro-optic based components for hollow core fibers," *Opt. Express*, vol. 28, no. 2, pp. 1518–1525, Jan 2020.

[85] W. Huang, Y. Cui, X. Li, Z. Zhou, Z. Li, M. Wang, X. Xi, Z. Chen, and Z. Wang, "Low-loss coupling from single-mode solid-core fibers to anti-resonant hollow-core fibers by fiber

tapering technique," *Opt. Express*, vol. 27, no. 26, pp. 37 111–37 121, Dec 2019.

[86] R. Zeltner, S. Xie, R. Pennetta, and P. S. Russell, "Broadband optomechanically stabilized coupling to liquid-filled hollow-core fiber using silica nanospike," in *Optics in the Life Sciences Congress*. Optical Society of America, 2017, p. OtW4D.2.

[87] C. Wang, R. Yu, B. Debord, F. Gérôme, F. Benabid, K. S. Chiang, and L. Xiao, "Ultralow-loss fusion splicing between negative curvature hollow-core fibers and conventional SMFs with a reverse-tapering method," *Opt. Express*, vol. 29, no. 14, pp. 22 470–22 478, Jul 2021.

[88] R. Slavík, G. Marra, E. N. Fokoua, N. Baddela, N. V. Wheeler, M. Petrovich, F. Poletti, and D. J. Richardson, "Ultralow thermal sensitivity of phase and propagation delay in hollow core optical fibres," *Scientific Reports*, vol. 5, p. 15447, 2015.

[89] G. A. Sanders, A. A. Taranta, C. Narayanan, E. N. Fokoua, S. A. Mousavi, L. K. Strandjord, M. Smiciklas, T. D. Bradley, J. Hayes, G. T. Jasion, T. Qiu, W. Williams, F. Poletti, and D. N. Payne, "Hollow-core resonator fiber optic gyroscope using nodeless anti-resonant fiber," *Opt. Lett.*, vol. 46, no. 1, pp. 46–49, Jan 2021.

[90] V. Michaud-Belleau, E. Numkam Fokoua, T. Bradley, J. Hayes, Y. Chen, F. Poletti, D. Richardson, J. Genest, and R. Slavik, "Backscattering in antiresonant hollow-core fibers: over 40 dB lower than in standard optical fibers," *Optica*, vol. 8, 01 2021.

[91] A. Ravaille, G. Feugnet, I. Fsaifes, A. Baz, B. Debord, F. Gérôme, G. Humbert, F. Benabid, and F. Bretenaker, "In-situ measurement of backscattering in hollow-core fiber based resonant cavities," *IEEE Photonics Journal*, vol. 9, no. 4, pp. 1–7, 2017.

[92] K. Nazeri, F. Ahmed, V. Ahsani, H.-E. Joe, C. Bradley, E. Toyserkani, and M. Jun, "Hollow-core photonic crystal fiber mach–zehnder interferometer for gas sensing," *Sensors*, vol. 20, p. 2807, 05 2020.

[93] Y. Zheng, P. P. Shum, S. Liu, B. Li, J.-L. Auguste, G. Humbert, and Y. Luo, "Strain sensitivity enhancement based on periodic deformation in hollow core fiber," *Opt. Lett.*, vol. 45, no. 14, pp. 3997–4000, Jul 2020.

[94] D. Liu, W. Li, Q. Wu, H. Zhao, F. Ling, K. Tian, C. Shen, F. Wei, W. Han, G. Farrell, Y. Semenova, and P. Wang, "Negative curvature hollow core fiber based all-fiber interferometer and its sensing applications to temperature and strain," *Sensors*, vol. 20, no. 17, 2020.

[95] X. Huang, J. Zang, and S. Yoo, "Multiple hollow-core anti-resonant fiber as a supermodal fiber interferometer," *Scientific Reports*, vol. 9, p. 9342, 2019.

[96] W. Zhu, E. R. Numkam Fokoua, A. A. Taranta, Y. Chen, T. Bradley, M. N. Petrovich, F. Poletti, M. Zhao, D. J. Richardson, and R. Slavík, "The thermal phase sensitivity of both coated and uncoated standard and hollow core fibers down to cryogenic temperatures," *Journal of Lightwave Technology*, vol. 38, no. 8, pp. 2477–2484, 2020.

[97] Z. Zhang, J. He, B. Du, K. Guo, and Y. Wang, "Highly sensitive gas refractive index sensor based on hollow-core photonic bandgap fiber," *Opt. Express*, vol. 27, no. 21, pp. 29 649–29 658, Oct 2019.

[98] H. Yu, Z. Luo, Y. Zheng, J. Ma, Z. Li, and X. Jiang, "Temperature-Insensitive Vibration Sensor With Kagomé Hollow-Core Fiber Based Fabry–Perot Interferometer," *Journal of Lightwave Technology*, vol. 37, no. 10, pp. 2261–2269, 2019.

[99] Z. Wu, B. Liu, J. Zhu, J. Liu, S. Wan, T. Wu, and J. Sun, "Ultrahigh resolution thickness

measurement technique based on a hollow core optical fiber structure," *Sensors*, vol. 20, p. 2035, 04 2020.

[100] P. Zhang, M. Tang, F. Gao, B. Zhu, Z. Zhao, L. Duan, S. Fu, J. Ouyang, H. Wei, P. P. Shum, and D. Liu, "Simplified hollow-core fiber-based fabry–perot interferometer with modified vernier effect for highly sensitive high-temperature measurement," *IEEE Photonics Journal*, vol. 7, no. 1, pp. 1–10, 2015.

[101] Y. Zhao, R.-j. Tong, M.-Q. Chen, and F. Xia, "Relative humidity sensor based on hollow core fiber filled with gqds-pva," *Sensors and Actuators B: Chemical*, vol. 284, 12 2018.

[102] H. Sakr, T. D. Bradley, Y. Hong, G. T. Jasion, J. R. Hayes, H. Kim, I. A. Davidson, E. N. Fokoua, Y. Chen, K. R. H. Bottrill, N. Taengnoi, P. Petropoulos, D. J. Richardson, and F. Poletti, "Ultrawide Bandwidth Hollow Core Fiber for Interband Short Reach Data Transmission," in *2019 Optical Fiber Communications Conference and Exhibition (OFC)*, 2019, pp. 1–3.

[103] A. Nespola, S. Straullu, T. Bradley, H. C. Mulvad, J. Hayes, G. Jasion, M. Alonso Gouveia, S. Sandoghchi, S. Bawn, F. Forghieri, D. Richardson, F. Poletti, and P. Poggiolini, "Record PM-16QAM and PM-QPSK transmission distance (125 and 340 km) over hollow-core-fiber," in *45th European Conference on Optical Communication (ECOC 2019)*, 01 2019, pp. 285 (4 pp.)–285 (4 pp.).

[104] Z. Liu, B. Karanov, L. Galdino, J. R. Hayes, D. Lavery, K. Clark, K. Shi, D. J. Elson, B. C. Thomsen, M. N. Petrovich, D. J. Richardson, F. Poletti, R. Slavík, and P. Bayvel, "Nonlinearity-free coherent transmission in hollow-core antiresonant fiber," *Journal of Lightwave Technology*, vol. 37, no. 3, pp. 909–916, 2019.

[105] J. R. Hayes, S. R. Sandoghchi, T. D. Bradley, Z. Liu, R. Slavík, M. A. Gouveia, N. V. Wheeler, G. Jasion, Y. Chen, E. N. Fokoua, M. N. Petrovich, D. J. Richardson, and F. Poletti, "Antiresonant hollow core fiber with an octave spanning bandwidth for short haul data communications," *Journal of Lightwave Technology*, vol. 35, no. 3, pp. 437–442, 2017.

[106] K. A. Clark, Y. Chen, E. R. N. Fokua, T. Bradley, F. Poletti, D. J. Richardson, P. Bayvel, R. Slavík, and Z. Liu, "Low thermal sensitivity hollow core fiber for optically-switched data centers," *Journal of Lightwave Technology*, vol. 38, no. 9, pp. 2703–2709, 2020.

[107] Y. Chen, Z. Liu, S. R. Sandoghchi, G. T. Jasion, T. D. Bradley, E. Numkam Fokoua, J. R. Hayes, N. V. Wheeler, D. R. Gray, B. J. Mangan, R. Slavík, F. Poletti, M. N. Petrovich, and D. J. Richardson, "Multi-kilometer long, longitudinally uniform hollow core photonic bandgap fibers for broadband low latency data transmission," *Journal of Lightwave Technology*, vol. 34, no. 1, pp. 104–113, 2016.

[108] B. Zhu, B. J. Mangan, T. Kremp, G. S. Puc, V. Mikhailov, K. Dube, Y. Dulashko, M. Cortes, Y. lian, K. Marceau, B. Violette, D. Cartsounis, R. Lago, B. Savran, D. Inniss, and D. J. DiGiovanni, "First demonstration of hollow-core-fiber cable for low latency data transmission," in *Optical Fiber Communication Conference Postdeadline Papers 2020*. Optical Society of America, 2020, p. Th4B.3.

[109] A. Saljoghei, M. Qiu, S. R. Sandoghchi, C. Laperle, M. Alonso, M. Hubbard, I. Lang, M. Pasandi, Y. Chen, M. Petrocich, A. Appleyard, A. Boyland, L. Hooper, T. Bradley, G. Jasion, H. Sakr, E. N. Fokoua, J. Hayes, F. Poletti, D. Richardson, M. Fake, and M. O'Sullivan. First Demonstration of Field-Deployable Low Latency Hollow-core Cable

Capable of Supporting >1000km, 400Gb/s WDM Transmission. [Online]. Available: https://arxiv.org/abs/2106.05343

[110] B. Debord, A. Foued, L. Vincetti, F. Gérôme, and F. Benabid, "Hollow-Core Fiber Technology: The Rising of "Gas Photonics"," *Fibers*, vol. 7, p. 16, 02 2019.

[111] A. V. V. Nampoothiri, A. M. Jones, C. Fourcade-Dutin, C. Mao, N. Dadashzadeh, B. Baumgart, Y. Wang, M. Alharbi, T. Bradley, N. Campbell, F. Benabid, B. R. Washburn, K. L. Corwin, and W. Rudolph, "Hollow-core Optical Fiber Gas Lasers (HOFGLAS): a review [Invited]," *Opt. Mater. Express*, vol. 2, no. 7, pp. 948–961, Jul 2012.

[112] M. Klimczak, D. Dobrakowski, A. N. Ghosh, G. Stępniewski, D. Pysz, G. Huss, T. Sylvestre, and R. Buczyński, "Nested capillary anti-resonant silica fiber with mid-infrared transmission and low bending sensitivity at 4000 nm," *Opt. Lett.*, vol. 44, no. 17, pp. 4395–4398, Sep 2019.

[113] F. Yang, W. Jin, Y. Cao, H. L. Ho, and Y. Wang, "Towards high sensitivity gas detection with hollow-core photonic bandgap fibers," *Opt. Express*, vol. 22, no. 20, pp. 24 894–24 907, Oct 2014.

[114] M. Nikodem, "Laser-based trace gas detection inside hollow-core fibers: A review," *Materials (Basel, Switzerland)*, vol. 13, 09 2020.

[115] J. F. Kelly, R. L. Sams, T. A. Blake, and J. M. Kriesel, "Further developments of capillary absorption spectrometers using small hollow-waveguide fibers," in *Quantum Sensing and Nanophotonic Devices XI*, vol. 8993, International Society for Optics and Photonics. SPIE, 2014, pp. 261 – 276.

[116] B. M. Masum, S. M. Aminossadati, M. S. Kizil, and C. R. Leonardi, "Numerical and experimental investigations of pressure-driven gas flow in hollow-core photonic crystal fibers," *Appl. Opt.*, vol. 58, no. 4, pp. 963–972, Feb 2019.

[117] J. Parry, B. Griffiths, N. Gayraud, E. McNaghten, A. Parkes, W. Macpherson, and D. Hand, "Towards practical gas sensing with micro-structured fibres," *Measurement Science and Technology*, vol. 20, p. 075301, 2009.

[118] W. Jin, Y. Cao, F. Yang, and H. L. Ho, "Ultra-sensitive all-fibre photothermal spectroscopy with large dynamic range," *Nature Communications*, vol. 6, p. 6767, 2015.

[119] P. Zhao, Y. Zhao, H. Bao, H. L. Ho, W. Jin, S. Fan, S. Gao, Y. Wang, and P. Wang, "Mode-phase-difference photothermal spectroscopy for gas detection with an anti-resonant hollow-core optical fiber," *Nature Communications*, vol. 11, p. 847, 2020.

[120] A. Knebl, D. Yan, J. Popp, and T. Frosch, "Fiber enhanced raman gas spectroscopy," *TrAC Trends in Analytical Chemistry*, vol. 103, pp. 230 – 238, 2018.

[121] C. Yao, L. Xiao, S. Gao, Y. Wang, P. Wang, R. Kan, W. Jin, and W. Ren, "Sub-ppm CO detection in a sub-meter-long hollow-core negative curvature fiber using absorption spectroscopy at 2.3 μm"," *Sensors and Actuators B: Chemical*, vol. 303, p. 127238, 2020.

[122] P. Zhao, H. L. Ho, W. Jin, S. Fan, S. Gao, Y. Wang, and P. Wang, "Gas sensing with mode-phase-difference photothermal spectroscopy assisted by a long period grating in a dual-mode negative-curvature hollow-core optical fiber," *Opt. Lett.*, vol. 45, no. 20, pp. 5660–5663, Oct 2020.

[123] P. Jaworski, K. Krzempek, G. Dudzik, P. J. Sazio, and W. Belardi, "Nitrous oxide detection at 5.26μm with a compound glass antiresonant hollow-core optical fiber," *Opt. Lett.*, vol. 45,

no. 6, pp. 1326–1329, Mar 2020.

[124] W. F. Krupke, R. J. Beach, V. K. Kanz, and S. A. Payne, "Resonance transition 795-nm rubidium laser," *Opt. Lett.*, vol. 28, no. 23, pp. 2336–2338, Dec 2003.

[125] Z. Zhou, N. Tang, Z. Li, W. Huang, Z. Wang, W. Wu, and W. Hua, "High-power tunable mid-infrared fiber gas laser source by acetylene-filled hollow-core fibers," *Opt. Express*, vol. 26, no. 15, pp. 19 144–19 153, Jul 2018.

[126] F. B. A. Aghbolagh, V. Nampoothiri, B. Debord, F. Gerome, L. Vincetti, F. Benabid, and W. Rudolph, "Mid ir hollow core fiber gas laser emitting at 4.6μm," *Opt. Lett.*, vol. 44, no. 2, pp. 383–386, Jan 2019.

[127] Y. Wang, M. K. Dasa, A. I. Adamu, J. E. Antonio-Lopez, M. S. Habib, R. Amezcua-Correa, O. Bang, and C. Markos, "High pulse energy and quantum efficiency mid-infrared gas Raman fiber laser targeting CO2 absorption at 4.2μm," *Opt. Lett.*, vol. 45, no. 7, pp. 1938–1941, Apr 2020.

[128] A. I. Adamu, M. S. Habib, C. R. Petersen, J. E. A. Lopez, B. Zhou, A. Schülzgen, M. Bache, R. Amezcua-Correa, O. Bang, and C. Markos, "Deep-UV to Mid-IR Supercontinuum Generation driven by Mid-IR Ultrashort Pulses in a Gas-filled Hollow-core Fiber," *Scientific Reports*, vol. 9, p. 4446, 2019.

[129] M. S. Habib, C. Markos, J. E. Antonio-Lopez, and R. Amezcua-Correa, "Multioctave supercontinuum from visible to mid-infrared and bend effects on ultrafast nonlinear dynamics in gas-filled hollow-core fiber," *Appl. Opt.*, vol. 58, no. 13, pp. D7–D11, May 2019.

[130] C. B. John C. Travers, Teodora F. Grigorova and F. Belli, "High-energy pulse self-compression and ultraviolet generation through soliton dynamics in hollow capillary fibres," *Nature Photonics*, vol. 13, p. 547–554, 2019.

[131] M. Triches, M. Michieletto, J. Hald, J. K. Lyngsø, J. Lægsgaard, and O. Bang, "Optical frequency standard using acetylene-filled hollow-core photonic crystal fibers," *Opt. Express*, vol. 23, no. 9, pp. 11 227–11 241, May 2015.

[132] Y. Chen, H. C. H. Mulvad, S. R. Sandoghchi, E. Numkam, T. D. Bradley, J. R. Hayes, N. V. Wheeler, G. T. Jasion, S. U. Alam, F. Poletti, M. N. Petrovich, and D. J. Richardson, "First demonstration of low loss, bend insensitive 37-cell hollow-core photonic bandgap fiber at 1μm for high power delivery applications," in *2016 Conference on Lasers and Electro-Optics (CLEO)*, 2016, pp. 1–2.

[133] A. V. Smith and B. T. Do, "Bulk and surface laser damage of silica by picosecond and nanosecond pulses at 1064 nm," *Appl. Opt.*, vol. 47, no. 26, pp. 4812–4832, Sep 2008.

[134] E. T. J. Nibbering, G. Grillon, M. A. Franco, B. S. Prade, and A. Mysyrowicz, "Determination of the inertial contribution to the nonlinear refractive index of air, N2, and O2 by use of unfocused high-intensity femtosecond laser pulses," *J. Opt. Soc. Am. B*, vol. 14, no. 3, pp. 650–660, Mar 1997.

[135] B. Debord, M. Alharbi, L. Vincetti, A. Husakou, C. Fourcade-Dutin, C. Hoenninger, E. Mottay, F. Gérôme, and F. Benabid, "Multi-meter fiber-delivery and pulse self-compression of milli-joule femtosecond laser and fiber-aided laser-micromachining," *Opt. Express*, vol. 22, no. 9, pp. 10 735–10 746, May 2014.

[136] F. Emaury, C. F. Dutin, C. J. Saraceno, M. Trant, O. H. Heckl, Y. Y. Wang, C. Schriber,

F. Gerome, T. Südmeyer, F. Benabid, and U. Keller, "Beam delivery and pulse compression to sub-50 fs of a modelocked thin-disk laser in a gas-filled kagome-type hc-pcf fiber," *Opt. Express*, vol. 21, no. 4, pp. 4986–4994, Feb 2013.

[137] E. Lee, J. Luo, B. Sun, V. L. Ramalingam, X. Yu, Q. Wang, F. Yu, and J. C. Knight, "45W 2 μm Nanosecond Pulse Delivery Using Antiresonant Hollow-Core Fiber," in *2018 Conference on Lasers and Electro-Optics (CLEO)*, 2018, pp. 1–2.

[138] S. Wu, B. Siwicki, R. M. Carter, F. Biancalana, J. D. Shephard, and D. P. Hand, "Impact of nonlinear effects on transmission losses of hollow-core antiresonant negative curvature optical fiber," *Appl. Opt.*, vol. 59, no. 16, pp. 4988–4996, Jun 2020.

[139] S. Eilzer and B. Wedel, "Hollow core optical fibers for industrial ultra short pulse laser beam delivery application," *Fibers*, vol. 4, no. 6, p. 80, 2018.

[140] F. Yu, M. Cann, A. Brunton, W. Wadsworth, and J. Knight, "Single-mode solarization-free hollow-core fiber for ultraviolet pulse delivery," *Opt. Express*, vol. 26, no. 8, pp. 10 879–10 887, Apr 2018.

[141] T. Tzu, K. Sun, R. Costanzo, D. Ayoub, S. M. Bowers, and A. Beling, "Foundry-enabled high-power photodetectors for microwave photonics," *IEEE Journal of Selected Topics in Quantum Electronics*, vol. 25, no. 5, pp. 1–11, 2019.

[142] P. A. Morton and M. J. Morton, "High-power, ultra-low noise hybrid lasers for microwave photonics and optical sensing," *Journal of Lightwave Technology*, vol. 36, no. 21, pp. 5048–5057, 2018.

[143] P. A. Morton, M. J. Morton, C. Zhang, J. B. Khurgin, J. Peters, C. D. Morton, and J. E. Bowers, "High-Power, High-Linearity, Heterogeneously Integrated III–V on Si MZI Modulators for RF Photonics Systems," *IEEE Photonics Journal*, vol. 11, no. 2, pp. 1–10, 2019.

[144] A. Hartog, A. Conduit, and D. Payne, "Variation of pulse delay with stress and temperature in jacketed and unjacketed optical fibres," *Optical and Quantum Electronics*, vol. 11, pp. 265–273, 01 1979.

[145] U. Mutugala, E. Numkam Fokoua, Y. Chen, T. Bradley, S. Sandoghchi, G. Jasion, R. Curtis, M. Petrovich, F. Poletti, D. Richardson, and R. Slavik, "Hollow-core fibres for temperature-insensitive fibre optics and its demonstration in an optoelectronic oscillator," *Scientific Reports*, vol. 8, 12 2018.

[146] F. Yang, F. Gyger, and L. Thévenaz, "Intense brillouin amplification in gas using hollow-core waveguides," *Nature Photonics*, vol. 14, pp. 700–708, 2020.

[147] S. Rikimi, Y. Chen, T. Bradley, M. A. Gouveia, R. J. Horley, A. T. Harker, S. Bawn, F. Poletti, M. Petrovich, D. Richardson, and N. Wheeler, "Long-term behaviour of water vapour absorption in hollow core fibres," in *Sixth International Workshop on Specialty Optical Fibers and Their Applications (WSOF 2019) (06/11/19 - 08/11/19)*, November 2019, p. 112061U.

[148] J. W. Nicholson, B. Mangan, L. Meng, A. DeSantolo, R. S. Windeler, J. M. Fini, K. Mukasa, E. M. Monberg, P. Vannasouk, E. Warych, and T. Taunay, "Low-loss, low return-loss coupling between SMF and single-mode, hollow-core fibers using connectors," in *2014 Conference on Lasers and Electro-Optics (CLEO) - Laser Science to Photonic Applications*, 2014, pp. 1–2.

[149] T. W. Kelly, P. Horak, I. A. Davidson, M. Partridge, G. T. Jasion, S. Rikimi, A. Taranta, D. J. Richardson, F. Poletti, and N. V. Wheeler, "Controlling the attenuation of hollow core fibers

using gas-induced differential refractive index," in *Conference on Lasers and Electro-Optics*. Optical Society of America, 2021, p. STh1A.4.

[150] N. Wheeler, M. G. Pappa, T. D. Bradley, Y. Chen, W. Brooks, J. Storey, M. Foster, D. J. Richardson, and M. N. Petrovich, "Spontaneous raman scattering in hollow core photonic crystal fibres," in *2017 IEEE SENSORS*, 2017, pp. 1–3.

[151] T. N. Bakhvalova, M. E. Belkin, M. Kamalian-Kopae, and S. K. Turitsyn, "Correcting the Chromatic Dispersion of a Fronthaul Fiber Link in Millimeter-Wave Radio -over-Fiber Networks," in *2019 27th Telecommunications Forum (TELFOR)*, 2019, pp. 1–4.

[152] Y. Cui, K. Xu, J. Dai, X. Sun, Y. Dai, Y. Ji, and J. Lin, "Overcoming Chromatic-Dispersion-Induced Power Fading in ROF Links Employing Parallel Modulators," *IEEE Photonics Technology Letters*, vol. 24, no. 14, pp. 1173–1175, 2012.

Appendix - Selected papers

Relevant publications, both from peer-reviewed journals and international conferences, are attached in their full text on the following pages.

Optical Engineering

OpticalEngineering.SPIEDigitalLibrary.org

Multimode fiber tapers for reproducible refractometric liquid detection

Matej Komanec
Tomas Martan
Tomas Nemecek
Stanislav Zvanovec

SPIE.

Optical Engineering 54(4), 047102 (April 2015)

Multimode fiber tapers for reproducible refractometric liquid detection

Matej Komanec,* Tomas Martan, Tomas Nemecek, and Stanislav Zvanovec
Czech Technical University in Prague, Department of Electromagnetic Field, Faculty of Electrical Engineering, Technicka 2, Prague 16627, Czech Republic

Abstract. This paper describes the refractometric detection of liquids based on silica multimode optical fibers which were tapered to increase the evanescent-wave overlap for higher sensor sensitivity. By precisely monitoring the production process, consistent sample parameters were achieved. More than 200 tapers with a taper waist diameter range from 6.0 to 76.3 μm were prepared from polymer-clad silica and gradient-index multimode fibers. U-shaped fiber taper sensitivities were analytically compared with straight tapers with resulting intensity sensitivities of over 200%/RIU. Crucial parameters for real sensor applications, such as measurement repeatability, reproducibility, and long-term stability, were further studied for polymer-clad silica straight tapers. Long-term stability was monitored showing stable measurement results over a 6 months long interval. Measurement repeatability and reproducibility with standard deviations of 0.55%/RIU and 2.26%/RIU, respectively, were achieved. [DOI: 10.1117/1.OE.54.4.047102]

Keywords: fiber optic sensors; refractometry; modes.

Paper 141861 received Dec. 4, 2014; accepted for publication Mar. 23, 2015; published online Apr. 8, 2015.

1 Introduction

Fiber optic liquid detection represents remarkable advantages in comparison, for instance, with semiconductor and electronic detection. The advantage of optical fibers lies in their immunity to surrounding electromagnetic fields. Additionally, optical silica fibers can withstand high temperatures and are resistant to a variety of chemical substances. Therefore, fiber optic sensors can be employed in extreme conditions, e.g., in explosive environments or in areas with high electromagnetic disruption.

Detection of liquids based on evanescent-wave overlap into measured analytes exploiting tapered optical fibers has been extensively studied for the last two decades. Refractometers employing tapered optical fibers were first presented[1] in a detailed study of evanescent-field overlap. More sophisticated refractometric applications have since been proposed including the tapered microstructured optical fiber refractometer presented in our previous work,[2] which features a tapered suspended-core microstructured optical fiber and an evanescent-field overlap which substantially increased from 0.29% to 29.16%.

The singlemode-multimode-singlemode (SMS) sensing structure represents a facile approach to enhancement of evanescent-wave overlap including a segment of multimode fiber between two single-mode fibers, resulting in optical mode spreading and subsequent interference in the multimode segment. A detailed study of in-line production monitoring and liquid sensing based on SMS structures was presented,[3] where 2946 nm/RIU (refractive index unit) was attained for tested analytes having a refractive index range of 1.42 to 1.43.

Surface plasmon resonance (SPR) refractometers were developed in parallel to tapered optical fiber-based refractometers allowing us to present achievements in extreme sensitivities and resolutions comparable to tapered fibers. In this scenario, SPR refractometers employing polymer-clad silica (PCS) fibers,[4] tapered fibers with multiple layers deposited,[5] and long-period grating sensors[6] were used. However, SPR refractometers require a multistep manufacturing process and more complex measurement configuration.

Tapered optical fiber sensors (TOFSs) are utilized either in transmissive[7] or reflective regimes,[8] whereas the sensor shape can be further tailored.[9] Furthermore, abrupt tapers (multiple in-line tapers on a single fiber) forming a Mach–Zehnder configuration were utilized for liquid sensing.[10]

Facile high-quality fabrication will determine the future success of TOFS applications. This paper focuses on straight and U-shaped polymer-clad silica TOFS for detecting liquids in the visible range and compares and analyzes conventional gradient-index multimode TOFS with polymer-clad silica TOFS. Our earlier studies[11,12] have been considerably extended, simulations have been carried out to provide preliminary results, prepared samples have been summarized and the measurement setup is, herein, described. Taper production quality and tapering process conditions are discussed, with a particular emphasis placed on stable taper parameters. A sensitivity analysis for all measured TOFS follows. Measurement repeatability (for a standalone TOFS) and measurement reproducibility (for a set of three TOFS) are studied in three consequent measurement cycles. Long-term stability, tested in periods of up to 6 months, is then presented. Our developed detection units can be employed as key instruments e.g., in petrochemical, automobile, or food industries.

2 Simulations

Preliminary simulations were carried out in the Synopsys BeamProp software for polymer-clad silica TOFS (PCS TOFS)

*Address all correspondence to: Matej Komanec, E-mail: komanmat@fel.cvut.cz

0091-3286 /2015/$25.00

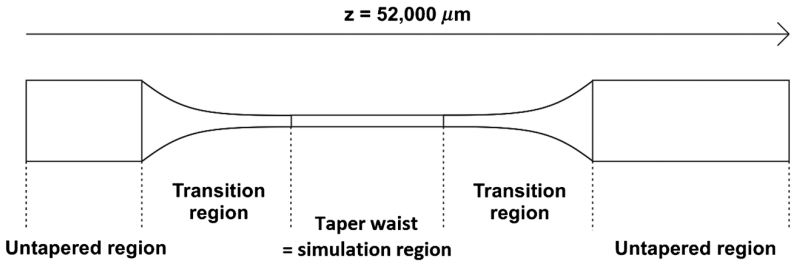

Fig. 1 Model of a taper structure with the taper waist as the simulation region.

of 200-μm outer diameter. The selected waist diameters were 3, 4, 5, 6, 8, 10, 15, and 20 μm, with the wavelength set at 632 nm. The full transparent boundary condition and a grid size notably below the evaluated wavelength were considered. In the simulations, external mediums with refractive index of 1.432, 1.380, and 1.361 were used to simulate ethylenglycol (EG), isopropylalcohol (IPA), and ethylalcohol (ETOH), respectively. The taper structure, set according to a real taper, is depicted in Fig. 1. For the simulation, we assumed an adiabatic transition region, all modes propagating (multimode launch field defined by the silica/cladding-polymer refractive indices) and only the taper waist was considered as the sensing region. One of the major parameters of tapers represents the tapering ratio, which defines how many times the final waist diameter is reduced to the original fiber diameter, as utilized e.g., by Kerttulla et al.[13]

The relative power loss summarized in Fig. 2, obtained for all three analytes and chosen waist diameters, occurs when higher propagating modes are being radiated into the analyte and no longer guided in the TOFS. Areas I and II depict a relative power loss saturation point where, for a particular waist diameter range, the evanescent-field overlap does not increase. If further tapered toward narrower diameters, most of the guided energy is transferred into higher (evanescent) modes and consequently radiated into the analyte with respect to the refractive index of the analyte. The saturation area is a boundary between the original mode set propagating in the untapered PCS (which is defined by silica/cladding-polymer refractive indices and is preserved for lower tapering ratios) and full mode excitation in the

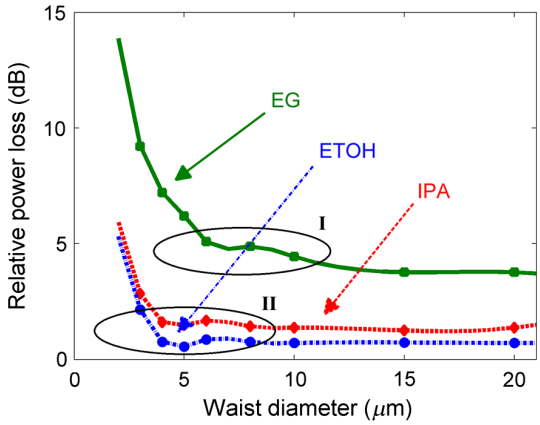

Fig. 2 Simulation results for 2-mm long taper waist immersed in selected analytes—dependence of relative power loss on waist diameter. Areas I and II depicting a saturation region.

case of a tapering ratio higher than approximately 15 for EG and 20 for IPA and ETOH.

3 Measurement Setup

All measurements were carried out in the wavelength range 450 to 1000 nm. The measurement setup included a broadband light source with a 2 m-long 200PCS fiber attached at the generator side. A calibration fiber and a mode stripper were inserted between the light source and the detector segment. For each fiber type, an appropriate calibration fiber (e.g., 125PCS in case of the 125PCS TOFS measurement) was employed. Afterward, TOFSs were inserted between the calibration fiber and the mode stripper. The detection was performed by a spectral analyzer with a 2 m-long 200PCS fiber attached. The measurement setup is depicted in Fig. 3.

4 Prepared Samples

Three conventional fiber types were used for fiber tapering: (1) Corning multimode 62.5/125 μm gradient-index fiber (62.5 MM), (2) CeramOptec Optran HWF 125/140 μm hard polymer-clad silica fiber (125PCS), and (3) CeramOptec Optran HWF 200/230 μm hard polymer-clad silica fiber (200PCS), which was the same as that considered in simulation. The 200PCS fiber was chosen based on simulations with the 125PCS fiber to provide comparisons in sensitivity and tapering limits. The 62.5MM fiber was selected as a representative of a conventional core/clad composition with a maximum core size typically available, while having a gradient-refractive index profile. A modified tapering technique, developed in our previous work,[14] where flame-heating, in conjunction with two synchronized motors pulling the fiber evenly in the opposite directions, was employed. We have utilized the exponential-linear taper profile which was also employed by Verma et al.[15] for SPR sensing, where a taper profile study was performed and the taper profile resulted in further improvement of the measurement sensitivity.

TOFS waist diameters from 79 μm to less than 10 μm were developed for enhanced evanescent-wave overlap with the selected analytes. The largest core diameter tapering ratio of almost 20 was achieved in the case of 200PCS fibers. For 125PCS fibers and 62.5MM fibers, the tapering ratios were approximately 15 and 10, respectively. Developed TOFSs were divided into four sets of waist diameters. For each TOFS set, at least five TOFSs were produced. Enhanced sensitivity was first achieved by fiber tapering and, further by shape-tailoring. U-shaped tapers were formed by preparing straight tapers and subsequently applying the U-profile, ensuring comparable outputs could be obtained for the same taper diameters in straight and

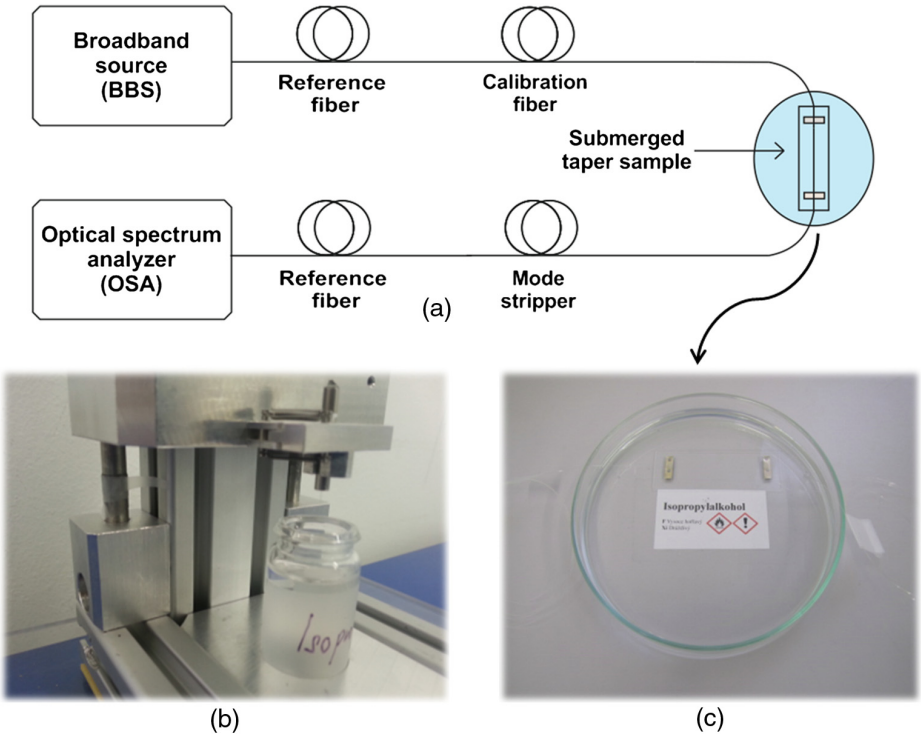

Fig. 3 Measurement setup for liquid sensing, (a) setup configuration; (b) a mini-tower for U-shaped tapered optical fiber sensor (TOFS) immersion; (c) immersion of straight TOFS.

U-shaped variants. A summary of the TOFS prepared is presented in Table 1.

For the U-shaped tapers, the radius was experimentally derived as the closest radius to the breakage point with emphasis on maintaining a repeatable radius (for all samples of a given fiber tapering ratio and fiber type). Table 2 summarizes the bending radii for all TOFSs, excluding the 47.5 μm 62.5MM TOFS, which it was not possible to shape-tailor and the 8.3 μm 125PCS TOFS where we experienced frequent breakage. The U-shape was conserved with a metallic tube located at the untapered part of the fiber, thus creating a fixed loop. A clear relation between the bending radius and tapering ratio can be observed – the higher the tapering ratio is set the smaller the bending radius that can be used, thus increasing sensitivity. The insertion loss of the detection unit also increases with bending radius, but since a reference for each measurement is utilized, this power loss can be neglected.

5 Results

Selected TOFSs were first submerged in IPA for approximately 5 min to remove small dust particles. To employ the TOFS after long-term storage, i.e., several months, a 30-minute purification period was utilized. Then a reference spectrum was recorded for TOFS exposed to air. Spectra were later recorded while the TOFSs were submerged in analytes: ETOH, IPA, and EG. A final spectrum was acquired for purified TOFS after the measurement cycle (again in IPA, to remove residual EG) with the temperature kept constant during the whole measurement cycle. Figure 4 illustrates an example of such a measurement. The figure shows the

Table 1 Taper waist diameters of utilized tapered optical fiber sensor (TOFS) sets.

	Taper waist diameters (μm)			
62.5MM	6.0	12.0	23.2	47.5
125 PCS	8.3	18.5	30.8	54.1
200 PCS	10.9	20.3	42.1	76.3

Table 2 U-shaped TOFS bending radius summary.

	Taper waist diameter (μm)	Bending radius (mm)
62.5MM	6.0	1.25
	12.0	1.32
	23.2	1.65
125PCS	18.5	0.92
	30.8	1.50
	54.1	1.62
200PCS	10.9	0.72
	20.3	1.11
	42.1	1.57
	76.3	1.70

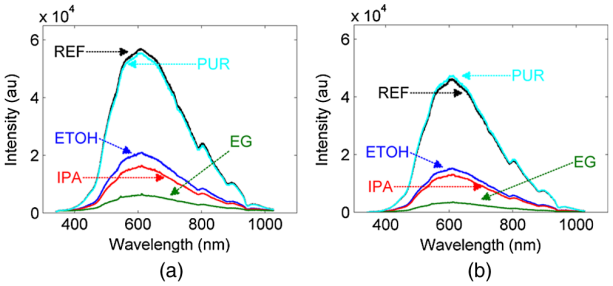

Fig. 4 Measured spectra for (a) straight and (b) U-shaped 200PCS 20.3 μm TOFS, REF—reference measurement, PUR — purification after measurement cycle.

measured spectra of the same 200PCS 20.3 μm TOFS, both in straight and U-shaped variants.

At first, we determined a significant parameter of the TOFS — the critical waist taper diameter. It was derived from the measured relative power loss for all 200PCS TOFS sets, both in straight and U-shaped variants (see dependences of average measured values with limits of minimum and maximum values reached in Fig. 5). The relative power loss represents a difference between the reference power level and power received after immersion in the analyte (ETOH, IPA, and EG) at the detector at 632 nm, which was derived from our spectral measurements. As can be seen, the measured relative power loss in the case of straight 200PCS TOFS saturates at a diameter of approximately 20 μm (marked areas in Fig. 5).

A similar phenomenon is observed for U-shaped 200PCS TOFS, where the saturation waist diameters are shifted to larger values, which is caused by the TOFS shape inducing a greater evanescent wave overlap.

5.1 *Production Process Enhancement*

To evaluate and enhance the production level, four sets (of three TOFS each) were produced from 125PCS and 200PCS fibers under monitored conditions. The best results were obtained for the 125PCS 21 μm TOFS set, with a waist diameter standard deviation of 0.25 μm. High-quality production was assured by maintaining stable production conditions, in particular, flame and ambient temperatures. The maximum fluctuation in ambient temperature was below 0.5°C during the manufacturing of all TOFS sets.

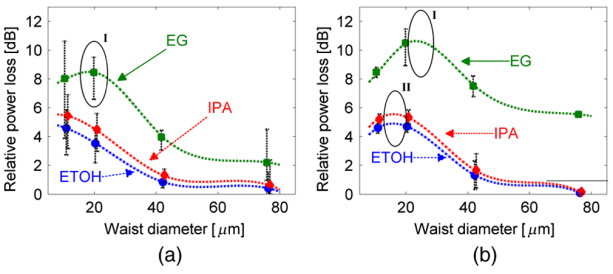

Fig. 5 Relative power loss for 200PCS TOFS sets: (a) straight and (b) U-shaped TOFS. Areas I and II depicting a saturation region.

5.2 *Sensitivity Study*

An intensity sensitivity analysis was used to compare obtained results with the intensity sensitivity (S) evaluated as[8]

$$S = \frac{\Delta I / I_0}{\Delta n} \times 100(\%/\mathrm{RIU}), \tag{1}$$

where ΔI stands for the analyte/reference measured intensity difference, I_0 represents the measured reference intensity, and Δn is the analyte/reference refractive index difference.

Figure 6 summarizes the maximum intensity sensitivities for the 200PCS TOFS sets at 632 nm. Here, it is more evident that, for all analytes, the sensitivity saturates around a waist diameter of 17 μm for straight TOFS and 20 μm for U-shaped TOFS. For straight TOFS, the values at the waist diameter of 76.3 μm for IPA are approximately 10%/RIU higher than for 42.1 μm, which is attributed to a measurement error because other intensity sensitivities show no variation in the 76.3 to 42.1 μm region. For U-shaped TOFS, the trend is linear and saturates at the same waist diameter as that of straight TOFS. Based on the results, an optimal tapering ratio in our experiment was derived to be 10 for 200PCS TOFS.

Derived maximum intensity sensitivities for the case of 125PCS TOFS sets are then presented in Fig. 7. Here, the saturation point can be found for waist diameters of approximately 25 μm for both straight and U-shaped variants (marked as area I). An interesting result was revealed for the U-shaped 125PCS TOFS sets submerged in EG, where we observed an almost independent intensity sensitivity on the change of the waist diameter. Therefore, for utilization of

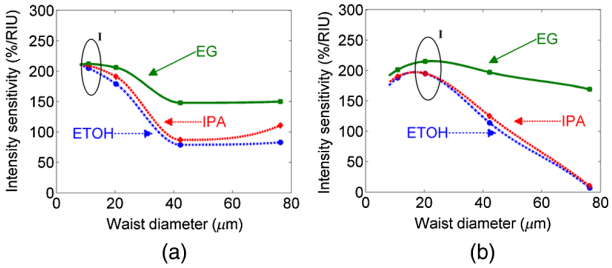

Fig. 6 Maximum intensity sensitivity of 200PCS TOFS sets: (a) straight and (b) U-shaped TOFS. Area I depicts the optimal waist diameter for highest sensitivity.

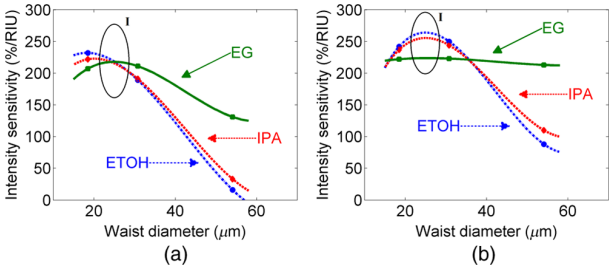

Fig. 7 Maximum intensity sensitivity of 125PCS TOFS sets: (a) straight and (b) U-shaped TOFS. Area I depicts the optimal waist diameter for highest sensitivity.

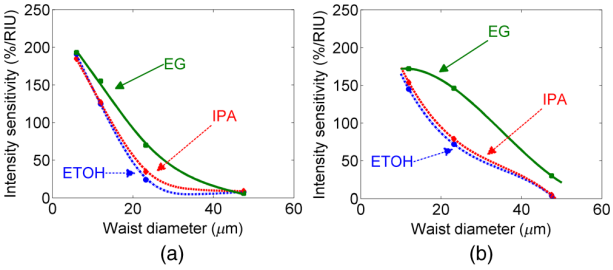

Fig. 8 Maximum intensity sensitivity of 62.5MM TOFS sets: (a) straight and (b) U-shaped TOFS.

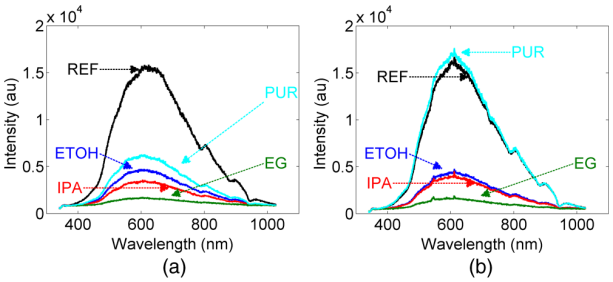

Fig. 9 Measured spectra of a straight 200PCS 10.9 μm TOFS measured (a) 4 months and (b) 6 months after production, REF — reference measurement, PUR — purification after measurement cycle.

such a sensor, a considerably lower tapering ratio could be required.

In comparison, intensity sensitivities of 62.5MM TOFS are depicted in Fig. 8. Here we observe, as expected, straight TOFS sets without any observable saturation in sensitivity. For the U-shaped 62.5MM TOFS, for EG detection only, saturation is evident. Therefore, to achieve an optimal waist diameter for straight and U-shaped TOFSs, a higher tapering ratio than 10 is required.

Resolutions for the most sensitive TOFS of each fiber type were evaluated both in straight and U-shaped variants, respectively. The results are summarized in Table 3 with the sensitivity values as comparisons.

5.3 *Measurement Repeatability and Reproducibility*

To verify production results and their impact on measurement output further, the 125PCS 21 μm TOFS set was selected and for a standalone TOFS of this set three subsequent measurement cycles were carried out to prove measurement repeatability. The standard deviations for standalone TOFSs were 7.17%/RIU for ETOH, 4.45%/RIU for IPA, and 0.55%/RIU for EG.

Table 3 Resolution and maximum sensitivity for measured TOFS.

	Taper waist diameter (μm)	Profile	Maximum sensitivity (%/RIU)	Resolution (RIU)
62.5MM	6.0	Straight	193 (EG)	1.3×10^{-2}
	6.0	U-shaped	172 (EG)	3.3×10^{-3}
125PCS	18.5	Straight	232 (ETOH)	2.5×10^{-3}
	18.5	U-shaped	242 (ETOH)	1.1×10^{-3}
200PCS	10.9	Straight	212 (EG)	2.0×10^{-3}
	20.3	U-shaped	215 (EG)	1.7×10^{-3}

Measurement reproducibility, i.e., obtaining the same results for different TOFSs of the same set, was evaluated for the whole 125PCS 21 μm TOFS set. For this purpose, we compared all the TOFS intensity sensitivities acquired and a standard deviation of 10.71%/RIU for ETOH, 8.11%/RIU for IPA, and 2.26%/RIU for EG was observed.

Results indicate 125 μm PCS TOFS (all tested variants) as ideal candidates for stable and repeatable sensing, in particular, for EG detection with a reproducibility deviation below 2.5%/RIU for the entire set and a repeatability deviation below 0.6%/RIU for standalone samples. For ETOH and IPA, the results allude to an application with less precise requirements. The overall difference between a standalone TOFS and the whole TOFS set is only several %/RIU, which further verifies the quality of our production process.

5.4 *Long-Term Stability*

Long-term stability was tested for a chosen TOFS within a time period of 6 months. Figure 9 depicts the spectra from the 10.9 μm 200PCS TOFS measured 2 months apart. During the first measurement cycle [see Fig. 9(a)], the TOFS was insufficiently purified after submerging in EG. After 4 months of storage we were able, by additional premeasurement purification, to remove all residual impurities.

6 Conclusion

We presented straight and U-shaped multimode tapered fibers for liquid sensing. Special emphasis was placed on multimode polymer-clad silica fibers' sensitivity, optimal waist diameter, and their measurement repeatability, measurement reproducibility, and long-term stability.

The production process was perfected with a taper waist standard deviation below 0.25 μm when manufacturing conditions were monitored and precautions, in particular with temperature, were taken. Further enhancement of taper parameter stability is possible with a more precise ambient temperature and relative humidity control.

Measurement results showed significant trends, such as saturation points in intensity sensitivities for different fiber types and analytes, and we defined an optimal taper waist for achieving maximum intensity sensitivity while keeping the tapering ratio as low as possible. For 125PCS fiber, a waist diameter of 25 μm with an intensity sensitivity over 200%/RIU is optimal. For the 200PCS fiber, the optimal waist diameter value is 11 μm with an intensity sensitivity again over 200%/RIU.

Measurement repeatability (for a standalone TOFS) was greatly increased for TOFS experiencing the monitored production process. The intensity sensitivity standard deviation measured below 8%/RIU for ETOH, 5%/RIU for IPA, and 1%/RIU for EG. This result leads to a promising application for precise liquid sensing with a refractive index in the range of 1.41–1.44 RIU. Long-term stability was examined and we have achieved more than 6 months' long-term stability.

In contrast to wavelength-based sensors such as SPRs, our TOFSs require only a single-step manufacturing process (double-step for U-shaped TOFS) and represent a low-cost option (cheap sensor, only a simple laser source and a

detector are needed) with reasonable sensitivity and stable measurement results. To conclude, a facile manufacturing process of tapered polymer-clad silica fiber sensors was presented, with optimized sensitivity, measurement repeatability, and reproducibility and proven long-term stability for liquid detection in the refractive index range of 1.36 to 1.43.

Acknowledgments

This work was supported by the Technological Agency of the Czech Republic under Grant No. TA03010060. The authors would like to thank SQS Fiber optics, Czech Republic for their close collaboration with the taper preparations.

References

1. S. Huntington et al., "Evanescent field characterisation of tapered optical fibre sensors in liquid environments using near field scanning optical microscopy and atomic force microscopy," *IEE Proc. Optoelectron.* **146**(5), 239–243 (1999).
2. T. Martan et al., "Tapered optical fibres for sensing," *Proc. SPIE* **7138**, 71380Z (2008).
3. C. R. Biazoli et al., "Multimode interference tapered fiber refractive index sensors," *Appl. Opt.* **51**, 5941–5945 (2012).
4. S. K. Srivastava, R. Verma, and B. D. Gupta, "Surface plasmon resonance based fiber optic sensor for the detection of low water content in ethanol," *Sens. Actuators B* **153**(1), 194–198 (2011).
5. R. Jha, R. Verma, and B. Gupta, "Surface plasmon resonance-based tapered fiber optic sensor: sensitivity enhancement by introducing a teflon layer between core and metal layer," *Plasmonics* **3**(4), 151–156 (2008).
6. C.-L. Tien et al., "Double-sided polishing long period fiber grating sensors for measuring liquid refractive index," presented at *Asia Communications and Photonics Conf. on Exhibition*, Paper WL93, pp. 1–6, Optical Society of America, Shanghai, China (2009).
7. P. Wang et al., "Enhanced refractometer based on periodically tapered small core single mode fiber," *IEEE Sens. J.* **13**, 180–185 (2013).
8. Y.-H. Tai and P.-K. Wei, "Sensitive liquid refractive index sensors using tapered optical fiber tips," *Opt. Lett.* **35**, 944–946 (2010).
9. E. OConnell et al., "Low cost hydrocarbon spillage sensor for the marine environment with interfacing to a mote platform," in *Proc. 2011 IEEE Sensors* pp. 1558–1561 (2011).
10. C.-L. L. Hun-Pin Chang, Chai-Ming Li and J.-M. Hsu, "Tapered fiber Mach–Zehnder interferometer for liquid level sensing," in *Proc. Progress in Electromagnetics Research Symposium*, Vol. 2528, pp. 734–736, Taipei (2013).
11. M. Komanec, T. Martan, and S. Zvanovec, "Tapered optical fibers for reproducible detection of liquids," presented at *Advanced Photonics 2013*, Paper JT3A.31, Optical Society of America, Río Grande, Puerto Rico (2013).
12. M. Komanec, T. Martan, and S. Zvanovec, "Polymer-clad silica tapers for liquid sensing: long-term measurement repeatability and production imperfections," presented at *Advanced Photonics*, Paper JM5A.63, Optical Society of America, Barcelona, Spain (2014).
13. J. Kerttula et al., "Mode evolution in long tapered fibers with high tapering ratio," *Opt. Express* **20**, 25461–25470 (2012).
14. T. Martan et al., "Workplace for manufacturing devices based on optical fiber tapers," *Proc. SPIE* **6609** 66090K (2007).
15. R. K. Verma, A. K. Sharma, and B. Gupta, "Surface plasmon resonance based tapered fiber optic sensor with different taper profiles," *Opt. Commun.* **281**(6), 1486–1491 (2008).

Matej Komanec is a research assistant at the Faculty of Electrical Engineering of the Czech Technical University in Prague. He received his MS and PhD degrees in radioelectronics from the Czech Technical University in Prague in 2009 and 2014, respectively. His current research interests include specialty optical fibers, nonlinear optics, optical interconnects, and fiber sensing. He is a member of OSA.

Tomas Martan is a research assistant at the Faculty of Electrical Engineering of the Czech Technical University in Prague. He received MS and PhD degrees in radioelectronics from the Faculty of Electrical Engineering of the Czech Technical University in Prague in 2001 and 2006, respectively. His current research interests include specialty fibers, optical fiber sensing, optoelectronics, and optical spectroscopy.

Tomas Nemecek is a PhD student at the Faculty of Electrical Engineering of the Czech Technical University in Prague. He received his MS degree in radioelectronics from the Faculty of Electrical Engineering of the Czech Technical University in Prague, in 2013. His current research interests include fiber sensing, specialty fibers, and measurement techniques.

Stanislav Zvanovec has been a professor at the Faculty of Electrical Engineering of the Czech Technical University in Prague since 2014. He received his MS and PhD degrees in radioelectronics from the Faculty of Electrical Engineering of the Czech Technical University in Prague in 2002 and 2006, respectively. His current research interests include fiber sensors and visible light communicatons.

applied optics

Suspended-core microstructured fiber for refractometric detection of liquids

TOMAS NEMECEK,* MATEJ KOMANEC, TOMAS MARTAN, REDWAN AHMAD, AND STANISLAV ZVANOVEC

Department of Electromagnetic Field, Faculty of Electrical Engineering, Czech Technical University in Prague, Technicka 2, 166 27 Prague 6, Czech Republic
**Corresponding author: nemect10@fel.cvut.cz*

Received 6 August 2015; revised 17 September 2015; accepted 17 September 2015; posted 18 September 2015 (Doc. ID 246959); published 14 October 2015

A silica suspended-core microstructured optical fiber sensor for detection of liquids, operating at 1550 nm, is analyzed. The sensing principle is based on the evanescent wave overlap into a tested analyte, which is filled via capillary forces into the cladding holes. Validations for analytes in the refractive index range of 1.35–1.43 are carried out with liquid-analyte-filling-length limits being studied both theoretically and experimentally. We prove, for the first time to our knowledge, that an extreme sensitivity of 342.86 dB/RIU and resolution of 4.4×10^{-5} can be achieved. This sensor represents a high-quality alternative for applications requiring a facile, low-cost solution.

OCIS codes: (280.4788) Optical sensing and sensors; (060.2370) Fiber optics sensors; (060.4005) Microstructured fibers.

http://dx.doi.org/10.1364/AO.54.008899

1. INTRODUCTION

Suspended-core microstructured optical fibers (SC-MOFs) were first presented in 2001 by Monro *et al.* [1] and have been studied and enhanced, achieving core sizes below 1 μm [2] utilizing various glass compositions [3,4] and developing inner surface functionalization [5,6]. SC-MOFs outperform conventional MOFs in terms of significantly increased nonlinearity, leading to extreme broadband supercontinuum generation [4] and enhanced evanescent wave overlap which substantially increases when cladding holes are filled with gases or liquids, making these fibers suitable for sensing purposes [7,8].

Optical sensors based on SC-MOFs have, therefore, attracted great attention due to their applications in hazardous environments for liquid-level [9] monitoring and biological DNA analysis [6]. For these applications the operating principle is, in some cases, based not only on refractometry, but is further evolved to fluorescence [6] or Raman spectroscopy [9]. To achieve enhanced sensitivities and resolution, a theoretical study has been carried out for SC-MOFs with core diameters below 1 μm [8] when considering glass materials. Exposed-core SC-MOFs for liquid filling were presented in [10], while other means were proposed in [11].

Significant sensitivity enhancements were achieved by SC-MOF surface functionalization [6], which demands precise deposition steps of the sensing layer, and by core diameter reduction [8], leading to coupling efficiency issues and waveguide losses. For widespread SC-MOF sensor applications, e.g., in petrochemistry and the automotive industry and for chemical analysis purposes, an easy sensing technique is required. Attenuation-based SC-MOF sensors provide a considerably less complicated solution than, e.g., functionalized-surface [6] or exposed-core [8] SC-MOF fluorescence-based sensors. Moreover attenuation-based SC-MOFs have never been studied in greater detail. This approach was only briefly considered with simulations carried out in [12] as an example of the theoretical limit of the utilized method.

In this paper, we present an attenuation-based SC-MOF liquid sensor analysis for the refractive index (RI) range of 1.35–1.43. Our sensor exploits the refractometric effect based on the enhanced evanescent wave overlap in the SC-MOF cladding holes filled with a tested analyte.

With a selected sensor and optimized measurement method, we achieved extreme sensitivity and resolution without the need for any additional fiber surface functionalization or SC-MOF core diameter reduction. The results provide substantial experimental knowledge in the respective fields of SC-MOF liquid sensors and MOF sensing.

2. EXPERIMENTAL BACKGROUND

The measurement setup is depicted in Fig. 1. A laser source with a wavelength of 1550 nm and output power of 10 mW irradiates polarized light. The laser beam is expanded by a graded-index (GRIN) collimator to 0.5 mm full width at half-maximum (FWHM) and, subsequently, collimated by a 40× objective (NA = 0.65) to the core of the SC-MOF.

1559-128X/15/308899-05$15/0$15.00

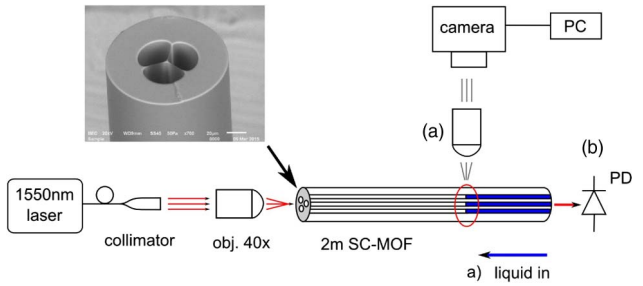

Fig. 1. Measurement setup of the SC-MOF liquid sensor. PD, photodetector; PC, microscope image processing. (a) Step one: filling the liquid analyte into the SC-MOF cladding holes. (b) Step two: attenuation measurement of the analyte-filled SC-MOF. Inset shows the SC-MOF cleave detail.

2 μm 3D stages are utilized to adjust the collimation assembly precisely. Coupling efficiency of over 10% is achieved with this setup. The total length of SC-MOF is 2 m. The analyte-filling length in SC-MOF is visualized and measured by microscope (see Figs. 1 and 4, respectively). Subsequently, an integral photodetector (PD) is used to measure attenuation at the cleaved end of the SC-MOF (filled with analyte).

The employed SC-MOF is composed of undoped silica with a core diameter of 2.75 μm, bridge width of 270 nm, and outer diameter of 122 μm. The radial diameters of the three cladding holes are all 29.73 μm. Material attenuation of an air-filled SC-MOF is 1 dB/m. The SC-MOF cross-section is depicted in Fig. 2(a) with detail of the SC-MOF core shown in Fig. 2(b).

To perform SC-MOF sensitivity analysis, seven liquid analytes are prepared, ranging from 1.3520–1.4269 RI with a continuous step of approximately 0.01 RI. Table 1 summarizes the prepared analytes with their RIs at 1550 nm, and these values are verified by an Abbe refractometer at 632 nm (recalculated to 1550 nm, employing refractive-index equations for each particular analyte).

Light coupled into the SC-MOF core is strongly guided thanks to the silica–air RI difference, and there is minimal evanescent wave overlap in the cladding holes. As the cladding holes are filled with analytes, the RI difference decreases and the evanescent wave overlap is enhanced, which is analyzed using COMSOL software for our specific SC-MOF (results depicted in Fig. 3).

The viscosity of selected analytes makes it possible to use capillary forces for filling. The main advantage of this technique

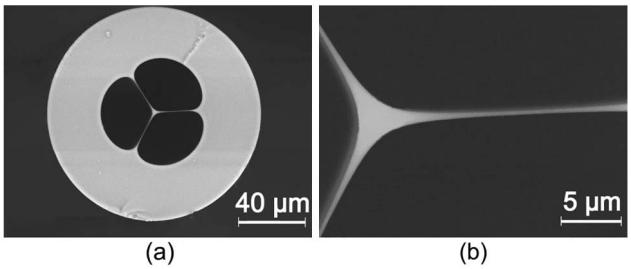

Fig. 2. SC-MOF scanning electron microscope photographs. (a) SC-MOF cross-section. (b) Detail of the SC-MOF core.

Table 1. Refractive Indices of Utilized Analytes at 1550 nm

Analyte	Denomination	RI
Ethyl alcohol	ETOH	1.3520
Isopropyl alcohol	IPA	1.3738
75% IPA + 25% EG	IPA75EG	1.3861
50% IPA + 50% EG	IPA50EG	1.3970
25% IPA + 75% EG	IPA25EG	1.4086
Ethylene glycol	EG	1.4204
76% Glycerol + 24% H20	GLY76H2O	1.4269

is that only a small amount of analyte, specifically 27.8 nL/cm (one cladding hole area is 925 μm^2), is required.

Filling length limit is set by the analyte properties in our experiment, whereas the whole measurement setup limit is set by the dynamic range, in our case to 45 dB. The maximum filling length F for the SC-MOF can be calculated as

$$F = 2\sigma \cos(\alpha)/\rho r g, \quad (1)$$

where σ represents surface tension, α is the contact angle, ρ is the analyte density, g is acceleration due to gravity, and r is the capillary radius, where we assume a capillary approximation for our SC-MOF cladding holes.

The determined maximum filling length for ethyl alcohol (ETOH) and isopropyl alcohol (IPA) is over 26 cm. For ethylene glycol (EG) and glycerol-water (GLY76H2O), it is possible to fill over 39 cm (the contact angle for both analytes is over 23°, but liquid densities and surface tensions are 1110 kg/m^3 and 48 mN/m for EG and 1290 kg/m^3 and 62.5 mN/m for glycerol).

The measurement setup is referenced with the air-filled SC-MOF for all subsequent measurements (one analyte, all filling lengths). Then SC-MOF is continuously filled with a particular analyte up to 25 mm in length, with a step lower than 5 mm. The filling length is monitored by microscopic side-viewing as shown in Fig. 4, guaranteeing a precise analyte filling length within 0.5 mm. For each filling step, the transmitted power is measured at the photodetector. Each analyte measurement is repeated at least three times to avoid inaccuracies.

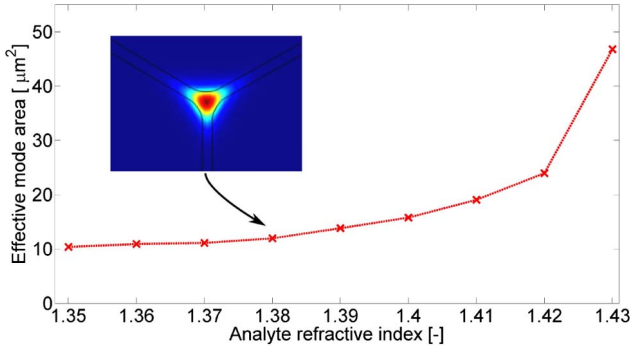

Fig. 3. Simulation of the effective mode area. Inset shows the effective mode area visualization of SC-MOF filled with an analyte of RI = 1.38.

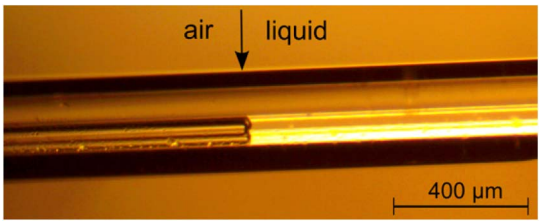

Fig. 4. Microscopic side view of SC-MOF filled with a liquid analyte. Arrow shows the air–analyte boundary.

3. EXPERIMENTAL RESULTS

The measurement results presented in Fig. 5 show loss with respect to the filling length F for each prepared liquid analyte, whereas Fig. 6 depicts attenuation dependence on analyte RI. Figures 5 and 6 show increasing sensitivity with increasing analyte RI and filling length, which is in accordance with the simulation results.

Analytes such as GLY76H20 and EG, where the analyte RI is close to the SC-MOF material RI (1.4454 at 1550 nm), show a significant increase in measured sensitivity with respect to filling length—in particular for GLY76H2O, where the first 5 mm filling step causes almost 20 dB loss though, for filling lengths longer than 6 mm, the slope of the loss curve decreases considerably. A similar effect is observed for EG, where loss increases more rapidly at the beginning. These phenomena are

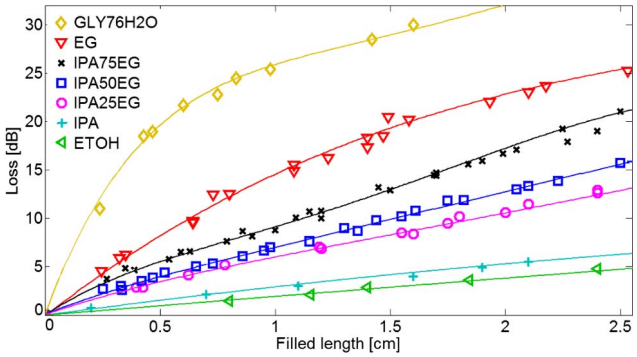

Fig. 5. Measured attenuation of SC-MOF dependent upon analyte filling length for all tested analytes.

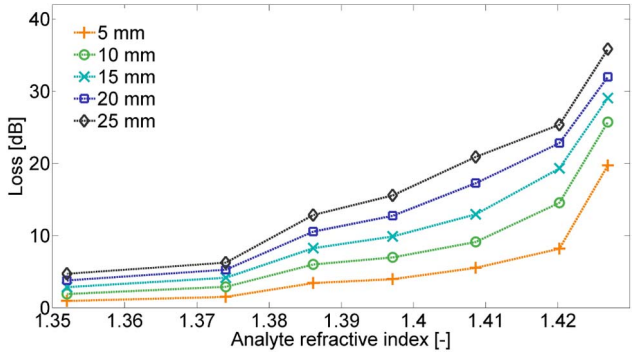

Fig. 6. Measured attenuation of SC-MOF dependent upon refractive index for selected filling lengths.

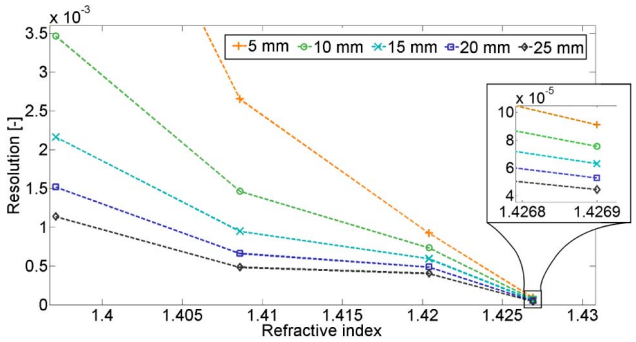

Fig. 7. Resolution of SC-MOF sensor dependent upon analyte refractive index for selected filling length. Inset shows a detail of the resolution values for GLY76H2O.

in contrast to other tested analytes, where trends are observed in near-linear fashion.

The SC-MOF sensor resolution R is calculated as [13]

$$R = \frac{\Delta n}{\Delta I / m_n}, \tag{2}$$

where Δn represents the RI difference between the two closest analytes, ΔI is the intensity difference, and m_n is measurement noise. The results are summarized in Fig. 7.

Our SC-MOF sensor reaches a resolution of 4.4×10^{-5} at RI of 1.4269 for filling length of 25 mm. The longer the filling length, the higher the resolution; therefore, resolution can be modified for sensing purposes, e.g., for a specific RI range. Longer filling lengths imply higher resolution, especially for analytes with 1.35–1.41 RI, where maximum filling lengths are limited by Eq. (1), not by the measurement setup dynamic range.

Sensitivity S is also enumerated for our SC-MOF sensor as [14]

$$S = \frac{\Delta I}{\Delta n}, \tag{3}$$

where Δn represents the RI difference between the two closest analytes; ΔI then stands for intensity difference. A maximal sensitivity of 324.86 dB/RIU (1341.61 μW/RIU), for filling length 25 mm at RI of 1.4269, has been achieved. For RI 1.43–1.44, sensitivity is predicted to increase as the dynamic range poses the limit.

A comparison to published results is provided in Table 2. So far, published results are based on several different methods of RI measurement: a RI fiber sensor based on a tilted fiber Bragg grating (FBG) interacting with multimode fiber [15], a RI sensor which consists of a combination of an intermodal photonic crystal fiber interferometer as a sensing head and FBG as a demodulating element [14], a sensing architecture consisting of a two-core chirped MOF [12], a sensor based on multimode interference (MMI) in the multimode fiber core section sandwiched between two single-mode fibers [16], a sensor based on MMI in the fiber tip [17], a laser-micromachined Fabry–Perot optical fiber tip sensor [18], a sensor based on Fresnel reflection modulated by Fabry–Perot interference [19], and an all-silica miniature dual-parameter fiber-optic Fabry–Perot sensors [20,21].

Table 2. Comparison of our Results from SC-MOF Liquid Sensor with State-of-Art Liquid Sensor References

References	RI	Sensitivity	Resolution (RIU)
[15]	1.37–1.43	28.5 μW/RIU	–
[14]	1.36–1.39	679 μW/RIU	1.5×10^{-5}
[12]	1.42	300/RIU	3×10^{-6}
[16]	1.38–1.45	300.4 dB/RIU	3.3×10^{-5}
[17]	1.33–1.38	110 dB/RIU	2.2×10^{-4}
[18]	1.33–1.441	27 dB/RI	3.7×10^{-5}
[19]	1.314–1.365	205 dB/RI	5×10^{-6}
[20][a]	1.38–1.45	1027 nm/RIU	$\sim 10^{-7}$
[21][a]	1.320–1.325	830 nm/RIU	2×10^{-5}
Our SC-MOF sensor			
	1.4269	1341.61 μW/RIU	4.4×10^{-5}
	1.4269	342.86 dB/RIU	4.4×10^{-5}

[a]Wavelength-shift based sensors.

In comparison with [17], without considering RI ranges, our maximal resolution is one order better and we also provide higher sensitivity. With similar RI range, Wang and Farrell [16] achieved comparable resolutions to our SC-MOF sensor. Slightly better resolution is provided by [14] and one order better resolution was presented in [12], but with a significantly more demanding sensor fabrication process and a complex measurement configuration. The best resolution is provided by the wavelength-shift-based sensor [20] for the major segment of the RI range; on the other hand, this approach employs spectral analysis.

The sensitivity achieved is a significant improvement over previously published results [14,16], in particular 47× higher sensitivity than [15] and 3× higher than [17] if we compare only the same RI ranges. This shows the remarkable sensing potential of SC-MOF and the possibility of further applications when detecting various analytes.

To acquire sufficient sensitivity and resolution for high-RI (≥1.42) analytes such as EG and GLY76H20, the optimal filling length is from 0.5 to 10 mm. For lower-RI (1.35–1.41) analytes, including IPA/EG mixtures and ETOH, it is desirable to increase the filling length as much as possible with respect to the dynamic range of the utilized measurement setup. We have presented experimental results of a liquid-filled SC-MOF sensor. Additionally, simulations of effective mode area evolution with respect to analyte RI were carried out.

4. CONCLUSION

We have analyzed the filling effects of analytes of various RIs and viscosities. The theoretical filling length limits the experimental measurement only when total loss for a particular analyte at the limit length is lower than the dynamic range of the whole measurement setup. This filling-length-limiting effect may occur for analytes in the RI range of 1.35–1.38.

Our measurement method with the SC-MOF sensor precisely distinguishes all tested analytes and has the potential to be used over a wide range of analyte refractive indices. Shorter filling lengths are suitable for measurements of high-RI analytes (EG, GLY76H2O) where the dynamic range could pose a limitation. Liquid analytes with RI less than 1.41 provide linear dependences of sensitivity curves, which is highly desired for real sensor applications.

Funding. Technological Agency of the Czech Republic (TA03010060).

REFERENCES

1. T. M. Monro, W. Belardi, K. Furusawa, J. C. Baggett, N. G. R. Broderick, and D. J. Richardson, "Sensing with microstructured optical fibers," Meas. Sci. Technol. **12**, 854–858 (2001).
2. H. Ebendorff-Heidepriem, S. C. Warren-Smith, and T. M. Monro, "Suspended nanowires: fabrication, design and characterization of fibers with nanoscale cores," Opt. Express **17**, 2646–2657 (2009).
3. X. Feng, F. Poletti, A. Camerlingo, F. Parmigiani, P. Petropoulos, P. Horak, G. M. Ponzo, M. Petrovich, J. D. Shi, W. H. Loh, and D. J. Richardson, "Dispersion controlled highly nonlinear fibers for all optical processing at telecoms wavelengths," Opt. Fiber Technol. **16**, 378–391 (2010).
4. U. Møller, Y. Yu, C. Petersen, X. Gai, L. Brilland, D. Mechin, C. Caillaud, J. Troles, B. Luther-Davies, and O. Bang, "Multi-milliwatt mid-infrared supercontinuum generation in a suspended core chalcogenide fiber," Opt. Express **23**, 3282–3291 (2015).
5. A. Csaki, F. Jahn, I. Latka, T. Henkel, D. Malsch, T. Schneider, K. Schröder, K. Schuster, A. Schwuchow, R. Spittel, D. Zopf, and W. Fritzsche, "Nanoparticle layer deposition for plasmonic tuning of microstructured optical fibers," Small **6**, 2584–2589 (2010).
6. E. Coscelli, M. Sozzi, F. Poli, D. Passaro, A. Cucinotta, S. Selleri, R. Corradini, and R. Marchelli, "Toward a highly specific DNA Biosensor: PNA-modified suspended-core photonic crystal fibers," IEEE J. Sel. Top. Quantum Electron. **16**, 967–972 (2010).
7. A. S. Webb, F. Poletti, D. J. Richardson, and J. K. Sahu, "Suspended-core holey fiber for evanescent-field sensing," Opt. Eng. **46**, 010503 (2007).
8. S. C. Warren-Smith, S. V. Afshar, and T. M. Monro, "Theoretical study of liquid-immersed exposed-core microstructured optical fibers for sensing," Opt. Express **16**, 9034–9045 (2008).
9. G. Tsiminis, F. Chu, S. C. Warren-Smith, N. A. Spooner, and T. M. Monro, "Identification and quantification of explosives in nanolitre solution volumes by Raman spectroscopy in suspended core optical fibers," Sensors **13**, 13163–13177 (2013).
10. S. Warren-Smith, H. Ebendorff-Heidepriem, T. Foo, R. Moore, C. Davis, and T. Monro, "Exposed-core microstructured optical fibers for real-time fluorescence sensing," Opt. Express **17**, 18533–18542 (2009).
11. C. M. B. Cordeiro, C. J. S. de Matos, E. M. dos Santos, A. Bozolan, J. S. K. Ong, T. Facincani, G. Chesini, A. R. Vaz, and C. H. B. Cruz, "Liquid-core, liquid-cladding photonic crystal fibers," Meas. Sci. Technol. **15**, 11207–11212 (2007).
12. P. Torres, E. Reyes-Vera, A. Díez, and M. V. Andrés, "Two-core transversally chirped microstructured optical fiber refractive index sensor," Opt. Lett. **39**, 1593–1596 (2014).
13. N. Díaz-Herrera, D. Viegas, P. A. S. Jorge, F. M. Araújo, J.-L. Santos, M.-C. Navarrete, and A. González-Cano, "Fibre-optic SPR sensor with a FBG interrogation scheme for readout enhancement," Sens. Actuators B **144**, 226–231 (2010).
14. W. Qian, C. C. Chan, C. L. Zhao, Y. Liu, T. Li, L. Hu, K. Ni, and X. Dong, "Photon. crystal fiber refractive index sensor based on a fiber Bragg grating demodulation," Sens. Actuators B **166**, 761–765 (2012).
15. Y. Jin, X. Dong, H. Dong, and C. Shen, "Refractive-index sensor based on tilted fiber Bragg grating interacting with multimode fiber," Microwave Opt. Technol. Lett. **52**, 1375–1377 (2010).
16. Q. Wang and G. Farrell, "All-fiber multimode-interference-based refractometer sensor: proposal and design," Opt. Lett. **31**, 317–319 (2006).
17. S. F. Silva, O. Frazão, J. L. Santos, and F. X. Malcata, "A reflective optical fiber refractometer based on multimode interference," Sens. Actuators B **161**, 88–92 (2012).
18. Z. Ran, Y. Rao, W. Liu, X. Liao, and K. Chiang, "Laser-micromachined Fabry–Perot optical fiber tip sensor for high-resolution temperature-

independent measurement of refractive index," Opt. Express **16**, 2252–2263 (2008).
19. J.-R. Zhao, X.-G. Huang, W.-X. He, and J.-H. Chen, "High-resolution and temperature-insensitive fiber optic refractive index sensor based on Fresnel reflection modulated by Fabry–Perot interference," J. Lightwave Technol. **28**, 2799–2803 (2010).
20. S. Pevec and D. Donlagic, "High resolution, all-fiber, micro-machined sensor for simultaneous measurement of refractive index and temperature," Opt. Express **22**, 16241–16253 (2014).
21. S. Pevec and D. Donlagic, "Miniature fiber-optic sensor for simultaneous measurement of pressure and refractive index," Opt. Lett. **39**, 6221–6224 (2014).

applied optics

Fiber optic refractometric sensors using a semi-ellipsoidal sensing element

Amalia Nallely Castro Martinez,[1,*] Matej Komanec,[2] Tomas Nemecek,[2] Stanislav Zvanovec,[2] and Sergei Khotiaintsev[1]

[1]Faculty of Engineering, Universidad Nacional Autónoma de México, Circuito Escolar sn, Ciudad Universitaria, D.F. 04510, Mexico
[2]Department of Electromagnetic Field, Faculty of Electrical Engineering, Czech Technical University in Prague, Technicka 2, 166 27 Prague 6, Czech Republic
*Corresponding author: ancm_0186@comunidad.unam.mx

Received 4 December 2015; revised 24 January 2016; accepted 24 January 2016; posted 22 February 2016 (Doc. ID 254312); published 24 March 2016

We present theoretical and experimental results for a fiber optic refractometric sensor employing a semi-ellipsoidal sensing element made of polymethyl methacrylate. The double internal reflection of light inside the element provides sensitivity to the refractive index of the external analyte. We demonstrate that the developed sensor, operating at a wavelength of 632 nm, is capable of measurement within a wide range of refractive indices from $n = 1.00$ to $n = 1.47$ with sensitivity over 500 dB/RIU. A comparison of the developed sensor with two more complex refractometric sensors, one based on tapered optical fiber and the other based on suspended-core microstructure optical fiber, is presented.

OCIS codes: (280.4788) Optical sensing and sensors; (060.2370) Fiber optics sensors; (160.5470) Polymers.

http://dx.doi.org/10.1364/AO.55.002574

1. INTRODUCTION

Optical refractometry is an effective tool for evaluating the refractive index (RI) of analytes to derive specific parameters such as density and liquid level for monitoring environmental contamination, leakage of liquids from pipes, and other hazards. The use of a fiber optic refractometric sensor (FORS) reduces the possibility of igniting an explosive or flammable medium, an attractive feature that allows FORS to be deployed in hazardous areas such as refineries and factories within the petrochemical industry. In addition, FORS can be integrated in remote monitoring applications.

FORSs are usually based on an intensity or wavelength measurement as they employ the total or partial reflection of light at the sensing element interface with the analyte. The corresponding reflection coefficient is a measure of the RI of the analyte [1]. The FORS with the external sensing element then employs the internal reflection of light at the surface of the sensing element that is in contact with the analyte. This kind of sensor operates in a wide range of measured analyte RI, for example, its utilization was discussed for cryogenic liquids (e.g., the RI of liquid helium is 1.0245 at 546 nm, and liquid nitrogen's RI is 1.205 at 589 nm [2,3]). This sensor was also proposed for aqueous solutions in order to evaluate the concentration of sugar [4] or salt [5] in industrial applications and for liquid level measurement in tanks and fuel reservoirs [6,7].

Sohn [8] proposed a liquid sensor consisting of a fiber Bragg grating (FBG) connected to a multimode silica fiber, whose operational principle is based on Fresnel's laws of reflection at the end face of a silica fiber; the FBG was used for monitoring the sensor head. The sensor operates in a RI range from 1.33 to 1.47. Kher *et al.* [9] measured the fuel adulteration through a long period grating (LPG) written in a B/Ge doped single-mode fiber with an average sensitivity of 1666 nm/RIU in the RI range from 1.33 to 1.43. Yan *et al.* [10] increased the sensor sensitivity in the RI range from 1.33 to 1.40 using a hybrid grating structure comprising 45° and 81° tilted fiber gratings that have been inscribed into a single-mode fiber. LPG- [10,11] and FBG- [12,13] based sensors allow the measurement of the liquid level. FORSs based on tapered silica optical fiber [14–16] are capable of measuring RI higher than silica's RI. Other structures based on a single-mode fiber (SMF) taper, such as a Michelson interferometer [17] and an asymmetrical fiber Mach–Zehnder interferometer based on a concatenating single-mode abrupt taper and core-offset section [18], can increase the sensitivity by modifying the diameter of the tapered section. Liang *et al.* [19] employed a LPG inscribed in a single-mode fiber that operates in the wide RI range from 1.32 to 1.47. Liquid level measurement of water and glycol was demonstrated via the multimode interference effect [20]. The development of novel optical fibers, such as

microstructure optical fibers (MOFs), brings a new range of possible applications. Webb *et al.* [21] used the cladding holes for acetylene gas sensing.

A FORS with an external sensing element offers certain advantages, none more significant than the ease in which it can be implemented and the wide RI range of measured analyte that is available. There are two standard configurations of FORS featuring an external sensing element: transmission and reflection [13,15,16,22]. A FORS operating in reflection mode brings two advantages when compared to the transmission mode. First, the sensitivity increases because the light travels twice inside the sensing element. Second, only one optical fiber is used in the sensor instead of the two used in the transmission mode. On the other hand, a directional optical device is required in the reflection mode.

We propose a sensor with an external semi-ellipsoidal sensing element that presents a facile approach to RI detection in a broad RI range from 1.00 to 1.47, whereby, with proper adjustment of the sensor parameters, sensitivity can be tuned to the selected RI range and sensitivity level. By employing polymethyl methacrylate (PMMA), material handling and processing is easy, and a low sensor cost is achieved. Our sensor can be utilized for detection of cryogenic fluids, water pollution monitoring, oil quality monitoring, and detection of water and oil leaks.

This paper is organized as follows. First, a FORS employing a semi-ellipsoidal sensing element made of PMMA is proposed, described theoretically, and optimized for measuring purposes. Experiments are then performed to validate its utilization. Finally, we present a comparison of our sensor with two developed FORSs based on a single-mode fiber taper (SMFT) and a suspended core microstructured optical fiber (SC-MOF).

2. THEORETICAL ANALYSIS

The proposed FORS with an external sensing element is formed using a multimode plastic optical fiber (MM-POF) coupled to a semi-ellipsoidal detection element made of PMMA and an aluminum mirror, allowing the doubling of the sensor working area. The proposed setup of the refractometric sensor in its generic form is shown in Fig. 1.

The variables used for the theoretical analysis were defined as: the half-width of the sensing element, a; the MM-POF core diameter, D; the numerical aperture of the MM-POF, NA; and the distance of the vertical axis of the sensing element to the MM-POF axis, L.

To perform analysis, dimensionless variables $\Lambda = L/a$ and $\Phi = D/a$ are introduced. The optical reflectance function of the sensor is given by $R = I_2/I_1$, where I_1 is the intensity of the optical signal transmitted by the fiber, and I_2 represents the optical intensity received by the fiber to account for the possibility of light traveling twice within the sensing element (see Fig. 1). Additionally, the relative reflectance has to be defined as $R^* = R_{\text{ana}}/R_{\text{air}}$, where R_{air} is the reflectance measured in air as an external analyte, and R_{ana} stands for the reflectance measured in an analyte apart from the air.

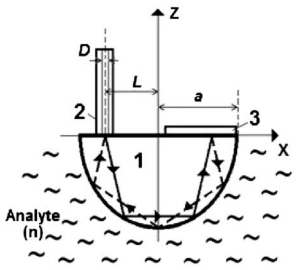

Fig. 1. Schematic of the sensor in reflection mode: 1, sensing element; 2, MM-POF; 3, mirror.

The theoretical analysis of the sensor was carried out by a numerical ray tracing method employing a refractometric fiber optical sensor [(SRFO) for its Spanish acronym: sensor refractométrico en fibras ópticas] and a specially developed computer program. It is possible to use geometrical optics because the dimension of the sensing element is greater than the wavelength of the signal.

SRFO allows us to introduce the physical and geometrical parameters of the optical fibers and detection elements such as the RI, NA, and the equation describing the shape of the sensing element. The mathematical model implemented considers nonpolarized and noncoherent light beams. The beam emerging from the fiber is composed of approximately 100,000 rays. Each ray is analyzed individually, from the angle it leaves the fiber's surface and next when it enters the sensing element along the path within the sensing element until it reaches the reflecting mirror. Next, the ray is analyzed along the return path through the sensing element, coupling again to the fiber or place where it leaves the detector surface elements. The Fresnel reflection coefficient was calculated at each reflection point, and the resulting intensity was determined for each ray. The element reflectance R was calculated by integrating the contributions of all rays reaching the fiber core within the limits of NA.

It was enumerated by a SRFO for three sensing elements of different shapes:

(a) hemisphere, which was presented in our previous works [2,20],
(b) semi-ellipsoidal element A, whose shape is described by the equation

$$x^2 + y^2 + 0.746z^2 = 1, \tag{1}$$

(c) a semi-ellipsoidal element B, whose shape is determined by the equation

$$0.92x^2 + 0.92y^2 + 1.27z^2 = 1. \tag{2}$$

In the simulations, we considered air as an external analyte, and the dimensionless distance Λ was varied in the range of 0.40–0.95 to find the best light coupling into the MM-POF core. Other parameters corresponded to the experimental setup (see Section 3). More specifically, we assumed the step-index optical fiber had a dimensionless core diameter $\Phi = 0.125$ and a $NA = 0.5$, and the same material of the optical fiber core and the sensing element PMMA had a RI of 1.492. The results of numerical modeling are shown in Fig. 2.

The performed simulation allowed us to choose a precise value of Λ to determine the best position of the MM-POF with respect to the center of the sensing element, to reach the best light coupling into the MM-POF, and to evaluate the response of the sensing element to changes of the external RI. The reflectance was then obtained as a function of RI, $R(n)$, for RIs

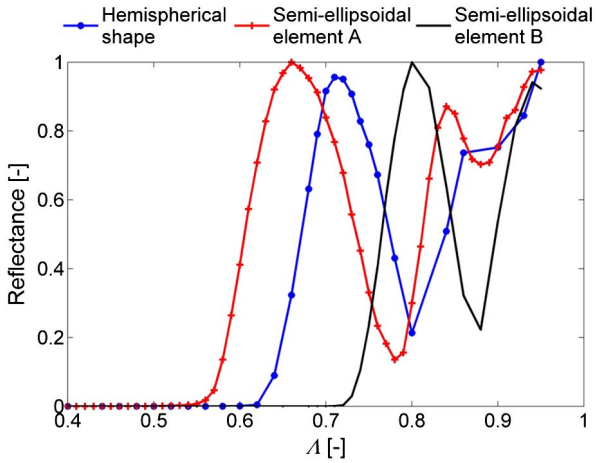

Fig. 2. Derived reflectance of the sensors as a function of dimensionless distance.

Table 1. Values of Λ Selected for Each Sensing Element

Element	Selected Values of Λ
Hemispherical shape	0.70, 0.86, 0.95
Semi-ellipsoidal element A	0.66, 0.84, 0.94
Semi-ellipsoidal element B	0.8, 0.94

ranging from $n = 1.00$ to $n = 1.47$ with increments of 0.005. The selected values of Λ for each sensing element are summarized in Table 1.

Figure 3 presents reflectance as a function of RI for specific values of Λ. It can be demonstrated that the sensing elements are sensitive to RI of the analyte at different intervals of n, indicating that the sensor could be used for detecting liquids with a relatively high RI such as gasoline [15,16] or even cryogenic liquids whose RI is relatively small [2]. Since the primary interest was to detect liquids with a RI within the interval of

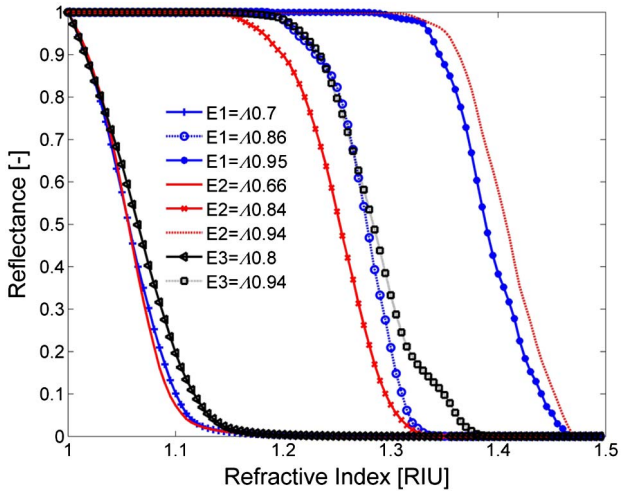

Fig. 3. Reflectance as a function of the refractive index for specific values of Λ. E1, hemispherical shape; E2, semi-ellipsoidal element A; E3, semi-ellipsoidal element B.

1.33–1.44, the hemispherical shape and semi-ellipsoidal element A can both be utilized in the desired RI range. However, the semi-ellipsoidal element A has a more linear response and more uniform sensitivity in comparison to the hemispherical element; therefore, element A better meets the performance requirements given at the beginning of FORS development.

3. EXPERIMENT SETUP

To validate analytical results, an experiment has been performed. The experimental setup (see Fig. 4) included a HeNe laser with a wavelength of 632.8 nm and a power output of 5 mW as the source. A step-index MM-POF (Jiangxi Daishing D-1000-1 made of PMMA with a core diameter of 0.98 mm, NA of 0.5, and a RI of 1.492) was used for connecting the laser source and the sensing element. The MM-POF was mounted on a translation stage that allowed movement along three axes. The semi-ellipsoidal element was fixed to the translation stage, and light was coupled from the MM-POF. An aluminum mirror was glued to the semi-ellipsoidal element. A PT331C phototransistor with a relative spectral sensitivity of ~0.74 at $\lambda =$ 632.8 nm was used as a photodetector. The output of the photodetector was connected to an Arduino UNO, which allowed us to process the data by MatLab.

For the experiment, a developed sensor with a semi-ellipsoidal element A was used (shown in Fig. 5). The semi-ellipsoidal element A, like the MM-POF, was made of PMMA to allow for better coupling from the fiber.

The experiment involved the characterization of the response of the semi-ellipsoidal element to variation of the RI of the analyte. The coupling position from the fiber in terms of Λ was changed to compare the experimental and theoretical data and to validate the sensor reflectance.

Five analytes featuring different RIs (see parameters in Table 2) were selected to evaluate the reflectance of the sensing element measured at a wavelength of 589 nm.

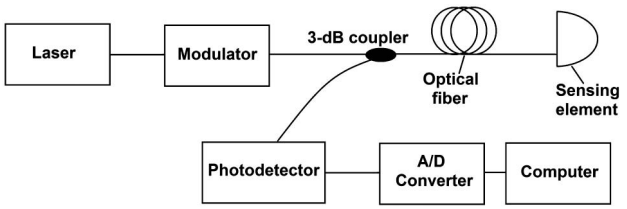

Fig. 4. Block diagram of the experimental setup.

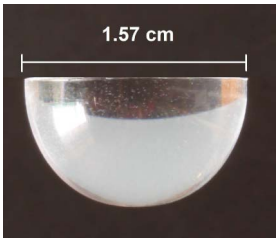

Fig. 5. Semi-ellipsoidal element A.

Table 2. Refractive Indices of Selected Analytes at $\lambda = 589$ nm and 20°C

Analyte	Refractive Index
Water	1.333
Salt water (120 ppm)	1.347
Salt water (350 ppm)	1.375
Antifreeze	1.392
Gasoline	1.432

To evaluate the main advantages of the proposed sensor, its performance was further compared with two other more complex FORSs developed by our team. The first sensor was based on a SMFT, and the second sensor was based on a SC-MOF.

The SMFT sensor was prepared using a flame-heating technique from a conventional silica SMF. The taper was created with two 1-cm-long adiabatic transition regions and with a 1-cm-long taper waist with a diameter of 4.3 μm. The SC-MOF sensor was made of pure silica glass with a core diameter of 2.75 μm, a bridge width of 170 nm, and cladding hole dimensions of 30 × 40 μm. The SC-MOF was precisely cleaved to achieve a perfect cleave with no surface distortion to provide equal capillary forces for all three cladding holes. Both sensors were stored at room temperatures of 22°C–25°C and at a humidity of 35%–45% before the measurements.

Both the SMFT and the SC-MOF sensors were tested with identical analytes, taking into account the wavelength dependence of RIs in both simulations and measurements (e.g., the RI of water $n_{H_2O} = 1.318$ at $\lambda = 1550$ nm and 20°C was calculated by the Cauchy equation [23]). The SMFT sensor was completely immersed in each analyte during the tests. In the case of the SC-MOF, the length of capillaries filled with analytes was 1 cm. A detailed description of the SC-MOF sensor measurement setup can be found in [24], and the SMFT measurement configuration is similar to the one presented in [14], with the modification of a laser source for the one working at 1550 nm, an appropriate photodetector, and single-mode optical fibers. The reference measurements were done with an SMFT sensor in air. Between measurements of particular analytes, each SMFT was first purified in isopropyl alcohol and then dried.

All measurements with the SMFT and SC-MOF were conducted at a wavelength of 1550 nm. We consider the use of different wavelengths completely justified because the semi-ellipsoidal sensor is made of PMMA, which is transparent in the visible and near-IR range. In contrast, the SMFT and SC-MOF sensors operate at longer wavelengths while having lower material attenuation, maintaining the single-mode regime and providing increased evanescent wave overlap. The main purpose was to validate optical sensors within the same RI range.

4. RESULTS

The reflectance function of the semi-ellipsoidal element A was obtained for five analytes with Λ ranging from 0.4 to 1.0 as determined by the previous simulation; note that no light is coupled for $\Lambda < 0.53$. The reflectance in air was the maximum value of reflectance that we used as a reference in sensor characterization.

The experimental results shown in Fig. 6 indicate that our proposed sensor can be set to a specific RI range by modifying the dimensionless parameter Λ. The range up to 0.66 is more suitable for gas measurement; higher values of Λ have to be set for liquid analytes.

The theoretical and experimental results presented in Fig. 7 exhibit a small deviation ($\sigma = 0.035$). We attribute this deviation to finite material absorption, material nonhomogeneity, and the nonperfect shape of the sensing element, which we did not consider in the theoretical analyses.

In the next step, we compared performance of our developed sensor with SMFT and SC-MOF. Furthermore, we added expected sensitivities for other values of Λ. To compare the sensors' performance, the intensity sensitivity parameter was determined as

$$S = \frac{\Delta I}{\Delta n}, \tag{3}$$

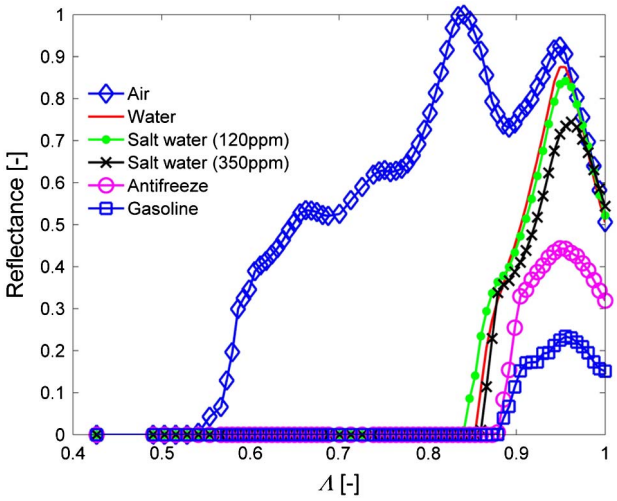

Fig. 6. Reflectance of the semi-ellipsoidal element A for selected analytes as a function of Λ.

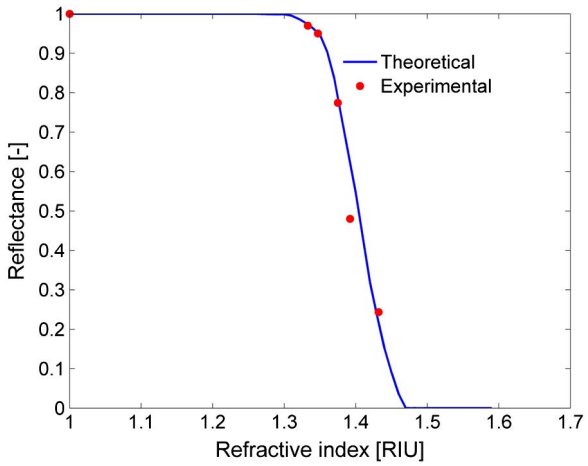

Fig. 7. Theoretical and experimental reflectance function $R(n)$ of the semi-ellipsoidal element under $\Lambda = 0.94$.

where ΔI is the difference between the optical intensity for the two analytes with the closest RI, and Δn is the RI difference. The observed sensitivity of the three sensors $S(n)$ is displayed by graphs in Fig. 8. The inset of Fig. 8 shows the predicted sensitivity of the semi-ellipsoidal sensor for different parameters Λ.

We can observe that the sensor with the semi-ellipsoidal element A can be utilized in the RI range of 1.00–1.47, where for particular regions of interest a specific parameter Λ must be set. For example, the inset in Fig. 8 shows a predicted sensibility of ~200 dB/RIU in the RI range of 1.00–1.20 under $\Lambda = 0.66$, with the peak sensitivity $S > 400$ dB/RIU at the RI of 1.04, thus being suitable for detection of cryogenic fluids.

By changing the Λ parameter to 0.84 (see inset in Fig. 8), the sensitivity increases up to 1500 dB/RIU in the RI range of 1.25–1.32. By further increasing Λ to 0.94, the RI range of operation shifts to 1.33–1.47. The sensor with an external sensing element and $\Lambda = 0.94$ (denoted as a sensor with semi-ellipsoid element A) was afterward compared to the SMFT and SC-MOF sensors.

Our sensor with semi-ellipsoid element A matched the simulation results (as depicted in Fig. 7) and provided a resolution of 3.08×10^{-4} in general laboratory conditions. (The ideal value is approximately one order smaller in the vicinity of RI = 1.40 when considering precise temperature stabilization of the whole measurement setup.)

In the range of 1.33–1.40, we obtained an increase in sensitivity of our sensor from 35 dB/RIU up to 180 dB/RIU, which is comparable to SMFT and SC-MOF sensor sensitivity in the same range. This is a quite good result, given that the sensor with the semi-ellipsoidal element is more simple and easy to fabricate than more complex SMFT and SC-MOF sensors.

The sensitivity range within a RI range of 1.41–1.43 is dominated by SMFT and SC-MOF with sensitivity above 500 dB/RIU for both sensors. The better performance, in comparison to the sensor with the semi-ellipsoidal element A ($S \approx 250$ dB/RIU), is attributed to the fact that the analyte's RI is close to the RI of the sensor material (silica) of both SMFT and SC-MOF.

For the FORS with semi-ellipsoidal sensing element A at Λ of 0.94, the simulations showed that the sensitivity S exponentially increased from ~300 dB/RIU at RIU of 1.42 and exceeded 500 dB/RIU at RIU > 1.452. Some oils have RIs in the range of 1.44–1.47; therefore, the aforementioned FORS sensor can find applications in the oil industry.

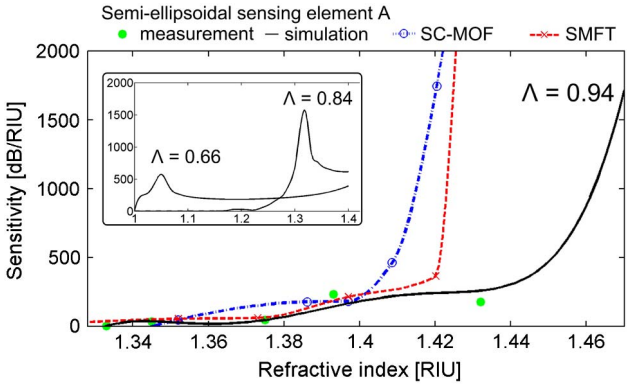

Fig. 8. Sensitivity of developed sensors as a function of the RI of an external analyte.

5. CONCLUSION

We presented a theoretical and simulation background for the development and optimization of a fiber optic refractometric sensor with a semi-ellipsoidal sensing element. The possibility of varying the number of serial reflections at the sensing element surface by changing the position of the optical fiber with respect to the axis of the sensing element was discussed. This change expressed by parameter Λ enables tuning of the working RI range. In particular, under $\Lambda = 0.66$, cryogenic liquids can be detected with high sensitivity (~500 dB/RIU at a RI of 1.04). Based on the aforementioned background, a sensor with a semi-ellipsoidal sensing element and parameter $\Lambda = 0.94$ was implemented and tested with five analytes in the RI range of 1.333–1.432. The difference between the predicted and observed behavior of the sensor was negligible ($\sigma = 0.035$). In the RI range of 1.333–1.392, the sensor exhibited a sensitivity of 180 dB/RIU (contaminated water fits in this particular RI range). The aforementioned sensitivity is close to that of two other, more complex sensors (SMFT and SC-MOF) that we also developed and tested. In the RI range of 1.44–1.47, the sensitivity of the sensor with the semi-ellipsoidal sensing element exceeded 500 dB/RIU (some oils fit in this specified range).

The main advantage of the sensor is its simplicity combined with its high sensitivity to the external RI and a capability to cover a broad measuring range between 1 and 1.47 RIU only by varying the position of the optical fiber with respect to the axis of the sensing element. Potential applications of this sensor include detection of cryogenic fluids, monitoring water pollution and some oils, and, in particular, detection of oil leaks.

Funding. Dirección General Asuntos del Personal Académico, Universidad Nacional Autónoma de México (DGAPA, UNAM) (IT102515); Technologická Agentura České Republiky (TA ČR) (TA03010060); České Vysoké Učení Technické v Praze (ČVUT) (SGS14/190/OHK3/3T/13).

Acknowledgment. A. N. C. M. acknowledges the scholarship of CONACYT, Mexico.

REFERENCES

1. S. Yin and P. Ruffin, *Fiber Optic Sensors* (Wiley, 2002).
2. K. E. Romo-Medrano and S. N. Khotiaintsev, "An optical-fibre refractometric liquid-level sensor for liquid nitrogen," Meas. Sci. Technol. **17**, 998–1004 (2006).
3. T. Chen, Q. Wang, R. Zhang, Y. Lin, and K. P. Chen, "Distributed liquid level sensors using self-heated optical fibers for cryogenic liquid management," Appl. Opt. **51**, 6282–6289 (2012).
4. M. Shao, X. Qiao, H. Fu, H. Li, Z. Jia, and H. Zhou, "Refractive index sensing of SMS fiber structure based Mach-Zehnder interferometer," IEEE Photon. Technol. Lett. **26**, 437–439 (2014).
5. S. Khotiaintsev, K. Khotiaintsev, and A. Garcia-Moreno, "Modeling of the fiber-optical water salinity sensor," in *8th International Conference on Laser and Fiber-Optical Networks Modeling*, Kharkiv, Ukraine, 2006, pp. 36–38.
6. S. Khotiaintsev, "Discrete POF liquid-level sensor for measuring the level of gasoline and detecting water in automobile tanks," in

Proceedings of the 18th International Conference on Plastic Optical Fibers (2009), pp. 1–4.
7. S. Khotiaintsev, E. Llanito-Caudillo, S. Perez-Garcia, and J. Morales-Farah, "Optical-fiber refractometric sensor with semi-cylindrical optical detection element for measuring the level of gasoline," in *Proceedings of the IEEE Conference on Electronics, Robotics and Automotive Mechanics* (IEEE, 2009), pp. 468–473.
8. K. R. Sohn, "Liquid sensors using refractive intensity at the end-face of a glass fiber connected to fiber-Bragg grating," Sens. Actuators A **158**, 193–197 (2010).
9. S. Kher, S. Chaubey, J. Kishore, and S. M. Oak, "Detection of fuel adulteration with high sensitivity using turnaround point long period fiber gratings in B/Ge doped fibers," Sens. J. **13**, 4482–4486 (2013).
10. Z. Yan, C. Mou, Z. Sun, K. Zhou, H. Wang, Y. Wang, and L. Zhang, "Hybrid tilted fiber grating based refractive index and liquid level sensing system," Opt. Commun. **351**, 144–148 (2015).
11. Y. Huang, B. Chen, G. Chen, H. Xiao, and S. U. Khan, "Simultaneous detection of liquid level and refractive index with a long-period fiber grating based sensor device," Meas. Sci. Technol. **24**, 095303 (2013).
12. Q. Jiang, D. Hu, and M. Yang, "Simultaneous measurement of liquid level and surrounding refractive index using tilted fiber Bragg grating," Sens. Actuators A **170**, 62–65 (2011).
13. G. Tsigaridas, D. Polyzos, A. Ioannou, M. Fakis, and P. Persephonis, "Theoretical and experimental study of refractive index sensors based on etched fiber Bragg gratings," Sens. Actuators A **209**, 9–15 (2014).
14. M. Komanec, T. Martan, T. Nemecek, and S. Zvanovec, "Multimode fiber tapers for reproducible refractometric liquid detection," Opt. Eng. **54**, 047102 (2015).
15. D. Wu, Y. Zhao, and O. Wang, *SMF Taper Evanescent Field Based RI Sensor Combined with Fiber Loop Ring Down Technology* (IEEE, 2015).
16. A. Mukherjee, D. Munsi, V. Saxena, R. Rajput, P. Tewari, V. Singh, and P. Gupta-Bhaya, "Characterization of a fiber optic liquid refractive index sensor," Sens. Actuators B **145**, 265–271 (2010).
17. Z. Tian, S. S. Yam, and H. P. Loock, "Refractive index sensor based on an abrupt taper Michelson interferometer in a single-mode fiber," Opt. Lett. **33**, 1105–1107 (2008).
18. G. Yin, S. Lou, and H. Zou, "Refractive index sensor with asymmetrical fiber Mach-Zehnder interferometer based on concatenating single-mode abrupt taper and core-offset section," Opt. Laser Technol. **45**, 294–300 (2013).
19. T. C. Liang, H. S. Huang, and M. H. Chuang, "Study on fiber grating sensors for concentration measurement of cottonseed oil adulteration in pure olive oil," Microelectron. Eng. **148**, 21–24 (2015).
20. J. E. Antonio-Lopez, J. J. Sanchez-Mondragon, P. LiKamWa, and D. A. May-Arrioja, "Fiber-optic sensor for liquid level measurement," Opt. Lett. **36**, 3425–3427 (2011).
21. A. S. Webb, F. Poletti, D. J. Richardson, and J. K. Sahu, "Suspended-core holey fiber for evanescent-field sensing," Opt. Eng. **46**, 010503 (2007).
22. V. Svirid, S. Khotiaintsev, and P. L. Swart, "Novel optical fiber refractometric transducer employing hemispherical detection element," Opt. Eng. **41**, 779–787 (2002).
23. M. Born and E. Wolf, *Principles of Optics* (Pergamon, 1980).
24. T. Nemecek, M. Komanec, M. Martan, R. Ahmad, and S. Zvanovec, "Suspended-core microstructured fiber for refractometric detection of liquids," Appl. Opt. **54**, 8899–8903 (2015).

applied optics

Refractometric detection of liquids using tapered optical fiber and suspended core microstructured fiber: a comparison of methods

T. Martan,* T. Nemecek, M. Komanec, R. Ahmad, and S. Zvanovec

Department of Electromagnetic Field, Faculty of Electrical Engineering, Czech Technical University in Prague, Technicka 2, Prague, Czech Republic
**Corresponding author: martant@fel.cvut.cz*

Received 22 December 2016; revised 13 February 2017; accepted 16 February 2017; posted 16 February 2017 (Doc. ID 283430); published 13 March 2017

Detecting explosive, flammable, or toxic industrial liquids reliably and accurately is a matter of civic responsibility that cannot be treated lightly. Tapered optical fibers (TOFs) and suspended core microstructured optical fibers (SC MOFs) were separately used as sensors of liquids without being compared to each other. We present a highly sensitive time-stable TOF sensor incorporated in the pipeline system for the in-line regime of measurement. This paper is furthermore focused on the comparison of this TOF and SC MOF of similar parameters for the detection of selected liquids. A validated method that incorporates TOF and SC MOF of small core (waist) diameter for refractometric detection is presented. The principle of detection is based on the overlap of an enhanced evanescent wave with a liquid analyte that either fills the cladding holes of the SC MOF or surrounds the waist area of the TOF. Optical power within the evanescent wave for both sensing structures and selected liquid analytes is analyzed. Measurement results concerning TOF and SC MOF are compared. Calculations to ascertain the limit of detection (*LOD*) for each sensor and the sensitivity (*S*) to refractive indices of liquid analytes in the range of 1.4269 to 1.4361 were performed at a wavelength of 1550 nm with the lowest refractive index step of 0.0007. Results affirming that $S = 600.96$ dB/RIU and $LOD = 0.0733$ RIU for the SC MOF and $S = 1143.2$ dB/RIU and *LOD* of 0.0026 RIU for the TOF sensor were achieved, clearly illustrating that TOF-based sensors can reach close to two times greater sensitivity and 30 times higher limit of detection. This paper extends the comparison of the fiber sensors by discussing the potential applications.

OCIS codes: (280.4788) Optical sensing and sensors; (060.2370) Fiber optics sensors; (060.4005) Microstructured fibers.

https://doi.org/10.1364/AO.56.002388

1. INTRODUCTION

Establishing systems for detecting explosive, flammable, or toxic liquids that are both reliable and fireproof are crucial for human safety and for protecting the environment, not to mention their role in controlling industrial chemical processes [1–3]. Detecting such liquids can be done by silica-based optical fibers (fiber optic sensors), which are not flammable and are immune to outer electromagnetic interferences. A variety of optical fibers, including conventional fibers with long-period gratings [4], fiber Bragg gratings [5] or etched fiber Bragg gratings [6,7], polymer clad silica (PCS) fibers [8] combined with coated adsorption layers for enhanced sensitivity or equipped by opto-chemical transducers to be able to distinguish specific chemical substance(s) [9], were used for the detection of liquids. To enhance sensing features, specialized optical fibers, such as tapered optical fibers (TOFs) [10–12] and microstructured optical fibers (MOFs), in particular, suspended core microstructured optical fibers (SC MOFs) [13,14], were designed for this purpose.

The basic principle of detecting liquids by TOFs and SC MOFs hinges upon an evanescent wave overlap in a liquid analyte resulting in a change in the attenuation of the guided light. An SC MOF is characterized by an inner structure consisting of an extremely small core (with its diameter in units of microns or less than one micron) surrounded by three large cladding air holes. Both the small SC MOF core size and a tested liquid filling the cladding holes contribute to an increase in loss due to the evanescent wave propagating in the holes. The SC MOF can be applied as a refractometric sensor for monitoring gasses or liquid analytes and for DNA analysis, as well as being used for fluorescence or Raman spectroscopy purposes [15–18]. A theoretical study has been carried out to capture the enhanced resolution and sensitivity of SC MOFs with core diameters below 1 μm [19]. Such a configuration leads to an

increase in the overlapping of the evanescent wave propagating along the core-cladding boundaries with the analyte. Exposed-core SC MOFs for liquid filling were presented in Ref. [20], while other means of liquid filling, including the filling of a hollow-core PCF with double selectivity resulting in a liquid-core and liquid-cladding fiber, were proposed in Ref. [21]. The SC MOFs, together with inner surface functionalization, e.g., equipped with a silver wire guided in one cladding hole, are suitable for use as surface plasmon resonance (SPR) sensors [22–24].

TOF sensors are usually based on tapered conventional optical fibers, as is the case with single-mode optical fibers (SMFs) or multimode optical fibers [25–27]. TOF can be defined as a fiber heated over a defined length and stretched to an extremely narrow filament resulting in a small diameter. Occasionally, the diameter of the taper waist can also be measured of the order of a few hundreds of nanometers or even below 100 nm in which case the tapers are called optical nanowires or nanotips [28–30]. TOFs are also applied as (bio) sensors in reflection (fiber probes) or transmission arrangements, e.g., in medicine, botany, or industrially, as a fiber optic refractometer, a SPR sensor, or a sensor equipped with an optical chemical transducer for pH measurement [31–33].

This paper introduces a new TOF principle incorporated in pipeline systems for the in-line regime of measurement. In the next step, it provides a comparison of SMF-based TOF and silica-based SC MOF sensors, which were designed, developed, and subsequently analyzed for the detection of selected liquid analytes. In particular, to validate simulation results and to illustrate the comparison better, TOF of comparable parameters to SC MOF, i.e., both having the same core diameters, were prepared. The sensitivity and limits of detection (*LOD*s) of both TOF and SC MOF of similar parameters were analytically and experimentally determined and validated. The comparison of both kinds of fiber sensors assesses additional benefits and drawbacks with regard to future applications.

2. TAPERED OPTICAL FIBER AND SUSPENDED CORE MICROSTRUCTURED OPTICAL FIBER

A. Tapered Optical Fiber

Tapered optical fiber was prepared by the flame brushing technique, i.e., by heating (to approximately 1700°C) a section of the SMF (core/cladding diameter of 9/125 μm) with a hydrogen–oxygen flame. A gas burner is moved from left to right between two fiber holders, while both ends of the fiber (fixed in holders) are pulled in opposite directions. The movement, stretching, and heating processes are fully PC controlled; see Fig. 1(a). The process gives rise to two specific parts of the TOF: the taper waist (defined by the movement of the gas burner) and two taper transition areas. The taper waist lies in the thinnest central section of the TOF and the taper transitions are regions with narrowing diameters between the untapered original fiber and the taper waist; see Fig. 1(b). A photograph of the tapering apparatus for the preparation of the TOF sensor can be seen in Fig. 1(c). The protective tube is prepared before the tapering process (it is laterally drilled for liquid input and output) and SMF is placed through the tube

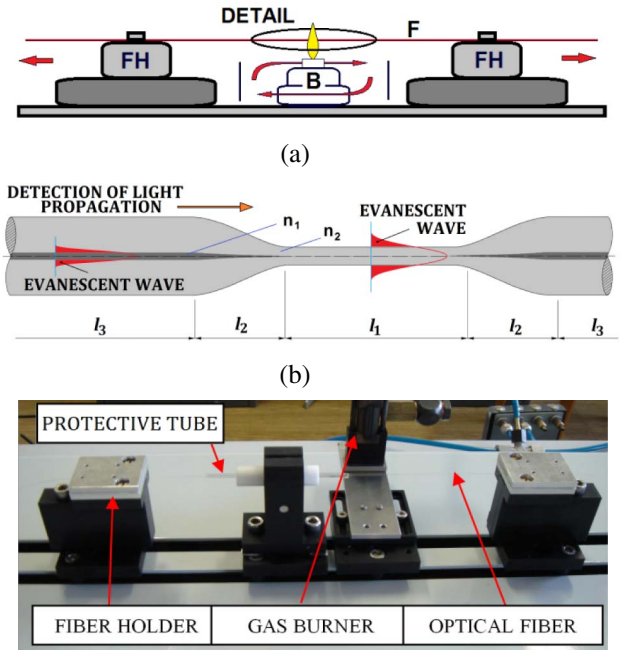

Fig. 1. (a) Schematic picture of the tapering process. F, optical fiber; B, burner; FH, fiber holder. (b) Details of a longitudinal structure of the TOF made from SMF—regions and evanescent wave. l_1, waist region; l_2, transition area; l_3, region of the untapered optical fiber; n_1, refractive index of the core (doped silica); n_2, refractive index of the cladding (pure silica). (c) Photograph of the tapering apparatus for preparation of the TOF sensor.

and fixed in holders; see Fig. 1(c). The TOF is covered by the protective tube and glued after the tapering process.

The TOF was prepared with the following parameters: a tapered waist diameter of 2.75 μm, a length of 5.0 mm, an exponential transition length of 16.0 mm, and the total length of the TOF was 37.0 mm. A scanning electron microscope (SEM) photograph of the longitudinal section of the developed TOF waist and the taper transition is shown in Figs. 2(a) and 2(b),

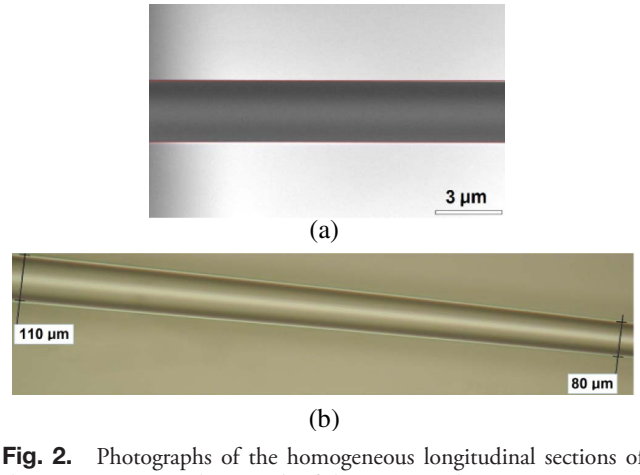

Fig. 2. Photographs of the homogeneous longitudinal sections of the TOF. (a) SEM photograph of the 2.75 μm diameter TOF waist. (b) The taper transition.

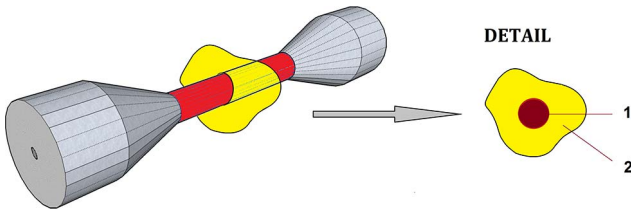

Fig. 3. Longitudinal structure of a TOF made from SMF. Detail: 1, cross section of the TOF waist (sensing) area; 2, the liquid analyte located around the TOF waist (cladding) region.

respectively. Photographs of the waist and the transition section of the TOF are presented to show the homogeneity of its surface. The diameter of the transition gradually (along 16.0 mm) decreases from the untapered part (diameter of 125 μm) to the waist (diameter of 2.75 μm) in order to minimize insertion loss. An example of part of the transition section is shown in Fig. 2(b) from the diameter of 110 μm down to 80 μm.

The germanium-doped core of the original SMF, with refractive index n_1, is narrowed by tapering over the transition area (with the core diameter decreasing) resulting in a tapered waist with the original doped core almost completely negligible. The taper waist is thus of pure silica. From this point of view, both the waist of the TOF and the SC MOF core consist of pure silica material. The TOF waist area is used for sensing because of its enhanced evanescent wave; see Figs. 1(b) and 2(a). In the case of the TOF waist, the original cladding acts as a new core and the surrounding liquid analyte represents a new cladding; see Fig. 3. The length of the TOF waist was optimized to be of similar length as the level of the liquid filled in the cladding holes of the SC MOF. The SMF-based TOF sensor has been designed for a wavelength of 1550 nm due to the low loss of the fused silica and the enhanced overlap of the evanescent wave in this band compared to the visible spectral band for reaching a higher sensitivity.

B. Suspended Core Microstructured Optical Fiber

For the detection, a silica-based SC MOF with a core diameter of 2.75 μm and three cladding holes has been designed for a wavelength of 1550 nm. Detailed descriptions of the inner structure of the SC MOF, in terms of its cross section and longitudinal structure showing particular regions and an evanescent wave, are presented in Figs. 4(a) and 4(b), respectively. Mode intensity distributions within the designed structure of

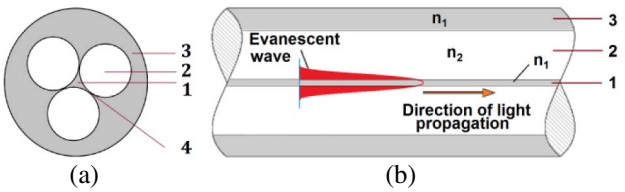

Fig. 4. (a) Cross section of the SC MOF. (b) Longitudinal structure of the SC MOF—regions and evanescent wave: 1, core area; 2, cladding holes; 3, outer silica cladding; 4, silica bridges; n_1, refractive index of the core or refractive index of outer cladding; n_2, refractive index of the cladding holes (filled by a liquid analyte).

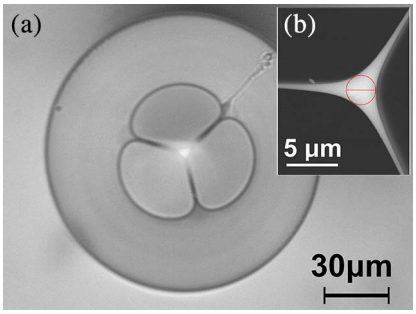

Fig. 5. SC MOF cross section. (a) Microscope photograph of the SC MOF cross section. (b) SEM photograph of the 2.75 μm core area.

the SC MOF were numerically analyzed using the finite element method (FEM) technique.

The SC MOF has been fabricated with a core diameter of 2.75 μm and a bridge thickness of 0.27 μm. The radial diameters of the three cladding holes are all 29.73 μm, i.e., the area of one cladding hole is 925 μm^2. The 125 μm outer diameter of the SC MOF was designed to provide a facile connection to SMFs.

A cross section of the SC MOF with a stripped polymeric jacket is shown in Fig. 5(a). Figure 5(b) shows the Jeol JSM-6510 SEM detail of the core area together with three silica bridges. The inscribed circle represents 2.75 μm diameter of the fiber core and corresponds to the diameter of the fiber core discussed further in this paper.

C. Detection Setup

1. Arrangement with the TOF

The set-up for liquid analyte detection containing the TOF sensor built within the pipeline system is shown in Fig. 6(a).

A superluminescent diode (SLED) radiating with a central wavelength of 1550 nm, a full width at half-maximum bandwidth of 56.0 nm, and maximal output power of 1.4 mW was used as a wideband light source. Light from the SLED was coupled into an SMF patchcord and then guided to the TOF sensor. The liquid analyte was pumped into the pipeline system from "input of liquid" to fill the area of the waist of the TOF sensor in Phase 1; see Fig. 6(a). The light was further guided from the TOF sensor to the second SMF patchcord and attenuation of light was measured by the detector (DET). In Phase 2 (after measuring the liquid analyte), the liquid analyte was pumped out from the area of the TOF sensor

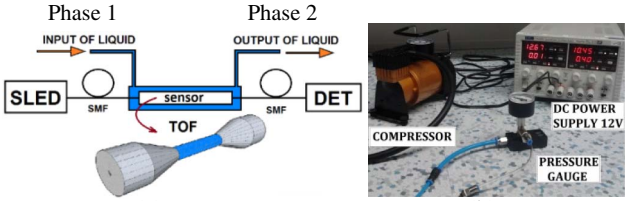

Fig. 6. (a) Schematic of the measurement setup for the detection of liquids using TOF. SLED, superluminescent diode; SMF, single-mode fiber patch cord; TOF, tapered optical fiber sensor; DET, detector. (b) System for liquid analyte pumping.

through "output of liquid"; see Fig. 6(a). An air compressor was used for the liquid analyte pumping in and pumping out utilizing negative pressure. The compressor was connected into the output part of the pipeline system. The pressure was controlled by a pressure gauge; see Fig. 6(b).

2. Arrangement with the SC MOF

The prepared and characterized SC MOF of a length of 1.5 m was used as a sensing element in the measuring setup (see Fig. 7), which consisted of two phases: Phase 1, which includes the air reference measurement [Fig. 7(a)] and the SC MOF filling process [Fig. 7(b)], and Phase 2, which involves the inspection of the liquid level in the SC MOF cladding holes [Fig. 7(c)] and cutting the SC MOF by a cleaver [Fig. 7(d)].

The same SLED as for TOF measurements was connected to the SMF, whereby light was further collimated (COL) and focused 40× by the objective (OBJ), with an NA = 0.65, directly into the core area of a section of the SC MOF; see Fig. 7.

Phase 1 was divided into two steps. First [Fig. 7(a)], the cladding holes of the SC MOF were filled only by air (without a liquid analyte) for reference measurement. The reference sensor attenuation was measured at the end of the SC MOF by the DET—a germanium photodiode with an optical power range of 50 nW to 40 mW and a wavelength range of 700–1800 nm. In the next step [Fig. 7(b)], the cladding holes of the SC MOF were filled by a liquid analyte by capillary forces.

Phase 2 is also divided into two steps. First [Fig. 7(c)], the level of liquid in the SC MOF cladding holes, filled with tested liquid analyte from previous step, was inspected by a microscope equipped with an objective (OBJ) for direct observation and by a digital camera (CAM) connected to a computer (PC) to evaluate data and pictures. Attenuation of light guided into the core of the SC MOF was measured for different liquid analytes by the DET. In the next step [Fig. 7(d)], the SC MOF was cut by a cleaver (CUT) in the region of those cladding holes filled by air (in front of the region filled by a liquid analyte), i.e., part of the SC MOF filled by a measured (tested) analyte is cut and discarded by a fiber cleaver, and the SC MOF is prepared to refill the cladding holes by a liquid analyte for another measurement. The measurement setup was kept at a constant room temperature of 20°C.

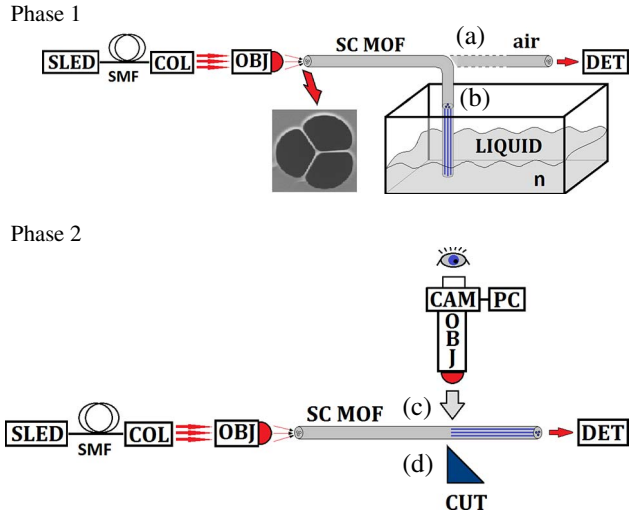

Fig. 7. Schematic of the measurement setup for the detection of liquid analytes using the SC MOF. Phase 1: (a) a section of the SC MOF whose cladding holes are filled by air, and (b) a section of the SC MOF whose cladding holes are filled by liquid analyte (reference). Phase 2: (c) a section of the SC MOF whose cladding holes are filled by a measured liquid analyte, and (d) CUT is the cleaver used for cutting the fiber in the region of the air-filled cladding holes (in the anterior region filled by liquid analyte). SLED, superluminescent diode; SMF, single-mode fiber patch cord; COL, collimator; OBJ, 40× objective used for focusing light; SC MOF, section of the suspended core microstructured optical fiber; OBJ, objective to observe liquid level; CAM, digital camera used for observation; PC, computer; DET, detector.

3. RESULTS

Laboratory testing of approaches employing the TOF or SC MOF on explosive and/or flammable or toxic liquids (e.g., on hydrocarbons, such as gasoline, heptane, hexane, toluene, tetrahydrofuran, or other toxic liquids as dioxane or chloroform) could be harmful to the health of laboratory personnel, so appropriate harmless liquid analytes were prepared to test the TOF or SC MOF sensor. We substituted the targeted dangerous liquids with environmentally friendly azeotropic liquid mixtures of glycerol dissolved in water in different ratios to achieve refractive indices comparable to hydrocarbons or mixtures of hydrocarbons in water. Glycerol (1,2,3-propanetriol) $C_3H_5(OH)_3$ represents a hygroscopic, colorless, viscous liquid (trihydric alcohol) that is not explosive, flammable, or toxic, thereby making it suitable for such tests. The glycerol molecule is polar. Therefore, it is unlimitedly miscible with water due to the presence of hydroxyl groups [34]. Refractive indices of these liquids must be lower than the refractive index of fused silica for a wavelength of 1550 nm. The liquid mixtures featuring refractive indices close to chloroform $CHCl_3$, which is toxic, volatile, and hazardous, or 1,4-Dioxane $C_4H_8O_2$, a volatile solvent used in laboratories, were prepared; see Table 1. Mixtures of glycerol (GLY) of defined concentrations dissolved in water (H_2O) and related refractive indices (RI) measured at 632 nm (at 20°C) and recalculated RI at 1550 nm are listed in Table 1. Values of RI of water (1.3180 at 1550 nm and 20°C) and glycerol (1.4594 at 1550 nm and 20°C) were calculated by the Cauchy equation [35]. Samples of 1-propanol (RI = 1.3738 at 1550 nm) were used as references for measuring these prepared liquid mixtures [36]. Refractive indices of liquid analytes

Table 1. Prepared Mixtures of Glycerol Dissolved in Water of Defined Concentrations and Corresponding Refractive Indices Measured at 632 nm and Recalculated at 1550 nm[a]

Mixture Name	RI at 632 nm	RI at 1550 nm	Concentration
1-propanol	1.3816	1.3738	100% 1-propanol
GLY77.0	1.4383	1.4269	77.0% GLY, 23.0% H_2O
GLY78.0	1.4399	1.4283	78.0% GLY, 22.0% H_2O
GLY80.5	1.4437	1.4318	80.5% GLY, 19.5% H_2O
GLY81.0	1.4445	1.4325	81.0% GLY, 19.0% H_2O
GLY83.5	1.4484	1.4361	83.5% GLY, 16.5% H_2O

[a]The reference is 1-propanol.

were continuously measured (controlled) by a WYA-Z Digital Refractometer working in the full automatic regime at 632 nm for refractive indices nD from 1.3000 to 1.7000, with a resolution of nD = 0.0001, featuring a measurement accuracy of ±0.0002 and recalculated at wavelength 1550 nm according to Ref. [36]. Determination of the refractive index of concentration was done by

$$\mathrm{RI}(m_n)_{1550} = \frac{\mathrm{CON(GLY)}}{100}\mathrm{RI(GLY)}_{1550} + \frac{\mathrm{CON(H_2O)}}{100}\mathrm{RI(H_2O)}_{1550}, \quad (1)$$

where $\mathrm{RI}(m_n)_{1550}$ is the recalculated refractive index at 1550 nm (and m_n stands for the mixture name), CON(GLY) is the percentage concentration of glycerol, $\mathrm{CON(H_2O)}$ is the percentage concentration of water, $\mathrm{RI(GLY)}_{1550}$ is the refractive index of glycerol at 1550 nm, and $\mathrm{RI(H_2O)}_{1550}$ is the refractive index of water at 1550 nm. For example, the recalculation of GLY77.0 at a wavelength of 1550 nm is calculated as

$$\mathrm{RI(GLY77.0)}_{1550} = \frac{77.0\%}{100}1.4594 + \frac{23.0\%}{100}1.3180 = 1.4269.$$

The total difference of the refractive indices in the measurement, i.e., between GLY83.5 and GLY77.0, is 0.0092, and the minimally reached difference of the prepared mixtures is 0.0007; see Table 1.

A. TOF Simulations and Measurements

A prepared TOF, particularly its waist area, was numerically analyzed in COMSOL Multiphysics. The fundamental core mode intensity profiles of the TOF were calculated by using the FEM technique at a wavelength of 1550 nm. Results of these simulations for the TOF waist surrounded by air and by 1-propanol are shown in Fig. 8.

The calculated n_{eff}, A_{eff}, and powers within the evanescent wave in SC MOF cladding holes filled by air, 1-propanol or by GLY77.0 to GLY83.5, are presented in Table 2. Numerical analyses show that the overlap of an evanescent wave (power of evanescent wave in the surrounding analyte) for 1-propanol is almost 11 times higher than the overlap of an evanescent wave for air; see the details in Table 2.

The TOF sensor incorporated in the protective glass tube was tested by filling this tube with a liquid analyte ranging from GLY77.0 to GLY83.5. The detection of other liquids was realized by using the pipeline developed for the insertion of testing liquids; see Fig. 9.

The SMF patchcord was connected to the light source on the input side, the TOF sensor was inside the protective glass tube, and the SMF patchcord was connected to the detector on the output side; see Fig. 9. A schematic picture of the measurement is shown in Fig. 6, which illustrates how the TOF sensor was completely surrounded (immersed) by a measured liquid analyte. After each measurement, the TOF sensor was cleaned by 1-propanol and dried by air, which was also used as a reference for measurements. Temporal changes of attenuation of the TOF based on refractive index changes for GLY77.0 to GLY83.5, together with the reference (1-propanol) and air level, i.e., the reversibility of the operation of the TOF, are shown in Fig. 10.

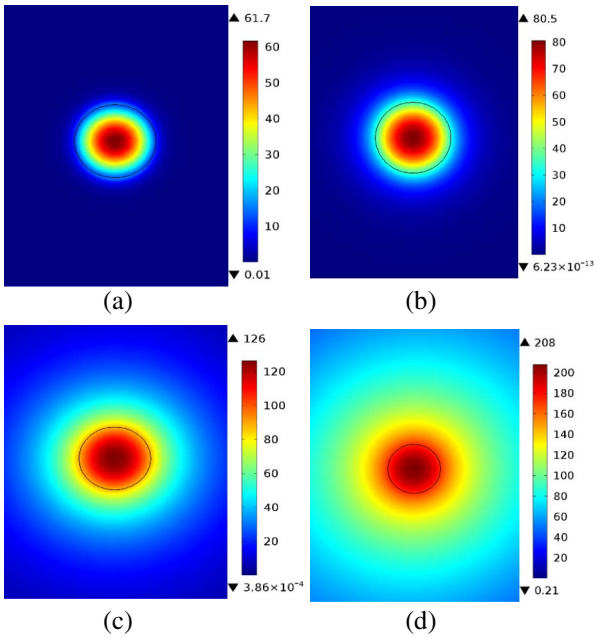

Fig. 8. Calculated, fundamental core mode, and normalized intensity of electric field profiles of the TOF. The taper waist is surrounded by (a) air, (b) 1-propanol, (c) GLY77.0, and (d) GLY83.5. The black ring represents the boundary of the TOF waist.

Table 2. Calculated Optical Power Carried by an Evanescent Wave of the TOF[a]

Analyte	Refractive Index	n_{eff} [–]	A_{eff} [$\mu\mathrm{m}^2$]	Power in Analyte [%]
Air	1.0002	1.3083	4.7114	1.53
1-propanol	1.3738	1.4120	7.3667	16.34
GLY77.0	1.4269	1.4289	21.0252	64.23
GLY78.0	1.4283	1.4299	23.3679	68.22
GLY80.5	1.4318	1.4324	32.9783	79.49
GLY81.0	1.4325	1.4330	35.8749	81.89
GLY83.5	1.4361	1.4362	56.3184	92.66

[a]The taper waist is surrounded by air or 1-propanol and then surrounded by a mixture of glycerol dissolved in water GLY77.0 to GLY83.5.

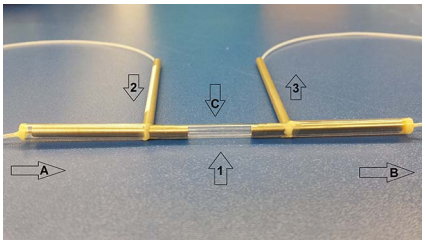

Fig. 9. Photograph of the pipeline with an inbuilt TOF sensor. (A) SMF fiber connected to the SLED source (on the left). (B) SMF connected to the detector (on the right). (C) TOF sensor. 1, protective glass tube filled with a measured liquid; 2, input of liquid; 3, output of liquid.

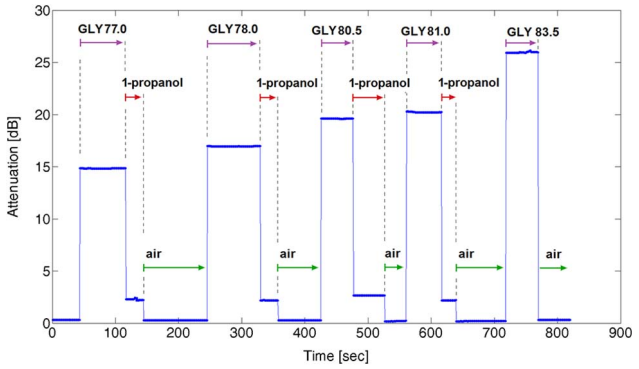

Fig. 10. Temporal changes in the attenuation of the TOF based on refractive index changes (GLY77.0 to GLY83.5). The basic reference level is represented by air and a TOF cleaning is represented by the 1-propanol level.

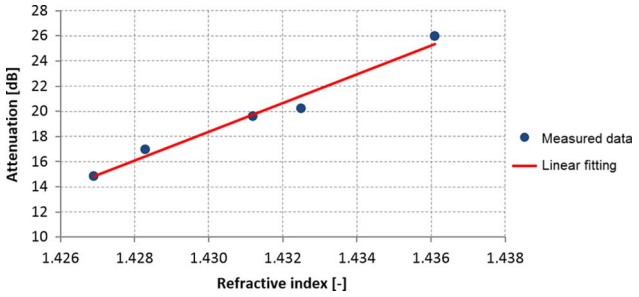

Fig. 11. Calibration curve—dependence of the attenuation on refractive index of the liquid surrounding the TOF (taper waist).

The calibration curve—dependence of attenuation on refractive index changes of the TOF—is shown in Fig. 11 and demonstrates how increasing attenuation for increasing refractive indices of the liquid analyte can be described by the linear dependence over the total measured interval of refractive indices. Please note, for a considerably wider RI range, the linearity of the calibration curve slightly decreases.

Sensitivity S of the TOF was determined mathematically from the slope of the linearly fitted calibration curve (see Fig. 11), and the correlation index R for this curve was calculated using the equation

$$R(X, Y) = \frac{\sum (x - \bar{x})(y - \bar{y})}{\sqrt{\sum (x - \bar{x})^2 \sum (y - \bar{y})^2}}, \quad (2)$$

where $\bar{x}$ and $\bar{y}$ are the mean values of fitted sample points on the x axis and the y axis, respectively.

Sensitivity S was calculated as

$$S = \frac{dY}{dX}. \quad (3)$$

Resulting values of the sensitivity and correlation index in the case of the TOF are $R = 0.9901$ and $S = 1143.2$ dB/RIU, respectively.

A LOD was determined from the noise level and sensitivity S, which is defined by the following equation:

$$LOD = \frac{3 \cdot \text{noise}}{\text{sensitivity}} = \frac{3 \cdot \frac{y+\Delta y}{y}}{S}. \quad (4)$$

LOD was calculated to reach 0.0026 RIU by using Fig. 11 and Eq. (4).

B. SC MOF Simulations and Measurements

The designed structure of the SC MOF was numerically analyzed using COMSOL Multiphysics, version 5.0, simulation software. Fundamental core mode intensity profiles of the SC MOF were calculated by using the FEM technique at a wavelength of 1550 nm. The calculated effective mode index (n_{eff}), effective area (A_{eff}), and powers within the evanescent wave in cladding holes of the SC MOF filled by air, 1-propanol, or by GLY77.0 to GLY83.5 (power in analyte) are presented in Table 3.

Numerical analyses show that an overlap of the evanescent wave (the power carried by the evanescent wave in the cladding holes) for the reference measurement, with cladding holes of the SC MOF filled by 1-propanol, is almost nine times higher than the overlap of an evanescent wave for cladding holes of the SC MOF filled by air; see Table 3.

The power in the cladding holes (evanescent wave overlap in cladding holes) filled by GLY83.5 is 1.5 times higher than the power in the cladding holes filled by GLY77.0 and 5.3 times higher than 1-propanol (reference). The calculated effective areas (A_{eff}) for GLY80.5 and GLY81.0 have high confinement losses, and GLY83.5 has exceedingly high confinement loss. A selected Visualization 1 of the results of these calculations, at 1550 nm for the SC MOF cladding holes filled by air ($n = 1.0002$), 1-propanol ($n = 1.3738$), and filled by GLY77.0 ($n = 1.4269$) and GLY83.5 ($n = 1.4361$), is shown in Fig. 12.

Light coupled into the SC MOF is strongly guided into the core of the fiber thanks to the high difference in the refractive index between the core material and the air-filled cladding holes. It implies that the overlap of an evanescent wave and the sensitivity of the SC MOF is minimal; see Fig. 12(a). When cladding holes are filled by a liquid analyte, whose refractive index is not dissimilar to the refractive index of the silica core, the overlap of the evanescent wave increases as does sensitivity; see Figs. 12(b)–12(d). A photograph of the longitudinal structure of the SC MOF in the area of the boundary between

Table 3. Calculated Effective Mode Index (n_{eff}), Effective Area (A_{eff}), and Optical Power Carried by an Evanescent Wave in the Cladding Holes of the SC MOF Filled by Air, 1-propanol, or by GLY77.0 to GLY83.5

Analyte	Refractive Index [–]	n_{eff} [–]	A_{eff} [μm^2]	Power in Analyte [%]
Air	1.0002	1.4074	6.76	1.33
1-propanol	1.3738	1.4218	11.41	11.58
GLY77.0	1.4269	1.4330	33.92	40.77
GLY78.0	1.4283	1.4336	37.20	43.22
GLY80.5	1.4318	1.4353	52.91	50.25
GLY81.0	1.4325	1.4356	56.84	52.04
GLY83.5	1.4361	1.4377	Too high confinement loss	61.32

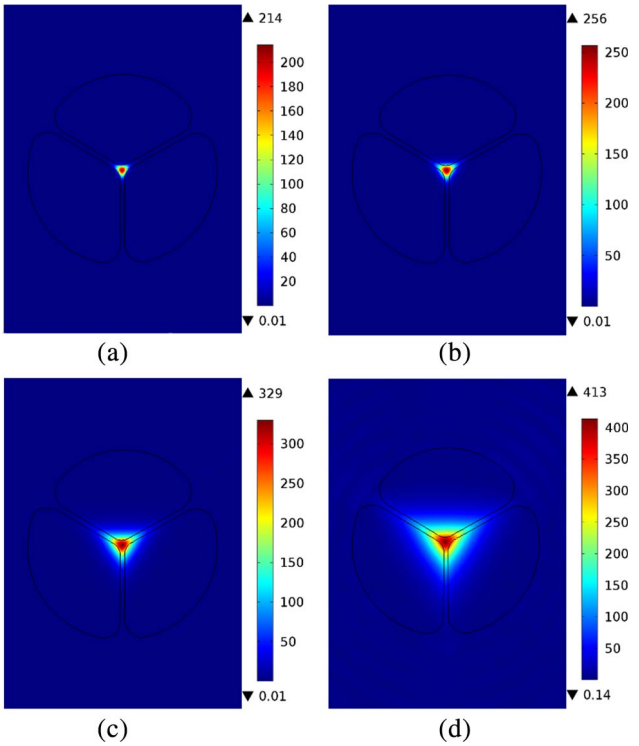

Fig. 12. Calculated fundamental, core mode normalized, intensity of electric field profiles of the SC MOF structure. The SC MOF cladding holes are filled by (a) air, (b) 1-propanol, (c) GLY77.0, and (d) GLY83.5.

air- (left) and liquid- (right) filled cladding holes is shown in Fig. 13.

The attenuation of the SC MOF was measured by the cut-back method using the setup shown in Phase 1 part (a) of Fig. 7. The analyzed attenuation of the air-filled cladding holes of the SC MOF, at a wavelength of 1550 nm, was 1 dB/m. The cladding holes of the SC MOF were then filled in the 5 mm length by the reference liquid (1-propanol) and then by experimental liquid analytes GLY77.0 to GLY83.5; see Table 1. The volume of the measured liquid analyte filled in the length of 5 mm in three cladding holes of the SC MOF is approx. 13.9 nl. In this case, the attenuation of the SC MOF was measured by the cut-back method using the setup shown in Phase 2 parts (a) and (b) of Fig. 7. Cladding holes of the SC MOF were filled by measured liquid

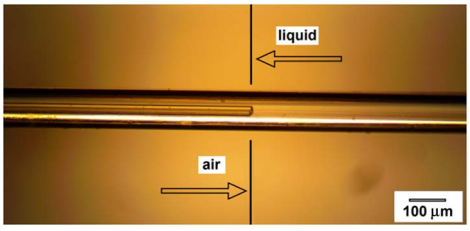

Fig. 13. Photograph of the longitudinal structure of the SC MOF in the region of the boundary between liquid-analyte- (right side) and air- (left side) filled cladding holes.

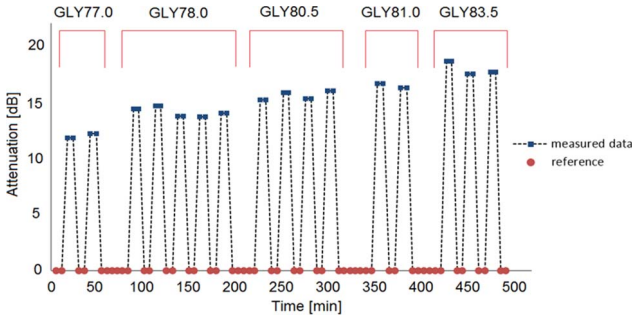

Fig. 14. Temporal changes in the attenuation of the SC MOF based on refractive index change.

analytes via capillary forces due to the relatively low viscosity of the liquid mixtures used.

Temporal changes in the attenuation of the SC MOF, based on the refractive index changes of particular mixtures (from GLY77.0 to GLY83.5), are shown in Fig. 14. Liquids of refractive indices of GLY77.0 to GLY83.5, which were used to fill the cladding holes of the SC MOF, caused changes to the refractive index of the cladding structure and induced changes in the attenuation of the guided light in the core of the SC MOF; see Fig. 14. The attenuation of each liquid was measured several times by repeatedly filling the cladding holes of the SC MOF by GLY77.0 to GLY83.5. Slight changes of attenuation for the given refractive index (GLY77.0 to GLY83.5) could be the result of different capillary forces in each cladding hole caused by a slightly different radial diameter for each hole.

A calibration curve—the dependence of the mean measured values of attenuation on the refractive index changes caused by different concentrations of GLY in water used to fill cladding holes of the SC MOF—is shown in Fig. 15 and demonstrates an increase in attenuation in correlation with higher refractive indices of the liquid analyte. The linear dependence was obtained for the total measured interval of refractive indices.

Using the calibration curve (see Fig. 15) and Eq. (3), the sensitivity S of the SC MOF was determined as 600.96 dB/RIU, and by using Eq. (2), the correlation index R was calculated to as 0.97098.

A LOD was calculated by using Fig. 15 and Eq. (4):

$$LOD = \frac{3 \cdot \frac{14.23+0.46}{14.23}}{600.96} = 0.0733 \text{ [RIU]}.$$

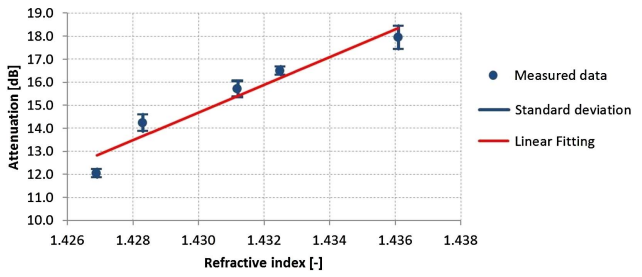

Fig. 15. Calibration curve—the dependence of the measured values of attenuation on refractive indices of SC MOF cladding holes filled with liquid.

4. DISCUSSION

The main advantage of the SC MOF is that it requires a minuscule amount of liquid analyte, specifically 27.8 nl/cm. In our case, the liquid filling length is 5.0 mm, i.e., the equivalent volume of liquid analyte in cladding holes of the SC MOF is 13.9 nl. The SC MOF measurement is more complex as the precise filling length must be controlled by a microscope examining various liquid analytes requires the SC MOF, as shown in Fig. 7 in the case of Phase 2, and to use another SC MOF section. It can be solved, e.g., by Ref. [20]. Calculations show that the effective area of the guided modes of the SC MOF, in particular for liquids from GLY 77 to GLY 83.5, is higher in comparison to the effective area of the guided modes of the TOF waist, implying that the SC MOF has a higher confinement loss, which may be explained by optical power being carried by the evanescent wave that is coupled out via the silica bridges. The measured attenuation for different refractive indices (of liquids) by the SC MOF sensor manifests small fluctuations; see Fig. 14. These measurement inaccuracies could be caused, in comparison with the TOF sensor, by manufacturing imperfections of the structural profile and symmetry of the SC MOF cladding holes. This means that each measurement of each liquid (with different viscosities) is slightly influenced by different capillary forces in each cladding hole, which affects individual filling lengths. The accuracy of measurement could also be affected by the cut-back method; a SC MOF section filled by a measured liquid is cleaved after each measurement. On the other hand, the SC MOF is mechanically more robust because the core is connected by the silica bridges to the outer silica cladding, in comparison to the TOF sensor, which is not protected by the outer cladding.

The TOF does provide a defined length of the waist (sensing area) so that the user is only required to immerse the waist of the TOF into the liquid analyte. Originally, the TOF sensor in the region of the taper waist is more fragile compared to the SC MOF. The fragility of the TOF waist is solved by the pipeline system formed by protective glass tube housing. The tube itself has the following dimensions: a length of 60 mm and an inner diameter of 2 mm, i.e., the inner volume is about 188 μl. However, the inner volume of the protective glass tube can be reduced (up to 16 times) to achieve a lower liquid sample volume and a shorter filling time for the liquid analyte. This can be achieved by inserting the TOF into a capillary fiber, which has an internal diameter >125 μm.

Both fiber optic sensors were stable during the whole measurement campaign. The fluctuation in output power during TOF testing was caused by an imperfect purification of the TOF waist surface (in the protective tube) during measurements when the liquid analytes were changed. Light coupling into the TOF was facile as the TOF is made from SMF. Light coupling into the SC MOF core area required a focusing apparatus because the core diameter was only 2.75 μm. Calculations show that the evanescent wave overlap to the liquid analyte and sensitivity of the TOF sensor is higher than the sensitivity of the SC MOF, which was confirmed by measurement.

A comparison of the price of both fiber sensors (SC MOF and TOF) is noteworthy. Current MOF fiber prices are significantly higher than an ordinary SMF, which is tapered to the desired waist diameter.

5. CONCLUSIONS

This paper focused on the application of a TOF sensor for the purposes of detecting prepared mixtures of glycerol dissolved in water to represent hazardous liquids with identical refractive indices. The new TOF principle incorporated in a pipeline system for the in-line regime of measurement was designed, characterized, and applied to liquid analyte detection. To provide a comparison of the TOF with a similar type of fiber sensor, a SC MOF featuring similar parameters to the TOF sensor was chosen. The SC MOF and TOF were tested on refractive indices in the range of 1.4269–1.4361 and at a wavelength of 1550 nm. Both fiber structures were numerically analyzed and the results of the measurements were compared.

A calculated sensitivity of $S = 600.96$ dB/RIU and a limit of detection $LOD = 0.0733$ RIU were achieved for SC MOF, whereas the TOF sensor achieved $S = 1143.2$ dB/RIU and $LOD = 0.0026$ RIU. The TOF has almost two times higher sensitivity and a 30 times higher limit of detection in comparison to the SC MOF sensor. Such differences are the result of a higher overlap of the evanescent wave to the liquid analyte (1.5 times higher power in an analyte for GLY83.5; see Tables 2 and 3) with respect to the symmetrical, cylindrical shape of the TOF waist (sensing area) when compared to the shape of the SC MOF core (sensing area). The SC MOF sensor can be used for applications where the amount of liquid is limited, as in certain medicinal or botanical situations where one-time detection is possible, and the TOF sensor can be used in applications where the amount of a liquid analyte is readily available, such as when detecting hydrocarbons in fuels or the toluene concentration in water.

Funding. Ceské Vysoké Ucení Technické v Praze (CVUT) (SGS14/190/OHK3/3T/13).

Acknowledgment. We thank SQS Vlaknova Optika A.S. for their close collaboration.

REFERENCES

1. L. C. Shriver-Lake, K. A. Breslin, P. T. Charles, D. W. Conrad, J. P. Golden, and F. S. Ligler, "Detection of TNT in water using an evanescent wave fiber-optic biosensor," Anal. Chem. **67**, 2431–2435 (1995).
2. E. Musayev and S. E. Karlik, "A novel liquid level detection method and its implementation," Sens. Actuators A **109**, 21–24 (2003).
3. R. Falate, R. C. Kamikawachi, M. Müller, H. J. Kalinowski, and J. L. Fabris, "Fiber optic sensors for hydrocarbon detection," Sens. Actuators B **105**, 430–436 (2005).
4. R. Slavik, "Extremely deep long-period fiber grating made with a CO_2 laser," IEEE Photon. Technol. Lett. **18**, 1705–1707 (2006).
5. V. V. Spirin, M. G. Shlyagin, S. V. Miridonov, E. Mitrani, J. Mendieta, and A. Marquez-Lucero, "Fiber optic Bragg-grating-based sensor for liquid hydrocarbon leak detection and localization," Proc. SPIE **3986**, 292–299 (2000).
6. B. N. Shivananju, M. Renilkumar, G. R. Prashanth, S. Asokan, and M. M. Varma, "Detection limit of etched fiber Bragg grating sensors," J. Lightwave Technol. **31**, 2441–2447 (2013).

7. J. Li, H. Wang, L.-P. Sun, Y. Huang, L. Jin, and B.-O. Guan, "Etching Bragg gratings in Panda fibers for the temperature-independent refractive index sensing," Opt. Express **22**, 31917–31923 (2014).
8. K. Cherif, J. Mrazek, S. Hleli, V. Matejec, A. Abdelghani, M. Chomat, N. Jaffrezic-Renault, and I. Kasik, "Detection of aromatic hydrocarbons in air and water by using xerogel layers coated on PCS fibers excited by an inclined collimated beam," Sens. Actuators B **95**, 97–106 (2003).
9. O. S. Wolfbeis, "Fiber-optic chemical sensors and biosensors," Anal. Chem. **72**, 81–90 (2000).
10. J. D. Love, W. M. Henry, W. J. Stewart, R. J. Black, S. Lacroix, and F. Gonthier, "Tapered single-mode fibers and devices. I. Adiabaticity criteria," IEEE Proc. J. Optoelectron. **138**, 343–354 (1991).
11. J. D. Love and W. M. Henry, "Quantifying loss minimisation in single-mode fiber tapers," Electron. Lett. **22**, 912–914 (1986).
12. A. W. Snyder and J. D. Love, *Optical Waveguide Theory* (Chapman & Hall, 1983).
13. T. M. Monro, W. Belardi, K. Furusawa, J. C. Baggett, N. G. R. Broderick, and D. J. Richardson, "Sensing with microstructured optical fibres," Meas. Sci. Technol. **12**, 854–858 (2001).
14. T. Martan, J. Aubrecht, O. Podrazký, V. Matějec, and I. Kašík, "Detection of hydrocarbons using suspended core microstructured optical fiber," Sens. Actuators B **202**, 123–128 (2014).
15. H. Ebendorff-Heidepriem, S. C. Warren-Smith, and T. M. Monro, "Suspended nanowires: fabrication, design and characterization of fibers with nanoscale cores," Opt. Express **17**, 2646–2657 (2009).
16. E. Coscelli, M. Sozzi, F. Poli, D. Passaro, A. Cucinotta, S. Selleri, R. Corradini, and R. Marchelli, "Toward a highly specific DNA biosensor: PNA-modified suspended-core photonic crystal fibers," IEEE J. Sel. Top. Quantum Electron. **16**, 967–972 (2010).
17. A. S. Webb, F. Poletti, D. J. Richardson, and J. K. Sahu, "Suspended-core holey fiber for evanescent-field sensing," Opt. Eng. **46**, 010503 (2007).
18. G. Tsiminis, F. Chu, S. C. Warren-Smith, N. A. Spooner, and T. M. Monro, "Identification and quantification of explosives in nanolitre solution volumes by Raman spectroscopy in suspended core optical fibers," Sensors **13**, 13163–13177 (2013).
19. S. C. Warren-Smith, S. V. Afshar, and T. M. Monro, "Theoretical study of liquid-immersed exposed-core microstructured optical fibers for sensing," Opt. Express **16**, 9034–9045 (2008).
20. S. Warren-Smith, H. Ebendorff-Heidepriem, T. Foo, R. Moore, C. Davis, and T. Monro, "Exposed-core microstructured optical fibers for real-time fluorescence sensing," Opt. Express **17**, 18533–18542 (2009).
21. C. J. S. de Matos, C. M. B. Cordeiro, E. M. dos Santos, J. S. K. Ong, A. Bozolan, and C. H. Brito Cruz, "Liquid-core, liquid-cladding photonic crystal fibers," Opt. Express **15**, 11207–11212 (2007).
22. N. Luan and J. Yao, "Surface plasmon resonance sensor based on exposed-core microstructured optical fiber placed with a silver wire," IEEE Photon. J. **8**, 4800508 (2016).
23. A. R. Hawkins and H. Schmidt, *Handbook of Optofluidics* (CRC Press/Taylor & Francis, 2010).
24. A. Mendez and T. Morse, *Specialty Optical Fibers Handbook* (Academic/Elsevier, 2007).
25. H. Latifi, M. I. Zibaii, S. M. Hosseini, and P. Jorge, "Nonadiabatic tapered optical fiber for biosensor applications," Photon. Sens. **2**, 340–356 (2012).
26. R. J. Black, S. Lacroix, F. Gonthier, and J. D. Love, "Tapered single-mode fibers and devices. II: experimental and theoretical quantification," IEEE Proc. J. Optoelectron. **138**, 355–364 (1991).
27. S. Pricking and H. Giessen, "Tapering fibers with complex shape," Opt. Express **18**, 3426–3437 (2010).
28. T. Vo-Dinh and C. P. Kasili, "Fiber-optic nanosensors for single-cell monitoring," Anal. Bioanal. Chem. **382**, 918–925 (2005).
29. K. Q. Kieu and M. Mansuripur, "Biconical fiber taper sensor," IEEE Photon. Technol. Lett. **18**, 2239–2241 (2006).
30. T. Vo-Dinh and Y. Zhang, "Single-cell monitoring using fiberoptic nanosensors," WIREs Nanomed. Nanobiotechnol. **3**, 79–85 (2011).
31. M. D. Marazuela and M. C. Moreno-Bondi, "Fiber-optic biosensors–an overview," Anal. Bioanal. Chem. **372**, 664–682 (2002).
32. A. M. Valadez, C. A. Lana, S. I. Tu, M. T. Morgan, and A. K. Bhunia, "Evanescent wave fiber optic biosensor for salmonella detection in food," Sensors **9**, 5810–5824 (2009).
33. I. Kasik, O. Podrazky, J. Mrazek, T. Martan, V. Matejec, K. Hoyerova, and M. Kaminek, "*In vivo* optical detection of pH in microscopic tissue samples of *Arabidopsis thaliana*," Mater. Sci. Eng. C **33**, 4809–4815 (2013).
34. http://www.sigmaaldrich.com/MSDS/MSDS/DisplayMSDSPage.do?country=CZ&language=EN-generic&productNumber=G9012&brand=SIAL&PageToGoToURL=http%3A%2F%2Fwww.sigmaaldrich.com%2Fcatalog%2Fproduct%2Fsial%2Fg9012%3Flang%3Den.
35. M. Born and E. Wolf, *Principles of Optics* (Pergamon, 1980).
36. http://refractiveindex.info/?shelf=organic&book=propanol&page=Moutzouris.

Optical Fiber Technology 47 (2019) 187–191

Contents lists available at ScienceDirect

Optical Fiber Technology

journal homepage: www.elsevier.com/locate/yofte

Structurally-modified tapered optical fiber sensors for long-term detection of liquids

Matej Komanec[a,*], Tomas Nemecek[a], Premysl Michal Vidner[a], Tomas Martan[a], Frantisek Lahodny[b], Stanislav Zvanovec[a]

[a] Department of Electromagnetic Field, Faculty of Electrical Engineering, Czech Technical University in Prague, Technicka 2, Prague 6 166 27, Czech Republic
[b] Department of Glass and Ceramics, Faculty of Chemical Technology, University of Chemistry and Technology, Technicka 5, Prague 6 166 27, Czech Republic

ARTICLE INFO

Keywords:
Optical fiber taper
Evanescent-wave
Refractometry
Liquid sensing
Long-term effects

ABSTRACT

We present an improvement of tapered optical fiber (TOF) sensor's response for the detection of liquids, which is achieved by TOF surface structural modification. Our TOF sensors utilize the refractometric principle with enhanced evanescent-wave overlap due to the wavelength of 1550 nm and TOF waist diameters of 4–6 μm. The structural modification is achieved by long-term TOF exposition to hygroscopic liquid analytes and ambient atmosphere. To analyze the structural modification process, long-term as well as proof-of-principle tests have been carried out to evaluate TOF sensors stability in terms of sensitivity and resolution. Maximum sensitivity of over 2100 dB/RIU has been reached when TOF is used to detect a liquid analyte with refractive index of 1.415. Increase of more than 1400 dB/RIU is attributed to the enhanced sensitivity. Sample TOF sensors were then linearly calibrated and have been tested in more than one year-long continuous measurement campaign. Resolution better than $7{\cdot}10^{-4}$ for a refractive index range of from 1.405 to 1.425 with working point drift below $2{\cdot}10^{-4}$ over 12 months period has been achieved. Our results and observations are suitable for reliable, low-cost and application-tailored TOF sensor development.

1. Introduction

Refractometric detection of liquids based on tapered optical fibers (TOFs) with an enhanced evanescent-wave overlap has been extensively studied, and a variety of configurations have been proposed [1–7]. The key difference of these measurement techniques lies in the intensity-based or the wavelength-shift-based measurement techniques. Wavelength-shift-based TOF sensors generally provide better performance in terms of sensitivity and resolution, on the other hand, they require a more complex processing system. Wavelength-shift-based TOF sensors utilizing periodically tapered fibers [1,2] with sensitivities up to 4000 nm/RIU at a refractive index (RI) of 1.45 were presented in [1]. An average sensitivity of 226 nm/RIU in the RI range from 1.33 to 1.38 was achieved in [2]. Microresonators with a sensitivity of 95.5 nm/RIU in the 1.38 to 1.41 RI range were demonstrated in [3]. To enhance sensor sensitivity, the TOF sensor was further shape-tailored in [4] resulting in $8.0{\cdot}10^{-5}$ RIU resolution in the RI range of 1.38–1.44. In-line production monitoring and liquid sensing based on single mode-multimode-single mode (SMS) structures were presented in [5] with a sensitivity of 2946 nm/RIU in the RI range of 1.42–1.43. Surface plasmon resonance (SPR) refractometers have also been developed in parallel while utilizing TOFs [6].

Intensity-based sensors remove the wavelength-shift-based sensor demands on the processing system and the complexity of SPR sensor preparation [6,8]. TOF sensors with ultra-thin tapered fiber tips with sensitivities over 8000%/RIU have been presented in [7]. Surface functionalization by additional layer deposition [9] or interferometric configuration can further increase TOF sensor performance but under cost of increased complexity. We have recently demonstrated a possible application of suspended-core microstructured optical fibers for the detection of liquids with a sensitivity of 342 dB/RIU at RI of 1.43 [10].

To provide a facile approach for the detection of liquid analytes, conventional silica single-mode TOF sensors can be applied as they further diminish the disadvantages of both intensity and wavelength-shift-based sensors, such as utilization of specialty optical fibers [1] and sensors' structure fragility [3,10].

Stability and long-term performance of TOFs have been studied only under laboratory conditions and from a short-term point of view within the range of multi-day time periods. An interesting evaluation of TOF degradation was presented in [11], where the primary contribution to the increase of TOF attenuation is attributed to dust particles attached to the nanotaper surface manifesting as scattering loss. The greatest

* Corresponding author.
E-mail address: komanmat@fel.cvut.cz (M. Komanec).

https://doi.org/10.1016/j.yofte.2018.11.010
Received 31 August 2018; Received in revised form 3 November 2018; Accepted 9 November 2018

impact was experienced in standard room conditions where, in the case of a TOF with 460 nm waist diameter, dust particles caused almost 10 dB attenuation within a time period of less than 10 h. The effects of humidity were found to be negligible in this study. Crack formations and their degradation effect on TOFs together with the humidity-induced hydrogen-bond formation and further attenuation increase was subsequently summarized in [12] for long microfibers. A 5 dB attenuation increase caused by 18 h long crack formation in a microfiber with a 2 µm waist diameter was observed in [12]. However, none of these publications have described any relation between TOF degradation and sensor performance for the detection of liquids.

This paper presents, for the first time, a long-term evaluation of TOF sensors for refractometric detection of liquids with focus on TOF surface structural modification. We analyze sensitivity enhancement and overall sensor response curve shift. We report on significant sensitivity enhancement, without any need for sol–gel or other functional layer deposition. We study freshly-produced TOF sample versus a structurally-modified TOF sample and we observe similar resolution with a significant shift of the sensors' response curve. Last a linear calibration is applied for selected TOF sensors, and results from sensor performance tests over more than a year-period of continuous measurement are discussed.

2. Sample preparation and measurement setup

Conventional silica single-mode fiber (SMF-28e, G.652) with 8.3/125 µm core/cladding diameters was chosen as the source fiber for development of TOF sensor samples. We used the flame-heating technique and aimed for a reproducible output. Flame temperature T_f, hydrogen generator temperature T_{HG}, room humidity R_H and ambient temperature T_a were controlled during the tapering process, while initial T_{HG} was kept constant for each singular sample. Fluctuations were kept at $\triangle T_a < 0.1$ °C and $\triangle R_H < 0.1\%$.

For the purposes of the long-term analysis, we produced two TOF sample series with the waist length of 10 mm and with waist diameters w_D of 4.5 µm and 5.5 µm (over 25 TOF samples in both series). The waist diameter deviations were kept under 10% for both series, which was verified by a scanning-electron microscope. TOF samples were then stored in normal conditions i.e., T_a = 22–25 °C and R_H = 35–45%.

The measurement configuration is depicted in Fig. 1. An integrated distributed-feedback laser diode (LD) emitted at 1550 nm. LD signal was divided via a 3 dB coupler to two outputs and two TOF sensor samples were placed between the source and detectors in order to measure both TOF sensor samples simultaneously (in the same liquid analyte) and to both verify performance and exclude temperature discrepancies. Two InGaAs PIN photodiodes (DET) were incorporated altogether with LD into a single stabilized monitoring system to cover both instantaneous and continuous data-readout statistics. All FC/APC connectors were fixed. We have furthermore analyzed long-term

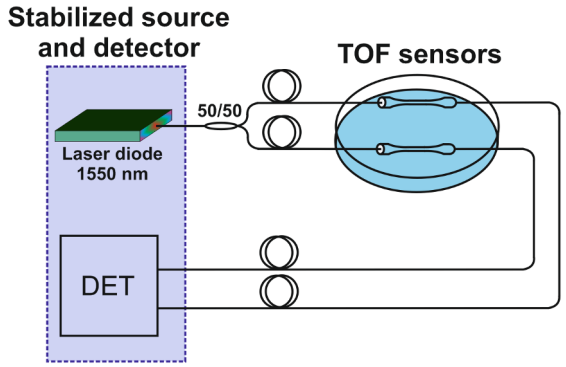

Fig. 1. Measurement configuration for the analysis of TOF sensor sample performance in selected liquid analytes.; DET – two InGaAs PIN photodetectors.

stability of the measurement configuration during a 3 weeks-long campaign and verified that our system is stable without any degradation. The measurement system dynamic range was limited to around 50 dB.

Laboratory testing of explosive or toxic liquids (e.g. hydrocarbons such as gasoline, toluene, or other toxic liquids as dioxane or chloroform) could be harmful to the health, so appropriate harmless liquid analytes were prepared to test our TOF samples. We substituted the above-mentioned hazardous liquids with environmentally friendly azeotropic mixtures of glycerol (GLY) dissolved in water to achieve refractive indices comparable to hydrocarbons or mixtures of hydrocarbons. Glycerol (1,2,3-Propanetriol) $C_3H_5(OH)_3$ represents a hygroscopic, colorless, viscous liquid (trihydric alcohol) which is neither explosive, flammable nor toxic, thereby suitable for such tests. The glycerol molecule is polar, therefore, it is unlimitedly miscible with H_2O. Mixtures of GLY with H_2O of defined concentrations were related via RI, which was measured at 632 nm (at 20 °C) and recalculated to RI at 1550 nm. Refractive index values at 1550 nm and 20 °C are for water 1.3180 and for glycerol 1.4594. Refractive indices of liquid analytes were continuously monitored with a digital refractometer. Refractive index of the GLY-H_2O mixture was then calculated as:

$$RI_{Mix,1550} = \frac{Con_{GLY}}{100} \cdot RI_{GLY,1550} + \frac{Con_{H20}}{100} \cdot RI_{H_20,1550}, \quad (1)$$

where $RI_{Mix,1550}$ is the recalculated refractive index of the GLY-H_2O mixture at 1550 nm, Con_{GLY} and Con_{H2O} represent the percentage concentration of both liquids and finally $RI_{GLY,1550}$ and $RI_{H2O,1550}$ are the refractive indices of both liquids at 1550 nm.

3. TOF sensitivity-modification process

First, we measured a randomly selected TOF sample with w_D = 5.20 µm immediately after the production. The second measurement was carried out after 18 months (meanwhile the TOF sample was stored in standard room conditions). Before both measurements we perfectly purified the TOF sample using several isopropyl-alcohol (IPA) purification cycles to achieve a stable performance (especially after 18 months to remove all dust particles on the TOF surface).

The test was performed on three selected liquid analytes, IPA (RI = 1.374), Ethylene–glycol (EG, RI = 1.420) and their 50/50 mixture (RI = 1.397). Measurement results are summarized in Table 1. Note 13.6 dB higher attenuation when submerged in EG after 18 months (16.7 dB) with respect to the attenuation value just after production (3.1 dB). This attenuation increase is attributed to the surface structural modification of the TOF sample.

The origin of this phenomenon can be understood as a multi-step process. First, optical fibers are formed by extremely pure silica, thus no alkali ions are present, so leaching can be neglected. The starting conditions are defined by the tapering process carried out by the flame-heating technique using a hydrogen-based flame, which causes H^+ and OH^- ions to penetrate into the TOF where concentration decreases in relation to the distance from the TOF surface. Only a few ppm of H_2O content can result in the OH^- ion formation process, where such a low H_2O content is already present after fiber manufacturing [13].

Tapering of silica fibers is achieved by laterally stretching the fiber. The stretching assists in breaking molecular bonds by distorting the SiO_2 tetrahedral structure. Thus non-bridging oxygen atoms are formed,

Table 1
Attenuation of a TOF sample after production and after 18 months of exposition to ambient atmosphere, measured in three liquid analytes at 1550 nm.

Analyte RI	After production (dB)	After 18 months (dB)
1.374	0.4	6.0
1.397	1.1	10.2
1.420	3.1	16.7

bound by one covalent bond to the glass network and holding one negative charge to compensate for the positive ions nearby [14]. The fiber is then less resistant to humidity effects [15].

These effects contribute to the modification of the TOF surface layer, with regard to hydrogen-bonding processes, resulting in a sol–gel layer formation. Note, that this sol–gel layer is formed from the fiber itself, due to the material change in the fiber surface layer, which is completely different from the well-known methods of sol–gel and other functional layer deposition on the fiber surface [9,16].

In the first step, a layer similar to a sol–gel is formed and gradually grows in thickness (in direction towards the TOF core) until equilibrium state is achieved, when TOF is exposed to a humid atmosphere, or submerged into an analyte (presuming the liquid analyte contains water or is able to form OH^- ions). Typically, the sol–gel layer thickness is in the order of nanometers. The sol–gel layer's physical properties differ from the pure silica glass material, in particular refractive index is lower [17]. Typically sensor sensitivity is expected to decrease when considering a modified layer on the TOF surface with a lower RI. This assumption is valid until the TOF is dried. Once the TOF is removed from the analyte (or placed in a lower humidity atmosphere), the sol–gel layer dries and micro-cracks develop [12].

The utilization of GLY and EG as liquid analytes further magnifies the effect of sol–gel layer formation as these liquids are highly hygroscopic. In addition, when IPA is used to purify the fibers, it can help even more to increase micro-crack formation. This is based on the fact that IPA (as a 96% alcohol) efficiently binds water, thus drawing the OH^- ions from the sol–gel layer. The effect of submerging/drying was observed for multiple TOF samples resulting in a high increase of attenuation, thus also in TOF sensor sensitivity enhancement and response curve shift, as will be described in the next chapter.

4. Measurement of TOF sensor response based on structural modification

We investigated the TOF sensor response and possibility of sensitivity enhancement on two randomly selected TOF sensor samples, with w_D = 4.80 µm and w_D = 5.50 µm, denoted as Samples A and B, respectively. Sample A was purified immediately after the production without any contact with GLY. Sample B was submerged into GLY immediately after the production, then purified and stored. After 12 months both TOF sensor samples were measured for the first time (such samples are hereafter marked by index 1, i.e., A_1, B_1). Both TOF sensor samples were then purified and stored in the same conditions for additional 6 months, resulting in a total of 18 months prior to the second measurement (indexed as A_2, B_2).

A GLY-H_2O solution was prepared for the measurement. The starting point was set to the RI of 1.435 and the solution was diluted, step-by-step in 19 measurement points, down to the RI of 1.360. For each of these points, refractive index of the mixture was analyzed by the refractometer. Increase in attenuation and thus sensitivity was observed for both TOF sensor samples submerged in the same liquid analytes after 18 months in contrast to the results after 12 months, as presented in Fig. 2.

To provide a comparison of studied TOF sensor samples, sensitivity S was introduced which can be expressed as the ratio of optical intensity difference $\triangle I$ to refractive index difference $\triangle n$ as:

$$S = \frac{\triangle I}{\triangle n} \tag{2}$$

Sensitivity enhancements of up to 1300 dB/RIU and 1400 dB/RIU were reached for Sample A and Sample B, respectively, for a liquid analyte RI of 1.415, when comparing results after 12 and 18 months. The achieved maximum sensitivity values after 18 months of exposure were S = 1920 dB/RIU and S = 2100 dB/RIU for Samples A and B, respectively. This is a significant sensitivity enhancement compared to previous results [18], where the studied TOFs were not sensitivity-enhanced.

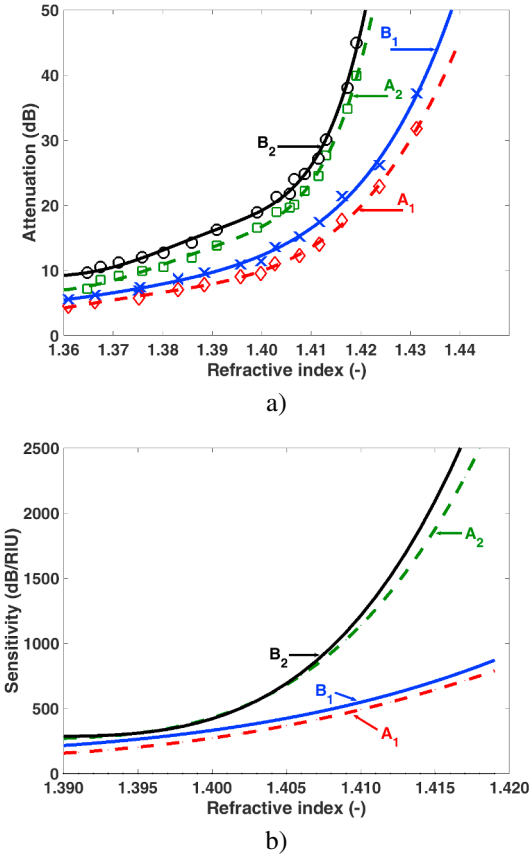

Fig. 2. Measured a) attenuation and b) sensitivity dependences on the liquid analyte RI at 1550 nm, Sample A and Sample B after 12 months of exposure (A_1, B_1) and 18 months of exposure (A_2, B_2).

Please note an interesting point of the TOF surface structural modification: Sample B, with wider w_D, provided greater sensitivity than Sample A (e.g. compare at RI of 1.415 in Fig. 2b). This is in contrast to the general taper theory which states that a thinner TOF should have a larger evanescent-wave overlap and, thus, greater sensitivity. The enhanced sensitivity in the case of Sample B is attributed to the TOF surface structural modification caused by the submersion of the TOF sample into GLY 12 months prior to the first measurement (right after the production).

5. Long-term measurement

Having achieved enhanced sensitivity, we further evaluated the performance of the structurally-modified TOF sensor samples in comparison to freshly-produced TOF sensor samples. Long-term stability of TOFs was studied in terms of sensitivity and resolution. Two selected TOF sensor samples were chosen, both with the identical w_D = 5.40 µm, to exclude the effect of waist diameter. First TOF sensor (Sample C) was picked from a freshly manufactured TOF set and was encapsulated in a protective metallic cover as depicted in Fig. 3. Sample D was structurally-modified (i.e. having an enhanced sensitivity) as described in the previous section. Both TOF sensor samples were purified before the test. Afterwards, continuous measurement was carried out for more than 12 months in total.

As the liquid analyte we used again the GLY-H_2O mixture where for the starting point the analyte was diluted to RI of 1.400 and, via water evaporation, the RI of the analyte continuously increased. Once RI of 1.440 was reached (after several weeks), we added H_2O and set RI again to 1.400 to start a new measurement cycle. The measurement

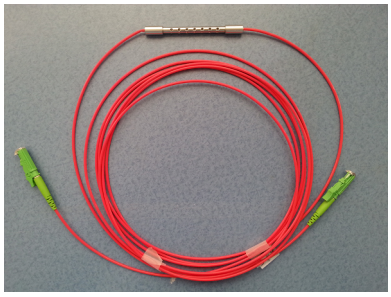

Fig. 3. TOF sensor sample encapsulation in protective metallic tubing, which allows liquid through-flow, equipped with E2000 connectors for easy inclusion in any optical system.

procedure was always the same step-wise process – first we measured actual attenuation of the submerged sensor, then we took a sample of the liquid analyte and measured its refractive index by a refractometer (which was then recalculated to 1550 nm and plotted with regard to attenuation/normalized power).

Calibration was performed for both TOF sensor samples during the first two measurement cycles, representing a relation between measured optical power (attenuation) and corresponding RI of liquid analyte. It is common that for real sensor application, the operation in the sensors' linear regime is desired. Sample C provided linear calibration in the RI region of interest (1.400–1.425). However, Sample D required a two-part linear calibration, where at liquid analyte RI range of 1.400–1.416 we can observe a significant increase of the calibration line steepness (denoted as "linear fit steep"). In the RI range of 1.416–1.425 we observe almost a flat response (denoted as "linear fit slow") for Sample D. Calibration lines with all measured data (over all cycles) are plotted in Fig. 4.

We see a clear trend of the structurally-modified TOF sensor sample, where the linear regime (steep) shifts to lower liquid analyte RIs (below 1.417) and is accompanied by enhanced sensitivity (derivation of the slope). Using the calibration (presented in Fig. 4) we were able to determine the TOF sensor long-term stability in over 12 months of continuous measurement. Sample C showed a standard deviation in measured RI of $6.6{\cdot}10^{-4}$ and drift of the working point (mean value) of only $1.3{\cdot}10^{-4}$. Sample D provided a standard deviation in measured RI of $12{\cdot}10^{-4}$ and drift of the working point of $15{\cdot}10^{-4}$.

To exactly compare both TOF sensor samples, we calculated their resolutions over all acquired data with regard to their calibration. Resolution (R) was calculated as:

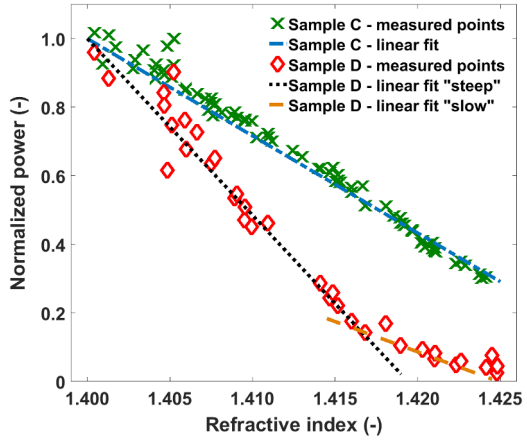

Fig. 4. All measured data points over more than 12 months and linear fits based on the first two measurement cycles further used as calibrations of Sample C (without structural modification) and Sample D (structurally-modified).

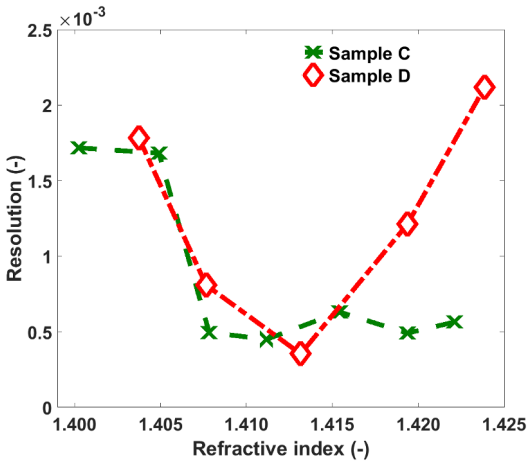

Fig. 5. Resolution of Sample C and Sample D with regard to the refractive index of the liquid analyte.

$$R = \frac{\triangle n}{\triangle I/\sigma_I}, \tag{3}$$

where σ_I stands for the standard deviation of the measured optical power with regard to the calibration.

Fig. 5 presents resolution dependence on the refractive index of the liquid analyte for Sample C and Sample D. For Sample C values around $5{\cdot}10^{-4}$ are experienced in the RI range above 1.405, Sample D has comparable values only in the RI range of 1.406–1.416. On the other hand sensitivity Sample C is 218 dB/RIU compared to Sample D with enhanced sensitivity of 883 dB/RIU for a liquid analyte with RI = 1.415.

6. Conclusion

TOF surface structural modification has been presented and discussed with regards to the detection of liquids. We determined a permanent TOF response curve shift and sensitivity enhancement caused by sol–gel development in the TOF inner surface layer. The structural modification was magnified by repeatedly submerging the TOF sensor sample into hygroscopic liquids (Ethylene–glycol or Glycerol) and then by subsequent drying in Isopropyl-alcohol.

We experimentally verified the sensitivity enhancement with an increase up to 1400 dB/RIU for a liquid analyte with a refractive index of 1.415 for the structurally-modified TOF sensor samples. We thus achieved an overall sensitivity of more than 2100 dB/RIU, which is almost ten times higher than for a freshly produced TOF having a sensitivity around 220 dB/RIU.

For the long-term continuous measurement of over 12 months, selected TOF sensor samples with linear calibration were evaluated. Experimental tests demonstrated high performance stability of a structurally-unmodified TOF sensor sample with an RI standard deviation of $6.6{\cdot}10^{-4}$ and working point drift below $2{\cdot}10^{-4}$. A structurally-modified TOF sensor sample provided significantly higher sensitivity. Working point drift was $15{\cdot}10^{-4}$.

Our results in TOF structural modification show that we can tailor the linear regime of the TOF sensor response curve to a desired RI range. Enhanced sensitivity can be achieved for a particular range of refractive indices. Measurements with duration of less than one month can expect stability of the sensitivity-enhanced TOF sensors in the order of 10^{-4}.

Acknowledgements

This work was supported by CTU project SGS17/182/OHK3/3T/13. The authors would like to thank SQS Vlaknova optika, a.s. for close cooperation.

References

[1] N. Chen, T. Yang, Z. Feng, Y. Chen, C. Lin, Cellular-Dimension Picoliter-Volume Index Microsensing Using Micro-Abrupt-Tapered Fiber Mach-Zehnder Interferometers, IEEE Photonics Technol. Lett. 24 (10) (2012) 842–844.

[2] P. Wang, G. Brambilla, M. Ding, T. Lee, L. Bo, Y. Semenova, Q. Wu, G. Farrell, Enhanced refractometer based on periodically tapered small core singlemode fiber, IEEE Sens. J. 13 (1) (2013) 180–185.

[3] H. Yu, L. Xiong, Z. Chen, Q. Li, X. Yi, Y. Ding, F. Wang, H. Lv, Y. Ding, Solution concentration and refractive index sensing based on polymer microfiber knot resonator, Appl. Phys. Exp. 7 (2) (2014) 022501 .

[4] F. Shi, J. Wang, Y. Zhang, Y. Xia, L. Zhao, Refractive index sensor based on s-tapered photonic crystal fiber, IEEE Photonics Technol. Lett. 25 (4) (2013) 344–347.

[5] C.R. Biazoli, S. Silva, M.A.R. Franco, O. Frazao, C.M.B. Cordeiro, Multimode interference tapered fiber refractive index sensors, Appl. Opt. 51 (24) (2012) 5941–5945.

[6] Y.-C. Kim, W. Peng, S. Banerji, K.S. Booksh, Tapered fiber optic surface plasmon resonance sensor for analyses of vapor and liquid phases, Opt. Lett. 30 (17) (2005) 2218–2220.

[7] Y.-H. Tai, P.-K. Wei, Sensitive liquid refractive index sensors using tapered optical fiber tips, Opt. Lett. 35 (7) (2010) 944–946.

[8] J. Homola, S.S. Yee, G. Gauglitz, Surface plasmon resonance sensors: review, Sens. Actuat. B: Chem. 54 (1) (1999) 3–15.

[9] Z. Qiang, L. Junyang, Y. Yanling, G. Libo, X. Chenyang, Micro double tapered optical fiber sensors based on the evanescent field-effect and surface modification, Optik 125 (17) (2014) 4614–4617.

[10] T. Nemecek, M. Komanec, T. Martan, R. Ahmad, S. Zvanovec, Suspended-core microstructured fiber for refractometric detection of liquids, Appl. Opt. 54 (30) (2015) 8899–8903.

[11] M. Fujiwara, K. Toubaru, S. Takeuchi, Optical transmittance degradation in tapered fibers, Opt. Express 19 (9) (2011) 8596–8601.

[12] S.-M. Chuo, L.A. Wang, Propagation loss, degradation and protective coating of long drawn microfibers, Opt. Commun. 284 (12) (2011) 2825–2828.

[13] M. Tomozawa, D.-L. Kim, V. Lou, Preparation of high purity, low water content fused silica glass, J. Non-Cryst. Solids 296 (1) (2001) 102–106.

[14] W. Wang, P. Lu, L. Han, C. Zhang, L. Wu, P. Guan, R. Su, J. Chen, Structural and electronic properties of peroxy linkage defect and its interconversion in fused silica, J. Non-Cryst. Solids 434 (2016) 96–101.

[15] N. Gougeon, M. Poulain, R.E. Abdi, Evolution of strength silica optical fibers under various moisture conditions, Opt. Mater. 27 (1) (2004) 75–79.

[16] D. Liu, W. Han, A.K. Mallik, J. Yuan, C. Yu, G. Farrell, Y. Semenova, Q. Wu, High sensitivity sol-gel silica coated optical fiber sensor for detection of ammonia in water, Opt. Express 24 (21) (2016) 24179–24187.

[17] Y. Tamar, M. Tzabari, C. Haspel, Y. Sasson, Estimation of the porosity and refractive index of sol-gel silica films using high resolution electron microscopy, Sol. Energy Mater. Sol. Cells 130 (2014) 246–256.

[18] T. Martan, T. Nemecek, M. Komanec, R. Ahmad, S. Zvanovec, Refractometric detection of liquids using tapered optical fiber and suspended core microstructured fiber: a comparison of methods, Appl. Opt. 56 (9) (2017) 2388–2396.

Multimode Chalcogenide Fibers for Evanescent Wave Sensing in the Mid-IR

Elena A. Romanova, Svetlana Korsakova, Matej Komanec, Tomas Nemecek, Alexander Velmuzhov, Maksim Sukhanov, and Vladimir S. Shiryaev

***Abstract*—Evanescent wave spectroscopy in the mid-infrared (MIR) is a powerful tool for remote real-time sensing. Chalcogenide fibers transparent in MIR are considered as a base for creation of a fiber-optical platform for the MIR sensing. In this paper, a rigorous theoretical approach has been applied for the analysis of evanescent modes propagation in a multimode chalcogenide fiber surrounded by an absorbing medium. A role of particular evanescent mode in power delivering through the fiber has been revealed. Strong absorption of water in this spectral range has been shown to be a main factor limiting sensitivity of the evanescent wave sensor. Possibilities of sensitivity enhancement by using waveguiding properties of the fiber have been discussed. The analysis is supported with an experimental measurement of a $[GeSe_4]_{95}I_5$ glass fiber partially immersed in an aqueous acetone solution, in the wavelength range of 2–5 μm.**

***Index Terms*—Optical fiber devices, infrared sensors, glass, electromagnetic propagation.**

I. Introduction

CONTROL of environmental hazards in cities, enterprises and objects of nature is necessary for health protection and safety. A basis of an effective control is real-time monitoring of air and water chemical composition, which gives information about the content of toxic impurities.

Technology for evanescent wave sensing based on silica fibers is limited to the near-infrared (NIR) and visible (VIS) spectral ranges due to the fibers are transparent at the wavelengths $\lambda = 0.4 - 2.0\,\mu\mathrm{m}$. Silica fibers and all supporting technology are already mature in the form of compact sources, detectors, connectors, gain media, which can route and exploit the NIR and VIS. However an unambiguous identification of molecular species is not possible in these spectral ranges. In the mid-infrared (MIR, $\lambda = 3 - 25\,\mu\mathrm{m}$) spectra of inorganic and organic molecular substances exhibit strong fundamental vibration bands much more suitable for spectroscopic analysis than the weak overtone absorption bands in NIR and VIS.

MIR spectroscopy provides a universal tool for quantitative detection of molecular species in gaseous or liquid form. Current state-of-the-art approach utilizes a sample chamber of an IR spectrometer in which any gas or liquid substance can be analyzed. For real-time remote molecular sensing outside of a laboratory, special technological platform is to be developed.

Chalcogenide glasses are known for their high transparency in MIR, which makes them attractive for the design of a MIR sensing platform. Compositional changes of the glass give rise to variations in optical, physical, chemical, thermal and mechanical properties important for subsequent fabrication of optical devices in both fiber and planar waveguide form.

In recent decades, there has been a significant progress in the design of chalcogenide glass fibers and integrated optical devices for chemical sensing [1], [2] that is often based on evanescent-wave absorption in an external medium and subsequent attenuation of the power transmitted by a fiber or waveguide at wavelengths corresponding to characteristic absorption bands of molecules in a studied medium.

For efficient interaction of the evanescent field with absorbing species, an unclad fiber or waveguide are to be used, or some part of the cladding is to be removed over a given sensing length. In NIR, refractive index of a chalcogenide glass ($n \approx 2.40 - 2.80$) is usually much greater than that of aqueous solutions of measureable analytes ($n \approx 1.30 - 1.50$) and propagating radiation is more confined in a chalcogenide fiber core in comparison with a silica one ($n \approx 1.45$). This is a drawback for the evanescent wave spectroscopy where amount of radiation propagating in the external medium is the key parameter.

Multimode chalcogenide fibers were used in [3]–[5] for measurements of the absorbance spectra of various chemical substances in aqueous solutions in MIR spectral range. In the experiments, linear dependencies of the absorbance on the analytes concentration were obtained. The importance of using multimode fibers to provide linear logarithmic output characteristics and high sensitivity was demonstrated in [6], [7] for a straight silica fiber acting as a sensing element in VIS. In [7], a multimode silica fiber with microbends over a length of 60 mm was used, where the evanescent-wave sensor was acting as a

Manuscript received June 1, 2016; revised October 17, 2016; accepted November 14, 2016. Date of publication November 18, 2016; date of current version December 23, 2016. This work was supported in part by the European Commission through the COST Action MP1401 "Advanced fibre laser and coherent source as tools for society, manufacturing, and lifescience"; in part by the Russian Science Foundation under Grant 16-13-10251, and by the Ministry of Education, Youth, and Sports of the Czech Republic under Grant COST LD15803.

E. A. Romanova and S. Korsakova are with the Physics Department, Saratov State University, Saratov 410012 Russia (e-mail: elena_rmnv@yahoo.co.uk; korsakova92@yandex.ru).

M. Komanec and T. Nemecek are with the Faculty of Electrical Engineering, Czech Technical University in Prague, Prague 16636, Czech Republic (e-mail: komanmat@fel.cvut.cz; nemect10@fel.cvut.cz).

A. Velmuzhov, M. Sukhanov, and V. S. Shiryaev are with the G.G. Devyatykh Institute of Chemistry of High-Purity Substances, Russian Academy of Sciences, Nizhny Novgorod 603950, Russia (e-mail: tej4@mail.ru; sukhanov@ihps.nnov.ru; Shiryaev@ihps.nnov.ru).

Color versions of one or more of the figures in this paper are available online at http://ieeexplore.ieee.org.

Digital Object Identifier 10.1109/JSTQE.2016.2630846

logarithmic detector with a dynamic range greater than six orders of magnitude.

In spite of several successful experimental demonstrations of optical fibers utilization for the evanescent-wave spectroscopy, a rigorous theoretical approach based on electrodynamics' calculation of evanescent modes of a fiber with an absorbing cladding has not been yet applied as a possible design tool.

Theoretical consideration of the evanescent-wave absorption was usually based on a simple approach using an assumption that the input power decreases only in a surrounding absorbing medium acting as the fiber cladding but it keeps constant in the fiber core [1], [6], [7]. In this case, normalised transmittance can be evaluated as:

$$T = P/P_0 = \sum_{i=0}^{N} \left(P_1^i + P_2^i \cdot \exp(-\alpha \cdot L)\right) / \sum_{i=0}^{N} \left(P_1^i + P_2^i\right)$$
$$= 1 - (1 - \exp(-\alpha \cdot L)) \cdot \sum_{i=0}^{N} r_2^i \quad (1)$$

Here P and P_0 are the total powers transmitted through the fiber, respectively, with and without an absorbing medium over an unclad section of length L, α represents the bulk absorption coefficient of the medium, N stands for the number of guided modes propagating in the fiber. P_1^i and P_2^i are powers of the i-th guided mode, respectively, inside and outside the fiber core in non-absorbing medium (air), r_2^i is the fraction of the i-th guided mode power outside the fiber core:

$$r_2^i = P_2^i / \sum_{i=0}^{N} \left(P_1^i + P_2^i\right). \quad (2)$$

In an assumption that $\alpha \cdot L << 1$, (1) can be reduced to:

$$T \approx 1 - \alpha \cdot L \sum_{i=0}^{N} r_2^i \approx \exp(-\sigma \cdot L), \quad (3)$$

where σ is the evanescent-wave absorption coefficient:

$$\sigma = \alpha \sum_{i=0}^{N} r_2^i \quad (4)$$

In MIR, the molecular absorption bands are strong and the condition $\alpha \cdot L << 1$ is not generally satisfied.

An approximate approach developed in the framework of geometric optics [8], [9] is relatively simple and efficient for analysis of launch conditions in multimode fibers. However being based on calculation of Fresnel reflections from an absorbing medium in the local plane wave approximation, it fails to describe penetration of radiation outside a fiber core.

Rigorous approach based on electromagnetic theory of optical waveguides [10] is a base of modern designs of fiber-optic devices. In this paper, we apply this approach for analysis of experimental results obtained in measurements of transmittance spectra of radiation passed through a chalcogenide fiber immersed into aqueous acetone solutions. Purpose of this analysis was twofold: first, to describe electromagnetic phenomena in the fiber for a particular experimental situation; second, to reveal specific features of the evanescent wave measurements in MIR spectral range.

II. Evanescent Modes of an Optical Fiber

In electromagnetic theory of optical fibers, complex-valued dielectric constants are used to describe light absorption in a fiber material. If a fiber segment is submerged into an absorbing medium, this medium acts as an absorbing fiber cladding [10]. Then propagation constants of the fiber modes are complex-valued, too, so that all the guided modes become evanescent. Power flow of an evanescent mode along the fiber axis is decreasing, radial and azimuthal components of the power flow in the fiber being non-zero that means constant power leakage outside the fiber core.

Amplitudes of the evanescent modes can be found from radiation launching conditions at the input facet of the fiber. When an input light beam is coaxial with a fiber axis, only azimuthally symmetric modes of the fiber can be excited. Azimuthally symmetric modes of a weakly guiding step-index fiber are known as $\mathrm{HE}_{1m}-$modes [10] with m being a mode radial order. If the difference between refractive indices of the core n_{co} and cladding n_{cl} is large, the weakly guiding approximation is not valid and solutions of the exact characteristic equation:

$$\left\{\frac{J_1'(u_m)}{u_m \cdot J_1(u_m)} + \frac{K_1'(w_m)}{w_m \cdot K_1(w_m)}\right\} \cdot \left\{\frac{J_1'(u_m)}{u_m \cdot J_1(u_m)} + \frac{n_{\mathrm{cl}}^2}{n_{\mathrm{co}}^2} \cdot \frac{K_1'(w_m)}{w_m \cdot K_1(w_m)}\right\} = \left(\frac{\beta_m}{k \cdot n_{\mathrm{co}}}\right)^2 \cdot \left(\frac{V}{u_m \cdot w_m}\right)^4 \quad (5)$$

are to be found. In (5), J_1, K_1 are, respectively, Bessel and Macdonald functions, J_1', K_1' represent derivatives of the functions, u_m and w_m are parameters, which describe transverse profile of the m-th fiber mode, $\beta_m = \sqrt{k^2 n_{\mathrm{co}}^2 - u^2/R^2}$ is a longitudinal propagation constant, $V = k \cdot R \cdot \sqrt{n_{\mathrm{co}}^2 - n_{\mathrm{cl}}^2}$ is the fiber parameter, $k = 2\pi/\lambda$, R stands for the fiber core radius. The refractive indices $n_{\mathrm{co}} = n_{\mathrm{co}}' + i \cdot n_{\mathrm{co}}''$, $n_{\mathrm{cl}} = n_{\mathrm{cl}}' + i \cdot n_{\mathrm{cl}}''$ are complex in general with the nonzero imaginary parts appearing due to material losses in the fiber.

Longitudinal propagation constants $\beta_m = \beta_m' + i \cdot \beta_m''$ of the evanescent modes can be found by numerical solution of (5). Attenuation coefficient $\eta_m = 2\beta_m''$ is related to the m-th fiber mode power decrease along the fiber axis z:

$$P_m(z) = P_{0m} \exp(-\eta_m z) \quad (6)$$

Here P_{0m} is the initial power of an evanescent mode at the fiber input facet, $P_m(z)$ is evaluated as longitudinal component of a power flow. The fraction of an evanescent mode power (2) outside a fiber core is a determining parameter for the attenuation coefficient magnitude. In fact, for each mode this fraction depends on the ratio R/λ [10]. At a given λ, this fraction grows with decrease of the core radius until the mode reaches its cutoff. For a given R, this fraction increases with wavelength.

As guided modes of an infinite dielectric cylinder used as a fiber model are orthogonal they propagate independently of each other and the power flow propagating in a multimode fiber is equal to the sum of powers of all the modes.

As follows from the theory of optical waveguides, number N of guided modes in a fiber is defined by the magnitude of

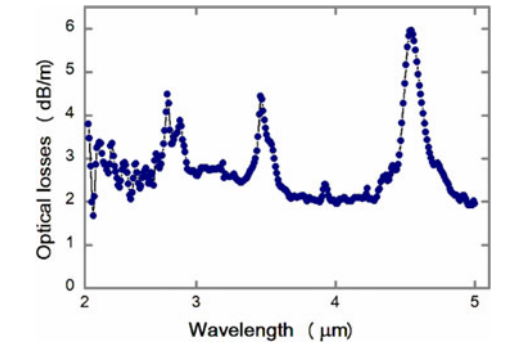

(a)

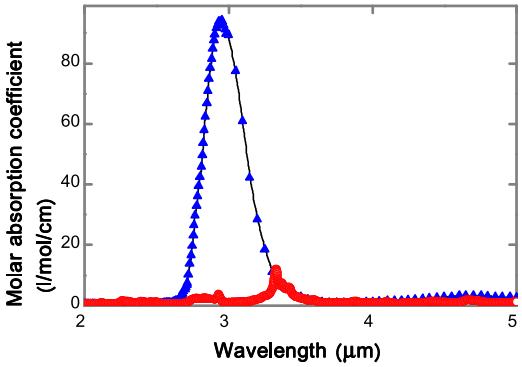

(b)

Fig. 1. Spectral dependencies of: optical losses in the [$GeSe_4$]$_{95}I_5$ fiber (a); molar absorption coefficients of water (triangles), acetone (open circles) (b).

parameter *V*. For each HE_{1m} mode, the cutoff parameter V_c can be found from the condition $J_1(V_c) = 0$ [10]. If $V_c < V$, the HE_{1m} mode is a guided mode. In an absorbing fiber, shape of the transverse profile of electromagnetic field of an evanescent mode does not vary along the fiber, but its power decreases [11]. Transformation of such an evanescent mode into a leaky one at the cutoff is rather complex [11], but the magnitudes of V_c calculated for a lossless fiber of the same geometry still can be used for *N* evaluation. A fundamental difference between an evanescent mode and a leaky mode is that electromagnetic field of a leaky mode grows in radial direction outside a fiber core.

III. Measurements of the Evanescent Modes Transmittance in Aqueous Acetone Solutions

In this work, measurements were carried out with a multimode single-index (unclad) fiber made of [$GeSe_4$]$_{95}I_5$ glass ($R = 145\,\mu$m). The [$GeSe_4$]$_{95}I_5$ fiber was fabricated from a melt from a single crucible as described in details in [12]. Addition of iodine atoms into the glass matrix reduces the formation of crystalline phases during bulk sample annealing and fiber drawing. The glass rod was placed in the crucible and heated to a plastic state (at the temperature about 300 °C). Inert gas (Ar) pressure was used to create the necessary melt flows through the die.

Optical losses of the fiber (Fig. 1(a)) were measured by using the conventional cut-back technique. Because of the low optical losses in the range of wavelengths 2–9 μm [12], this fiber is very promising for MIR spectroscopy. Refractive index of this glass is around 2.4 in NIR [13] and can be taken of this magnitude in MIR because the refractive index is almost constant in spectral range far from the fundamental absorption band edge that is at $\lambda \approx 0.6\,\mu$m for the [$GeSe_4$]$_{95}I_5$ glass.

Aqueous acetone solutions were used in [3]–[5], [12] in similar experiments.

Spectral dependencies of the molar absorption coefficients shown in Fig. 1(b) have been obtained from the IR spectra of bulk water and bulk acetone recorded by using a Fourier - Transform Infrared Spectrometer (FTIR) in zinc-selenide cells with the optical path-length of 18 μm. At around $\lambda = 3.33\,\mu$m, an absorption band is observed that is attributed to acetone molecular vibrations.

From these measurements, the molar absorption coefficient of pure acetone ($\alpha_m^a = 12.01/\text{mol/cm}$) and pure water ($\alpha_m^w = 9.01/\text{mol/cm}$) have been obtained at $\lambda = 3.33\,\mu$m. As the molar concentration of water ($c^w = 55.5\,\text{mol/l}$) is much greater than that one of acetone ($c^a = 13.5\,\text{mol/l}$), the resulting absorption coefficient of water is much greater than that of acetone ($\alpha_m^a c^a << \alpha_m^w c^w$). These conditions are absolutely different than in VIS range measurements where water absorption is negligible.

For experimental treatment, a broadband 50 W silicon-nitride bulb-based MIR light source with the maximum intensity at $\lambda = 2.5\,\mu$m was used. The light source was free-space coupled to the $[GeSe_4]_{95}I_5$ fiber, which was cleaved at a 90° angle with a specialized low-tension cleaver.

The whole fiber facet area was coaxially and uniformly irradiated. Output signal was then detected by an FTIR within the spectral range $\lambda = 2 - 6\,\mu$m.

The [$GeSe_4$]$_{95}I_5$ fiber was inserted into a slightly curved silica glass tube of the length of 24 cm, diameter of 7 mm and radius of curvature of 15 cm (Fig. 2(a)). This tube was used to decrease acetone evaporation that is quite fast in an open vessel.

At first, transmittance T_0 of the fiber without the liquid analyte was acquired. Next, an aqueous acetone solution was poured into the tube in a total volume of 5 ml, and the transmittance T_1 was measured again. Relevant length *L* of the fiber submerged into the solution was equal to 14 cm. By evaluating the normalized transmittance $\tau = T_1/T_0$ for each concentration of the solution, the influence of reflections from the fiber facets was minimized.

Spectral dependencies of τ shown in Fig. 2(b) have been obtained for several volume concentrations of acetone. As water absorption was strong, the absorption peak of acetone at $\lambda = 3.33\,\mu$m was not observable at its volume concentration less than 50%.

IV. Electromagnetic Analysis

Number *N* of the evanescent modes of the [$GeSe_4$]$_{95}I_5$ fiber varies over the spectral range of the fiber transmittance measurements (Fig. 3(a)). At $\lambda = 5\,\mu$m, *N* is more than two times less than at $\lambda = 2\,\mu$m. As refractive indices of water and acetone have similar values ($n^w = 1.33$ and $n^a = 1.35$), *N* does not depend on the acetone solution concentration. The number of modes is less in a fiber section immersed in the solution than

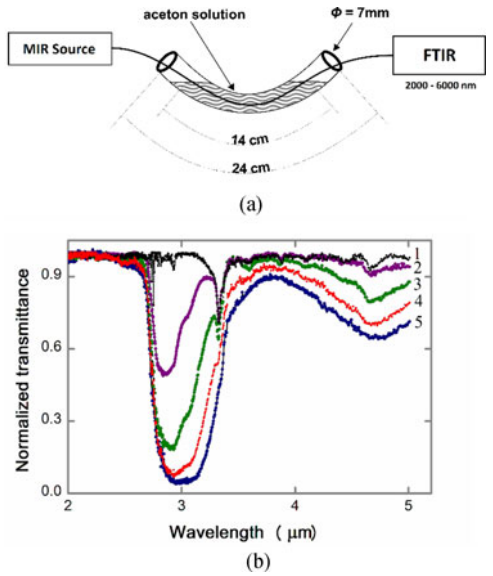

Fig. 2. Measurement configuration schematic with a glass tube filled with an aqueous acetone solution. (a); measurement results for various volume concentrations of acetone: 100% (1), 90% (2), 75% (3), 50% (4), 0% (pure water) (5)(b).

that in the same fiber in the air. This is a reason for some additional radiation losses when electromagnetic field is propagating through the boundary between air and the acetone solution.

In order to evaluate attenuation coefficients of the evanescent modes, imaginary parts of refractive indices of the fiber material and surrounding medium are to be quantified.

In the $[\,GeSe_4]_{95}I_5$ fiber, material absorption coefficients of the bulk glass samples of the compositions $[\,GeSe_4]_{95}I_5$ in the spectral range 2–5 μm are no more than 0.01 cm^{-1} [12] that is significantly less than the absorption coefficients of aqueous acetone solutions at $\lambda = 3.33\,\mu m$ (for ex., $\alpha_m^a c^a = 162\ cm^{-1}$). Then absorption of the fiber material can be neglected ($n''_{co} = 0$).

As absorbance of a solution in bulk is:

$$A = (\alpha_m^w c^w + \alpha_m^a c^a) \cdot L, \tag{7}$$

in accordance with the Bouguer-Lambert-Beer law, the imaginary part of the refractive index of the solution can be defined as:

$$n''_{cl} = (\alpha_m^w c^w + \alpha_m^a c^a) \cdot \ln(10)/(2k). \tag{8}$$

In Fig. 3(b), magnitudes of the attenuation coefficient η_m evaluated at $\lambda = 3.33\,\mu m$ by numerical solution of (5) are plotted for pure water and for pure acetone at each radial order *m* of the HE_{1m} modes of the $[GeSe_4]_{95}I_5$ fiber. In accordance with the theory of optical fibers [10], higher-order modes of the fiber have greater penetration into the cladding than the lower-order ones (an example is shown in Fig. 3(c), inset). That is why magnitudes of η of the higher-order modes shown in Fig. 3(b) are more than ten times greater than that of the fundamental mode.

In the analysis, it is reasonable to find out how η_m depends on the fiber core radius. If the $[\,GeSe_4]_{95}I_5$ fiber would have a greater or a lesser *R*, the number of modes would increase or decrease, respectively, at a given wavelength as shown in

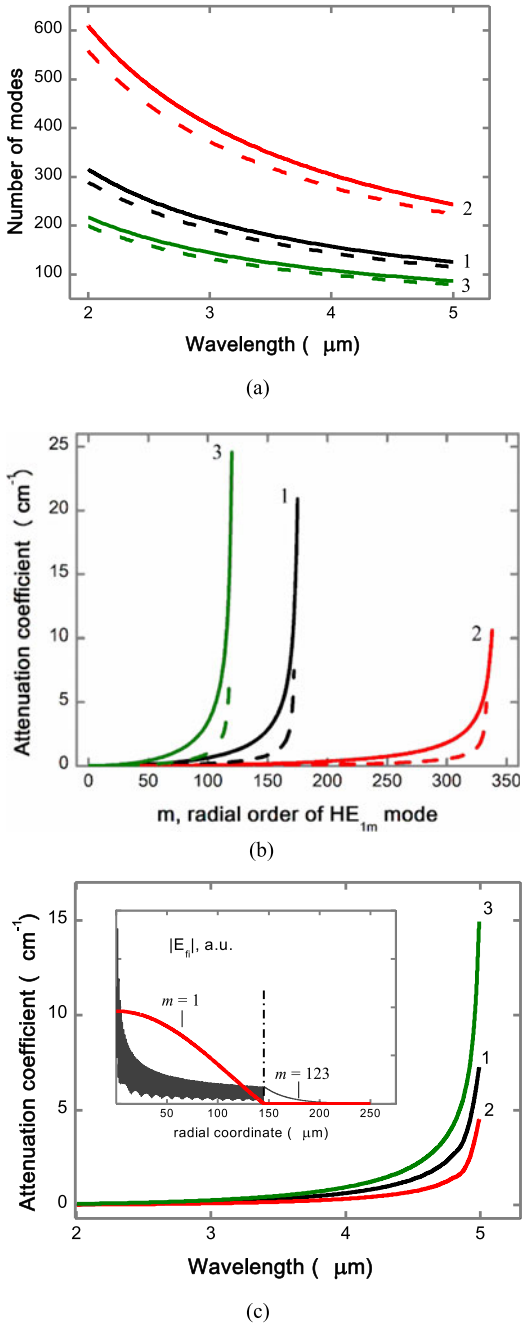

Fig. 3. Number of the HE_{1m} modes of the $[\,GeSe_4]_{95}I_5$ fiber in air (solid lines), immersed in aqueous acetone solution (dashed lines) (a); attenuation coefficient of the HE_{1m} modes of the fiber immersed in pure water (solid lines), in pure acetone (dashed lines) at $\lambda = 3.33\,\mu m$ (b); attenuation coefficients of the HE_{1m} modes with $m = 114$ (1), 221 (2), 79 (3) (c); Inset: radial profiles of electrical field components of the HE1m modes with $m = 1$ and $m = 123$ at $\lambda = 4.6\,\mu m$. $R = 145\,\mu m$ (1), 280 μm (2), 100 μm (3).

Fig. 3(a). Attenuation coefficient of each evanescent mode of a given *m* grows with an *R* decrease (Fig. 3(b)) because of greater penetration of the mode filed into the absorbing medium (see Section II). From this point of view, it would be optimal to decrease *R* as much as possible taking into account relating technological restrictions. However, as was mentioned in Section I, a multimode propagation has an advantage in providing a log-

arithmic output characteristics and a large dynamic range [6], [7].

Another important feature is that at a given core radius, $\eta_{\rm m}$ of each radial mode grows with wavelength due to greater penetration of a mode field into the cladding (see Section II). In Fig. 3(c), the magnitudes of η_m have been calculated in assumption that the absorption coefficient of a liquid was the same at all the wavelengths (equal to $\alpha^a_m = 12\,{\rm l/mol/cm}$ at $\lambda = 3.33\,\mu{\rm m}$). The observed η_m increase with wavelength is specifically due to the waveguiding properties of the fiber. It is shown here that if the $[{\rm GeSe_4}]_{95}{\rm I_5}$ fiber would be of 100 μm core radius it would be more efficient for the evanescent wave spectroscopy. Over the range $\lambda = 2-5\,\mu{\rm m}$ (Fig. 3(c)), attenuation coefficients of the highest-order $\rm HE_{1m}$ mode ($m = 79$) of the fiber with $R = 100\,\mu{\rm m}$ are larger than those of the fibers with greater radii ($m = 114$ for $R = 145\,\mu{\rm m}$, $m = 221$ for $R = 280\,\mu{\rm m}$).

This wavelength dependence of the attenuation coefficients reveals why decrease of the fiber transmittance measured at $\lambda = 4.7\ \mu{\rm m}$ (Fig. 2(b)) is significant in spite of the bulk absorption coefficients of water and acetone are small at this wavelength (Fig. 1(b)).

When several evanescent modes propagate in a fiber, total transmittance depends on initial amplitudes of the modes at the input facet of the fiber. In general, the initial amplitudes depend on radiation launching conditions.

In our analysis, we assume at first that all the input power was launched into just one *m*-th evanescent mode. For this case, the normalized transmittance $\tau = P_m(L)/P_{0m}$ has been calculated for several evanescent modes of the fiber immersed in pure acetone (Fig. 4(a)) or in pure water (Fig. 4(b)).

Transmittance of some higher-order modes at some wavelengths is equal to zero because their attenuation length $L_m = \eta_m^{-1}$ is much less than the length of fiber length immersed in the solution $L = 14\,{\rm cm}$ (for ex., in Fig. 4(b), for the evanescent mode with $m = 100$ at $\lambda = 3.33\,\mu{\rm m}$, $L_m \approx 1\,{\rm cm}$).

This means that if only the higher-order modes be excited at the input facet, L can be significantly reduced for sensing purposes. In comparison with the higher-order modes, the lower-order ones are delivering power over longer distances. Attenuation coefficient of the fundamental evanescent mode ($m = 1$) is so small that $L_m >> L$ and the mode transmittance is equal to unity over all the spectral range. Then we can conclude that the observed decrease of transmittance measured in the experiment (Fig. 2(b)) is due to absorption by a group of evanescent modes having the attenuation length $L_m \approx L$. For the $[\,{\rm GeSe_4}]_{95}{\rm I_5}$ fiber, these are modes with $m > 10$ (Fig. 4).

As a next step of the analysis, we assume that the input power is equally distributed between all the evanescent modes. Then the normalized transmittance can be evaluated as

$$\tau = N^{-1} \sum_{m=1}^{N} \exp(-\eta_m L), \tag{9}$$

In spectroscopic sensors based on measurements of power decrease over a path length in a bulk liquid substance, transmittance can be evaluated separately for water T^w and acetone T^a

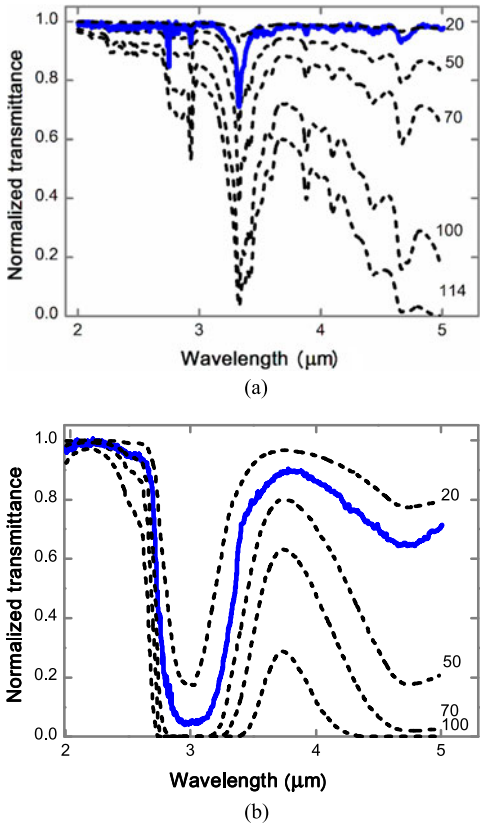

Fig. 4. Normalized transmittance (τ) of the $[{\rm GeSe_4}]_{95}{\rm I_5}$ fiber immersed in pure acetone (a) and in pure water (b): measured (solid lines) and calculated for $\rm HE_{1m}$ modes with m = 20,50,70,100,114 (dashed lines). $R = 145\ \mu$m, $L = 14$ cm.

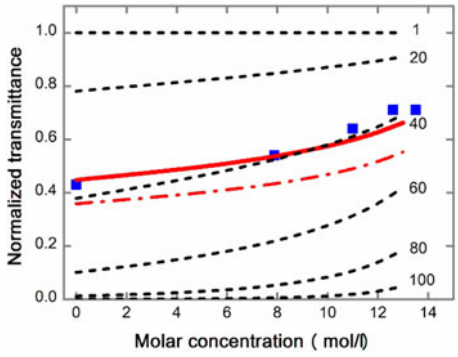

Fig. 5. Normalized transmittance (τ) at $\lambda = 3.33\,\mu{\rm m}$ of the $[\,{\rm GeSe_4}]_{95}{\rm I_5}$ fiber immersed in the acetone solution: measured (squares), calculated for the $\rm HE_{1m}$ modes with $m = 1, 20, 40, 60, 80, 100$ (dashed lines), calculated by using (9) with $N = 80$ (solid line), $N = 100$ (dash-dot line). $R = 145\,\mu{\rm m}$, $L = 14\,{\rm cm}$.

so that the total transmittance is equal to their product:

$$T = 10^{-A} = 10^{-\alpha^a_m\, c^a\, L} \cdot 10^{-\alpha^w_m\, c^w\, L} = T^a \cdot T^w \tag{10}$$

However for a fiber with an absorbing cladding, (10) is not valid because the magnitude of β''_m of each evanescent mode is defined by the profile of the complex refractive index over all the fiber cross-section with the imaginary part defined by (8).

In Fig. 5, the magnitudes of τ at different molar concentrations of acetone are shown: calculated separately for some

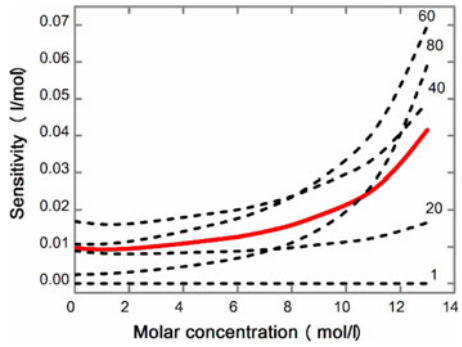

Fig. 6. Sensitivity (S) calculated at $\lambda = 3.33\,\mu\mathrm{m}$ for the HE_{1m} modes of the $[\,GeSe_4]_{95}I_5$ fiber with $m = 1, 20, 40, 60, 80$ (dashed lines) and by using (9) (solid line). $R = 145\,\mu\mathrm{m}$, $L = 14\,\mathrm{cm}$.

evanescent modes (dashed curves) and calculated in approximation of equally distributed input power (solid curves) by using (9). Due to the stronger absorption of water rather than acetone, the transmittance grows with acetone concentration that is unusual in comparison with the absorption spectroscopy in VIS or NIR where an analyte has a stronger absorption than water.

In spite of $N = 114$ at $\lambda = 3.33\,\mu\mathrm{m}$ in the $[\,GeSe_4]_{95}I_5$ fiber immersed in the solution, we can see in Fig. 5 that some higher-order modes cannot reach the fiber output because of the stronger absorption. For example, transmittance of the 100-th evanescent mode is negligibly small at low concentrations of acetone. As in fact the input power was not equally distributed between the fiber modes at the input facet, actual number of the evanescent modes delivering power to the fiber output depends on both the initial amplitudes and attenuation coefficients of each mode. Then the 100-th mode of the $[\,GeSe_4]_{95}I_5$ fiber (and some other higher modes) might have a small amplitude and a small impact into the total transmittance. In our approximate calculations, indeed, the curve calculated by using (90 with $N = 80$ provides a good fit with the experimental results (Fig. 5), but the curve obtained with $N = 100$ is located much lower.

For sensitivity characterisation, the derivatives

$$S = d\tau/dc^a \tag{11}$$

have been evaluated and plotted in Fig. 6 for several individual modes and for τ calculated by using (9) with $N = 80$. For the fundamental mode ($m = 1$) magnitudes of S are close to zero and do not depend on the acetone concentration. The mode with $m = 80$ is strongly absorbed by water at low acetone concentrations but at greater c^a its sensitivity increases because of partial replacement of water by acetone. In the range of concentrations $c^a = 0-2\,\mathrm{mol/l}$, magnitudes of S calculated by using (9), (11) at low c^a are defined mostly by the evanescent modes with m from 20 to 60. At larger concentrations, some higher-order modes, which has not been totally absorbed at $L = 14\,\mathrm{cm}$, impact into the total sensitivity.

In general, magnitudes of S depend on the slopes of the curves shown in Fig. 5, and the slopes depend on the difference between the pure water and pure acetone absorption coefficients at a given λ.

In addition to the HE_{1m} modes considered in this paper, other types of evanescent modes having potentially greater attenuation coefficients can be excited if an input light beam is not co-axial with the fiber. These modes are not azimuthally symmetric and correspond to tilted rays, which may have greater penetration into the absorbing medium.

V. Conclusions

We have applied a rigorous electrodynamics' model of a multimode optical fiber with an absorbing cladding for analysis of evanescent wave absorption in a chalcogenide fiber immersed in an aqueous acetone solution. Azimuthally symmetric evanescent modes of a single-index (unclad) fiber have been considered. We have demonstrated that higher-order modes of the fiber have greater attenuation coefficients than the lower-order ones because of greater penetration of the higher-order modes into the absorbing solution. By this, we have revealed that a selective excitation of the higher-order modes can be used for optimisation of fiber-optic sensing elements by decrease of the fiber length immersed into an absorbing medium.

As modal fields penetration into an absorbing cladding grows with decrease of the ratio of the fiber core radius to radiation wavelength, attenuation coefficient of an evanescent mode increases with wavelength. From this point of view, MIR spectral range is more attractive for evanescent wave sensing than VIS or NIR. This is especially important when using chalcogenide fibers, which generally have large refractive indices (2.4 or more). However strong absorption of water is a serious limitation in the MIR spectroscopy. To achieve high sensitivity, absorption coefficient of an analyte should by much greater than that one of pure water at a given wavelength.

For real-time remote sensing, supercontinuum sources are considered as a reasonable alternative to the heat sources used in laboratories. The supercontinuum sources provide coherent high-intensity radiation (more than three orders higher power spectral density than incoherent sources). Recently a new commercially available 1.7–4.2 μm mid-IR supercontinuum source has been presented by NKT photonics, thus representing a significant enhancement for spectroscopic applications. Furthermore a supercontinuum generation in chalcogenide fibers in the spectral range of 1–14 μm has been demonstrated in laboratory conditions [14], providing an excellent possibility for the future of the MIR spectroscopy.

References

[1] J. D. Musgraves, S. Danto, K. Richardson, and J. Hu, "Chalcogenide glass thin-film and fiber structures for chemical and biological sensing," in *Amorphous Chalcogenides: Advances and Applications*, R. Wang, Ed. Singapore: Pan Stanford Publ., 2014.

[2] R. R. Gattass *et al.*, "Review of infrared fiber-based components," *Appl. Opt.*, vol. 54, no. 31, pp. F25–F34, 2015.

[3] J. Heo, M. Rodrigues, S. J. Saggese, and G. H. Sigel, Jr., "Remote fiber-optic chemical sensing using evanescent-wave interactions in chalcogenide glass fibers," *Appl. Opt.*, vol. 30, no. 7, pp. 3944–3951, 1991.

[4] J. S. Sanghera, F. H. Kung, L. E. Busse, P. C. Pureza, and I. D. Aggarwal, "Infrared evanescent absorption spectroscopy of toxic chemicals using chalcogenide glass fibers," *J. Amer. Ceram. Soc.*, vol. 78, no. 8, pp. 2198–2202, 1995.

[5] K. Michel *et al.*, "Monitoring of pollutant in waste water by infrared spectroscopy using chalcogenide glass optical fibers," *Sensors Actuators B, Chem.*, vol. 101, pp. 252–259, 2004.
[6] P. S. Kumar, C. P. G. Vallabhan, V. P. N. Nampoori, V. N. Sivasankara Pillai, and P. Radhakrishnan, "A fibre optic evanescent wave sensor used for the detection of trace nitrites in water," *J. Opt. A, Pure Appl. Opt.*, vol. 4, pp. 247–250, 2002.
[7] L. S. Thomas *et al.*, "Chemical sensing with microbent optical fiber," *Opt. Lett.*, vol. 26, pp. 1541–1543, 2001.
[8] A. Messica, A. Greenstein, and A. Katzir, "Theory of fiber-optic, evanescent-wave spectroscopy and sensors," *Appl. Opt.*, vol. 35, no. 13, pp. 2274–2284, 1996.
[9] Y. Xu, A. Cottenden, and N. Barrie Jones, "A theoretical evaluation of fibre-optic evanescent wave absorption in spectroscopy and sensors," *Opt. Lasers Eng.*, vol. 44, pp. 93–101, 2006.
[10] A. W. Snyder and J. D. Love, *Optical Waveguide Theory*. London, U.K.: Chapman & Hall, 1983.
[11] L. A. Melnikov and E. A. Romanova, "Transformation of HE1m guided mode into the leaky one in absorbing optical fiber," *Opt. Commun.*, vol. 141, pp. 10–16, 1997.
[12] A. P. Velmuzhov *et al.*, "Preparation and investigation of [GeSe4]100xIx glasses as promising materials for infrared fiber sensors," *Opt. Mater.*, vol. 60, pp. 438–442, 2016.
[13] G. Boudebs *et al.*, "Linear optical characterization of chalcogenide glasses," *Opt. Commun.*, vol. 230, pp. 331–336, 2004.
[14] C. R. Petersen *et al.*, "Mid-infrared supercontinuum covering the 1.4–13.3 μm molecular fingerprint region using ultra-high NA chalcogenide step-index fibre," *Nature Photon.*, vol. 8, pp. 830–834, Nov. 2014.

Elena A. Romanova received the Ph.D. degree in optics and the Dr.Sc. degree in laser physics from the Saratov State University, Saratov, Russia, in 1988 and 2004, respectively. She is currently a Professor at the Chair of Computational Physics and Metamaterials, Saratov State University. She spent one year in research at the University of Nottingham as a Marie Curie Fellow. She specializes in theory and modeling of laser beams and pulses propagation in linear and nonlinear dielectric waveguides and optical fibers. Her research interests include the study of nonlinear optical response of noncrystalline semiconductors and the development of the technology of optical materials processing by the ultrashort laser pulses. She has been involved into several research projects supported by the European Commission and the Royal Society.

Svetlana Korsakova received the M.S. degree in laser physics and nonlinear optics from the Faculty of Physics, Saratov State University, Saratov, Russia, in 2015, where she is currently working toward the Ph.D. degree in the Faculty of Physics. Her research interests include fiber sensing, IR-spectroscopy, and computer modeling.

Matej Komanec received the M.S. and Ph.D. degrees in radioelectronics from the Czech Technical University in Prague, Prague, Czech Republic, in 2009 and 2014, respectively, where he is currently a Research Assistant at the Faculty of Electrical Engineering. His research interests include specialty optical fibers, nonlinear optics, optical interconnects, and fiber sensing. He is a member of OSA and SPIE.

Tomas Nemecek received the M.S. degree in radioelectronics from the Faculty of Electrical Engineering, Czech Technical University in Prague, Prague, Czech Republic, in 2013, where he is currently working toward the Ph.D. degree. His research interests include fiber sensing, specialty fibers, and measurement techniques. He is a member of SPIE.

Alexander Velmuzhov received the Graduate (Hons.) degree from the Department of Inorganic Chemistry, Nizhniy Novgorod State University, Nizhniy Novgorod, Russia, in 2009. In 2009, he started a postgraduate course in the Institute of Chemistry of High-Purity Substances, Russian Academy of Sciences and began to work in the Laboratory of Chemistry of the High-Purity Non-Oxide Glasses. In March 2012, he defended his Ph.D. thesis on "Preparation of Special Pure Ge-Sb-S(Se)-I Glass Systems Via Volatile Iodides of Germanium and Antimony." His research interests include high-purity substances, optical materials, inorganic chemistry, optical spectroscopy, thermodynamics simulations, infrared glasses, and iodids and chalcogenids of p-elements. Main results of his research work were published in 22 scientific publications.

Maksim Sukhanov received the Graduate degree from the Department of Inorganic Chemistry, Nizhniy Novgorod State University, Nizhniy Novgorod, Russia, in 2003 and the Ph.D. degree in chemistry in 2006. Since 2010, he has been working as a Senior Researcher in the Laboratory of Chemistry of the High-Purity Non-Oxide Glasses, Institute of Chemistry of High-Purity Substances, Russian Academy of Sciences. His research interests include high-purity substances, optical materials, inorganic chemistry, optical spectroscopy, infrared glasses, and isotopes and chalcogenide glasses. Main results of his research work were published in 35 scientific publications.

Vladimir S. Shiryaev received the Graduate degree from the Department of Applied Physics and Microelectronics, Nizhny Novgorod State University, Nizhny Novgorod, Russia, in 1983 , the Ph.D. degree in chemistry in 1992, and the Dr.Sc. degree in chemistry in 2007. Since 1985, he has been working in the Laboratory of Chemistry of the High-Purity Non-Oxide Glasses, Institute of Chemistry of High-Purity Substances, Russian Academy of Sciences, Nizhniy Novgorod, Russia. Since 1996, he has been a Lecturer in optical fibers and chemistry of glassy state, Nizhny Novgorod State University. He is involved in several international research programs. He has more than 180 scientific articles and contributed papers. He has been involved in research work on the preparation and investigation of various properties of infrared transmitting glasses for ultralow-loss fiber optics. His current research interests include synthesis and investigation of chalcogenide and fluoride glasses, and preparation of low-loss optical fibers (multimode, single-mode, microstructured, activated with REE).

Circular Lattice Photonic Crystal Fiber for Mid-IR Supercontinuum Generation

Redwan Ahmad, Matej Komanec, and Stanislav Zvanovec

***Abstract*— This letter introduces specific design features of a proposed chalcogenide photonic crystal fiber for ultra-wideband supercontinuum generation in the mid-infrared region. The fiber is optimized to include a circular photonic crystal lattice having tremendous potential in the fields of spectroscopy, food quality control, pulse compression, gas sensing, and various nonlinear applications. By tailoring the zero-dispersion wavelength up to 2 and 2.5 μm, we have reached supercontinuum generation in the anomalous dispersion regime with the entire design hinging upon fibers based on two types of chalcogenide glass-arsenic-selenide and arsenic-sulfide, where supercontinuum broadening from 1.2 to 9.3 μm is made possible.**

***Index Terms*— Optical fiber dispersion, optical propagation in nonlinear media, optical solitons.**

I. Introduction

PHOTONIC crystal fibers (PCFs) consisting of a solid core, surrounded by an ordered array of air-holes are attracting considerable interest thanks to their widespread applications in optical fiber communication, nonlinear devices, optical fiber sensors, and other areas [1]. A wide variety of soft-glass fibers and pump lasers have been considered during the development of broadband mid-infrared supercontinuum sources (MIR-SC). Research on non-silica fibers such as tellurite, chalcogenide, and fluoride glass for supercontinuum generation (SCG) applications [2]–[4] has been ongoing for many years. Chalcogenide glass has a high nonlinear refractive index and wider transparency range compared to tellurite and fluoride glass [5]. Such types of glass can substantially enhance supercontinuum generation as they have a nonlinear refractive index about 100 to 1000 times that of silica [5]. In such cases, dispersion control becomes a critical design stage as it allows higher flexibility regarding the choice of the SC pump wavelength.

Several research groups have proposed novel designs or procedures to generate ultra-broadband MIR-SC [6]–[10]. More recently Saini *et al.* numerically proposed a design featuring a triangular core PCF exhibiting ultra-broadband supercontinuum in the range of 2–15 μm when pumped by a 50 fs laser at 4.1 μm [6]. Theoretically, Jonathan *et al.* introduced a procedure for maximizing the bandwidth of SCG in arsenic- selenide (As_2Se_3) fiber with a hexagonal geometry, when pumping at 2.5 μm, can generate an optical bandwidth wider than 4 μm [7]. Recently Robichaud *et al.* proposed first fiber-based mid-IR supercontinuum generated in a low-loss commercial step index As_2Se_3 fiber up to 8 μm [8]. In [9] Weiqing *et al.* theoretically and experimentally demonstrated an SCG optical bandwidth wider than 4 μm by using a suspended core As_2S_3 PCF with the pumping wavelength set at 2.5 μm. They experimentally investigated SCG parameters by changing the fiber length, pump peak power and pump wavelength. Wei *et al.* numerically investigated an As_2Se_3PCF by using 10 cm of PCF pumped at 2.78 μm with 800 fs pulses covering broadband SC in the range of 2-12 μm [10].

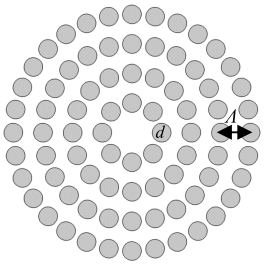

Fig. 1. Cross-section view of the proposed C-PCF.

This letter provides a principle of PCF design for SCG with main focus on the simplicity of manufacturing and tolerance for manufacturing imperfections. Our proposal features a PCF design based on a four circular ring structure with the same air-hole filling fraction ratio in all rings. By using two types of chalcogenide glass (As_2S_3 and As_2Se_3) and customizing ZDW to 2.0 μm and 2.5 μm, we analyze SCG in an anomalous dispersion regime. In the case of As_2Se_3 glass, we achieved a broadening in the wavelength range of 1.2 - 9.3 μm. In both cases, only 0.5 cm long circular PCF (C-PCF) were used.

II. Design Methodology

We investigated SCG by using a C-PCF structure. Though C-PCFs have been already used in different applications such as in [11]–[14]. However, to the best of our knowledge, no one has analyzed SCG by using C-PCF with chalcogenide glasses. Besides compared to hexagonal PCF, C-PCF has more air-holes in corresponding rings which in turns enhances the confinement performance. Figure 1 illustrates the cross-sectional view of the proposed C-PCF. It contains four rings, each having $8\times n$ air-holes ($n = 1, 2, 3, 4$). We optimized our C-PCFs to obtain simultaneously high nonlinearity, ZDW within 2.5 μm and simplified design for a manufacturing facility, where the diameters of all air-holes are equal.

Manuscript received July 19, 2016; revised September 16, 2016; accepted October 1, 2016. Date of publication October 6, 2016; date of current version October 31, 2016. This work was supported by the Ministry of Education Youth and Sports of the Czech Republic, under the Framework of COST Action MP1401 under Grant COST LD15803.

The authors are with the Wireless and fiber optics group, Department of Electromagnetic Field, Faculty of Electrical Engineering, Czech Technical University in Prague, Prague 16627, Czech Republic (e-mail: redwan.ruet.eee@
gmail.com; komanmat@fel.cvut.cz; xzvanove@fel.cvut.cz).

Color versions of one or more of the figures in this letter are available online at http://ieeexplore.ieee.org.

Digital Object Identifier 10.1109/LPT.2016.2615657

The proposed design can then be fabricated, e.g., by using a conventional stack and draw technique [15]. We investigated the modal properties of the proposed C-PCF by using As_2Se_3 chalcogenide glass. For a better demonstration of the design principle, we as well included the second chalcogenide glass (As_2S_3) having the same PCF design parameters. The wavelength dependence of the refractive indexes of the As_2S_3 chalcogenide glass is determined by:

$$n(\lambda) = \sqrt{1+\frac{B_1\lambda^2}{\lambda^2-C_1^2}+\frac{B_2\lambda^2}{\lambda^2-C_2^2}+\frac{B_3\lambda^2}{\lambda^2-C_3^2}+\frac{B_4\lambda^2}{\lambda^2-C_4^2}+\frac{B_5\lambda^2}{\lambda^2-C_5^2}} \quad (1)$$

With the following Sellmeier coefficients $B_1 = 1.898367$, $B_2 = 1.922297$, $B_3 = 0.87651$, $B_4 = 0.11887$, $B_5 = 0.95699$, $C_1 = 0.15$, $C_2 = 0.25$, $C_3 = 0.35$, $C_4 = 0.45$ and $C_5 = 27.3861$ [16]. The refractive index of the As_2Se_3 is then determined using the AMTIR-II Sellmeier equation proposed by [17]:

$$n = \sqrt{1+\sum_{n=1}^{N}\frac{A_n\lambda^2}{\lambda^2-a_n^2}} \quad (2)$$

with Sellmeier coefficients $A_1 = 1.308575$, $A_2 = 0.347441$, $A_3 = 2.234921$, $a_1 = 0.48328$ μm, $a_2 = 19$ μm and $a_3 = 0.24164$ μm [17].

III. Numerical Method

An efficient finite element method (FEM) relying on commercial full-vector finite element software (COMSOL Multiphysics 5.0) is used to investigate the modal properties of the proposed C-PCF. Total chromatic dispersion $D(\lambda)$, including the waveguide and the material dispersion, is calculated by:

$$D(\lambda) = -\frac{2\pi c}{\lambda^2}\beta_2 = -\frac{\lambda}{c}\frac{d^2 Re[n_{eff}]}{d\lambda^2} \quad (3)$$

$$\gamma = \frac{2\pi n_2}{\lambda A_{eff}} \quad (4)$$

Where $\mathrm{Re}[n_{eff}]$ represents the real part of the effective refractive index, c is the velocity of light and $\beta_2$is the second order dispersion known as group velocity dispersion (GVD). The nonlinear coefficient of C-PCF represents a significant parameter during SCG analysis as the nonlinear coefficient (γ) is directly proportional to the nonlinear refractive index (n_2) and inversely proportional to the effective area (A_{eff}). The nonlinear coefficient of the analyzed C-PCF is evaluated based on the Equ. 4 [18]. Propagation and broadening of an ultrashort pulse in C-PCF can be described by the nonlinear Schrödinger equation (NLSE) [18]:

$$\frac{\partial}{\partial z}A(z,t) = -\frac{\alpha}{2}A(z,t) + \sum_{m\geq 2}\beta_m\frac{i^{m+1}}{m!}\frac{\partial^m}{\partial t^m}A(z,t) + i\gamma\left(1+\frac{i}{\omega_0}\frac{\partial}{\partial t}\right)\left[A(z,t)\int_{-\infty}^{\infty}R(t')\left|A(z,t-t')\right|^2 dt'\right] \quad (5)$$

TABLE I
Parameters of Glass Materials

Material	τ_1 [fs]	τ_2 [fs]	f_R [-]	n_2 [m^2W^{-1}]
As_2S_3 [9],[19]	15.2	230.5	0.031	3.0×10^{-18}
As_2Se_3 [20]	23.1	195.0	0.100	2.4×10^{-17}

Where $A(z, t)$ is the slowly varying envelope of the electric field of the optical pulse and α represents the propagation loss coefficient in C-PCF which is neglected here since only a short length of C-PCF (0.5 cm) is used.

In our simulation the hyperbolic secant pulse is assumed to act as an input pulse defined as:

$$A(z=0,t) = \sqrt{P_0}\,\mathrm{sec}\,h\left(\frac{t}{T_0}\right) \quad (6)$$

Here T_0 is the pulse duration related to T_{FWHM} (Full width at half maximum) as $T_0 = T_{FWHM}/1.7627$. Higher order dispersion coefficients can be determined by:

$$\beta_m = \frac{\delta_m\beta}{\delta\omega^m} \quad (7)$$

where m =2,3,4,…represents the m^{th} order dispersion coefficients in the Taylor series expansion. The nonlinear response function $R(t)$ can be defined as:

$$R(t) = (1-f_R)\delta(t) + f_R h_R(t) \quad (8)$$

$$h_R(t) = \frac{\tau_1^2+\tau_2^2}{\tau_1\tau_2^2}\exp\left(-\frac{t}{\tau_2}\right)\sin\left(\frac{t}{\tau_1}\right) \quad (9)$$

where f_R is the fractional contribution of the Raman response and $h_R(t)$ is the Raman response function with Raman period (τ_1) and lifetime (τ_2). The material parameters (f_R,τ_1, τ_2) are summarized in Tab. I.

IV. Simulation Results and Discussion

Based on the optimization the following parameters for our C-PCFs were determined: the pitch of the lattice Λ = 1.9 μm; the diameter of each air hole d = 1.3 μm; and core diameter ($2\times(\Lambda$-$d/2)$)=2.5 μm. The ZDW of the proposed C-PCF (As_2S_3) is 1985 nm. For our analysis, the pumping wavelength at 2000 nm was chosen (anomalous dispersion), where the proposed C-PCF exhibits A_{eff} =3.98 μm^2 and γ = 2362 $W^{-1}km^{-1}$. By taking $\lambda\lambda$ = 2000 nm as the pumping wavelength of the input pulse, the calculated dispersion coefficient values of the Taylor expansion are listed in Tab. II. In the case of the As_2Se_3 glass material, we obtained the ZDW at 2466 nm and we chose the pumping wavelength at 2500 nm. The proposed As_2Se_3C-PCF offers γ of 14923 $W^{-1}km^{-1}$, which helps to make the SCG broader in the mid-IR region and A_{eff} of 4.042 μm^2. By taking λ = 2.50 μm as the pumping wavelength of the input pulse, the calculated dispersion coefficient values of the Taylor expansion are described in Tab. II.

During manufacturing, a tolerance of ±2% from the parameters designed for the proposed C-PCF is expected [24]. So the next step includes a tolerance analysis on the proposed C-PCF by varying pitch (up to approximately ±5%) and air hole's diameter (up to approximately ±8%) In As_2S_3 C-PCF we vary pitch parameter (Λ =1.8, 1.9 and 2.0 μm) while

TABLE II
HIGHER ORDER DISPERSION COEFFICIENTS

β_n / Material	As_2S_3 C-PCF	As_2Se_3 C-PCF
β_2	-0.0107 ps^2/m	-0.0313 ps^2/m
β_3	1.45×10^{-3} ps^3/m	3.08×10^{-3} ps^3/m
β_4	-3.92×10^{-6} ps^4/m	-1.06×10^{-5} ps^4/m
β_5	2.1×10^{-8} ps^5/m	7.17×10^{-8} ps^5/m
β_6	-1.25×10^{-10} ps^6/m	-5.3×10^{-10} ps^6/m
β_7	8.50×10^{-13} ps^7/m	4.80×10^{-12} ps^7/m
β_8	-5.68×10^{-15} ps^8/m	-3.7253×10^{-14} ps^8/m
β_9	1.51×10^{-17} ps^9/m	1.1885×10^{-16} ps^9/m
β_{10}	6.51×10^{-19} ps^{10}/m	1.0076×10^{-17} ps^{10}/m

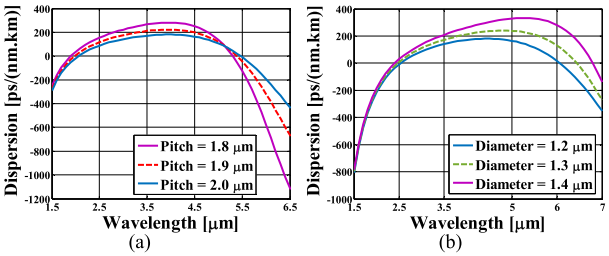

Fig. 2. Dispersion curve as a function of wavelength (a) varying pitch in As_2S_3 C-PCF, (b) varying the air hole's diameter (d) in As_2Se_3 C-PCF.

keeping the diameter of the air holes fixed, and in As_2Se_3 C-PCF we vary air hole diameters (d =1.2, 1.3 and 1.4 μm) while keeping pitch fixed. From Fig. 2, showing wavelength dependence of dispersion on different parameters of air holes.

It is clear that we do not experience a significant change in the dispersion curve while varying pitch and air hole's diameter.

We have chosen power of input pulses by considering damage threshold of chalcogenide glass fibers as it was demonstrated e.g. by high pulsed laser power in arsenic sulfide fibers (2 - 5 μm region) in [26]. By using chalcogenide fibers (As_2Se_3) in [27] Yuan has numerically shown Mid-IR SC in the range of 2 - 10 μm when pumped with femtosecond pulses having 10 kW peak power at 4.1μm. Kubat *et al.* theoretically demonstrated MIR-SC broadening from 0.9 to 9 μm by using concatenated fluoride and chalcogenide glass fibers pumped with a standard pulsed Thulium (Tm) laser even with peak power of 20 kW [28].

A. Supercontinuum Generation Analysis in As_2S_3 C-PCF

In our simulation hyperbolic secant pulse was selected as the input pulse with T_{FWHM} = 50 fs and peak powers (P_{peak}) of 1 kW, 5 kW and 10 kW respectively. And their corresponding pulse energy values are 56.8 pJ, 0.28 nJ and 0.56 nJ. The simulation results show that by using peak power of 10 kW we can observe spectral broadening from 1100 nm to 4100 nm (Fig. 3b). Moreover, by using peak power of 1 kW and 5 kW, we obtained spectral broadening of about 1300 nm (Fig. 3a) and 2300 nm (1200 nm to 3500 nm) respectively. In all of the above cases, we employed only 0.5 cm-long PCF with T_{FWHM} = 50 fs. The simulation results show that as peak power increases from 5 kW to 10 kW, there is a slight change in spectral broadening. For pumping at 2.00 μm, a mode-locked Thulium fiber laser can be used [21], [22]. The nonlinear length ($L_{NL} = 1/\gamma P_0$) and the dispersion length

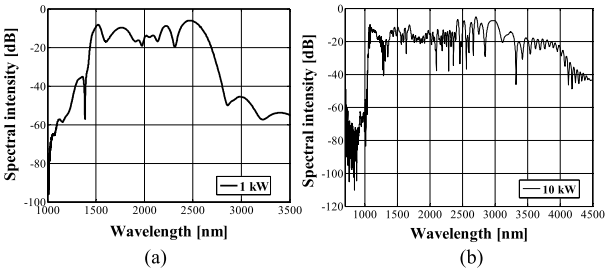

Fig. 3. Spectra of broadening in 0.5 cm long As $_2S_3$C-PCF using pump pulse with T_{FWHM} = 50 fs and peak power of (a) 1 kW, (b) 10 kW.

($L_D = T_0^2/|\beta_2|$) of the proposed C-PCF, using As_2S_3materials, are 4.23×10^{-5}m and 7.5×10^{-2}m, respectively, (P_{peak} = 10 kW and T_0 = 0.0284 ps) at 2000 nm pumping wavelength. So the nonlinear effects initially play a significant role in spectral broadening. By fulfilling conditions as ($L_{NL} < L_D$) and ($L_{NL} < L_{PCF}$) [25], the nonlinear effect is dominant here and, initially, the self-phase modulation (SPM) leads to a symmetric spectral broadening of the input pulse. In next step, we have analyzed the effects on broadening by varying pulse duration using fixed P_{peak} as 2 kW. The pulse duration T_{FWHM} was set as 50 fs, 100 fs, and 150 fs, respectively with 1 cm long C-PCF (Figures are not shown here). Simulation results show that as pulse duration increases, the starting length of broadening shifts with a slight increase. In all above cases, the spectral broadening range is the same as that of a different intensity level. From Fig. 3 it is seen that the SC spectra exhibit some ripples formed mainly by the effect of SPM. For low peak power of 1 kW, the spectral flatness is with a maximal 10 dB fluctuation over a 1250 nm optical bandwidth (Fig.3a). As peak power increases, ripples become more significant, rising to 20 dB.

B. Supercontinuum Generation Analysis in As_2Se_3 C-PCF

In our simulation, we selected hyperbolic secant pulse as input pulse with T_{FWHM} = 50 fs and pulse energy of 0.56 nJ, 0.85 nJ and 1.13 nJ respectively. In [7]–[9] they have used 2.5 μm as a pumping wavelength for demonstration of SCG in microstructured optical fiber. For pumping at 2.5 μm, we can use passively mode-locked Tm:fiber lasers and fiber-based Cr:ZnS lasers operating at 2.0-2.5 μm. Which offers sub-100 femtosecond pulses, tens of Nano joule pulse energies, frequency combs with average output powers of several Watt and peak powers of hundreds of kilowatts [23]. There are several advantages of the 2.0-2.5 μm window such as the broad tuning range, comparatively eye-safe laser within this window, low cost InGaAs detectors operating at room temperatures and one may employ conventional silica fibers as well as optical components such as lenses, mirrors and optical filters etc. for the receiver part [23]. Simulation results demonstrate that by using T_{FWHM} = 50 fs and pulse energy as 0.56 nJ (Peak power= 10 kW), we reach spectral broadening from 1200 nm to 6700 nm (Fig. 4a). By using pulse energy of 0.85 nJ with T_{FWHM} = 50 fs, the spectral broadening is primarily around 6600 nm, from 1200 nm to 7800 nm (Fig. 4b). Spectral broadening from 1200 nm to 9300 nm is experienced when using 1.13 nJ pulse energy (Fig. 4c). L_{NL} and L_D of the proposed As_2Se_3C-PCF are 6.70×10^{-6}m and 2.57×10^{-2}m respectively (P_{peak} = 10 kW and T_0 = 0.0284 ps) at 2.50 μm pumping wavelength. Initial spectral

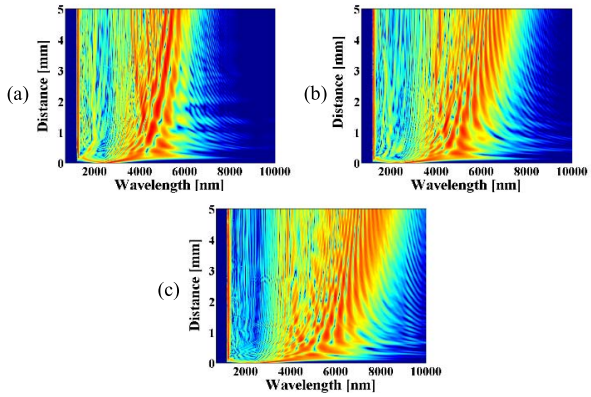

Fig. 4. Spectral evolution of broadening in 0.5 cm long C-PCF (As_2Se_3) for pump pulse of $T_{FWHM} = 50$ fs and energy of (a) 0.56 nJ, (b) 0.85 nJ, (c) 1.13 nJ.

broadening of input pulse mainly lead by SPM though the nonlinear effect is dominant here ($L_{NL} < L_D$).

V. Conclusion

The design of a circular ring lattice photonic crystal fiber based on chalcogenide glass and tailored dispersion for supercontinuum generation with pumps being placed at 2.0 μm and 2.5 μm has been presented. Numerical studies show the proposed C-PCFs as being suitable for mid-IR supercontinuum generation especially via $As_2Se_3$where only a 0.5 cm-long C-PCF was needed to obtain spectral broadening in an optical bandwidth of 8000 nm. The major advantage of our proposed design is the simplicity of manufacturing it and its tolerance for manufacturing imperfections. Moreover due to having dominant non-linear effect, slight change in ZDW (tolerance analysis) of the proposed C-PCF will not cause any significant change in spectral broadening. With ultra-wideband SCG, the proposed C-PCF has the potential to be used in numerous applications such as spectroscopy, gas sensing and various nonlinear applications. In next steps, we would like to further extend this principle for other laser sources moved towards MIR [6], [8], [10], [27].

References

[1] P. Russell, "Photonic crystal fibers," *Science*, vol. 299, no. 5605, pp. 358–362, 2003.
[2] M. Liao, X. Yan, Z. Duan, T. Suzuki, and Y. Ohishi, "Tellurite photonic nanostructured fiber," *J. Lightw. Technol.*, vol. 29, no. 7, pp. 1018–1025, Apr. 1, 2011.
[3] L. Liu, G. Qin, Q. Tian, D. Zhao, and W. Qin, "Numerical investigation of mid-infrared supercontinuum generation up to 5 μm in single mode fluoride fiber," *Opt. Exp.*, vol. 19, no. 11, pp. 10041–10048, May 2011.
[4] C. R. Petersen *et al.*, "Mid-infrared supercontinuum covering the 1.4–13.3 μm molecular fingerprint region using ultra-high NA chalcogenide step-index fibre," *Nature Photon.*, vol. 8, pp. 830–834, Nov. 2014.
[5] J. M. Harbold *et al.*, "Highly nonlinear As–S–Se glasses for all-optical switching," *Opt. Lett.*, vol. 27, no. 2, pp. 119–121, Jan. 2002.
[6] T. S. Saini, A. Kumar, and R. K. Sinha, "Broadband mid-infrared supercontinuum spectra spanning 2–15 μm using As_2Se_3 chalcogenide glass triangular-core graded-index photonic crystal fiber," *J. Lightw. Technol.*, vol. 33, no. 18, pp. 3914–3920, Sep. 15, 2015.
[7] J. Hu, C. R. Menyuk, L. B. Shaw, J. S. Sanghera, and I. D. Aggarwal, "Maximizing the bandwidth of supercontinuum generation in As_2Se_3 chalcogenide fibers," *Opt. Exp.*, vol. 18, no. 7, pp. 6722–6739, Mar. 2010.
[8] L.-R. Robichaud *et al.*, "Supercontinuum generation up to 8 μm in a low loss As_2Se_3 step-index fiber," in *Proc. Adv. Photon.*, 2016, p. JW4A-2.
[9] W. Gao *et al.*, "Mid-infrared supercontinuum generation in a suspended-core As_2S_3 chalcogenide microstructured optical fiber," *Opt. Exp.*, vol. 21, no. 8, pp. 9573–9583, Apr. 2013.
[10] C. Wei, X. Zhu, R. A. Norwood, F. Song, and N. Peyghambarian, "Numerical investigation on high power mid-infrared supercontinuum fiber lasers pumped at 3 μm," *Opt. Exp.*, vol. 21, no. 24, pp. 29488–29504, Dec. 2013.
[11] W. Zhong and X. Zhang, "Localized modes in defect-free two-dimensional circular photonic crystals," *Phys. Rev. A*, vol. 81, p. 013805, Jan. 2010.
[12] P. S. Maji and P. R. Chaudhuri, "Studies of the modal properties of circularly photonic crystal fiber (C-PCF) for high power applications," *Photon. Nanostruct. Fundam. Appl.*, vol. 19, pp. 12–23, Apr. 2016.
[13] H. Xu, J. Wu, K. Xu, Y. Dai, C. Xu, and J. Lin, "Ultra-flattened chromatic dispersion control for circular photonic crystal fibers," *J. Opt.*, vol. 13, no. 5, p. 055405, Mar. 2011.
[14] V. Rastogi and K. S. Chiang, "Holey optical fiber with circularly distributed holes analyzed by the radial effective-index method," *Opt. Lett.*, vol. 28, no. 24, pp. 2449–2451, Dec. 2003.
[15] K. Suzuki, H. Kubota, S. Kawanishi, M. Tanaka, and M. Fujita, "Optical properties of a low-loss polarization-maintaining photonic crystal fiber," *Opt. Exp.*, vol. 9, no. 13, pp. 676–680, Dec. 2001.
[16] L. Shuo and L. Shu-Guang, "Numerical analysis of photonic crystal fiber with chalcogenide core tellurite cladding composite microstructure," *Chin. Phys. B*, vol. 22, no. 7, p. 074206, 2013.
[17] H. G. Dantanarayana *et al.*, "Refractive index dispersion of chalcogenide glasses for ultra-high numerical-aperture fiber for mid-infrared supercontinuum generation," *Opt. Mater. Exp.*, vol. 4, no. 7, pp. 1444–1455, Jul. 2014.
[18] G. P. Agrawal, *Nonlinear Fiber Optics*, 4th ed. San Francisco, CA, USA: Academic, 2007.
[19] M. El-Amraoui *et al.*, "Strong infrared spectral broadening in low-loss As-S chalcogenide suspended core microstructured optical fibers," *Opt. Exp.*, vol. 18, no. 5, pp. 4547–4556, 2010.
[20] J. Hu, C. R. Menyuk, L. B. Shaw, J. S. Sanghera, and I. D. Aggarwal, "Raman response function and supercontinuum generation in chalcogenide fiber," in *Proc. Conf. Lasers Electro-Opt. (CLEO)*, May 2008, pp. 1–2.
[21] J. Swiderski, M. Michalska, and G. Maze, "Mid-IR supercontinuum generation in a ZBLAN fiber pumped by a gain-switched mode-locked Tm-doped fiber laser and amplifier system," *Opt. Exp.*, vol. 21, no. 7, pp. 7851–7857, 2013.
[22] O. P. Kulkarni *et al.*, "Supercontinuum generation from ~1.9 to 4.5 μm in ZBLAN fiber with high average power generation beyond 3.8 μm using a thulium-doped fiber amplifier," *J. Opt. Soc. Amer. B*, vol. 28, no. 10, pp. 2486–2498, 2011.
[23] I. T. Sorokina, V. V. Dvoyrin, N. Tolstik, and E. Sorokin, "Mid-IR ultrashort pulsed fiber-based lasers," *IEEE J. Sel. Topics Quantum Electron.*, vol. 20, no. 5, Sep./Oct. 2014, Art. no. 0903412.
[24] F. Poletti, V. Finazzi, T. M. Monro, N. G. R. Broderick, V. Tse, and D. J. Richardson, "Inverse design and fabrication tolerances of ultra-flattened dispersion holey fibers," *Opt. Exp.*, vol. 13, no. 10, pp. 3728–3736, 2005.
[25] J. M. Dudley, G. Genty, and S. Coen, "Supercontinuum generation in photonic crystal fiber," *Rev. Mod. Phys.*, vol. 78, p. 1135, Oct. 2006.
[26] I. D. Aggarwal, L. E. Busse, L. B. Shaw, B. Cole, and J. S. Sanghera, "IR transmitting fiber and applications: High-power delivery, sources, and amplifiers," in *Proc. Diode Laser Tech. Rev.*, 1998, pp. 2–4.
[27] W. Yuan, "2–10 μm mid-infrared supercontinuum generation in As_2Se_3 photonic crystal fiber," *Laser Phys. Lett.*, vol. 10, no. 9, p. 095107, Aug. 2013.
[28] I. Kubat *et al.*, "Thulium pumped mid-infrared 0.9–9 μm supercontinuum generation in concatenated fluoride and chalcogenide glass fibers," *Opt. Exp.*, vol. 22, no. 4, pp. 3959–3967, Feb. 2014.

Modified Octagonal Photonic Crystal Fiber for Residual Dispersion Compensation over Telecommunication Bands

Redwan Ahmad [1], Matej Komanec [2], Dmytro Suslov [2], Stanislav Zvanovec [2]

[1] Dept. of Electrical and Electronic Engineering, World University of Bangladesh, Dhaka, Bangladesh
[2] Dept. of Electromagnetic Field, Czech Technical University in Prague, Czech Republic

redwan.ahmad@eee.wub.edu.bd, komanmat@fel.cvut.cz, suslodmy@fel.cvut.cz, xzvanove@fel.cvut.cz

Manuscript received

Abstract. *A modified octagonal photonic crystal Fiber (MO-PCF) is proposed and numerically investigated for the purpose of residual dispersion compensation in the optical transmission link. The results show that the proposed fiber with optimized parameters exhibits ultra-flattened negative dispersion over the 300 nm band (1380 nm-1680 nm) with an average dispersion of -506 ps/(nm·km) and an absolute dispersion variation of 11.3 ps/(nm·km). In addition to large negative dispersion, the proposed MO-PCF also exhibits high birefringence in the order of 0.0207 at the 1550 nm wavelength. The proposed MO-PCF can be advantageously used especially for residual chromatic dispersion compensation in the wavelength-division-multiplexing optical fiber transmission system. The proposed fiber design is easy to draw and is tolerant to manufacturing imperfections.*

Keywords

Finite element method, negative flat dispersion, residual dispersion compensation, high birefringence, photonic crystal fiber.

1. Introduction

In optical fiber transmission systems, chromatic dispersion in a single mode fiber (SMF) is challenging as it causes broadening of the optical pulse and limits the link bandwidth especially for higher data rates. Typical standard single-mode fiber has positive dispersion in the range of ~10 to 20 ps/(nm·km), therefore dispersion compensating fibers (DCFs) are extensively used to compensate for the chromatic dispersion [1]. However, some flattened positive dispersion still remains even after dispersion compensation, which could result in serious restrictions in the transmission data rates [2]. Hence, a fiber having flattened negative dispersion becomes an essential component of optical communication systems. Moreover, dispersion compensation over a wide wavelength range is particularly required for wavelength division multiplexing (WDM) [3] over the entire range 1260 nm – 1675 nm of the telecommunication bands. On the other hand, to minimize losses and reduce costs, the inserted residual dispersion compensating fiber (R-DCF) should be as short as possible with high negative dispersion and flattened characteristics to compensate for dispersion in wavelength-division-multiplexing systems effectively [4-5].

Photonic crystal fibers (PCFs) with high negative and flattened dispersion characteristics have been proposed by several groups studying residual dispersion [6-10, 18, 20, 21, 24]. Franco *et al.* [6] proposed a PCF with seven defected air-holes in the core region and having a low average negative dispersion of -179 ps/(nm·km) over the S+C+L+U wavelength bands. Another PCF has been proposed in [7] based on a genetic algorithm with resulting average negative dispersion of -212 ps/(nm·km) and an absolute dispersion variation of 11 ps/(nm·km) over the S+C+L+U wavelength bands. By having low average dispersion, the PCFs mentioned above require a long length to compensate a standard SMF-based link. One of the main disadvantages lies in the core doping as presented in [7] when describing, in particular, fabrication difficulties. An equiangular spiral PCF (ES-PCF) proposed by Islam *et al*. in [8] had an average negative dispersion of -227 ps/(nm·km) along with high birefringence. Though this design exhibited high negative dispersion, in addition to promising polarization-maintaining characteristics, the main drawback was introduced by the elliptical air hole in the center core which made the whole design and future fabrication processes more complex. More recently PCF in PCF design has been proposed by [9] which showed an extremely high negative dispersion of -457.4 ps/(nm·km) over the E+S+C+L+U wavelength bands. However, small air holes in the inner PCF structure make the complex design extremely difficult to fabricate, as was as well mentioned in [9]. In previous work [10], Samiul *et al*. proposed MO-PCF with a specific core region shape exhibiting a negative dispersion of -465.5 ps/(nm·km) with an absolute dispersion variation of 10.5 ps/(nm·km) covering a 215 nm flat band. In the same year, Hasan *et al*. [18] published a similar design as in [10], where they achieved flatness over 240 nm band with higher negative

DOI: 10.13164/re.2017.0001

dispersion value compared to [10]. A pentagonal PCF design has been proposed by Xuyou *et al*. [21] where they achieved 250 nm flatness with an average negative dispersion of -474 ps/(nm·km) and birefringence in the order of 1.75×10^{-2}. On the other hand, MO-PCF has been proposed by Shubi, F. *et al*. [20] where they reported only 95 nm flatness with negative dispersion value from -226 ps/(nm·km) to -290 ps/(nm·km). A square photonic crystal fiber has been proposed by Mahmud *et al*. [24], where they achieved flatness over only 170 nm using silica PCF and 230 nm using lead-silicate PCF. However, compared to silica PCF, the fabrication cost is much higher in the case of lead-silicate PCF as a dispersion compensating fiber. Our main research goal was to propose a new improved design of a photonic crystal fiber which can cover wider wavelength band (flattened) while also providing high negative dispersion value. This was achieved by inserting an extra elliptical ring in the PCF core region, which in turns also gave a higher negative dispersion value while also providing wider wavelength band compared to above-mentioned results.

In this paper, we propose a new design based on a modified octagonal photonic crystal fiber acting as R-DCF with a double row elliptical shape core region that ensures higher average negative dispersion with flattened characteristics, ultra-high birefringence and low confinement loss. The paper presents a considerable extension of our previous work presented in [10]. The newly proposed MO-PCF exhibits negative dispersion of -506 ps/(nm·km) covering a 300 nm flat band (from 1380 nm to 1680 nm) with negative dispersion -511 ps/(nm·km) at wavelength 1550 nm. Thanks to having a modest number of design parameters, it makes the design significantly less complex compared to other approaches [7-9] and therefore, our MO-PCF is considerably easier to fabricate.

2. Structure Design of Proposed MO-PCF

Figure 1 shows the proposed MO-PCF with optimized air-hole diameters d and d_1. We have selected an octagonal structure for R-DCF, as this structure offers smaller confinement losses along with better dispersion accuracy [10-12]. The spacing between the air-hole centers is indicated as Λ, whereas Λ_1 depicts the spacing between air-hole centers on the same ring. Octagonal structure Λ_1 is related to Λ by the relation Λ_1=0.765 Λ. By replacing the first ring of air holes with an elliptical core shape (see in Fig. 1 (a) within the full structure and in Fig. 1 (b) inner elliptical ring), birefringence increases and negative dispersion characteristics are flattened. Moreover, we designed two air holes in the first ring with a diameter equal in size to the air holes in the outer ring to increase the range of flatness [10]. Two air hole elliptical rings in our new design with ten extra air holes result in a new structure design that leads, in turn, to the broadening of the flatness band of the proposed R-DCF.

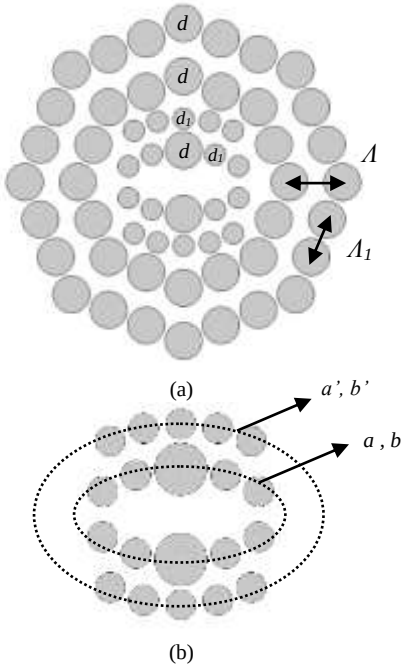

Fig 1. (a) Cross section of 3 ring MO-PCF (b) Elliptical core shape (where a , b and a', b' denote the lengths of the major and minor axes of 1st and 2nd ring).

The lengths of the major and minor axes of the elliptical shapes of the 1st and 2nd rings were denoted as a, b, a' and b' respectively (see Fig. 1 b). The optimum values of a, b, a' and b' are 1.2 µm, 0.6 µm, 1.6 µm and 1.2 µm respectively. By using only two optimized diameters d and d_1, the proposed R-DCF is formed.

3. Simulation Results and Discussion

To optimize the proposed structure, we have used COMSOL multiphysics software featuring the full-vector finite element method (FEM) with a perfectly matched boundary layer (PML). The material dispersion obtained from the three-term Sellmeier formula is directly included in the calculation. The dispersion, confinement loss and effective area of the proposed MO-PCF are evaluated based on the following equations [13]:

$$D(\lambda) = -\frac{\lambda}{c}\left(\frac{d^2 \mathrm{Re}[n_{eff}]}{d\lambda^2}\right) \text{ ps/(nm·km)} \quad (1)$$

$$L_c = 8.686 \times k_0 \,\mathrm{Im}[n_{eff}] \times 10^3 \text{ dB/ km} \quad (2)$$

$$A_{eff} = \left(\iint |E|^2 dxdy\right)^2 / \left(\iint |E|^4 dxdy\right) \text{ µm}^2 \quad (3)$$

where Re[n_{eff}] and Im[n_{eff}] are the real and imaginary parts of the effective refractive index, c is the velocity of light, $k_0 = 2\pi/\lambda$ free-space wave number in vacuum and E is the electric field intensity derived by solving the Maxwell equations. Polarization-maintaining (PM) fibers have highly asymmetrical core region, which in turn provide an extremely high effective index difference between the two orthogonal polarization modes. The modes of a perfect six-fold symmetric core and cladding structure are not birefringent [23]. In practice, however, the large glass-air

index difference means that even slight asymmetry in the structure yields a degree of birefringence. The propagating mode is then split into two co-propagating polarization orthogonal modes. Birefringence is the difference between the mode indices of material/structure for two orthogonal polarization fundamental modes.

$$B = |n_x - n_y| \quad (4)$$

where n_x and n_y are the effective refractive indices of x and y polarization state respectively. In high bit-rate fiber transmission systems, PM fiber plays an important role. Such as PM fibers can eliminate the influence of polarization mode dispersion (PMD) or stabilize the operation of optical devices [19]. The numerical results are reported for an optimized structure with the number of rings N_r = 5, d/Λ=0.7, d_1/Λ =0.4 and Λ = 1 μm for R-DCF. Typically, for better compensation, a R-DCF should have flattened negative dispersion with significantly high magnitude across the whole bands of the wavelength of interest. The proposed and optimized design exhibits an average value of chromatic dispersion equal to -506 ps/(nm·km) with a dispersion variation of 11.3 ps/(nm·km) between -500.5 ps/(nm·km) and -511.8 ps/(nm·km) in the wavelength range 1380 nm to 1680 nm for the fundamental slow axis mode – see figure 2.

As the effective refractive index of the y-axis mode is higher than the x-axis, the y-polarization mode acts in slow-axis mode and the x-polarization mode acts as the fast-axis mode. Meanwhile confinement loss represents one of the most important issues when designing the R-DCF, though such losses can be minimized by inserting extra rings of air holes surrounding the core of the MO-PCF without affecting the characteristics of the dispersion curve [14]. Figure 3 presents confinement loss values for the R-DCF designed for the test case with four to ten rings of air holes surrounding the core. It can be clearly demonstrated, that confinement loss at 1550 nm reaches 5 dB/km, 0.46 dB/km and 0.045 dB/km when N_r (number of rings) is 8, 9 and 10 respectively.

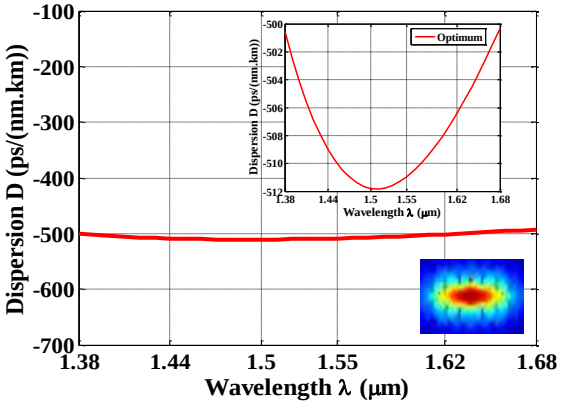

Fig. 2. Chromatic dispersion as a function of wavelength with field distribution (for number of rings N_r =5); inset shows electric field distribution for slow axis mode (y polarization).

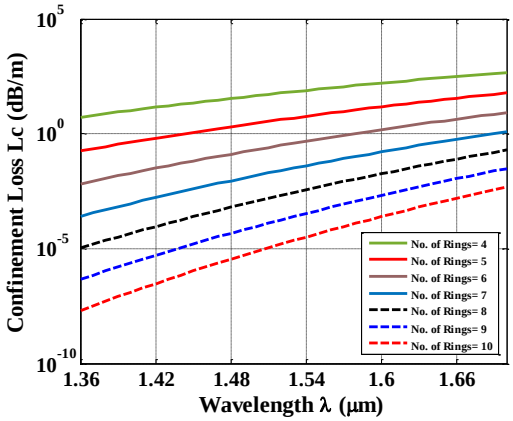

Fig. 3. Confinement loss as a function of wavelength for a different number of rings.

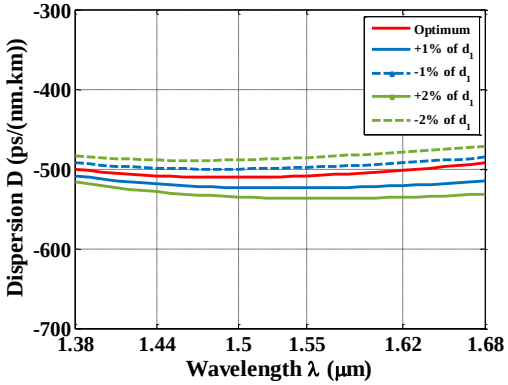

Fig. 4. Dispersion as a function of wavelength for variation of d_1 from ±1% to ±2%.

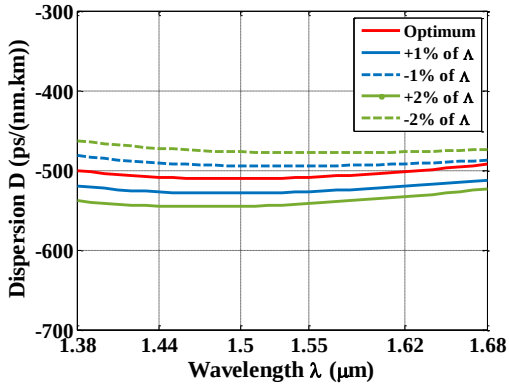

Fig. 5. Dispersion as a function of wavelength for variation of pitch (Λ) from ±1% to ±2%.

Uncertainties, which can be experienced during fiber fabrication, need to be considered, where a 1% variation of structural parameters is typically acquired while the fiber is being drawn [15]. For that reason, when numerically analysing proposed fiber performance, we have included the influence of fabrication by up to a 2% variation uncertainty in global diameters of the proposed MO-PCF. Results including uncertainties of particular parameters are plotted in figures 4 to 6 (all for the case of N_r=5). From the tolerance analysis, it can be seen that +2% variation in d_1 has a meager effect in the dispersion curve flatness, but

increases the average chromatic dispersion up to +4% from the optimum value (when almost all fiber parameters such as dispersion, birefringence and flatness are met). Moreover, for the purpose of the sensitivity of final design parameters during fabrication, we have also performed a tolerance analysis of pitch (Λ) variation which is plotted in figure 5. From the figure it can be determined that for the variations of pitch of +1%, +2%, -1% and -2%, the average dispersion becomes -524 ps/(nm·km), -542 ps/(nm·km), -488 ps/(nm·km) and -470 ps/(nm·km), respectively, with flattened characteristics. Afterwards, we set the tolerance analysis of the major and minor axes of the central core shape. It is evident that changes in parameters *a*, *b*, *a'* and *b'* of up to a 2% variation increase the average dispersion towards -557 ps/(nm·km) without affecting the flattening of characteristics (figure 6). With the exception of the results mentioned above, where we analyzed the MO-PCF by using ring number N_r =5 for the optimum condition, we have demonstrated the effect on dispersion flatness by changing the ring number (see the influence on increased and decreased number on N_r in figure 7). From figure 7 it is evident that there is no such effect on average dispersion value while increasing the number of rings and a limited effect when decreasing to 4. Figure 8 shows that the birefringence of the MO-PCF reaches 2.07× 10^{-2} at 1.55 μm for N_r = 5. It can be seen that there is no noteworthy influence on birefringence value when we change the number of rings.

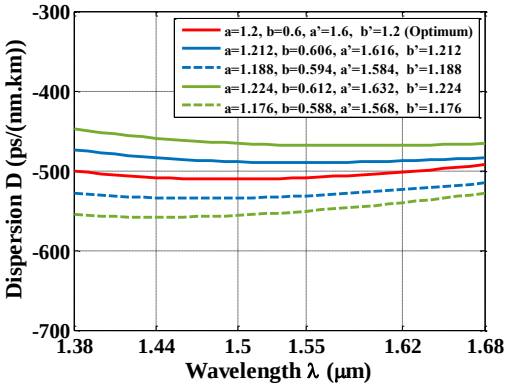

Fig. 6. Dispersion as a function of wavelength for variation of *a*, *b*, *a*' and *b*' from ±1% to ±2% (units of *a*, *b*, *a*' and *b*' are in μm).

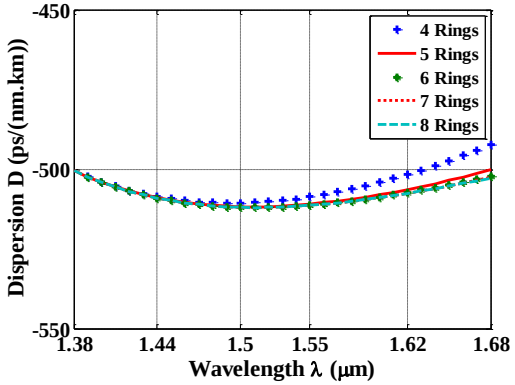

Fig. 7. Dispersion as a function of wavelength for variation of number of rings.

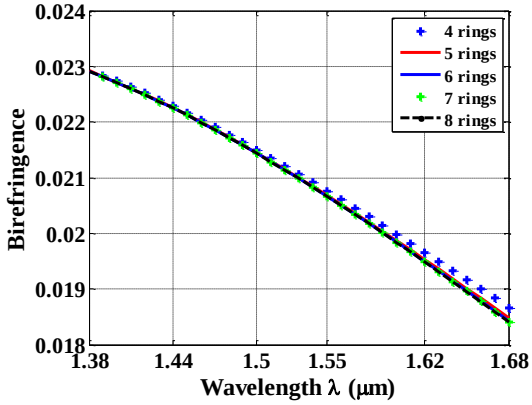

Fig. 8. Birefringence as a function of wavelength for optimum design parameters with variation of number of rings.

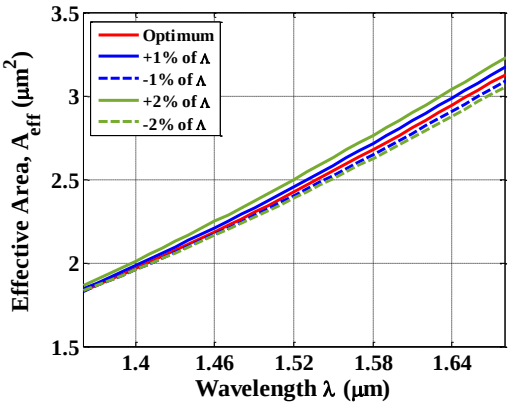

Fig. 9. Effective area as a function of wavelength for optimum design parameters with variation of pitch (Λ).

Due to the elliptical shape of the center core, the high birefringence of the proposed structure is formed. A fiber of this property can be used to eliminate the effect of polarization mode dispersion (PMD) in transmission systems and many other areas where high birefringence is required. On the other hand, the proposed MO-PCF will be a suitable candidate for applications in optical fiber sensing and polarization maintaining transmission systems as it exhibits high birefringence. Furthermore highly birefringent fibers are extensively used in extremely precise fiber interferometers especially in fiber optic gyroscopes and as a major component for optical fiber sensing applications [22].

One important aspect of the residual dispersion compensating fiber introduces a splice loss, which can be found when coupling between PCFs and conventional SMFs for splice loss is inversely related to effective area and this should be reduced to ensure the optimum performance of the proposed R-DCF. There have been reports of splice-free interconnection techniques between PCFs of almost any structure and SMFs, provided the PCF is drawn from individual stackable units as reported by [16]. From figure 9 it is seen that the proposed R-DCF exhibits an effective area of about 2.6 μm^2 at wavelength 1550 nm. We have carried out a tolerance analysis of the effective area by varying the pitch size from ± 1% to ±2%,

which is shown in figure 9. Owing to a small effective mode area; the proposed modified octagonal PCF is expected to be insensitive to bending losses [17].

Fabrication complexity is one of the important challenges in the realization of any proposed PCF. There are several methods, which could be used for fabrication of PCF including the stack and draw method, sol-gel casting, extrusion, ultrasonic drilling etc. Stack and draw method is cost-effective and allows easy control over shape [25]. Several complex PCF designs have been already fabricated by using the stack and draw method, which is explained in detail in [19, 26]. Besides using sol-gel casting technique, many complex structures of PCF have been fabricated by [27]. Sol-gel casting method offers a wide range of design flexibility which is required for dispersion compensation designs [27]. Both stack and draw and sol-gel casting technique are well suited for fabrication of PCF having circular air holes. As our proposed MO-PCF consists of only circular air holes, both methods could be used to fabricate our proposed MO-PCF.

4. Conclusion

A new type of modified octagonal PCF with dual-elliptical core structure, which can be used as a residual dispersion compensating fiber operating over a 300 nm bandwidth, has been proposed. The proposed structure exhibits an average dispersion of -506 ps/(nm·km) with a variation of 11.3 ps/(nm·km) in the range from 1380 nm to 1680 nm. It was shown that the confinement loss of the proposed R-DCF is 0.045 dB/km for ten rings. All of these guiding properties make our design a promising cost-effective broadband dispersion compensator in WDM optical fiber transmission system while maintaining a single polarization state. In particular, it allows tolerance to fabrication processes when average dispersion and its flatness remain resistant to slight changes of the designed structural parameters during fiber drawing. This fabrication tolerance represents a major advantage of our proposed fiber in contrast to other rather complex PCF structures designed for dispersion compensation [7-9]. Apart from dispersion compensation, this design also maintains single polarization thanks to its high birefringence.

Acknowledgments

The research is supported by the Ministry of Education Youth and Sports of the Czech Republic, grant COST LD15803 within the framework of COST Action MP1401 and by the Technology Agency of the Czech Republic, grant TE02000202.

References

[1] Y. LIU, J. WANG, Y. LI, R. WONG, J. LI, X. XIE. A novel hybrid photonic crystal dispersion compensating fiber with multiple windows. *Opt. Laser Technol*., 2012, vol. 44, no. 7, p. 2076–2079.

[2] G. P. Agrawal, *Fiber-Optic Communication Systems*. 3rd ed. New York (USA): Wiley, 2002, p. 15–64.

[3] F. GEROME, J. L. AUGUSTE, J.-M. BLONDY. Design of dispersion-compensating fibers based in a dual-concentric-core photonic crystal fiber. *Opt. Lett*., 2004, vol. 29, no. 23, p. 2725–2727.

[4] M. KOSHIBA, K. SAITOH. Structural dependence of effective area and mode field diameter for holey fibers. *Opt. Exp*., 2003, vol. 11, no.15, p. 1746-1756.

[5] MD AMINUL ISLAM, REDWAN AHMAD, MD SHARAFAT ALI, K M NASIM. Proposal for highly residual dispersion compensating defected core decagonal photonic crystal fiber over S+C+L+U wavelength bands. *Optical Engineering*, 2014, vol. 53, no.7, p. 076106.

[6] M. A. R. FRANCO, V. A. SERRÃO, F. SIRCILLI. Microstructured optical fiber for residual dispersion compensation over S + C + L + U wavelength bands, *IEEE Photon. Technol. Lett*., 2008, vol. 20, no. 9, p. 751–753.

[7] J. P. DA SILVA, D. S. BEZERRA, V. F. R. ESQUERRE, I. E. FONSECA, H. E. H. FIGUEROA. Ge-doped defect-core microstructured fiber design by genetic algorithm for residual dispersion compensation. *IEEE Photon. Technol. Lett*. , 2010, vol. 22, no. 18, p. 1337–1339.

[8] M. A. ISLAM, M. S. ALAM. Design of a polarization maintaining equiangular spiral photonic crystal fiber for residual dispersion compensation over E + S + C + L + U wavelength bands. *IEEE Photon. Technol. Lett*. 2012, vol. 24, no. 11, p. 930–932.

[9] D. C. TEE, M. H. A. BAKAR, N. TAMCHEK, F. R. M. ADIKAN. Photonic crystal fiber in photonic crystal fiber for residual dispersion compensation over E + S + C + L + U wavelength bands. *IEEE Photon. J.*, 2013, vol. 5, no. 3, p. 7200607.

[10] M. S. HABIB, REDWAN AHMAD, M. S. HABIB, M. I. HASAN. Residual dispersion compensation over the S +C +L +U wavelength bands using highly birefringent octagonal photonic crystal fiber. *Appl. Opt*., 2014, vol. 53, no. 14, p. 3057–3062.

[11] S. M. A. RAZZAK, Y. NAMIHIRA. Tailoring dispersion and confinement losses of photonic crystal fibers using hybrid cladding. *J. Lightwave Technol*., 2008, vol. 26, no. 13, p. 1909–1914.

[12] S. M. A. RAZZAK, Y. NAMIHIRA, A. Y. SABER, M. A. G. KHAN. Dispersion tolerance of various photonic crystal fibers. *Int. J. Optomechatron*., 2007, vol. 1, no. 4, p. 359–368.

[13] S. M. A. RAZZAK, Y. NAMIHIRA. Proposal for highly nonlinear dispersion-flattened octagonal photonic crystal fibers. *IEEE Photon. Technol. Lett*. , vol. 20, no. 4, p. 249–251.

[14] G. RENVERSEZ, B. KUHLMEY, R. MCPHEDRAN. Dispersion management with microstructured optical fibers: ultraflattened chromatic dispersion with low losses. *Opt. Lett*., 2003, vol. 28, no. 12, p. 989–991.

[15] F. POLETTI, V. FINAZZI, T. M. MONRO, N. BRODERICK, V. TSE, D. J. RICHARDSON. Inverse design and fabrication tolerances of ultra-flattened dispersion holey fibers. *Opt. Exp*., 2005, vol. 13, no. 10, p. 3728–3736.

[16] S. G. L. SAVAL, T. A. BIRKS, N. Y. JOY, A. K. GEORGE, W. J. WADSWORTH, G. KAKARANTZAS, P. ST. J. RUSELL. Splice-free interfacing of photonic crystal fibers. *Opt. Lett*., 2005, vol. 30, no. 13, p. 1629–1631.

[17] H. ADEMGIL, S. HAXHA, F. ABDELMALEK. Highly nonlinear bending insensitive birefringent photonic crystal fibres. *Engineering*, 2010, vol. 2, no. 8, p. 608–616.

[18] MD. I. HASAN, S. M. ABDUR RAZZAK, MD. S. HABIB. Design and Characterization of Highly Birefringent Residual Dispersion Compensating Photonic Crystal Fiber. *Journal of Lightwave Technology*, 2014, vol. 32, no. 23, p.4578-4584.

[19] K. SUZUKI, H. KUBOTA, S. KAWANISHI, M. TANAKA, M. FUJITA. Optical properties of a low-loss polarization-maintaining photonic crystal fiber. *Opt. Express*, 2001, vol. 9, no.13, p.676-680.

[20] S. F. KAIJAGE, Y. NAMIHIRA, N. H. HAI, F. BEGUM, S. M. A. RAZZAK, T. KINJO, K. MIYAGI, N. ZOU. Broadband Dispersion Compensating Octagonal Photonic Crystal Fiber for Optical Communication Applications. *Japanese Journal of Applied Physics*, 2009, vol. 48, p. 052401.

[21] X. LI, P. LIU, Z. XU, Z. ZHANG. Design of a pentagonal photonic crystal fiber with high birefringence and large flattened negative dispersion. *Appl. Opt.*, 2015, vol.54, no.24, p.7350-7357.

[22] S. KIM, C. S. KEE, C. G. LEE. Modified rectangular lattice photonic crystal fibers with high birefringence and negative dispersion. *Opt. Express*, 2009, vol.17, no.10, p.7952–7957.

[23] M. J. STEEL, T. P. WHITE, C. MARTIJN DE STERKE, R. C. MCPHEDRAN, L. C. BOTTEN. Symmetry and degeneracy in microstructured optical fibers. *Opt. Lett.*, 2001, vol.26, no. 8, p. 488-490.

[24] RUSSEL R. MAHMUD, M. A. G. KHAN, S. M. A. RAZZAK. Design and Comparison of SF57 over SiO2 on Same Structured PCF for Residual Dispersion Compensation. *Photonics Journal*, 2016, vol. 8, no. 6, p. 7102710.

[25] D. GHOSH, S. BOSE, S. ROY, S. K. BHADRA. Design and Fabrication of Microstructured Optical Fibers with Optimized Core Suspension for Enhanced Supercontinuum Generation. *J. Lightwave Technol.*, 2015, vol. 33, no. 19, p. 4156-4162.

[26] Z. LIU, C. WU, MING-LEUNG V. TSE, C. LU, HWA-YAW TAM. Ultrahigh birefringence index-guiding photonic crystal fiber and its application for pressure and temperature discrimination. *Opt. Lett.*, 2013, vol. 38, no. 9, p.1385-1387.

[27] R. T. BISE, D. J. TREVOR. Sol-gel derived microstructured fiber: fabrication and characterization. *OFC/NFOEC Tech. Dig. Optical Fiber Communication Conference*, 2005.

About the Authors

REDWAN AHMAD was born in Rajshahi, Bangladesh. He received his B.Sc. from Rajshahi University of Engineering and Technology in 2013 and M.Sc from Czech Technical University in Prague in 2016. He also worked as research assistant in wireless and fiber optics group, Czech Technical University in Prague from 2014 to 2016. Currently he is working as lecturer in department of Electrical and Electronic Engineering in World University of Bangladesh. His research interests include super-continuum Generation, dispersion compensation, sensing applications etc. using photonic crystal fiber.

MATEJ KOMANEC is a research assistant at the Faculty of Electrical Engineering of the Czech Technical University in Prague. He received his M.S. and Ph.D. degrees in radioelectronics from the Czech Technical University in Prague in 2009 and 2014, respectively. His current research interests include specialty optical fibers, nonlinear optics, optical interconnects, and fiber sensing. He is a member of OSA, SPIE.

DMYTRO SUSLOV is a PhD student at the Faculty of Electrical Engineering of the Czech Technical University in Prague. He received his M.S. degree in radioelectronics from the Czech Technical University in Prague in 2016. His current research interests include specialty optical fibers, nonlinear optics, optical interconnects.

STANISLAV ZVANOVEC received M.Sc. in 2002, a Ph.D. in 2006 at the Czech Technical University in Prague. Now he is a full professor and deputy-head of the Department of Electromagnetic Field at the Faculty of Electrical Engineering, Czech Technical University in Prague. He leads a Free-space and fiber optics team from Faculty of Electrical Engineering, CTU and several research projects. His current research interests include wireless optical communications, visible light communications, remote sensing and optical fiber sensors.

Optical Fiber Technology 45 (2018) 295–299

Contents lists available at ScienceDirect

Optical Fiber Technology

journal homepage: www.elsevier.com/locate/yofte

Experimentally and analytically derived generalized model for the detection of liquids with suspended-core optical fibers

Tomas Nemecek[a,*], Matej Komanec[a], Bryan Nelsen[b,c], Tomas Martan[a], Dmytro Suslov[a], Peter Hartmann[b,c], Stanislav Zvanovec[a]

[a] Department of Electromagnetic Field, Faculty of Electrical Engineering, Czech Technical University in Prague, Technicka 2, Prague 6 166 27, Czech Republic
[b] Fraunhofer-Institut für Werkstoff- und Strahltechnik IWS, 01277 Dresden, Germany
[c] Institute of Leupold-Institute for Applied Natural Sciences/Optical Technologies, University of Applied Sciences Zwickau, 08056 Zwickau, Germany

ARTICLE INFO

Keywords:
Sensors
Fiber optics systems
Microstructured fibers
Refractometry

ABSTRACT

A generalized model for the detection of liquids within suspended-core microstructured optical fibers has been experimentally and theoretically derived. The sensor detection is based on the refractometric principle of transmission losses due to the overlap of the evanescent field with the liquid analyte. A number of parameters, including fiber core diameter and filling length, have been included in the general model. Specially tailored suspended-core fibers were manufactured with the core diameters within the range of 2.4 μm to 4.0 μm. Five selected liquid analytes were used to cover the refractive index range of 1.35 to 1.42. Based on experiments, the characteristics of the parameters of the semi-empirical model have been determined by a genetic algorithm using 283 measurement data sets. The model can be used to design sensors for the detection of liquid analytes as it provides a set of parameters allowing to optimize the sensor's sensitivity for a wide scale of applications. Finally, numerical simulations of the system were carried out by an eigenmode routine to support the results of the generalized model.

1. Introduction

Remote monitoring of the quality of liquids in toxic, explosive or flammable environments is essential for safety and is required in various industrial and agricultural processes. Fiber-optic sensors provide many advantages over electronic sensors, including their small size and low weight, their immunity to electromagnetic interference, the absence of any sparks, their long lifetime and easy system integration.

To enhance fiber-optic sensor features, especially sensitivity and resolution, special optical fiber designs have been developed employing microstructured optical fibers (MOFs) [1,2]. The potential of MOFs for optical detection lies in the possibility of tailoring the MOF structure to achieve enhanced sensor performance [3]. Among MOFs, suspended-core MOFs (SC-MOFs) can provide significantly increased evanescent field overlap with the measured analyte, making them exceptionally suitable for the purposes of the detection of liquid analytes. An overview of SC-MOF sensor applications is summarized in [4,5]. SC-MOF sensors focusing on specific liquid analytes or in-liquid particles were developed using plasmon resonance [6,7] and other spectroscopic sensing methods [8]. Even though the abovementioned SC-MOF sensors provide high sensitivity, they require a complex multi-step sensor preparation, often including opto-chemical transducers.

Refractive index-based sensors represent a simplified and universal sensor approach for the detection of liquid analytes, e.g. in petrol quality analysis, where the refractive index of gasoline change as a result of blending with bioalcohol was studied in [9] and similarly ethanol-gasoline concentration was measured by long-period gratings in [10]. Several SC-MOF structural modifications for the detection of liquid analytes have been previously presented as an exposed-core fiber [11,12]. Conventional and selective hole filling of SC-MOF was also examined [13,14]. The combination of fiber Bragg gratings and SC-MOF was presented in [15], where the achieved sensitivity was up to 100 nm/RIU. Resonance based RI sensing was demonstrated by MOF tapering, resulting in air-hole collapse [16], where the resolution acquired by this approach was around 1×10^{-5} RIU. An interference-based sensor, consisting of two air-clad MOFs spliced between standard single-mode fibers, was presented in [17], indicated sensitivity was 230 nm/RIU and achieving resolution of 3.4×10^{-5} RIU.

This paper significantly extends our previous work [18] by developing an analytical description of optical signal propagation within a liquid analyte filled SC-MOF. Based on an extensive amount of experimental data, a generalized model is derived, which describes the

* Corresponding author.
E-mail address: nemect10@fel.cvut.cz (T. Nemecek).

https://doi.org/10.1016/j.yofte.2018.08.005
Received 25 May 2018; Received in revised form 18 July 2018; Accepted 3 August 2018
Available online 23 August 2018

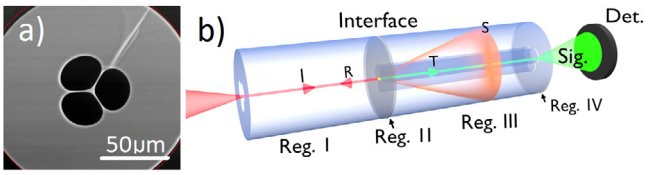

Fig. 1. a) Scanning-electron microscope (SEM) image of the end-face of a 4 μm core diameter SC-MOF and b) a schematic representation the studied interactions inside the SC-MOF studied; Det – Detector, Sig – Signal, I – Incident, R – Reflected, T – Transmitted and S – Scattered light. Region I – air-filled cladding holes, Region II – air-clad liquid-clad interface, Region III – liquid-filled cladding holes, Region IV – liquid-filled cladding free-space interface.

theoretical and empirical behavior of the SC-MOF sensor. This model can be used as a universal tool for SC-MOF sensor design.

2. Light propagation in SC-MOF structure

The mechanisms which cause losses in a partially liquid-filled SC-MOF (shown in Fig. 1) can be divided into two essential loss contributions. The major loss sources are illustrated in Fig. 1 b). The first of them is represented by reflection and scattering losses at the boundary where the air-filled cladding (depicted as Region I) interfaces the liquid-filled cladding (depicted as Region II), as well as in the case of the interface of liquid-filled cladding (depicted as Region III) and free-space at the end of the SC-MOF (depicted as Region IV). Region IV further represents radiation from the SC-MOF end-face. The second type of loss is caused by the evanescent component of the SC-MOF mode being either absorbed or scattered by the liquid analyte itself (Region III).

A numerical-based solution of the losses in the liquid-filled SC-MOF was carried out by a self-developed eigenmode routine using a finite-difference method with a sparse-matrix eigenvalue solver which we utilized to solve the propagation of modes in both the air- and liquid-filled sections of the SC-MOF sensor (Region I and Region III). It was important to consider the full-polarization form of the wave equation because the tight confinement of the modes depends strongly on the boundary conditions between glass and air, or, glass and the liquid analyte (previously defined in [18]). A set of first-order polarized guided modes derived for SC-MOF, with a core diameter (d_{core}) of 4 μm, is shown in Fig. 2.

It was assumed, for the purpose of simplicity, that only the fundamental mode is excited in Region I. The model can be written as:

$$\overrightarrow{E_{III}} = a_0 \overrightarrow{E_O} + \overrightarrow{E_s}, \tag{1}$$

where $\overrightarrow{E_s}$ is light scattered at the interface, $\overrightarrow{E_0}$ is the normalized fundamental mode electric field in Region III and $|a_0|^2$ gives the fraction of power coupled into the outgoing fundamental mode [19], used as the input field for Region III. It is assumed that the remaining power $(1-|a_0|^2)$ is scattered into the cladding modes and mostly lost due to scattering out of SC-MOF. The power, therefore, transferred to the fundamental mode of Region III at the interface (Region II) is given by:

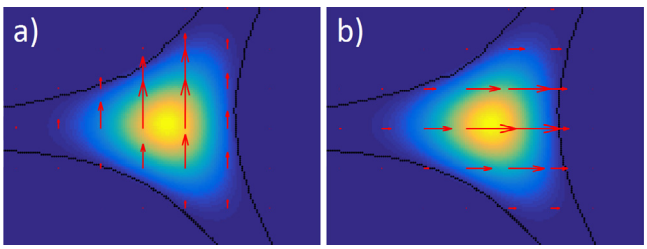

Fig. 2. Numerically calculated polarized fundamental modes of the SC-MOF with a 4 μm core diameter at 1550 nm. a) and b) are orthogonal to each other, $\beta = 5.788\,\mu m^{-1}$.

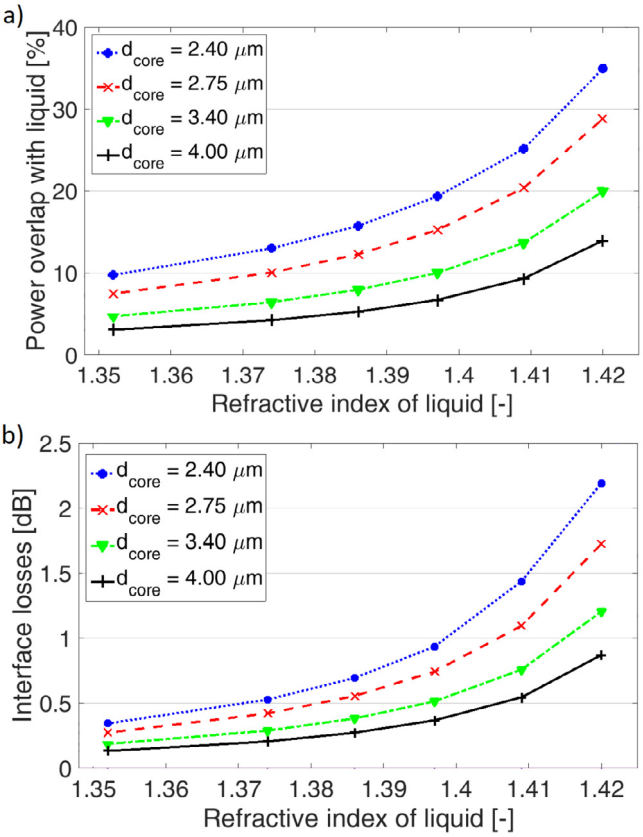

Fig. 3. Finite difference results of a) the power overlap with liquid analytes with respect to SC-MOF core diameters for Region III (see Eq. (1)) and b) losses due to reflection and scattering at the interface (Eq. (2)).

$$P_{III} = |a_0|^2 P_I, \tag{2}$$

with P_I, P_{III} being the power in Regions I and III, respectively (reflection at this interface was calculated to be extremely small because the mode in Region I is very tightly confined in the glass core of the SC-MOF). Once the light has entered Region III, the liquid analyte gives rise to both absorption losses and weak scattering losses. Both loss coefficients are proportional to the distance traveled through the liquid analyte and the power overlap of the fundamental mode with the liquid analyte. The differential power loss in Region III can be expressed as:

$$\frac{\partial P}{\partial z} = -(\rho_a \sigma_{abs} + \rho_s \sigma_{scatt})\eta P, \tag{3}$$

where P is the power along the length of SC-MOF, σ_{abs}, σ_{scatt} are the absorption and scattering cross-sections, respectively, ρ_a and ρ_s are the density of absorbing and scattering centers in the liquid analyte, respectively, and η is the percentage of mode intensity overlap with the liquid analyte. The derived dependencies of power overlapping with liquid and interface losses on RI and core diameter are shown in Fig. 3. The solution to Eq. (3), considering the full length of the liquid-filled section, can be written as:

$$P = P_{III} e^{-(\rho_a \sigma_{abs} + \rho_s \sigma_{scatt})\eta l_{fill}}, \tag{4}$$

where l_{fill} is the length of liquid-filled SC-MOF, and P_{III} stands for the power at the input interface of Region III.

The losses in Region IV do not change significantly from the completely unfilled SC-MOF to the filled case. Since the losses of the filled SC-MOF will be calculated relative to that of the completely unfilled SC-MOF, losses due to Region IV are not included in the final equation.

Finally, inserting Eq. (2) into Eq. (4), the attenuation caused by liquid analyte in the SC-MOF sensor can be determined in [dB] by:

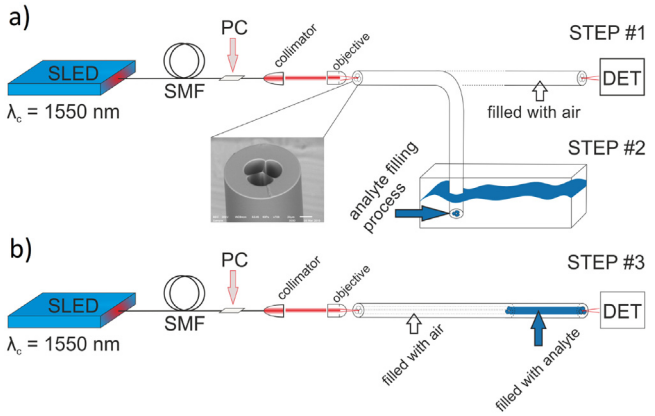

Fig. 4. Scheme of the measurement setup using SC-MOF for detection of liquid analytes, a) Step 1 – reference measurement, followed by Step 2 – SC-MOF filling process, b) Step 3 – liquid analyte measurement process. SMF – single mode fiber, PC – polarization controller, DET – detector.

$$L_{att} = 10log_{10}(e)((\rho_a\sigma_{abs} + \rho_s\sigma_{scatt})\eta l_{fill} - ln|a_0|^2). \quad (5)$$

3. Analyte measurements

To derive a generalized model of the SC-MOF sensor, an extensive measurement campaign has been performed. In our measurement setup (see Fig. 4), a super-luminescent LED (SLED) diode centered at a wavelength of 1545 nm with a 40 nm full-width at half-maximum intensity distribution was used. The polarization of the SLED output was adjusted by a polarization controller (PC), collimated by a GRIN collimator and, subsequently, focused via an objective (with a 40x magnification and a numerical aperture of NA = 0.60) into the selected silica SC-MOF (RI at 1545 nm is 1.441). The detector was a Ge-based photodiode with a sensitivity level of 50 nW. SC-MOFs were filled with selected liquid analytes and the filling length was monitored with a digital microscope, which allowed us to achieve a filling-length precision better than 20 μm.

To cover a wide range of liquid analyte RIs, we prepared liquid analytes: Ethyl-alcohol (RI = 1.3520) and mixtures of Isopropyl-alcohol and Ethylene-glycol (EG) (with RI = 1.3861, 1.3970, 1.4085 and 1.4204 at EG concentrations by volume of 25%, 50%, 75% and 100%, respectively). All RI data assumes a wavelength of 1545 nm. Each liquid analyte was used to characterize the performance of each SC-MOF sample with inner core diameters of 2.40, 2.75, 3.40, and 4.00 μm. Clading outer diameter ranged from 108 μm to 157 μm. In each measurement step (see Fig. 4) the reference power was first measured with the air-filled SC-MOF (Step 1). Subsequently, a defined length of the SC-MOF was filled with a liquid analyte via capillary forces (Step 2). Filling lengths ranged from 0 cm to 4.5 cm (the upper limit was set by the dynamic range of the measurement setup). We measured each liquid analyte three times within the above-mentioned Steps 1–3. The temperature was kept constant within the range of ±1 °C during the measurement to eliminate RI drifts of the liquid analytes. Fundamental-mode excitation was optimized by near-field measurements of the guided light within SC-MOF.

The measured dependencies of attenuation (L_{att}) of an SC-MOF sensor (determined as the difference from the reference measurement) with a core diameter of 3.40 μm for the range of tested liquid analytes and different filling lengths are illustrated in Fig. 5 a). Note that the slope of the curve is linear in the case of filling lengths ranging from 0.5 cm up to 4.5 cm. This is in contrast to shorter filling lengths where the scattered light from the air-to-liquid interface (illustrated in Fig. 1 b) still has a significant intensity at the point it reaches the detector.

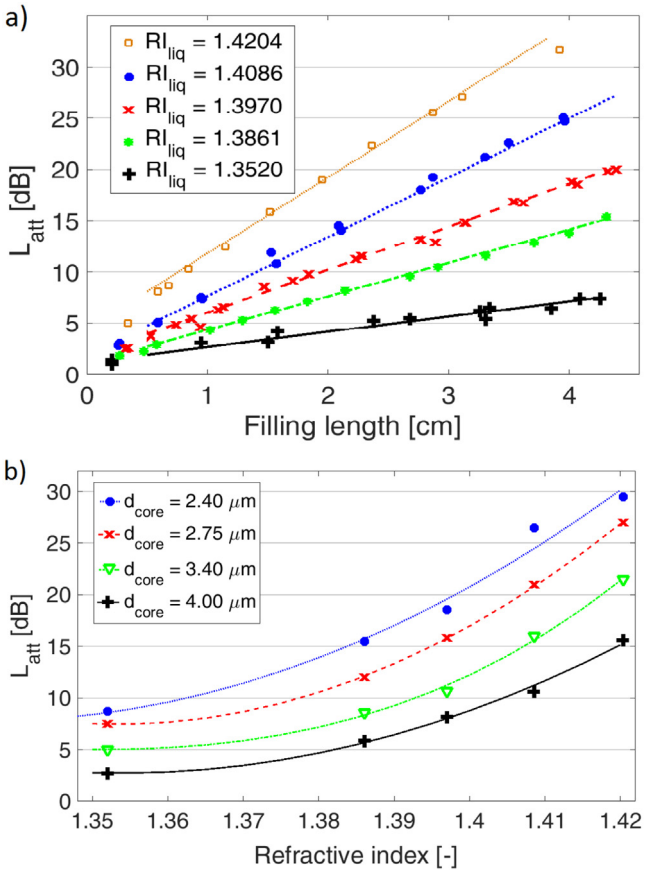

Fig. 5. Measured dependencies of SC-MOF sensor attenuation on a) filling length for SC-MOF with a core diameter of 3.40 μm, b) RIs of liquid analytes and SC-MOF core diameters when filling length = 2.5 cm.

4. Generalized model

Parameters generated by the numerical model require a large computational effort to determine a detailed description of a specific sensor system, thus we have derived a generalized model of a SC-MOF sensor for the detection of liquid analytes based on experimental data and validated by simulation. The performance of the SC-MOF sensor can be determined in relation to L_{att} caused by the: i) dependence on the filling length (l_{fill} ranging from 0.5 cm to 4.5 cm); ii) dependence on the RI of the liquid analyte (RI_{liq} from 1.35 to 1.42); and iii) dependence on the power overlap in the liquid analyte corresponding to the core diameter (from 2.4 μm to 4.0 μm). The following generalized model of overall sensor attenuation has been derived based on Eq. (5) and the measured data:

$$L_{att}(l_{fill}, RI_{liq}, d_{core}) = l_{fill} \times c_1(RI_{liq}, d_{core}) + c_2(RI_{liq}, d_{core}), \quad (6)$$

where c_1 and c_2 are experimentally derived coefficients dependent on RI_{liq} and d_{core} based on 283 measurements. While the coefficient c_1 represents attenuation in the liquid-filled SC-MOF (Region III), c_2 is then influenced by conditions on the interface between the air and the liquid-filled cladding holes (Region II, IV) corresponding to the scattering and reflection of the optical signal. The dependencies of the coefficients c_1 and c_2 have been empirically determined, see the visualization with respect to RI_{liq} and d_{core} in Fig. 6.

The general description of c_1 [dB/cm] and c_2 [dB] dependencies has been derived utilizing a genetic algorithm [20] on the experimentally collected data. A population of 10^6 generations was used to obtain a precise solution. The following dependencies have been derived using the genetic algorithm:

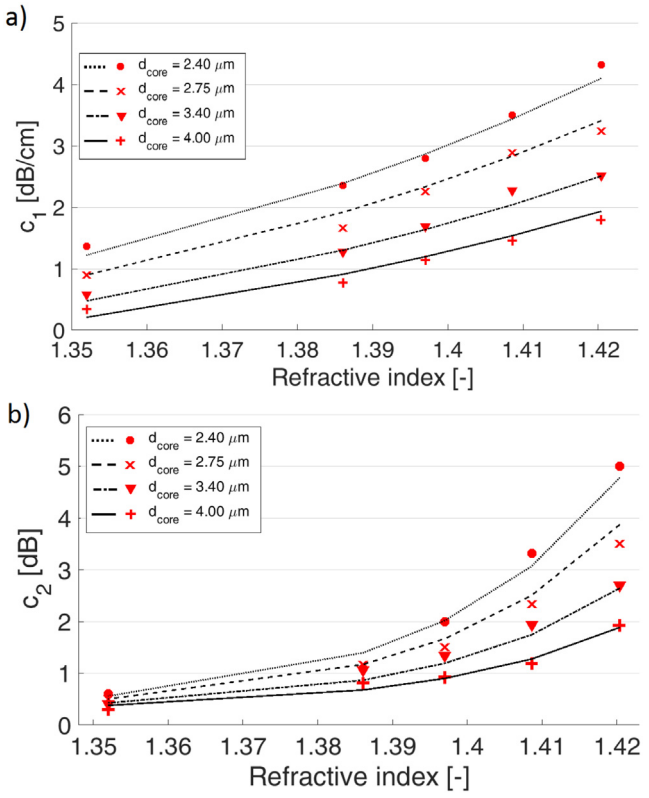

Fig. 6. Coefficient evolution of analyzed SC-MOF. a) c_1 values, b) c_2 values from measurements (symbols) and curves calculated from the generalized model (lines).

$$c_1 = a_1 \times \left(\left(1 + \frac{a_2}{d_{core}}\right)\right) \times (e^{(a_3(RI_{liq}-1))}-1), \tag{7}$$

$$c_2 = e^{\left(b_1+\left(\frac{b_2}{d_{core}}\right)\right)} \times (e^{(b_3(RI_{liq}-1))}-1), \tag{8}$$

values of the variables are summarized in Table 1. The results of these equations are plotted as lines on top of the measured data points shown in Fig. 6 a) and b). Fig. 6 a) is the same as the theoretically derived Fig. 3 a) up to an overall, analyte-dependant proportionality constant (this constant is seen in the first term of Eq. (5)), whereas, Figs. 6 b) and 3 b) are comparable and represent interface losses.

The standard deviation of the generalized model is below 0.9 dB over the entire studied RI range. Sensor resolution, based on experimental data, is better than 10^{-4} RI over the whole RI range 1.35 to 1.42 and SC-MOF core diameter from 2.4 μm up to 4 μm.

The utilization of the derived model can be illustrated in the following example of the design of a sensor for Ethylene-glycol (i.e., antifreeze) monitoring. The desired detection RI ranges from RI = 1.3861 to 1.4204 representing water-diluted Ethylene-glycol and pure Ethylene-glycol, respectively. For the purposes of this example, we assume that a standard source/detector deployment limits the measurement setup up to the maximum dynamic range of 20 dB. The main aim is to design a sensor with the highest sensitivity. Based on the input

Table 1
Derived variables for determination of c_1 (Eq. 7) and c_2 (Eq. 8), with losses measured in decibels.

Variables for c_1		Variables for c_2	
a_1 [1/cm]	−0.0027	b_1 [−]	−14.9012
a_2 [μm]	−7.3708	b_2 [μm]	5.0225
a_3 [−]	18.0144	b_3 [−]	34.1974

Table 2
Example of sensor design based on a constant dynamic range of 20 dB for Ethylene–glycol monitoring.

SC-MOF		
Core size [μm]	Filling length [cm]	Sensitivity [dB/RIU]
2.5	1.77	334.1
3.0	2.32	375.7
3.5	3.01	411.3
4.0	3.92	441.8

limits, the model proposes a set of SC-MOFs of various core diameters. For each core diameter the maximum filling length is limited by the maximum dynamic range. Final solutions of the sensor are summarized in Table 2, where the sensitivity S is determined as:

$$S = \frac{\Delta L_{att}}{\Delta RI_{liq}} \tag{9}$$

The highest sensitivity, based on data from the derived model, can be reached in this case for an SC-MOF of 4 μm core diameter and a filling length of 3.92 cm.

For this specific situation, more options can be generated by the model, which mainly provides the sensitivity evaluation of the SC-MOF sensor and also the possibility of an application-tailored approach. Generally, a larger core diameter would be preferred to provide higher coupling efficiency and longer filling length to increase the sensitivity.

5. Conclusions

The semi-empirical generalized model of SC-MOF for the detection of liquid analytes has been derived. The model serves as a universal tool for a specific sensor design given a wide scale of input parameters such as refractive index range, dynamic range or minimal sensitivity requirements. The generalized model is based on an immense experimental data set, which also eliminated the need for the computationally expensive eigenvalue routine which still requires additional input parameters such as the scattering and absorption cross sections of the analyte. We carried out 283 measurements of SC-MOFs with core diameters in the range of 2.4 μm to 4.0 μm, and with liquid analyte refractive index in the range of 1.35 to 1.42. A genetic algorithm was applied to find a simplified general description of sensor behavior over a wide range of SC-MOF parameters.

Using the genetic algorithm, we found two key coefficients to describe the sensor. The first coefficient represents optical signal attenuation in the liquid analyte, while the second represents signal loss at the air-analyte interface. These results are in strong correlation with the analytical description based on the numerical solutions, where a developed theoretical approach has been applied to describe the complete system performance using an eigenmode solver. The standard deviation of the semi-empirical model is below 0.9 dB for the entire refractive index range and the whole scale of SC-MOF parameters that we investigated. The resolution and sensitivity of the proposed SC-MOF sensors are more than sufficient for detection of a broad range of liquid analytes, e.g. petrol quality analysis in Ethylene-glycol and gasoline blends monitoring.

Acknowledgements

This work has been supported by the project of Ministry of Industry and Trade FV10519, by CTU project SGS17/182/OHK3/3T/13, and by the European Commission through the COST Action MP1401.

Appendix A. Supplementary data

Supplementary data associated with this article can be found, in the

online version, athttps://doi.org/10.1016/j.yofte.2018.08.005.

References

[1] A.M. Cubillas, S. Unterkofler, et al., Photonic crystal fibres for chemical sensing and photochemistry, Chem. Soc Rev. 42 (22) (2013) 8629–8648.
[2] M. Calcerrada, C. Garcia-Ruiz, M. Herraez, Chemical and biochemical sensing applications of microstructured optical fiber-based systems, Laser Photonics Rev. 9 (6) (2015) 604–627.
[3] R. Kostecki, H. Ebendorff-Heidepriem, S.C. Warren-Smith, T.M. Monro, Predicting the drawing conditions for microstructured optical fiber fabrication, Opt. Mat. Exp. 4 (2014) 29–40.
[4] O. Frazao, et al., Suspended-core fibers for sensing applications, Phot. Sens. 2 (2) (2012) 118–126.
[5] T.M. Monro, et al., Sensing with suspended-core optical fibers, Opt. Fiber Tech. 16 (2010) 343–356.
[6] Y. Zhao, D. Ze-qun, J. Li, Photonic crystal fiber based surface plasmon resonance chemical sensors, Sens. Actuators B: Chem. 202 (2014) 557–567.
[7] J.P.B. Lee, S. Roh, Current status of micro- and nano-structured optical fiber sensors, Opt. Fiber Technol. (2009) 209–221.
[8] T.G. Euser, J.S.Y. Chen, M. Scharrer, P.S.J. Russell, N.J. Farrer, P.J. Sadler, Quantitative broadband chemical sensing in airsuspended solid-core fibers, Appl. Phys. 103 (1) (2008) 103108.
[9] I. Nita, E. Geacai, S.O.O. Iulian, Study of the refractive index of gasoline + alcohol pseudo-binary mixtures, Ovidius Univ. Ann. Chem. (2017) 18–24.
[10] G.R.C. Possetti, M. Muller, J.L. Fabris, Refractometric optical fiber sensor for measurement of ethanol concentration in ethanol-gasoline blend, Int. Microwave Optoelectron. Conf. (2009) 616–620.
[11] C. Warren-Smith, H. Ebendorff-Heidepriem, et al., Exposed-core microstructured optical fibers for real-time fluorescence sensing, Opt. Exp. 17 (2009) 18533–18542.
[12] R. Kostecki, H. Ebendorff-Heidepriem, et al., Silica exposed-core microstructured optical fibers, Opt. Mater. Expr. 2 (11) (2012) 1538–1547.
[13] C.M.B. Cordeiro, E.M. dos Santos, C.H.B. Cruz, D. Ferreira, Lateral access to the holes of photonic crystal fibers – selective filling and sensing applications, Opt. Exp. 14 (18) (2006) 8403–8412.
[14] Y.P. Wang, S.J. Liu, X.L. Tan, W. Jin, Selective-fluid-filling technique of microstructured optical fibers, J. Lightwave Techol. 28 (22) (2010) 3193–3196.
[15] S.C. Warren-Smith, T. Monro, Exposed core microstructured optical fiber bragg gratings: refractive index sensing, Opt. Exp. 22 (2) (2014) 1480–1489.
[16] V.P. Minkovich, J. Villatoro, et al., Holey fiber tapers with resonance transmission for high-resolution refractive index sensing, Opt. Exp. 13 (19) (2005) 7609–7614.
[17] S. Silva, J.L. Santos, F.X. Malcata, J. Kobelke, K. Schuster, O. Frazao, Optical refractometer based on large-core air-clad photonic crystal fibers, Opt. Lett. 36 (6) (2011) 852–854.
[18] T. Nemecek, M. Komanec, M. Martan, R. Ahmad, S. Zvanovec, Suspended-core microstructured fiber for refractometric detection of liquids, Appl. Opt. 54 (30) (2015) 8899–8903.
[19] K. Kataoka, Estimation of coupling efficiency of optical fiber by far-field method, Opt. Rev. 17 (5) (2010) 476–480.
[20] S.M. Lothar, Theory of genetic algorithms, Theor. Comput. Sci. 259 (2001) 1–61.

Optical Fiber Technology 56 (2020) 102177

Contents lists available at ScienceDirect

Optical Fiber Technology

journal homepage: www.elsevier.com/locate/yofte

Exact modeling of photonic crystal fibers for determination of fundamental properties

Dmytro Suslov*, Matěj Komanec, Tomáš Němeček, Jan Bohata, Stanislav Zvánovec

Department of Electromagnetic Field, Faculty of Electrical Engineering, Czech Technical University in Prague, Technicka 2, Prague 6 166 27, Czech Republic

ARTICLE INFO

Keywords:
Photonic crystal fiber
Optical fiber modeling
Mode-field distribution
Supercontinuum generation

ABSTRACT

We present a simple but highly accurate modeling technique for real photonic crystal fibers (PCFs) characterization. We determine the influence caused by idealized model parameters. Our technique can be applied to arbitrary PCF air-hole structures, as it takes into account all structural distortions. It requires only an image of the PCF cross-section to create an accurate PCF model. Model outputs are presented in comparison with the measurement of chromatic dispersion curve and the effective mode area. We provide a study on the impact of imprecise determination of glass refractive index on the PCF model accuracy. We demonstrate how the simplification of the air-hole deformations can influence the chromatic dispersion curve. Finally, we show the effect of precise PCF modeling on example of supercontinuum generation.

1. Introduction

Photonic crystal fibers (PCFs) are widely used thanks to the versatility and freedom of their design. This allows to specifically tailor PCF properties towards individual applications such as supercontinuum generation (SCG) [1,2], sensing [3,4] or signal filtering [5].

Various methods have been proposed for efficient PCF design and tailoring of their properties [6,7]. These methods enable us to derive the PCF chromatic dispersion (CD) curve, mode-field distribution, or effective mode area (A_{eff}) [8]. Moreover, results of PCF application, such as SCG, can be predicted even prior to the drawing of the PCF.

The PCF drawing process, however, can introduce distortions to the designed PCF air-hole structure causing significant differences from the pre-draw PCF design. The effect of such distortions has been studied in hollow-core fibers in [9–11], as well as in index-guided PCFs [12]. These distortions were found to cause an increase in insertion loss (IL) by a factor of ten [10], as well as a more than a 0.2 μm reduction in the PCF transmission bandwidth [10].

It is possible to predict the PCF structure evolution during the fiber drawing process by considering the pressure applied to the outer cladding and the surface tension, pressure and the viscosity of the air-hole microstructure (using the fluid dynamics model) [13]. However, this approach has its limitations and requires exact knowledge of the drawing process and as such, it is impossible to apply this method to characterize already drawn PCFs.

PCF parameters (CD, mode-field distribution, A_{eff}) can be measured directly [8]. However, such approach is often time and cost-intensive. A fast and accurate method capable of deriving PCF properties based on the simulation model is preferable.

In this paper, we present an easy, straightforward and precise technique of PCF characterization based on the creation of an exact model of the post-draw PCF. This technique works well even with a short PCF segment (with length less than 1 m) and can be carried out in just 3 subsequent steps: i) At first, an accurate photograph of the PCF structure is acquired; ii) next refractive index (RI) of the glass is obtained; and iii) finally, the PCF model is created. Even though separate steps of this technique are known, a comprehensive study of the entire process is missing. Moreover, the impact of the modelling precision and air-hole structure deformation is provided, with regard to CD and SCG.

To demonstrate this technique, two models of a sample lead-silicate PCF are presented. The first one presents a precise post-draw PCF model with accurate PCF properties and the second model includes a simplified air-hole structure. Finally, the presented technique is verified by measurement of CD and A_{eff}.

2. PCF model

We start our model with the PCF structure by acquiring the image of the unknown PCF cross-section. Then we determine the refractive index of the PCF glass material. Combining these two steps, we create the whole PCF model and calculate PCF properties using a finite element method (FEM) solver.

* Corresponding author.
E-mail address: suslodmy@fel.cvut.cz (D. Suslov).

https://doi.org/10.1016/j.yofte.2020.102177
Received 26 August 2019; Received in revised form 29 January 2020; Accepted 19 February 2020
Available online 06 March 2020

The following sections describe each of these steps in detail.

2.1. Air-hole structure

In literature, PCF structures are typically described by parameters such as the core diameter, the diameter of the air-holes (for each ring) and the distance between the air-holes (lattice constant/pitch) [14–16]. These parameters are often used in the PCF design process and therefore may lead to the assumption that the drawn PCF would have the same regular structure. However, this is usually not the case, as during the PCF drawing process distortions of the air-hole structure occur. These can then change/shift the shape/position of the air-holes, which can also lead to the change or deformation of the core area diameter. The distortions can influence each individual air-hole differently.

To obtain a precise PCF model, these distortions must be taken into account. For FEM based model, it is necessary to create a mesh that provides a representation of the PCF structure. This mesh must include all the distortions, therefore a detailed image of the PCF cross-section is needed. A scanning electron microscope (SEM) is typically used to capture the image, however we have found that for some types of PCFs an ordinary light microscope (OLM) can be used as well. An OLM with at least 400x magnification can provide enough detail for some simpler PCF structures, such as suspended-core PCFs. For more complicated structures with many air-holes, the use of SEM is necessary as OLM typically does not provide high enough resolution to capture the exact dimensions of the air-holes with a diameter in the order of micrometers. The comparison of microscopes usage can be seen in Fig. 1, where the image of suspended-core PCF cross-section is obtained with OLM as shown in Fig. 1a) and with SEM shown in Fig. 1b). The same comparison is then shown for a honeycomb PCF with small air-holes - see OLM image in Fig. 1c) and SEM image in Fig. 1d).

The captured image is then converted into a mesh using vector graphic software, where the outlines of the air-holes are drawn as vector elements which then form the PCF model. This allows us to capture all the distortions of the PCF structure. Since only the image of PCF cross-section is required, a very short piece of PCF is sufficient (e.g. cleaved-off PCF segments).

2.2. Refractive index

The second step of the PCF model is getting the RI dependence on wavelength, i.e. RI curve of the glass material. For a glass material, RI is described by the well-known Sellmeier equation [17]:

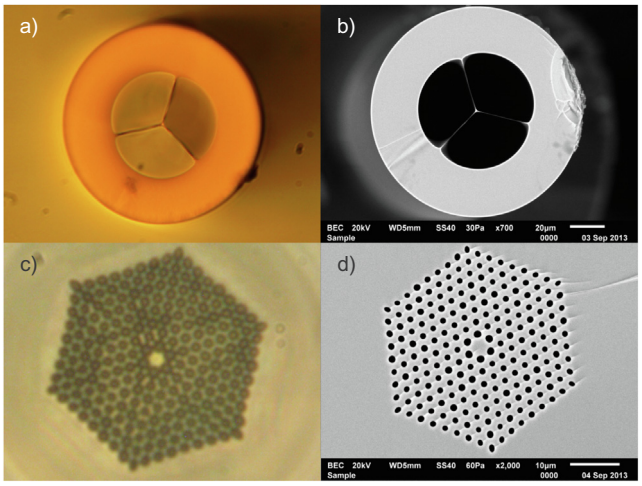

Fig. 1. Comparison of cross-sections of: a) suspended core PCF end-facet obtained with 400× magnification using OLM, b) suspended core PCF obtained with 700× magnification using SEM, c) PCF obtained with 1000× magnification using OLM, d) PCF obtained with 2000× magnification using SEM.

$$n(\lambda) = \sqrt{1 + \sum_{n=1}^{N} \frac{B_n \lambda^2}{\lambda^2 - C_n}} \quad (1)$$

where λ is wavelength, B_n and C_n are n-th fitting coefficients.

Many of glass materials commonly used for manufacturing PCF have already been well defined and their fitting coefficients are readily available [18]. Glass RI values for each wavelength are commonly described with the precision of 10^{-4} and wavelength spanning from visible to near-infrared region.

However, newly developed glass materials require a detailed study of their respective RI curves. For proper PCF characterization, the RI curve must be measured with the above-mentioned precision of 10^{-4} for each value of RI. For this purpose, the Abbe refractometer is commonly used with the modification for the infrared region [19].

2.3. Modelling approach

One of the commonly used methods for the computation of modal properties in a PCF is FEM, which is a well-described method [20] [21] with many of the commercially available solvers. In this paper, we use Comsol Multiphysics 5.1 as a direct full-vector FEM eigenvalue solver.

The derived mode field distribution can provide several parameters like effective refractive index (n_{eff}), electric field intensity E and the propagation constant (β) for a given wavelength. Also CD and A_{eff} can be investigated. Especially CD curve can be used as a good tool for PCF examination since it is susceptible even to the small changes of the air-hole structure or glass material RI. The CD coefficient for each wavelength is determined as [22]:

$$D(\lambda) = \frac{-2\pi c}{\lambda^2}\beta_2 = \frac{\lambda}{c}\frac{\partial^2 \mathrm{Re}(n_{\text{eff}})}{\partial \lambda^2} \quad (2)$$

where c is the speed of light and β_2 is the group velocity dispersion.

A_{eff} represents a significant parameter for nonlinear applications, which are typical uses of many PCFs. We calculate A_{eff} by integrating the intensity of the electric field over the surface of the fiber end (A) as [22]:

$$A_{\text{eff}} = \frac{(\int I dA)^2}{\int I^2 dA} = \frac{(\int |E^2| dA)^2}{\int |E^4| dA} \quad (3)$$

where I is the near-field optical intensity.

3. PCF model example

To demonstrate the impact of air-hole distortions and imprecise RI determination, a sample PCF is examined. We have selected a hexagonally-structured PCF made of lead-silicate glass (denoted as PBG-08_1) with the composition of PbO: 39.17%, Bi_2O_3: 27.26%, Ga_2O_3: 14.26%, SiO_2: 14.06% and CdO: 5.26%. Image of the sample PCF structure can be seen in Fig. 1d). We have created two models of this sample PCF.

3.1. PCF air-hole structure models

"Model 1" is based on the real post-draw PCF. This model is created by vectorization of the image of the PCF cross-section obtained with SEM. Therefore, this PCF model provides an accurate representation of the real post-draw PCF and the properties derived from this model match the properties of the real PCF (as will be shown later). This model is an exact copy of the PCF cross-section, it includes all air-hole shape deformations and size changes that occurred during drawing process. For this reason this model is not described by standardized PCF parameters that describe air-hole structure (air-hole diameters, pitch, core diameter).

"Model 2" is a commonly used, but simplified model. We present it to demonstrate how even small changes in the PCF air-hole structure

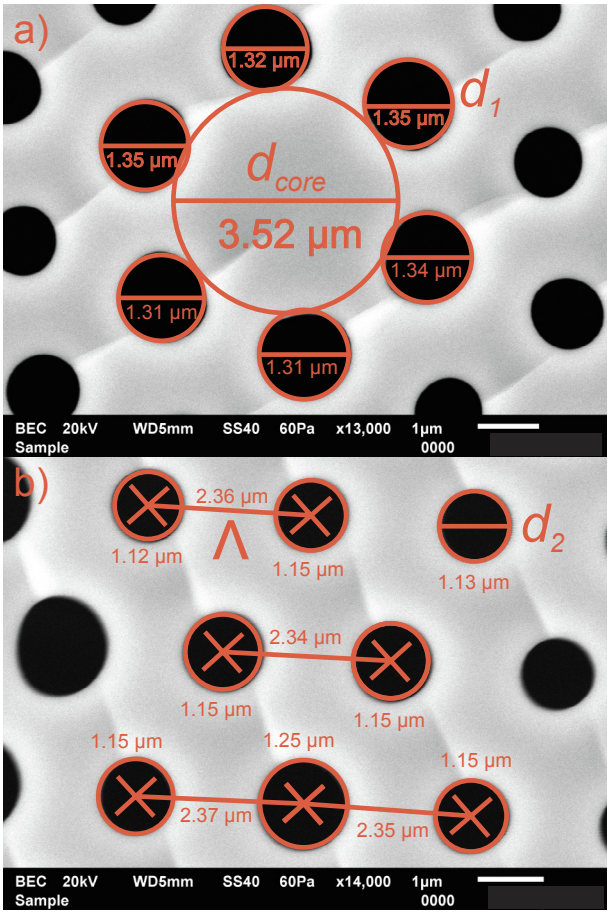

Fig. 2. Example of PCF air-hole structure parameter measurement for Model 2. Details of a) the measured diameter d_1 of the innermost rings, b) measured diameter d_2 of outer rings and the distance between air-holes (Λ).

(comparable to varying real parameters) can influence the derived PCF properties and that at first look reasonable simplifications of the PCF air-hole structure can lead to significantly incorrect results.

Model 2 is created using post-draw PCF structure as a template (the identical SEM image of the PCF cross-section that is used for Model 1), however in this case we consider all of the air-holes to be perfectly circular having the same specific air-hole diameter d_1 for all air-holes in the innermost ring and d_2 for all air-holes in the outer rings, the same distance between air-holes (pitch—Λ) and a core diameter (d_{core}).

Each of these parameters is obtained by averaging the measured values that can be seen in Fig. 2. First, we average all of the innermost ring air-holes to obtain parameter d_1 and then air-holes in outer rings to obtain parameter d_2. Last, we average distances between the air-holes to obtain parameter Λ. In our case, we have measured $d_1 = 1.33$ µm, $d_2 = 1.15$ µm, $\Lambda = 2.35$ µm and $d_{core} = 3.52$ µm. The core areas of the resulting air-hole structures of Model 1 and Model 2 are compared in Fig. 3.

3.2. Refractive index curves

Following the PCF model creation step, we now examine the impact of imprecise glass RI determination on the PCF model outputs. The Sellmeier coefficients of the lead-silicate glass (PBG-08$_1$) of the sample PCF were published in [16]. Refractive index is dependent on wavelength, thus precise characterization of RI is necessary to obtain correct PCF model results. This can sometimes present a challenge for new and experimental PCF materials, such as one used in our sample PCF. To demonstrate the effect of such an imprecision, we have constructed a

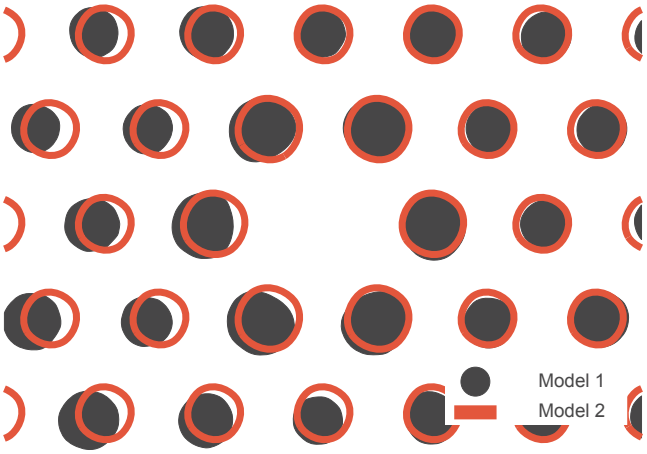

Fig. 3. Detail of the sample PCF core area. Model 1 is drawn in full black and Model 2 is represented by the red outlines.

Table 1
Sellmeier equation coefficients of the PBG-08 glass. PBG-08$_1$ are data presented in [16], PBG-08$_2$ are derived coefficients of the shifted RI curve.

	PBG-08$_1$	PBG-08$_2$
B_1	2.0118814	−0.385
B_2	0.5467324	3.264
B_3	1.3948861	−0.3491
C_1	0.011537	−0.1281
C_2	0.063552	0.004391
C_3	141.65405	−0.1265

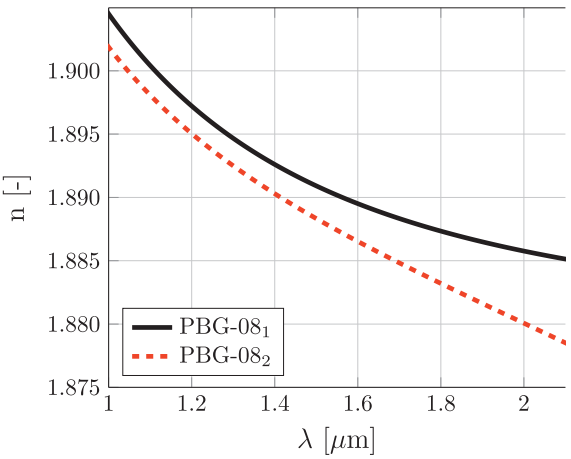

Fig. 4. Refractive index curves of PBG-08 glass; PBG-08$_1$ are data presented in [16], PBG-08$_2$ is shifted RI curve.

second RI curve (PBG-08$_2$), which is shifted and diverges in the longer wavelength region from the RI curve in [16] (PBG-08$_1$). Both examined RI Sellmeier equation coefficients are presented in Table 1 and in Fig. 4.

Here we can see that the two RI curves are merely shifted in the shorter wavelength region, but at longer wavelengths the two curves begin to diverge with difference in order of 0.005.

3.3. Model results

We have evaluated the impact of the RI curves on CD, which can be determined using Eq. 2. The calculation is carried out for Model 1 using two RI curves depicted in Fig. 4. We use a single model (Model 1) of air-hole structure, since a dominant part of CD in PCFs is formed by waveguide dispersion. Therefore, to demonstrate only the impact of RI on

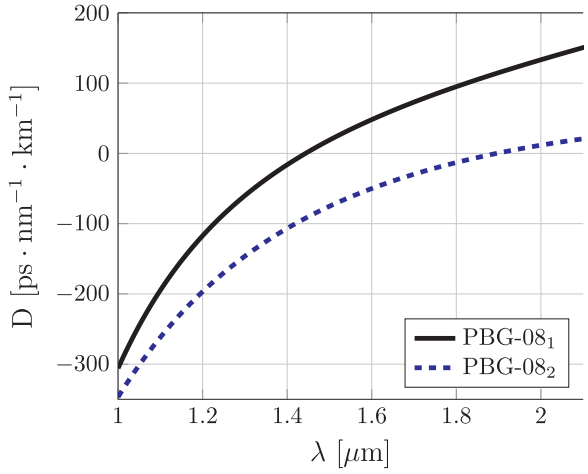

Fig. 5. Calculated chromatic dispersion curves using Model 1 with RI curve PBG-08_1 obtained from [16] and PBG-08_2 obtained from derived coefficients of the shifted RI curve.

the resulting CD, a single PCF model must be used. Calculated CD curves are then shown in Fig. 5.

This result underlines the fact that even small differences in RI such as ~ 0.005 can cause a significant divergence in the CD curves with a zero-dispersion wavelength (ZDWL) shift of up to 0.450 μm ($ZDWL_{PBG-08_1}$ = 1.445 μm and $ZDWL_{PBG-08_2}$ = 1.895 μm).

Seeing the strong effect of the glass RI, we study the effect of the air-hole structure deformation. CD curves are calculated for Model 1 and Model 2 using Sellmeier coefficients of PBG-08_1. The results can be seen in Fig. 6. The CD curves for Model 1 and Model 2 are in a good agreement for shorter wavelengths, but as wavelength increases the CD plots begin to diverge significantly (difference of 23.46 ps·nm^{-1}·km^{-1} at 1.550 μm and 49.57 ps·nm^{-1}·km^{-1} at 2 μm). The ZDWL shift between Model 1 and Model 2 is 0.077 μm (1.445 vs 1.522 μm). Such differences in CD curves can have significant consequences for practical applications which are discussed more in Chapter 5.

A_{eff} is calculated for both Models using Eq. 3. The values of the electric field of the examined mode were obtained from FEM solver at λ = 1.550 μm. The results are shown in Table 2.

These results show that there are only minor differences (0.01 μm^2) in A_{eff} between the RI curves. However, there are noticeable differences in the A_{eff} between the two models (0.71 μm^2), as the changes in the air-hole structure significantly affect the physical dimensions of the waveguide and therefore the mode-field distribution of the fundamental mode in PCF.

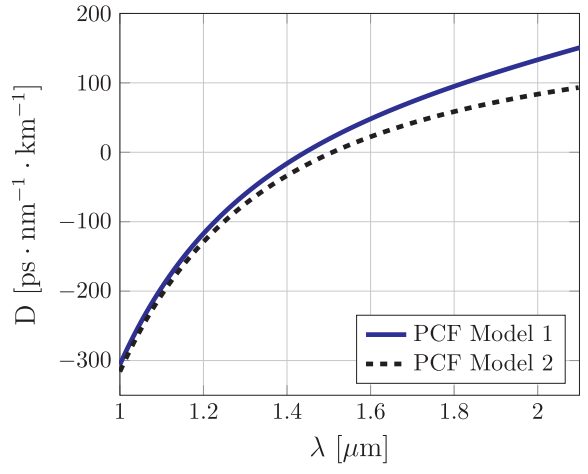

Fig. 6. Comparison of the CD curves for Model 1 and Model 2. Both models consider PBG-08_1 glass.

Table 2
Calculated A_{eff} values at λ = 1.550 μm.

	PBG-08_1	PBG-08_2
$A_{\text{eff model1}}$ [μm^2]	7.92	7.91
$A_{\text{eff model2}}$ [μm^2]	7.20	7.20

4. Verification of PCF model parameters

To demonstrate that our technique yields accurate values, we have verified the presented PCF model via the CD curve and A_{eff}. Note that these measurements are not necessary to create the PCF model.

4.1. Chromatic dispersion measurement

The CD curve of the sample PCF is measured using the free-space interferometric method [23], which is based on the measurement of the optical path difference between two signals propagating in the reference (free-space) path and measured (sample PCF) path – see the setup of the measurement depicted in Fig. 7.

In this setup we use a supercontinuum (SC) source (NKT SuperK Extreme EXR-15) as a broadband light source which allows us to measure the entire spectrum at once. The 6 W output of the supercontinuum source is launched via a free-space collimator and split in a 96/4 ratio via a wedge glass prism, where the 4% signal is further filtered using an optical filter (Thorlabs FELH0750) to remove the visible part of the SC spectrum. The signal is then split into two arms in free-space using a 50/50 beam splitter (BS) (Thorlabs PBSW-1550). The measurement arm contains the PCF and lens 1 and lens 2 (both Thorlabs C660TME-C) used to couple the signal into and out of the PCF. These lenses are positioned on the micromovement stage to enable alignment with sub-micron precision. The reference arm contains a micromovement stage with two mirrors (Thorlabs PF10-03-P01) that allow the tuning of the optical path length. The output of both arms is then combined on another 50/50 BS (Thorlabs PBSW-1550) and coupled into the output fiber using lens 3 (convex lens with f = 5 cm). Resulting data are visualized via the optical spectrum analyzer (OSA) (Yokogawa AQ6370C).

These measurements provide a spectral interferogram which can be observed at OSA as a beat signal at specific wavelengths. From the interference pattern it is possible to calculate the resulting CD as [23]:

$$D = \frac{1}{c}\frac{\partial N_{\text{PCF}}}{\partial \lambda}, \tag{4}$$

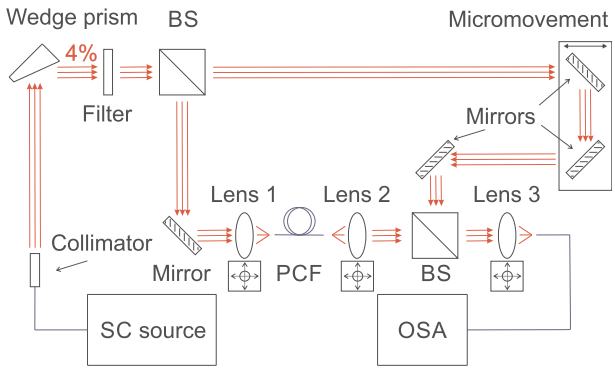

Fig. 7. Interferometric setup for the measurement of the CD curve using a broadband source. Supercontinuum source (SC source), beam splitter (BS), optical spectrum analyzer (OSA).

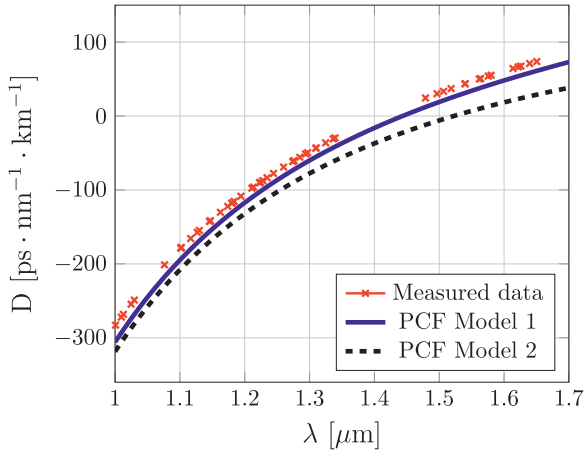

Fig. 8. Simulated and measured CD curve of sample PCF. Simulation results are based on Model 1 and Model 2 using PBG-08_1 glass material.

$$N_{\mathrm{PCF}} = \frac{2\Delta l - \Delta l_{\mathrm{lenses}}}{l_{\mathrm{PCF}}} + 1 \tag{5}$$

where N_{PCF} is given as the group refractive index of PCF, l_{PCF} is the PCF length, Δl is the optical path difference between the measurement and reference arms, $\Delta l_{\mathrm{lenses}}$ is the additional optical path difference caused by the signal passing through the lenses in the measurement arm.

To validate our PCF model (Model 1 using PBG-08_1) measured and calculated CD curves are compared. We illustrate the results in Fig. 8.

The ZDWL obtained from our CD measurement is $ZDWL_{\mathrm{meas}} = 1.412$ μm, while the ZDWL obtained from the simulation Model 1 using PBG-08_1 is $ZDWL_{\mathrm{sim}} = 1.443$ μm. This result is in agreement with the model. The 0.031 μm blue shift of the measured CD curve is caused by the unknown lens thickness at the point of the signal as well as imprecision in determining the wavelength of interference maximum.

4.2. Effective mode area

The second validation of the PCF model is done via A_{eff} of the sample PCF, which is obtained by measuring the PCF mode-field distribution in the near-field. Effective mode area is calculated using Eq. 3. The measurement setup can be seen in Fig. 9.

The laser signal at 1.55 μm (ID Photonics Cobrite DX4) is coupled into our sample PCF with lens 1 (Thorlabs C660TME-C, 40% coupling efficiency). The PCF output signal is then collimated using lens 2 (Thorlabs C660TME-C) and propagates to the BS (Thorlabs PBSW-1550). 50% of the signal is captured with the CCD camera (Gentec Beamage 4 M IR), the other 50% is deflected and is not used.

For correct measurement of the near-field distribution, PCF end-facet must be positioned precisely in the focus of lens 2 and the magnification of lens 2 must be determined. To ensure that, we use laser 2 (ID Photonics Cobrite DX4) with lens 3 (convex lens with focus

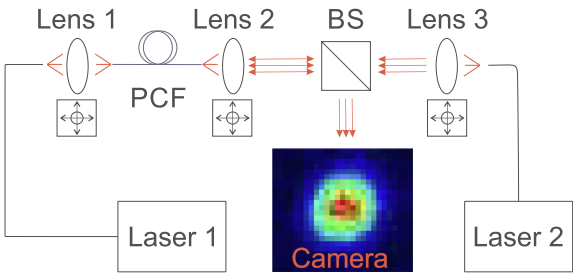

Fig. 9. Setup for measuring the mode-field distribution of sample PCF in the near-field.

distance = 5 cm) that serves to illuminate the PCF end-facet. The image of the air-hole structure of the sample PCF is then reflected back on the BS and to the CCD camera. Therefore, when we can see the sharp image of the PCF air-hole structure on the CCD camera, we are sure that the PCF is in the focus of lens 2. The magnification of the lens 2 can be then easily determined from the image captured by the CCD camera, as the reflected image of the air-hole structure passes through lens 1 and BS, it is subjected to same magnification as mode-field distribution of the PCF and the dimensions of the PCF air-hole structure are already known.

Using this method we are able to obtain $A_{\mathrm{eff_{meas.}}} = 7.87$ μm^2 at $\lambda = 1.550$ μm, which is in good agreement with the data obtained from the Model 1 with $A_{\mathrm{eff}} = 7.92$ μm^2. The small 0.05 μm^2 difference in A_{eff} is contributed to the finite resolution of the camera (2048 × 2048 px), inherent noise of the camera and the uncertainty in determining the focus of the PCF end-facet.

5. Discussion

From the presented results, it is clear that to achieve accurate PCF characterization we need to transfer the exact PCF air-hole structure into the proposed model (Model 1). Defining a PCF by using uniform parameters (Model 2) is not suitable as the model does not include all deformations of shape, size, or position of the air-holes.

We have shown that in some cases an OLM with 400x magnification is sufficient to obtain a detailed enough image of the PCF air-hole structure. Using OLMs can simplify the model preparation process and make it less cost-intensive.

The precise characterization of the RI curve of studied PCF glass material has proven to be critical. In this paper, we have studied a sample PCF made from experimental lead-silicate glass. As shown in Fig. 4 and Fig. 5, even small RI variations in the order of 10^{-3} can produce significant differences in the resulting CD curve and 0.077 μm ZDWL shift. On the other hand, typically well known glass materials are used, such as silica glasses, which have already been precisely characterized and then the RI measurement step can be omitted.

Now we want to emphasize the importance of the precise PCF modeling in the context of a practical application. For this purpose, SCG was calculated using [24] with the parameters of Model 1 and Model 2. The sample PCF nonlinear coefficient γ and the propagation constants β_2 - β_m at the pump wavelength were calculated. β_2 can be obtained using Eq. 2, or derived from the models, while β_3 - β_m are calculated by the derivation of subsequent β as [22]:

$$\beta_m = \frac{\partial^m \beta}{\partial \omega^m}, \qquad (m = 1, 2, 3, \ldots) \tag{6}$$

where ω is the central frequency of the pump pulse spectrum.

The nonlinear coefficient γ is calculated as [22]:

$$\gamma = \frac{2\pi n_2}{\lambda A_{\mathrm{eff}}} \tag{7}$$

where n_2 is the nonlinear refractive index; $n_2 = 4.3 \cdot 10^{-19}$ m^2/W (measured at $\lambda = 1.240$ μm) for PBG-08_1 glass [25]. A_{eff} is calculated using the COMSOL simulation for a particular wavelength and the PCF model. We consider the input pulse duration $t = 400$ fs with 30 kW peak power and 20% PCF coupling efficiency. A comparison of the derived A_{eff} and γ is presented in Table 3.

Considering the ZDWL results shown in Fig. 6 (Model 1 = 1.445 μm and Model 2 = 1.522 μm with PBG − 08_1) and based on the values obtained with Model 2 it would lead to the assumption that optimal SCG could be achieved with sources centered at around 1.575 μm region. We have confirmed this by calculating SCG with such source and using values in Table 3. We could observe the SCG formation starting at 3 cm PCF length and fully forming at 4 cm PCF length with SCG spanning from 0.860 to 2.900 μm. However, for the same setup and with 4 cm of real drawn PCF (PCF model 1) we can observe SCG spanning only from 1.150 to 2.600 μm.

Table 3
Calculated A_{eff} and γ of sample PCF. Results are calculated for two PCF models considering PBG-08$_1$ glass material.

	λ = 1.450 μm	λ = 1.575 μm
$A_{eff\ model1}$ [μm^2]	7.82	8.11
$A_{eff\ model2}$ [μm^2]	7.10	7.20
γ_{model1} [W^{-1} km^{-1}]	223.00	211.51
γ_{model2} [W^{-1} km^{-1}]	262.44	242.09

To effectively pump real post-draw PCF, a laser source centered at 1.450 μm must be used, which produces SCG spanning from 0.600 to 2.900 μm with using only 3.5 cm of PCF. For practical applications, it is thereby necessary to use precise PCF modeling technique.

6. Conclusion

We presented an easy straightforward technique to obtain an accurate model of the real post-draw PCF, which gives reliable outputs for subsequent applications. The advantage of our approach is in time and cost saving without the need for a detailed experimental measurement campaign. In many cases, where the PCF glass material is already known only a several centimeters long PCF segment is all that is required to construct the accurate PCF model. Additionally, our PCF model (Model 1) was verified by CD and mode effective area measurements.

We then compared our accurate PCF Model 1 to a commonly used simplified model (Model 2) considering a sample lead-silicate hexagonally-structured PCF. We calculated the CD curve, γ and A_{eff} for both PCF models. We show a ZDWL shift of 0.077 μm between the two models and even 0.450 μm between the two presented RI curves. An impact on a selected application of supercontinuum generation is discussed showing that considering simplified Model 2 can lead to the use of non-optimal laser pump and therefore narrow SCG spanning only 1.150–2.600 μm as compared to the Model 1 with SCG spanning 0.600–2.900 μm.

These differences in model outputs illustrate the imprecision that occurs when even seemingly reasonable simplification of the PCF structure is considered (Model 2). The model differences in CD, A_{eff} and SCG highlight the need to use real post-draw PCF design with all air-hole distortions and to define glass RI with the precision of at least 10^{-4}.

CRediT authorship contribution statement

Dmytro Suslov: Methodology, Software, Investigation, Writing - original draft, Visualization. **Matěj Komanec:** Validation, Resources, Writing - review & editing, Supervision. **Tomáš Němeček:** Software, Validation, Investigation, Writing - review & editing. **Jan Bohata:** Validation, Investigation, Writing - review & editing. **Stanislav Zvánovec:** Validation, Resources, Writing - review & editing, Supervision.

Declaration of Competing Interest

The authors declare that they have no known competing financial interests or personal relationships that could have appeared to influence the work reported in this paper.

Acknowledgement

This research was supported by the CTU in Prague grant SGS17/182/OHK3/3T/13 and by the project of the Ministry of Industry and Trade of the Czech Republic, TRIO FV10519.

References

[1] J.H.V. Price, T.M. Monro, H. Ebendorff-Heidepriem, F. Poletti, P. Horak, V. Finazzi, J.Y.Y. Leong, P. Petropoulos, J.C. Flanagan, G. Brambilla, X. Feng, D.J. Richardson, Mid-IR supercontinuum generation from nonsilica microstructured optical fibers, IEEE J. Sel. Top. Quantum Electron. 13 (3) (2007) 738–749.
[2] L.E. Hooper, P.J. Mosley, A.C. Muir, W.J. Wadsworth, J.C. Knight, Coherent supercontinuum generation in photonic crystal fiber with all-normal group velocity dispersion, Opt. Express 19 (6) (2011) 4902–4907.
[3] O. Frazão, J.L. Santos, F.M. Araújo, L.A. Ferreira, Optical sensing with photonic crystal fibers, Laser Photon. Rev. 2 (6) (2008) 449–459.
[4] A.M. Cubillas, J. Hald, J.C. Petersen, High resolution spectroscopy of ammonia in a hollow-core fiber, Opt. Express 16 (6) (2008) 3976–3985.
[5] K.S. Hong, H.C. Park, B.Y. Kim, I.K. Hwang, W. Jin, J. Ju, D.I. Yeom, 1000nm tunable acousto-optic filter based on photonic crystal fiber, Appl. Phys. Lett. 92 (3) (2008) 031110.
[6] K. Saitoh, M. Koshiba, T. Hasegawa, E. Sasaoka, Chromatic dispersion control in photonic crystal fibers: application to ultra-flattened dispersion, Opt. Express 11 (8) (2003) 843–852.
[7] A. Ferrando, E. Silvestre, P. Andrés, J.J. Miret, M.V. Andrés, Designing the properties of dispersion-flattened photonic crystal fibers, Opt. Express 9 (13) (2001) 687–697.
[8] S. Xing, D. Grassani, S. Kharitonov, A. Billat, C.-S. Brés, Characterization and modeling of microstructured chalcogenide fibers for efficient mid-infrared wavelength conversion, Opt. Express 24 (9) (2016) 9741–9750.
[9] E.N. Fokoua, D.J. Richardson, F. Poletti, Impact of structural distortions on the performance of hollow-core photonic bandgap fibers, Opt. Express 22 (3) (2014) 2735–2744.
[10] M.J. Li, J.A. West, K.W. Koch, Modeling effects of structural distortions on air-core photonic bandgap fibers, J. Lightwave Technol. 25 (9) (2007) 2463–2468.
[11] G.T. Jasion, F. Poletti, J.S. Shrimpton, D.J. Richardson, Volume manufacturing of hollow core photonic band gap fibers: challenges and opportunities, Optical Fiber Communication Conference, Optical Society of America, 2015page W2A.37.
[12] M. Zghal, R. Cherif, Impact of small geometrical imperfections on chromatic dispersion and birefringence in photonic crystal fibers, Opt. Eng. 46 (12) (2007).
[13] G.T. Jasion, S.R. Sandoghchi, Y. Chen, N.V. Wheeler, T. Bradley, N. Baddela, J. Hayes, M. Petrovich, D.J. Richardson, J.S. Shrimpton, F. Poletti, Novel fluid dynamics model to predict draw of hollow core photonic band-gap fibres, in: 2014 The European Conference on Optical Communication (ECOC), 2014, pp. 1–3.
[14] F. Poli, A. Cucinotta, S. Selleri, Hotonic Crystal Fibers: Properties and Applications, Springer, 2007.
[15] I. Kaminow, T. Li, A.E. Willner, Optical fiber telecommunications VA: systems and networks, Elsevier, 2008.
[16] G. Stepniewski, R. Kasztelanic, D. Pysz, M. Klimczak, R. Buczynski, Temperature sensitivity of chromatic dispersion in nonlinear silica and heavy metal oxide glass photonic crystal fibers, Opt. Mater. Express 6 (8) (2016) 2689–2703.
[17] W. Sellmeier, Zur erklärung der abnormen farbenfolge im spectrum einiger substanzen, Ann. Phys. 219 (6) (1871) 272–282.
[18] Advanced Optics SCHOTT AG. Optical glass catalogue, 2018.
[19] J. Rheims, J. Köser, T. Wriedt, Refractive-index measurements in the near-IR using an Abbe refractometer, Meas. Sci. Technol. 8 (6) (1997) 601–605.
[20] P.G. Ciarlet, J.L. Lions, General preface, Finite Element Methods (Part 1), Handbook of Numerical Analysis, vol. 2, Elsevier, 1991.
[21] P.G. Ciarlet, J.L. Lions, General preface, Finite Element Methods (Part 2), Numerical Methods for Solids (Part 2), Handbook of Numerical Analysis, vol. 4, Elsevier, 1996.
[22] G. Agrawal, Nonlinear Fiber Optics. Optics and Photonics, Elsevier Science, 2012.
[23] P. Hlubina, M. Szpulak, D. Ciprian, T. Martynkien, W. Urbańczyk, Measurement of the group dispersion of the fundamental mode of holey fiber by white-light spectral interferometry, Opt. Express 15 (18) (2007) 11073–11081.
[24] J.R. Taylor, J.M. Dudley, Supercontinuum Generation in Optical Fibers, Cambridge University Press, 2010.
[25] G. Sobon, M. Klimczak, J. Sotor, K. Krzempek, D. Pysz, R. Stepien, T. Martynkien, K.M. Abramski, R. Buczynski, Infrared supercontinuum generation in soft-glass photonic crystal fibers pumped at 1560 nm, Opt. Mater. Express 4 (1) (2014) 7–15.

Low-Loss and Low-Back-Reflection Hollow-Core to Standard Fiber Interconnection

M. Komanec, D. Suslov, S. Zvánovec, Y. Chen, T. Bradley, S. R. Sandoghchi, E. R. Numkam Fokoua, G. T. Jasion, M. N. Petrovich, F. Poletti, D. J. Richardson, and R. Slavík

***Abstract*— We present a new approach to permanently inter-connect hollow-core fiber (HCF) to solid-core fiber, which does not involve fusion splicing. Our approach is based on a modification of the glue-based fiber-array technology routinely used for fiber pigtailing of planar lightwave circuits. The resulting interconnection provides for a low insertion loss due to the fact that the HCF microstructure is not deformed during the gluing (low temperature) process that is almost impossible to achieve with the standard (high temperature) fusion splicing method. Furthermore, this low-temperature technique enables the deposition and preservation of thin films deposited at the solid-to-hollow core fiber interface, allowing for additional functionality without the introduction of extra losses or any increase in complexity. To demonstrate this, we have applied an anti-reflection (AR) coating. A further feature of our approach is the ability to control very precisely the length of the graded-index (GRIN) fiber mode field (MF) adapter inserted in between the standard single-mode fiber (SMF-28) and the HCF. We show experimentally how the length of the GRIN fiber MF adapter influences the coupling between the SMF-28 and the fundamental as well as the higher-order modes of the HCF. We coupled between SMF-28 [10 μm mode field diameter (MFD)] and the fundamental mode of a 19-cell hollow-core photonic bandgap fiber (HC-PBGF, 21.1 μm MFD) with the lowest-ever reported insertion loss of 0.30 dB per interface.**

***Index Terms*— Optical components, optical fiber connecting, optical fibers.**

I. Introduction

HOLLOW-CORE fibers such as hollow-core photonic bandgap fibers (HC-PBGFs) offer many advantages over conventional solid-core fibers due to the strongly reduced interaction of the guided light with the glass material. Examples of the benefits of this are the extremely low fiber non-linearity, low and stable [1] signal latency, the possibility to construct long-length gas cells [2], etc.

Manuscript received December 11, 2018; revised February 9, 2019; accepted February 22, 2019. Date of publication March 4, 2019; date of current version May 7, 2019. This work was supported in part by the Czech Technical University (CTU) in Prague under Grant SGS17/182/OHK3/3T/13, in part by the Optoelectronics Research Centre (ORC), University of Southampton, U.K., RAEng (Senior Research Fellowship - RCSFR1718\6\15), and in part by the Engineering and Physical Sciences Research Council (EPSRC) under Grant EP/P030181/1. *(Corresponding author: M. Komanec.)*

M. Komanec, D. Suslov, and S. Zvánovec are with the Faculty of Electrical Engineering, Czech Technical University in Prague, 16627 Prague, Czech Republic (e-mail: komanmat@fel.cvut.cz).

Y. Chen, T. Bradley, S. R. Sandoghchi, E. R. Numkam Fokoua, G. T. Jasion, M. N. Petrovich, F. Poletti, D. J. Richardson, and R. Slavík are with the Optoelectronics Research Centre, University of Southampton, Southampton SO17 1BJ, U.K.

Color versions of one or more of the figures in this letter are available online at http://ieeexplore.ieee.org.

Digital Object Identifier 10.1109/LPT.2019.2902635

A key property of any optical fiber is attenuation. In HC-PBGF the attenuation is defined principally by the fiber design. The common forms are the so-called 7-cell and 19-cell designs (made by removing 7 and 19 glass capillaries respectively to form the core in the preform from which the fiber is subsequently drawn). 7-cell HC-PBGFs typically have smaller cores (and mode field diameters, MFDs) and higher attenuation than 19-cell HC-PBGFs due to the increased interaction between the guided mode and the glass core surround (cladding). However, 7-cell HC-PBGF remains popular as it can be more straightforwardly interconnected to SMF-28 since both have a similar MFD. By contrast, when interconnecting 19-cell HC-PBGF [3] to SMF-28 there is a significant mismatch in MFD that needs to be managed e.g., using a mode field (MF) adapting bridge fiber.

Whilst generally operating in the single-mode regime both, 7-cell and 19-cell HC-PBGFs are inherently multi-moded, making the interconnection with SMF-28 prone to the unwanted coupling of part of the energy into higher-order modes (HOMs). This is highly undesirable in most applications, as it causes multi-path interference (MPI). To avoid this unwanted effect, the MFD and the MF profile of the fundamental modes of both interconnecting fibers must be very well matched; this is also needed to minimize the insertion loss (IL) of the interconnection.

There is sometimes an inconsistency in the literature when reporting insertion loss measurements for SMF-28-HC-PBGF interconnections. In some cases, the signal from the SMF-28 is coupled into the HC-PBGF and the power at the HC-PBGF output (total power in all of the excited guided modes) is measured. However, this does not represent the coupling loss between the fundamental mode of the SMF-28 and HC-PBGF. Moreover, due to multi-mode nature of HC-PBGFs, such measurements typically do not yield symmetric insertion loss values, i.e. the measured IL is different depending on whether the signal is propagating from the SMF-28 into the HC-PBGF, or vice-versa [4]. To properly characterize the coupling between the two fundamental fiber modes, it is important to measure only the power in the fundamental mode of HC-PBGF.

Apart from mitigating MPI and minimizing IL, the remaining challenges for hollow-core to solid-core fiber interconnection are the relatively strong Fresnel back-reflection and distortion of the HC-PBGF microstructure during the splicing process.

Regarding the solid-core to hollow-core interconnection IL, the best result reported up to date is 0.3 dB [5]. This result, however, was not achieved using standard SMF-28, but a custom-made large mode area single-mode fiber. The insertion loss was measured for a HC-PBGF interconnected to SMF-28 fiber at both ends. Both interconnections exhibited a loss of 0.3 dB, confirming efficient coupling into the fundamental mode of the HC-PBGF. An anti-reflection (AR) coating was deposited on the large mode area fiber and this reduced the back-reflection to −31 dB at 1550 nm. The connection [5] was housed in a connector-style arrangement. This result is impressive and gives a benchmark as to how a coupling loss and back-reflection can be achieved with AR coatings. The main areas of improvements, however, are: (i) how to realize the low-loss connection with SMF-28, and (ii) how to hermetically seal the interconnection to avoid any degradation in the HCF loss with time (e.g., humidity-caused increase of attenuation).

Back-reflections can also be reduced by splicing angle-cleaved fibers to HC-PBGFs. The main drawback of this approach so far is in the relatively high level of IL > 3 dB [6] when 19-cell HC-PBGF was used (although an excellent −60 dB level of back-reflection was achieved). With further refinement a reduced IL of 1-2 dB with a slight compromise in back-reflection (−50 dB) was reported [7]. The main challenges of this approach are the difficulty in reliably achieving accurate angle cleaves on such delicate structures and the high sensitivity of the IL to the cleave quality.

In this letter, we demonstrate a novel approach for low-loss, low back-reflection and highly-efficient fundamental-mode coupling between SMF-28 fiber and HC-PBGF. Our approach is based on fiber-array (FA) interconnection technology [8] which can be used to create a robust and permanent HC-PBGF to SMF-28 interconnection, whilst at the same time hermetically sealing the end-facet of the HC-PBGF.

We incorporate a graded-index (GRIN) fiber based MF adapter and demonstrate how sensitive low-loss coupling between the SMF-28 and the fundamental mode of the HC-PBGF is to the precise length of the GRIN fiber used. We achieved ILs as low as 0.30 dB between the fundamental modes of the two fibers (a record value); with a reduced back-reflection loss of −30 dB. We also characterized the level of MPI and measured the polarization-dependent loss.

II. Modified Fiber-Array Technology

Our approach is based on the FA assembly technique, which is a well-established method to pigtail photonic lightwave circuits (PLCs) with solid-core optical fibers. The fibers are first glued into a V-groove array, which is then glued onto the PLC end-facet. Adaptation is required to apply this basic approach to the case of HC-PBGF to solid-core fiber interconnection and a schematic of the modified FA assembly is depicted in Fig. 1 along with the principle of MF adaptation using a GRIN fiber segment.

First we use a 1-channel FA for the solid-core fiber and MF adaptation, we fusion splice GRIN fiber to the end of the input

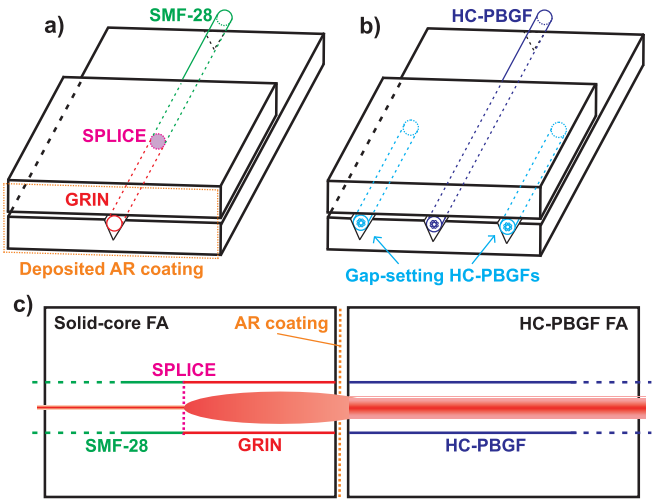

Fig. 1. Illustration of the developed 1-channel FA, a) containing SMF-28 spliced on GRIN, with the GRIN length precisely polished and with a subsequently deposited AR coating, b) containing HC-PBGF inserted and aligned with the FA end-facet. Two short segments of the same-diameter HC-PBGF are used to set the vertical gap size, c) with a schematic of the MF propagation and MF matching at the GRIN-HC-PBGF interface.

SMF-28. This MF adaptation technique has previously been used to make connectors for high power laser applications [9] in which a large MFD (and thus lower power density) is required at the point of interconnection. We cleave the GRIN fiber to a length longer than the target length and insert the spliced SMF-28 and GRIN segment into the V-groove before gluing it in place. Finally, we polish the fiber-array end-face until the desired GRIN length is achieved. This process allows for very precise control of the GRIN fiber length (μm-level), which is essential for low-loss interconnection, as we shall show later. Subsequently, for this proof-of-principle demonstration, we deposit a simple TiO_2/SiO_2 2-layer AR coating on the GRIN end-facet (see the SMF-28-GRIN component in Fig. 1a). The AR coating had the minimum reflection of −32 dB at 1600 nm and a 3-dB bandwidth of 60 nm.

Simulations (ray-tracing in ZEMAX) indicated that the best commercially available GRIN fiber has a core diameter of 62.5 μm (standard OM1 graded-index multi-mode fiber). For a fully-collimating (quarter-pitch, length 265 μm) GRIN, it gives MFD of 24.6 μm, which is close to the MFD of the fundamental mode in HC-PBGF.

HC-PBGF cannot be polished in the V-groove in the same way as the solid-core GRIN fiber because of fear of damage to the delicate microstructure and ingression of polishing products. Thus, we modified the FA assembly procedure for HC-PBGF, which also takes into account the fact that HC-PBGFs generally have non-standard outer diameters which can vary from HC-PBGF sample to sample. The FA is a 1-channel type, but includes three V-grooves. The two side V-grooves are used to set the vertical gap between the upper and lower blocks of the FA by using HC-PBGF segments made of the same fiber (same diameter) as that to be used in the interconnection. At this stage, we intentionally leave the central V-groove empty. Subsequently, the HC-PBGF FA

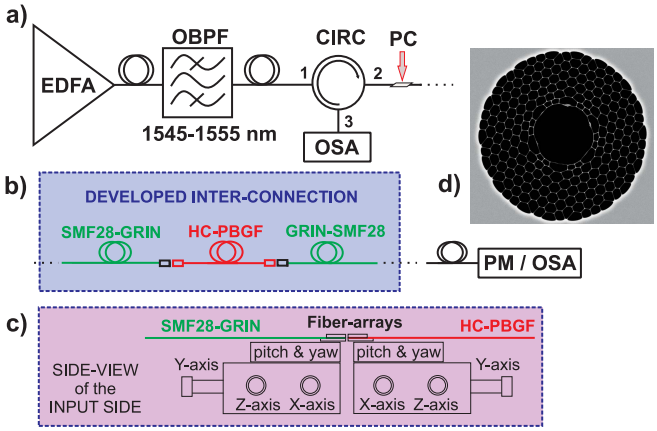

Fig. 2. Measurement configuration including a) input signal generation, b) developed interconnection with output power/spectral measurement, c) side-view of the alignment apparatus, and d) 19-cell HC-PBGF structure. EDFA - Erbium-doped fiber amplifier, OBPF - optical bandpass filter, CIRC - circulator, PC - polarization controller, GRIN - graded-index fiber MF adapter, PM - power meter, OSA - optical spectrum analyzer.

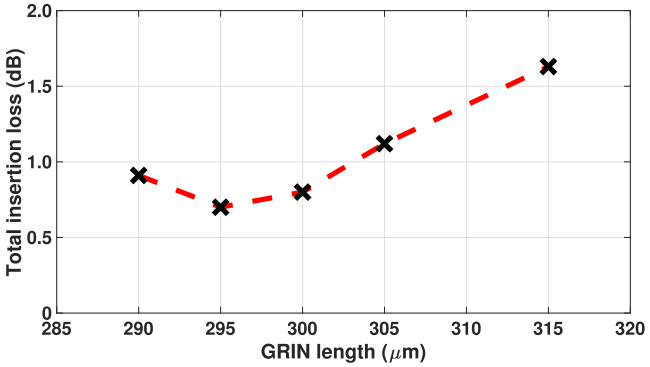

Fig. 3. Dependence of total insertion loss of the whole SMF-GRIN-HC-PBGF-GRIN-SMF component on the GRIN fiber MF adapter length (the same GRIN length was always used on both sides), utilizing a 10-m long 19-cell HC-PBGF.

is polished and cleaned. After that, we insert a freshly cleaved HC-PBGF into the central V-groove and precisely align its end-face with the front edge of the FA (see the HC-PBGF component in Fig. 1b).

III. Measurement Setup

The HC-PBGF used in our experiments was an in-house made 19-cell HC-PBGF with a 230 μm outer diameter and a 31.4 μm central air-hole diameter. The MFD of the fundamental mode was calculated (in COMSOL) to be 21.1 μm at 1550 nm. Calculated interconnection loss between the calculated shape of the HC-PBGF mode and a Gaussian beam of 21.1 μm (ideal) and 24.6 μm (our quarter-pitch GRIN lens) was 0.13 dB and 0.23 dB, respectively. We prepared two samples, having 10 m and 50 m HC-PBGF lengths, and made interconnections to SMF-28 fiber pigtails at each side.

For precise alignment, the FAs were placed on 5-axis micropositioning stages (X,Y,Z, pitch, and yaw), as shown in Fig. 2. We used a stabilized Erbium-doped fiber amplifier (EDFA) as a broadband light source. The EDFA output (ASE) was coupled into an optical bandpass filter (OBPF) with 10 nm bandwidth. The light then passed through a circulator (CIRC), a fiber polarization controller (PC), and the first SMF28-GRIN-HC-PBGF. After the HC-PBGF sample, the signal was coupled through the second HC-PBGF-GRIN-SMF-28 (again, using 5-axis micropositioning stage) and was measured with the optical spectrum analyzer (OSA) or power meter (PM). The spectrum of the reflected signal was measured at the 3rd CIRC port.

IV. Results

First, we measured the IL dependence on the GRIN length. Our preliminary experimental results (not shown here) indicated that the optimum GRIN length is slightly longer than that expected from the theoretical analysis. We used five pairs of GRIN-SMF-28 FA with the 2-layer ARC and GRIN lengths (the same lengths in each pair) of 290, 295, 300, 305 and 315 μm, respectively. The GRIN lengths were measured using an optical microscope, measuring the splice to end-facet distance with a measurement uncertainty of $\pm 1\,\mu$m. The measured IL for the whole SMF-28-GRIN-HC-PBGF-GRIN-SMF-28 assembly is plotted in Fig 3.

The minimum IL was obtained with a GRIN length of 295 μm. It is worth noting that deviation as little as 5 μm from the optimum GRIN length leads to the insertion loss increase of >0.1-0.2 dB (see Fig. 3). A similar level of insertion loss increase is expected (based on a numerical analysis) in the case of longitudinal or transverse misalignment of $\sim$5 μm. Note that besides slightly increased insertion loss, any misalignment will result as well in stronger unwanted HOM excitation.

Besides optimizing the IL using the two 5-axes stages, we also monitored the quality of the launch into the fundamental mode by observing the transmitted signal with the OSA. Any component of power launched into HOMs presents itself as MPI and is visible as spectral ripples on the transmitted broadband spectrum measured at the OSA. This technique is simpler than conventional measurements of MPI based on the time-of-flight technique [10] or S^2 measurement [10], [11]. The HOMs contributing most to MPI are the LP_{11} mode and the LP_{02} mode with differential modal delays of 8.7 ps/m and 21.4 ps/m respectively [11]. We should be able to observe MPI from these modes in HC-PBGF with lengths up to 45 m and 18 m length respectively when operating the OSA at its highest resolution of 20 pm.

The MPI for various GRIN lengths used for the 10-m long HC-PBGF sample is shown in Fig. 4, together with the measured IL for the entire SMF28-GRIN-HC-PBGF-GRIN-SMF-28 assembly.

The minimum MPI (demonstrated as the smallest amplitude spectral ripples) was achieved for a GRIN fiber length of 295 to 300 μm (the minimum IL was achieved for the 295 μm length).

Once we optimized the optical performance, we glued the FAs together. Apart from ensuring that the connection does not move during the glue-curing process, we had also to ensure

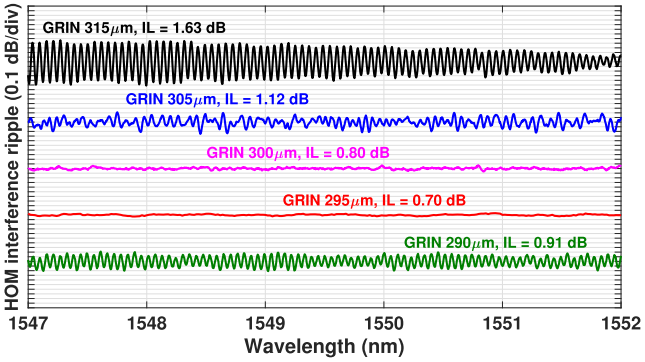

Fig. 4. HOM interference ripples in transmitted spectra for various GRIN fiber MF adapter lengths measured for the whole SMF28-GRIN-HC-PBGF-GRIN-SMF28 configuration including a 10-m long HC-PBGF.

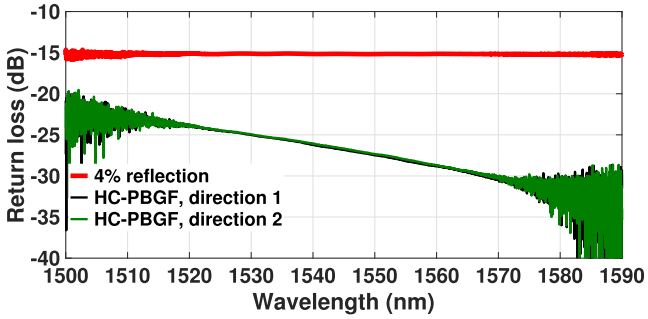

Fig. 5. Back-reflection spectra of the final component including 50-m long HC-PBGF.

that the glue does not creep into the HC-PBGF microstructured region - we used a fast (< 5 s) UV-curable, high viscosity glue for this purpose. First, we aligned both 5-axis stages for the entire SMF-28-GRIN-HC-PBGF-GRIN-SMF-28 assembly. During the gluing, (the first interconnection followed by the second one), we observed a maximum increase in the IL per interface of 0.05 dB.

Subsequently, we interconnected a 50-m long HC-PBGF. We achieved an IL of 0.87±0.05 dB (which also includes the PDL) for the complete SMF-28-GRIN-HC-PBGF-GRIN-SMF-28 glued assembly. Considering the loss of the 50-m long HC-PBGF (4.0 dB/km), we calculated IL per connection of 0.30 dB. Figure 5 shows the measured back-reflection spectrum of the 50-m long HC-PBGF after the assembly process (without the OBPF). We observed 15 dB lower back-reflection at 1580 nm (the used ARC showed minimum reflection there) with respect to the measured 4 % reflection from a flat interface.

V. Conclusion

In this letter we have presented for the first time a FA based approach to create a permanent hermetically sealed interconnection of HC-PBGF to SMF-28s. Our method provides signal propagation in the fundamental mode, with the signal propagating in the higher-order modes being significantly suppressed, reducing multipath propagation effects.

Using our approach, a coating can be applied to the interface. As a proof-of principle, we have reduced back-reflections by 15 dB compared to the typical silica-air interface by depositing a simple 2-layer AR coating. Apart from reducing the back-reflection, the AR coating is also expected to reduce IL by 0.17 dB per silica-air interface.

We reached best-ever reported insertion loss between SMF-28 and 19-cell HC-PBGF of 0.30 dB, confirmed both for a 10-m long and 50-m long HC-PBGF. The interconnection was reciprocal, with IL difference of only 0.03 dB for both propagation directions, confirming good coupling between fundamental modes of both fibers. Furthermore we have presented a simple approach of single-mode launch verification by monitoring MPI with a spectrum analyzer.

An additional advantage of the presented method lies is the fact that it can be straightforwardly extended to simultaneously interconnecting several (e.g., 64) HC-PBGFs with multiple SMF-28s or even with a multi-port planar lightwave circuit (e.g., a 64x64 PLC coupler).

Acknowledgment

The data in this letter is accessible through the University of Southampton research repository (DOI: 10.5258/SOTON/D0831).

References

[1] R. Slavík *et al.*, "Ultralow thermal sensitivity of phase and propagation delay in hollow core optical fibres," *Sci. Rep.*, vol. 5, p. 15447, Oct. 2015.
[2] N. Dadashzadeh *et al.*, "Near diffraction-limited performance of an OPA pumped acetylene-filled hollow-core fiber laser in the mid-IR," *Opt. Express*, vol. 25, no. 12, pp. 13351–13358, Jun. 2017.
[3] Y. Chen *et al.*, "Multi-kilometer long, longitudinally uniform hollow core photonic bandgap fibers for broadband low latency data transmission," *J. Lightw. Technol.*, vol. 34, no. 1, pp. 104–113, Jan. 2016.
[4] R. Thapa, K. Knabe, K. L. Corwin, and B. R. Washburn, "Arc fusion splicing of hollow-core photonic bandgap fibers for gas-filled fiber cells," *Opt. Express*, vol. 14, no. 21, pp. 9576–9583, Oct. 2006.
[5] J. W. Nicholson *et al.*, "Low-loss, low return-loss coupling between SMF and single-mode, hollow-core fibers using connectors," in *Proc. Conf. Lasers Electro-Optics (CLEO) Laser Sci. Photonic Appl.*, Jun. 2014, pp. 1–2.
[6] F. Couny, F. Benabid, and P. S. Light, "Reduction of Fresnel back-reflection at splice interface between hollow core PCF and single-mode fiber," *IEEE Photon. Technol. Lett.*, vol. 19, no. 13, pp. 1020–1022, Jul. 1, 2007.
[7] G. A. Miller and G. A. Cranch, "Reduction of intensity noise in hollow core optical fiber using angle-cleaved splices," *IEEE Photon. Technol. Lett.*, vol. 28, no. 4, pp. 414–417, Feb. 15, 2016.
[8] N. Hiroi, Y. Hashimoto, and K. Matsumoto, "Optical fiber array," U.S. Patent US 20090285533 A1, May 3, 2011.
[9] Y. Shou and J. Zhao, "Mode field expanded fiber collimator," U.S. Patent US 7920763 B1, Aug. 5, 2011.
[10] D. R. Gray *et al.*, "Complementary analysis of modal content and properties in a 19-cell hollow core photonic band gap fiber using time-of-flight and S^2 techniques," in *Proc. 38th Eur. Conf. Exhibit. Opt. Commun.*, Sep. 2012, pp. 1–4.
[11] D. R. Gray *et al.*, "Accurate calibration of S^2 and interferometry based multimode fiber characterization techniques," *Opt. Express*, vol. 23, no. 8, pp. 10540–10552, Apr. 2015.

Hollow-Core Optical Fibers

Matěj Komanec, Daniel Dousek, Dmytro Suslov and Stanislav Zvánovec

Department of Electromagnetic Field, Faculty of Electrical Engineering, Czech Technical University in Prague, Technicka 2, 166 27 Prague, Czech Republic

komanmat@fel.cvut.cz

Submitted January 1, 2020 / Accepted January 2, 2020

Abstract.

Today hollow-core optical fibers (HCF) are on the verge of surpassing the attenuation benchmark of silica single-mode optical fibers used in optical communication. Compared to solid-core optical fibers, HCFs exhibit ultra-low nonlinearity, high damage threshold, low latency and temperature insensitivity, making them ideal candidates for high-speed data communication, high-resolution sensing, high-power delivery and precise interferometry. The main challenges of low insertion loss, suppressed back-reflections and fundamental mode coupling must be addressed to incorporate HCFs into existing fiber-optic systems to fully exploit their potential.

This paper provides an overview of the HCF history, from early papers in the 1980s, over the invention of photonic-bandgap HCFs, to the recent achievements with antiresonant HCFs. Then light guiding mechanisms are presented and key HCF properties are discussed. Interconnection techniques to standard optical fibers are compared with respect to possible HCF applications. Fusion splicing results are presented with an alternative interconnection solution based on a modified fiber-array technique newly developed by our team. Finally, cutting-edge HCF applications that take advantage of our HCF interconnection, are discussed.

Keywords

Hollow-core fibers, Photonic crystal fibers, Antiresonant, Photonic bandgap, Interconnection, Fabry-Perot

1. Introduction

Silica single-mode optical fibers (SMFs) form the core of today's high-capacity telecommunication networks. However, network capacity is limited and a so-called "capacity crunch" is inevitable in the near future. Further improvement of the SMF performance will not be possible due to the physical limit of the Rayleigh scattering and the nonlinear Shannon limit [1]. Today's record-low attenuation for SMF of only 0.14 dB/km at 1550 nm was achieved in 2018 [2].

Contrary to solid-core fibers, guiding light over long lengths in air (ideally in a vacuum) is extremely appealing. Hollow-core optical fibers (HCFs) have an air-filled core surrounded with microstructured glass cladding allowing high level of light confinement. Figure 1 gives an example of a 19-cell hollow-core photonic bandgap fiber (PBGF).

HCFs offer extremely low nonlinearity [3], low latency [4], high damage threshold [5] and temperature insensitivity [6–8]. HCFs can be advantageously used in many applications, e.g., long-length gas cells [9], high-power delivery [10], pulse compression [11], nonlinear phenomena [12], mid-infrared (MIR) propagation and sensing [13], MIR gas-filled lasers [14], ultra-precise fiber-optic gyroscopes [15] or Fabry-Perot resonators [16].

In telecommunications, HCFs are now challenging the attenuation of standard SMFs [17]. An 11-km-long HCF has already been drawn [18], while predictions of a more than 100 km-long HCF drawing were presented in [19]. To effectively use HCFs in conventional fiber-optic systems, it is essential to connect HCFs to solid-core optical fibers, in most cases to SMFs. Three main challenges exist for such an HCF-SMF interconnection: *i)* the air-silica boundary causing unwanted back-reflections; *ii)* state-of-the-art low-loss HCFs have a significantly larger mode-field diameter (MFD) compared to SMFs; and *iii)* HCFs with large MFD are inherently multi-modal, therefore higher-order mode (HOM) excitation must be suppressed to ensure only fundamental mode coupling.

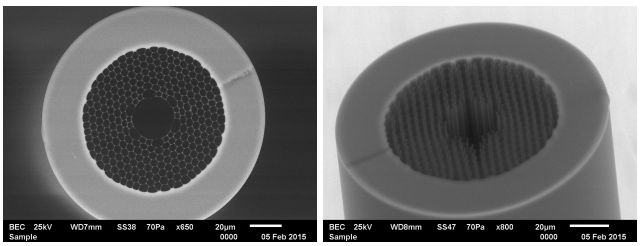

Fig. 1. Photographs of a 19-cell PBGF developed at the University of Southampton, acquired by a scanning-electron microscope

Fusion splicing is a method that is typically used for permanent, low-loss interconnection of solid-core optical fibers. This method can be reasonably well applied [20]

to the HCF-SMF interconnection, but does not address back-reflections that occur on a glass-air interface. To suppress back-reflections, angled-splicing of HCFs was proposed, but proved to be quite lossy [21, 22].

We have developed an alternative approach for an HCF-SMF interconnection based on a modified fiber-array technology [23], which solves the issue with back-reflections by applying optical coatings (optical coatings cannot be used in fusion splicing because of high temperatures). Furthermore, fundamental mode coupling is achieved by using mode-field adapters in the form of graded-index multimode fibers.

This paper begins with a historical overview of the evolution of HCFs from the first real HCF samples to current state-of-the-art hollow-core nested antiresonant nodeless fibers (NANFs) with only 0.28 dB/km attenuation at 1550 nm [17]. The section after the historical overview discusses the main HCF guidance mechanisms, from Bragg fibers, PBGFs to antiresonant fibers (ARFs), followed by a section summarizing HCF key properties, comparing PBGFs and ARFs, which are the main focus of this article. In the next section we show HCF interconnection techniques. Fusion splicing results are compared to our modified fiber-array technology. Advantages of our interconnection technique are discussed with regard to HCF applications in the last section.

2. Historical overview

The idea of wave guidance in a hollow-core has existed since the end of the 19th century, when J. Thomson [24] and Lord Rayleigh [25] first discussed the possibility of metallic waveguides. Later in the 1960s, at the Bell labs, E. A. J. Marcatili and R. A. Schmeltzer [26] proposed a hollow-core metal-coated dielectric waveguide for short-range transmission of millimeter waves. The main length-limiting factor was attributed to waveguide bend-induced losses, e.g., a minimal attenuation of 1.85 dB/km was predicted, whereas the attenuation doubled for a curvature radius of $R{\sim}10$ km. With the advent of optical fibers later in the 1960s, the focus had shifted to solid-core fibers and the development of hollow-core waveguides for light delivery was significantly limited.

HCFs first appeared in the early 1980s in the form of hollow-core metal-coated fibers, which were designed for the 10.63 μm (940 cm^{-1}) band to guide light from CO_2 lasers [27]. These hollow-core fibers were made of Pb-oxide glass and exhibited attenuation of 7.7 dB/m. Just ten years later, in 1991, silica-glass-based HCF was presented for CO_2 laser delivery with attenuation below 1 dB/m [28]. It is important to mention that these HCFs typically had core diameters larger than 1 mm.

In 1993 two interesting studies on HCFs appeared that were based on the silica-air design. First, HCFs in the vicinity of 10 μm were used to measure gas concentration where HCF, with a 1.5 mm inner core diameter and of 1 m length, acted as a gas cell to analyze NH_3 content [29]. Second, an interferometric HCF-based fiber sensor was published in [30], where the HCF was formed by a glass capillary with a 70 μm inner diameter and length of 137 μm. Later, in 1995, a simple-glass capillary HCF was used to transport atoms by optical forces [31]. In this work the main limitation originated from glass capillary attenuation, proving the need for better light guidance. Annular core fibers were mentioned as a possible substitute for glass capillaries.

Bragg HCFs have subsequently superseded the older HCF-type metal-coated capillary fibers [28] thanks to their lower attenuation at identical wavelengths. To give an example, the first Bragg HCF, denoted as an Omniguide fiber, was presented in 2002 [32] with high-refractive-index glass and a low-refractive-index polymer microstructure. Omniguide fibers exhibited less than 1 dB/m attenuation at 10.6 μm while it was possible to get tens of meters of Omniguide fiber in a single draw. Later the focus was primarily placed on Bragg fibers from pure silica where the rings were held together by glass struts [33].

Parallel to this, in 1996, a fundamental breakthrough was made in the field of optical fibers when J. C. Knight published experimental results of the very first photonic crystal fiber (PCF) and thus revolutionized the fiber-optic world [34]. The idea of PCF came from P. St. J. Russell and was based on the paper by Y. Jablonovitch [35] and S. John [36], who first showed the possibilities of 2D and 3D photonic crystals and derived the photonic bandgap conditions. The invention of PCFs allowed unprecedented freedom in PCF parameter tailoring (such as the chromatic dispersion curve, zero-dispersion wavelength, single-mode cut-off wavelength, mode-field diameter) which can be easily modified by changing the design of the PCF microstructure. Endlessly-single mode PCFs appeared a year after [37], group-velocity dispersion management became possible [38] and soon supercontinuum generation was first demonstrated using PCFs with zero-dispersion wavelength at 800 nm producing broadband radiation from visible to near-infrared [39].

The first photonic crystal HCF was presented in 1999 by Cregan et al. [40], members of the P. St. J. Russel team at the University of Bath, where most of the pioneering research in HCFs was carried out in the following years. In [40], a silica-based HCF with honeycomb microstructure and a core diameter of 14.8 μm was fabricated. The guidance mechanism was attributed to the 2D photonic bandgap (PBG) effect. This first hollow-core photonic bandgap fiber (HC-PBGF, or more simply PBGF) led to numerous application areas where HCF were afterwards advantageously used such as gas sensing [41], gas-filled lasers [42], fiber-optic gyroscopes [15], high-speed data transmission [17], and many more [5,16,43].

Considering telecommunication, i.e. optical networks, the most important parameters are fiber attenuation in the 1550 nm band (denoted as C-band) and fiber transmission bandwidth. In 2002, a 7-cell PBGF with attenuation of 13 dB/km was reported [44], while, in 2004, attenuation was improved to 1.7 dB/km [45] and to 1.2 dB/km [46] in

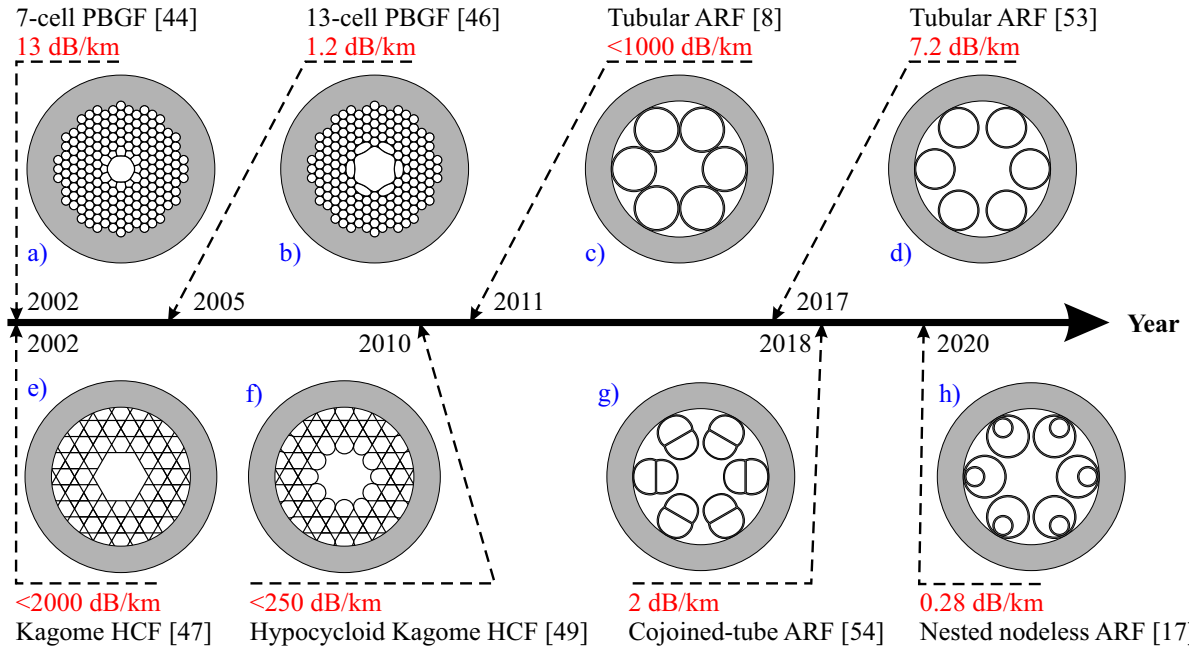

Fig. 2. Timeline of the hollow-core optical fiber evolution including both fiber design and attenuation milestones, values are given for the wavelength of 1550 nm.

2005 which is, until today, still the record-low attenuation for PBGFs (see Fig. 2b). The design of the PBGF eventually limited the progress in achieving low-attenuation and broadband performance (e.g., in [46] the achieved bandwidth was only 70 THz) and an alternative HCF design was pursued.

The first alternative appeared in 2002 when a new type of HCF, denoted as Kagome HCF, was invented [47]. Kagome HCFs provide an extremely delicate structure of thin triangular-lattice struts with no cladding nodes (see Fig. 2e), which leads to multi-band transmission and much lower mode-field overlap with the glass cladding thanks to inhibited coupling. Even then was the attenuation of Kagome HCF higher than that of PBGFs by more than two orders of magnitude due to the high confinement loss [48].

The next milestone in HCF development occurred in 2010 with the development of negative curvature Kagome HCFs, denoted as hypocycloid fibers [49]. These Kagome HCFs worked on the principle of antiresonance and are thus a representative of an ARFs. The negative curvature represents the shape of the first ring around the ARF core (see Fig. 2f) which led to a decrease of fiber attenuation down to hundreds of dB/km with a bandwidth of 1000 nm. Although the attenuation of this negative curvature Kagome HCF was significantly higher than that of PBGF, the bandwidth was superior to that of the PBGF. Later, in 2016 a Kagome HCF with attenuation of 12.3 dB/km at 1 μm was presented [50].

Parallel efforts focused on exploiting the negative curvature while simultaneously reducing the microstructure complexity. In 2010 and 2011, the first ARFs with a simplified design appeared, showing a simplified PBGF lattice [51], a simplified hypocycloid Kagome lattice [52] and, finally, a tubular lattice [8]. These ARFs did not require a periodic lattice and worked just on the principle of antiresonance. Among the lattice variants, the tubular ARF provided the simplest design and best performance and has been further developed (see Fig. 2c,d). The lowest current attenuation of a single-ring tubular ARF is 7.7 dB/km at 750 nm [53].

The results presented in [53] were impressive, though still far from conventional SMFs. Three years earlier, in 2014, a fundamental study was published [6] showing the potential of ARFs when including an additional (nested) resonator inside of each existing tubes, forming the so-called nested antiresonant nodeless fibers (NANFs). It was envisioned that NANFs could eventually surpass the attenuation of other HCF types and eventually that of SMFs. This is due to the negligible optical field overlap with the glass leading to low surface scattering losses. Generally, ARFs suffered from significantly higher confinement losses, however those were addressed by the proposed NANF design by including more antiresonant elements.

By 2018 a cojoined-tube fiber (CTF) with a minimal loss of 2 dB/km at 1512 nm was demonstrated [54] (see Fig. 2g). In parallel, NANFs have undergone rapid development (see Fig. 2h). NANF with only 1.3 dB/km was presented the same year [55] and this attenuation value was significantly decreased just a year later by NANF with attenuation of 0.65 dB/km [56]. Recently, in 2020, a NANF with a record-low attenuation of only 0.28 dB/km has been presented [17], challenging the long-held record of SMFs.

3. HCF fabrication and waveguiding

The most common fabrication method of HCFs is the stack-and-draw principle [34] where multiple glass capillaries are stacked in a large capillary, then drawn to a preform, and, finally, drawn to the final HCF structure [40]. Extreme care needs to be taken especially when applying specific pressures or a vacuum to the capillaries to achieve the desired HCF design. Less common methods to obtain a preform are extrusion, drilling or sol-gel casting, techniques often used for short fiber samples and glass materials other than silica (e.g., chalcogenide glass). As HCF drawing is a time-consuming and extremely costly process, virtual HCF drawing was presented in 2014 by G. Jasion in [57].

HCF waveguiding principles can be divided into three categories according to HCF design:

- Bragg hollow-core fibers with a layered structure of cladding (1D photonic crystal) - find example in Fig. 3.
- Hollow-core photonic bandgap fiber (PBGF) with a large number or periodic air-holes arranged in rings surrounding the central air-core - see example in Fig. 1, 2a and 2b.
- Antiresonant hollow-core fiber (ARF) with a Kagome or a simple cladding structure - examples given in Fig. 2c-h.

This section overviews the basic principles for each HCF type mentioned-above with focus on ARFs which are the state-of-the-art HCFs.

3.1 Bragg HCF guidance

Bragg HCFs have a simple inner structure that can be described as a 1D photonic crystal formed by a series of layers with periodically changing refractive indices n_1 and n_2. Bragg's law is given as:

$$N\lambda = 2\Lambda \sin\phi, \tag{1}$$

where N is a positive integer, λ is the wavelength, Λ is the period of the cladding and ϕ is the angle of the incident wave. Total reflection then occurs for a range of wavelengths around λ and a range of angles around ϕ. To acquire high reflectance, i.e. low guiding losses, a significant difference in refractive indices Δn (high n_1/n_2 ratio) is needed. This condition applies to glass materials having high-refractive indices, thereby exhibiting higher material losses limiting possibly low Bragg HCF attenuation. However, for short ranges in order of meters attenuation is not critical and Bragg fibers are, therefore, an excellent candidate for CO_2 laser delivery.

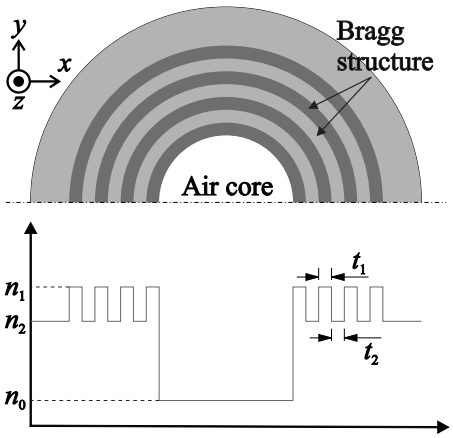

Figure 3. Example of a Bragg fiber structure with its refractive index profile, n_1 and n_2 are refractive indices of the Bragg layers, n_0 is refractive index of air, t_1 and t_2 are layer thicknesses.

3.2 Photonic bandgap guidance

Hollow-core PBGF is formed by introducing a defect in the periodic photonic crystal structure. Light is then trapped in the defect as it cannot escape through the cladding due to the photonic bandgap (PBG) effect, and is guided along the fiber. The defect can be created by removing a capillary from the center of the preform (e.g., to form a symmetric low-index core we can remove 7, 19 or 37 capillaries, thus so-called 7-,19- and 37-cell PBGFs are drawn).

The analogy between electronic bandgaps and photonic bandgaps originates from the periodic arrangement of atomic potentials and two different dielectrics, respectively. The periodicity of the two dielectrics (representing the cladding) gives rise to a frequency band where propagation of photons is forbidden.

The PBG effect is described in great detail in [40,58,59]. Here we briefly overview three approaches, from the oldest to the current one:

1. Using numerical approaches from solid-state physics.
2. Brute-force techniques, such as a finite difference methods, finite element method (FEM) or plane-wave expansion.
3. An antiresonance description of a number of resonators in the cladding.

The first description of the guidance mechanism, based on the analogy with solid-state physics, appeared in 1999 [40] and presented the 2D PBG effect principle, which was denoted as "frustrated tunneling PBG guidance". The cladding structure was considered as a double layer dielectric stack with an air-core in between. Light was confined once the stacks provided PBG for a range of propagation constants ($\beta = k\, n \cos\phi$) at fixed optical frequencies.

In the following effort to find the best lattice configuration, numerical approaches from solid-state physics were

applied to calculate the PBGs supporting the air-guided mode of a unit cell with periodic boundary conditions as a function of the wavevector direction [60, 61]. These first papers brought noteworthy PBGF design optimizations, such as a triangular lattice outperforming a honeycomb lattice [62] and the introduction of bandwidth scaling based on the air-filling fraction (percentage of air content to glass material) [63]. However, these approaches considered only a perfectly symmetric PBGF microstructure.

With rapid increase in computational power, methods such finite difference method [64] became more common. These methods allowed for a far more accurate description of mode distribution in HCFs as they consider the real HCF microstructure instead of the idealized one, which was the case of previously used analytical models. However, these methods did not explain the physical mechanisms, nor did they provide any more-in-depth understanding. Nevertheless, they have since often been applied due to improved computational capacities and satisfactory approximate results.

In the last decade, researchers have moved towards describing PBGFs by antiresonance, which we will discuss in greater detail after introducing the basic antiresonance waveguiding principles.

3.3 Antiresonant guidance mechanism

For some HCFs the light guidance cannot be explained by the formation of PBGs as the glass membrane (strut) thickness t is typically hundreds of nm, which is one or two orders of magnitude thicker than the boundary condition for PBG. Here, antiresonant reflection confines light in the air-core (or generally lower refractive index region) without the need for periodic cladding and the PBG effect. The antiresonant reflecting optical waveguide (ARROW) model has been often used to describe ARFs, where the first idea appeared in 2002 [65] and has been further evolved [66]. The principle of ARROW assumed high-index circular layers around the low-index (air) core, where each layer acts as a Fabry-Perot resonator.

We will describe the antiresonant guidance with simplified examples of a 1D slab waveguide, an annular core fiber and a negative curvature fiber. Then we will return to the PBG effect and describe its interpretation via antiresonance reflection.

1D slab waveguide approach

To understand the antiresonance principle, the example of a 1D slab waveguide is often given. The situation is depicted in Fig. 4 with $D_{\text{core}} >> \lambda$. The resonance condition (phase difference is $2m\pi$) for the transversal wave vector k_{T} is described as [67]:

$$k_{\text{T}}\, t = \pi m \tag{2}$$

$$k_T = \sqrt{k^2 n_1^2 - \beta^2} = k\sqrt{n_1^2 - 1}, \tag{3}$$

where we consider n_1 as the refractive index of the glass material and the refractive index of air is $n_{\text{air}} = 1$. The parameter m is a real positive integer and t is the glass thickness. We can then find a resonance wavelength λ_{res}, where all the light is transmitted in the transversal direction given as [67]:

$$\lambda_{\text{res}} = \frac{2t\sqrt{n_1^2 - 1}}{m}, \qquad m = 0, 1, 2, \ldots \tag{4}$$

For wavelengths other than λ_{res}, light is confined inside the air-core with low leakage loss. The solution of the 1D slab waveguide based on anti-resonance leads to a number of resulting glass thicknesses based on m. These solutions provide high leakage loss for given wavelengths. Fiber transmission bands are present between them (see example cases given in [67]).

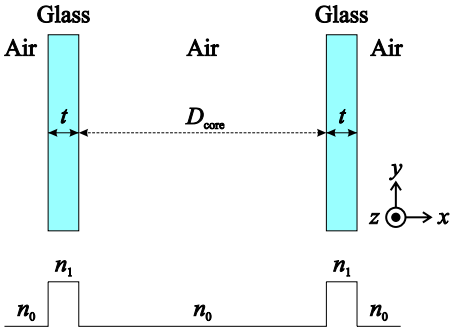

Fig. 4. 1D slab waveguide structure, glass with refractive index n_1, air with refractive index n_0, t is the glass thickness and D_{core} is the slab width corresponding the the fiber core diameter.

For the fundamental mode, not only does t play a critical role, but also air-core diameter D_{core}. The transmission bands do not change with D_{core}, but leakage loss increases as D_{core} gets larger [67].

Annular core fiber

Moving from the 1D slab waveguide to the simplest case of a fiber structure, we can assume a high-index glass ring around the air-core, which forms two reflective surfaces. This configuration is denoted as an annular core fiber and is depicted in Fig. 5. For a mode existing in the glass ring, the effective index is between that of glass and air. For a mode propagating in the air-core, the effective refractive index is lower than that of air. Depending on glass thickness t, multiple transmission bands will be present, with losses dependant on t and D_{core}. The modes of the annular core fiber can be easily calculated using FEM [67] or mode-matching methods [68]

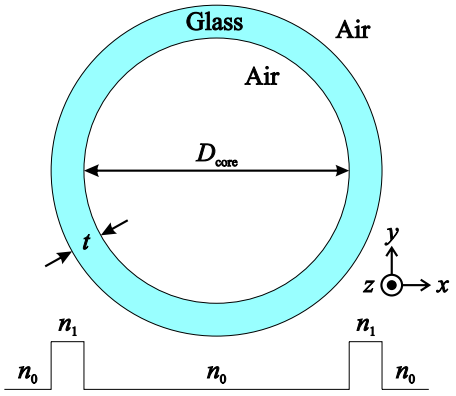

Fig. 5. Annular core fiber structure, glass with refractive index n_1, air with refractive index n_0, t is the glass thickness, D_{core} is the annular fiber core diameter and z is the direction of light propagation.

Negative curvature fiber

Let us consider a simple tubular ARF, as shown in Fig. 6 with a set of capillaries around the central air-core, which are in touch with each other. The core boundary is now formed by glass membranes (capillary walls) having a negative curvature with respect to the radial direction. The overall geometry of such negative curvature fiber is described by D_{core}, capillary thickness t, capillary diameter D_{cap} and the number of capillaries p as [67]:

$$D_{\text{core}} = \frac{D_{\text{cap}} + 2t}{\sin(\pi/p)} - (D_{\text{cap}} + 2t). \tag{5}$$

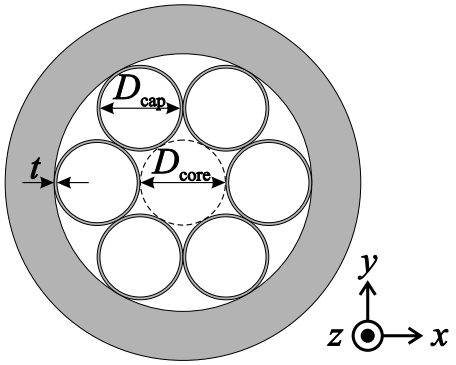

Fig. 6. Tubular fiber structure.

For negative curvature fibers, the effective refractive index of the fundamental mode is larger than that for the same D_{core} of annular fibers due to the negative curvature , given an empirical 5% increase [67]. This fact is interconnected with the required glass membrane thickness t, which is smaller for negative curvature fibers than for annular core fibers thanks again to the negative curvature effect [69].

Figure 7 shows an example of an advanced type of the negative curvature fiber with non-touching capillaries, parameter g then defines the gap. These fibers eliminate the remaining glass nodes which are not in anti-resonance. The nodes can be seen e.g., in Fig. 6 at the point where the capillaries touch each other. The addition of the gap leads to better confinement of the core mode and therefore lower attenuation of the tubular ARF. Furthermore, HOMs are significantly attenuated due to the added gaps.

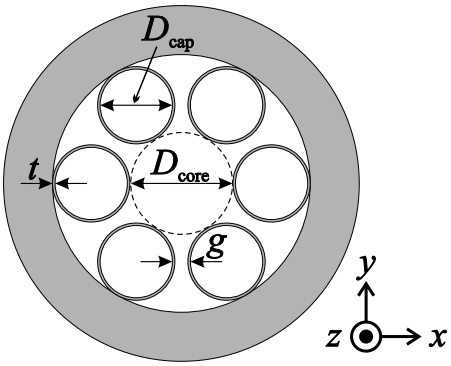

Fig. 7. Tubular fiber structure with non-touching glass capillaries.

The effect of D_{core} on transmission bands and leakage loss is identical to annular core fibers.

Inhibited coupling

Antiresonance prohibits the air-core mode from overlapping with the glass material (glass capillaries). This leads to low surface scattering and low material-induced attenuation which is required for low loss propagation. Nevertheless, to achieve competitive losses to standard SMFs greater coupling suppression between the air-core mode and the cladding modes is required. This coupling suppression is denoted as inhibited coupling [53]. Inhibited coupling is achieved by the already mentioned low overlap between the core and cladding modes and furthermore by a mismatch of core and cladding modes effective refractive indices.

For a more detailed description and illustrative calculated examples of the 1D slab waveguide, annular core and negative curvature fibers and inhibited coupling see [67].

PBGF described by antiresonance

In the last decade research has turned to antiresonance principles in order to describe light guiding mechanism of the PBGF [59]. The idea is illustrated in Fig. 8 showing a simplified formation of the bandgap formation as the PBGF is being assembled.

At first, we assume just a single silica rod in an infinite air-cladding (see inset of Fig. 8a), the guided modes are described by the well-known dispersion equation, using the normalized frequency V and rod radius r as:

$$V = \frac{2\pi r}{\lambda}(n_1^2 - n_0^2). \tag{6}$$

Then we can set the air-line as given e.g., in [59] as:

$$w^2 = (\beta^2 - k_0^2)r^2 = 0, \tag{7}$$

where β is the propagation constant (in the direction of propagation) and k_0 is the wavenumber in air. No modes can propagate above air-line (in the white regions) as they

are in antiresonance with the rod modes and also they cannot propagate in the cladding. Below the air-line is a continuum of plane-wave-like air modes [59], see Fig. 8a.

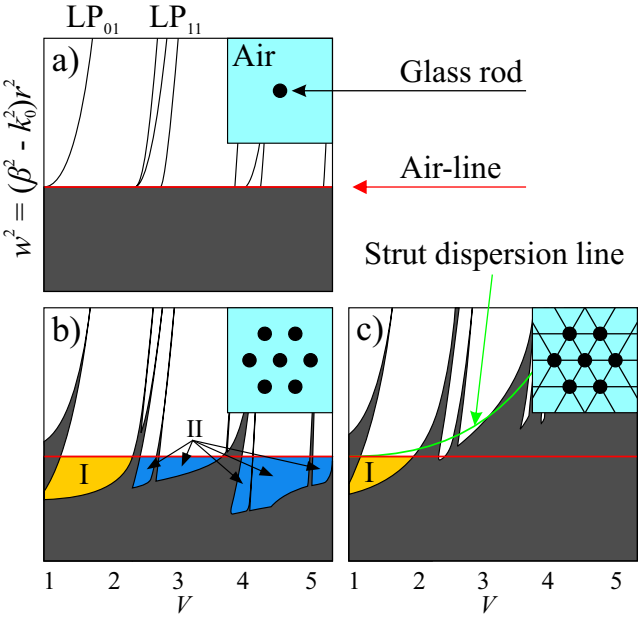

Fig. 8. Creation of an air-guiding PBG, simplified from [59]

When more rods are arranged in a symmetric/periodic fashion to form a single ring around the central rod (see inset of Fig. 8b), the dispersion equation changes and conditions broaden around the particular mode cut-offs (intersection of the mode curves with the air-line). In fact, the rod modes become so expanded that they overlap with the other rod modes and a spatial superposition occurs. Meanwhile, periodic forbidden bands appear below the air-line (coloured regions in Fig. 8b, marked as I and II).

If we create a defect, i.e., remove one of the rods, light can be coupled into the defect region and propagate in the PBG regions. Further addition of more rods in the 2nd, 3rd, etc. rings increases the confinement (considering we create the defect in the fiber center). By placing the rods closer to each other (decreasing the so-called pitch) we decrease the bandwidth of the PBG while allowing more modes to propagate in the PBG, which is often unwanted as HOMs are detrimental to various applications.

To create a real PBGF, we need to interconnect the rods so that the fiber holds together. We achieve this by introducing struts (see Fig. 8c). The struts are not in antiresonance to the air-core mode (confined in the defect). We can see in Fig. 8c that high frequency PBGs disappeared (blue regions marked as II) due to the effective refractive index being raised by the glass struts above the air-line. This is the reason behind PBGF having only one transmission band in contrary to ARFs where multiple transmission bands are present.

4. HCF losses and modes

This section will briefly explain the main HCF parameters and state-of-the-art results.

4.1 HCF attenuation

Hollow-core fibers are envisioned to surpass the minimal intrinsic attenuation of silica SMFs [2] in the near future. Currently, the lowest HCF attenuation at 1550 nm for PBGF is 1.2 dB/km, achieved in 2005 [46], and 0.28 dB/km for NANF as presented in 2020 [17]. There is negligible Rayleigh scattering loss in HCFs compared to silica fibers, on the other hand, surface-scattering loss (SSL) and confinement loss (CL), i.e., leakage loss can be detrimental.

SSL is dominant for PBGFs. The struts supporting the rods in the PBGF microstructure are made as thin as possible to widen the transmission bandwidth and, thus, are not in anti-resonance. Therefore, a mode-field overlap with the struts occurs. This overlap results in scattering at the air-glass interface, which is dependent on the inner surface roughness and HCF non-uniformity. This roughness is caused by the surface capillary waves that are thermodynamically locked-in when the HCF cools during HCF drawing. Compared to the SSL effect, CL is negligible in PBGF thanks to the possibility of increasing the number of rings (resonators). Considering bending losses, PBGFs are the most resistant of all above-mentioned HCFs [70].

ARFs (excluding Kagome fibers) perform oppositely to PBGFs, regarding sources of fiber losses. Thanks to their negative curvature, inhibited coupling and antiresonance, SSL is negligible (there is minimal mode-field overlap with the glass material). For state-of-the-art NANFs, SSL is lower than 10^{-1} dB/km. Contrary to SSL, confinement loss is detrimental to many ARFs due to the gaps between tubes and since only one ring of the antiresonant structure is included. For ARFs, CL is typically around 10^{-6}. NANFs have introduced a solution to increase the mode-field confinement by adding nested tubes and have thus achieved lower CL of only 10^{-8} [6]. In [6] it was also shown that for $D_{\mathrm{core}} = 50\,\mu$m, SSL and CL are equal, with CL scaling with the core radius R_{core} as R_{core}^{-8} and SSL with R_{core}^{-3}. Furthermore, F. Poletti predicted in [6] that for $D_{\mathrm{core}} = 40\,\mu$m it would bring fiber attenuation to the 0.1 dB/km level, which would surpass SMFs in the wavelength region of 1.5 to 2.3μm. Increasing the size of D_{core} promises to reach even lower fiber attenuation.

The combination of negligible SSL and lowered CL led to NANFs with sub-1 dB/km attenuation achieved in 2019 [56] and 2020 [17].

4.2 Higher-order modes

To minimize SSL and reduce the mode-field overlap with glass material, PBGFs and ARFs are designed with a large $D_{\mathrm{core}}/\lambda$ ratio (typically above 10). This leads to an increased number of guided modes and lower HOM atten-

uation. For PBGFs, the number of modes is given by the PBG - approximately 12 modes are present in case of a 7-cell PBGF, around 40 modes for 19-cell PBGF and approximately 80 modes in case of 37-cell PBGF [71]. In PBGF, the lowest-order HOM (LP_{11}) propagates with attenuation of only about 2.5 times larger than the fundamental mode(LP_{01}) and, therefore, HOMs can propagate even over longer PBGF lengths [70]. In NANFs HOMs propagate with attenuation in orders of hundreds or even thousands of dB/km, which allows effective single-mode guidance to be obtained even at short fiber lengths.

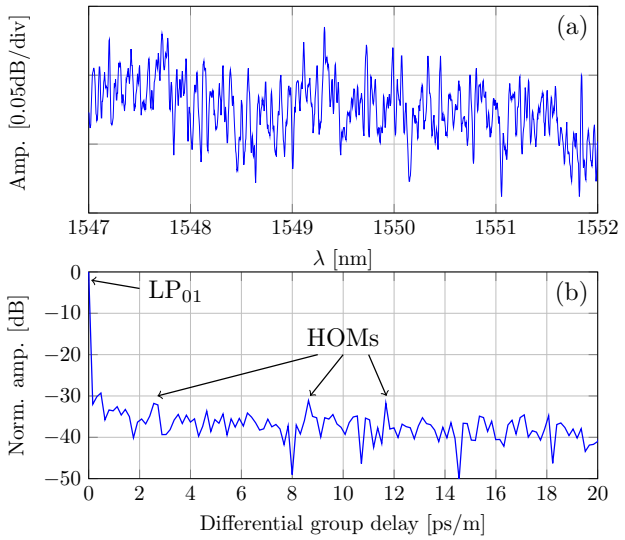

Fig. 9. Higher-order mode interference pattern in a 10-m-long PBGF. (a) Measured using optical spectrum analyzer and (b) it's Fourier transform.

It is possible to suppress HOMs significantly by precise alignment of input light source (either free-space optics or fiber) while exciting only the fundamental mode. We show a measured interference pattern of the fundamental mode (LP_{01}) with HOMs for a 10-m-long PBGF in Fig. 9a). From this interference pattern and by using a Fourier transform, it is possible to calculate the relative amplitude of the propagating modes and know which HOMs propagate in the particular HCF [72]. This is depicted in Fig. 9b), where we can also see greater than 30 dB suppression of HOMs. In this case, mode-field adapters based on a graded-index multimode fibers were used to match the mode-field of an SMF to a PBGF [23] and, according to the match quality, we observed interference (HOM amplitude) of various levels.

5. HCF to SMF interconnection

The practical implementation of HCFs is generally limited to laboratory applications. This is due to the difficulty in connecting HCFs with existing optical systems that are mostly based on standard SMFs. This is especially true for 19- and 37-cell PBGFs and the state-of-the-art NANFs having D_{core} over 30 μm. Additionally, precise MFD matching must be carried out so that HOMs are not excited. Using lenses with precise alignment is not a viable long-term solution due to limited time stability. Connectors are challenging as well, as the exposed HCF is susceptible to mechanical damage or a humid environment [73]. Therefore permanent and hermetic interconnection is required, as with conventional fiber-optic components.

Key requirements on the interconnection, apart from being permanent and hermetic, are:

- Low insertion loss (IL)
- Suppressed back-reflections on the silica-air interface, i.e., low return loss, RL
- Strict fundamental mode excitation (suppression of HOMs)

5.1 Fusion splicing

A common practice of creating a permanent interconnection of two optical fibers is fusion splicing. This is typically done using an arc-discharge that heats the two fiber ends, which are then pressed together to form a permanent, robust, repeatable and low-loss splice. When splicing two SMFs we can obtain virtually loss-less interconnection with no unwanted back-reflections. After the appearance of HCFs, modified splicing techniques have emerged with focus on maintaining the delicate microstructure, which easily collapses if overheated [9, 74]. The main modification is typically done by using a heating offset (by arc, filament or CO_2 laser) so that the SMF is heated more than the PCF and the HCF is then softly pushed onto the HCF. Unfortunately, this generally leads to low strength splices.

The first efforts in HCF splicing occurred in 2005, where the effect of an HCF microstructure collapse via an arc-discharge was studied [74], and in the same year, HCFs were spliced for use in gas-cells [9] with IL of 1.7 dB. In 2006 a deeper HCF splicing analysis was published [75], focusing on 7-cell (MFD ~ 7.5 μm) and a 19-cell (MFD ~ 13 μm) PBGFs. For an SMF to 7-cell PBGF splice, IL of 1.5-2.0 dB was observed for SMF-PBGF transition and 2.6-3.0 dB for the HCF-SMF transition. In the case of the 19-cell PBGF, IL was 0.3-0.5 dB and over 2.0 dB for SMF-HCF and HCF-SMF transitions, respectively. This unbalanced result of SMF-HCF and HCF-SMF insertion loss is extremely important, as it shows a huge effect of HOM excitation on measured IL once the MFD and numerical aperture of the SMF and HCF are not well matched. It is necessary to always measure two splices (generally interconnections), the input and output together so that the effect of the HOM is neglected. Or if just one splice is evaluated, fundamental mode coupling must be ensured or the effect of the HOM corrected (using a long enough HCF so that all HOMs would be attenuated).

Further attempts at HCF-SMF splicing brought improved IL and were focused on suppressing unwanted back-reflections that occur at the glass-air interface. In 2007,

splicing of flat and angled-cleaved 7-cell PBGFs was presented [21], with IL of 0.9 dB and 3.0 dB for flat and angled-cleaved HCFs, respectively, with RL of -16 dB and -60 dB. In 2016, splicing of 7-cell and 19-cell angled-cleaved PBGFs [22] brought improved IL of 1-2 dB with slightly lower RL of −50 dB. IL in this work was measured including HOMs which explains the great range of obtained IL values, furthermore, the obtained cleave angle variation was significant, from 7 to 12 degrees. In the same year, high-strength fusion splicing of 7-cell PBGF was demonstrated with IL of 1.3 dB [76].

To achieve sub-1 dB insertion losses, the move to bridge fibers acting as mode-field adapters was necessary. In 2014, MFD accommodation using a few-mode fiber to a 7-cell PBGF was published [20], showing the potential of bridge fibers formed by thermally-expanded core (TEC) fibers. Splice loss of only 0.73 dB was obtained for an SMF-TEC-PBGF interconnection.

5.2 Fiber-array based interconnection

When we first came with the idea of an alternative HCF-SMF interconnection approach, the best interconnection result had not yet been reached by a splice, but by using an HCF connector [77] and a large-mode area (LMA) single-mode fiber acting as a mode-field adapter (afterwards spliced to SMF) with a benchmark IL of 0.3 dB and RL of -31 dB thanks to a deposited anti-reflective (AR) coating on the LMA fiber.

Prior to HCFs, we already had some experience with interconnecting solid-core chalcogenide fibers to conventional SMFs, where AR coating was used to accommodate the difference in refractive indices and a bridge fiber was used to accommodate MFD. The deposition of AR coating or generally any optical coating was extremely appealing for HCFs, as fusion splicing prohibits the use of optical coatings due to high temperatures during splicing. Therefore, we developed a new alternative interconnection technology for HCFs, which, at that time, was envisioned to provide MFD accommodation, low IL and suppress unwanted back-reflections.

As a result, we published a low-loss, low-back-reflection reciprocal HCF-SMF interconnection in 2019 [23] based on the fiber-array technology and graded-index (GRIN) multi-mode fibers as mode-field adapters. In this first result we showed state-of-the-art IL per a single interconnection of 0.30 dB for fundamental mode coupling and RL of almost -30 dB, which are comparable values to [77]. However, in [77] the interconnection was based on a connectorized PBGF and, thus, the interconnection was not permanent and hermetic as the interconnection we developed is. In the development of our interconnection technique, we also devised a new method for HOM content monitoring (seen in Fig. 9), which is described in detail in [23]. The basic principle of the interconnection is depicted in Fig. 10, where both fiber-arrays are then glued together at temperatures below 80°C, thus also considered as a "cold splice" technique. Our interconnection can essentially work for any HCF with any solid-core fiber, while any optical coating can be deposited.

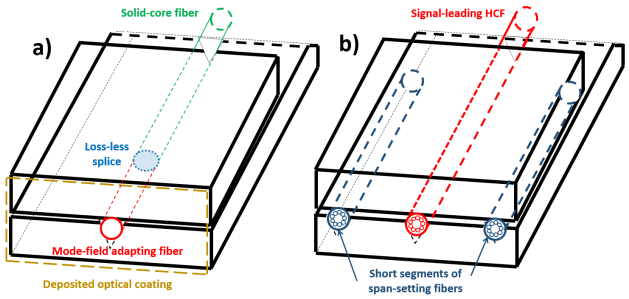

Fig. 10. Principle of the fiber-array-based interconnection of hollow-core to solid-core fiber, a) solid-core fiber with spliced mode-field adapting fiber segment in a 1-channel fiber-array, b) hollow-core fiber in a 3-channel fiber-array, where the side channels serve for precise gap setting.

In our first result [23], we observed very low HOM excitation, which is welcomed in many HCF applications as is shown in Fig. 9. Nevertheless, as mentioned above, PBGFs are inherently multi-modal and HOMs propagate with low attenuation, so even with high HOM suppression PBGF still exhibits multi-modal behavior. The next logical step was to move to ARFs, which have currently surpassed PBGFs in most aspects (other than bend loss resistance). The most promising of all ARFs are NANFs.

Using our interconnection approach, we modified our graded-index mode-field adapters for NANFs and the prior results showed IL below 0.5 dB with RL of -35 dB using an improved AR coating [78]. An image of an experimental NANF overlapped with its mode-field distribution can be seen in Fig. 11. As the NANF has a closer mode shape to a Gaussian than a PBGF and close to single-mode behavior, we expect to achieve record-low IL of the interconnection soon.

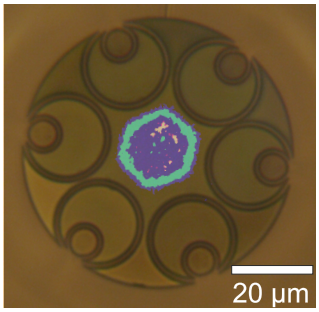

Fig. 11. NANF overlapped with its measured mode-field distribution.

5.3 Other interconnection solutions

An interesting solution has recently appeared using micro-optic collimator technology [79], where IL of 0.53 dB was presented for a single SMF-HCF interconnection with RL better than -45 dB and good HOM suppression (> 20 dB).

A tapered SMF as a coupling option has been theoretically and experimentally investigated [80], where the taper was inserted into the ARF core area. The resulting IL was approximately 0.8 dB for an SMF-NANF coupling, whereas back-reflections were suppressed well below -60 dB (considered as Fresnel-loss free). The design was based on a tapered coupling of an SMF-HCF published previously, in 2017, by R. Pennetta [41].

Regarding HCF to HCF interconnection, an interconnection has already been demonstrated via fusion splicing with only 0.16 dB average splice loss [81].

6. Interconnected HCF applications

In this section we present an overview of the main application fields where our HCF-SMF interconnection technology can be advantageously used.

6.1 HCF-based interferometers

In interferometric applications, HCFs offer the advantages of low nonlinearity thanks to the negligible light-glass interaction and HCF thermal insensitivity [7].

The flagship representative among all fiber-optic interferometric sensors is the Sagnac interferometer acting as a fiber-optic gyroscope (FOG). Use of HCFs in FOGs is especially desired due to their low nonlinearity and thermal polarization stability. A proposal for a HCF-based FOG was presented in [15] using a 7-cell PBGF of 20 m length. HCF-SMF interconnection was found to be one of the key challenges for further FOG development. Mach-Zehnder interferometer based on HCFs has been predominantly used as a gas/pressure sensor, such as the one shown in [82].

Our interconnection technology brings the advantages of low IL, optical coatings deposition to reduce back-reflection, fundamental mode excitation and also possible gas-cell formation (by adding gas inlets in the interconnection) which can serve to apply purge gases for further increase of interferometer stability and performance.

Recently, we have been focusing on fiber-based Fabry-Perot interferometers (FPIs) which permit us to build on our interconnection technique. Using a highly-reflective (> 98 %) coating we created two long-length FPIs [16] with lengths of 5 m and 22 m. Achieved finesse was over 120 for both FPIs with transmission peaks of only 47 kHz. Furthermore thermal stability of our HCF-based FPIs was evaluated and was measured to be 14.5 times better than for an identical FPI made of SMF.

6.2 Data transmission

HCFs are especially suitable for data transmission thanks to their low latency [4], low nonlinearity [3], and in the case of NANFs, extreme bandwidth and low attenuation. In 2019, data transmission over a 1-km-long NANF was demonstrated, where the tested NANF exhibited bandwidth of 700 nm with attenuation of 6.6 dB/km at 1550 nm which allowed 50 Gbit/s On-off keying (OOK) and 100 Gbit/s 4-level Pulse Amplitude Modulation (4PAM) signals [83]. The same year, 4.8-km-long NANF segment with attenuation of 1.18 dB/km at 1550 nm was used in a recirculating loop. This allowed for a data transmission of over 341-km-long NANF link with better pre-forward error correction bit error rate than 3E-2 [84].

To enable NANF application in real optical networks, fusion splicing may serve well when back-reflections are not a limiting factor. Otherwise, our interconnection technology provides better performance. Nevertheless for all interconnection approaches long-term stability must be ensured.

6.3 Gas sensing

HCFs have evolved significantly over the last two decades and are excellent candidates for highly sensitive gas sensing applications [85]. This is especially due to their almost 100 % mode-field overlap with the studied gas analyte. HCFs also allow the possibility to construct long-length gas cells which substitute the need for conventional multi-path free-space cells [14]. Among HCFs, ARFs provide a homogeneous and low-defect structure with substantial mitigation of HOMs, thus becoming the most suitable choice to form gas cells. Further advantage of silica HCFs for gas sensing is their MIR transparency. Even though silica is opaque above 2.4 μm, thanks to the negligible overlap of the core mode with the glass material, silica HCFs can work up to 4.0-4.5 μm with reasonable attenuation [43].

The common approach to analyzing gases is to use infra-red (IR) spectroscopy [86]. A complementary detection technique is Raman spectroscopy which is especially advantageous when studying multi-component gas analytes as it does not require a strict wavelength to match the respective absorption line [87].

Nevertheless, the gas-cell is mostly built in a laboratory environment where light is coupled via lens-systems. Alternatively, gas cells are sometimes fusion spliced to solid-core fibers resulting in higher IL and unwanted back-reflections.

Using our fiber-array interconnection technology we can either significantly suppress back-reflections or, as in the case of Fabry-Perot interferometers, we can increase the reflection and allow multi-path propagation to increase the interaction length by a factor of 10-100 depending on HCF attenuation and coating reflectivity. Furthermore, we can ensure fundamental mode excitation and thus reduce noise of the sensing system dramatically.

6.4 Other application fields

Gas-filled MIR lasers based on HCFs [42] can also benefit from providing a permanent interconnection of HCF to

solid-core fibers, most likely not SMFs, but MIR transparent fibers, such as fluoride (ZBLAN). Nevertheless, the interconnection methodologies (of both fusion splicing and using fiber-arrays) will need to be modified to work with other glass materials.

For high-power delivery, HCFs are extremely interesting due to their high damage threshold [5]. From particular power levels (depending on a continuous-wave or pulsed regime and on wavelength) HCFs, or more specifically ARFs, are the only option, as glass fibers are limited by the material damage threshold. Increasing power places higher requirements on the optical coatings, heat transfer from the interconnection and high HOM suppression. Our fiber-array approach has already shown very good HOM suppression, nevertheless efficient heat transfer and high-power optical coatings must still be investigated.

7. Conclusion

We have presented an overview of hollow-core optical fibers which are considered to be the future successors of conventional solid-core optical fibers, from their early stages all the way to current state-of-the-art antiresonant optical fibers.

Light guiding mechanisms of Bragg, photonic-bandgap and antiresonant fibers were discussed. Nested antiresonant nodeless fibers and conjoined-tube fibers are the two most promising antiresonant fiber designs for achieving ultra-low attenuation.

We have discussed interconnection options of hollow-core fibers to standard single-mode silica fibers. An alternative interconnection technique developed by our team was presented. Thanks to the mode-field adaptation using graded-index multimode fiber we achieved record-low insertion loss and also suppressed higher-order modes. Deposition of anti-reflective coating allowed us to reduce unwanted back-reflections. Finally, cutting-edge application of hollow-core fibers have been summarized with respect to the advantages of our proposed interconnection technology.

Hollow-core optical fibers are undoubtedly the future of fiber-optic communication, gas sensing, metrology, ultra-precise interferometry or mid-infrared lasers. Therefore, they definitely are worthy of scientific attention.

Acknowledgments

We would like to thank the members of the Advanced Fibre Technologies & Applications group, Optoelectronics Research Centre, Zepler Institute for Photonics and Nanoelectronics, University of Southampton for their collaboration in the hollow-core fiber research and for providing samples of photonic-bandgap and nested antiresonant nodeless fibers.

References

[1] ELLIS, A.D., MCCARTHY, M.E., KHATEEB, M.A.Z.A., et al., Performance limits in optical communications due to fiber nonlinearity, *Adv. Opt. Photon.*, 2017, vol. 9, no. 3, pp. 429–503, doi: 10.1364/AOP.9.000429

[2] TAMURA, Y., SAKUMA, H., MORITA, K., et al., The First 0.14-dB/km Loss Optical Fiber and its Impact on Submarine Transmission, *Journal of Lightwave Technology*, 2018, vol. 36, no. 1, pp. 44–49, doi: 10.1109/JLT.2018.2796647

[3] ROBERTS, P., COUNY, F., BIRKS, T., et al., Achieving low loss and low nonlinearity in hollow core photonic crystal fibers, in *Lasers and Electro-Optics*, 2005, pp. 1240–1242 Vol. 2, doi:10.1109/CLEO.2005.202085

[4] KUSCHNEROV, M., MANGAN, B.J., GONG, K., et al., Transmission of commercial low latency interfaces over hollow-core fiber, *Journal of Lightwave Technology*, 2016, vol. 34, no. 2, pp. 314–320, ISSN 1558-2213, doi:10.1109/JLT.2015.2469144

[5] SHEPHARD, J., COUNY, F., RUSSELL, P., et al., Improved hollow-core photonic crystal fiber design for delivery of nanosecond pulses in laser micromachining applications, *Applied Optics*, 2005, vol. 44, no. 21, pp. 4582–4588, doi:10.1364/AO.44.004582

[6] POLETTI, F., Nested antiresonant nodeless hollow core fiber, *Opt. Express*, 2014, vol. 22, no. 20, pp. 23807–23828, doi:10.1364/OE.22.023807

[7] SLAVÍK, R., MARRA, G., FOKOUA, E.N., et al., Ultralow thermal sensitivity of phase and propagation delay in hollow core optical fibres, *Scientific Reports*, 2015, vol. 5, p. 15447, doi:10.1038/srep15447

[8] PRYAMIKOV, A.D., BIRIUKOV, A.S., KOSOLAPOV, A.F., et al., Demonstration of a waveguide regime for a silica hollow - core microstructured optical fiber with a negative curvature of the core boundary in the spectral region > 3.5 μm, *Opt. Express*, 2011, vol. 19, no. 2, pp. 1441–1448, doi:10.1364/OE.19.001441

[9] BENABID, F., COUNY, F., KNIGHT, J.C., et al., Compact, stable and efficient all-fibre gas cells using hollow-core photonic crystal fibres, *Nature*, 2005, vol. 434, pp. 488–491, doi:10.1038/nature03349.

[10] HUMBERT, G., KNIGHT, J.C., BOUWMANS, G., et al., Hollow core photonic crystal fibers for beam delivery, *Opt. Express*, 2004, vol. 12, no. 8, pp. 1477–1484

[11] GÉRÔME, F., DUPRIEZ, P., CLOWES, J., et al., High power tunable femtosecond soliton source using

hollow-core photonic bandgap fiber, and its use for frequency doubling, *Opt. Express*, 2008, vol. 16, no. 4, pp. 2381–2386, doi:10.1364/OE.16.002381

[12] COUNY, F., BENABID, F., ROBERTS, P.J., et al., Generation and photonic guidance of multi-octave optical-frequency combs, *Science*, 2007, vol. 318, no. 5853, pp. 1118–1121, doi:10.1126/science.1149091

[13] WHEELER, N.V., HEIDT, A.M., BADDELA, N.K., et al., Low-loss and low-bend-sensitivity mid-infrared guidance in a hollow-core-photonic-bandgap fiber, *Opt. Lett.*, 2014, vol. 39, no. 2, pp. 295–298, doi: 10.1364/OL.39.000295

[14] NAMPOOTHIRI, A.V.V., JONES, A.M., FOURCADE-DUTIN, C., et al., Hollow-core Optical Fiber Gas Lasers (HOFGLAS): a review [Invited], *Opt. Mater. Express*, 2012, vol. 2, no. 7, pp. 948–961, doi:10.1364/OME.2.000948

[15] TERREL, M.A., DIGONNET, M.J.F., FAN, S., Resonant fiber optic gyroscope using an air-core fiber, *J. Lightwave Technol.*, 2012, vol. 30, no. 7, pp. 931–937, doi:10.1109/JLT.2011.2177959

[16] DING, M., KOMANEC, M., SUSLOV, D., et al., Long-length and thermally stable high-finesse fabry-perot interferometers made of hollow core optical fiber, *Journal of Lightwave Technology*, 2020, vol. 38, no. 8, pp. 2423–2427, doi:10.1109/JLT.2020.2973576

[17] JASION, G.T., BRADLEY, T.D., HARRINGTON, K., et al., Hollow Core NANF with 0.28 dB/km Attenuation in the C and L Bands, in *Optical Fiber Communication Conference Postdeadline Papers 2020*, Optical Society of America2020, p. Th4B.4, doi: 10.1364/OFC.2020.Th4B.4

[18] CHEN, Y., LIU, Z., SANDOGHCHI, S.R., et al., Multi-kilometer long, longitudinally uniform hollow core photonic bandgap fibers for broadband low latency data transmission, *Journal of Lightwave Technology*, 2016, vol. 34, no. 1, pp. 104–113, doi: 10.1109/JLT.2015.2476461

[19] JASION, G.T., POLETTI, F., SHRIMPTON, J.S., et al., Volume manufacturing of hollow core photonic band gap fibers: Challenges and opportunities, in *Optical Fiber Communication Conference*, Optical Society of America2015, p. W2A.37, doi:10.1364/OFC.2015

[20] GAO, S., WANG, Y., TIAN, C., et al., Splice Loss Optimization of a Photonic Bandgap Fiber via a High V-Number Fiber, *IEEE Photonics Technology Letters*, 2014, vol. 26, no. 21, pp. 2134–2137, doi: 10.1109/LPT.2014.2349519

[21] COUNY, F., BENABID, F., LIGHT, P.S., Reduction of Fresnel Back-Reflection at Splice Interface Between Hollow Core PCF and Single-Mode Fiber, *IEEE Photonics Technology Letters*, 2007, vol. 19, no. 13, pp. 1020–1022, doi:10.1109/LPT.2007.898770

[22] MILLER, G.A., CRANCH, G.A., Reduction of intensity noise in hollow core optical fiber using angle-cleaved splices, *IEEE Photonics Technology Letters*, 2016, vol. 28, no. 4, pp. 414–417, doi: 10.1109/LPT.2015.2496873

[23] KOMANEC, M., SUSLOV, D., ZVÁNOVEC, S., et al., Low-loss and low-back-reflection hollow-core to standard fiber interconnection, *IEEE Photonics Technology Letters*, 2019, vol. 31, no. 10, pp. 723–726, doi: 10.1109/LPT.2019.2902635

[24] J. J. THOMSON, *Notes on Recent Researches in Electricity and Magnetism: Intended as a Sequel to Professor Clerk-Maxwell's Treatise on Electricity and Magnetism*, The Clarendon press1893, doi: 10.1017/CBO9780511659034

[25] LORD RAYLEIGH F.R.S., XVIII. On the passage of electric waves through tubes, or the vibrations of dielectric cylinders, *The London, Edinburgh, and Dublin Philosophical Magazine and Journal of Science*, 1897, vol. 43, no. 261, pp. 125–132, doi: 10.1080/14786449708620969

[26] MARCATILI, E.A.J., SCHMELTZER, R.A., Hollow metallic and dielectric waveguides for long distance optical transmission and lasers, *The Bell System Technical Journal*, 1964, vol. 43, no. 4, pp. 1783–1809, doi:10.1002/j.1538-7305.1964.tb04108.x

[27] HIDAKA, T., MORIKAWA, T., SHIMADA, J., Hollow-core oxide-glass cladding optical fibers for middle-infrared region, *Journal of Applied Physics*, 1981, vol. 52, p. 4467, doi:10.1063/1.329373

[28] NAGANO, N., SAITO, M., MIYAGI, M., et al., TiO2-SiO2 based glasses for infrared hollow waveguides, *Appl. Opt.*, 1991, vol. 30, no. 9, pp. 1074–1079, doi: 10.1364/AO.30.001074

[29] SAITO, Y., KANAYA, T., NOMURA, A., et al., Experimental trial of a hollow-core waveguide used as an absorption cell for concentration measurement of NH3 gas with a CO2 laser, *Optics Letters*, 1993, vol. 18, no. 24, pp. 2150–2152, doi:10.1364/OL.18.002150

[30] SIRKIS, J.S., BRENNAN, D.D., PUTMAN, M.A., et al., In-line fiber étalon for strain measurement, *Opt. Lett.*, 1993, vol. 18, no. 22, pp. 1973–1975, doi: 10.1364/OL.18.001973

[31] RENN, M.J., MONTGOMERY, D., VDOVIN, O., et al., Laser-guided atoms in hollow-core optical fibers, *Phys. Rev. Lett.*, 1995, vol. 75, pp. 3253–3256, doi: 10.1103/PhysRevLett.75.3253

[32] TEMELKURAN, B., HART, S.D., BENOIT, G., et al., Wavelength-scalable hollow optical fibres with large photonic bandgaps for CO2 laser transmission, *Nature*, 2002, vol. 420, pp. 650–653, doi: doi.org/10.1038/nature01275

[33] VIENNE, G., XU, Y., JAKOBSEN, C., et al., Ultra-large bandwidth hollow-core guiding in all-silica Bragg fibers with nano-supports, *Opt. Express*, 2004, vol. 12, no. 15, pp. 3500–3508, doi:10.1364/OPEX.12.003500

[34] KNIGHT, J.C., BIRKS, T.A., RUSSELL, P.S.J., et al., All-silica single-mode optical fiber with photonic crystal cladding, *Opt. Lett.*, 1996, vol. 21, no. 19, pp. 1547–1549, doi:10.1364/OL.21.001547

[35] YABLONOVITCH, E., Inhibited spontaneous emission in solid-state physics and electronics, *Phys. Rev. Lett.*, 1987, vol. 58, pp. 2059–2062, doi: 10.1103/PhysRevLett.58.2059

[36] JOHN, S., Strong localization of photons in certain disordered dielectric superlattices, *Phys. Rev. Lett.*, 1987, vol. 58, pp. 2486–2489, doi: 10.1103/PhysRevLett.58.2486

[37] BIRKS, T.A., KNIGHT, J.C., RUSSELL, P.S.J., Endlessly single-mode photonic crystal fiber, *Optics Letters*, 1997, vol. 22, no. 13, pp. 961–963, doi: 10.1364/OL.22.000961

[38] MOGILEVTSEV, D., BIRKS, T.A., RUSSELL, P.S.J., Group-velocity dispersion in photonic crystal fibers, *Opt. Lett.*, 1998, vol. 23, no. 21, pp. 1662–1664, doi: 10.1364/OL.23.001662

[39] RANKA, J.K., WINDELER, R.S., STENTZ, A.J., Visible continuum generation in air–silica microstructure optical fibers with anomalous dispersion at 800 nm, *Opt. Lett.*, 2000, vol. 25, no. 1, pp. 25–27, doi: 10.1364/OL.25.000025

[40] CREGAN, R., MANGAN, B., KNIGHT, J., et al., Single-mode photonic band gap guidance of light in air, *Science*, 1999, vol. 285, no. 5433, pp. 1537–1539, ISSN 0036-8075, doi:10.1126/science.285.5433.1537

[41] PENNETTA, R., XIE, S., LENAHAN, F., et al., Fresnel-Reflection-Free Self-Aligning Nanospike Interface between a Step-Index Fiber and a Hollow-Core Photonic-Crystal-Fiber Gas Cell, *Physical Review Applied*, 2017, vol. 8, no. 1, 014014, doi: 10.1103/PhysRevApplied.8.014014

[42] DADASHZADEH, N., THIRUGNANASAMBANDAM, M.P., WEERASINGHE, H.W.K., et al., Near diffraction-limited performance of an OPA pumped acetylene-filled hollow-core fiber laser in the mid-IR, *Opt. Express*, 2017, vol. 25, no. 12, pp. 13351–13358, doi:10.1364/OE.25.013351

[43] KLIMCZAK, M., DOBRAKOWSKI, D., GHOSH, A.N., et al., Nested capillary anti-resonant silica fiber with mid-infrared transmission and low bending sensitivity at 4000 nm, *Opt. Lett.*, 2019, vol. 44, no. 17, pp. 4395–4398, doi:10.1364/OL.44.004395

[44] VENKATARAMAN, N., GALLAGHER, M.T., SMITH, C.M., et al., Low Loss (13 dB/km) Air Core Photonic Band-Gap Fibre, in *2002 28TH European Conference on Optical Communication*, vol. 5, 2002, pp. 1–2

[45] MANGAN, B.J., FARR, L., LANGFORD, A., et al., Low loss (1.7 dB/km) hollow core photonic bandgap fiber, in *Optical Fiber Communication Conference*, Optical Society of America2004, p. PD24

[46] ROBERTS, P.J., COUNY, F., SABERT, H., et al., Ultimate low loss of hollow-core photonic crystal fibres, *Opt. Express*, 2005, vol. 13, no. 1, pp. 236–244, doi: 10.1364/OPEX.13.000236

[47] BENABID, F., KNIGHT, J.C., ANTONOPOULOS, G., et al., Stimulated raman scattering in hydrogen-filled hollow-core photonic crystal fiber, *Science*, 2002, vol. 298, no. 5592, pp. 399–402, doi: 10.1126/science.1076408

[48] PEARCE, G.J., WIEDERHECKER, G.S., POULTON, C.G., et al., Models for guidance in kagome-structured hollow-core photonic crystal fibres, *Opt. Express*, 2007, vol. 15, no. 20, pp. 12680–12685, doi: 10.1364/OE.15.012680

[49] WANG, Y.Y., COUNY, F., ROBERTS, P.J., et al., Low loss broadband transmission in optimized core-shape Kagome Hollow-Core PCF, in *Conference on Lasers and Electro-Optics 2010*, Optical Society of America2010, p. CPDB4, doi:10.1364/CLEO.2010

[50] WHEELER, N., BRADLEY, T., HAYES, J., et al., Low loss kagome fiber in the 1 μm wavelength region, in *Advanced Photonics 2016 (IPR, NOMA, Sensors, Networks, SPPCom, SOF)*, Optical Society of America2016, p. SoM3F.2

[51] FÉVRIER, S., BEAUDOU, B., VIALE, P., Understanding origin of loss in large pitch hollow-core photonic crystal fibers and their design simplification, *Opt. Express*, 2010, vol. 18, no. 5, pp. 5142–5150, doi: 10.1364/OE.18.005142

[52] YU, F., WADSWORTH, W.J., KNIGHT, J.C., Low loss silica hollow core fibers for 3–4 μm spectral region, *Opt. Express*, 2012, vol. 20, no. 10, pp. 11153–11158, doi:10.1364/OE.20.011153

[53] DEBORD, B., AMSANPALLY, A., CHAFER, M., et al., Ultralow transmission loss in inhibited-coupling guiding hollow fibers, *Optica*, 2017, vol. 4, no. 2, pp. 209–217, doi:10.1364/OPTICA.4.000209

[54] GAO, S.F., WANG, Y.Y., DING, W., et al., Hollow-core conjoined-tube negative-curvature fibre with ultralow loss, *Nature Communications*, 2018, vol. 9, p. 2828, doi:10.1109/IPCon.2016.7831157

[55] BRADLEY, T.D., HAYES, J.R., CHEN, Y., et al., Record Low-Loss 1.3dB/km Data Transmitting Antiresonant Hollow Core Fibre, in *2018 European Conference on Optical Communication (ECOC)*, 2018, pp. 1–3, doi: 10.1109/ECOC.2018.8535324

[56] BRADLEY, T.D., JASION, G.T., HAYES, J.R., et al., Antiresonant hollow core fibre with 0.65 dB/km attenuation across the C and L telecommunication bands, in *45th European Conference on Optical Communication (ECOC 2019)*, 2019, pp. 1–4, doi: 10.1049/cp.2019.1028

[57] JASION, G.T., SANDOGHCHI, S.R., CHEN, Y., et al., Novel fluid dynamics model to predict draw of hollow core photonic band-gap fibres, in *2014 The European Conference on Optical Communication (ECOC)*, 2014, pp. 1–3, doi:10.1109/ECOC.2014.6964003

[58] RUSSELL, P.S., Photonic-crystal fibers, *J. Lightwave Technol.*, 2006, vol. 24, no. 12, pp. 4729–4749, doi: 10.1109/JLT.2006.885258

[59] POLETTI, F., PETROVICH, M.N., RICHARDSON, D.J., Hollow-core photonic bandgap fibers: technology and applications, *Nanophotonics*, 2013, vol. 2, no. 5-6, pp. 315 – 340, doi:10.1515/nanoph-2013-0042

[60] BARKOU, S.E., BROENG, J., BJARKLEV, A., Silica–air photonic crystal fiber design that permits waveguiding by a true photonic bandgap effect, *Opt. Lett.*, 1999, vol. 24, no. 1, pp. 46–48, doi:10.1364/OL.24.000046

[61] MARADUDIN, A., MCGURN, A., Out of plane propagation of electromagnetic waves in a two-dimensional periodic dielectric medium, *Journal of Modern Optics*, 1994, vol. 41, no. 2, pp. 275–284, doi: 10.1080/09500349414550321

[62] BROENG, J., BARKOU, S.E., SøNDERGAARD, T., et al., Analysis of air-guiding photonic bandgap fibers, *Opt. Lett.*, 2000, vol. 25, no. 2, pp. 96–98, doi: 10.1364/OL.25.000096

[63] MORTENSEN, N.A., NIELSEN, M.D., Modeling of realistic cladding structures for air-core photonic bandgap fibers, *Opt. Lett.*, 2004, vol. 29, no. 4, pp. 349–351, doi:10.1364/OL.29.000349

[64] ZAMANI AGHAIE, K., FAN, S., DIGONNET, M.J.F., Birefringence Analysis of Photonic-Bandgap Fibers Using the Hexagonal Yee's Cell, *IEEE Journal of Quantum Electronics*, 2010, vol. 46, no. 6, pp. 920–930, doi:10.1109/JQE.2010.2040369

[65] LITCHINITSER, N.M., ABEELUCK, A.K., HEADLEY, C., et al., Antiresonant reflecting photonic crystal optical waveguides, *Opt. Lett.*, 2002, vol. 27, no. 18, pp. 1592–1594, doi:10.1364/OL.27.001592

[66] RENVERSEZ, G., BOYER, P., SAGRINI, A., Antiresonant reflecting optical waveguide microstructured fibers revisited: a new analysis based on leaky mode coupling, *Opt. Express*, 2006, vol. 14, no. 12, pp. 5682–5687, doi:10.1364/OE.14.005682

[67] WEI, C., WEIBLEN, R.J., MENYUK, C.R., et al., Negative curvature fibers, *Adv. Opt. Photon.*, 2017, vol. 9, no. 3, pp. 504–561, doi:10.1364/AOP.9.000504

[68] CHOUDHURY, P., YOSHINO, T., A rigorous analysis of the power distribution in plastic clad annular core optical fibers, *Optik*, 2002, vol. 113, no. 11, pp. 481 – 488, ISSN 0030-4026, doi:10.1078/0030-4026-00195

[69] WEI, C., ALVAREZ, O., CHENARD, F., et al., Empirical glass thickness for chalcogenide negative curvature fibers, in *2015 IEEE Summer Topicals Meeting Series (SUM)*, 2015, pp. 187–188, doi: 10.1109/PHOSST.2015.7248259

[70] JUNG, Y., SLEIFFER, V.A.J.M., BADDELA, N., et al., First demonstration of a broadband 37-cell hollow core photonic bandgap fiber and its application to high capacity mode division multiplexing, in *2013 Optical Fiber Communication Conference and Exposition and the National Fiber Optic Engineers Conference (OFC/NFOEC)*, 2013, pp. 1–3, doi:10.1364/OFC.2013

[71] MORIOKA, T., AWAJI, Y., RYF, R., et al., Enhancing optical communications with brand new fibers, *IEEE Communications Magazine*, 2012, vol. 50, no. 2, pp. s31–s42, doi:10.1109/MCOM.2012.6146483

[72] NICHOLSON, J.W., YABLON, A.D., FINI, J.M., et al., Measuring the modal content of large-mode-area fibers, *IEEE Journal of Selected Topics in Quantum Electronics*, 2009, vol. 15, no. 1, pp. 61–70, doi: 10.1109/JSTQE.2008.2010239

[73] RIKIMI, S., CHEN, Y., BRADLEY, T., et al., Long-term behaviour of water vapour absorption in hollow core fibres, in *Sixth International Workshop on Specialty Optical Fibers and Their Applications (WSOF 2019) (06/11/19 - 08/11/19)*, 2019, p. 112061U

[74] XIAO, L., JIN, W., DEMOKAN, M.S., et al., Fabrication of selective injection microstructured optical fibers with a conventional fusion splicer, *Opt. Express*, 2005, vol. 13, no. 22, pp. 9014–9022, doi: 10.1364/OPEX.13.009014

[75] THAPA, R., KNABE, K., CORWIN, K.L., et al., Arc fusion splicing of hollow-core photonic bandgap fibers for gas-filled fiber cells, *Opt. Express*, 2006, vol. 14, no. 21, pp. 9576–9583, doi:10.1364/OE.14.009576

[76] WU, C., SONG, J., ZHANG, Z., et al., High strength fusion splicing of hollow-core photonic bandgap fiber and single-mode fiber, in *Photonics and Fiber Technology 2016 (ACOFT, BGPP, NP)*, Optical Society of America2016, p. AW4C.7, doi: 10.1364/ACOFT.2016.AW4C.7

[77] NICHOLSON, J.W., MANGAN, B., MENG, L., et al., Low-loss, low return-loss coupling between SMF and single-mode, hollow-core fibers using connectors, in *2014 Conference on Lasers and Electro-Optics (CLEO) - Laser Science to Photonic Applications*, 2014, pp. 1–2, doi:10.1364/CLEO.AT.2014

[78] SUSLOV, D., KOMANEC, M., ZVÁNOVEC, S., et al., Highly-efficient and low return-loss coupling of standard and antiresonant hollow-core fibers, in *Frontiers in Optics + Laser Science APS/DLS*, Optical Society of America2019, p. FW5B.2, doi: 10.1364/FIO.2019.FW5B.2

[79] JUNG, Y., KIM, H., CHEN, Y., et al., Compact micro-optic based components for hollow core fibers, *Opt. Express*, 2020, vol. 28, no. 2, pp. 1518–1525, doi: 10.1364/OE.28.001518

[80] HUANG, W., CUI, Y., LI, X., et al., Low-loss coupling from single-mode solid-core fibers to anti-resonant hollow-core fibers by fiber tapering technique, *Opt. Express*, 2019, vol. 27, no. 26, pp. 37111–37121, doi: 10.1364/OE.27.037111

[81] WOOLER, J.P., GRAY, D., POLETTI, F., et al., Robust low loss splicing of hollow core photonic bandgap fiber to itself, in *2013 Optical Fiber Communication Conference and Exposition and the National Fiber Optic Engineers Conference (OFC/NFOEC)*, 2013, pp. 1–3

[82] NAZERI, K., AHMED, F., AHSANI, V., et al., Hollow-core photonic crystal fiber machâ€“zehnder interferometer for gas sensing, *Sensors*, 2020, vol. 20, p. 2807, doi:10.3390/s20102807

[83] SAKR, H., BRADLEY, T.D., HONG, Y., et al., Ultra-wide Bandwidth Hollow Core Fiber for Interband Short Reach Data Transmission, in *2019 Optical Fiber Communications Conference and Exhibition (OFC)*, 2019, pp. 1–3, doi:10.1109/JLT.2019.2943178

[84] NESPOLA, A., STRAULLU, S., BRADLEY, T., et al., Record PM-16QAM and PM-QPSK transmission distance (125 and 340 km) over hollow-core-fiber, in *45th European Conference on Optical Communication (ECOC 2019)*, 2019, pp. 285 (4 pp.)–285 (4 pp.), doi: 10.1049/cp.2019.1019

[85] DEBORD, B., FOUED, A., VINCETTI, L., et al., Hollow-Core Fiber Technology: The Rising of "Gas Photonics", *Fibers*, 2019, vol. 7, p. 16, doi: 10.3390/fib7020016

[86] YANG, F., JIN, W., CAO, Y., et al., Towards high sensitivity gas detection with hollow-core photonic bandgap fibers, *Opt. Express*, 2014, vol. 22, no. 20, pp. 24894–24907, doi:10.1364/OE.22.024894

[87] KNEBL, A., YAN, D., POPP, J., et al., Fiber enhanced raman gas spectroscopy, *TrAC Trends in Analytical Chemistry*, 2018, vol. 103, pp. 230 – 238, ISSN 0165-9936, doi:https://doi.org/10.1016/j.trac.2017.12.001

About the Authors . . .

Matej KOMANEC was born in 1984. He received his M.S. and Ph.D. degrees in radioelectronics from the Czech Technical University in Prague (CTU) in 2009 and 2014, respectively. His research interests include specialty optical fibers, hollow-core fibers, optical interconnects, fiber-optic sensing, radio-over fiber and microwave photonics. He is a member of the Optical Society of America.

Daniel DOUSEK is a PhD student at CTU. He received his M.S. degree in radioelectronics from CTU in 2019. His current research interests include specialty optical fibers, optical components and interferometry.

Dmytro SUSLOV is a PhD student at CTU. He received his M.S. degree in radioelectronics from the CTU in 2016. His current research interests include specialty optical fibers, nonlinear optics, optical interconnects.

Stanislav ZVANOVEC received M.Sc. in 2002, a Ph.D. in 2006 at CTU.Now he is a full professor and deputy-head of the Department of Electromagnetic Field at the Faculty of Electrical Engineering, CTU. He leads a Free-space and fiber optics team from Faculty of Electrical Engineering, CTU and several research projects. His current research interests include wireless optical communications, visible light communications, remote sensing and optical fiber sensors.

scientific reports

Check for updates

OPEN

Low loss and high performance interconnection between standard single-mode fiber and antiresonant hollow-core fiber

Dmytro Suslov[1]✉, Matěj Komanec[1], Eric R. Numkam Fokoua[2], Daniel Dousek[1], Ailing Zhong[1], Stanislav Zvánovec[1], Thomas D. Bradley[2], Francesco Poletti[2], David J. Richardson[2] & Radan Slavík[2]

We demonstrate halving the record-low loss of interconnection between a nested antiresonant nodeless type hollow-core fiber (NANF) and standard single-mode fiber (SMF). The achieved interconnection loss of 0.15 dB is only 0.07 dB above the theoretically-expected minimum loss. We also optimized the interconnection in terms of unwanted cross-coupling into the higher-order modes of the NANF. We achieved cross-coupling as low as −35 dB into the LP_{11} mode (the lowest-loss higher-order mode and thus the most important to eliminate). With the help of simulations, we show that the measured LP_{11} mode coupling is most likely limited by the slightly imperfect symmetry of the manufactured NANF. The coupling cross-talk into the highly-lossy LP_{02} mode (> 2000 dB/km in our fiber) was measured to be below −22 dB. Furthermore, we show experimentally that the anti-reflective coating applied to the interconnect interface reduces the insertion loss by 0.15 dB while simultaneously reducing the back-reflection below −40 dB over a 60 nm bandwidth. Finally, we also demonstrated an alternative mode-field adapter to adapt the mode-field size between SMF and NANF, based on thermally-expanded core fibers. This approach enabled us to achieve an interconnection loss of 0.21 dB and cross-coupling of −35 dB into the LP_{11} mode.

Hollow core fibers (HCFs) have been reported to reduce the attenuation from 1.3 dB/km a year ago[1] to the current state-of-the-art of 0.28 dB/km[2], making the prospect of obtaining an optical fiber with attenuation below that of solid silica single-mode fiber (SMF) a distinct possibility in the near future. The latest three low-loss records in HCFs (1.3 dB/km[1], 0.65 dB/km[3], and 0.28 dB/km[2]) were reported in the Nested Antiresonant Nodeless Fiber (NANF), which therefore emerges as the most promising geometry in the quest for lower losses than the SMF. Besides this potential for ultra-low attenuation, HCFs have a range of additional advantages including low latency of propagation[4], low thermal sensitivity of latency as well as accumulated phase[5], low nonlinearity[6,7], high damage threshold[8], etc., making them of interest in a wide range of applications. To fully benefit from these advantages, however, an efficient low-loss and low-back-reflection interconnection between HCFs and mainstream SMFs is needed.

Recently, we demonstrated a new permanent, low-loss SMF-HCF interconnection technique based on gluing rather than splicing[9]. Fiber gluing is a widely-used process in demanding and cost-sensitive applications including telecoms, e.g., for pigtailing of planar lightwave splitters[10]. As gluing does not require any heating of the fibers (as opposed to fusion splicing), there is no deformation to the HCF micro-structure, which otherwise increases the interconnection loss. Further, no heating means that an optical coating can be applied in between the HCF and SMF. When anti-reflective (AR) coating is deposited, it significantly reduces the unwanted 3.5% back-reflection occurring at the glass-air interface in between the air core of the HCF and the solid silica glass core of the SMF. In addition to reducing the back-reflection, it also lowers the insertion loss (by up to 3.5% that would otherwise be lost in the back-reflection). The most important aspect, however, that must be addressed to achieve low-loss SMF-HCF interconnection, is to adapt the mode-field diameter, which at 1550 nm is typically 10.4 μm for the SMF and > 20 μm for low-attenuation HCF[9].

[1]Department of Electromagnetic Field, Czech Technical University in Prague, Technická 1902/2, 166 27 Prague 6, Czech Republic. [2]Optoelectronics Research Centre, University of Southampton, Southampton SO17 1BJ, UK. ✉email: suslodmy@fel.cvut.cz

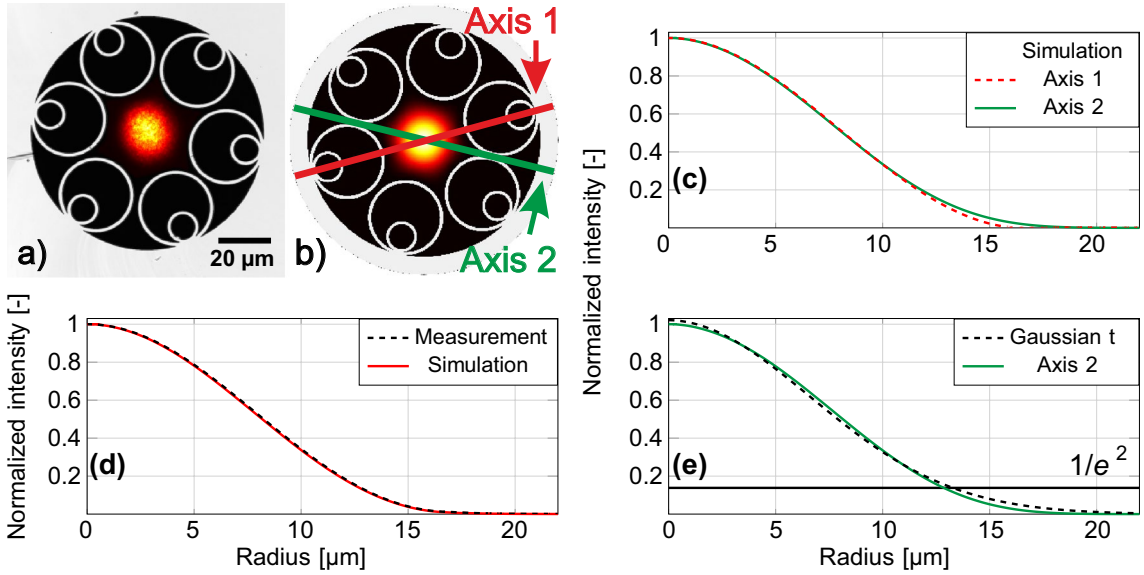

Figure 1. (**a**) Measured mode field distribution at the output of NANF overlaid with the captured image of the NANF core area. (**b**) Simulated fundamental mode field distribution overlaid with the NANF microstructure, extracted from the used NANF end-face photograph. (**c**) Mode field profiles from (**b**) along the two principal axes shown in (**b**). (**d**) Averaged axis 1 and 2 mode field profiles from measurement and simulation. (**e**) Mode field profile from (**c**) and its Gaussian fit.

In[9], we inserted a short segment of graded-index multi-mode fiber (GRIN) in between the SMF and HCF, which served as a lens that adapted the mode field size. When complemented with the AR coating, an HCF-SMF insertion loss (IL) as low as 0.3 dB and back-reflection below −30 dB were achieved. This was demonstrated with a photonic bandgap type of HCF, which was the state-of-the-art in terms of attenuation before the NANF emerged. These two types of HCFs are fundamentally different in their guiding mechanism (photonic bandgap guiding versus antiresonant effect guiding) as well as structure (delicate photonic bandgap with a large number of thin glass membranes versus a small number of tubes). As the antiresonant HCFs emerged as a low-attenuation solution only recently, there is only a limited number of reports on their interconnection with SMF. To the best of our knowledge, the lowest interconnection loss reported is 0.5 dB for simple SMF-NANF interconnection[11] or 1.5 dB for a more complex device (1×2 splitter[12]).

Although the lowest-loss value reported for a HCF-SMF interconnection of 0.3 dB is acceptable for a wide range of applications, it is 0.17 dB higher than expected from simulations[9]. Additionally, there are no data on how much of the light is coupled into the HCF's higher-order modes (HOMs) in these low-loss interconnections, and (even more importantly) how and how much this can be suppressed. From the practical point of view, loss lower than 0.3 dB will be of interest in high-power applications and laser resonators. Lower unwanted coupling into HOMs is of interest in applications sensitive to modal noise, e.g., interferometry[13], precise time[14], frequency transfer[15] and even telecommunications[16,17].

In this paper, we show a record low-loss SMF-NANF interconnection of 0.15 dB (which increases slightly to 0.16 dB when permanently glued), which is only 0.07 dB higher than the theoretically predicted minimum loss of 0.08 dB (calculated from the mode-field overlap between the field in NANF and a Gaussian field profile). This represents over 2 times improvement from the previous result in which the interconnection loss of 0.30 dB was 0.17 dB above the theoretical limit[9]. This improvement is thanks to the use of a mode-field adapter that is better matched to the mode of the HCF used. Simultaneously, we report a low-back-reflection level of −40 dB over 60 nm bandwidth thanks to a high-performance AR coating. Furthermore, we calculated and measured the coupling into the HOMs and show that: (1) the coupling magnitude to the LP_{11} mode was measured to be below −35 dB (calculated value: −41 dB) and that it is likely to be limited by the symmetry of the fabricated NANF, and (2) coupling magnitude to the LP_{02} mode was measured to be below −22 dB (calculated value: −24 dB). In addition to the GRIN-based mode field adaptation, we also present a new configuration based on thermally-expanded core fibers (TECs), showing experimentally a NANF-SMF interconnection loss of 0.21 dB.

Simulations of NANF mode field profile and higher-order modes

NANF HCF used in our experiment is of the same geometry as reported in[1], operating in the 2nd antiresonant window at 1550 nm. It has six large tubes with smaller tubes placed inside them, see Fig. 1a. The measured core diameter is 32.5 µm.

Firstly, we measured the field profile of light at the NANF output. The result together with an image of the used NANF end-face are shown in Fig. 1a. Subsequently, we simulated the fundamental mode-field profile of the NANF used in our experiments (obtained using the fiber end-face image shown in Fig. 1a and technique described in detail in[18]) using COMSOL Multiphysics. Both simulated and measured mode field profiles show that NANF mode is not circularly symmetric—it actually has a six-fold symmetry, following the symmetry of

the fiber microstructure. This is also visualized in Fig. 1c, where the mode field profile is plotted along the two principal axes (that are shown in Fig. 1b).

Let us consider light coupling between the NANF fundamental mode and a Gaussian-profile beam. A priori, we expect the mismatch between the circular symmetry of the Gaussian beam and the six-fold symmetry of the NANF fundamental mode to impose a fundamental limit on the achievable interconnection loss. However, the symmetry is not the only limiting factor, as we can see by analyzing the data shown in Fig. 1e, where one of the mode field profiles from Fig. 1c is fitted with a Gaussian profile. Clearly, the NANF mode field profile is not Gaussian, which is especially visible in the mode field tails, where the Gaussian profile vanishes more slowly than the profile of the NANF fundamental mode. Both of these phenomena (the non-circular symmetry and non-Gaussian mode field profile) contribute to: (1) the minimum-achievable coupling loss between a Gaussian-profile beam and the fundamental mode of NANF, and (2) coupling into HOMs. Theoretical analysis (calculating overlap integrals between the Gaussian mode and the NANF modes) shows that the minimum coupling loss from a Gaussian beam into NANF fundamental mode is 0.08 dB, with simultaneous coupling into LP_{02} mode (essentially a cross-talk) of −24 dB. Coupling into the LP_{11} mode is −41 dB. The LP_{11} coupling occurs due to the small deviations from the ideal symmetry (fabrication errors) of the manufactured NANF structure, this coupling would ideally be zero thanks to the different symmetries of the fundamental mode and the LP_{11} mode. The attenuation of the fundamental, LP_{11}, and LP_{02} modes (limited by confinement loss) is calculated to be ∼ 0.6 dB/km, ∼ 35 dB/km and ∼ 2100 dB/km, respectively.

Mode field adaptation

There are two aspects to be addressed to obtain ultra-low-loss interconnection between NANF and standard SMF: (1) The differences in mode field profile between the NANF and SMF-28 and (2) the Fresnel losses and back-reflection caused by the difference in refractive indices at a glass–air interface (about 3.5% for a silica glass–air interface).

As for the mode field adaptation, we would ideally need to transform the mode field profile and size of the SMF to match those of the NANF. As discussed earlier, transforming the mode field profile is challenging due to the different symmetry (circular for SMF and six-fold for NANF) as well as the slightly different field profiles: both SMF and NANF modes are almost Gaussian, but as we have shown in Fig. 1e they do not fit the Gaussian profile perfectly. Thus, we attempt to match the mode field size only, accepting this will limit the minimum-achievable coupling loss. As shown in our theoretical analysis, this limitation is expected to be 0.08 dB (provided we generate a perfectly-Gaussian mode field profile of optimum size).

To enlarge the mode field diameter (MFD) of SMF (10.4 μm) to that of our NANF (∼ 24 μm), we use here two approaches: the first one uses commercially available graded-index multi-mode fiber (GRIN) as mode field adapters (MFA), the other one uses SMF-based TEC mode field adapters.

GRIN and TEC fiber based MFAs. An optical signal that propagates from SMF to GRIN enlarges and shrinks its MFD in a periodic/sinusoidal fashion along the length of the GRIN (one period is referred to as 'one pitch'). It is therefore possible to achieve the desired MFD by controlling the length of the GRIN segment. The largest MFD is obtained when the GRIN length is at 1/4 of the pitch, which is also the length at which the output beam is collimated. In our experiment, we splice the GRIN fiber to SMF-28, put it into a single-channel glass fiber array (FA) and polish it to the desired length, which depends on the required MFD. We described this technique in detail in our previous publication[9].

We consider commercially available GRIN fibers of type OM1 (core diameter 62.5 μm, numerical aperture NA = 0.275) and OM2 (core diameter 50 μm, NA = 0.20). We used BeamProp software to model propagation through the GRIN fibers (OM1 and OM2) to get an estimate of the 1/4 pitch length as well as the output MFD. The modelling results for GRIN length in the vicinity of the 1/4 pitch (which is the region of our interest, as we show later) are shown in Fig. 2a. MFD is calculated at the $1/e^2$ of the intensity profile. We see that OM1 type GRIN provides a MFD up to 19.1 μm (at 1/4 pitch length of 260 μm), while OM2 type GRIN offers a MFD up to 23.2 μm (at 1/4 pitch length of 300 μm). The main reason OM2 provides larger MFD as compared to OM1 is its lower NA. Fig. 2b shows coupling loss between the mode generated by the GRIN MFA (which we measured in the near-field to be Gaussian) and a Gaussian mode with 24.1 μm MFD (MFD value obtained by fitting the NANF mode with a Gaussian profile). We see that OM2 should provide close to 0 dB loss for coupling into a Gaussian mode of 24.1 μm MFD for a GRIN length of 250–350μm. Fig. 2c shows the coupling loss between the mode generated by the GRIN MFA (considered to be Gaussian) and mode of our NANF (which includes the loss due to the mode field diameter mismatch (shown in Fig. 2b) together with loss due to NANF's 6-fold symmetry and its slightly non-Gaussian field profile) with the earlier-discussed limit of 0.08 dB. However, MFD is not the only parameter of the beam leaving GRIN fiber. Unless it is at 1/4 pitch, the beam is converging (focusing) or diverging, introducing phase curvature across the mode profile. This effect is not considered in our simulations.

To overcome Fresnel losses, we use an AR coating applied on to the polished GRIN surface[9]. To deposit this coating, particular care must be given to the coating deposition temperature, as the GRIN is glued inside the FA. Glue may not withstand high temperatures used for standard thin-film coating procedures and lower deposition temperature may compromise the coating quality. This is why in our previous report, we achieved a back-reflection level of −30 dB only. Although this level of back-reflection does not degrade the interconnection loss (−30 dB back-reflection corresponds to 0.1% of transmission loss, which is negligible as compared to the expected insertion loss of 0.08 dB (1.8%) transmission loss), better back-reflection suppression would be of interest in many applications. Here, we improved the control of the AR deposition process, achieving more than 10 dB better back-reflection suppression. The AR coating is a 4-layer TiO_2/SiO_2 design, which allows suppression of back-reflection by up to 48 dB, with >40 dB suppression over a 60 nm bandwidth (1550–1610 nm) (Fig. 3).

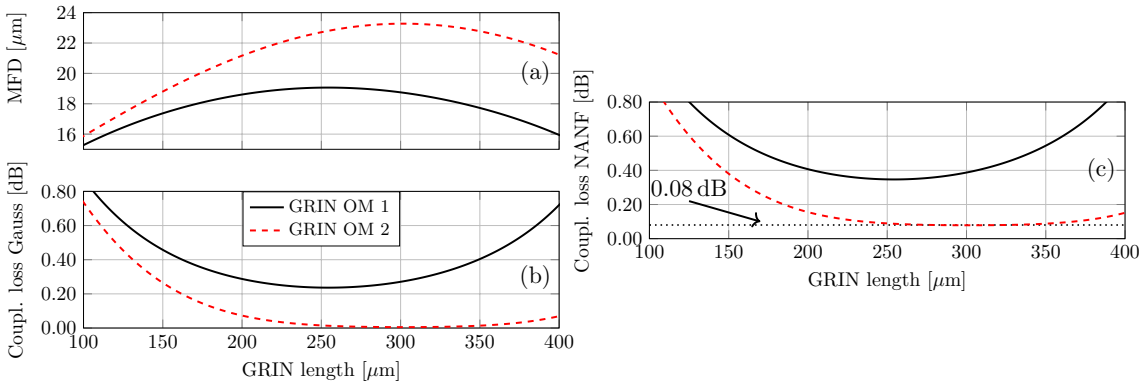

Figure 2. (**a**) Calculated MFD of OM1 (solid line) and OM2 (dashed line) type GRIN as a function of its length. (**b**) Coupling loss between Gaussian mode with MFD of 24.1 μm and output of GRIN mode field adapter shown in (**a**). (**c**) Coupling loss between NANF fundamental mode and output of GRIN mode field adapter shown in (**a**).

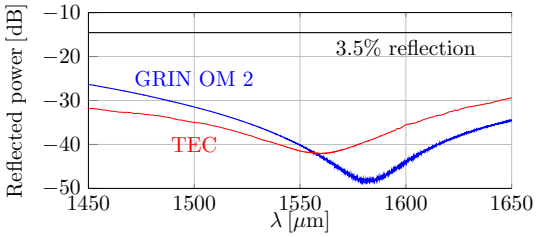

Figure 3. Measured back-reflection of SMF-GRIN and SMF-TEC MFAs as a function of wavelength.

TECs are commercially-available and typically provide 2-3 times magnification of the mode field size of standard SMF. We purchased TECs with mode field diameters of 20, 24, and 26 μm and a deposited AR coating of 40-dB back-reflection-level at 1550 nm as shown in Fig. 3.

SMF-NANF interconnection characterization

Measurement setup. As NANF can support the guidance of HOMs, we need to be cautious when measuring a single SMF-NANF interconnection to accurately characterize the coupling between the SMF and the NANF fundamental mode. This is because measuring power directly at the NANF output includes contributions from all the propagating modes and HOMs can carry an appreciable fraction of the total optical power.

One way to measure coupling between the SMF and NANF fundamental mode is to use a long length of NANF in which all HOMs are attenuated (thanks to the relatively high differential loss between the NANF fundamental mode and HOMs), obtaining only the fundamental mode power at the NANF output.

We chose another approach, using a short NANF (10 m) and performing interconnection with the SMF at both ends using a pair of identical MFAs (Fig. 4). This method allows for accurate coupling loss measurement between the fundamental modes of the two fibers[9] and also allows for estimation of the coupling efficiency into HOMs, which is not possible using a single interconnection and a long length NANF (HOMs will already be attenuated and no interference pattern will be visible). This approach provides additional means of characterization of the interconnection performance.

We took a set of GRIN and TEC MFA pairs with various mode field sizes. For each MFA pair, we aligned them with a 10 m long NANF sample and measured the total insertion loss as shown in Fig. 4. We used an Erbium-doped fiber amplifier (EDFA) operated in automatic power control mode as a broadband light source (Keyopsys KPS-BT2-C-10-LN-SA). We chose this source as it is broadband and unpolarized, avoiding effects of polarization dependent loss or interference during the alignment. The EDFA signal was filtered with a 10 nm wide optical band-pass filter (OBPF) (1545–1555 nm). The output of OBPF was then passed through a circulator (CIRC) to the input of the first MFA. The MFA output was precisely aligned with NANF using a 5-axis micropositioning stage (Thorlabs NanoMax MAX313D/M with pitch and yaw tilt platform APY002/M). Port 3 of CIRC enabled measurement of the back-reflection. The NANF output was aligned in a similar fashion to the second MFA.

There are two important aspects of our measurement we would like to emphasise: firstly, the use of the 5-axis stages that enables pitch and yaw alignment. Besides angular misalignment compensation, it also allows for compensation of small imperfections in the NANF cleave angle, which was always below 1° in our experiments. Secondly, the accurate calibration of transmitted power for accurate insertion loss measurement. For this, we firstly measured the transmitted power using an SMF patchcord and considered it as our reference (zero loss)

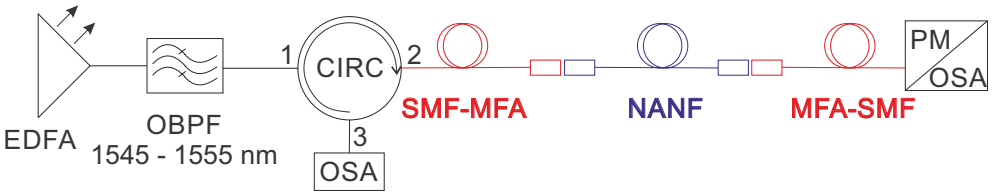

Figure 4. Setup used for insertion loss and back-reflection measurement of SMF-NANF-SMF interconnect for GRIN/TEC MFA pairs.

value. Subsequently, we cut this patchcord in the middle and spliced the two MFAs in. Finally, we inserted the NANF sample in between the two MFAs and measure the total insertion loss of the SMF-NANF-SMF interconnections. Loss of a single SMF-NANF interconnection is then given as half of this value. This, however, means our loss measurement includes two SMF-SMF splices, which we do not account for in our analysis and which may cause up to 0.01 dB loss each. Although this makes for a slightly overestimated loss value, this is, however, at the level of accuracy of our power measurement (0.01 dB) and is thus considered negligible.

The output signal was captured using either a power meter (PM, Thorlabs S154C, to characterize insertion loss) or an optical spectrum analyzer (OSA, Yokogawa AQ6370C, to characterize back-reflection and HOM interference). This approach allows us to repeatably achieve the insertion loss of 0.15 dB within ± 0.01 dB accuracy.

As analyzed in simulations, we expect some level of coupling into HOMs even when perfectly aligning the MFA with the NANF. As we mentioned, analysis of the optical spectrum of a broadband signal that propagates through NANF interconnected on both ends with SMF enables observation of coupling into HOMs. This manifests itself as an interference pattern. The light that is coupled into a HOM at the first MFA-NANF interface propagates in that mode and a fraction of it is coupled back into the fundamental mode of SMF after the second NANF-MFA interface. As the fundamental mode and the HOM have different effective refractive indices, the power recorded at the OSA shows a signature interference pattern. The amplitude of the interference pattern is proportional to the magnitude of the HOM excitation, while the interference period is proportional to the difference in propagation constants between the HOM and the fundamental mode of the NANF. Thus, we can distinguish between coupling to various HOMs too. This approach is significantly faster and easier to use than the traditional time of flight method[19], which is especially of interest during the alignment of the interconnection, in which we try to simultaneously maximize the output power (hence coupling into the fundamental mode) and minimize the HOM interference pattern amplitude observed at the OSA (to minimize coupling into HOMs). It is important to note that in practice this technique is only possible with short pieces of fiber due to the limitation of the OSA resolution. E.g. our OSA (Yokogawa AQ6370C) with a minimum resolution of 0.02 nm allows the use of 44 m long fiber.

Interconnection loss with GRIN MFAs. In this work we consider commercially available GRIN fibers to find the best MFD match. For our NANF we found the OM2 GRIN fiber to provide the closest match with the OM1 coming the second. However, depending on the particular NANF and its corresponding MFD, different type of GRIN fiber can provide an optimal mode-field adaptation. The insertion loss of SMF-NANF interconnections was measured for each GRIN MFA pair, see Fig. 5.

For OM1-based AR-coated MFA, a minimum loss of 0.32 dB was achieved with the GRIN fiber 1/4 pitch long (250 μm, Fig. 5), corresponding to the largest MFD that can be provided by the OM1 based MFA, Fig. 2. This MFD (19.1μm) is smaller than what is necessary for our NANF (Fig. 1d, MFD about 24 μm). The expected loss is 0.35 dB (Fig. 2c), which is close to the measured loss of 0.32 dB. We speculate this small discrepancy is caused by the small gap between the GRIN MFA and NANF fiber that was made during the alignment targeted to find the best value, which may have slightly enlarged the beam MFD (an effect we have not accounted for in our theoretical analysis).

The OM2-based MFA is expected to give significantly better match of the mode field size (up to 23.2 μm in 1/4 pitch GRIN length, which is achieved for 300 μm, Fig. 2a) to that of our NANF. As coupling between Gaussian fields of 23.2 μm and 24 μm MFDs leads to a negligible loss (< 0.01 dB, Fig. 2b), we expect the NANF-MFA interconnection loss to be dominated by the 0.08 dB additional loss due to the symmetry and shape mismatch. Our experiments show a loss only slightly higher than expected: 0.15 dB. This was achieved for a slightly shorter GRIN length (265 μm), which however is, similarly to the optimum 1/4 pitch length, expected to bring negligible (< 0.01 dB) mode field size mismatch loss, Fig. 2b. The 0.15 dB loss includes the loss of the SMF-GRIN splice. We measured this splice loss and found it to be below our power measurement resolution (≤ 0.01 dB). To evaluate the effect of the AR coating on the insertion loss, we also measured IL with the GRIN-MFAs before applying the coating, Fig. 5, showing 0.15 dB increase in the IL (corresponding to 3.5%), which is exactly in line with the value expected theoretically for the air-silica glass interface.

Unlike our previous study with photonic bandgap HCFs[9] in which we concluded that the GRIN length in MFA is very critical (± 5 μm length change produced almost 0.1 dB interconnection loss increase), here we see that significantly larger GRIN length variation in here-used HCF and GRIN MFA should produce negligible interconnection increase (Fig. 2c). Specifically, a change of up to ± 50 μm in GRIN length is predicted to produce insertion loss degradation below 0.01 dB. Experimentally, we confirm this, albeit over only a limited GRIN length variation of 15 μm. This improvement is thanks to the MFA used in combination with the HCF which was designed to ensure that the MFD of the mode generated with the quarter-pitch length GRIN is well matched to

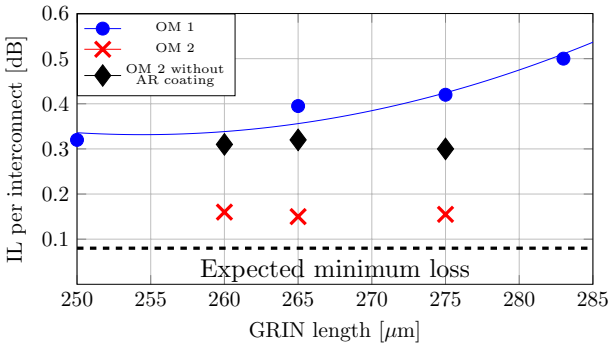

Figure 5. Insertion loss of SMF-28-NANF interconnect using OM1 (AR coated, blue circles, solid blue line represents fitted measurement data) and OM2 with (red crosses) and without (black diamonds) AR coating GRIN MFAs.

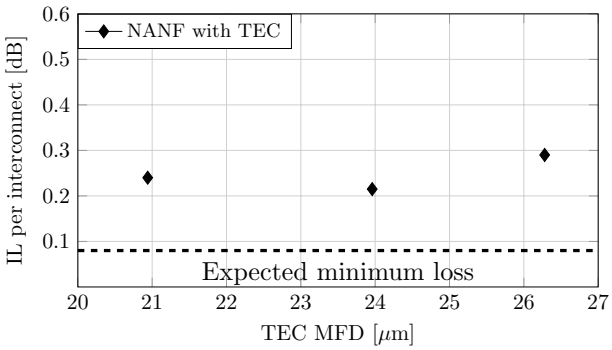

Figure 6. Insertion loss of SMF-28-NANF interconnect using TEC-based MFAs of various MFDs.

the MFD of the NANF. The larger margin on the GRIN length we show here can be achieved with cleaving[20], reducing the complexity of preparing an optimum-length GRIN MFA.

Interconnection loss with TEC MFAs. The insertion loss for each TEC MFA pair was measured, Fig. 6. As expected, the TEC producing a MFD of 24 μm gives the lowest insertion loss. We measured 0.21 dB, which is 0.13 dB above the mode symmetry and shape mismatch limit of 0.08 dB. For 21 and 26.5 μm MFD TECs, we measured an insertion loss of 0.24 and 0.29 dB, respectively. Based on the mode size mismatch, we would expect degradation of 0.08 dB for 21 μm and 0.04 dB for 26.5 μm as compared to the optimum 24 μm. These very small values do not correlate well with the experiment (although they are of the same magnitude as measured). This can be caused either by mode shape mismatch (the TEC-MFA mode can deviate more from the Gaussian shape for larger MFDs) or by inner TEC insertion loss (larger TEC-MFA having higher insertion loss). Both of these are plausible, as larger MFD TEC expansion requires longer heat processing and thus provides less control over the shape of the output TEC refractive index and mode field profile.

Measurement of higher-order mode content. HOM interference patterns (optical spectrum measured at the SMF-MFA-NANF-MFA-SMF output) measured when using the best-performing pairs of GRIN and TEC MFAs are shown in Fig. 7.

We see very weak (below 0.05 dB peak-to-peak) spectral oscillations of the transmitted power. The period of the oscillation is directly proportional to the propagation delay in NANF between the fundamental mode and a HOM that is being excited. Thus, a Fourier transform of the spectrum enables us to analyze the HOMs that are being excited, as we know the guided modes propagation constants from simulations. Figure 8 shows the Fourier transform of data from Fig. 7, in which we have identified two HOMs that were predominantly excited: LP_{11} (expected from simulations to be at 3.1 ps/m) and LP_{02} (expected from simulations to be at 8.7 ps/m) modes. To estimate how much power is carried by these two modes, we have to find the relationship between the coupling efficiency for these HOMs and the measured quantities.

Considering only the fundamental mode and a single HOM, the detected power is:

$$|E + \alpha E \cos(\Delta\tau L)|^2 = |E|^2 + 2\alpha|E|^2 \cos(\Delta\tau), \quad (1)$$

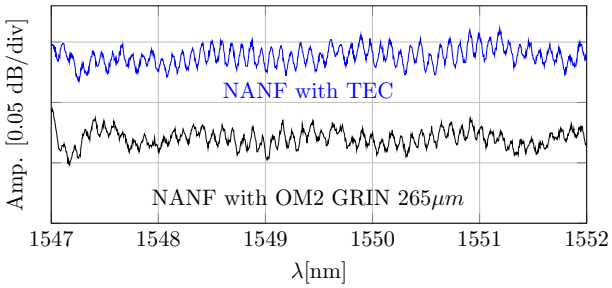

Figure 7. Interference pattern due to coupling into HOMs measured with the best-performing GRIN and TEC MFAs.

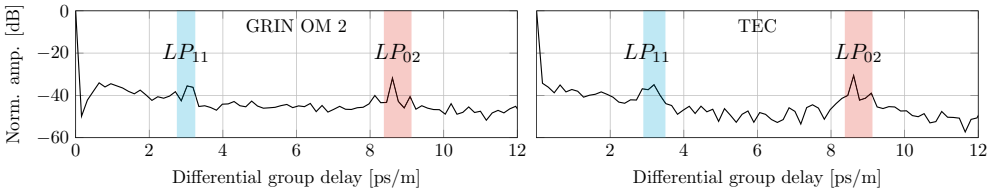

Figure 8. Fourier transform of spectral trances shown in Fig. 7. Positions of LP_{11} and LP_{02} modes expected from simulations are 3.1 and 8.7 ps/m.

where α is the fraction of energy that couples into the HOM, propagates in the HOM, and then couples back into the fundamental mode. $\Delta\tau$ is the normalized differential delay between the two modes inside the NANF. L is the fiber length and E is the intensity of the electric field. We have neglected the term proportional to α^2. Then, the Fourier transform of the measured data is:

$$\mathscr{F}\left(|E+\alpha E|^2\right) = |E|^2\delta(t) + \alpha|E|^2(\delta(t-\Delta\tau)+\delta(t+\Delta\tau)). \tag{2}$$

In Fig. 8, we see the tone at $t-\Delta\tau$ (due to the beating between the NANF fundamental mode and the HOM) which has a normalized amplitude of α. When taking into account the calculated attenuation of the LP_{11} and LP_{02} modes mentioned earlier (we need to separate the α contributions due to attenuation and due to coupling at the MFA-NANF interfaces) and assuming the HOM coupling is identical at both MFA-NANF interfaces, we calculated that the coupling magnitude at a single GRIN-MFA interface into the LP_{11} and LP_{02} modes is −35.3 dB and −21.3 dB, respectively. The LP_{11} mode has negligible loss for the 10-m long NANF sample used (35 dB/km), and thus the measured tone amplitude in Fig. 8 corresponds directly to the coupling into the LP_{11} mode. However, the loss for LP_{02} (2100 dB/km) cannot be neglected (21 dB in 10 m of NANF) and contributes significantly to the calculated coupling efficiency into the LP_{02} mode. For TECs, the LP_{11} coupling is very similar, −35.0 dB, but coupling into LP_{02} is slightly higher at −20.1 dB.

The measured results for coupling into the LP_{11} (−35 dB) and those simulated considering slight deviation from the perfect symmetry of the used NANF sample (−41 dB) are very close, especially considering measurement and simulation errors (due to limited resolution of the trace in Fig. 8 and limited accuracy of extracting data from the measured cross-sectional fiber image used in the simulations). In light of this, we conclude that coupling into the LP_{11} mode at a single MFA-NANF interconnection is most likely limited by the symmetry in the fabricated NANF rather than by other effects such as poor cleave quality. This conclusion is further supported by the fact that we measured an almost identical level of LP_{11} coupling using both, GRIN and TEC MFAs, suggesting this coupling is more related to the NANF properties rather than anything else. As for the LP_{02} results, we measured slightly higher values than predicted (−24 dB), suggesting the mode field profile generated in MFAs deviates slightly from a Gaussian (as the simulations were based on an MFA with Gaussian mode field profile). This slight deviation may also explain why we have not achieved an insertion loss closer to the expected value of 0.08 dB (which is also calculated considering a Gaussian-profile input beam). Furthermore, in the GRIN-MFA, the measured value of −22.3 dB is closer to the prediction (−24 dB) than the value measured for a TEC-MFA (−20.1 dB), suggesting the mode field profile at the TEC output deviates more from the Gaussian than at the GRIN-MFA output. This may explain why we measured the insertion loss with the GRIN-MFA to be slightly smaller (0.15 dB) than for TEC-MFA (0.21 dB).

It is worth mentioning that a low-level of cross-coupling into LP_{11} mode (e.g., −35 dB in our experiment) is more critical than coupling into other HOMs due to the relatively low LP_{11} mode attenuation. The relatively high level of cross-talk into the LP_{02} mode is then less critical for most applications due to the very high attenuation of the LP_{02} mode in typical NANFs. Apart from the LP_{11} mode, all HOMs suffer attenuation similar to or higher than LP_{02} mode.

We conclude that the predominant loss mechanism of our interconnection is through coupling into the LP_{02} mode. We expect this could be minimized by designing the GRIN fiber (to have a refractive index profile that slightly deviates from parabolic) or by optimizing the fiber (refractive index profile) used in the TEC process. As far as reduction of the LP_{11} mode coupling concerns, this would require more symmetric structure of the fabricated NANF. Since better symmetry will also bring lower attenuation[2], LP_{11} mode coupling will be further reduced for lower-attenuation NANFs that have been already reported recently[2].

Permanent interconnection. Based on the results shown in Fig. 5 we have proceeded to creating a permanent interconnection using a technique described in detail in[9]. We used a slightly modified setup from Fig. 4, where we added fiber-array holders (Thorlabs HFA001) onto the 5-axis stages.

The GRIN MFA, as discussed above, is glued in a fiber array and then polished to the desired length and AR coated. NANF fiber array, however, is prepared slightly differently, because the end-face of the NANF cannot be polished, as debris would get into the holes. This modified procedure has three steps. Firstly, after striping the protective coating from the small portion of NANF, we cleaved it, and inserted it into an empty pre-polished fiber array. Then, the NANF cleaved end-face was aligned with the pre-polished fiber-array end-face, so that both NANF and fiber-array end at the same point. Finally, we applied a UV-curable glue to the back-side of the NANF fiber array to secure NANF inside it.

Afterwards, we put both fiber arrays (with GRIN MFA and NANF) into the fiber-array holders, which we fixed on our 5D stages (Thorlabs NanoMax MAX313D/M with pitch and yaw tilt platform APY002/M), enabling precise alignment in the same way that was used previously for characterization. After aligning the two fiber arrays, we applied a viscous UV-curable glue in between the two fiber arrays (ensuring the glue does not creep into the NANF microstructure) and cured the glue to form a permanent interconnection. During the curing process, we continuously monitored IL of the interconnection and observed an IL degradation of 0.01 dB, which is within our measurement accuracy. Thus, we conclude that the gluing did not degrade the interconnection performance.

It is worth mentioning that although we made the interconnections manually (as a proof of concept), the entire process can be in principle fully automated, as it is for conventional gluing-based fiber array assembly in the photonic industry.

Conclusion

We have demonstrated record low-loss interconnect between NANF and SMF with insertion loss of only 0.15 dB. This is 0.07 dB above the theoretically-expected minimum loss due to the mode shape and symmetry mismatch between the NANF mode and an ideal Gaussian mode. The interconnect was based on a modified fiber-array technology, which is industry-proven, used, e.g., in telecom when attaching SMFs to high-port-number planar lightwave splitters (e.g., 1×64). As gluing is a cold process (no fusion splicing involved), it allows for deposition of optical coatings in between NANF and the SMF-GRIN mode field adapter. Anti-reflective coatings strongly-reduce the SMF-NANF 3.5% back-reflection due to the hollow core (air) to glass core interface. We experimentally demonstrated better than −40 dB back-reflection over 60 nm bandwidth while reducing the interconnection insertion loss by 0.15 dB (corresponding to the theoretically-expected reduction by 3.5%).

We used two approaches for adaptation of the mode field size between the SMF and NANF. The first mode field adapter used a short segment of telecom-standard (OM2) graded-index multimode fiber. The interconnection insertion loss was 0.15 dB, where we showed that a length variation as large as 15 μm (such accuracy can be straightforwardly achieved with a modified standard fiber cleaver) does not degrade the excellent interconnection insertion loss performance.

The second mode field adaptation approach used a thermally-expanded core of SMF. TECs are available commercially at low cost and can be manufactured with advanced commercially-available fusion splicers. We achieved NANF-SMF interconnection loss of 0.21 dB with TEC mode field adapters.

We studied the unwanted coupling into higher-order modes of NANF. We measured HOMs using a simple method based on an analysis of optical spectra. For the lowest-attenuation HOM (LP_{11}, about 35 dB/km in our NANF), we found unwanted coupling below −35 dB being most likely limited by the slight asymmetry of the fabricated NANF (rather than alignment or NANF end-face cleaving imperfection). The second most prominent HOM into which a small portion of light was coupled is the LP_{02} mode (attenuation of 2100 dB/km in our NANF). Coupling into this mode, which has the same symmetry as the LP_{01} mode, is mainly due to the mismatch of the shape of the mode field adapter output and the NANF LP_{01} fundamental mode profile. We show that GRIN-based mode field adapter produces slightly smaller coupling into the LP_{02} mode (−21.3 dB) than the TEC mode field adapter (−20.1 dB), suggesting the first one has a mode field shape better adapted to the LP_{01} mode than the latter. This agrees with our insertion loss measurements, which show slightly worse result for TEC mode field adapters (0.21 dB versus 0.15 dB).

We then show that permanent glued interconnection of NANF with a GRIN-based mode field adapter brings negligible (0.01 dB in our measurement, which is at our resolution limit) degradation to the final interconnection.

This work represents a new benchmark in hollow core fiber interconnection, showing simultaneously low loss, low coupling into higher-order modes, and low level of back-reflection. It also outlines further necessary steps to improve this even further (e.g., by improving the symmetry of the hollow core fiber or engineering the mode field profile generated by mode field adapters to better match the shape of the hollow core fiber fundamental mode).

Received: 27 January 2021; Accepted: 6 April 2021
Published online: 22 April 2021

References

1. Bradley, T. D. et al. Record low-loss 1.3 dB/km data transmitting antiresonant hollow core fibre. In *44th European Conference on Optical Communication (ECOC 2018)*, 1–3. https://doi.org/10.1109/ECOC.2018.8535324 (2018).
2. Jasion, G. T. et al. Hollow core NANF with 0.28 dB/km attenuation in the C and L bands. In *Optical Fiber Communication Conference Postdeadline Papers 2020, Th4B.4*. https://doi.org/10.1364/OFC.2020.Th4B.4 (Optical Society of America, 2020).
3. Bradley, T. et al. Antiresonant hollow core fibre with 0.65 dB/km attenuation across the C and L telecommunication bands. In *45th European Conference on Optical Communication* (ECOC 2019) (2019).
4. Kuschnerov, M. *et al.* Transmission of commercial low latency interfaces over hollow-core fiber. *J. Lightw. Technol.* **34**, 314–320. https://doi.org/10.1109/JLT.2015.2469144 (2016).
5. Mutugala, U. *et al.* Hollow-core fibres for temperature-insensitive fibre optics and its demonstration in an optoelectronic oscillator. *Sci. Rep.* https://doi.org/10.1038/s41598-018-36064-1 (2018).
6. Roberts, P. *et al.* Achieving low loss and low nonlinearity in hollow core photonic crystal fibers. *Lasers Electro-Opt.* **2**, 1240–1242 (2005).
7. Liu, Z. *et al.* Nonlinearity-free coherent transmission in hollow-core antiresonant fiber. *J. Lightw. Technol.* **37**, 909–916. https://doi.org/10.1109/JLT.2018.2883541 (2019).
8. Shephard, J. *et al.* Improved hollow-core photonic crystal fiber design for delivery of nanosecond pulses in laser micromachining applications. *Appl. Opt.* **44**, 4582–4588. https://doi.org/10.1364/AO.44.004582 (2005).
9. Komanec, M. *et al.* Low-loss and low-back-reflection hollow-core to standard fiber interconnection. *IEEE Photon. Technol. Lett.* **31**, 723–726. https://doi.org/10.1109/LPT.2019.2902635 (2019).
10. Xiao, G., Zhang, Z. & Grover, C. Adhesives in the packaging of planar lightwave circuits. *Int. J. Adhesion Adhesives* https://doi.org/10.1016/j.ijadhadh.2003.11.003 (2004).
11. Suslov, D. et al. Highly-efficient and low return-loss coupling of standard and antiresonant hollow-core fibers. In *Frontiers in Optics + Laser Science APS/DLS, FW5B.2*. https://doi.org/10.1364/FIO.2019.FW5B.2 (Optical Society of America, 2019).
12. Jung, Y. *et al.* Compact micro-optic based components for hollow core fibers. *Opt. Express* **28**, 1518–1525. https://doi.org/10.1364/OE.28.001518 (2020).
13. Choi, H. *et al.* Miniature fiber-optic high temperature sensor based on a hybrid structured Fabry-Perot interferometer. *Opt. Lett.* **33**, 2455–2457. https://doi.org/10.1364/OL.33.002455 (2008).
14. Xin, M. *et al.* Attosecond precision multi-kilometer laser-microwave network. *Light Sci. Appl.* https://doi.org/10.1038/lsa.2016.187 (2017).
15. Lisdat, C. *et al.* A clock network for geodesy and fundamental science. *Nat. Commun.* https://doi.org/10.1038/ncomms12443 (2016).
16. Sakr, H. et al. Ultrawide bandwidth hollow core fiber for interband short reach data transmission. In *2019 Optical Fiber Communications Conference and Exhibition (OFC)*, 1–3 (2019).
17. Nespola, A. et al. Record PM-16QAM and PM-QPSK transmission distance (125 and 340 km) over hollow-core-fiber. In *45th European Conference on Optical Communication (ECOC 2019)*, 285 (4). https://doi.org/10.1049/cp.2019.1019 (2019).
18. Fokoua, E. N. *et al.* Accurate modelling of fabricated hollow-core photonic bandgap fibers. *Opt. Express* **23**, 23117–23132. https://doi.org/10.1364/OE.23.023117 (2015).
19. Gray, D. R. et al. Complementary analysis of modal content and properties in a 19-cell hollow core photonic band gap fiber using time-of-flight and S^2 techniques. In *2012 38th European Conference and Exhibition on Optical Communications,* 1–4 (2012).
20. Chang, M. P. & Buscher, D. F. Cleaving optical fibre lengths to high relative accuracy. *Opt. Commun.* **157**, 282–290. https://doi.org/10.1016/S0030-4018(98)00440-4 (1998).

Acknowledgements

This work was supported by EPSRC project "Airguide Photonics", under Grant EP/P030181/1 and the Czech Technical University in Prague project through SGS20/166/OHK3/3T/13. F. Poletti gratefully acknowledges EU ERC (Grant 682724); R. Slavík and E. Numkam Fokoua were supported by RAEng Fellowships. The data in this paper is accessible through the University of Southampton research repository (DOI: https://doi.org/10.5258/SOTON/D1774).

Author contributions

D.S. and R.S. wrote the manuscript and prepared figures with input from M.K. and S.Z.. D.S. and D.D. carried out the experiments. M.K., A.Z. and E.R.N.F. conducted the simulations and calculations. T.D.B., F.P. and D.J.R. designed and manufactured the fiber. The manuscript results were discussed by all authors and all authors provided comments on the draft of the manuscript.

Competing interests

The authors declare no competing interests.

Additional information

Correspondence and requests for materials should be addressed to D.S.

Reprints and permissions information is available at www.nature.com/reprints.

Publisher's note Springer Nature remains neutral with regard to jurisdictional claims in published maps and institutional affiliations.

Long-Length and Thermally Stable High-Finesse Fabry-Perot Interferometers Made of Hollow Core Optical Fiber

Meng Ding, Matěj Komanec, Dmytro Suslov, Daniel Dousek, Stanislav Zvánovec, Eric R. Numkam Fokoua, Thomas D. Bradley, Francesco Poletti, David J. Richardson, *Fellow, IEEE*, and Radan Slavík, *Senior Member, IEEE*

***Abstract*—We made and characterized two Fabry-Perot interferometer samples made of the latest-generation hollow core fiber with sub-1-dB/km loss. Thanks to this low transmission loss, we achieved a finesse of over 140 and 120, for interferometer lengths of 5 and 23 m, respectively. This resulted in transmission peaks as narrow as 47 kHz. Our all-fiber Fabry-Perot interferometers have standard single-mode fiber pigtails (for easy integration in conventional fiber optic systems) and employ fiber mode field adapters to enable low-loss coupling between the pigtails and the low-loss hollow core fiber. The high-reflectivity mirrors (>98%) were deposited directly on the fiber mode field adapters, which were glued to the hollow core fiber, resulting in permanently-aligned Fabry-Perot interferometers. We also measured how the position of the transmission peaks change with temperature (an important performance metrics for most applications, e.g., when used as a narrow-band band-pass filter) and found that it changed 14.5 times less in our Fabry-Perot interferometer relative to a similar device made of standard single mode fiber.**

***Index Terms*—Fabry-Perot, optical fiber applications, optical fiber devices.**

I. Introduction

FABRY-PEROT interferometers (FPs) have many unique properties including high wavelength selectivity, high extinction ratios, the capability to enhance light intensity, etc. Their applications include, amongst others: lasers [1]–[3], metrology [4], [5] and sensing [6]–[8]. The full width at half maximum, FWHM of the transmission peaks is the key parameter of a FP, as a narrower peak provide better capability to discriminate frequency [6], of relevance, e.g., in reference cavities [2] or a ultra-high resolution sensors [5]. Another important parameter is the free spectral range (FSR), which is the spacing between neighboring transmission peaks and which is inversely proportional to the FPs optical length nL, where n is the refractive index and L is the length. The finesse (F) is then defined as the ratio FSR/FWHM. A small FWHM can be achieved with a high finesse or small FSR (or both). In free-space FPs (made, e.g., by drilling a hole in a low-expansion glass rod and then attaching high reflectivity mirrors at both ends [4]), L is usually limited by practical constraints to less than 50 cm, limiting the achievable FSR. Thus, if a small FWHM is desired, ultra-high finesse (sometimes $>10^5$) is needed, making such FPs highly sensitive to alignment. Thus, an alternative implementation using single-mode fiber FPs (SMF-FPs) has been widely investigated. SMF-FPs can have long lengths (e.g., 100's of meters) and can be very compact and lightweight. Although the finesse of SMF-FPs [7], [8] does not reach that achievable in free-space FPs (due to the fiber transmission loss), their small FSR enables narrow transmission peaks similar to those of short, high-finesse free-space FPs. Unfortunately, SMF-FPs have several drawbacks that make free-space FPs the preferred approach for many applications, despite free-space FPs larger size and the alignment challenges. The two primary drawbacks are the large sensitivity to temperature variations [8] and unwanted nonlinear effects like stimulated Brillion scattering (SBS) [9], especially in high-finesse FPs where the intra-cavity power is strongly enhanced by the resonant effect. Both of these parasitic effects are mainly due to the interaction of light with the silica glass material in SMFs. For example, the thermal sensitivity of the FSR (determined by the temperature dependence of the optical length nL of the SMF) is dominated (95%) by thermally-induced changes in the n of silica glass (thermo-optic effect) with the thermally-induced fiber length (thermal expansion effect) change providing the other 5% [10].

Hollow core fibers (HCFs) in which the glass-light interaction is very weak should address shortcomings discussed above. Firstly, the thermo-optic effect is practically eliminated, making HCF 20 times less thermally sensitive than SMF of equal L [10]. When considering equal optical length nL, this advantage

Manuscript received December 13, 2019; revised February 8, 2020; accepted February 9, 2020. Date of publication February 12, 2020; date of current version April 15, 2020. This work was supported in part by the EPSRC project "Airguide Photonics", under Grant EP/P030181/1 and in part by the Czech Technical University in Prague under Grant SGS SGS17/182/OHK3/3T/13. The work of Meng Ding was supported by CSC scholarship. The work of Francesco Poletti was supported by EU ERC under Grant 682724. The work of Radan Slavík was supported by RAEng Fellowship. *(Corresponding author: Meng Ding.)*

Meng Ding, Eric R. Numkam Fokoua, Thomas D. Bradley, Francesco Poletti, David J. Richardson, and Radan Slavík are with the Optoelectronic Research Centre, University of Southampton, SO17 1BJ Southampton, U.K. (e-mail: m.ding@soton.ac.uk; eric.numkam-fokoua@soton.ac.uk; t.bradley@soton.ac.uk; frap@orc.soton.ac.uk; djr@orc.soton.ac.uk; r.slavik@soton.ac.uk).

Matěj Komanec, Dmytro Suslov, Daniel Dousek, and Stanislav Zvánovec are with the Faculty of Electrical Engineering, Czech Technical University in Prague, 16627 Prague, Czech Republic (e-mail: komanmat@fel.cvut.cz; suslodmy@fel.cvut.cz; dousedan@fel.cvut.cz; xzvanove@fel.cvut.cz).

Color versions of one or more of the figures in this article are available online at https://ieeexplore.ieee.org.

Digital Object Identifier 10.1109/JLT.2020.2973576

is reduced (as $n\sim1$ in HCF compared to $n\sim1.45$ in SMF) to about 14 times [11], [12]. Nonlinearities are also substantially weaker in HCF as compared to SMF, enabling several orders of magnitude higher powers to be launched into HCF-FPs as compared to SMF-FPs [1].

Several recent works have reported high-finesse HCF-FPs. The cavity mirrors were formed using photonic crystal slabs [13] or high-reflectivity dielectric coatings [14]. However, all these reports dealt with cm-long fiber lengths limiting their use for applications requiring narrow FWHM transmission peaks. Generally, they used 7-cell photonic bandgap HCF designs, which offer good coupling into SMF, but whose high loss (>10 dB/km [15]) does not allow the construction of high-finesse long-length HCF-FPs (e.g., for 20-m long FP made with 10-dB/km fiber, the fiber-loss-limited maximum achievable finesse is 68). Furthermore, the reported HCF-FPs were not designed for long-term operation since their ends were not sealed, enabling air-born pollution like water vapor and dust to enter the hollow core, possibly causing long-term HCF-FP performance degradation.

Concerning ongoing efforts to reduce HCF loss, antiresonant type HCFs have recently witnessed tremendous progress [16]–[18]. The most recent results obtained with the Nested Antiresonant Node-less Fiber (NANF) geometry have broken the 1-dB/km barrier (0.65 dB/km across a bandwidth of 120 nm [18]). This has opened up a host of new application opportunities, including the possibility of making long length high-finesse HCF-FPs.

In this paper, we demonstrate and characterize two HCF-FPs with lengths of 5 and 23 m, with finesse > 120 over a wavelength range from 1530–1565 nm, made using NANF with sub-1 dB/km loss and pigtailed with SMF. These HCF-FPs are two orders of magnitude longer than previously-demonstrated. We compare their thermal stability with that of an SMF-FP, demonstrating more than an order of magnitude better performance. Besides improving the stability of fiber-based FPs, this also represents the first demonstration of such low thermal sensitivity in antiresonant HCFs; to date this has only been previously demonstrated for photonic bandgap type HCFs.

II. Fabrication of HCF-FPs

The schematic of the pigtailed HCF-FP is shown in Fig. 1. The HCF used is a NANF similar to the one reported in [18] with a loss of 0.9 dB/km, operating in the 1550-nm wavelength region. The HCF-FP is pigtailed with SMF. Because of the mode mismatch between the fundamental mode of the HCF used (21 μm) and standard SMF (10 μm), a suitable piece of GRIN fiber was inserted in between the two to enable mode field adaptation [19]. The GRIN fiber was first fusion spliced to the SMF. Before connecting it to the HCF, a FP mirror was deposited on its end-face. We used a 13-layer Ta2O5/SiO2 dielectric coating-based mirror with a reflectivity of >98% (from 1500–1570 nm). We did not use fusion splicing to interconnect the mirrors to the HCF, as this would destroy the mirror and could cause deformation of the HCF microstructure. We also did not use mechanical splice as shown in [14], since this approach does not allow for active alignment of the angle between the NANF and the

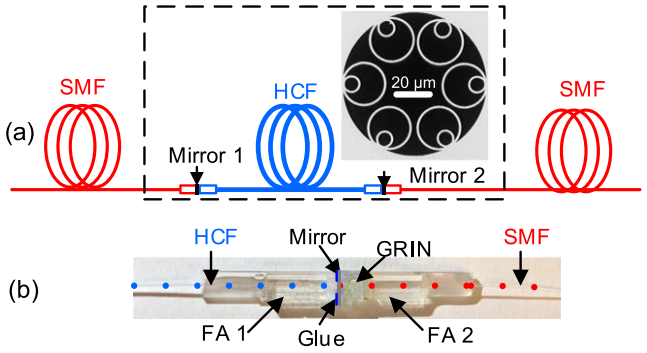

Fig. 1. (a) Configuration of the pigtailed HCF-FP with a cross-sectional scanning electron microscope (SEM) image of the HCF used. (b) Photograph of the fully assembled SMF-GRIN-Mirror-HCF interconnection. FA: fiber array, GRIN: Graded-index fiber based mode field adapter.

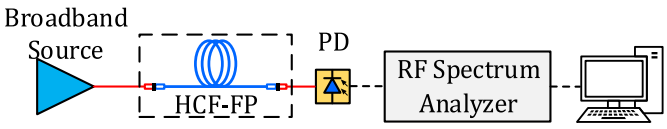

Fig. 2. Set-up for characterization of FPs in the radio-frequency (RF) domain. The broadband source is formed by two cascaded Erbium-doped fiber amplifiers (EDFAs) with a tunable bandpass filter inserted in between them. PD: photodetector.

mirror, imposing inherent limitation to reproducibility as well as the maximum achievable finesse. Instead, we used a modified fiber-array technique (used industrially for fiber pigtailing of planar lightwave circuits, PLCs) which we have refined for low-loss interconnection (<0.3 dB/interconnection) between HCFs and SMF [19]. Here, the SMF spliced to the GRIN is first glued into a V-groove array, polished to the desired GRIN fiber length, and afterwards, a coating is deposited on the end facet (the mirror in the work presented here). Then the carefully cleaved NANF is inserted into another fiber array V-groove and glued in to that. The two fiber arrays are actively aligned (in x, y, z, pitch, and yaw) before gluing the fiber arrays together (to obtain a permanent and sealed interconnection, which does not allow any air-born pollutants to enter the hollow core cavity, and thus ensures no degradation in the long-term performance). A Photograph of a typical glued interconnection is shown in Fig. 1b.

Since we target long length high-finesse FPs which have very narrow transmission peaks, optical scanning method used, e.g., in [13] is not ideal for active cavity alignment prior to gluing. This is because too many parameters are changing during the alignment (FP peaks spectral position, insertion loss, polarization, etc.), making alignment tedious and slowly converging. We found that in practice, the following two methods (for coarse and fine alignments) allowed us to align the HCF-FP cavity relatively quickly. For the coarse alignment, we optimized transmitted optical power of the HCF-FP using a 10-nm wide broadband incoherent light source and a photodetector. Once maximum power has been reached, we analyzed the photodetected signal with a radio-frequency (RF) spectrum analyzer observing RF beats (discussed in detail later) [20], Fig. 2. In the

coarse method, the transmitted power is insensitive to HCF-FP peaks spectral position and polarization state inside the FP. By maximizing the transmitted power, coupling loss between the HCF and the mirrors (i.e., how much light at the HCF output is coupled back into it) is minimized, which in practice allows for almost-optimum HCF-FP cavity alignment. The RF beat analysis technique allowed us to measure FP finesse directly (as we show below) enabling us to fine tune the FP. The signal shown on the RF spectrum analyzer is proportional to the convolution of the FP's optical coefficient with its conjugate:

$$P(f) \propto \frac{1}{1+\left(\frac{2F_e}{\pi}\right)^2 \sin^2\left(\frac{\pi f}{FSR}\right)}. \tag{1}$$

Here, f is the signal frequency shown on the RF spectrum analyzer and F_e is:

$$F_e = \frac{\pi R}{1-R^2} \approx \frac{\pi\sqrt{R}}{2(1-R)} = \frac{F}{2}. \tag{2}$$

where $R = \sqrt{R_1}\sqrt{R_2}\alpha$ is the effective reflectivity of the interferometer with $R_{1,\,2}$ being the reflectivities of the mirrors, and α the single-trip loss including the coupling loss between the HCF and the mirrors (i.e., how much light at the HCF output is coupled back into it) and fiber transmission loss. Although Eq. (1) is identical in form to the expression for the FP's optical transmission transfer function [13] it is not the same since F_e is different to the finesse F. For a high-finesse FP in which $R \sim 1$, we have derived that $F \sim 2F_e$ based on the first order Taylor series approximation. Thus, the FP's RF spectrum has twice as large peaks compared to the optical spectrum. In our experiment, data from the RF spectrum analyzer were acquired with a computer, where they were fitted with Eq. (1) in LABVIEW, enabling the FSR and finesse to be output in real-time, allowing for active FP alignment.

We made two HCF-FP samples using 5 and 23 m long HCFs. When aligned (prior to gluing), their Finesses were 195 and 160, respectively. After gluing using a UV-curable glue, we witnessed a slight finesse reduction to 153 and 133, respectively. Although we believe this may be improved by further refining the gluing process, the high-finesse (>120) FPs obtained are robust and have not degraded with time (we have not seen any degradation in four months since gluing them).

The 23-m HCF-FP had a smaller finesse both before and after the gluing as compared to the 5-m device. By considering the HCF loss of 0.9 dB/km and mirror reflectivity of 98.6%, analysis using Eqs. (1, 2) suggests that it is due to the HCF's transmission loss.

III. Characterization

Following the fabrication, we characterized the FPs using two techniques - besides the convenient, fast, and high-dynamic range RF technique we have described; we also measured it directly in the optical domain. We measured all of the important parameters (insertion loss, birefringence, and dependence on the wavelength). Finally, we measured the FPs' thermal sensitivity.

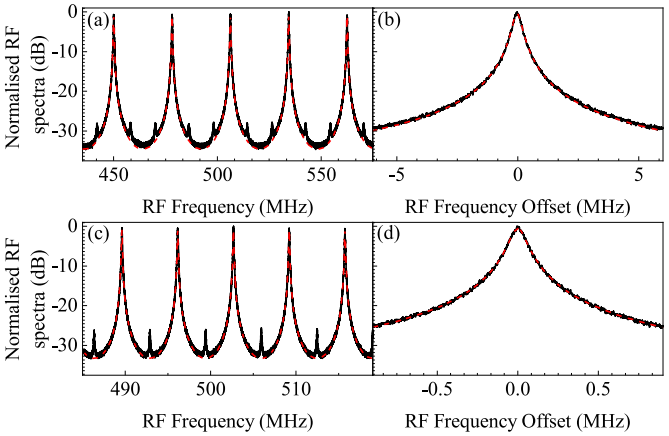

Fig. 3. Measured results for 5 m-HCF-FP (a, b) and 23 m HCF-FP (c, d). Normalized RF power spectra around 500 mHz (a,c) and their details around one peak (b, d). Solid black: measured, red dashed: fitted with Eq. (1).

A. Characterization in the RF Domain

The FP's transmission spectra including information about FSR and finesse were measured in RF domain using the method described previously. Normalized RF power spectra showing 5 peaks around 500 MHz and normalized RF power spectra showing one peak with fitted curves for the fabricated HCF-FPs are shown in Fig. 3. The broadband source used for this measurement had a 1 nm optical bandwidth (this narrow bandwidth allowed us to perform spectrally-dependent characterization shown later) with a central wavelength of 1550 nm (given by the optical bandpass filter used in the source set-up, Fig. 2). The small spikes at bottom of the RF power spectra are artefacts originating from noise in the EDFA electronics. We saw them in all our experiments. When fitting the experimental data with Eq. (1), we used only data above -10 dB to avoid any contribution from the measurement noise. Despite this, we achieved a very good fit across the entire fitting range. The FSR and F were 28.1 MHz and 153 for the 5 m HCF-FP and 6.5 MHz and 133 for the 23 m HCF-FP.

Subsequently, we measured the RF spectrum of the HCF-FPs over the entire C band (by tuning the wavelength of the 1-nm bandwidth tunable bandpass filter, Fig. 2). The results of both FPs are displayed in Fig. 4(a) (finesse) and Fig. 4(b) (FSR). The finesse values range from 140 to 160 for the 5-m HCF-FP and from 120 to 138 for the 23-m HCF-FP. Considering this measurement data and their variation across the C-band, the effective reflectivity (reflectivity that includes the coupling loss of light from the HCF to the mirror and back and HCF transmission loss) was calculated to be between 97.8% and 98.1% (5-m HCF-FP) and 97.4% to 97.75% (23 m HCF-FP). The FSRs, Fig. 4(b) slightly decrease with wavelength (by 150 Hz for 5-m HCF-FP and 600 Hz for 23-m HCF-FP over the entire C-band). This is due to the HCF chromatic dispersion, which we confirmed by fitting the data in Fig. 4(b) and calculating HCF chromatic dispersion from them, obtaining value of 2 ps/nm/km. This is consistent with value expected for our NANF-type HCF [18]. It is worth mentioning that this value of chromatic dispersion is 8

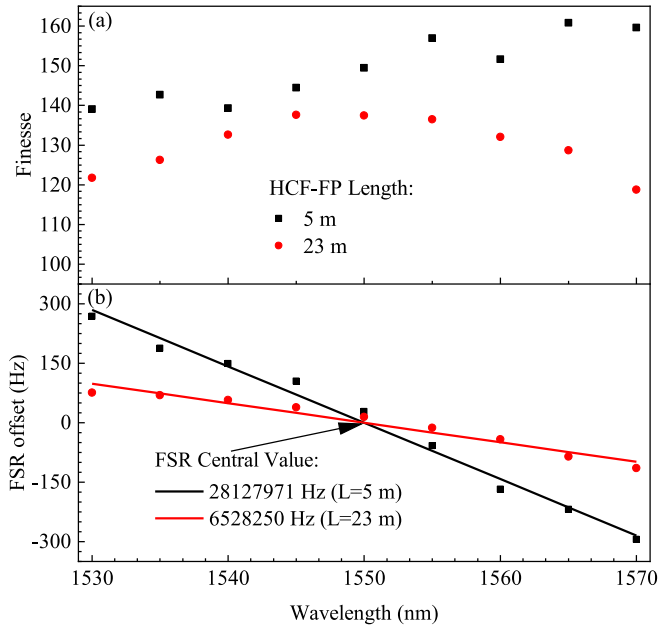

Fig. 4. (a) Finesse and (b) FSR offset of the two HCF-FP samples measured with the RF method every 5 nm across the C band.

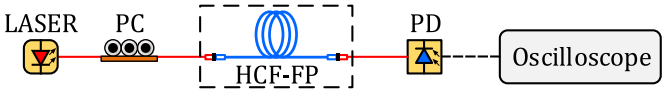

Fig. 5. Set-up to characterize the HCF-FPs in the optical domain. PC: polarization controller; PD: photodetector.

times lower than SMF and thus our HCF-FP is expected to have 8 times smaller variation of its FSR as compared to SMF-FP.

B. Characterization in the Optical Domain

Further FP parameters such as insertion loss (FP transmission loss at resonance) and polarization dependence are less straightforward to measure using the RF analysis technique. Thus, we implemented a characterization technique operating directly in the optical domain, Fig. 5.

We scanned the input light frequency of a narrow-linewidth (<10 kHz) fiber laser (NP Photonics, 1556 nm) by applying a sawtooth waveform on its RF port. The output was photodetected and visualized on an oscilloscope. The laser RF port response was calibrated to obtain the spectral characteristics of the FP transfer.

Due to the birefringence of the HCF (caused by the fabricated HCF inner structure not being perfectly symmetric and by HCF bending/coiling [21]), transmission peaks occur at two different positions within one FSR period when varying the polarization state of the launched light (via a polarization controller, Fig. 5). It is worth mentioning that this phenomenon is also observed with SMF-FPs [22] in which a very small residual fiber birefringence causes this splitting. The transmitted spectra for the two polarization eigenstates of two HCF-FPs are displayed in Fig. 6. The polarization peak spectral splitting was 15.1 and 2.42 MHz for the 5 and 23 m HCF-FPs, respectively. If the two peaks for the

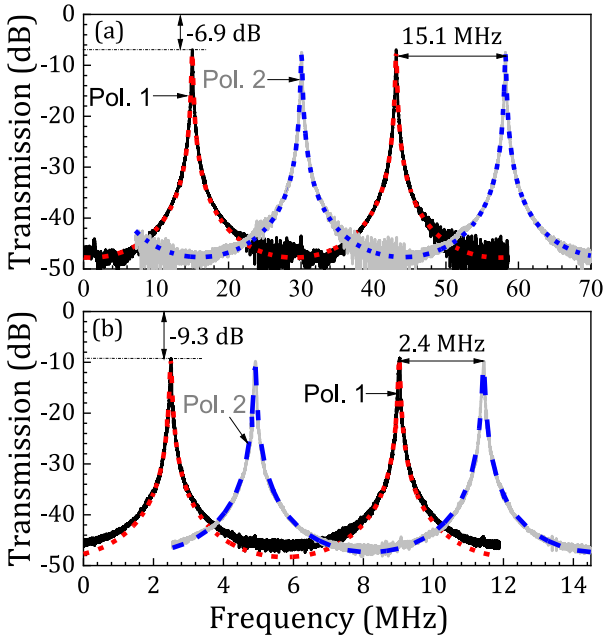

Fig. 6. Measured optical transmission spectra along the two principal axes of birefringence (Pol. 1, black and Pol. 2, grey solid) of (a) 5 m and (b) 23 m HCF-FPs. The insertion loss and polarization-induced spectral splitting are also shown. The red and blue dashed lines are data fitted by the transmission function of FP.

5 m HCF-FP were within the same FP resonance order (which we have not confirmed yet), HCF phase birefringence would have been 8×10^{-8} with corresponding beat length of 20 m.

We measured the FP's insertion loss to be 6.9 dB for the 5 m HCF-FP, Fig. 6, with the fitted finesse of 166 and 154 for the two polarization eigenstates, respectively. For the 23 m HCF-FP, the FP insertion loss was 9.3 dB and the fitted finesse was 139 and 130 (corresponding to 3-dB transmission peak width of 47 and 50 kHz), respectively. The obtained finesses are consistent with the RF method. Based on our theoretical analysis using Eqs. (1, 2), the FP insertion loss is mainly caused by the mirror loss (∼0.5% for the mirrors used). Replacing the current mirrors with improved mirrors with a loss of 0.1% would reduce the FPs insertion loss by ∼3 dB. Furthermore, by improving the gluing technique (i.e., no degradation of finesse during the gluing process), we could further improve the FP insertion loss by ∼2 dB for the two HCF-FPs.

C. Characterization of the Thermal Response

Thermal response here refers to how the transmission peaks frequency shifts with temperature. We characterized the thermal response of our 5 m HCF-FP using the set-up shown in Fig. 7. For comparison purposes we placed the 5 m HCF-FP together with a 3.6 m SMF-FP (which has the same optical length *nL* as the 5 m HCF-FP) into the same thermal chamber. The light source (NP Photonics used earlier, but here operated at fixed wavelength) was split and launched simultaneously into both FPs. PCs were used at both interferometer inputs to align the input polarization to one of the two FPs' eigenstates. The output power of both FPs was monitored using two photodiodes.

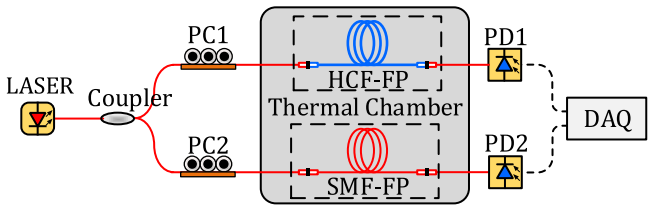

Fig. 7. Set-up for the thermal response measurement. DAQ: Data Acquisition System.

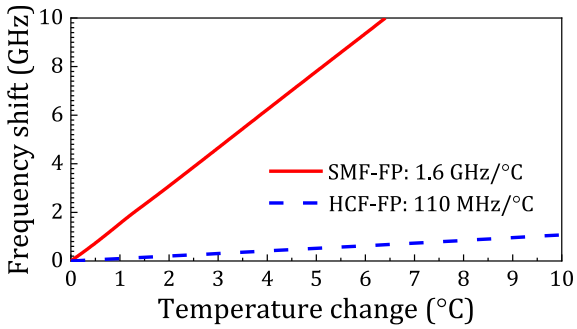

Fig. 8. Frequency shift of a selected transmission peak in the HCF-FP and a SMF-FP (of equivalent optical length) as the temperature is increased.

From the results shown in Fig. 8 we see that the transmission peak of the HCF-FP moved at a rate of 110 MHz/°C while in the SMF-FP it moved by 1.6 GHz/°C. Thus, the temperature sensitivity of HCF-FP is 14.5 times lower than that of SMF-FP, which matches well with the theoretical prediction. This is also the first demonstration of such a low sensitivity using an antiresonant HCF.

IV. Conclusion

In conclusion, we fabricated 5-m and 23-m long HCF-FPs. Our fully assembled permanent-connection based FPs have finesse >120 over the entire C band, which represents the first demonstration of long length (>1 m) HCF-FPs with such a high finesse. This was enabled by the combination of the latest-generation of low-loss (sub-1dB/km) HCFs and the recently developed technique for permanent, low loss, fusion-splice-less sealed HCF interconnection with standard optical fibers. We achieved a FP transmission peak width as narrow as 47 kHz (with an equivalent time delay of 3.2 km). This is only a factor of three wider than for state-of-the-art bulk FP cavities that are typically 10 cm long and have a finesse in excess of 10^5. We also showed HCF-FPs to have 14.5 times lower thermal sensitivity than SMF-FPs, which is due to the HCF's low thermal phase sensitivity. Our work represents the first demonstration of this property for antiresonant type HCF. The performance we demonstrate here, together with the expected high nonlinear threshold [9], will be of interest in many applications in which SMF-FPs cannot be used and free-space FPs are impractical.

Acknowledgment

The data in this paper is accessible through the University of Southampton research repository (DOI: 10.5258/SOTON/D1233).

References

[1] A. V. V. Nampoothiri *et al.*, "Hollow-core optical fiber gas lasers (HOFGLAS): A review [Invited]," *Opt. Mater. Express*, vol. 2, no. 7, pp. 948–961, 2012.
[2] A. V. V. Nampoothiri, B. Debord, M. Alharbi, F. Gérôme, F. Benabid, and W. Rudolph, "CW hollow-core optically pumped I_2 fiber gas laser," *Opt. Lett.*, vol. 40, no. 4, pp. 605–608, Feb. 2015.
[3] M. Xu, F. Yu, M. R. Hassan, and J. C. Knight, "Continuous-wave mid-infrared gas fiber lasers," *IEEE J. Sel. Top. Quantum Electron.*, vol. 24, no. 3, May-Jun. 2018, Art no. 0902308.
[4] S. Häfner *et al.*, "8×10^{-17} fractional laser frequency instability with a long room-temperature cavity," *Opt. Lett.*, vol. 40, no. 9, pp. 2112–2115, May 2015.
[5] T. Kessler *et al.*, "A sub-40-mHz-linewidth laser based on a silicon single-crystal optical cavity," *Nat. Photon.*, vol. 6, no. 10, pp. 687–692, Oct. 2012.
[6] G. Gagliardi, M. Salza, S. Avino, P. Ferraro, and P. De Natale, "Probing the ultimate limit of fiber-optic strain sensing," *Science*., vol. 330, no. 6007, pp. 1081–1084, Nov. 2010.
[7] J. Chen, Q. Liu, X. Fan, and Z. He, "Ultrahigh resolution optical fiber strain sensor using dual pound–drever–hall feedback loops," *Opt. Lett.*, vol. 41, no. 5, pp. 1066–1069, 2016.
[8] N. M. R. Hoque and L. Duan, "Ultrahigh-resolution fiber-optic sensing using a high-finesse, meter-long fiber fabry-perot resonator," Aug. 2019, *arXiv:1908.08595*.
[9] M. B. Gray, J. H. Chow, K. McKenzie, and D. E. McClelland, "Using a passive fiber ring cavity to generate shot-noise-limited laser light for low-power quantum optics applications," *IEEE Photon. Technol. Lett.*, vol. 19, no. 14, pp. 1063–1065, Jul. 2007.
[10] R. Slavík *et al.*, "Ultralow thermal sensitivity of phase and propagation delay in hollow core optical fibers," *Sci. Rep.*, vol. 5, no. 1, Dec. 2015, Art. no. 15447.
[11] M. Tateda, S. Tanaka, and Y. Sugawara, "Thermal characteristics of phase shift in jacketed optical fibers," *Appl. Opt.*, vol. 19, no. 5, pp. 770–773, 1980.
[12] S. Meiselman and G. A. Cranch, "Optical phase response to temperature in a hollow-core photonic crystal fiber," *Opt. Express*, vol. 25, no. 22, pp. 27581–27594, Oct. 2017.
[13] J. Flannery, R. Al Maruf, T. Yoon, and M. Bajcsy, "Fabry-pérot cavity formed with dielectric metasurfaces in a hollow-core fiber," *ACS Photon.*, vol. 5, no. 2, pp. 337–341, Feb. 2018.
[14] Y. Tan *et al.*, "Hollow-core fiber-based high finesse resonating cavity for high sensitivity gas detection," *J. Light. Technol.*, vol. 35, no. 14, pp. 2887–2893, 2017.
[15] R. Amezcua-Correa, F. Gèrôme, S. G. Leon-Saval, N. G. R. Broderick, T. A. Birks, and J. C. Knight, "Control of surface modes in low loss hollow-core photonic bandgap fibers," *Opt. Express*, vol. 16, no. 2, pp. 1142–1149, Jan. 2008.
[16] S. Gao *et al.*, "Hollow-core conjoined-tube negative-curvature fiber with ultralow loss," *Nat. Commun.*, vol. 9, no. 1, 2018, Art. no. 2828.
[17] T. D. Bradley *et al.*, "Record low-loss 1.3 dB/km data transmitting antiresonant hollow core fiber," in *Proc. Eur. Conf. Opt. Commun.*, 2018, no. 1, pp. 1–3.
[18] T. D. Bradley *et al.*, "Antiresonant hollow core fiber with 0.65 dB/km attenuation in the C and L telecommunication bands," in *Proc. Eur. Conf. Opt. Commun.*, 2019, Art. no. PDP3.1.
[19] M. Komanec *et al.*, "Low-loss and low-back-reflection hollow-core to standard fiber interconnection," *IEEE Photon. Technol. Lett.*, vol. 31, no. 10, pp. 723–726, May 2019.
[20] H. Tsuchida, "Characterization of optical resonators with an incoherent light," *Opt. Express*, vol. 20, no. 28, pp. 29347–29352, Dec. 2012.
[21] C. Rohrer *et al.*, "Phase shift introduced degradation of polarization caused by bends in inhibited-coupling guiding hollow-core fibers, " *IEEE Photon. Technol. Lett.*, vol. 31, no. 16, pp. 1362–1365, Aug. 2019.
[22] T. Yoshino, K. Kurosawa, K. Itoh, and T. Ose, "Fiber-optic fabry-perot interferometer and its sensor applications," *IEEE Trans. Microw. Theory Tech.*, vol. 30, no. 10, pp. 1612–1621, Oct. 1982.

Research Article | Vol. 29, No. 17 / 16 Aug 2021 / Optics Express 27768
Optics EXPRESS

Experimental comparison of DSB and CS-DSB mmW formats over a hybrid fiber and FSO fronthaul network for 5G

J. Bohata,[1,*] D. N. Nguyen,[1] J. Spáčil,[1] M. Komanec,[1] B. Ortega,[2] L. Vallejo,[2] Z. Ghassemlooy,[3] and S. Zvánovec[1]

[1]Department of Electromagnetic Field, Czech Technical University in Prague, Technicka 2, Prague 6, 166 27, Czech Republic
[2]Polytechnic University of Valencia, Camí de Vera, 46022 Valencia, Spain
[3]Northumbria University, 2 Sandyford Rd, NE1 8QH, Newcastle upon Tyne, UK
[*]bohatja2@fel.cvut.cz

Abstract: The telecommunication world is experiencing the 5th generation (5G) networks deployment including the use of millimeter wave (mmW) frequency bands to satisfy capacity demands. This leads to the extensive use of optical communications, especially the optical fiber connectivity at the last mile access and the edge networks. In this paper we outline fiber and free space optics (FSO) technologies for use as part of the 5G optical fronthaul network. We investigate two different mmW transmission schemes based on (*i*) the conventional analog radio over fiber transmission using one Mach-Zehnder modulator (MZM) with double sideband (DSB) optical modulation, and (*ii*) an optical-based frequency doubling with one MZM biased at the null point to introduce carrier suppression DSB (CS DSB) transmission and second MZM used for data modulation. Both systems are assessed in terms of the error vector magnitude, signal-to-noise ratio, dynamic range and phase noise. We consider a configuration for the fronthaul network in the frequency range 2 (FR2) at 27 and 39 GHz with the scale of bandwidth up to 400 MHz with M-quadrature amplitude modulation and quadrature phase shift keying. Results are also shown for FR1 at 3.5 GHz. Moreover, we investigate for the first time the 5G new radio signal transmission under strong turbulence conditions and show the turbulence-induced FSO link impairment. We finally demonstrate the CS DSB scheme performs well under chromatic dispersion-induced fading for the frequency up to 40 GHz and single mode fiber length of 30 km, whereas the DSB format seems more appropriate for an antenna seamless transmission.

1. Introduction

The 5th generation (5G) wireless networks [1], which have been deployed since 2019, are expected to account for approximately 10% of the global mobile devices (i.e., 1.4 billion out of the total of 13.1 billion according to the CISCO forecast [2]) and connections in 2023. The networks transmission capacity, and thus the requirement for new resources, need to satisfy the increasing end users' demand for access to information, more specifically for the video streaming via smart devices. High frequencies are well recognized worldwide as being the key component for the high-speed 5G services. The use of the unlicensed frequency bands above 6 GHz in 5G (and beyond) networks, which is labeled as frequency range 2 (FR2), is one complementary option to the licensed bands to offer ultrahigh speed mobile broadband communications. The most promising bands in FR2 are 27 and 39 GHz [3] providing sufficient bandwidth and covering a reasonably large service area, although the main limitation is due to big losses experienced by the high frequencies free space propagation.

#434334 https://doi.org/10.1364/OE.434334
Journal © 2021 Received 16 Jun 2021; revised 29 Jul 2021; accepted 29 Jul 2021; published 12 Aug 2021

Optics EXPRESS

The use of high frequency bands, i.e., millimeter wave (mmW), together with the need for massive data capacity places high demands on the adopted wireless technologies in terms of reliability, cost, efficiency (power and bandwidth), and robustness. The mmW technology is most widely needed in ultra-dense urban areas and hot-spot regions (e.g., football stadiums etc.) where the use of cloud radio access network (C-RAN) architecture has been considered as an interesting solution to save resources [4]. In C-RAN architectures, the baseband units (BBUs), hosted in the central office (CO), and the remote radio heads (RRHs) are physically decoupled. The RRH, which is kept at the base station (BS), and BBU, which is moved to the cloud infrastructure, are connected via an optical fronthaul network with increased demands on coverage, capacity and reduced latency and pressure on core network operations. This can be effectively implemented in 5G and beyond networks by a seamless convergence of the optical fiber and wireless technologies as reported in [5]. In [6], the analog radio over fiber (RoF) technology was introduced by moving all baseband processing, analog-to-digital conversion, up-conversion and electrical-to-optical conversion to the CO and keeping only the optical-to-electrical conversion, filtering, and amplification in the remote stations with reduced complexity [7]. An overview of RoF technologies adopted for wireless systems with an emphasis on the C-RAN architecture is given in [8].

To enhance the optical networks deployment and flexibility, particularly in urban areas, the free space optics (FSO) technology is considered as a potential solution [9]. The FSO offers optical fiber-based systems features including very large bandwidth at unlicensed frequency bands, immunity to electromagnetic interference, etc. However, in line with other wireless technologies, FSO links performance is affected by the channel conditions (i.e., fog, haze, and more importantly atmospheric turbulence (AT)) [10]. The latter is caused by the thermal distribution along the light signal propagation in the air that results in time variant beam refraction and beam width changes, thus leading to irradiance fluctuations known as scintillation [11].

1.1. Related works

In the literature, several radio over fiber (RoF), i.e. standard single mode optical fiber (SMF), radio over FSO (RoFSO) and a combination of both links for transmission of mmW signals using different modulation schemes such as double-sideband (DSB) and carrier-suppressed double sideband (CS DSB) have been reported. In [12], a 25 GHz 16-quadrature amplitude modulation (QAM) DSB signal based on either direct or external modulation was transmitted over 100 m SMF and 50 m long outdoor mmW links with the signal bandwidth limited to 20 MHz only. In [13], a CS DSB scheme for doubling the frequency to obtain the 40 GHz mmW signal with a 2 GHz bandwidth over a 20 km SMF was experimentally demonstrated. However, the 32-QAM signal was only evaluated at the intermediate frequency (IF) of 2 GHz, not at 40 GHz. In [14], a simple RoF link (20 km) with 3.5 Gbps on-off keying, which is not used in 5G networks, downstream link using the 72 GHz mmW based on all-optical CS DSB frequency eightfold technique and only a single external Mach-Zehnder modulator (MZM) was reported. A 60 GHz 4- and 16-QAM DSB signals with a bandwidth up to 400 MHz over a SMF were investigated in [15]; however fiber distance was limited to a 1 km of SMF, which is relatively short for optical fronthauling in 5G. In [16], the transmission of the 5G new radio (NR) standard signal of 26 GHz 16-QAM DSB with a bandwidth of 400 MHz over a 12.5 km of SMF, as well as 1 and 8 m long FSO and RF wireless channels, respectively was reported. However, the link performance was not investigated under the AT.

It is worth mentioning that in [17], we reported a detailed investigation of the AT distribution for the FSO path in a hybrid SMF and FSO channel using CS DSB-based frequency doubling technique at 40 GHz with a 2 GHz bandwidth and using 16-QAM. In [18] and [19], we also demonstrated the transmission of 25 GHz QPSK and 16/64-QAM signals using CS DSB-based frequency doubling technique over SMF, FSO and RF wireless links focusing on the impact

Optics EXPRESS

of AT on the FSO link. The signal performance was directly evaluated at 25 GHz; however, we only used a LTE signal with a 20 MHz bandwidth and thus the potential toward incoming telecommunication standards is limited.

1.2. Contributions

From the literature reviews, no works have been reported on the followings:

1. Transmission of the 5G NR signal at the mmW frequency bands of 27 and 39 GHz with a bandwidth up to of 400 MHz over the hybrid SMF, FSO and mmW wireless link and the system evaluation.
2. Experimental investigation and comparison of 39 GHz mmW DSB and CS DSB with QPSK and 64/256-QAM over the hybrid SMF and FSO channels with AT.
3. Characterization of the spurious-free dynamic range (SFDR) and the phase noise for both setups.

To the best of authors' knowledge, in this work for the first time we investigate the transmission of 5G NR signals at 39 GHz for DSB and CS DSB schemes over the combined analog RoF and RoFSO link. In addition, we experimentally demonstrate the implementation of 5G optical fronthaul with the hybrid SMF and FSO link at 3.5, 27, and 39 GHz bands. The paper is organized as follows. The experimental schemes are described in section 2, while results and discussion are provided in section 3. Finally, a summary of the main results of the paper is presented in section 4.

2. Experimental setup

As mentioned above, we have tested two setups for performance comparison of the mobile mmW fronthaul network as illustrated in Fig. 1(a). Both setups employ a continuous wave (CW) laser signal source (CoBrite DX4) with 16 dBm of output optical power. In Setup A, representing a classic analog MPL with DSB modulation and direct detection (DD), a 5G NR mmW signal at a particular carrier frequency is produced by a vector signal generator (R&S SMW200A) and applied to the MZM (Optilab IML-1550-50-PM), which is biased at its quadrature point. The output optical power of the MZM is 7 dBm. In Setup B, a radio signal at the half of the target carrier frequency, i.e., 12.5 GHz for 27 GHz and 18.5 GHz for 39 GHz transmission, produced by a signal generator (R&S SMF100A) is applied to MZM1 (Fujitsu FTM7938EZ/201), which is biased at its null point. The carrier-suppressed DSB (CS DSB) signal is led to low-speed MZM2 (Covega 10TM 081), which is biased at its linear point and modulated by the 2 GHz IF data signal from a vector signal generator (R&S SMW200A). The externally modulated optical signal with a power of -2 dBm is launched into the optical channel for transmission. In both Setups, the optical signal is directly detected at the optical receiver (Rx) (Optilab PD 40) and the resulting converted signal is captured by a signal analyzer (R&S FSW) for performance assessment. In the case of setup B, the beating of the optical sidebands at the optical Rx generates the signal at the double frequency of the original signal, i.e., 25 and 37 GHz with an additional IF of 2 GHz. Note that, due to the lower output optical power level in Setup B, an erbium doped fiber amplifier (EDFA) is required while in Setup A, the EDFA is only used when the FSO link is included. The optical channel used in Setups A & B consists of a fixed 10 km long SMF reel, providing a satisfactory range for connection between a CO and RRH, and a 4 m long FSO link as depicted in Fig. 1(b), to demonstrate a proof of concept. The latter offers a flexible solution to establish connectivity in high-density urban areas where burying fibers is costly and time consuming. The FSO link is composed of the Tx and the Rx with optical doublet collimators (Thorlabs F810APC-1550) for

Optics EXPRESS

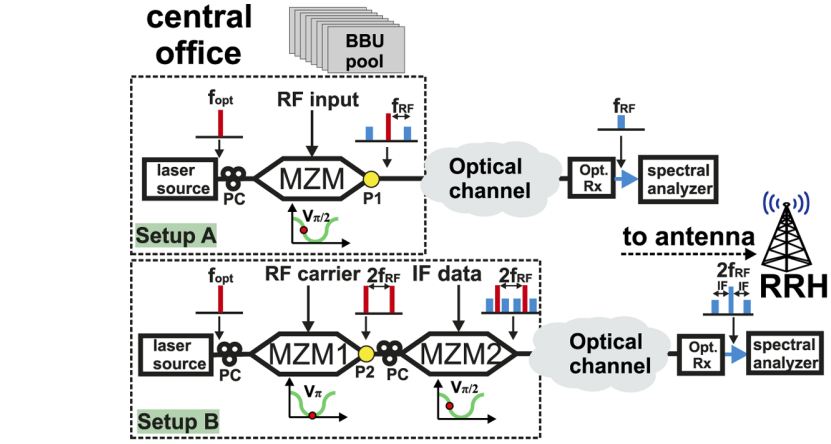

(a)

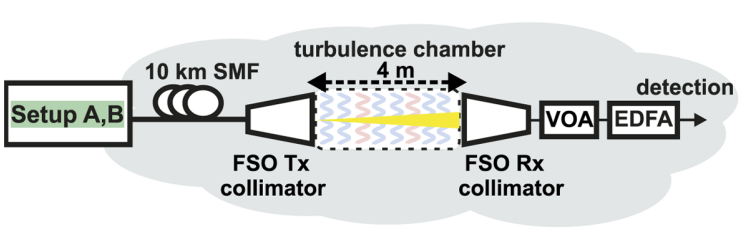

(b)

(c)

Fig. 1. (a) Setups A and B for an optical fronthaul network, (b) the full configuration of the optical channel, and (c) turbulent chamber.

launching and capturing the optical signal from and to the optical fiber, respectively. A laboratory AT chamber with controlled temperature distribution is employed for the FSO channel.

Table 1. System parameters

Parameter	Value
Laser wavelength	1550.6 nm
Laser output power	16 dBm
FSO length	4m
FSO loss	6 dB
FSO collimator aperture	2.4 cm
SMF length	10 km
SMF loss	2.5 dB
Opt. Rx responsivity	0.8 A/W
EDFA output power	3 dBm
EDFA noise figure	< 4 dB
PD bandwidth (-6dB)	> 40 GHz

Optics EXPRESS

Note that, in the FSO link the optical loss is 6 dB and a variable optical attenuator (VOA, Oz optics DA-100-SC-1300/1550-9/125-S-40) is used to control the input to the EDFA whose output power is set to 3 dBm. All the key parameters are summarized in Table 1.

3. Results and discussion

3.1. System characterization

The optical spectra with the RF carrier frequency of 27 GHz, measured in both Setups, are shown in Fig. 2. For Setup A, the spectrum captured in point P1 according to Fig. 1 evinces DSB optical modulation with sidebands located away from the optical carrier by the input RF, i.e., at 27 GHz, whereas Setup B shows the spectrum, obtained in point P2, of the suppressed carrier with two sidebands having the frequency difference between them equal to the double of the incoming electrical signal frequency to the modulator, which is 25 GHz in this case. Note that the original carrier frequency in Setup B is half, i.e., 12.5 GHz. Due to the absence of the optical carrier and beating of these sidebands at PD, a new RF carrier emerges in the frequency corresponding to the frequency difference between the sidebands, i.e., 25 GHz. Note, there is a second modulator MZM2 in Setup B, modulating data at the IF frequency of 2 GHz to the optical signal, so the total system output electrical carrier frequency is 27 GHz. Note that 2 GHz IF signal cannot be distinguished in optical spectral spectrum measured at the output of MZM2 even though we used high-quality spectral analyzer (Yokogawa AQ6370D), whose maximal resolution is 0.02 nm. Therefore, we have only shown the spectrum after MZM1 to demonstrate the transmission properties.

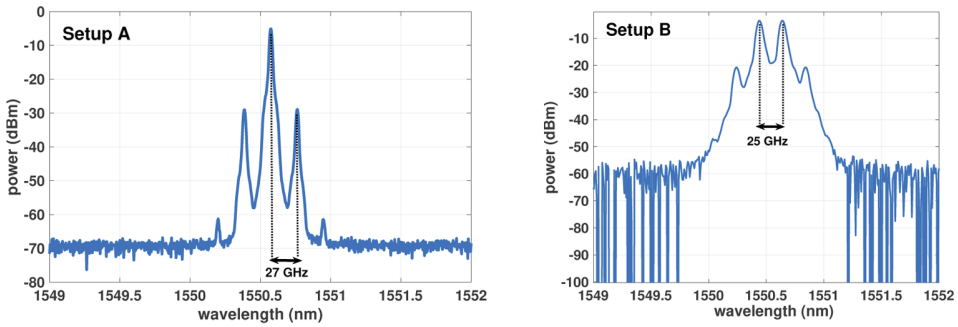

(a) (b)

Fig. 2. Optical spectra of the modulated optical signal for transmission at the frequency of 27 GHz for Setups: (a) A, and (b) B, which were obtained in points P1 and P2, respectively, according to Fig. 1(a).

Both setups have been characterized in terms of the spurious free dynamic range (SFDR) to demonstrate the impact of the third-order intermodulation distortion. For this purpose, we have used a two-tone test signal with 1 MHz spacing. It is worth to mention that, comparing to Setup A, the input power for the two-tone test in Setup B was applied to the the MZM2, i.e. low-frequency modulator, because the MZM2 is responsible for data modulation and thus most affects the overall performance. Measured results are depicted in Fig. 3. Note, in Setups A and B the noise floor levels are -158.0 and -156.5 dBm/Hz, respectively with the corresponding SFDR values of 88 and 89 dB $\times$ $Hz^{-2/3}$, respectively while there was employed EDFA in this test in Setup B. Based on the achieved results, both setups show very comparable dynamic range in terms of SFDR.

Optics EXPRESS

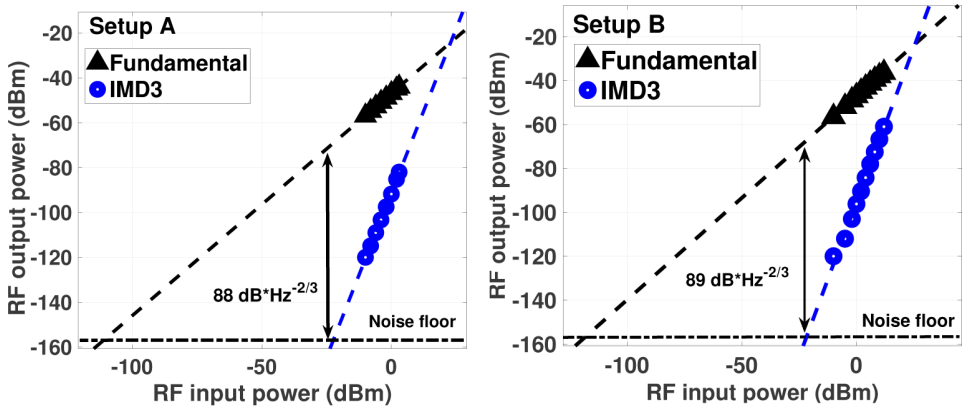

Fig. 3. Measured SFDR for Setups: (a) A, and (b) B.

For the overall system performance evaluation, 5G NR signals have been adopted according to the 3GPP 5G specifications in release 15, namely pre-defined test models TM1.1, TM3.1, and TM3.1a [20]. The test models use time division duplexing with a bandwidth range of 50 to 400 MHz, which is the maximum considered single bandwidth in 5G NR. These models are used, for example, for testing the output power dynamics or the quality of transmitted signal. Based on the 5G NR recommendations [21], we have selected frequency bands 3.5, 27, and 39 GHz for Setup A and 27 and 39 GHz for Setup B. Considering the fact that, the frequency multiplication technique (i.e., doubling) adopted in Setup B is preferably used only for higher frequency generation to relax the demands on the signal source, i.e., over 20 GHz, the frequency band 3.5 GHz has been tested only in the case of Setup A. Note that, the main focus is to characterize 27 GHz band, which is the closest band above FR1 for 5G, i.e., above 6 GHz [22]. The details of the adopted 5G NR signals are listed in Table 2. All used test models contain normal cyclic prefix with 14 OFDM symbols per slot.

Table 2. Used 5G NR signals – BW: bandwidth, ScS: subcarrier spacing, Thpt: throughput

Test model for 5G-NR	BW (MHz)	ScS (kHz)	CP (μ s)	Modul. Format	EVM limit (%)	Thpt (Mb/s)	Spectr. Eff. (b/s/Hz)
TM3.1	50	60	1.17	64QAM	9	178	3.56
TM3.1a	90	60	1.17	256QAM	4.5	444	4.93
TM3.1	100	60	1.17	64QAM	9	360	3.46
TM3.1	200	120	0.58	64QAM	9	692	3.46
TM3.1	400	120	0.58	64QAM	9	1386	3.47
TM3.1	400	120	0.58	QPSK	18.5	462	1.16

Note, (*i*) the highest throughput of 1.386 Gb/s is achieved at the bandwidth of 400 MHz and 64-QAM; and (*ii*) the best spectral efficiency of 4.93 b/Hz for a single channel without considering multiplexing techniques is at 90 MHz and 256-QAM, where the error vector magnitude (EVM) limit is the lowest i.e., 4.5 %.

3.2. *Chromatic dispersion-induced fading*

At first, we investigate the systems with only the SMF link (5 to 30 km) for (*i*) Setup A with no EDFA and an optical output power level of 7 dBm; and (ii) Setup B with EDFA, which is used to

Optics EXPRESS

compensate optical losses due to MZMs for the sake of comparison with Setup A. The EDFA output power is also 7 dBm and is placed behind the MZM2. Figure 4 depicts the EVM plots as a function of the SMF length for 400 MHz bandwidth quadrature phase shift keying (QPSK) and 200 and 400 MHz bandwidth 64-QAM signals for both setups at 27 GHz. The EVM limits of 9 and 18.5 % for QPSK and QAM, respectively, that are defined by 3GPP [20], are also shown in Fig. 4. For Setup A with optical DSB modulation format and with no filtering, we observe that the EVM limits are not met at fiber lengths of 5, 15 and 25 km, because of the chromatic dispersion, see marked measured points in Fig. 4.

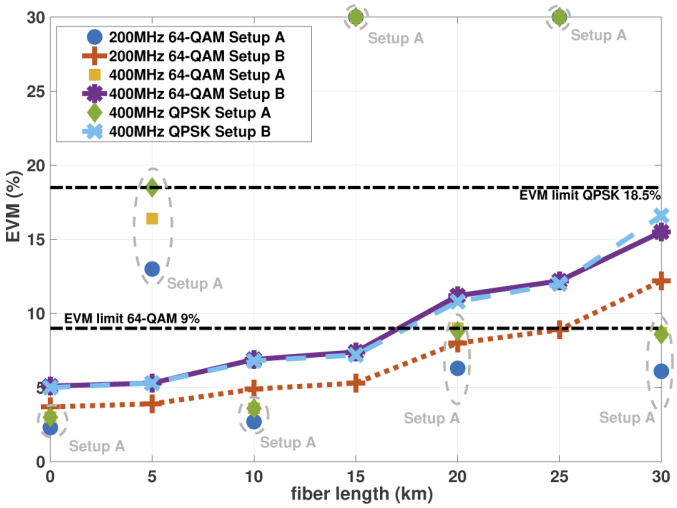

Fig. 4. The EVM versus SMF length for Setups A and B using QPSK and QAM with different bandwidth at 27 GHz.

The received optical power is the same for both Setups A and B. Considering an ideal intensity-modulated analog optical link, the RF signal transmission as a function of frequency will be constant. However, the transmission of the DSB signal evinces a substantial power drop in the RF spectrum due to the chromatic dispersion-induced fading. At the frequencies where RF response vanishes, intensity modulation of light is fully converted to the optical phase modulation, i.e., the optical intensity becomes constant, thus giving rise to no measurable RF response at the PD [6]. Setup B with the suppressed carrier displays maximal transmission link spans of (*i*) 17 and 25 km for 400 and 200 MHz 64-QAM, respectively for the EVM limits of 9%; and (*ii*) > 30 km for 400 MHz QPSK for the EVM limit of 18.5%.

The comparison of the RF frequency responses over a MPL with optical DSB and CS-DSB schemes, i.e. Setups A and B, respectively, for back to back (B2B) and different SMF lengths is shown in Fig. 5. For Setup B, the power transmission plots display a gradual decrease in the magnitude with the increasing SMF length, which follows the B2B plot, in contrast with Setup A, where a number of dips can be seen in the spectrum, which depends on the SMF lengths.

Considering the phase shift between both sidebands, the RF transmitted power corresponds to [23]:

$$P_{RF} \approx cos^2\left(\frac{\pi L D \lambda_0^2 f_{RF}^2}{c}\right) \tag{1}$$

where c is the light speed, L is the length of the fiber, D is the chromatic dispersion coefficient, λ_0 is the central optical wavelength and f_{RF} is the electrical frequency. Note, for the DSB schemes the chromatic dispersion induced power fading can be compensated, for example, by using a filter

Optics EXPRESS

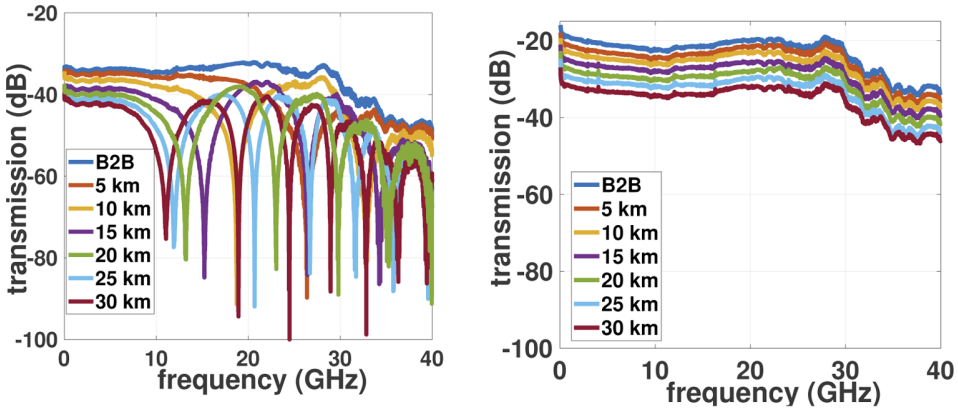

Fig. 5. The RF signal transmission response for different SMF lengths in: (a) Setup A, and (b) Setup B.

[24] to introduce optical single sideband transmission or by simultaneous intensity and phase modulation [25], but at the cost of increased complexity of the system.

3.3. *Full optical channel configuration with no AT*

Here, we consider both setups with a full configuration consisting of 10 km SMF and 4 m FSO link, as depicted in Fig. 1(b). Figure 6 shows the measured EVM values as a function of the data throughput at frequencies of 3.5, 27 and 39 GHz for Setup A and at 27 and 39 GHz for Setup B for QPSK and 64-QAM with the bandwidth range from 50 to 400 MHz. For Setup A, the EVM values are well below the limits for all cases at 3.5, 27 and 39 GHz, except for 400 MHz 64-QAM (highest data throughput of 1.4 Gb/s) at 39 GHz, which does not satisfy the 9 % threshold level. The same pattern is also observed in Setup B in Fig. 6(b), where all EVM values are below the limits except for 400 MHz 64-QAM at 39 GHz. It is worth to mention that for both 27 and 39 GHz tests, an optical Rx having lower frequency response at 39 GHz, compared to 27 GHz, was chosen.

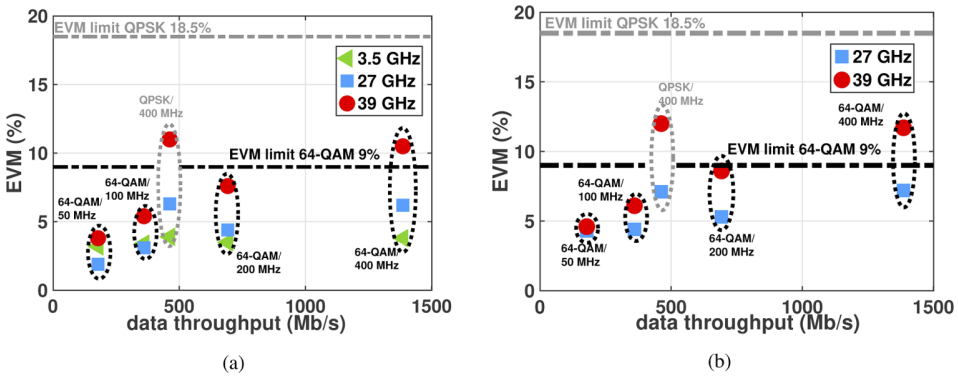

Fig. 6. Measured EVM after transmission over 10 km SMF and 4 m FSO optical channel for different signals and data throughput in: (a) Setup A, and (b) Setup B.

Presented results offer a better insight to the transmission capacity of fronthaul networks employing different MPL of SMF and FSO in comparison with digital fronthaul interface.

Optics EXPRESS

In another perspective, an appropriate modulation scheme and the signal bandwidth can be adopted to meet the data throughput requirement in 5G hybrid fronthaul links. Given that, 5G communication uses orthogonal frequency division multiplexing with the subcarrier spacing in the range of 15 to 120 kHz [26], the signal integrity in terms of the phase noise is critical. Characterizing and improving the phase noise performance of optically generated RF carrier signal is important for practical applications. Additive phase noise is the key parameter for accurately characterizing the phase noise due to the optical components [27,28]. Here, we show the phase noise performance for both microwave photonics setups, which are measured at the same frequencies and are illustrated in Table 3.

Table 3. Measured phase noise magnitudes for Setups A and B for the system with both SMF and FSO channels.

	Setup A			Setup B	
Frequency offset	@3.5 GHz (dBc/Hz)	@27 GHz (dBc/Hz)	@39 GHz (dBc/Hz)	@27 GHz (dBc/Hz)	@39 GHz (dBc/Hz)
1 kHz	-107	-108	-103	-99	-96
10 kHz	-102	-105	-109	-102	-100
100 kHz	-126	-118	-118	-110	-108
1 MHz	-136	-128	-127	-120	-121
10 MHz	-141	-132	-134	-132	-135

Note that, at the low frequency offset of 1 kHz Setup A offers improved phase noise by 7 to 10 dB compared with Setup B, whereas at the high frequency offset of 10 MHz, the phase noise levels are comparable in both cases. Figure 7 depicts the phase noise against the frequency offset for the optical channel composed of 10 km SMF and 4 m FSO at frequencies of 3.5, 27 and 39 GHz in Setup A and 27 and 39 GHz in Setup B, and also shows the results obtained for a B2B link for both setups. Note that, the performance varies with the carrier frequency significantly in Setup A, especially for the frequency offset < 1 MHz, while Setup B exhibits a minimal difference between 27 and 39 GHz over the given frequency offset and almost identical performance to that of B2B and the full channel compared with Setup A.

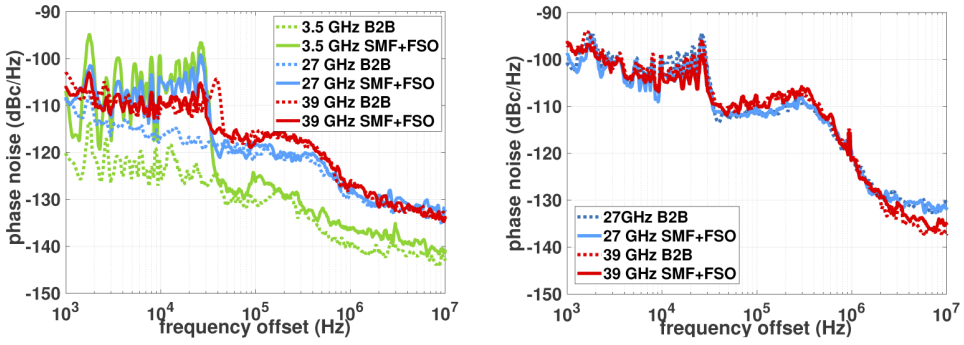

(a) (b)

Fig. 7. The phase noise performance for Setups: (a) A, and (b) B for 10 km SMF and 4 m FSO optical channel at different frequencies.

Next, we have investigated the EVM as a function of SNR for both setups at 27 GHz, as illustrated in Fig. 8. To measure the SNR, a combination of an electrical attenuator at the input stage and a signal analyzer at the Rx was adopted. Following the 5G NR standard, we evaluated 90 MHz bandwidth using 256-QAM, and 400 MHz bandwidth using QPSK and 64-QAM. As

Optics EXPRESS

expected, the EVM results for QPSK and 64-QAM show similar trends in both setups, since they have identical bandwidth of 400 MHz, however, each is subject to a different EVM limit. The highest required SNR is observed for 256-QAM. This is because the bandwidth is only 90 MHz comparing to 400 MHz for a fixed RF input power, i.e., 7 dBm, resulting in the highest power spectral density compared to the 400 MHz bandwidth. The 256-QAM transmission in Setup A offers improved performance in terms of the gain in the maximum SNR by 6 dB, and lower EVM by 2% compared with Setup B. In Setup A, the lowest EVM values of 1.3 and 2.1 % at the SNR of 35 dB are observed for 256-QAM/QPSK, and 64-QAM, respectively. In Setup B, the lowest EVM values are achieved at SNR of 28 and 35 dB for 64-QAM/QPSK, and 256-QAM, respectively. Thus in both setups, 256-QAM with 90 MHz bandwidth offers the best performance in terms of EVM, which is confirmed by the constellations shown for the selected SNR values.

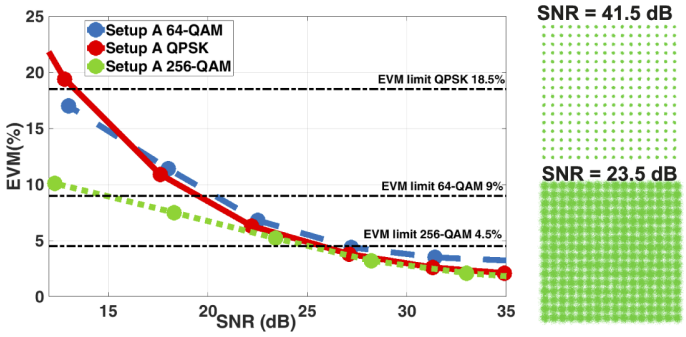

(a)

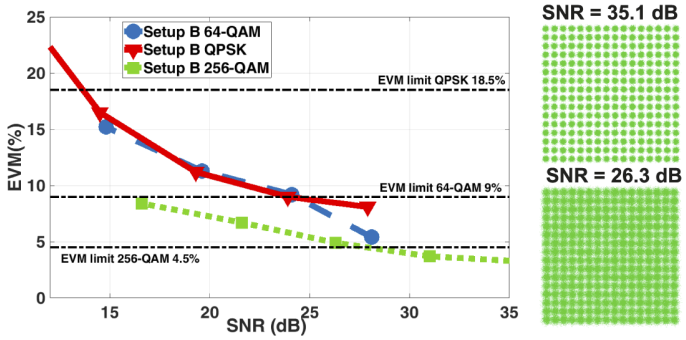

(b)

Fig. 8. EVM versus the SNR at 27 GHz for: (a) Setup A, and (b) Setup B. Inset are the constellations for 256-QAM at maximum SNR values and behind the edge of the EVM limit.

3.4. Full optical channel configuration with AT

As stated in the introduction, the FSO channel is affected by the atmospheric conditions including AT, which can lead to significant fluctuations of both amplitude and phase of the optical signal and thus leading to performance deterioration [29]. In this work, we have emulated a turbulent channel using an indoor atmospheric chamber. For this purpose, we have used (*i*) 20 temperature sensors, spaced 20 cm apart, which were placed within the chamber along the optical propagation path; (*ii*) two fan heaters blowing hot air perpendicular to the optical beam to generate a thermal gradient; and accordingly, the AT strength is calculated by using the equations given in [17]. To investigate the impact of different AT levels (i.e., scintillation index, which is proportional to

Optics EXPRESS

Rytov variance σ_R^2) on the hybrid link in a 5G fronthaul optical network, we have used weak (T0) and strong (T1) AT regimes defined by the refractive index structure parameter C_n^2 of 5.54×10^{-14} $m^{-2/3}$($\sigma_R^2 = 8.78\times10^{-6}$) and 1.15×10^{-11} $m^{-2/3}$ ($\sigma_R^2 = 1.83\times10^{-3}$), respectively. Note that, these values can be recalculated through σ_R^2 [10] for longer transmission spans maintaining the overall scintillation effect. For example, if we consider common FSO distances of 100 and 500 m in urban areas, then we have the turbulence levels of T0 with C_n^2 of 1.52×10^{-16} and 7.93×10^{-18} $m^{-2/3}$ and T1 with 3.14×10^{14} and 1.65×10^{-15} $m^{-2/3}$, respectively. The QPSK and 64-QAM signals with the 400 MHz bandwidth at 27 GHz were transmitted to compare the EVM performance under turbulence conditions as a function of SNR in both setups, see Fig. 9.

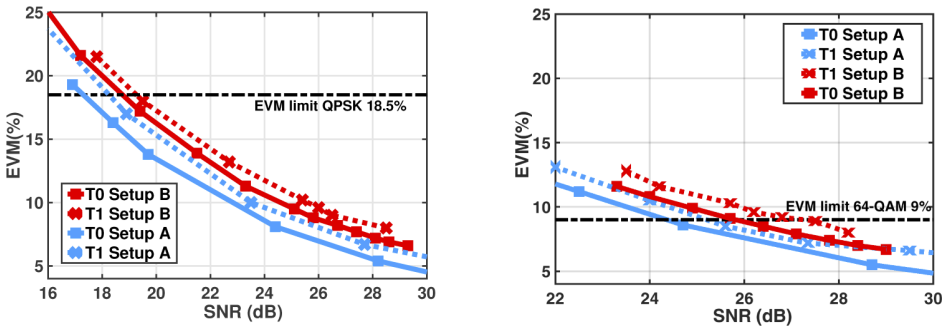

(a) (b)

Fig. 9. EVM against SNR for Setups A (blue) and B (red) at 27 GHz with a 400 MHz of bandwidth for weak and strong AT regimes for: (a) QPSK, and (b) 64-QAM.

Note, the optical loss along the links was adjusted by using VOA. Once again, we observe that Setup A offered the highest SNR of 36 dB (not shown in Fig. 9 due to the limited x-axis scale) for both modulation schemes, and lower average EVM by 3 and 1% for QPSK and 64-QAM, respectively, compared with Setup B. Under AT and for a given SNR, the average EVM increased by 2 and 1% for QPSK and 64-QAM, respectively. In any case, we have shown that EVM values are below the EVM thresholds for both setups and modulation formats even under the strong AT regime. Figure 10 depicts the electrical power spectra for Setup A with 400 MHz 64-QAM for T0 and T1. Note, the in-band power variation of $\pm2-3$ dB around the average electrical received power value of -77 dBm for the case with T1 (orange curve) compared to T0 (grey curve), which is highly stable, i.e., flatter. The similar power variation in electrical spectrum under turbulence conditions in FSO channel has been observed e.g., in [17].

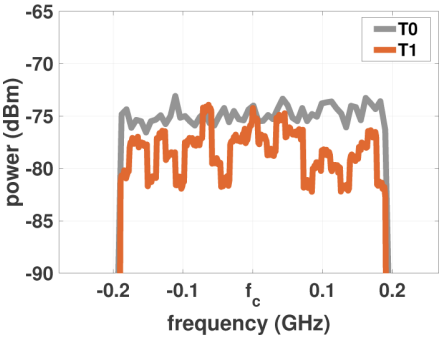

Fig. 10. Electrical spectra for Setup A with 400 MHz/64-QAM for T0 and T1.

Optics EXPRESS

Finally, we investigate the impact of AT on the EVM performance of both setups at 39 GHz for QPSK with the 400 MHz bandwidth. As depicted in Fig. 11, EVM shows a linear trend with reduced SNR for all cases and marginal difference between T0 and T1 compared with the case at 27 GHz. At the EVM limit of 18.5 %, the SNR penalties are within the range of 0.2-0.5 dB with the highest and lowest observed between T0 and T1 for Setups A and B, respectively. In particular, Setup B evinces very comparable EVM dependence on SNR for both low and strong turbulence regimes at 39 GHz. However, under strong turbulence conditions, there is about 1 dB lower maximal achieved SNR.

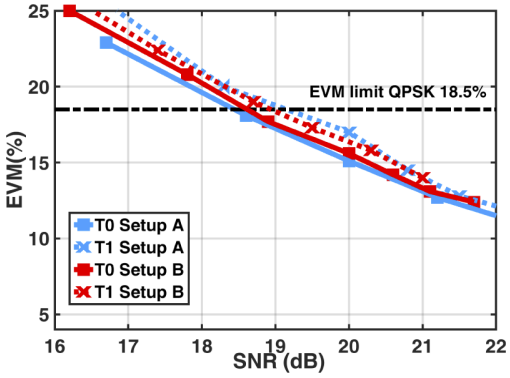

Fig. 11. EVM against SNR for Setups A (blue) and B (red) at 39 GHz with 400 MHz QPSK for T0 and T1 turbulence regimes.

3.5. Discussion and implementation

Two selected MPL systems' performances have been evaluated for the mobile fronthaul network application. In addition to the results shown along the paper, requirements and problems of RF antenna seamless transmission following optical-to-electrical conversion at the PD have to be taken into account for proper discussion.

The insignificant difference in the EVM performance between both setups under AT at 39 GHz highlights the advantage of Setup B with doubling of the original frequency (i.e., 18.5 GHz with 2 GHz of IF), and high frequency mmW signal transmission with the reduced phase noise. In other words, even though Setup B has some limitation, as discussed above, it shows a good performance for higher frequencies with the benefit of reduced requirements for RF equipment and less sensitivity to the chromatic dispersion-induced fading. The latter is crucial in systems with the DSB schemes at high frequencies employing long SMF, i.e., over 5 km, section. However, in Setup B using the carrier suppressed mode, there is a need for higher carrier suppression ratio (i.e., at least 20 dB) with sufficient optical and RF power levels to generate a strong electrical carrier at twice the original frequency. Moreover, the optical carrier is never completely suppressed. Also, the MZM2 is fed by the useful data signal with the IF offset, whose power is split (*i*) dominantly to DSB modulation at the new frequency; and (*ii*) then partially to DSB modulation at the residual original electrical frequency and a minimum to a frequency equal to the IF offset originated from the residual of the optical carrier. As a result, following optical transmission and the beating of the sidebands at the PD, a RF signal with a very strong carrier signal and two less powerful sidebands at the desired frequencies are generated. To transmit the signal via the free space path using the antenna relay, the signal needs to be amplified using at least a single RF amplifier on both the Tx and the Rx. However, by doing so the amplifier (or other active RF devices) may be overloaded by too strong carrier signal and the cost of lower power level for the data signal. Consequently, the data signal bandwidth, comparing to the RF

Optics EXPRESS

carrier, is not sufficiently amplified for antenna transmission and thus leading to lower SNR and worse EVM performance. This is more critical when large bandwidth signals are employed. Here, we bring part of our tests carried out along the experimental scenario, which have not been shown yet in the paper.

For example, in Setup B for the optical B2B configuration with an additional 3.5 m long RF link (antennas RFspin DRH40 with a gain of 15 dBi at 27 GHz) with two electrical amplifiers (Miteq AMF-4F-260400-40-10p), the measured received electrical power was about -33 dBm for 64-QAM with the 100 MHz bandwidth. The same amount of power was however assigned also for the 200 and 400 MHz bandwidth resulting in lower power spectral densities of 3 and 6 dB, respectively, which cannot be effectively compensated by amplification from the aforementioned reasons related with too strong RF carrier. More specifically, for the 400 MHz 64-QAM B2B link with no SMF and FSO links, the measured EVM following mentioned antenna transmission was 5.1%, which is below the EVM limit of 9%. However, increasing the optical path loss to 4 dB (e.g., corresponding to the loss of 20 km of SMF) by using the VOA, the received RF power is decreased by 8 dB with the EVM value of 10.6%, which is already above the EVM limit. This is adverse especially for higher bandwidth, i.e., $\geq$ 200 MHz, in contrast to much lower narrower bandwidth, i.e., 20 MHz, which can operate over relatively long free space path with much lower EVM as was demonstrated in [30]. This issue can, for example, be avoided using filtering to transform the spectrum to the electrical single side-band with the suppressed carrier signal. Note that, biasing MZM at its null transmission point results also in higher optical loss, which requires the use of EDFA in Setup B at the increased noise level and high costs. It has been verified that, the optimal optical power level at receiver for this configuration is at least 3 dBm to ensure the 64-QAM EVM limit with 400 MHz bandwidth. Note that, by including the mmW wireless link, the optical power requirement would be even higher. The optical channel (i.e., 4 m FSO and 10 km SMF) exhibits a loss of about 8.5 dB, and the two-MZM cascade introduces an additional loss of 18 dB. Therefore, without EDFA, the transmit power needs to get higher by at least 13.5 dB to main the link performance (i.e., the laser output power is 16 dBm). This can be achieved by using higher power lasers, but in risk of high power handling, or by adopting phase modulation (i.e., external modulation of the light signal) instead of intensity modulator to minimize the MZM loss. Nevertheless, Setup B (*i*) the CS-DSB scheme is immune to the chromatic dispersion-induced fading; (*ii*) offers improved stability under strong AT; (*iii*) maintains the same phase noise magnitudes across the frequency range; and (*iv*) significantly reduces requirements for the high frequency equipment, i.e., optical modulator and RF generators, thus reduces costs. Therefore, MZM at 18.5 GHz could be used instead of MZM at 39 GHz. Note, the same also applies to the both active and passive RF devices at the transmitter side.

On the other hand, Setup A, using a classic analog approach with a single MZM biased in the linear point with DD, represents a simple and universal solution for seamless RF signal transmission, i.e., 5G, over a fronthaul network even for high frequency mmW signals. Moreover, Setup A exhibits a 9 dB lower loss, comparing to Setup B, which implies the potential implementation of it without the need for EDFA under certain conditions. However, the drawbacks are the need to eliminate the chromatic-induced fading and the use of high frequency components. To conclude, both systems are applicable as an effective approach in 5G C-RAN each with its advantages and disadvantages as discussed above.

4. Conclusion

The experimental comparison of two MPL approaches for the 5G fronthaul network based on SMF and FSO links to transmit the 5G NR signal in different frequency bands was presented. We evaluated the performance of two setups using a conventional DSB analog MPL approach with an externally modulated laser and a CS DSB scheme to double the input carrier frequency, respectively, considering the data throughput, fiber chromatic dispersion, phase noise, SNR and

Optics EXPRESS

AT. We showed that, the CS DSB approach offered immunity to chromatic dispersion-induced fading for the frequency range up to 40 GHz and a SMF length of 30 km. We evinced no significant difference in the performance at 27 and 39 GHz thus making it as an attractive solution for higher frequency bands. Moreover, the CS-DSB scheme can be implemented with frequency n-multiplication to further relax the bandwidth requirements. Contrary, although the conventional DSB analog MPL approach is highly sensitive to dispersion-induced fading and requires higher bandwidth, it offers improved EVM performance since MZM is biased at the quadrature point instead of the null point as in CS DSB, higher SNR, lower phase noise, and reduced complexity. In addition, it was shown seamless deployment of antennas is another important issue, which needs to be considered especially in links with a large bandwidth ($\geq$ 200 MHz). To conclude, we showed that both approaches can operate at 27 and 39 GHz with the bandwidth up to 400 MHz even under the strong turbulence regime. Based on the measured results and validated by the analytical data, the EVM performance fulfilling the limit was achieved for the 500 m long outdoor FSO link under a moderate turbulence level (i.e., $C_n^2 = 1.65 \times 10^{-15}$ m$^{-2/3}$). The highest achieved data throughput was 1.4 Gb/s, which is sufficient for the chosen unlicensed single band. Finally, we proved that up to 256-QAM could be used in the proposed scheme with the hybrid SMF and FSO fronthaul network.

Funding. European Cooperation in Science and Technology (CA19111); Ministerstvo Průmyslu a Obchodu (FV40089); České Vysoké Učení Technické v Praze (SGS20/166/OHK3/3T/13).

Disclosures. The authors declare no conflicts of interest.

Data availability. Data underlying the results presented in this paper are not publicly available at this time but may be obtained from the authors upon reasonable request.

References

1. D. He, W. Wang, Y. Xu, X. Huang, H. Cheng, X. Duan, Y. Huang, H. Hong, Y. Zhang, and W. Zhang, "Overview of physical layer enhancement for 5G broadcast in release 16," IEEE Trans. Broadcast. **66**(2), 471–480 (2020).
2. CISCO, "Cisco Annual Internet Report (2018–2023) White paper," https://www.cisco.com/c/en/us/solutions/collateral/executive-perspectives/annual-internet-report/white-paper-c11-741490.html.
3. G. Gampala and C. J. Reddy, "Design of millimeter wave antenna arrays for 5G cellular applications using FEKO," in *2016 IEEE/ACES International Conference on Wireless Information Technology and Systems (ICWITS) and Applied Computational Electromagnetics (ACES)*, (2016), pp. 1–2.
4. T. R. Raddo, S. Rommel, B. Cimoli, and I. T. Monroy, "The optical fiber and mmwave wireless convergence for 5G fronthaul networks," in *2019 IEEE 2nd 5G World Forum (5GWF)*, (2019), pp. 607–612.
5. P. T. Dat, A. Kanno, N. Yamamoto, and T. Kawanishi, "Seamless convergence of fiber and wireless systems for 5G and beyond networks," J. Lightwave Technol. **37**(2), 592–605 (2019).
6. V. Urick, K. Williams, and J. McKinney, *Fundamentals of Microwave Photonics*, Wiley Series in Microwave and Optical Engineering (Wiley, 2015).
7. S. Rommel, D. Dodane, E. Grivas, B. Cimoli, J. Bourderionnet, G. Feugnet, A. Morales, E. Pikasis, C. Roeloffzen, P. van Dijk, M. Katsikis, K. Ntontin, D. Kritharidis, I. Spaleniak, P. Mitchell, M. Dubov, J. B. Carvalho, and I. Tafur Monroy, "Towards a scaleable 5G fronthaul: Analog radio-over-fiber and space division multiplexing," J. Lightwave Technol. **38**(19), 5412–5422 (2020).
8. D. Novak, R. B. Waterhouse, A. Nirmalathas, C. Lim, P. A. Gamage, T. R. Clark, M. L. Dennis, and J. A. Nanzer, "Radio-over-fiber technologies for emerging wireless systems," IEEE J. Quantum Electron. **52**(1), 1–11 (2016).
9. J. Bohata, M. Komanec, J. Spáčil, Z. Ghassemlooy, S. Zvánovec, and R. Slavík, "24-26 GHz radio-over-fiber and free-space optics for fifth-generation systems," Opt. Lett. **43**(5), 1035–1038 (2018).
10. L. Andrews and R. Phillips, *Laser Beam Propagation Through Random Media*, Online access with subscription: SPIE Digital Library (Society of Photo Optical, 2005).
11. N. A. M. Nor, Z. Ghassemlooy, J. Bohata, P. Saxena, M. Komanec, S. Zvanovec, M. R. Bhatnagar, and M.-A. Khalighi, "Experimental investigation of all-optical relay-assisted 10 Gb/s FSO link over the atmospheric turbulence channel," J. Lightwave Technol. **35**(1), 45–53 (2017).
12. J. Bohata, M. Komanec, J. Spacil, R. Slavik, and S. Zvanovec, "Transmitters for combined radio over a fiber and outdoor millimeter-wave system at 25 GHz," IEEE Photonics J. **12**(3), 1–14 (2020).
13. L. Vallejo, B. Ortega, J. Bohata, S. Zvanovec, and V. Almenar, "Photonic multiple millimeter wave signal generation and distribution over reconfigurable hybrid SSMF/FSO links," Opt. Fiber Technol. **54**, 102085 (2020).
14. H. Zhang, L. Cai, S. Xie, K. Zhang, X. Wu, and Z. Dong, "A novel radio-over-fiber system based on carrier suppressed frequency eightfold millimeter wave generation," IEEE Photonics J. **9**(5), 1–6 (2017).

Optics EXPRESS

15. K. Kanta, A. Pagano, E. Ruggeri, M. Agus, I. Stratakos, R. Mercinelli, C. Vagionas, P. Toumasis, G. Kalfas, G. Giannoulis, A. Miliou, G. Lentaris, D. Apostolopoulos, N. Pleros, D. Soudris, and H. Avramopoulos, "Analog fiber-wireless downlink transmission of IFoF/mmWave over in-field deployed legacy pon infrastructure for 5G fronthauling," J. Opt. Commun. Netw. **12**(10), D57–D65 (2020).
16. C. H. d. S. Lopes, E. S. Lima, L. A. M. Pereira, R. M. Borges, A. C. Ferreira, M. Abreu, W. D. Dias, D. H. Spadoti, L. L. Mendes, and A. C. S. Junior, "Non-standalone 5G NR fiber-wireless system using FSO and fiber-optics fronthauls," J. Lightwave Technol. **39**(2), 406–417 (2021).
17. L. Vallejo, M. Komanec, B. Ortega, J. Bohata, D.-N. Nguyen, S. Zvanovec, and V. Almenar, "Impact of thermal-induced turbulent distribution along FSO link on transmission of photonically generated mmw signals in the frequency range 26–40 GHz," IEEE Photonics J. **12**(1), 1–9 (2020).
18. D.-N. Nguyen, J. Bohata, J. Spacil, D. Dousek, M. Komanec, S. Zvanovec, Z. Ghassemlooy, and B. Ortega, "M-QAM transmission over hybrid microwave photonic links at the K-band," Opt. Express **27**(23), 33745–33756 (2019).
19. D.-N. Nguyen, J. Bohata, M. Komanec, S. Zvanovec, B. Ortega, and Z. Ghassemlooy, "Seamless 25 GHz transmission of LTE 4/16/64-QAM signals over hybrid SMF/FSO and wireless link," J. Lightwave Technol. **37**(24), 6040–6047 (2019).
20. ETSI, "5G release description, release 15," ETSI, TS 138 141-1 v15.0.0 (2019).
21. A. Tikhomirov, E. Omelyanchuk, and A. Semenova, "Recommended 5G frequency bands evaluation," in *2018 Systems of Signals Generating and Processing in the Field of on Board Communications*, (2018), pp. 1–5.
22. M. Sung, S.-H. Cho, J. Kim, J. K. Lee, J. H. Lee, and H. S. Chung, "Demonstration of IFoF-based mobile fronthaul in 5G prototype with 28-GHz millimeter wave," J. Lightwave Technol. **36**(2), 601–609 (2018).
23. M. Oishi, Y. Nishikawa, S. Akiba, J. Hirokawa, and M. Ando, "2-dimensional beam steering by 2 × 3 photonic antenna using millimeter-wave radio over fiber," in *2013 IEEE International Topical Meeting on Microwave Photonics (MWP)*, (2013), pp. 130–133.
24. T. Bakhvalova, M. Belkin, M. Kamalian-kopae, and S. Turitsyn, "Correcting the chromatic dispersion of a fronthaul fiber link in millimeter-wave radio -over-fiber networks," in *27th Telecommunications Forum, TELFOR 2019*, (IEEE, United States, 2020), pp. 1–4. 2019 27th Telecommunications Forum (TELFOR) ; Conference date: 26-11-2019 Through 27-11-2019.
25. Y. Cui, K. Xu, J. Dai, X. Sun, Y. Dai, Y. Ji, and J. Lin, "Overcoming chromatic-dispersion-induced power fading in ROF links employing parallel modulators," IEEE Photonics Technol. Lett. **24**(14), 1173–1175 (2012).
26. P. K. Yadav, V. K. Dwivedi, B. T. Maharaj, V. Karwal, and J. P. Gupta, "Performance enhancement of 5G OFDM systems using modified raised cosine power pulse," Wirel. Pers. Commun. **106**(4), 2375–2386 (2019).
27. W. Li and J. Yao, "Investigation of photonically assisted microwave frequency multiplication based on external modulation," IEEE Trans. Microwave Theory Tech. **58**(11), 3259–3268 (2010).
28. J. Yao, "Microwave photonics," J. Lightwave Technol. **27**(3), 314–335 (2009).
29. J. Libich and S. Zvanovec, "Influences of turbulences in near vicinity of buildings on free-space optical links," IET Microw. Antennas Propag. **5**(9), 1039–1044 (2011).
30. J. Bohata, J. Spacil, D.-N. Nguyen, S. Zvanovec, L. Vallejo, and B. Ortega, "Radio over 50 km fiber and joint 80 m FSO/wireless links using photonic frequency doubling for 5G," in *2019 IEEE Global Communications Conference (GLOBECOM)*, (2019), pp. 1–6.

Optics Letters

24–26 GHz radio-over-fiber and free-space optics for fifth-generation systems

Jan Bohata,[1,*] Matěj Komanec,[1] Jan Spáčil,[1] Zabih Ghassemlooy,[2] Stanislav Zvánovec,[1] and Radan Slavík[3]

[1]Czech Technical University in Prague, Faculty of Electrical Engineering, Technicka 2, 166 27 Prague, Czech Republic
[2]Optical Communications Research Group, Northumbria University, Newcastle-upon-Tyne NE1 8ST, UK
[3]Optoelectronics Research Centre, University of Southampton, Southampton SO17 1BJ, UK
*Corresponding author: bohatja2@fel.cvut.cz

Received 21 November 2017; revised 15 January 2018; accepted 18 January 2018; posted 24 January 2018 (Doc. ID 314050); published 22 February 2018

This Letter outlines radio-over-fiber combined with radio-over-free-space optics (RoFSO) and radio frequency free-space transmission, which is of particular relevance for fifth-generation networks. Here, the frequency band of 24–26 GHz is adopted to demonstrate a low-cost, compact, and high-energy-efficient solution based on the direct intensity modulation and direct detection scheme. For our proof-of-concept demonstration, we use 64 quadrature amplitude modulation with a 100 MHz bandwidth. We assess the link performance by exposing the RoFSO section to atmospheric turbulence conditions. Further, we show that the measured minimum error vector magnitude (EVM) is 4.7% and also verify that the proposed system with the free-space-optics link span of 100 m under strong turbulence can deliver an acceptable EVM of <9% with signal-to-noise ratio levels of 22 dB and 10 dB with and without turbulence, respectively.

OCIS codes: (060.2310) Fiber optics; (060.2605) Free-space optical communication; (010.7060) Turbulence.

https://doi.org/10.1364/OL.43.001035

In order to satisfy the demand for ever-increasing data rates in the mobile networks, the new millimeter wave band (20–30 GHz) has been selected by 5GPPP (Public Private Partnership) [1] to be used in the emerging fifth-generation (5G) mobile networks. The vision of the 5G network poses many challenges, as it plans to reach ultra-low latency of 1 ms, 10 Gbps maximal throughput, and cover more than 100 billion devices [2]. A typical architecture addressing these challenges is shown in Fig. 1. A central office services and coordinates a number of remote micro-, pico-, and femto-cells, which reduces both the energy consumption and costs [3]. For this architecture, and especially for the fronthaul network, novel fiber/optical wireless approaches are highly desirable.

The mentioned 20–30 GHz "pioneer" spectral band is the first to be used in mobile networks above 6 GHz, requiring a number of challenges to be addressed, including a significantly high attenuation (i.e., ∼3 dB/m) when the radio frequency (RF) signal is transmitted over metallic cables, which limits the transmission span. To address this, the radio-over-fiber (RoF) technology was proposed [4], e.g., for usage between a central office and the pico- or femto-cell base stations. In [5], an alternative concept of radio-over-free-space optics (FSO) (RoFSO) transmission was proposed for deployment in dense urban areas, where installation of new optical fiber cables is not cost effective. For example, transmission of the RF signal over a 1 km long RoFSO link was experimentally demonstrated at wavelength of 1550 nm in [6]. It was shown that RoF and RoFSO links offer the benefit of increased transmission span between the base station and the antenna while ensuring sufficient signal-to-noise ratio (SNR). In any case, the key advantage of the RoFSO links is deployment flexibility; however, their performance is affected by weather conditions (i.e., turbulence, fog, etc., [7]).

For RoF and RoFSO applications, both the directly modulated laser (DML) and externally modulated laser (EML) can be used [8]. In [9], an integrated fiber-wireless system using EML was demonstrated, employing coherent detection and adaptive

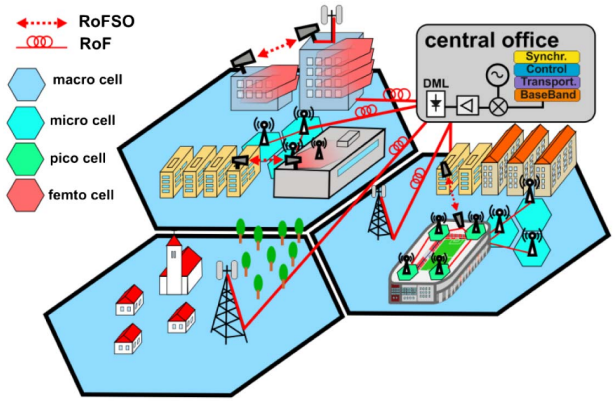

Fig. 1. RoF and RoFSO deployment for connection of micro-, pico-, and femto-cells in 5G architecture.

polarization-multiplexed quadrature-phase-shift-keying (PM-QPSK) modulation. The authors achieved an impressive 108 Gbps data rate over an 80 km of single-mode fiber (SMF) and over the 1 m long wireless link at a carrier frequency of 100 GHz. Although EML (as compared to DML) gives better performance (e.g., no modulation chirp), DML represents the simplest (and thus potentially the cheapest and most compact) option with additional benefits such as high transmitter power, high energy efficiency, and linear modulation characteristics (which is of particular importance in RoF systems [10]). Apart from the modulation chirp, DML typically does not allow for operation at frequencies above 20 GHz. In [11], a 1 Gbps RoF DML link at 24 GHz over a 50 km of SMF was demonstrated with help of an erbium-doped fiber amplifier (EDFA). Error vector magnitude (EVM) was, however, strongly frequency dependent and insufficiently high at 24 GHz, while EVM as low as 3.4% was achieved at the carrier frequency f_c of 3.5 GHz, it increased to 20% at 24 GHz.

In this Letter, we address the main challenge of DML RoF and RoFSO systems by means of the DML optimized to operate in the 5G-selected 20–30-GHz spectrum band. We present experimental results for the entire system composed of RoF, RoFSO, and free-space RF within the frequency range of 24–26 GHz. To the best of the authors' knowledge, this is the first experimental investigation of the proposed scheme, which includes three technologies of (i) the optical fiber, (ii) FSO link, and (iii) RF free-space link simultaneously, all in the spectrum band of 24–26 GHz. We have used 64 quadrature amplitude modulation (64-QAM), which potentially facilitates transmission of a net data rate of 10 Gbps (with 20% overhead) within the used spectrum band. In addition, we assess the impact of turbulence on the RoFSO section. The presented results demonstrate the full potential of the DML-based RoFSO, RoF, and their combination in the emerging 24–26 GHz band as part of the future 5G mobile networks, as shown Fig. 1.

The experimental setup is shown in Fig. 2. The long-term evolution advanced (LTE-A) baseband signal, composed of five 20 MHz bands of evolved universal terrestrial radio access (E-UTRA) test model 3.1 [12] with 64-QAM—the largest bandwidth of today's mobile network standard, is generated using a signal generator (R&S SMW200A). LTE-A is then up-converted to the 24–26 GHz band using a RF signal generator (R&S SMF100A) and a RF modulator, prior to being amplified (by Wisewave AGP- 33142325-01) to a level of 12 dBm. The amplified signal is then combined in a bias tee with a DC signal and sent to the DML, which is a monolithically integrated passive feedback laser described in detail in [13]. The DC current for biasing of the DML is provided by a laser diode controller (Newport modulator controller 8000).

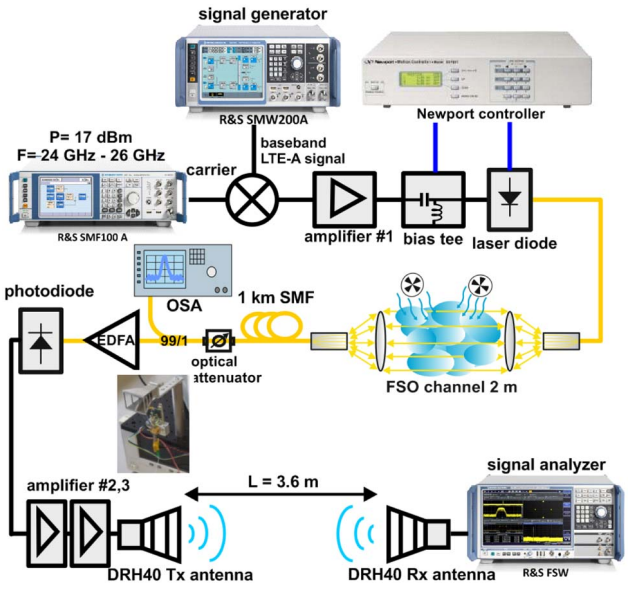

Fig. 2. Experimental setup consisting of RoF (1 km), RoFSO (2 m), and RF over free space (3.6 m).

The fiber-coupled laser output (with the average optical power of 4.8 dBm at the wavelength of 1549 nm) is launched into the free space via the combination of a short length SMF, graded-index (GRIN), and plano-convex lenses. Following propagation over a 2 m long free space (i.e., the FSO path), the optical beam is launched into a 1 km of SMF via a plano-convex and GRIN lenses. An optical spectrum analyzer is used for real-time monitoring of the data stream via a 99/1 tap coupler. An EDFA (Keopsys KPS-BT2-C-10-LN-SA, noise figure <5 dB) with a 15 dB gain (5 dBm of output power) is used prior to photodetection (Optilab PD-40 photodiode with the bandwidth of 40 GHz). The photodetected RF signal is passed through two-stage amplifiers #2,3 (Miteq AMF-4F-260400-40-10p, Analog devices HMC1131), amplifying it to the power of 4 dBm prior to transmission over a 3.6 m long free space using a double-ridged waveguide horn antenna (DRH40—RFspin, s.r.o.) with a 14 dBi gain at the frequency of 24 GHz. At the Rx, we have used the same type of antenna to capture the signal and analyze it using a signal analyzer (R&S FSW). The total loss of the RF free-space channel, including the gains of antennas, is 43.2 dB at 24 GHz. All the key system parameters are summarized in Table 1. First, we characterized the frequency response of the entire system, depicted in Fig. 2, using a vector network analyzer (R&S ZVA67). The spectral characteristic of the link loss, described by the S_{21} parameter, is shown in Fig. 3. As can be seen, the optimum frequency range (with loss below 35 dB) is around 23–27 GHz (inset in Fig. 3). In the proposed system, the most significant noise contributor is amplified spontaneous emission (ASE) signal from EDFA detected at the photodiode. The non-flat response of S_{21} in Fig. 3 is due to the combined effect of laser modulation, antenna transmission/reception, and photodiode properties—all of them having ripples in their spectral characteristics. The measured EVM, with the 64-QAM LTE-A signal for carrier frequencies of 24 GHz, 25 GHz, and 26 GHz, and with no turbulence, is shown in Fig. 4(a). Also shown is the

Table 1. Key System Parameters

Parameter	Value
Radio frequency	24–26 GHz
RF bandwidth	100 MHz
LTE test model	TM 3.1
RF output power	−15.3 dBm
Antenna distance	3.6 m
Wavelength	1549 nm
Laser power	4.79 dBm
FSO link length	2 m
FSO loss	12 dB

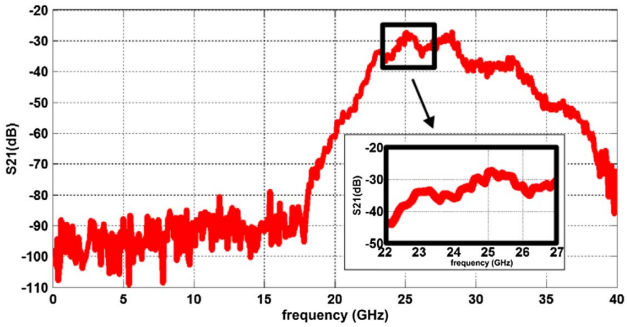

Fig. 3. Measured spectral characteristics of the entire link (RoF + FoFSO + RF over free space).

9% EVM limit (dotted black line) adopted in 3GPP [12]. Note that the 24 GHz displays the best EVM performance closely followed by 25 GHz although 25 GHz evinces better S_{21} performance in Fig. 3. This is because the adopted modulator has been designed and optimized for the 24 GHz band, and the optimization has no effect on S_{21} measurement. At 26 GHz, we observe the SNR penalty of 8 dB (for EVM = 9%) as compared to 24 GHz. At a moderate SNR of 20 dB, the EVM values for all three carrier frequencies are below the limit of 9%. Also shown are the constellation diagrams for 64-QAM at the SNR values of 10 dB and 27 dB for 24 GHz, illustrating the quality of signal transmission at higher SNR.

Next, we characterized the entire link performance by considering the impact of the atmospheric turbulence on the FSO path. Reproducible turbulence levels were achieved using two heating fans, which generated a varying thermal distribution along the optical propagation path, as described in [14]. The atmospheric turbulence-induced degradation on the received signal was characterized by using the commonly used refractive index structure parameter C_n^2 and Rytov variance, which are derived from the thermal distribution along the FSO path [5]. We carried out system measurements for up to a strong turbulence level (i.e., $C_n^2 = 2.4 \times 10^{-10}$ m$^{-2/3}$) for a 2 m long FSO link. Note that this high level of turbulence for a short FSO link can be recalculated using Rytov variance [7] to reflect the turbulence values, which can be observed in longer outdoor FSO links. Thus, $C_n^2 = 2.4 \times 10^{-10}$ m$^{-2/3}$ corresponds to the magnitudes of 1.8×10^{-13} m$^{-2/3}$, 9.5×10^{-15} m$^{-2/3}$, and 2.7×10^{-15} m$^{-2/3}$ for FSO link spans of 100 m, 500 m, and 1000 m, respectively, by maintaining the same level of signal variance. In further examples, we show the measured system performance recalculated for a 100 m long FSO link to better illustrate real outdoor conditions. It should be noted that the impact of increased attenuation in 100 m can be neglected when operating under clear weather conditions with high visibility, since signal attenuation is less than 0.05 dB when considering 10 km visibility. Figure 4(b) depicts the EVM performance for the complete system under strong turbulence $C_n^2 = 1.8 \times 10^{-13}$ m$^{-2/3}$ as a function of the SNR, which was measured at the output of the RF Rx antenna (i.e., using the signal analyzer). As shown, both 24 GHz and 25 GHz bands display similar EVM performance meeting the EVM limit of 9% at the SNR values of 22 dB and 25 dB, respectively, whereas the 26 GHz band exceeds the EVM profile above the EVM limit for the entire

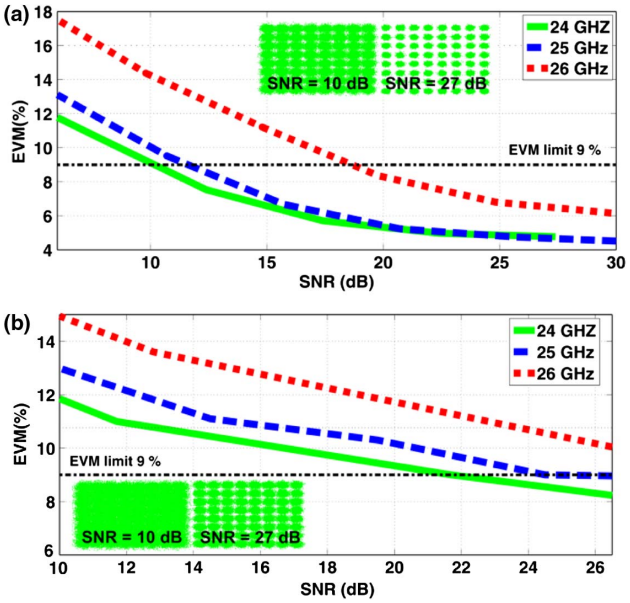

Fig. 4. Measured EVM for various SNRs and three carrier frequencies for the entire link with no turbulence (a) and strong turbulence corresponding to $C_n^2 = 1.8 \times 10^{-13}$ m$^{-2/3}$ for 100 m long link (b).

SNR range. Figure 5 further compares the EVM performance of the link with various strengths of turbulence (recalculated to a 100 m FSO outdoor link) at the frequency of 24 GHz. The EVM limit of 9% is achieved for all turbulence levels for the SNR range of 27–22 dB. However, for the strongest level of turbulence ($C_n^2 = 1.8 \times 10^{-13}$ m$^{-2/3}$), the SNR penalties are 10.0 dB, 9.0 dB, 8.5 dB, and 6.5 dB as compared to performance without any turbulence and turbulence corresponding to C_n^2 of 5.7×10^{-14} m$^{-2/3}$, 7.5×10^{-14} m$^{-2/3}$, and 1.2×10^{-13} m$^{-2/3}$, respectively. Next, we characterized the link tolerance to the optical attenuation (using the variable optical attenuator; see Fig. 2) to determine the maximum potential transmission span. Figure 6 illustrates the EVM as a function of the optical attenuation at 24 GHz for a range of C_n^2 values recalculated to the 100 m long FSO link. The results show that the proposed system can operate (EVM < 9%) in clear atmospheric conditions with up to a 15 dB of additional optical loss, which corresponds to an increased fiber link span

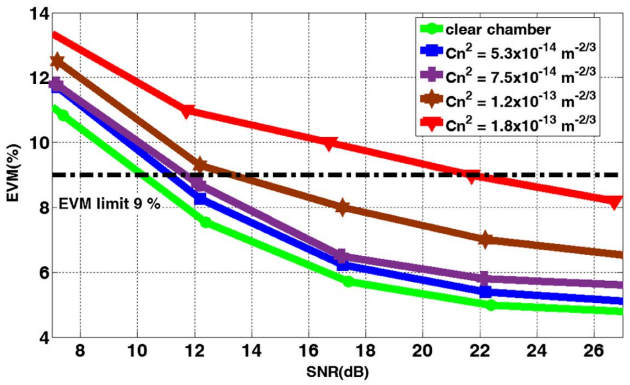

Fig. 5. Measured EVM for various SNRs and 24 GHz carrier frequency for the entire link with 100 m long FSO link.

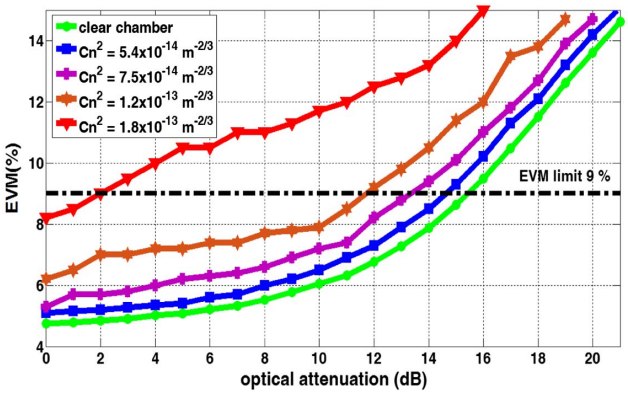

Fig. 6. Measured EVM as a function of the optical attenuation at 24 GHz for C_n^2 values corresponding to the 100 m FSO link.

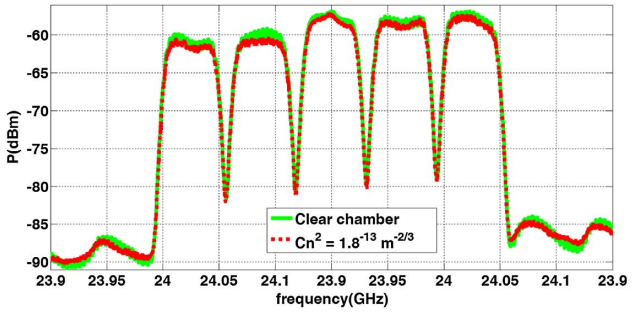

Fig. 7. LTE-A measured spectrum for the clear chamber (green) and with turbulence corresponding to the 100 m long FSO link (red).

by 60 km (neglecting the fiber dispersion) or, e.g., ∼2 km of FSO link span under moderate visibility conditions. In turbulence, we observe performance degradation due to the RoFSO link section. More specifically, the attenuation tolerance is reduced by 2.5 dB and 13.0 dB for the moderate (i.e., $C_n^2 = 7.5 \times 10^{-14}$ m$^{-2/3}$) and very strong (i.e., $C_n^2 = 1.8 \times 10^{-13}$ m$^{-2/3}$) turbulence regimes, respectively. Acceptable performance (EVM < 9%) is achieved up to the strong turbulence regime (i.e., $C_n^2 = 1.2 \times 10^{-13}$ m$^{-2/3}$) with a 4 dB of power penalty compared with the no turbulence scenario, which shows about 2% improvement in the EVM performance. We believe that both the RoF and RoFSO EVM performance can be further improved by including supplementary optical bandpass filters, which would suppress out-of-band noise (e.g., from the EDFA). As this would be at the cost of increased complexity, we have not used any filter in our system. Finally, we provide a comparison of the detected LTE-A spectra for the link with no turbulence and with strong turbulence in Fig. 7. Note that the decrease in the total RF power caused by turbulence is 0.4 dB. Moreover, the noise floor is increased by 1.4 dB, which results in 1.8 dB degradation of the SNR.

In this Letter, we experimentally investigated, to the best of our knowledge for the first time, the complete RoF and RoFSO mobile network scenario, including transmission of the RF signal and using a wideband DML at a carrier frequency band of 24–26 GHz. We showed that EVM as low as 4.7% can be reached at 24–25 GHz for the 100 MHz bandwidth with 64-QAM. Further, we verified that in a real outdoor scenario the proposed system is capable of operating over a 100 m long FSO link under strong turbulence conditions (and even for longer FSO links ∼500 m and 1000 m with reduced turbulence level) with the EVM level kept under the 9% limit. Moreover, we showed that the proposed system could cope with the additional 15 dB of optical loss, which allows for an additional link extension. Presented results therefore confirmed the feasibility of the new RoF and RoFSO system deployment, utilizing DML with broadband transmission and operating in the 24–26 GHz band for small mobile cells. We showed that the proposed scheme is capable of delivering higher data rates using the high-frequency band over longer transmission spans by means of optical transmission, thus illustrating its potential in 5G networks. The proposed scheme can be extended up to 10 Gbps using the explored spectrum bandwidth, which will be part of our future experimental investigations.

Funding. European Cooperation in Science and Technology (COST) (CA16220, MP1401); Ministry of Industry and Trade (FV30427); Engineering and Physical Sciences Research Council (EPSRC) (EP/P030181/1).

Acknowledgment. The data are accessible through the Soton Repository (DOI: 10.5258/SOTON/D0390).

REFERENCES

1. A. Gupta and R. K. Jha, IEEE Access **3**, 1206 (2015).
2. A. Checko, H. L. Christiansen, Y. Ying, L. Scolari, G. Kardaras, M. S. Berger, and L. Dittmannal, IEEE Commun. Surv. Tutorials **17**, 405 (2015).
3. "The 5 G infrastructure public private partnership," https://5g-ppp.eu/.
4. D. Pham Tien, A. Kanno, and T. Kawanishi, IEEE Wireless Commun. **22**, 67 (2015).
5. M. Uysal, C. Capsoni, Z. Ghassemlooy, A. Boucouvalas, and E. Udvary, *Optical Wireless Communications: An Emerging Technology* (Springer, 2016).
6. C. B. Naila, K. Wakamori, M. Matsumoto, A. Bekkali, and K. Tsukamoto, IEEE Commun. Mag. **50**(8), 137 (2012).
7. L. C. Andrews and R. L. Phillips, *Laser Beam Propagation through Random Media* (SPIE, 2005).
8. D. Wake, A. Nkansah, N. J. Gomes, G. de Valicourt, R. Brenot, M. Violas, L. Zhansheng, F. Ferreira, and S. Pato, J. Lightwave Technol. **28**, 2416 (2010).
9. X. Li, Z. Dong, J. Yu, N. Chi, Y. Shao, and G. K. Chang, Opt. Lett. **37**, 5106 (2012).
10. X. Zhang, R. Zhu, D. Shen, and T. Liu, Photonics **1**, 455 (2014).
11. K. V. Gasse, J. V. Kerrebrouck, A. Abbasi, G. Torfs, H. Chen, X. Yin, J. Bauwelinck, and G. Roelkens, *Microwave Photonics* (IEEE, 2016), p. 328.
12. "The 3rd generation partnership project," www.3gpp.org.
13. J. Kreissl, IEEE Photon. Technol. Lett. **24**, 362 (2012).
14. J. Bohata, S. Zvanovec, P. Pesek, T. Korinek, M. M. Abadi, and Z. Ghassemlooy, Appl. Opt. **55**, 2109 (2016).

IEEE Photonics Journal
An IEEE Photonics Society Publication

Open Access

Transmitters for Combined Radio Over a Fiber and Outdoor Millimeter-Wave System at 25 GHz

Volume 12, Number 3, June 2020

Jan Bohata, *Member, IEEE*
Matej Komanec
Jan Spacil
Radan Slavik, *Senior Member, IEEE*
Stanislav Zvanovec, *Senior Member, IEEE*

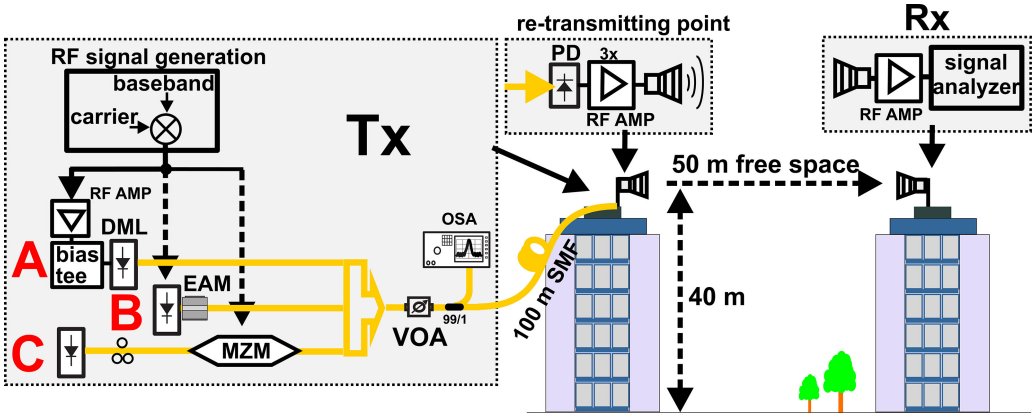

DOI: 10.1109/JPHOT.2020.2997976

Transmitters for Combined Radio Over a Fiber and Outdoor Millimeter-Wave System at 25 GHz

Jan Bohata,[1] ***Member, IEEE***, **Matej Komanec**,[1] **Jan Spacil**,[1]
Radan Slavik,[2] ***Senior Member, IEEE***,
and Stanislav Zvanovec,[1] ***Senior Member, IEEE***

[1]Department of Electromagnetic Field, Faculty of Electrical Engineering, Czech Technical University in Prague, 166 36 Prague, Czech Republic
[2]Optoelectronics Research Centre, Faculty of Engineering and Physical Sciences, University of Southampton, SO17 1BJ Southampton, UK

DOI:10.1109/JPHOT.2020.2997976

Manuscript received April 16, 2020; revised May 20, 2020; accepted May 24, 2020. Date of publication May 27, 2020; date of current version June 22, 2020. This work was supported in part by a project from the Ministry of Industry and Trade in the Czech Republic (FV30427) in part by Grant Agency of the CTU in Prague (SGS20/166/OHK3/3T/13), and in part by COST action CA 16220. Corresponding author: Jan Bohata (e-mail: bohatja2@fel.cvut.cz).

Abstract: In the modern wireless networks, millimeter-wave radio-frequency (RF) bands are becoming more attractive as they provide larger bandwidth and higher data rates than the today-used systems operating at frequencies below 6 GHz. In addition, according to the fact that coaxial cables exhibit extremely high attenuation for millimeter-wave RF signals, analog radio over fiber techniques (RoF) form a promising technology for delivering unaltered radio waveform to a remote antenna. This paper experimentally analyzes three types of RoF modulations, namely a directly modulated laser, an electro-absorption modulator, and a Mach-Zehnder Modulator. The primary focus is on the implementation of each RoF transmitter in an RoF system, such as those in 5G networks. The experimental study includes a detailed characterization of an RoF system with a 50-m long outdoor free-space RF channel operating in the frequency band of 25 GHz. Frequency response (S-parameters) and third-order nonlinear distortion are investigated in detail. Tests of EVM performance were conducted using an orthogonal frequency division multiplexing signal modulated with 16-quadrature amplitude modulation (16-QAM) with a long-term evolution signal. It is demonstrated that the transmitters studied can operate under a 13.5% EVM limit given for 16-QAM. Apart from the detailed system performance, the considerable power fluctuations in the 25 GHz free-space RF outdoor channel are reported.

Index Terms: Microwave photonics, optical fiber, millimeter wave, radio over fiber, optical modulator.

1. Introduction

Global data traffic in wireless networks is increasing exponentially, mainly due to video applications and high-resolution streaming, and it is expected that about 75% of the 69 Exabytes of total worldwide mobile data traffic will be used for video by 2022 [1]. This demand is driving the rapid evolution of wireless technology and incorporates higher frequency bands than those used today to offer significantly greater bandwidth, which is of particular importance for the 5th generation (5G) mobile networks. In addition to higher bandwidths, 5G networks need to deliver latency as low as

1 ms and data rates in the order of tens of Gb/s delivered to a high number of users, e.g., through highly directional beamforming [2].

High-frequency bands for 5G are mostly planned in the millimeter-wave (mm-wave) range of the electromagnetic spectrum. Due to the presence of atmospheric absorption across the mm-wave spectrum and a critical lack of available frequency bands, 24–28 GHz, 37–40 GHz and 64–71 GHz are the best candidates for 5G [2], in particular for smaller cells in cloud radio access network (C-RAN) architecture which tends to centralize the control of remote base stations. In C-RAN networks, radio over fiber (RoF) technology is very likely to be used for mm-wave transfers due to low attenuation and extremely large signal bandwidths [3], [4]. The usage of RoF system for mobile fronthaul networks can be digital or analog. However, especially for 5G networks, the analog RoF implementation helps in shifting of expensive analog-to-digital and digital-to-analog converters to the central office. [5] In the analog RoF approach with direct detection, a radio signal for wireless transmission is modulated onto an optical carrier, propagated via a standard single-mode optical fiber (SSMF) and directly detected by a photodiode keeping the radio frequency (RF) signal in original form, which is ready for antenna transmission. [6]. In this case, the distance between the RoF transmitter and receiver, e.g., for a remote antenna system, can be up to 50 km [7], [8]. Notwithstanding the long distance, RoF technology can operate for upper 5G mm-wave bands as was shown, for example, at 60 GHz for a 2.2-km long RoF link with a laboratory tested 4-m long free-space RF channel with leaky-wave antennas [9]. A comprehensive review of mm-wave frequency RoF systems was provided in [10].

As mentioned, an RoF transmission requires the RF signal to be first modulated on an optical carrier. The most established scheme for high-end RoF links is based on an external modulation performed in a lithium-niobate ($LiNbO_3$) based Mach-Zehnder Modulator (MZM), which is biased in quadrature bias point. Its advantages are large bandwidth ($>$40 GHz), negligible modulation chirp, low insertion loss (IL), low distortion, high power handling, and a relatively high extinction ratio (ER) [6]. Disadvantages include large size, high cost, low output optical power when operating in a linear area resulting in the need for a high power optical source, and low RF-to-optical modulation efficiency. However, the size of MZM can be reduced by integrating, as shown for example in [11]. Note that by using single drive MZM in the null transmission point, a carrier suppressed regime can be achieved, resulting in frequency doubling of the original RF signal after beating in a photodiode, as experimentally demonstrated in laboratory conditions [12], [13]. However, the operation in the null transmission point further reduces optical signal power due to high losses and second MZM needs to be used for data modulation.

The second option for external modulation is to use an electro-absorption modulator (EAM) capable of operating at high frequencies (up to 40 GHz). It is small in size and can be integrated with the laser source [14]. Its disadvantages include a slight modulation chirp, relatively low power handling, and modest ER in a trade-off with modulator losses. [15]

Another option for the RoF transmitter is the direct modulation of a high-bandwidth, directly modulated laser (DML). It represents the simplest and most compact solution as light generation and modulation occur within a single device. Direct modulation offers satisfactory RF to optical conversion efficiency and linearity but has relatively low output power and the modulation chirp is generally higher than the external modulation techniques [16]. A comparison of DML and external modulation using MZM for RoF links has already been presented e.g. in [17] states that MZM type links suffer from relatively high cost and complexity, especially when compared to DML links. Therefore, it seems that DMLs and EAMs are more suitable for microwave/photonic networks thanks to their low price and small size. Another experimental comparison between direct and external modulation at 60 GHz has been presented in [18], however, authors substituted real channel just by a variable attenuator, which cannot fully mimic the free space transmission channel parameters.

Published results on mm-wave transmissions over optical infrastructures mostly report on experiments performed in a laboratory environment. Recently, a 1 Gb/s full-duplex transmission using a silicon ring modulator and integrated III-V photodiode with downstream/upstream carriers at 15/11.5 GHz was presented in [19]. In [20] a DML transmission of 1 Gb/s RoF at 24 GHz over a

50-m long SSMF was demonstrated. To compensate for losses in the optical link, an erbium-doped fiber amplifier (EDFA) was used. Although error vector magnitude (EVM) was as low as 3.4% at the carrier frequency of 3.5 GHz, it was unacceptably high (20.5%) at 24 GHz when using quadrature phase-shift keying modulation. In [21], a 28 GHz 5G RoF system, using universally filtered orthogonal frequency division multiplexing with optical heterodyning, was presented. It used externally injected gain-switched distributed feedback laser realizing transmission over 25 km of SSMF and a 10-cm free-space RF channel with Vivaldi antennas. The total aggregated data rate was 4.56 Gb/s. In [22], the photonic generation of an RF multiple-input-multiple-output signal, in a dense wavelength division multiplexing RoF setup with MZMs, has been described and a 1 Gb/s transmission through 2 km of RoF, and an additional 6-m free-space RF channel was demonstrated. Another published work showed an experimental long-term evolution (LTE) transmission in a multi-service RoF system at 26 GHz [23]. This demonstration contained a 0.75-m long indoor RF channel and achieved 8% of EVM with 64-quadrature amplitude modulation (64-QAM), 10 MHz bandwidth, and an SNR of 30 dB. An RoF transmission over 20 km of SSMF and 10 m long RF free space channel including photonic mm-wave generation at 60 GHz for 5G fronthaul using MZM was presented in [24]. A microwave photonic link using the combination of free space optics (FSO) and 1 m long RF wireless channel operating at a frequency of 28 GHz was shown in [25] [26]. In addition, our previously published work [27] showed the most detailed experimental demonstration of RoF using DML that includes radio over free-space optics and a 3.3 m long indoor wireless free-space RF channel in the frequency band of 24–26 GHz.

Several papers reporting on an outdoor free-space RF transmission within RoF system have been also published. A 60 GHz RF transmission over a combined optic link for broadband photonic transmission wireless links was realized in [28] using self-pulsating mode-locked lasers and high output power photodetectors. In this case, two setups using EAM and MZM were demonstrated for the testing of an outdoor RF transmission for distances up to 25 m. Another report showed the possible integration of a W-band RoF link with passive optical networks [29]. For this purpose, a common, small, form-factor pluggable laser module was used for a 2.5 Gb/s transmission over 15 km of SSMF and an up to 225-m long free-space RF channel with parabolic antennas at a W-band frequency of 86 GHz. However, none of these outdoor experiments was carried out at the 25 GHz mm-wave band, which is the most probable spectral band to be adopted in early 5G and future wireless networks.

In this paper, we present experimental results from a mm-wave RoF outdoor system with a free-space RF channel operating in the 25 GHz band. We analyze the implementation of three transmitter topologies, including MZM, EAM and DML. The proposed transmission scheme and the environment represent real RoF deployment in an urban scenario for transmitting a wideband signal. The paper is organized as follows: The experimental setup is described in Section II, results from the indoor and outdoor measurements are presented in Section III and IV, respectively, a discussion is given in Section V and finally, the summary is provided in Section V.

2. Experimental Setup

At first, we performed an indoor measurement whose laboratory scheme is shown in Fig. 1. To emulate real data transmission format, the RF signal was composed of a baseband (BB) signal containing an orthogonal frequency division multiplexing (OFDM) LTE evolved universal terrestrial radio access (E-UTRA) test model TM3.2 with 16-QAM used for testing output power dynamic and transmitted signal quality [30]. The 20-MHz wide LTE bandwidth was generated by an R&S SMW200A signal generator and up-converted into an RF modulator (RF-MOD) by a 25 GHz single-tone carrier frequency provided by another signal generator R&S SMF100A. It resulted in output power of −10 dBm in the given signal bandwidth. Subsequently, the RF signal was modulated onto an optical carrier using three transmitter modulation techniques with particular parameters given in Tab. 1.

Note that mm-wave generation, providing high-quality signal with low phase noise, can also be realized in the optical domain as was shown e.g. in [4] and [28].

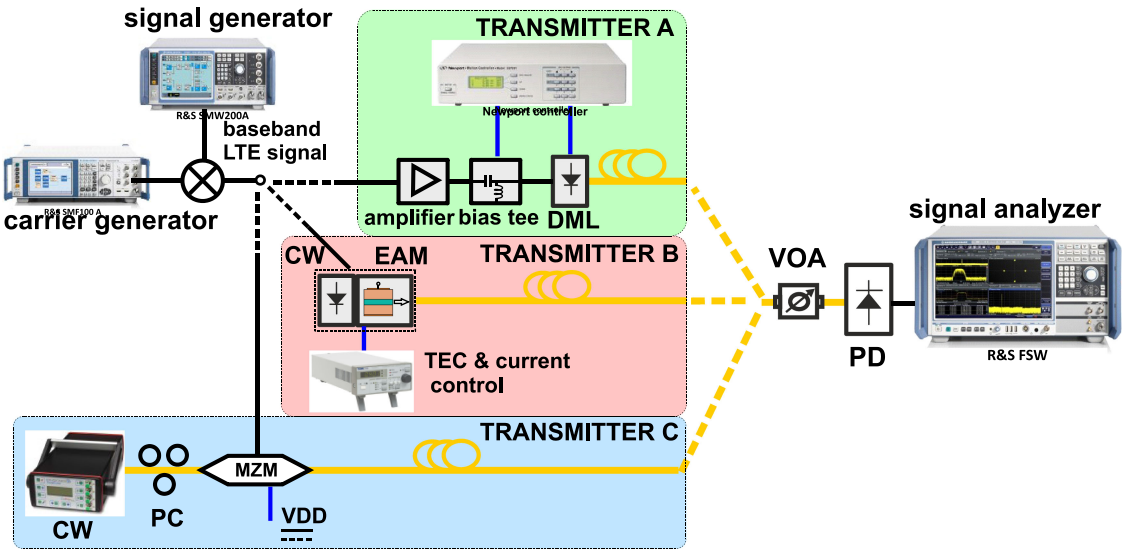

Fig. 1. Indoor laboratory set-up in which Transmitter A, B, or C is used.

TABLE 1
Comparison of Selected Transmitters Parameters

Transmitter	Employed scheme	Modulation bandwidth -3 dB (GHz)	Optical output power (dBm)	side-mode suppression ratio (dB)	Static extinction ratio (dB)
Transmitter A	DML	≥ 35	≥ 1.6	≥ 50	≥ 30
Transmitter B	EAM	≥ 32 GHz	6.7	≥ 35	≥ 15
Transmitter C	MZM	> 25 GHz	6.6	≥ 40 (external CW laser)	≥ 20

Although we use here only 20 MHz bandwidth, the testbed is examined over larger transmission bandwidth at the target frequency band of 25 GHz with emphasis on the comparison of particular modulation techniques. The DML (manufactured in HHI Berlin, commercially available) employed to form Transmitter A was a monolithically-integrated passive feedback laser [31]. It required a bias-tee (SigTek SB12D2) with bias current control and temperature stabilization (both driven by a Newport 8000 modulator controller). The input RF signal was first amplified by an RF amplifier (Wisewave AGP- 33142325-01) to optimize power at the output of the RoF link. Optical output power (laser bias current of 59 mA and temperature of 35 °C) was 1.6 dBm.

Transmitter B was based on an external EAM (OKI OSC-LDS-EML-C-500C) packaged with a continuous wave (CW) laser in a butterfly assembly. It was of comparable size to the DML, which was also in a butterfly package. The EAM required temperature control (Thorlabs TED200C, set to 35 °C in our experiments) and a bias current (Thorlabs LDC205C) set to 100 mA. Its average optical output power was 6.7 dBm.

Finally, Transmitter C used a CW laser (CoBrite DX4) with an external $LiNbO_3$ 40 Gb/s MZM (Fujitsu FTM7938EZ/201) biased at the quadrature point with optical power of 6.6 dBm at the output of the MZM.

The highest requirement for power consumption of the tested transmitters lay in RF signal generation, which was the same for all transmitters, although Transmitter A used an additional

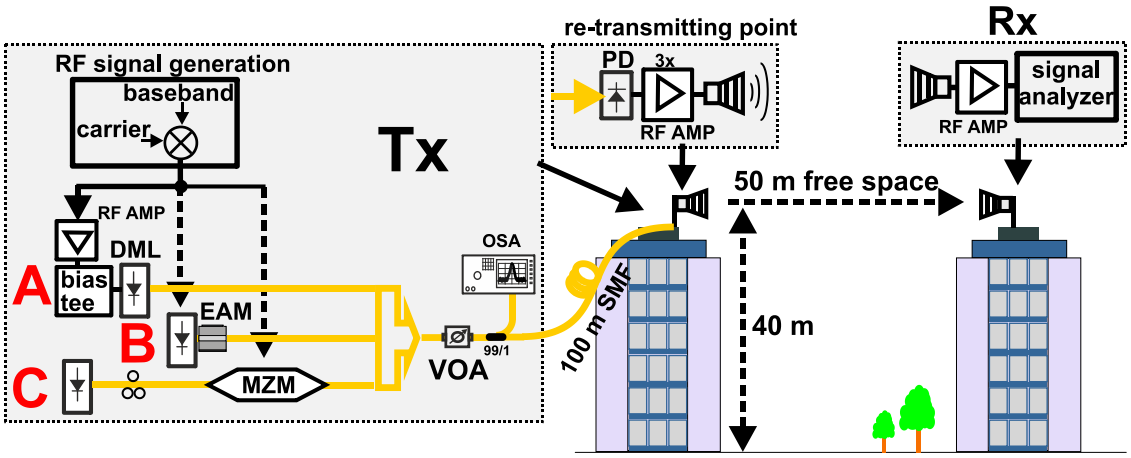

Fig. 2. Outdoor RoF link and 50-m long free-space RF channel. All three transmitters (A, B, and C) are shown. In the experiment, only one transmitter was used at a time.

low noise RF amplifier to compensate bias tee losses. Another power consumption requirement arose from the temperature control, which was however, needed for all laser sources and optical signal generation. The tested optical sources consumed approx. 0.5 W with strictest demands to Transmitter C, which needed to produce the highest optical power, whereas the lowest power consumption had DML in Transmitter A.

The signal from the transmitter under test (A, B, or C) firstly passed through a variable optical attenuator (VOA, Oz optics - DA-100-SC-1300/1550-9/125-S-40 with 1.5 dB of IL) and a 100-m long SSMF. For indoor measurements, the signal was further detected by a photodetector (Optilab PD-40) and analyzed with an R&S FSW signal analyzer.

In the next step, the outdoor setup was proposed to compare indoor and outdoor system performance. Outdoor measurements included a free-space RF channel, which was comprised of two antennas (transmitter antenna - Tx and receiver antenna - Rx) placed on the rooftops of two 9-story building towers, both of which are part of the campus of the Faculty of Electrical Engineering, Czech Technical University in Prague. This enabled 50-m long free-space RF transmission in real atmospheric conditions about 40 m above ground level. The entire setup is shown in Fig. 2, where the 100-m long SSMF between the VOA and the photodetector represented a typical distance of an RoF link, such as what is needed to connect a roof-top antenna with a ground-level central office. Note that the 100-m long SSMF was part of the installed network to mimic a real scenario, e.g. inside a large business building. As will be shown later, SSMF length can be significantly extended without introducing any system performance degradation. To compensate for the relatively large loss of the 50-m long free-space RF channel, the photo-detected signal was amplified with a cascade of three low-noise amplifiers (LNAs) (Miteq AMF-4F-260400-40-10p, Analog devices HMC1131, and Qorvo TGA4536-SM), boosting the power at the transmitting antenna input up to 14.3 dBm. The two RF antennas used to transmit the signal over the free-space RF channel between the buildings (see Fig. 3) were double ridged horn antennas (DRH40–RFspin, s.r.o.) with 14.7 dBi gain at 25 GHz. The free-space loss for antenna transmission at 25 GHz over the 50-m long channel was 94.4 dB, reduced to 65 dB by the antenna gains.

The RF signal received by the receiver antenna was boosted with an LNA (Miteq AMF-4F-260400-40-10p) to compensate for losses of the free-space transmission and the 3-m long coaxial cable (9 dB loss at 24 GHz [32]) connecting the antenna to the signal analyzer. Note that the additional internal amplifier of the signal analyzer was used for Transmitter A enabling the incoming signal, which was weaker in the case of Transmitter A, to set a comparable power level for all three transmitters.

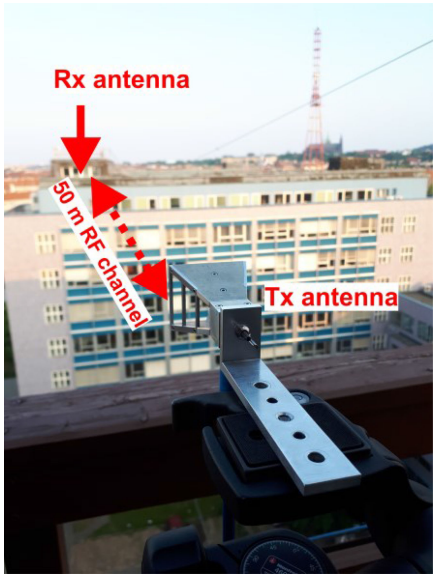

Fig. 3. 50-m long free-space RF channel with detail on the transmitting antenna (Tx).

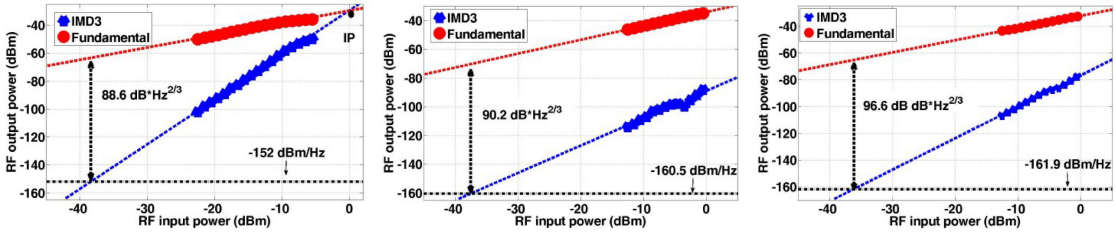

Fig. 4. System response (denoted as "Fundamental") and IMD3 for (a) Transmitter A (DML), (b) Transmitter B (EAM), and (c) Transmitter C (MZM). SFDR and IP are also shown.

Additionally, another measuring setup was built to characterize the free-space RF channel. The scheme consisted of the RF parts shown in Fig. 2 without any optics, i.e., it comprised signal generators with RF-MOD, a combination of Tx and Rx antennas, and two LNAs (Miteq AMF-4F-260400-40-10p and Analog devices HMC1131).The received signal was evaluated by the signal analyzer.

Our experimental work consisted of two subsequent experiments – a laboratory characterization of the RoF part, followed by the characterization of the entire RoF link with an outdoor free-space RF channel.

3. Indoor Experimental Results

Firstly, the linearity of the three transmitters (A, B, and C) using the laboratory setup (Fig. 1) was compared. Third-order intermodulation distortion (IMD3) was measured using a standard two-tone test with enabling the IMD3, spurious-free dynamic range (SFDR) and the third-order intercept point (IP3) to be evaluated. The results, measured at a frequency of 25 GHz with 1 MHz spacing between two tones, for all three transmitters using the same photodetector, are shown in Figs. 4a), b) and c).

SFDRs of 88.6, 90.2 and 96.6 dB·Hz$^{2/3}$ for Transmitters A, B and C, respectively, were obtained with corresponding input IP3s of 0, 50, and 31 dBm. Results show that Transmitter C had the lowest

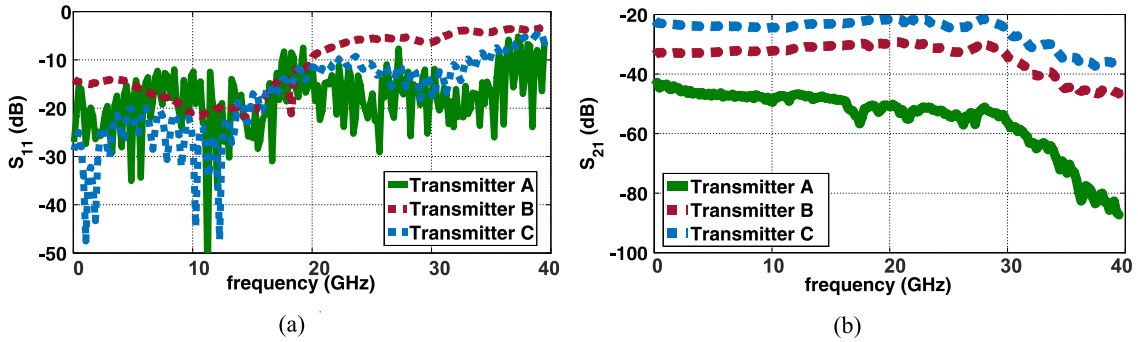

Fig. 5. (a) S_{11} and (b) S_{21} measured characteristics for Transmitters A (green solid line), B (red dotted line), and C (blue dashed line) in the frequency range 0–40 GHz.

third-order distortion (SFDR = 96.6 dB·Hz$^{2/3}$), followed by Transmitter B (SFDR = 90.2 dB·Hz$^{2/3}$). Transmitter A had the highest nonlinearity in terms of IMD3, mainly due to a considerably higher noise floor, but on the other hand, the input power did not exceed a critical value to generate significant nonlinear distortion. It is worth noting that the linearity measurement of Transmitter A was influenced by the bias-tee and especially by the additional RF amplifier that was necessary to boost RF power at its input to maintain the same power level as Transmitters B and C what resulted in the lowest linearity in terms of the SFDR. Transmitter B had the highest level of allowable input power in terms of IP3, i.e. 50 dBm. In the next step, S_{11} and S_{21} parameters for frequencies up to 40 GHz were measured using a vector network analyzer (R&S ZVA67). Measured data for all three transmitters are presented in Fig. 5. The vector measurement was carried out for an optical back-to-back setup without any other components, i.e., without the RF amplifier otherwise used with Transmitter A.

Note that S_{11} result of Transmitter A (Fig. 5a) involved the input matching load of the bias tee since the DML had no direct RF input and show an excellent matching with S_{11} mostly below -10 dB in bandwidth between 20 and 30 GHz. Transmitter B evinced at the input a very low impedance match of -5.5 dB in terms of S_{11} at 25 GHz compared to -11 dB and -16.5 dB for Transmitters A and C, respectively. Nevertheless, the results imply low frequency-dependent transmission in terms of S_{21} for all three transmitters with frequencies up to 30 GHz (Fig. 5b) showing a comparable course. Additionally, Transmitters B and C have an almost identical shape of S_{21} curves, suggesting the measured performance is predominantly given by the photodetector. The average S_{21} magnitude difference between Transmitters B and C was 7 dB, mainly caused by the modulation depth. The DML in Transmitter A was designed to operate over a wider frequency range of up to 40 GHz [26], however, its S_{21} performance was highly influenced by the frequency profile of the photodetector used and, in particular, by the bias tee. It resulted in a less flat characteristic compared to Transmitters B and C. The S_{21} measured at frequency of 25 GHz were -53.9, -32.3 and -24.2 dB for Transmitters A, B and C, respectively. Note that considerably lower transmission with Transmitter A was caused by the exclusion of an RF amplifier in front of its bias tee input. The IL, meaning the RF signal transfer to optical and back from optical to the RF domain, measured in an indoor scenario for a particular setup with parameters given in section II at a frequency of 25 GHz, was 32.4 dB (53.3 dB without an amplifier in front of the DML), followed by 38.9 dB and 30.2 dB for Transmitters A, B and C, respectively.

Furthermore, the RoF link performance without the free-space RF channel was analyzed in laboratory conditions. Its performance was first characterized in terms of EVM over a frequency range of 22.5 GHz to 26.5 GHz by using a 20 MHz LTE signal bandwidth and 16-QAM modulation from the test model TM 3.2. Results are then shown in Fig. 6. The highest received RF power and corresponding absolute lowest EVM of 2.3% in the selected frequency range were achieved with Transmitter C. The measured EVM values at 25 GHz were 3.7, 3.7 and 2.4% for Transmitters A, B and C, respectively, showing comparable performance of Transmitters A and B for indoor scenario.

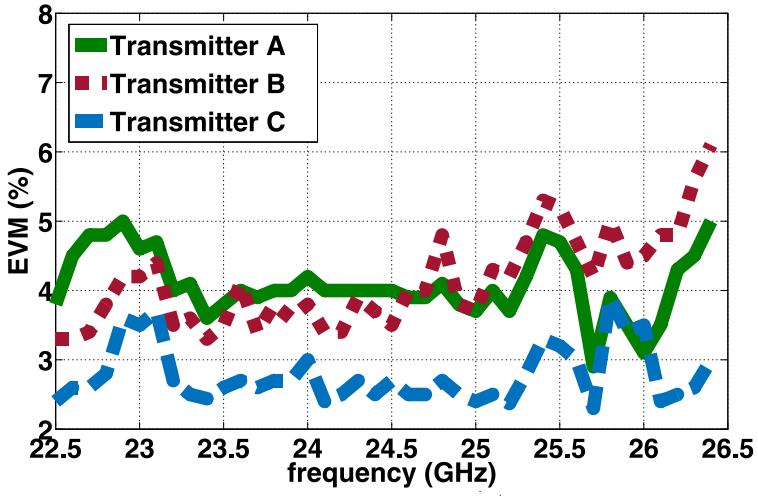

Fig. 6. Measured EVM for Transmitters A (green solid line), B (red dotted line), and C (blue dashed line) in the frequency range of 22.5 GHz–26.5 GHz in laboratory conditions.

The best EVM performance while using Transmitter C has been achieved especially due to the above mentioned high RF power transmission and low IMD3, which directly affects the signal in used bandwidth.

It can be observed that the profile of EVM for all transmitters partially follows the frequency response of the jointly-used equipment/components, which can be seen, e.g., at 23.1 or 25.8 GHz where all three curves evince similar peaks. However all performances in selected bandwidth keep under the EVM of 6%, which is greatly under the EVM limit for 16-QAM. In order to evaluate potential margins in the system power budget, we tested the resilience of the laboratory RoF setup to additional optical loss, which was introduced by using a VOA as depicted in Fig. 1. Measured results for indoor setup at 25 GHz are shown in Fig. 7. The black-dotted horizontal line indicates the 13.5% limit given by the 3GPP for the 16-QAM modulation scheme [30]. Constellation diagrams with EVM of 3.3, 3.7 and 2.4% for Transmitter A, B and C, respectively, are shown in Fig. 7b).

The maximum margins for additional optical losses were 9.2, 6.7, and 11.2 dB for Transmitters A, B, and C, respectively. In other perspectives, the EVM magnitudes were 6.5, 11.5 and 4.9% when setting the allowable margin to 6 dB to keep all scenarios with EVM under 13.5% and providing large margin for e.g. fiber length extension.

4. Outdoor Experimental Results

A large unlicensed bandwidth is provided by the mm-wave band between 24–28 GHz though significant challenges remain, in particular, high free-space propagation loss. As shown below, another limitation is introduced by significant power fluctuations due to perturbations in the atmosphere.

4.1. Free-space RF channel characterization

To characterize the free-space RF channel stability in RoF system, received RF power fluctuations were monitored by using both data and single-carrier transmission at the 25 GHz frequency described in Chapter II. For the sake of comparison, a single-carrier transmission at 5 GHz was also tested. Results from a one-hour measurement of the received LTE signal power fluctuation within test model TM 3.2, with 20 MHz bandwidth and 16-QAM modulation at 25 GHz, are shown in Fig. 8. Note that the data were taken each 100 ms to capture even fast signal fades. As can be seen, the signal experienced high power fluctuations around the mean power level of -45.7 dBm with a standard deviation of 1.9 dB, which follows the probability density function of normal distribution

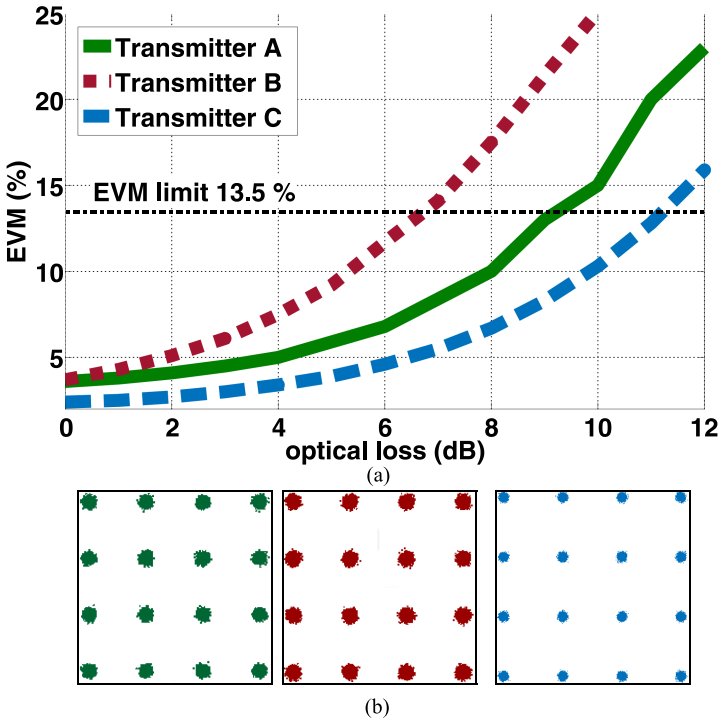

Fig. 7. (a) EVM vs. additional optical loss for indoor links with Transmitters A (green solid line), B (red dotted line), and C (blue dashed line) at a frequency of 25 GHz and (b) corresponding constellation diagrams for Transmitter A, B, and C with 16-QAM at 0 dB of optical attenuation.

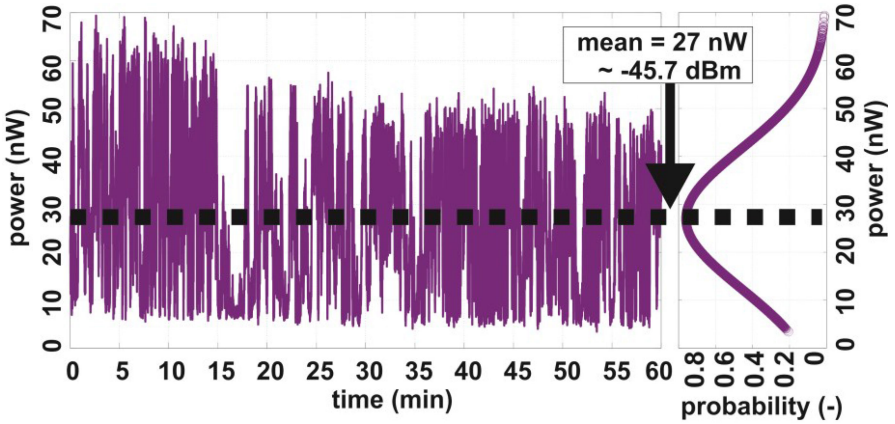

Fig. 8. Measured received power fluctuations following propagation through 50-m long free-space RF channel at a carrier frequency of 25 GHz with the 20 MHz bandwidth LTE data including the corresponding probability density function.

as depicted in the inset in Fig. 8. Note, this result is in line with calculations and measurements presented in the literature. For example, the experimental measurements and empirical-based propagation channel models at 28 GHz reported a standard deviation of 1.1 dB for the directional path loss model with line-of-sight [33].

Another study [34] presented data from a path loss model for usage within 5G in urban macrocells, microcells and indoor scenarios. The standard deviation of power fluctuation was modeled to be as large as 3.2 dB at 28 GHz for a distance range of 31–54 m [34]. Moreover, the free-space channel condition has been examined especially in terms of atmospheric effects

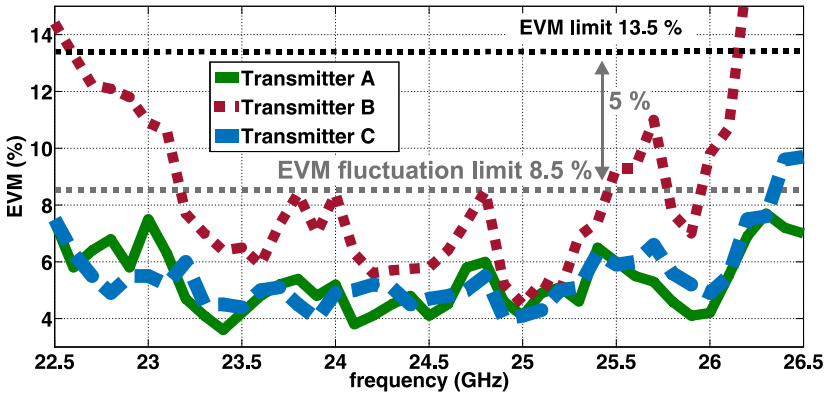

Fig. 9. Measured EVM for Transmitters A (green solid line), B (red dotted line), and C (blue dashed line) in the frequency range of 22.5–26.5 GHz for outdoor measurement.

that revealed a non-negligible correlation between received RF signal power with wind speed and consequently with air humidity, which was between 50–62% in given measuring interval. The magnitude of Pearson correlation coefficient of received RF power and humidity was 0.31 denoting weak correlation with the presence of the water particles in the air. To further gain insight into the measured power fluctuations, additional tests transmitting only a single-tone (instead of the LTE signal) were performed at 25 GHz. Power fluctuations in terms of a standard deviation of 2.3 dB were observed. When the single-tone signal frequency was decreased to 5 GHz, power fluctuations were reduced to 0.8 dB, making 1.5 dB difference compared to the 25 GHz frequency.

All our measurements were carried out during clear, sunny September days with similar conditions (temperatures around 14 °C). To confirm the achieved results, we repeated the measurement several times with comparable weather conditions and acquired similar results. As we did not observe any power fluctuations of such magnitude in our indoor experiment using the same hardware published earlier [27], we conclude that the fluctuations were caused exclusively by the atmospheric conditions.

Considering our experiments were carried out during clear days suggests that significantly stronger power fluctuations may be expected during harsh weather conditions. As the power fluctuations may significantly influence system performance (and especially power margins), weather conditions must be carefully considered and their influence on power fluctuations needs to be characterized when designing a free-space RF channel operating at the 25 GHz band.

4.2. Overall optical and RF system performance

In the final step, the whole system, including RoF and the outdoor free-space RF channel, was tested according to the indoor measurement campaign. The performance was again characterized in terms of EVM over a frequency range of 22.5 GHz to 26.5 GHz using a 20 MHz LTE signal bandwidth and test model TM 3.2 with 16-QAM modulation. Note that the EVM values were captured as a mean value according to received power fluctuations whose distribution is displayed in Fig. 8. Results from the EVM measurement are shown in Fig. 9. Due to the lower output optical power, the configuration of Transmitter A used an internal RF amplifier at the signal analyzer to obtain a similar level of detected signal power as that obtained with Transmitters B and C. As expected, the highest received power, as well as the lowest EVM in the selected frequency range, was achieved by Transmitter C with MZM like in indoor scenario. However, Transmitter A performed quite similarly to Transmitter C also thanks to activated additional RF amplifier in the receiver, which improved the signal power. We achieved a mean EVM below 6%, well below the limit of 13.5%, for all three transmitters at 25 GHz. However, Transmitter B only evinced an EVM under 13.5% over a reduced frequency range of 22.6–26.1 GHz. This is surprising as Transmitters A and C performed

sufficiently well over the entire spectral range studied, whereas optical power of Transmitter C was at the same level as for Transmitter B. We attribute the overall poorer performance of Transmitter B to its relatively lower ER and worse impedance matching and lower S_{21} transmission, as compared to Transmitters A and C. As concerns EVM values obtained for the outdoor setup, it was as low as 4.1% when using Transmitters A and C, and 4.5% when using Transmitter B at 25 GHz. This represents only a modest degradation when compared to the laboratory setup performance. The considered 4-GHz bandwidth is reduced, especially for Transmitter B on both edges of the considered spectrum. For all transmitters, the EVM increases above the frequency of approximately 25.2 GHz due to frequency-dependent losses, a small drop in S21 characteristics (see Fig. 5b) at this frequency and increased noise of the receiver, which steeply rises above 26 GHz and results in the degradation of SNR. We can also observe the increased EVM values for frequencies below 23.4 GHz for all transmitters because of the frequency-dependent gain of used amplifiers. The aforementioned reasons led to significantly increased EVM values for Transmitter B, having about 8 dB lower power transmission, about 6 dB worse impedance matching and 6.4 dB lower dynamic range compared to Transmitter C and whose different transmission parameters have become apparent in outdoor system usage. Moreover, the Transmitter B evinced the lowest SNR from all transmitters in outdoor scenario, namely 29.8 dB at 25 GHz. Whereas the SNR of the Transmitter B was lower by 3.5 and 2.2 dB at 25 GHz, comparing to the Transmitters A and C, respectively, the SNR at 24 GHz was lower by 5.5 and 6 dB, respectively and lower by 4.5 and 3.5 dB at the frequency of 26 GHz, comparing to the Transmitter A and C, respectively. Therefore the overall performance was more deteriorated in the edges of considered bandwidth for Transmitter B. Note that the displayed EVM figures are mean values. When taking power fluctuations into account, the EVM also fluctuated, with up to a maximal $\pm$5% variation for the test model used at the 20 MHz bandwidth and 16-QAM. The updated limit, providing enough margin and ensuring a fluctuating EVM below the original limit, is shown as the grey dashed horizontal line at EVM of 8.5%. Unfortunately, this reduces the useful bandwidth for Transmitter B from 23.2 GHz to 25.4 GHz and for Transmitter C from 22.5 to 26.3 GHz.

Finally, we analyzed the effect of additional optical losses using the same approach as described in Section III. Measured results of EVM dependence on optical loss for all three transmitters are depicted in Fig. 10. As can be seen, there is a smaller maximum margin for additional optical losses for the outdoor setup than for the laboratory setup without the free-space RF channel. The maximum observed difference was 3.6 dB for Transmitter C. The optical loss of the outdoor system can be increased up to 6.8, 4.2 and 7.6 dB for Transmitters A, B, and C, respectively while keeping mean EVM below 13.5%.

On the other hand, when maximum RF received power fluctuation induced in the free-space RF channel at 25 GHz was accounted for, the margin for additional optical losses was reduced to 4.0, 3.1 and 5.0 dB for Transmitters A, B and C, respectively. These values were obtained without the use of an optical amplifier whose use would significantly extend the power budget margin to provide, e.g., SSMF link extension. The higher margin for optical losses achieved with Transmitter C is due to high optical power when using MZM, the linear characteristic of the MZM, and its high ER as well as the high transmission in terms of S_{21}. Fig. 10b) depicts constellation diagrams while using particular Transmitter with 0 dB of optical attenuation with corresponding EVM values of 4.3, 4.6 and 3.9% for Transmitter A, B and C, respectively.

5. Discussion

In the conducted experiment, we have shown that all three transmitters exhibit satisfactory performance for deployment in real-world RoF systems. Achieved results are in agreement with commonly observed differences in the performance of particular modulation configurations and we have shown which parameters can highly affect such a RoF link including a real outdoor antenna link. Based on our results, the importance of high signal power transmission, i.e. around 30 dB of IL or better for passive RoF, over optical infrastructure in terms of S21 parameter and impedance

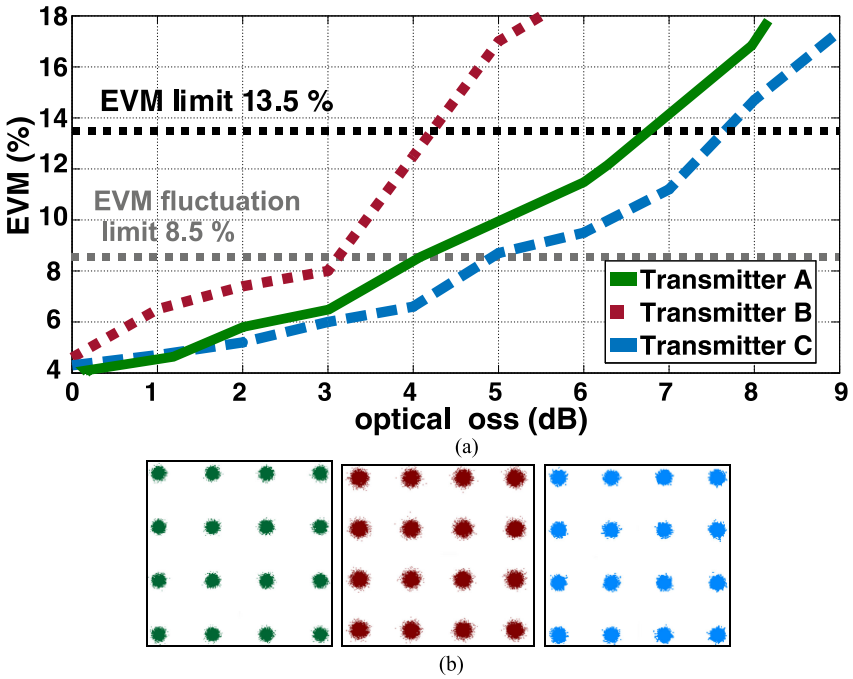

Fig. 10. EVM vs. additional optical losses when using Transmitters A (green solid line), B (red dotted line), and C (blue dashed line) at a frequency of 25 GHz in the outdoor setup and (b) corresponding constellation diagrams for Transmitter A, B, and C with 16-QAM at 0 dB of optical attenuation.

matching over a large frequency range can be clearly highlighted. Higher ER and immunity to IMD3 influencing the quality of the signal are also vital.

Apart from the above-mentioned observations, which may be straightforward for researchers in the RoF field, we examined real outdoor free-space RF link and we found that signal fluctuations affect the RoF system performance severely. Captured data analysis provided a nice insight into the channel behavior and proved to have the most significant effect on the overall RoF system. The main outcome is that even in a clear, sunny day, strong signal fluctuations of over 2-3 dB are present at 25 GHz, whereas lower frequencies are more resilient. Therefore, for RoF system analyses including antennas, it is important to measure in real conditions instead of laboratory verifications or at least to include the channel behavior based on published empirical data.

The delivery of sufficient RF power to the antenna depends, amongst others, also on the optical transmitter power and therefore we have added an additional RF amplifier in the RF receiver when using Transmitter A. Interestingly, with this additional RF amplifier, the RoF system performance was as good as with Transmitter C. Moreover, we demonstrated in [27] the excellent system performance under laboratory conditions with identical DML when the optical power was 3 dB higher and EDFA has been adopted to compensate the low DML output power. Based on the results, it is worth mentioning that the most appropriate approach for a specific solution needs to be considered in the context of other parameters like cost, size or integrability, which favours DML approach, even in the frequency band between 20 and 30 GHz.

The optical link serves here as a medium for radio signal transmission over longer distances than would be possible to reach with RF cable or antenna and therefore, margin for additional losses have been tested for both indoor and outdoor link and all presented approaches can be used with some limitations according to their particular parameters. Moreover, the complete RoF system including the RF wireless transmission at the frequency around 25 GHz needs more used RF components, namely RF amplifiers to compensate high atmospherical attenuation in this band and high losses due to antenna broadcasting (note that in our case the RF free space losses

including antenna gain were 65 dB over 50 m distance because the used antenna has relatively wide radiating beam $> 30°$). Thus there is a number of RF amplifiers, which are necessary to get sufficient RF power budget. This considerably affects the overall system performance by the uneven amplifier gain in the given bandwidth and also noise floor increases.

In our study, we used a lower data rate (TM 3.2 LTE test model with 20 MHz bandwidth and 16-QAM modulation scheme), nevertheless, the achieved results suggest the system has the potential to operate even at 100 MHz bandwidth or more. This we demonstrated in [27] for an indoor-only based system where we achieved 375 Mb/s throughput with the same DML as we used in this study for Transmitter A.

6. Conclusions

We have demonstrated an experimental RoF transmission of mm-wave signal with a 50-meter long outdoor free-space RF channel in the frequency band of 25 GHz. The best system performance has been achieved by using Transmitter A (based on a DML) and Transmitter C (based on MZM). In the outdoor scenario, the mean EVM for the aforementioned transmitters was below 8.5% over the entire tested 4 GHz bandwidth window, giving reasonable margin for the 16-QAM requirement of $<$13.5% EVM, budgeting for the expected power variations due to the received power fluctuations in the free-space RF channel. The Transmitter A compared to Transmitter C is potentially significantly cheaper, simpler, and more compact, making it a better candidate for large-scale deployment, e.g., in 5G networks. Moreover, we have shown that the lower output optical power in the case of Transmitter A can be compensated by additional RF amplifier in the receiver and therefore equalize the Transmitter C with MZM. Transmitter B (based on EAM) achieved adequate overall EVM performance but with degradation towards both edges of the spectral band studied in the outdoor experiment. The EAM performance suffers from an achieved trade-off between satisfactorily high ER (i.e., 15 dB vs. 20 dB with MZM) and acceptable IL, lower linearity, RF transmission and impedance matching when compared to Transmitter C what led in real outdoor system with additional RF equipment to considerable signal fading. However, Transmitters A and B represent an integrated and, thus, potentially low cost and compact solution. Furthermore, we characterized all three transmitters in the RoF channel to evaluate potential margins in the system power budget. All of them can provide more than 3 dB (Transmitter C up to 6 dB) when considering maximal EVM variation due to a wireless transmission at 25 GHz. Finally, we reported on a significant signal power fluctuation for the free-space RF channel at 25 GHz, whose impact needs to be taken into account (e.g., considering higher power margins) when designing such a link. The standard deviation of received power, while using a 16-QAM transmission with a 20 MHz bandwidth at 25 GHz over a 50-m long wireless channel, was 1.9 dB resulting in maximal EVM variation of $\pm$5%.

References

[1] S. Mattisson, "Overview of 5G requirements and future wireless networks," in *Proc. 43rd IEEE Eur. Solid State Circuits Conf.*, 2017, pp. 1–6.
[2] T. S. Rappaport *et al.*, "Millimeter wave mobile communications for 5G cellular: It will work!," *IEEE Access*, vol. 1, pp. 335–349, 2013.
[3] B. Lannoo *et al.*, "Radio-over-fibre for ultra-small 5G cells," *Proc. 17th Int. Conf. Transparent Opt. Networks*, 2015, pp. 1–4.
[4] P. T. Dat, A. Kanno, and T. Kawanishi, "Radio-on-radio-over-fiber: efficient fronthauling for small cells and moving cells," *IEEE Wirel. Commun.*, vol. 22, no. 5, pp. 67–75, Oct. 2015.
[5] P. J. Urban, G. C. Amaral, and J. P. Von Der Weid, "Fiber monitoring using a sub-carrier band in a sub-carrier multiplexed radio-over-fiber transmission system for applications in analog mobile fronthaul," *J. Lightw. Technol.*, vol. 34, no. 13, pp. 3118–3125, 2016.
[6] C. H. Lee, *Microwave Photonics*, 2nd ed., New York, NY, USA: Taylor & Francis, 2013.
[7] T. Kanesan, W. P. Ng, Z. Ghassemlooy, and C. Lu, "Experimental demonstration of the compensation of nonlinear propagation in a LTE RoF system with a directly modulated laser," in *Proc. IEEE Int. Conf. Commun.*, 2013, pp. 3884–3888.
[8] D. Novak *et al.*, "Radio-over-fiber technologies for emerging wireless systems," *IEEE J. Quantum Electron.*, vol. 52, no. 1, pp. 1–11, Jan. 2016.

[9] U. Habib, M. Steeg, A. Stöhr, and N. J Gomes, "Radio-over-fiber-supported 60 GHz multiuser transmission using leaky wave antenna," in *Proc. Int. Topical Meeting Microw. Photon.*, 2017, pp. 1–4.
[10] J. Beas, G. Castanon, I. Aldaya, A. Aragon-Zavala, and G. Campuzano, "Millimeter-wave frequency radio over fiber systems: A survey," *IEEE Commun. Surv.*, vol. 15, no. 4, pp. 1593–1619, Oct. –Dec. 2013.
[11] T. Yeyu, C. Chow, G. Chen, C. Peng, C. Yeh, and H. Tsang, "Integrated silicon photonics remote radio frontend (RRF) for single-sideband (SSB) millimeter-wave radio-over-fiber (ROF) systems," *IEEE Photon. J.*, vol. 11, no. 2, Apr. 2019, Art. no. 7202108.
[12] D.-N. Nguyen *et al.*, "M-QAM transmission over hybrid microwave photonic links at the K-band," *Opt. Express*, vol. 27, pp. 33745–33756, 2019.
[13] L. Vallejo, B. Ortega, J. Bohata, S. Zvanovec, and V. Almenar, "Photonic multiple millimeter wave signal generation and distribution over reconfigurable hybrid SSMF/FSO links," *Opt. Fiber Technol.*, vol. 54, 2020, Art. no. 102085.
[14] H. Li *et al.*, "Real-time 100-GS/s sigma-delta all-digital radio-over-fiber transmitter for 22.75–27.5 GHz band," in *Proc. Opt. Fiber Commun. Conf. Exhib*, 2019, pp. 1–3.
[15] S. H. Lee, H. J. Kim, and J.I. Song, "Simultaneous multichannel photonic frequency up-conversion based on an EAM and an optical interleaver for radio-over-fiber systems," in *Proc. IEEE Int. Topical Meeting Microw. Photon.*, 2012, pp. 220–223.
[16] S. A. Khwandah, J. P. Cosmas, I. A. Glover, P. I. Lazaridis, N. R. Prasad, and Z. D. Zaharis, "Direct and external intensity modulation in OFDM RoF links," *IEEE Photon. J.*, vol. 7, no. 4, Aug. 2015Art. no. 7902710.
[17] D. Wake *et al.*, "A comparison of radio over fiber link types for the support of wideband radio channels," *J. Lightw. Technol.*, vol. 28, no. 16, pp. 2416–2422, Aug. 2010.
[18] A. Lebedev, X. Pang, J. J. V. Olmos, S. Forchhammer, and I. T. Monroy, "Simultaneous 60-GHz RoF transmission of lightwaves emitted by ECL, DFB, and VCSEL," *IEEE Photon. Technol. Lett.*, vol. 26, no. 7, pp. 733–736, Apr. 2014.
[19] Z. Tang, J. Zhang, S. Pan, G. Roelkens, and D. Van Thourhout, "RoF system based on an III-V-on-silicon transceiver with a transfer-printed PD," *IEEE Photon. Technol. Lett.*, vol. 31, no. 13, pp. 1045–1048, Jul. 2019.
[20] K. V. Gasse *et al.*, "480 Mbps/1 Gbps radio-over-fiber link based on a directly modulated III-V-on-Silicon DFB laser," in *Proc. IEEE Int. Topical Meeting Microw. Photon.*, 2016, pp. 328–331.
[21] E. Martin *et al.*, "28 GHz 5G radio over fibre using UF-OFDM with optical heterodyning," in *Proc. IEEE Int. Topical Meeting Microw. Photon.*, 2017, pp. 1–4.
[22] A. Naemat, S. M. Mohd Hassan, N. F. I. Muhammad, A. S. M. Marzuki, and N. Kushairi, "Experimental study on LTE signal transmission in multi-service Radio-over-Fiber (RoF) system," in *Proc. IEEE 13th Malaysia Int. Conf. Commun.*, 2017, pp. 300–304.
[23] U. Habib, A. E. Aighobahi, C. Wang, and N. J. Gomes, "Radio over fiber transport of mm-wave 2 $\times$ 2 MIMO for spatial diversity and multiplexing," in *Proc. IEEE Int. Topical Meeting Microw. Photon.*, 2016, pp. 39–42.
[24] S.E. Alavi, M. R. K. Soltanian, I. S. Amiri, M. Khalily, A. S. M. Supa'at, and H. Ahmad, "Towards 5G: A photonic based millimeter wave signal generation for applying in 5G access fronthaul," *Sci. Rep.*, vol. 6, 2016, Art. no. 19891.
[25] O. Alkhalifah, O. Alrabiah, A. Ragheb, M. A. Esmail, and S. Alshebeili, "Investigation and demonstration of 5G signal transmission over fiber/FSO/wireless links," in *Proc. Int. Conf. Elect. Comput. Technologies Appl.*, 2017, pp. 1–4.
[26] M. A. Esmail, A. M. Ragheb, H. A. Fathallah, M. Altamimi, and S. A. Alshebeili, "5G-28 GHz signal transmission over hybrid all-optical FSO/RF link in dusty weather conditions," *IEEE Access*, vol. 7, pp. 24404–24410, 2019.
[27] J. Bohata, J. Spáčil, Z. Ghassemlooy, S. Zvánovec and R. Slavík, "24-26 GHz radio-over-fiber and free-space optics for fifth-generation systems," *Opt. Lett.*, vol. 43, no. 5, pp. 1035–1038, 2018.
[28] A. Stohr *et al.*, "Millimeter-wave photonic components for broadband wireless systems," *IEEE Trans. Microw. Theory Techn.*, vol. 58, no. 11, pp. 3071–3082, Nov. 2010.
[29] S. Rommel *et al.*, "225 m Outdoor W-band radio-over-fiber link using an optical SFP+ module," in *Proc. Opt. Fiber Commun. Conf. Exhib.*, 2016, pp. 1–3.
[30] The 3rd Generation Partnership Project. [Online]. Available: www.3gpp.org
[31] J. Kreissl, V. Vercesi, U. Troppenz, T. Gaertner, W. Wenisch, and M. Schell, "Up to 40-Gb/s Directly modulated laser operating at low driving current: buried-heterostructure passive feedback laser (BH-PFL)," *IEEE Photon. Technol. Lett.*, vol. 24, no. 5, pp. 362–364, Mar. 2012.
[32] J. Bohata, J. Spacil, S. Zvanovec, Z. Ghassemlooy, and R. Slavik, "Hybrid RoF-RoFSO system using directly modulated laser for 24–26 GHz 5G Networks," in *Proc. 11th Int. Symp. Commun. Syst., Networks Dig. Signal Process.*, 2018, pp. 1–5.
[33] T. S. Rappaport, G. R. MacCartney, M. K. Samimi, and S. Sun, "Wideband millimeter-wave propagation measurements and channel models for future wireless communication system design," *IEEE Trans. Commun.*, vol. 63, no. 9, pp. 3029–3056, Sep. 2015.
[34] S. Sun *et al.*, "Investigation of prediction accuracy, sensitivity, and parameter stability of large-scale propagation path loss models for 5G wireless communications," *IEEE Trans. Veh. Technol.*, vol. 65, no. 5, pp. 2843–2860, May 2016.

IEEE Photonics Journal
An IEEE Photonics Society Publication

Open Access

Polarization Division Multiplexing-Based Hybrid Microwave Photonic Links for Simultaneous mmW and Sub-6 GHz Wireless Transmissions

Volume 12, Number 6, December 2020

Dong-Nhat Nguyen, ***Member, IEEE***
Jan Bohata
Jan Spacil
Matej Komanec
Nobby Stevens
Zabih Ghassemlooy, ***Senior Member, IEEE***
Pham Tien Dat, ***Member, IEEE***
Stanislav Zvanovec, ***Senior Member, IEEE***

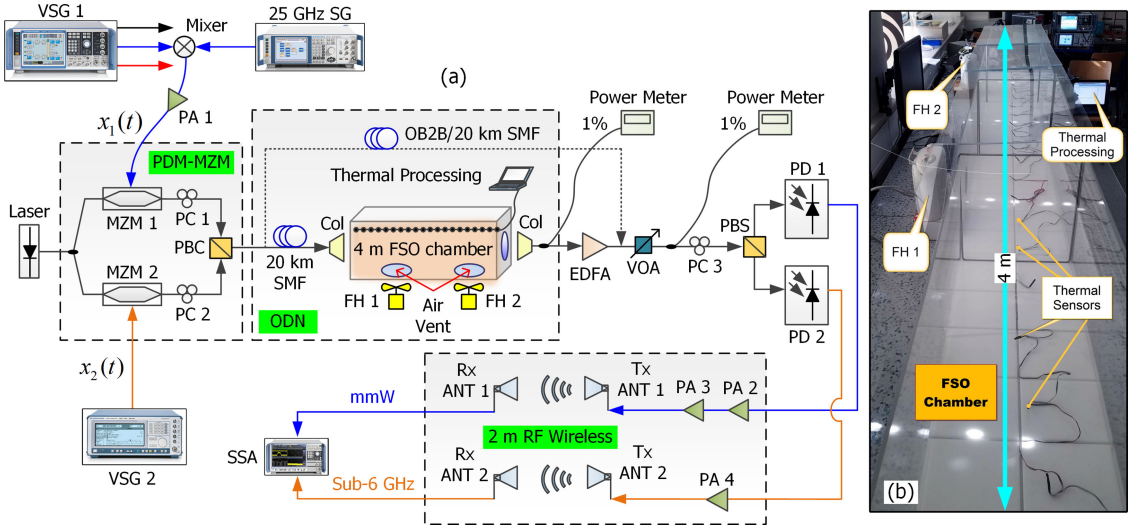

DOI: 10.1109/JPHOT.2020.3036440

Polarization Division Multiplexing-Based Hybrid Microwave Photonic Links for Simultaneous mmW and Sub-6 GHz Wireless Transmissions

Dong-Nhat Nguyen,[1] ***Member, IEEE***, **Jan Bohata**,[1] **Jan Spacil**,[1]
Matej Komanec,[1] **Nobby Stevens**,[2]
Zabih Ghassemlooy,[3] ***Senior Member, IEEE***,
Pham Tien Dat,[4] ***Member, IEEE***,
and Stanislav Zvanovec,[1] ***Senior Member, IEEE***

[1]Department of Electromagnetic Field, Czech Technical University in Prague, Prague 16627, Czech Republic
[2]ESAT-DRAMCO, KU Leuven, Leuven 3000, Belgium
[3]Optical Communication Research Group, Faculty of Engineering and Environment, Northumbria University, Newcastle upon Tyne NE1 8ST, U.K.
[4]Network System Research Institute, National Institute of Information and Communication, Tokyo 184-8795, Japan

DOI:10.1109/JPHOT.2020.3036440

Manuscript received September 22, 2020; revised October 25, 2020; accepted November 3, 2020. Date of publication November 6, 2020; date of current version December 2, 2020. This work was supported by International Mobility of Researchers in CTU (CZ.02.2.69/0.0/0.0/16_027/0008465); Central Europe Leuven Strategic Alliance (CELSA) Project PICNIC. Corresponding author: Dong-Nhat Nguyen (email: dongnhat@fel.cvut.cz).

Abstract: A new hybrid microwave photonic link based on a polarization division multiplexing Mach-Zehnder modulator (PDM-MZM) is proposed. The link enables co-transmission of millimeter-wave (mmW) and sub-6 GHz wireless signals over a seamless single-mode fiber (SMF) and free-space optics (FSO) channels. Optimization of the chromatic dispersion (CD)-induced power fading regardless of the power fading due to the non-deterministic atmospheric turbulence (AT) is simultaneously demonstrated. Extensive simulation analysis is first presented to examine (i) the impact of CD on mmW (25 GHz) and sub-6 GHz (2.6 GHz) signals, envisioned for the 5th generation networks, and (ii) optimization of CD-induced power fading by changing the phase relations between the optical carrier and optical sidebands in each polarization channel using single tunable polarization controller. A proof-of-concept experiment is finally performed to simultaneously deliver 25 GHz and 2.6 GHz signals with 4/16/64-quadrature amplitude modulation over (i) 20 km SMF and 2 m radio wireless link and (ii) 20 km SMF, 4.2 m FSO (with AT) and 2 m radio wireless links. The optimization of the CD-induced power fading is experimentally verified and link performance shows high tolerance to CD with no power penalties and the measured error vector magnitudes well below the required limits. The predicted bit error rates are also below the forward error correction threshold of 2×10^{-4}.

Index Terms: Millimeter-wave, sub-6 GHz, multi-RAT, radio-over-fiber, free-space optics, microwave photonic link.

1. Introduction

The data traffic on wireless communications is growing exponentially due to the use of ever-increasing number of devices, e.g., smartphones, laptops, tablets, etc., requiring access to multi-Gb/s bandwidth-demanding applications and services. The sub-6 GHz radio access technology (RAT) has been developed for the 5th generation (5G) wireless networks to address this demand [1], [2]. These sub-6 GHz bands offer promising attributes for mobile broadband and possess interesting propagation characteristics to support wide area coverage. However, to support the growing demand for the bandwidth, the communication industry is moving to the higher radio frequency (RF) range in the millimeter-wave (mmW) bands, e.g., mmW RAT [3]. In 2016, the Federal Communications Commission officially announced the frequency slots in the mmW bands of 24.75 $-$25.25, 27.5 $-$28.35, 38.6 $-$40 and 57 $-$71 GHz as part of 5G [4]. In early 2020, Global System for Mobile Communications Association updated the 5G spectrum public policy position with the emphasizes on 26, 28 and 40 GHz frequencies, which has currently received the most international support and strong momentum from operators due to the widest harmonization with minimized user equipment complexity [2].

Despite the fact that the mmW frequency bands are capable of offering ultra-high broadband services, i.e., multi-Gb/s data rate (R_b), which is envisioned for the broadband access network in 5G, the high signal attenuation due to the atmospheric condition (gaseous, rain, snow, turbulence, etc.) limits the transmission range d. For example, a 28 GHz mmW point-to-point communication system was demonstrated in [5] with R_b of 2 Gb/s at d of 1 km, which implies that only users close to the cell site will receive the full benefit of mmW-based wireless service. In addition, mmW signals are unable to penetrate most solid materials very well, since they are more susceptible to blockages such as walls, buildings and trees. E.g., at 40 GHz the signal attenuation through 10 cm concrete materials is 175 dB compared to $\sim$18 dB at sub-6 GHz (i.e., $<$ 3 GHz) [5].

Therefore, to (*i*) reuse the transport networks of current sub-6 GHz RAT for the new mmW RAT and (*ii*) offer more widespread 5G deployments for supporting all use cases at a low cost and reduced time, co-transmission of the sub-6 GHz and mmW wireless signals over the current mobile transport i.e., mobile fronthaul/backhaul are highly desirable and attractive. The microwave photonic link (MPL), i.e., radio-over-fiber, has been represented as an attractive alternative technology with numerous advantages such as low attenuation, ultra-broad bandwidth, excellent flexibility and immunity to RF electromagnetic interference [6]–[10]. In the centralized radio access network architecture using MPL, multiple RF signals are generated at the central station (CS) and directly transmitted to the base station (BS) via an optical distribution network (ODN), e.g., optical fiber, with no protocols and interfaces modifications and therefore significantly reducing cell site hardware complexity and cost [11]. At the BS, the received multiple RF signals are electrically amplified and then radiated via antennas (ANTs) to the user equipment. Furthermore, as demonstrated in [12], the MPL is also applicable for the implementation of multiple-input multiple-output technology, which increases the link capacity enormously.

The simplest method for simultaneous transmission of mmW and sub-6 GHz wireless signals is to employ the MPL-based wavelength-division-multiplexing technology. However, assigning an optical wavelength per RAT is a costly and bulky solution due to the use of multiple optical transmitters (Txs) and receivers (Rxs), i.e., lasers, optical modulators and high-speed photodetectors (PDs) [13]. It is worth mentioning that high-speed PDs are relatively expensive; they however can be reused for future wireless networks, where mmW RATs are widely operated. In addition, with the ongoing development of optoelectronic devices and integration technologies, commercial high-speed PDs (i.e., $>$ 20 GHz bandwidth) could become more cost-effective in the next few years. Therefore, the option of adopting MPL for supporting multi-RAT in a compact and cost-effective manner using only a single laser would be highly desirable. There are two possible solutions, which have been proposed and demonstrated recently using:

1) Subcarrier multiplexing via an electrical combiner [14], [15]. This solution is simple and cost-effective. However, the intermodulation distortion owing to the combination of two electrical signals is high and more importantly, the effect of fiber chromatic dispersion (CD) is severe,

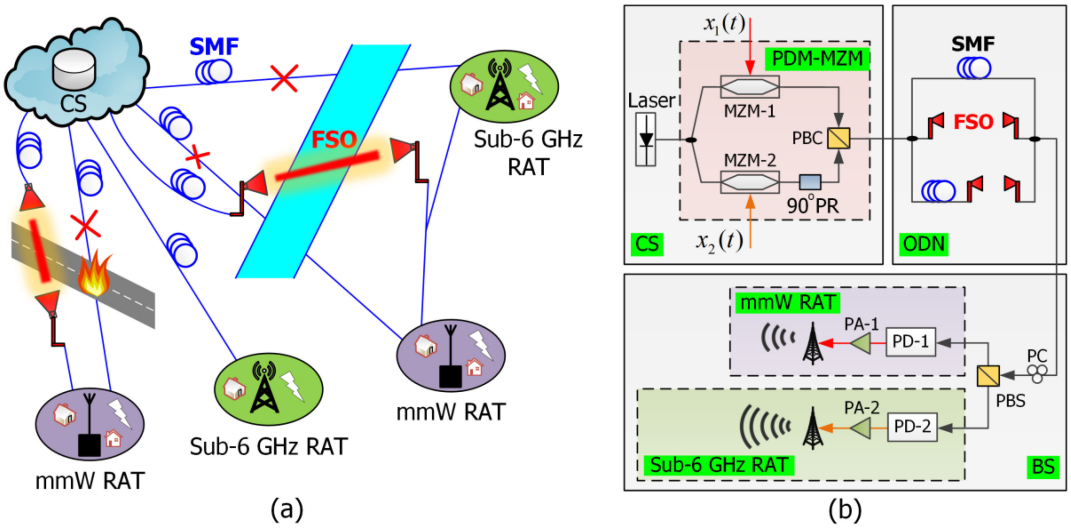

Fig. 1. (a) A converged fiber-FSO-wireless systems for 5G and beyond networks and (b) schematic of the proposed system with PDM-MZM for the co-transmission of mmW and sub-6 GHz signals.

especially for the mmW signal when simple optical double-sideband (DSB) modulation is employed [14].

2) Dual-drive MZM technique [16], [17]. This approach requires the optimization of both bias voltages applied to the dual-drive MZM and an optical interleaver to separate the multi-RF signals [17].

In these works, only a single-mode fiber (SMF) channel was employed for the signal transmission. In addition, no sub-6 GHz wireless link was carried out. In this work, for the first time, to the best of our knowledge, we propose and experimentally demonstrate the co-transmission of mmW (i.e., 25 GHz) and sub-6 GHz (i.e., 2.6 GHz) signals based on the polarization division multiplexing-MZM (PDM-MZM) technique over two configurations of ODN, which consists of (*i*) only a SMF channel, namely PDM-MPL and (*ii*) a hybrid optical link (i.e., of SMF and FSO) known as PDM-hybrid microwave photonic link (PDM-HMPL) under atmospheric turbulence (AT).

Note that, in ultra-dense urban areas, the deployment of optical fiber cables is costly, complex and requires the right of access. Therefore, in such cases as well as in areas where there are very limited coverage or no coverage at all due to damaged optical fibers or environmental disasters, the FSO technology could be deployed at reduced cost and time to provide flexible wireless services prior to the final RF transmission from nodes to users, see Fig. 1(a). However, both RF (especially mmW) and optical signals will experience attenuation and distortions imposed by the channels. In the SMF channel, CD is more severe for the DSB-based modulation scheme because of the relative phase changes between the optical carrier (f_{oc}) and sidebands (f_{sb}) frequencies, which will seriously deteriorate the quality of transmission signals [18]. In the FSO channel, the propagating signal will experience both attenuation and fluctuations due to fog and AT. The latter is due to random small-scale temperature variations along free-space channel, which results in changes of the refractive index and thus irradiance variations [19]. These detrimental effects lead to an extremely low received RF power (P_{rRF}) level at the Rx, thus resulting in a reduction of demodulated signal quality in terms of distorted quadrature amplitude modulation (QAM) constellation diagrams, high error vector magnitude (EVM) and bit error rate (BER). In this work, to compensate for the CD-induced relative phase changes, we propose a simple technique based on a tunable polarization controller (PC) at the BS to adjust the phase of f_{oc}. By properly controlling the PC, the CD-induced power fading on RF wireless signals are optimized independently regardless of the AT-induced power fading effect. We have observed no performance degradation due to CD for mmW and sub-6 GHz signals using the optical DSB modulation. By adopting the proposed scheme, P_{rRF} is

maintained at the desirable level with discernible constellation diagrams and improved EVM and BER without employing complex high-speed digital signal processing [20]. This, ultimately, leads to the reduced complexity and cost of the transport system.

It is worth to mention that, in [18] tunable PCs were used to optimize the CD-induced power fading in 6 GHz MPL. Two tunable PCs were employed since the two vector signals at the Tx were independently intensity- and phase-modulated by a complex in-phase-quadrature MZM, which consisted of 4 phase modulators and a polarization rotator (PR). However, no work has been reported on the hybrid SMF-FSO and RF wireless system.

The remainder of this paper is structured as follows. Section 2 describes the proposed system and provides simulation analysis on the simultaneous transmission of 5G-envisioned mmW and sub-6 GHz signals and the CD-induced power fading optimization. Section 3 describes the proof-of-concept experimental setup, while Section 4 discusses the extensive experimental results. Finally, Section 5 outlines the conclusions of the work.

2. Operating Principle and Simulation Analysis

2.1 Link Structure

The schematic diagram of the proposed system is shown in Fig. 1(b). At the CS, the laser output at a central wavelength of 1550 nm is equally split into two branches, which are applied to two MZMs for external modulation by the mmW $x_1(t)$ and sub-6 GHz $x_2(t)$ signals via the RF input ports of the MZM-1 and MZM-2, respectively. To ensure orthogonality of both polarization states, a PR at the output of MZM-2 is used to rotate the state of polarization of the optical signal by 90°. Both optical signals are subsequently multiplexed using a polarization beam combiner (PBC), the output of which is transmitted to ODN via a SMF. Note that, the PDM-MZM is a commercially available integrated device, as recently demonstrated in [21].

In ODN, the polarized optical signal can be transmitted via three paths of (*i*) SMF, (*ii*) FSO, and (*iii*) hybrid SMF-FSO. Next, the output of ODN is applied to two Rxs at the BS via the tunable PC, which is employed to optimize the CD-induced power fading, and a polarization beam splitter (PBS). The regenerated $x_1(t)$ and $x_2(t)$ signals are further amplified using power amplifiers (PAs) prior to being wirelessly transmitted via commercial ANTs.

2.2 Simulation Results

For the initial link analysis, we first use OptiSystem-MATLAB co-simulation platform to evaluate the performance of the simultaneous transmission of mmW and sub-6 GHz signals over the SMF channel. Since the distance of 5G optical fronthaul links between CS and BS is typically below 20 km, we consider 10 and 15 km of SMF to represent practical links. As a benchmark, the optical back-to-back (OB2B) link (i.e., no ODN) is also considered. Note that, the optical power at the output of the PDM-MZM is set at 0 dBm. We first investigate the co-transmission of $x_1(t)$ and $x_2(t)$ signals, i.e., 25 and 2.6 GHz 4-QAM, respectively at R_b of 4 Gb/s (2 GHz bandwidth) with the input RF power levels of 10 and 0 dBm, respectively. To assess the impact of CD, we have not used PC. Fig. 2(a–c) depicts the simulated optical spectra for x_1 and x_2-polarization multiplexed signals at the input of PD-1 for OB2B, 10 and 15 km SMF, respectively. As can be seen in Fig. 2(a), the optical spectra clearly show the DSB intensity-modulated scheme for $x_1(t)$ with 25 GHz frequency spacing from the optical-data-tone to $f_{\rm oc}$. However, for the cases of 10 and 15 km SMFs, see Figs. 2(b) and (c), we observe not only the reduction in optical power of $x_1(t)$ compared with OB2B but also the optical signal leakage of $x_2(t)$ (i.e., 2.6 GHz carrier component). This is due to the crosstalk between the two polarizations in a PDM system over a long SMF. The longer SMF distances, the more pronounced leakage, which in turn, leads to polarization misalignment and especially, the CD-induced power fading effect at the Rx. However, by controlling the PC, we can flexibly adjust the polarization misalignment between the optical signals from the two MZMs and compensate for the CD [18].

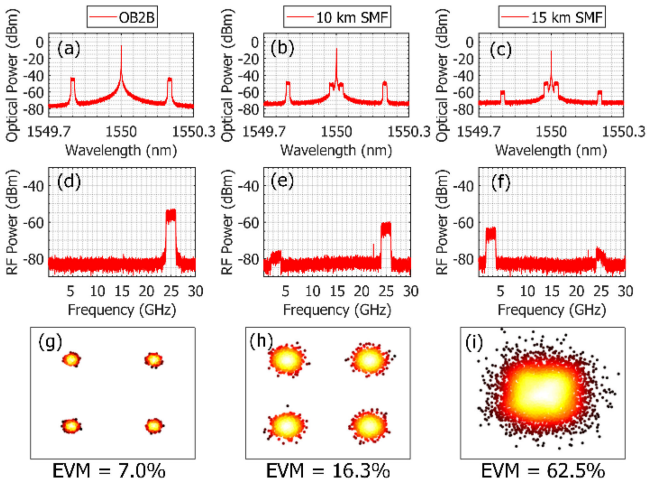

Fig. 2. Simulated optical spectra (a–c); received electrical spectra (d–f); and constellation diagrams of the $\boldsymbol{x}_1(\boldsymbol{t})$–25 GHz 4-QAM signal (g–i) for OB2B, 10 and 15 km SMF links.

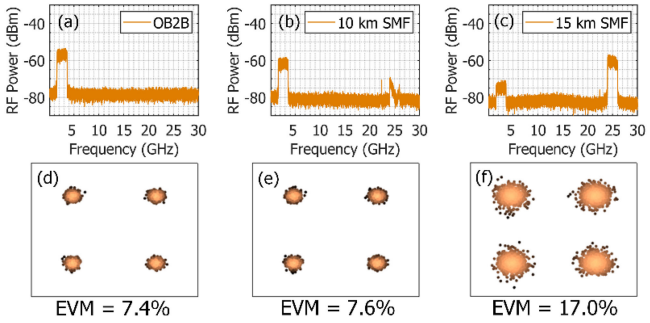

Fig. 3. Simulated received electrical spectra (a–c); and constellation diagrams of the $\boldsymbol{x}_2(\boldsymbol{t})$–2.6 GHz 4-QAM signal (d–f) for OB2B, 10 and 15 km SMF links.

Fig. 2(d–f) depicts the corresponding spectra of the electrical signals at the output of PA-1 for OB2B, 10 and 15 km SMF links. Note that, for 15 km SMF, P_{rRF} of $x_1(t)$ is reduced by 22 and 15 dB compared with OB2B and 10 km SMF, respectively. The constellation diagrams for OB2B, 10 and 15 km SMF links are illustrated in Fig. 2(g–i). For the OB2B and 10 km SMF links, the EVM values are 7.0 and 16.3%, respectively, which are below the 17.5% EVM requirement. For the 15 km SMF link, it is not possible to demodulate the signal due to the significant reduction of received power.

Similarly, Fig. 3 depicts the performance of the $x_2(t)$, where the spectra at the output of PA-2 for OB2B, 10 and 15 km SMF links are shown in Fig. 3(a–c). We also observe the inter-channel interference from $x_1(t)$ (i.e., 25 GHz carrier component) following transmission over 10 and 15 km SMFs. The constellation diagrams depicted in Fig. 3(d–f) show reduced distortions compared with Fig. 2(g–i). However, unlike $x_1(t)$, the effect of CD-induced power fading on $x_2(t)$ is less severe since the signal power periodically fades with the increasing of the carrier frequency [18]. The EVM values for OB2B, 10 km and 15 km SMF links are 7.4, 7.6 and 17.0%, which are below the 17.5% EVM level.

2.3 Optimization of the CD-induced Power Fading

In the previous section, we investigated the effect of CD-induced power fading due to the relative phase changes between f_{oc} and f_{sb} for mmW and sub-6 GHz signals. However, the phase difference can be tuned using a tunable PC at an angle of ϕ and thus the compensation of power fading for $x_1(t)$ and $x_2(t)$ can be achieved. The results are depicted in Fig. 4.

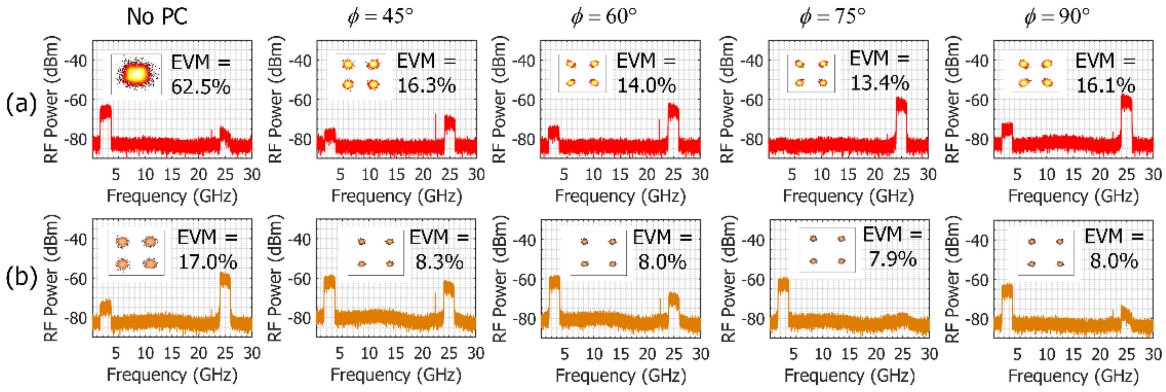

Fig. 4. Simulated received electrical spectra of: (a) $x_1(t)$ and (b) $x_2(t)$ for different PC angles for 15 km SMF transmission. Insets are the corresponding constellation diagrams.

As shown previously, for $x_1(t)$ with no tunable PC we observe significantly reduced P_{rRF} and the presence of $x_2(t)$ following transmission over a 15 km SMF link. However, using a tunable PC with ϕ set within the range of 45°–90° (at a step of 15°), the effect of power fading for $x_1(t)$ is gradually improved and the optimum P_{rRF} of −60 dBm is achieved at ϕ of 75°, see Fig. 4(a). Note that, by controlling the PC, the existence of $x_2(t)$ is simultaneously suppressed. At ϕ of 75° the constellation diagram is stable with an EVM of 13.4%, which is well below the 17.5% EVM level for 4-QAM. Similar for $x_2(t)$, see Fig. 4(b), at ϕ of 75° we observe (*i*) full recovery of $x_2(t)$ with reduced interference (i.e., 19 dB) due to $x_1(t)$ and (*ii*) a clear constellation diagram with the best EVM of 7.9% (i.e., 9.1% EVM improvement in comparison to the case with no PC). It is worth mentioning that the EVM performance of both $x_1(t)$ and $x_2(t)$ can be further improved by suitably increasing the input RF power. This is important because higher signal bandwidth and modulation formats (i.e., 256-QAM) with the low required EVM limit of 3.5% are considered in future wireless networks.

3. Experimental Setup

A complete experimental proof-of-concept system schematic is shown in Fig. 5(a). A continuous wave from the laser source (ID Photonics Cobrite-DX4) is applied to a PDM-MZM module, which is composed of two zero-chirp single-drive MZMs (MZM-1–Fujitsu FTM7938EZ/210 and MZM-2–Covega Mach-10^{TM} 081), via a 50/50 coupler.

Because of the equipment limitation, we could generate relatively narrow bandwidth signals and transmit them over the system to prove the proposed concept. Different modulations i.e., 4-, 16- and 64-QAM with a bandwidth range of 5 to 20 MHz can be adaptively configured. However, for the upper branch, we investigate only the maximum signal bandwidth of 20 MHz for 4/16/64-QAM with the corresponding highest R_b of 40, 80 and 120 Mb/s, respectively [22], which are generated by a vector signal generator (VSG-1–R&S SMW200A). These are the evolved universal terrestrial radio access 3.3, 3.2 and 3.1 test models, respectively as defined by the standard. The mmW signal $x_1(t)$ is then electrically up-converted to 25 GHz using a signal generator (R&S SMF100A) via an electronic mixer prior to being amplified by a power amplifier (PA-1–Wisewave AGP-33142325-01) to a level of 10 dBm. For the lower branch, the sub-6 GHz signal $x_2(t)$, i.e., the 4/16-QAM microwave vector signals with the carrier frequency and signal bandwidth of 2.6 GHz and 17 MHz, is generated using a VSG-2 (R&S SMIQ3B). Note that, for 4- and 16-QAM R_b values are 34 and 68 Mb/s, respectively, and the input RF power of $x_2(t)$ is set to 0 dBm.

The outputs of externally modulated MZMs are applied to two PCs, which are properly adjusted to achieve the desired orthogonal state of polarization prior to being multiplexed using a PBC for transmission over (*i*) a 20 km SMF and (*ii*) a hybrid SMF-FSO link i.e., 20 km and 4.2 m, respectively. Considering that the optical power measured after the PBC is 0 dBm, the optical

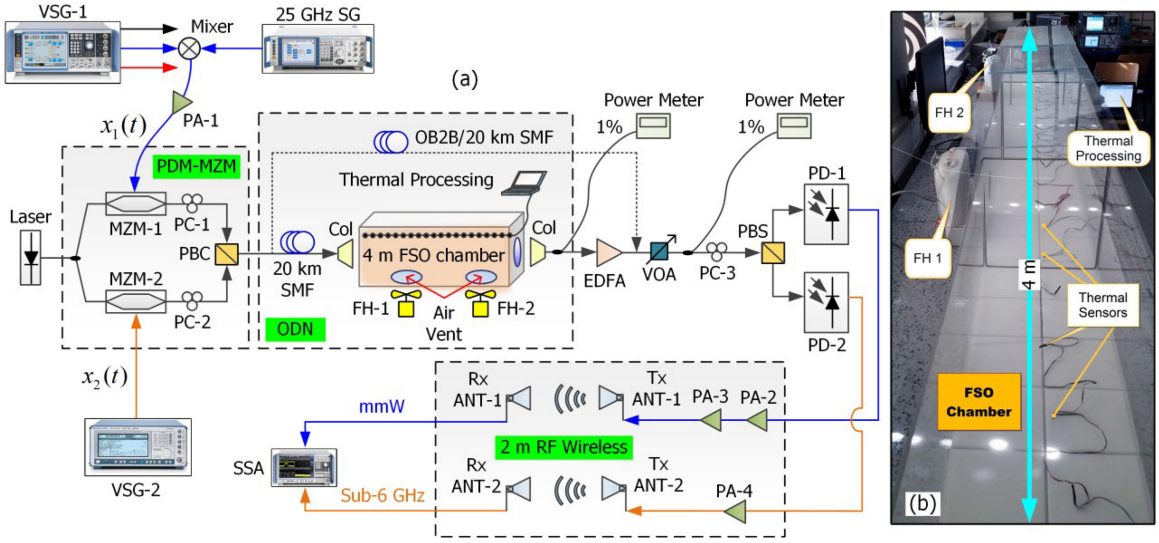

Fig. 5. (a) Experimental setup and (b) turbulent FSO chamber. MZM: Mach-Zehnder modulator, PC: polarization controller, PBC: polarization beam combiner, SMF: single-mode fiber, FSO: free-space optics, FH: fan heater, Col: collimator, EDFA: erbium-doped fiber amplifier, VOA: variable optical attenuator, PD: PIN photodiode, PA: power amplifier and ANT: antenna.

nonlinear effect in SMF therefore can be neglected. For the FSO link, we used (*i*) a pair of air-spaced doublet collimators (Col–Thorlabs F810APC-1550) and (*ii*) an indoor atmospheric turbulent chamber with a dimension 4 × 0.4 × 0.4 m, see Fig. 5(b), to investigate the impact of AT on the signal quality. Note that, the AT strength is usually characterized by the refractive index structure parameter C_n^2 ($m^{-2/3}$) ranging from 10^{-17} to 10^{-13} $m^{-2/3}$ for weak-to-strong AT regimes in outdoor environments [23]. To generate AT within the chamber, we used two external fan heaters (FHs) located at both ends of the chamber blowing hot air perpendicularly to the propagating direction the optical beam and 20 temperature sensors positioned along the chamber to measure the temperature profile and thus C_n^2. Note that, the performance of a short laboratory FSO link can be equivalent to a longer outdoor FSO link by retaining the Rytov variance (σ_R^2). Details of the AT generation, σ_R^2 and C_n^2 levels processing can be found in [13].

The optical signal after the FSO link is amplified using an erbium doped fiber amplifier (EDFA–Keopsys CEFA-C-HG-SM-50-B130-FA-FA) with the pump power kept constant for all measurements with and without AT to maintain the same noise conditions for a fair comparison between different QAM formats. Following amplification, the optical signal is applied to a variable optical attenuator (VOA), which is used to vary the received optical power and corresponding P_{rRF} values at the receiving end. The transmission performance of each RF signal is comprehensively evaluated in terms of EVM, BER, signal-to-noise-ratio (SNR), P_{rRF} and constellation diagrams. Note that, P_{rRF} is the critical parameter for link performance evaluation since it is measured at the user equipment and used to estimate the achievable *d* under different weather conditions. Next, the two orthogonally polarized light waves are applied to the 3-tunable-knob PC-3 and PBS and then detected by two different PDs (i.e., PD-1–Optilab PD-40 and PD-2–New Focus 1554-B), respectively. By properly controlling the PC-3, the CD-induced power fading can be optimized for $x_1(t)$ and $x_2(t)$, resulting in enhanced recovered RF power, clear constellation diagrams and low EVMs. Note that, the measured optical power at both PD inputs is approximately 0 dBm.

The output of the PD-1 is further amplified using a cascaded PAs (PA-2–Miteq AMF-4F-260400-40-10p and PA-3–Analog device HMC1131) prior to being transmitted over a 2 m RF wireless channel using a pair of double ridged waveguide horn ANTs (Tx ANT-1 and Rx ANT-1–RFSpin DRH40). The output of the PD-2 is also amplified using a PA-4 (Mini circuits ZVA-213-S+) for transmission over a 2 m RF wireless link using pair of double ridged waveguide horn ANTs (Tx

TABLE 1
Key Parameters used in Experiments

Parameter			**Value**
Optical domain	Laser	Wavelength	1550 nm
		Output power	15 dBm
	SMF	Length and attenuation	20 km and 0.2 dB/km
		Chromatic dispersion	17 ps/(nm·km)
	FSO	Collimator aperture	24 mm
		Length and loss	4.2 m and 8 dB
	EDFA	Output power	7.2 dBm
		Noise figure	< 5 dB
$x_1(t)$, **($x_2(t)$)**	Carrier frequency		25 GHz **(2.6 GHz)**
	Modulation format		4/16/64-QAM **(4/16-QAM)**
	Bit rate		40/80/120 Mb/s **(34/68 Mb/s)**
	PD-1 **(PD-2)**	Responsivity	0.8 A/W **(0.85 A/W)**
		Bandwidth	33 GHz **(12 GHz)**
	PA-2 **(PA-4)**	Gain	22 dB **(26 dB)**
		Noise figure	1.7 dB **(3 dB)**
		Bandwidth	24 – 27 GHz **(0.8 – 21 GHz)**
	PA-3	Gain	27 dB
		Noise figure	2 dB
		Bandwidth	18 – 26.5 GHz
	ANT-1 **(ANT-2)**	Frequency range	4 – 40 GHz **(0.74 – 10.5 GHz)**
		Gain	15 dBi **(11 dBi)**
		Wireless channel length	2 m **(2 m)**

ANT-2 and Rx ANT-2–RFSpin DRH10). The received mmW and sub-6 GHz signals are captured using a signal and spectrum analyzer (SSA–R&S FSW) for performance evaluation. Note that, (*i*) all ANTs are fixed at the height of 1 m for the ideal alignment to maximize the signal strength at the Rx, (*ii*) the separation of two Tx ANTs and two Rx ANTs is 12 cm, and (*iii*) transmitting and receiving ANTs are in line-of-sight and operating at different frequency regions in order to minimize the interchannel interference. All the key system parameters adopted in the experimental setup are summarized in Table 1.

4. Experimental Results and Discussion

4.1 Link Performance of PDM-MPL (SMF and RF Wireless)

We first evaluate the link performance in terms of EVMs and BERs as a function of P_{rRF} for the 25 GHz mmW signal with 16-QAM i.e., $x_1(t)$ for OB2B + 2 m RF wireless link (denoted as OB2B) and 20 km SMF with a 2 m RF wireless link (denoted as PDM-MPL) as shown in Fig. 6.

As shown in Fig. 6(a), for OB2B and PDM-MPL the lowest EVM values are 2.1 and 5.4% at P_{rRF} of −44 and −55 dBm, respectively. A corresponding 16-QAM constellation for OB2B is clearly observed, as can be seen in the inset. The resultant RF power reduction between OB2B and PDM-MPL is attributed to the loss of the 20 km SMF since the EDFA is not used in this case. Also shown is the required limit of 12.5% EVM for 16-QAM according to 3rd generation partnership project (3GPP) standard [24]. Noticeably, almost no RF power penalty is observed at the EVM required limit. This is because the polarization misalignment and CD-induced power fading are

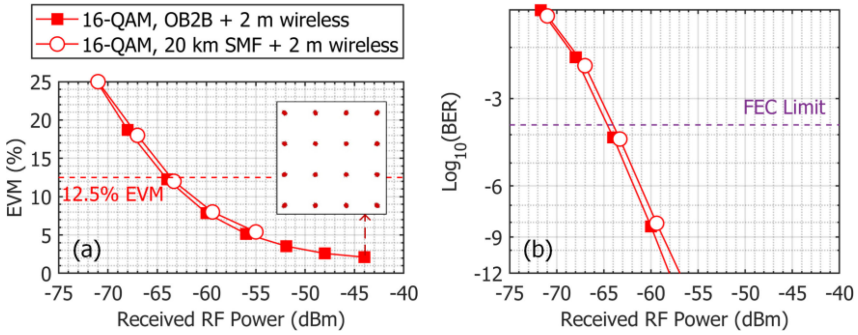

Fig. 6. (a) Measured EVMs and (b) calculated BERs versus received RF power for 25 GHz signal with 16-QAM format. Inset is the constellation obtained at $\boldsymbol{P}_{\mathrm{rRF-Max}}$ for OB2B.

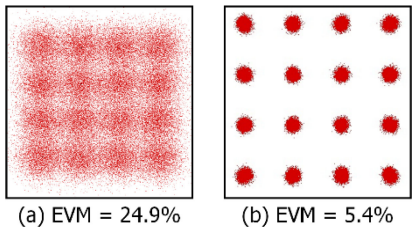

Fig. 7. The constellation diagrams of the received 25 GHz signal with 16-QAM: (a) before and (b) after optimization of CD-induced power fading.

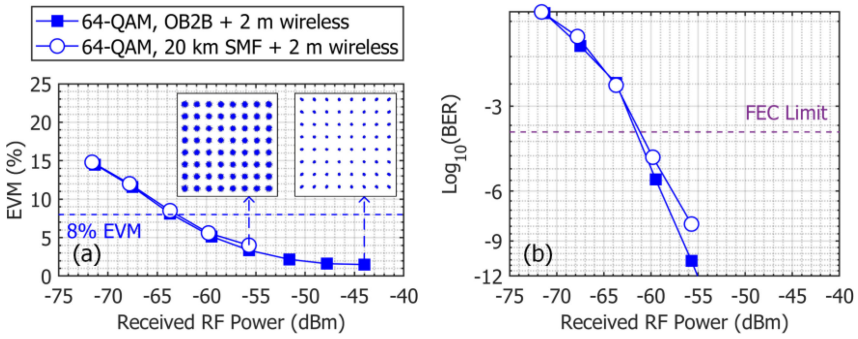

Fig. 8. (a) Measured EVMs and (b) calculated BERs versus the received RF power for 25 GHz 64-QAM. Insets are the constellations obtained at $\boldsymbol{P}_{\mathrm{rRF-Max}}$ for OB2B and PDM-MPL.

optimized by properly controlling the PC-3 as we have described in Section 2. The BER versus P_{rRF} is depicted in Fig. 6(b) based on the EVM-BER relationship for M-QAM as given in [13]. We see that, the BERs of the 16-QAM signal for OB2B and PDM-MPL cases are lower than the BER of 1×10^{-12} for P_{rRF} larger than -58 dBm, which indicates error-free transmissions. Comparing at the FEC limit of 2×10^{-4}, both cases are met at P_{rRF} of -64.5 dBm.

To demonstrate the mitigation of CD-induced power fading, we have determined the constellation diagrams before and after the optimization for the PDM-MPL, as shown in Figs. 7(a) and (b), respectively. As can be clearly seen, without optimization the constellation diagram is highly distorted, thus leading to a high EVM of 24.9%, which is well above the required EVM limit of 12.5%. With optimization, the constellation diagram is clear and stable with the EVM of 5.4%, i.e., considerably less than 12.5% limit.

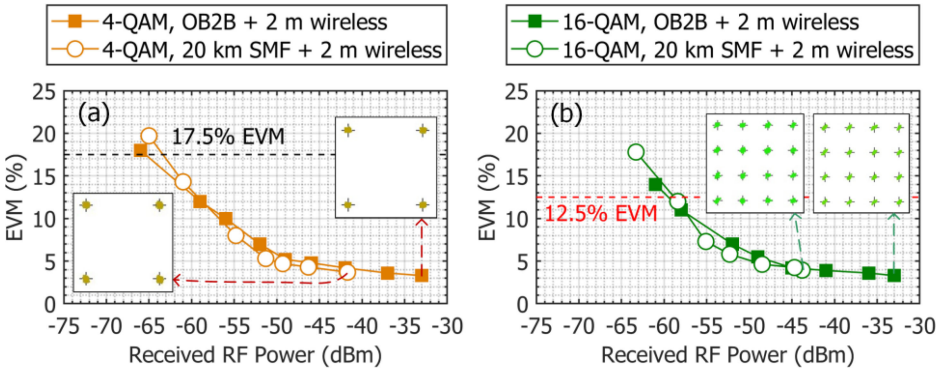

Fig. 9. Measured EVMs versus the received RF power for 2.6 GHz with (a) 4-QAM and (b) 16-QAM. Insets are the constellations obtained at $P_{\mathrm{rRF-Max}}$ for OB2B and PDM-MPL.

Similarly, the results for the mmW signal with 64-QAM are shown in Fig. 8. For OB2B and PDM-MPL, the best EVM values are 1.5 and 4%, which are below the 8% EVM requirement for 64-QAM [24], at P_{rRF} of -44 and -56 dBm, respectively, see Fig. 8(a). For PDM-MPL, following compensation of the CD-induced power fading, P_{rRF} has been well recovered, which therefore results in a discernable 64-QAM constellation, see inset. In addition, no RF power penalty is observed in comparison to OB2B, confirming also the effectiveness of the optimization technique for higher-order QAM. As for the BER performance, an error-free transmission (i.e., BER $< 1 \times 10^{-12}$) is observed for OB2B, see Fig. 8(b). While the best BER for PDM-MPL is about 1.4×10^{-8}, which is well below the FEC threshold. Comparing at the FEC limit, both cases are met at P_{rRF} of -61.5 dBm. Relating to the 16-QAM signal in Fig. 6(b), we observe only 3 dB RF power penalty when changing from 16- to 64-QAM format. The performance of 64-QAM is worse than 16-QAM signal regardless of transmission scenarios owing to the fact that the SNR requirement is more stringent for higher-order modulation, that is investigated in the next sub-section.

We have further evaluated the EVM performance for $x_2(t)$ with 4- and 16-QAM format for both OB2B and PDM-MPL configurations, as shown in Fig. 9. As illustrated, for 2.6 GHz 4- and 16-QAM the measured EVMs are well below the EVM limits over a wide range of P_{rRF}. Note that, the performance of lower frequency bands is superior compared with $x_1(t)$ due to the lower signal propagation losses.

In detail, under OB2B, the 2.6 GHz 4- and 16-QAM signals have the lowest EVM of 3.3% measured at the maximum P_{rRF} of -33 dBm. For the 2.6 GHz 16-QAM signal at P_{rRF} of -44 dBm, the measured EVM is 4.1%, which is about 2% higher than that of $x_1(t)$, see Fig. 6(a). For the 2.6 GHz 16-QAM signal at P_{rRF} of -44 dBm, the measured EVM is 4.1%, which is about 2% higher than that of $x_1(t)$, see Fig. 6(a). This agrees well with the simulation results in Section 2 since $x_1(t)$ has a higher input RF power. Comparing between PDM-MPL and OB2B configuration, almost no RF power penalty is observed for each signal. Based on the measured EVMs, the resultant BERs are also calculated with the values well below the BER of 10^{-12}, which indicate error-free transmissions for $x_2(t)$ with both 4- and 16-QAM formats. The received constellation diagrams for all cases are depicted in the insets. The practicality of the proposed PDM-based system for the co-transmission and optimization of the CD-induced power fading for 25 and 2.6 GHz wireless signals is therefore validated.

4.2 Link Performance of PDM-HMPL (Hybrid SMF-FSO and RF Wireless)

In this section, we investigate the performance of PMD-HMPL (i.e., a hybrid optical channel of 20 km SMF and 4.2 m FSO) without and with AT and a 2 m RF wireless link (denoted as PDM-HMPL).

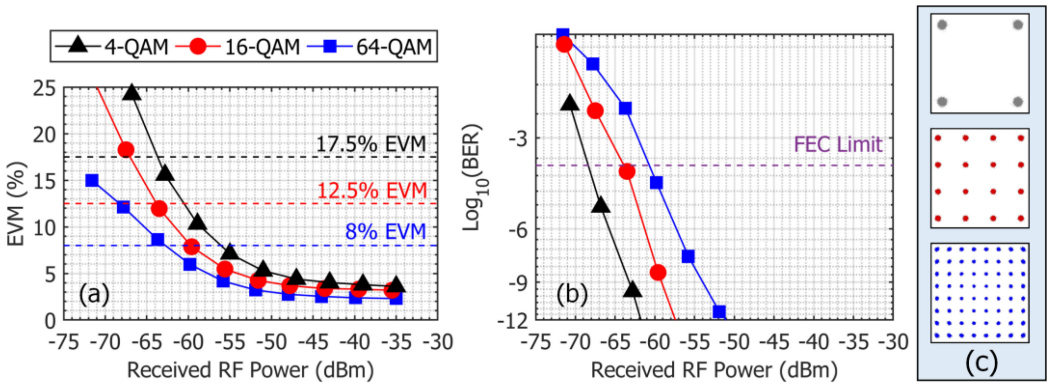

Fig. 10. (a) Measured EVMs and (b) calculated BERs versus the received RF power for 25 GHz with 4/16/64-QAM. (c) Constellation diagrams obtained at $\boldsymbol{P}_{\mathrm{rRF-Max}}$ for PDM-HMPL without AT.

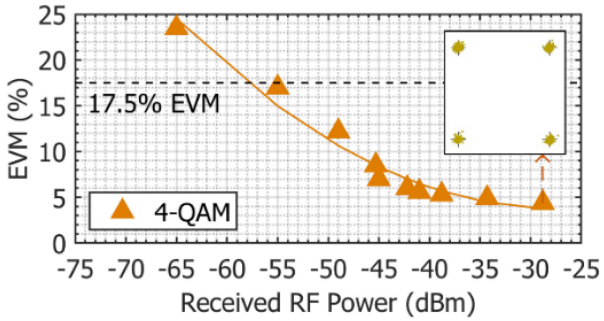

Fig. 11. Measured EVMs versus the received RF power for 2.6 GHz with 4-QAM. Inset is the constellation diagram at $\boldsymbol{P}_{\mathrm{rRF-Max}}$ for PDM-HMPL without AT.

4.2.1. Measurements Without AT: Fig. 10(a) shows the post-optimization EVM as a function of P_{rRF} for $x_1(t)$ with 4-, 16- and 64-QAM under no AT i.e., C_n^2 is 2.59×10^{-14} $\mathrm{m}^{-2/3}$. As shown, the EVM plots display exponential drop with P_{rRF} having the lowest EVM values of 3.6, 3.2 and 2.3% at P_{rRF} of -35 dBm for 4-, 16- and 64-QAM, respectively. Note that, the extended P_{rRF} range (i.e., lower EVMs) is due to the use of EDFA. The BER plots for 4-, 16- and 64-QAM are illustrated in Fig. 10(b) together with the FEC limit. The lowest EVM values of 3.6, 3.2 and 2.3% correspond to error-free transmissions i.e., BER of less than 10^{-12}. The constellation diagrams at P_{rRF} of -35 dBm for QAM signals are also displayed in Fig. 10(c), which are clear and stable. Compared with 64-QAM in OB2B, see Fig. 8(a), at P_{rRF} of -44 dBm we observe the EVM penalty of 1%, which demonstrates the benefit of adopting FSO in ODN.

For $x_2(t)$ in PDM-HMPL, we have evaluated only the microwave vector signal with 4-QAM. The EVM performance is given in Fig. 11. As expected, the lowest EVM is 4.4% at P_{rRF} of -28.8 dBm with a clear constellation shown in the inset, thus demonstrating full recovery of the 2.6 GHz signal following optimization. In comparison to 4-QAM in OB2B, see Fig. 9(a), at P_{rRF} of -33 dBm, the EVM penalty is only 1%, which indicates the practicality of the proposed HMPL for the co-transmission of mmW and sub-6 GHz wireless signals.

To further evaluate the proposed PDM-HMPL as part of the future converged mmW and sub-6 GHz RATs, we measured the EVM values and then converted them to BERs as a function of the electrical SNR for both 25 GHz 4/16/64-QAM and 2.6 GHz 4-QAM signals under no AT, see Fig. 12(a) and (b), respectively. All cases show the best BERs below the FEC threshold. For the 25 GHz signal, the minimum SNR required for 4-QAM to satisfy the FEC limit is about 16.5 dB.

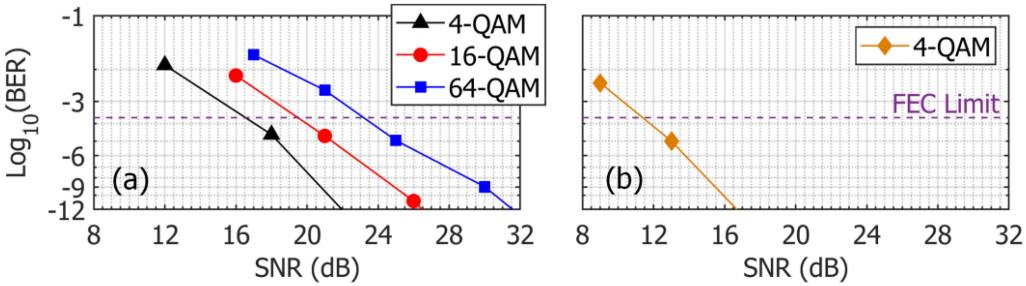

Fig. 12. Calculated BERs versus SNR at the Rx for: (a) 25 GHz with 4/16/64-QAM and (b) 2.6 GHz with 4-QAM.

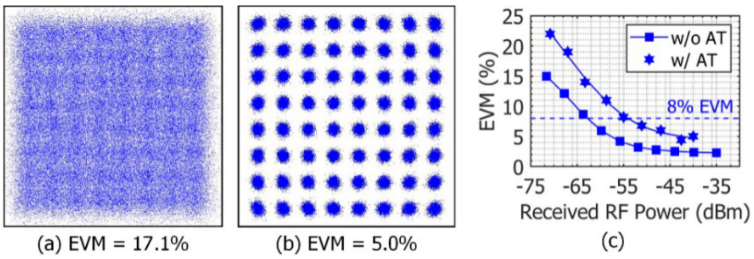

Fig. 13. The constellation diagram of the received 25 GHz with 64-QAM: (a) before and (b) after the optimization of the power fading. (c) Measured EVMs versus P_{rRF}.

While that of 16- and 64-QAM are about 19.5 and 23.5 dB leading to 3 and 7 dB more in comparison to 4-QAM. For the 2.6 GHz signal, the required SNR for 4-QAM is only 11.5 dB, which is 5 dB lower than that of 25 GHz 4-QAM signal since it is operated in the sub-6 GHz frequency band.

4.2.2. Measurements With AT: In this case, we examine only $x_1(t)$ with 64-QAM under AT. After offline processing the recorded temperature profile based on Equations (2) and (3) in [13], the σ_R^2 and C_n^2 are calculated about 0.011938 and 1.49×10^{-11} $\mathrm{m}^{-2/3}$, respectively. As expected, the joint effect of CD- and AT-induced power fading significantly limits the performance of the mmW wireless service, as seen from the constellation diagram in Fig. 13(a). The constellation diagram is highly distorted due to the strong correlation between adjacent symbols, which results in a high EVM level of 17.1% (i.e., higher than the required EVM limit) and a corresponding BER of 5.9×10^{-2} (i.e., above the FEC threshold). The CD-induced power fading, however, can be separately optimized regardless of the AT-induced power fading through properly controlling the PC-3. Following optimization, P_{rRF} is recovered, which, in turn, leads to an improved constellation diagram with a low EVM of 5.0% (i.e., lower than the required EVM limit) as depicted in Fig. 13(b) and the corresponding BER of 3.7×10^{-6} (i.e., below the FEC threshold). The EVM and BER performance of the 25 GHz mmW with 4- and 16-QAM can also be expected to satisfy the requirements.

Finally, Fig. 13(c) shows the EVM dependency on P_{rRF} for the link with and without AT. Note that, under AT, the propagating optical signals experience a higher degree of intensity and phase fluctuations, thus leading to the fluctuations in EVM. We observe that, with AT, the best EVM achieved is 5.0% and the corresponding BER is 3.7×10^{-6}. However, in contrast to the link without AT, the EVM quickly fails to meet the EVM criterion of 8% for $P_{\mathrm{rRF}} < -54$ dBm, while that of without AT is -63 dBm, see Fig. 10(a), which leads to a 9 dB RF power penalty. This shows clearly the power fading due to the effect of strong AT in FSO. At P_{rRF} of -44 dBm, the measured EVM is 5.2%, thus resulting in the EVM penalty of 3.7% compared with 64-QAM in OB2B, see Fig. 8(a). It is worth mentioning that by remaining the same σ_R^2 of 0.011938, the short indoor FSO link under

strong C_n^2 of 1.49×10^{-11} $m^{-2/3}$ is equivalent to the outdoor FSO link length of 760 m under the practical C_n^2 of 10^{-15} $m^{-2/3}$. This shows the viability of real-world implementation of the proposed PDM-HMPL with 20 km SMF and up to 760 m FSO for use in converged mmW and sub-6 GHz RATs. The performance of $x_2(t)$ signal with different QAM formats can also be anticipated to satisfy the requirements. In order to maximize the signal quality of both mmW and sub-6 GHz wireless services in a long-term practical implementation of the proposed PDM-HMPL, an adaptive digital PC should replace the PC-3 for an automatic optimization.

5. Conclusion

In this paper, a hybrid microwave photonic link containing a SMF and FSO under the AT using a PDM-MZM with the optimization of the CD-induced power fading regardless of the AT-induced power fading is proposed to support the co-existence of mmW and sub-6 GHz RAT. We first carried out in simulation the co-transmission of the multi-Gb/s intensity-modulated 25 and 2.6 GHz 4-QAM signals. The numerical simulation allowed us to obtain the optical and electrical spectra at different nodes of the proposed converged mmW and sub-6 GHz RATs and analyze the impact of CD-induced power fading on both multi-Gb/s link performances. We also showed the effectiveness of optimizing the single PC at the Rx to compensate for the relative phase changes between the optical carrier and the sidebands as they propagate over SMF, which, in turn, mitigates the CD-induced power fading. We then experimentally demonstrated the simultaneous transmission of both signals over a hybrid optical channel consisting of a 20 km SMF and 4 m FSO under the AT effect to comprehensively observe the impact of power fading due to CD and AT. After optimization, we achieved no performance degradation caused by the CD with the measured EVMs and predicted BERs for both signals using the optical DSB modulation. We also showed that, FSO link length can be equivalently extended up to 760 m in outdoor environments with a typical AT of 10^{-15} $m^{-2/3}$, which is adequate to cover ultra-dense, hotspot areas and emergency situations. As an advantage, the proposed PDM-based system can be reused to implement the transmission of both signals with the identical mmW carrier frequency, which therefore offers (*i*) high-capacity and (*ii*) seamless 2×2 multiple-input multiple-output transmissions for future wireless networks.

References

[1] "In the matter of expanding flexible use in the 3.7–4.2 GHz band," 2020. [Online]. Available: https://www.fcc.gov/document/fcc-expands-flexible-use-c-band-5g-0

[2] "5G spectrum GSMA public policy position," 2020. [Online]. Available: https://www.gsma.com/

[3] L. Wei, R. Hu, Y. Qian, and G. Wu, "Key elements to enable millimeter wave communications for 5G wireless systems," *IEEE Wirel. Commun.*, vol. 21, no. 6, pp. 136–143, Dec. 2014.

[4] "FCC takes steps to facilitate mobile broadband and next generation wireless technologies in spectrum above 24 GHz," 2016. [Online]. Available: https://www.fcc.gov/document/fcc-adopts-rules-facilitate-next-generation-wireless-technologies

[5] Z. Pi and F. Khan, "An introduction to millimeter-wave mobile broadband systems," *IEEE Commun. Mag.*, vol. 49, no. 6, pp. 101–107, Jun. 2011.

[6] X. Li, J. Yu, and G.-K. Chang, "Photonics-aided millimeter-wave technologies for extreme mobile broadband communications in 5G," *J. Lightw. Technol.*, vol. 38, no. 2, pp. 366–378, Jan. 2020.

[7] C. Lim, Y. Tian, C. Ranaweera, A. Nirmalathas, E. Wong, and K. Lee, "Evolution of radio-over-fiber technology," *J. Lightw. Technol.*, vol. 37, no. 6, pp. 1647–1656, Mar. 2019.

[8] H. Y. Wang, C. H. Cheng, C. T. Tsai, Y. C. Chi, and G. R. Lin, "28-GHz wireless carrier heterodyned from orthogonally polarized tri-color laser diode for fading-free long-reach MMWoF," *J. Lightw. Technol.*, vol. 37, no. 13, pp. 3388–3400, Jul. 2019.

[9] X. Chen and J. Yao, "Data rate quadrupled coherent microwave photonic link," *IEEE Photon. Technol. Lett.*, vol. 29, no. 13, pp. 1071–1074, Jul. 2017.

[10] E. Martin *et al.*, "28 GHz 5G radio over fibre using UF-OFDM with optical heterodyning," in *Proc. Int. Top. Meet. Microw. Photon.*, 2017, Paper. Th2.4.

[11] Y. Chen, J. Xiao, and Z. Dong, "Delivering dual polarization-division-multiplexing millimeter-wave signals at W-Band by one pair of antennas," *IEEE Photon. J.*, vol. 11, no. 5, pp. 1–10, 2019.

[12] X. Li *et al.*, "Delivery of 54-Gb/s 8QAM W-band signal and 32-Gb/s 16QAM K-band signal over 20-km SMF-28 and 2500-m wireless distance," *J. Lightw. Technol.*, vol. 36, no. 1, pp. 50–56, Jan. 2018.

[13] D.-N. Nguyen, J. Bohata, M. Komanec, S. Zvanovec, B. Ortega, and Z. Ghassemlooy, "Seamless 25 GHz transmission of LTE 4/16/64-QAM signals over hybrid SMF/FSO and wireless link," *J. Lightw. Technol.*, vol. 37, no. 24, pp. 6040–6047, Dec. 2019.
[14] P. T. Dat, A. Kanno, N. Yamamoto, and T. Kawanishi, "Full-duplex transmission of LTE-A carrier aggregation signal over a bidirectional seamless fiber-millimeter-wave system," *J. Lightw. Technol.*, vol. 34, no. 2, pp. 691–700, Jan. 2016.
[15] J. Zhang *et al.*, "Full-duplex quasi-gapless carrier aggregation using FBMC in centralized radio-over-fiber heterogeneous networks," *J. Lightw. Technol.*, vol. 35, no. 4, pp. 989–996, Feb. 2017.
[16] R. M. Borges *et al.*, "Integration of a GFDM-based 5G transceiver in a GPON using radio over fiber technology," *J. Lightw. Technol.*, vol. 36, no. 19, pp. 4468–4477, Oct. 2018.
[17] L. Huang *et al.*, "Simple multi-RAT RoF system with 2 $\times$ 2 MIMO wireless transmission," *IEEE Photon. Technol. Lett.*, vol. 31, no. 13, pp. 1025–1028, Jul. 2019.
[18] W. Zhang, A. Wen, Y. Li, and J. Ma, "A high spectral efficiency microwave photonic link with optimization of chromatic-dispersion-induced power fading," *J. Lightw. Technol.*, vol. 37, no. 4, pp. 1123–1132, Feb. 2019.
[19] Z. Ghassemlooy, W. O. Popoola, and S. Rajbhandari, in *Optical Wireless Communications–System and Channel Modelling With Matlab.* 2nd ed. Boca Raton, FL, United States: CRC Press, 2019.
[20] L. Li *et al.*, "Mitigation for turbulence effects in a 40-Gbit/s orbital-angular-momentum-multiplexed free-space optical link between a ground station and a retro-reflecting UAV using MIMO equalization," *Opt. Lett.*, vol. 44, no. 21, Nov. 2019, Art. no. 5181.
[21] R. Zheng, E. H. W. Chan, X. Wang, X. Feng, and B. Guan, "Broadband high dynamic range fiber optic link based on a dual-polarization modulator," *Opt. Express*, vol. 27, no. 4, 2019, Art. no. 4734.
[22] K. Van Gasse *et al.*, "III-V-on-silicon photonic transceivers for radio-over-fiber links," *J. Lightw. Technol.*, vol. 36, no. 19, pp. 4438–4444, Oct. 2018.
[23] H. Kaushal and G. Kaddoum, "Optical communication in space: Challenges and mitigation techniques," *IEEE Commun. Surv. Tutorials*, vol. 19, no. 1, pp. 57–96, Jan./Mar. 2017.
[24] 3GPP TS 36.104. "Base station (BS) radio transmission and reception," 2018.

Seamless 25 GHz Transmission of LTE 4/16/64-QAM Signals Over Hybrid SMF/FSO and Wireless Link

Dong-Nhat Nguyen, *Member, IEEE*, Jan Bohata, Matej Komanec, Stanislav Zvanovec, *Senior Member, IEEE*, Beatriz Ortega, *Member, IEEE*, and Zabih Ghassemlooy, *Senior Member, IEEE*

***Abstract*—We propose and experimentally demonstrate a photonics-assisted converged radio-over-fiber (RoF), radio-over-free-space optics (RoFSO) and millimeter-wave (MMW) wireless transmission system for use in broadband wireless access (BWA) networks. The focus is at the emerging frequency band of 25 GHz, as recommended for fifth-generation networks. As a proof-of-concept demonstration, all-optical up-converted long-term evolution test models with 4-, 16- and 64-quadrature amplitude modulation (QAM) are transmitted and evaluated over the proposed hybrid link under weak-to-strong atmospheric turbulence regimes. Link performance shows that, the error vector magnitudes are below the 3GPP standard for 4-, 16- and 64-QAM. We also show that, for all QAM signals under turbulence conditions, the bit error rate performance is below the forward error correction limit of 10^{-3}. Simulation analysis is also performed for the 10 Gb/s hybrid systems under turbulence for an extended FSO link up to 500 m to emulate a practical outdoor environment. Furthermore, we analytically estimate the attainable MMW wireless range for different rain rates in Prague, Czech Republic. The obtained experimental and simulation results confirm the feasibility and potential of the proposed hybrid system for next-generation last mile BWA networks.**

***Index Terms*—Atmospheric turbulence, free-space optics, millimeter-wave communication, radio-over-fiber.**

I. Introduction

FUTURE broadband wireless access (BWA) and optical front-haul systems need to support multigigabit bandwidth-intensive applications and services due to the continuous growth in mobile broadband data subscriptions and mobile data traffic [1], [2]. Existing BWA systems, which mainly operate at lower microwave frequency regions (<5 GHz), are unable to offer high-speed data transmission due to the spectral congestion. To overcome this problem, BWA schemes operating at higher-frequency carriers, i.e., the millimeter-wave (MMW) bands, has been proposed [3]. Radio-over-fiber (RoF), inspired by photonics-assisted technologies i.e., external modulator-based all-optical up-conversion for MMW generation, has been stated as the key enabler in BWA for directly connecting central stations to base stations using optical fibers (OFs) [4]–[7]. The unlicensed 60 GHz RoF has gained considerable attention since the introduction of 60 GHz standards (i.e., IEEE 802.15.3c) and WirelessHD [8], [9]. However, the use of 60 GHz MMW in access networks would mean close proximity of the access point to the customer unit due to high propagation losses, thus limiting the coverage range.

The new MMW band of 24 – 28 GHz radio frequency (RF) has received significant international support to meet the ultra-high broadband speeds and reliability envisioned for the fifth generation (5G) mobile networks [10]. RoF systems at this frequency band have also been recently demonstrated [11], [12]. However, in RoF schemes, installation of optical fibers (OF) as the transmission medium is (i) time-consuming and costly in urban areas; (ii) requires permission from public administrations; and (iii) impractical in many situations considering the geographical constraints and physical obstacles. Therefore, in such scenarios the radio-over-free-space optics (RoFSO) technology could be one of the potential complementary alternative solutions. RoFSO is also standardized by International Telecommunication Union [13]. Ultra-high-capacity of FSO transmission systems using the wavelength division multiplexing technology has also been considered [14]. Alternatively, the hybrid RoF-FSO could be adapted to extend the coverage range and therefore delivering BWA to rural areas and underserved communities. However, laser beams propagating over the free space channel are highly susceptible to atmospheric conditions in particular the turbulence. We have recently demonstrated 100 MHz 64-quadrature amplitude modulation (64-QAM) over a 24-26 GHz hybrid RoF-FSO link with the error vector magnitude (EVM) of 4.7% [15].

Manuscript received July 9, 2019; revised September 5, 2019 and September 30, 2019; accepted October 2, 2019. Date of publication October 4, 2019; date of current version December 10, 2019. This work was supported in part by the International Mobility of Researchers in CTU (CZ.02.2.69/0.0/0.0/16_027/0008465) and in part by the MEYS INTERCOST project LTC18008 within COST CA16220. *(Corresponding author: Dong-Nhat Nguyen.)*

D.-N. Nguyen, J. Bohata, M. Komanec, and S. Zvanovec are with the Department of Electromagnetic Field, Czech Technical University in Prague, Prague 166 27, Czech Republic (e-mail: dongnhat@fel.cvut.cz; bohatja2@fel.cvut.cz; komanmat@fel.cvut.cz; xzvanove@fel.cvut.cz).

B. Ortega is with the Instituto de Telecomunicaciones y Aplicaciones Multimedia, ITEAM, Universitat Politècnica de València, Camino de Vera 46022, Spain (e-mail: bortega@dcom.upv.es).

Z. Ghassemlooy is with the Optical Communication Research Group, Northumbria University, Newcastle upon Tyne NE1 8ST, U.K. (e-mail: z.ghassemlooy@northumbria.ac.uk).

Color versions of one or more of the figures in this article are available online at http://ieeexplore.ieee.org.

Digital Object Identifier 10.1109/JLT.2019.2945588

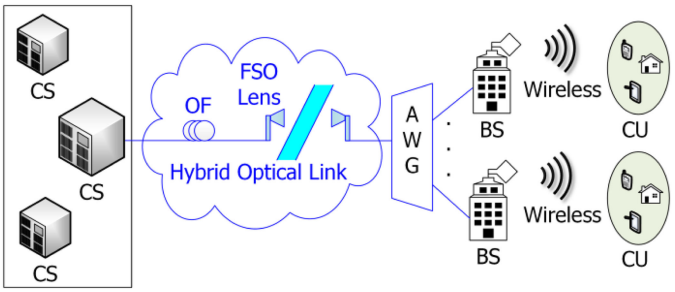

Fig. 1. System schematic of the proposed seamless connectivity for next-generation last mile BWA networks. CS: central station, OF: optical fiber, FSO: free-space optics, AWG: arrayed-waveguide grating, BS: base station and CU: customer unit.

Motivated by the aforementioned technologies, in this work we propose a seamless converged 25 GHz RoF-FSO and wireless system as illustrated in Fig. 1 for the last mile access network applications.

The long-term evolution (LTE) *M*-QAM signals for $M = 4$, 16 and 64 are generated and transmitted over the proposed link. More specifically, the main contributions of this work are as follows:

1) Evaluation of the transmission performance of seamless converged photonics-assisted link including three technologies of (i) RoF, (ii) RoFSO and (iii) 25 GHz MMW wireless in terms of EVM and the bit error rate (BER).
2) Experimental evaluation of the impact of turbulence-induced fading on all-optical up-converted LTE 4-, 16- and 64-QAM signals.
3) Simulation analysis of a 10 Gb/s *M*-QAM RoF-FSO link with the extended FSO link of 500 m for the last mile application under different turbulence regimes.
4) Analytical estimation of the achievable MMW wireless transmission range under rain conditions.

The paper is organized as follows. Section II provides a brief analysis of free space channels for both FSO and MMW. Section III describes the experimental setup, measurement and simulation results. Finally, Section IV provides concluding remarks.

II. Principle of Free-Space Channels

A. FSO Channel

The atmospheric turbulence is due to thermal variation induced changes in the refractive index of the air, which will cause in both intensity and phase fluctuation of the propagating optical beam [16]. The turbulence strength is best characterized by Rytov variance and the refractive index structure parameter [16]–[18], which are given, respectively as:

$$\sigma_R^2 = 1.23 C_n^2 k^{7/6} R^{11/6}, \tag{1}$$

$$C_n^2 = \left(79 \times 10^{-6} \frac{P}{T^2}\right) C_T^2, \tag{2}$$

where temperature structure constant is:

$$C_T^2 = (T_1 - T_2)^2 \, / {d_i}^{2/3}, \tag{3}$$

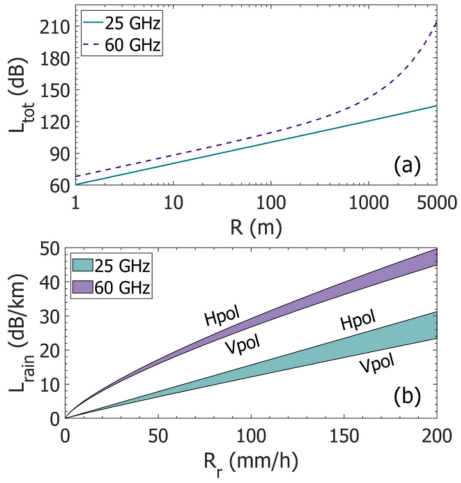

Fig. 2. (a) Total path and atmospheric losses and (b) the predicted specific rain attenuation for 25 and 60 GHz MMW.

$k = 2\pi/\lambda$ is the optical wavenumber, R is a free-space range, P and T are the atmospheric pressure (millibar) and average temperature (Kelvin) along the free-space path, respectively. T_1 and T_2 are measured temperatures at two points separated by a distance d_i. Note, the temperature profile along the transmission path is used to estimate the turbulence strength. C_n^2 ($\mathrm{m}^{-2/3}$) is the key parameter used to measure the turbulence strength, which is highly dependent on the small-scale temperature fluctuations and C_T^2. To relate C_n^2 to a real-time outdoor measurement, it is worth mentioning that C_n^2 values measured over L of 2200 m during summer 2011 in Prague, Czech Republic [19] have the lower and upper limits of 10^{-17} and 10^{-13} $\mathrm{m}^{-2/3}$, respectively. The typical value for C_n^2 was about 10^{-15} with Rytov variance of 0.0845, which can be considered as weak turbulence.

B. MMW Wireless Channel

The MMW signal propagating along the line of sight (LoS) path experience both path L_{PL} and atmospheric L_{atm} losses. The former is given by the Friis transmission equation:

$$L_{\mathrm{PL}}\ (\mathrm{dB}) = 20\log\left(\frac{4\pi R}{\lambda_{\mathrm{MMW}}}\right), \tag{4}$$

where λ_{MMW} is the wavelength of MMW signal.

Fig. 2(a) shows the total loss $L_{\mathrm{tot}} = L_{\mathrm{PL}} + L_{\mathrm{atm}}$ as a function of R for LoS 25 and 60 GHz MMW links. Note, the 60 GHz V-band is shown for comparison. L_{atm} of 0.1 and 15 dB/km are used for 25 and 60 GHz, respectively as in [20]. As can be seen, at 60 GHz the loss is >160 dB for the transmission range longer than 2 km, therefore the 25 GHz system is considered in this work.

The link availability is paramount under all weather conditions. For the MMW link, rain-induced attenuation L_{rain} (dB/km) is the most critical, which affects the link availability, and is given by [21]:

$$L_{\mathrm{rain}}\,(\mathrm{dB/km}) = aR_r^b, \tag{5}$$

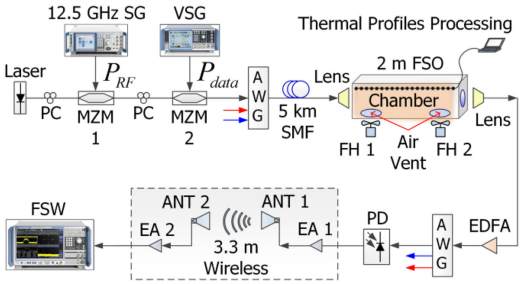

Fig. 3. Experimental setup. MZM: Mach-Zehnder modulator, SMF: standard single-mode fiber, FH: fan heater, EDFA: erbium-doped fiber amplifier, PD: PIN photodiode, EA: electrical amplifier and ANT: antenna.

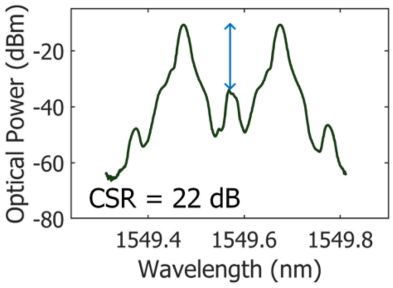

Fig. 4. Output optical spectra of MZM 1 at a bias voltages of 3.4 V.

where parameters a and b are frequency dependent, and R_r the rainfall rate (mm/h). For specified values of a, b and R_r at frequencies of 25 and 60 GHz see ITU-R P.838-3 recommendations for horizontal and vertical polarization (Hpol and Vpol) [21]. Fig. 2(b) shows the rain attenuation against $R_{\rm r}$ for Hpol and Vpol at frequencies of 25 and 60 GHz. As can be seen, 25 GHz in general shows much lower rain attenuation than 60 GHz links.

Following transmission over the free-space channel, the received power $P_{\rm rMMW}$ for the MMW signal is given as:

$$P_{\rm rMMW}\ ({\rm dBm}) = P_t\ ({\rm dBm}) + G_{\rm Tx} + G_{\rm Rx} - 20\log_{10}\left(\frac{4\pi R}{\lambda_{\rm MMW}}\right) - (L_{\rm atm} + L_{\rm rain})\,R, \quad (6)$$

where P_t is the transmit power at the antenna (ANT), $G_{\rm Tx}$ and $G_{\rm Rx}$ are the gains of transmitter (Tx) and receiver (Rx) ANTs, respectively [22]. Note, these parameters are helpful when scaling the system performance from indoor to outdoor wireless environments [23], [24].

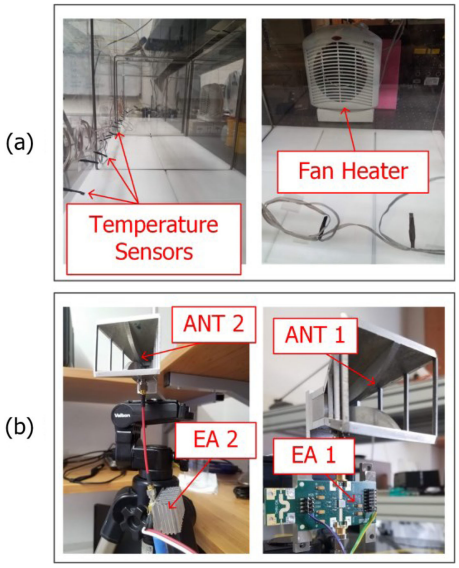

Fig. 5. (a) A FSO chamber and (b) a RF wireless link.

III. Experimental Setup and Results

In this section, we outline the complete setup for the 25 GHz RoF-FSO and MMW wireless link for the transmission of LTE 4/16/64-QAM signal as a proof of concept and experimentally evaluate its performance in terms of the EVM and BER.

A. Experimental Setup

Fig. 3 shows the experimental setup of the proposed scheme. A continuous wave laser source (ID Photonics CoBrite-DX4) is applied to a zero-chirp single-drive Mach-Zehnder modulator (MZM 1 – Fujitsu FTM7938EZ/201), which is externally modulated by a 12.5 GHz input signal with the power $P_{\rm RF}$ of 18 dBm from a microwave signal generator (12.5 GHz SG). Note, MZM 1 is biased at the minimum transmission point has a photonic MMW output which is a suppressed carrier double-sideband (SC-DSB) signal with a frequency spacing between the sidebands of 25 GHz (also known as all-optical up-conversion). Fig. 4 depicts the output optical spectra of MZM 1 at a bias voltage V_b of 3.4 V, which results in the highest optical carrier to sideband ratio (CSR) of 22 dB and therefore been adopted in all experiments regardless of modulation formats for a fair comparison. Also note that, this approach of generating the SC-DSB signal offers the advantages of (i) relaxed requirements for RF components, (ii) wavelength reuse for the uplink and (iii) improved receiver sensitivity compared to other modulation schemes such as conventional double-sideband and single-sideband [5]. Polarization controllers (PCs) are used to minimize the polarization-dependent loss. The output of MZM 1 is further modulated using MZM 2 (Covega 10TM 081) by LTE M-QAM signals which is generated by a vector signal generator (VSG). We used 4-, 16- and 64-QAM for test models of 3.3, 3.2 and 3.1, respectively, which are defined by universal terrestrial radio access (E-UTRA) [25] with a carrier frequency $f_{\rm c}$ of 50 MHz. The spectrum of the signals at the output of RF wireless transmission therefore features DSB signal with frequency components of 25 GHz $- f_{\rm c}$, 25 GHz and 25 GHz $+$ $f_{\rm c}$. Note that, the M-QAM signals have the same bandwidth of 20 MHz.

The up-converted signals are then applied to the arrayed-waveguide grating (AWG)-based multiplexer, the output of which is launched into a 5 km of standard single-mode fiber (SMF). Using a collimator lens (Thorlabs F810APC-1550), light from the SMF is launched into the atmospheric chamber of a dimension 2.0 m $\times$ 0.4 m $\times$ 0.4 m, see Fig. 5(a). At the end of the chamber, another collimator lens is used to launch the received light back into a SMF the output of which is optically

TABLE I
KEY PARAMETERS USED IN EXPERIMENT

Parameter	Value
Laser (Tunable)	
• Wavelength	1549.57 nm
• Output power	16 dBm
MMW carrier frequency	25 GHz
LTE test models (power)	3.3, 3.2, 3.1 (+6 dBm)
Modulation formats	4-, 16-, 64-QAM
Tested LTE signal bandwidth	20 MHz
EDFA	
• Output power and noise figure	3 dBm and < 5 dB
SMF	
• Length	5 km
• Dispersion	17 ps/(nm·km)
Collimator lens	
• Aperture	24 mm
• Focal length	37.13 mm
• Beam divergence	280 μrad
FSO length and loss	2 m and 4 dB
Optical Rx	
• PD responsivity	0.8 A/W @ 1550 nm
• Dark current	10 nA
• Optical return loss	30 dB
MMW wireless length	3.3 m
RF ANT gain	15 dBi
EA 1 gain	22 dB
• Noise figure	1.7 dB
• Bandwidth	24 – 27 GHz
EA 2 gain	27 dB
• Noise figure	2 dB max
• Bandwidth	18 – 26.5 GHz

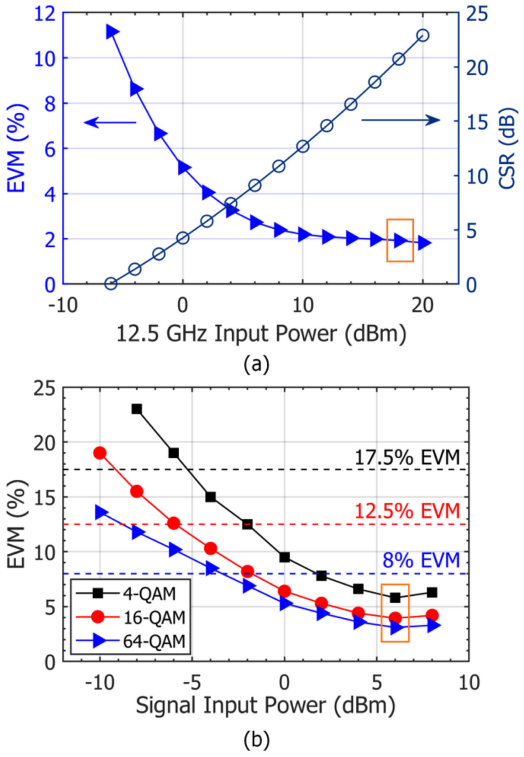

Fig. 6. B2B link: (a) EVM and CSR as a function of *P*RF for 64-QAM and (b) EVM as a function of *P*data for 4-, 16- and 64-QAM. Orange boxes mark the selected input powers used in the experiments.

amplified using an erbium-doped fiber amplifier (EDFA) (Keopsys KPS-BT2-C-10-LN-SA). The amplified signal is applied to AWG prior to detection by a 40 GHz optical Rx (a PIN photodiode – Optilab PD-40). The regenerated electrical signal is amplified (EA 1 – Analog device HMC1131) prior to transmission over a 3.3 m wireless channel using a horn ANT (RFSpin DRH40), see Fig. 5(b). Following wireless transmission, the RF signal is amplified by EA 2 (Miteq AMF-4F-260400-40-10p), prior to being captured by a signal and spectrum analyzer (Rohde&Schwarz FSW) for further signal analysis. Note, ANTs 1 and 2 are mounted on adjustable tripods at a height of 1.5 m for ideal alignment. All the key system parameters adopted in the experimental setup are summarized in Table I.

B. Back-to-Back (B2B) Link Measurements

First, we carried out measurements for the B2B link (i.e., no hybrid SMF and FSO and no RF wireless transmission) in order to determine the optimum power levels for the 12.5 GHz sinusoidal and LTE signals. Fig. 6(a) depicts the EVM and CSR as a function of 12.5 GHz input power P_{RF}. This is carried out because increasing P_{RF} results in higher CSR and therefore improved EVM performance due to the higher power at desired frequency. Note that, 64-QAM is used in this case. As can be seen from Fig. 6(a), EVM drops exponentially reaching a constant level of 2% at $P_{\mathrm{RF}} \geq 12$ dBm. The CSR plot increases linearly with P_{RF} with the highest level of 22 dB at P_{RF} of 20 dBm. The optimum P_{RF} therefore can be chosen within the range of 12 to 20 dBm. Here, we have selected P_{RF} of $+18$ dBm, which was optimized with regards to the EVM performance, high CSR and low nonlinear distortion.

Fig. 6(b) shows the measured EVM performance as a function of the LTE signal input power P_{data} for 4/16/64-QAM. Note that, EVM values were obtained from 90000 points averaged over 50 EVMs. Also shown in Fig. 6(b) are the EVM required limits of 17.5, 12.5 and 8% for 4-, 16- and 64-QAM, respectively as defined in 3GPP specifications [25]. We notice that, for low values of P_{data} i.e., <-7 dBm, the EVM values for *M*-QAM signals do not satisfy their corresponding standard requirements. For P_{data} larger than $+6$ dBm, the EVM performance is degraded due to the impact of nonlinear distortion. Therefore, P_{data} should be set to the optimal value to ensure high-quality signal transmission over the hybrid system. The lowest EVM values of 6, 4 and 3% are observed at P_{data} of $+6$ dBm for 4-, 16- and 64-QAM, which is adopted in this work.

Fig. 7 illustrates the EVM against the received MMW power P_{rMMW} for the B2B link for 4-, 16- and 64-QAM at the output of optical Rx. For P_{rMMW} of -50 dBm the EVM values are 4, 2.5 and 2% for 4-, 16- and 64-QAM, respectively, which were used as the benchmark. Note, these EVM values correspond to error-free transmission with a predicted BER of $<10^{-12}$ [26], [27]. At the required EVM limit of 8%, P_{rMMW} is found to be -64.5 dBm for B2B 64-QAM transmission. This value is critical in order to estimate MMW power penalty following transmission over the hybrid link under different turbulence

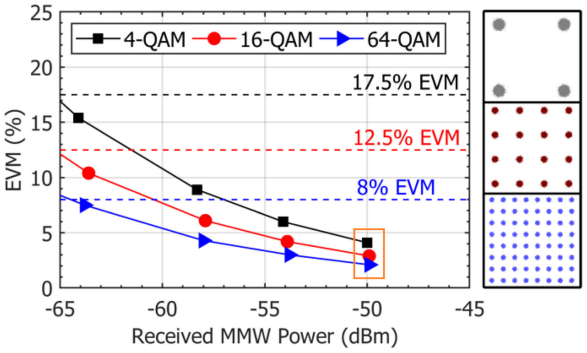

Fig. 7. EVM versus the received MMW power for the B2B link. Orange box marks the *P*rMMW of −50 dBm illustrating the constellation diagrams of 20 MHz 4-, 16- and 64-QAM as shown in insets.

levels. Also shown in insets in Fig. 7 are the clear constellation diagrams at P_{rMMW} of −50 dBm.

C. Hybrid Link Measurements

To generate turbulence within the chamber, two external fans located at both ends of the chamber are used to blow hot air perpendicularly to the propagating optical beam. 20 temperature sensors (equidistantly spaced by 10 cm) are positioned along the chamber are used to accurately measure the temperature profile in order to determine C_n^2 (see Fig. 5(a)). Note that, the statistical mean of a large number of temperature readings (i.e., 1400 data sets) along the chamber is for each turbulence level is considered to ensure identical test and measurement conditions. C_n^2 therefore can be determined based on the recorded thermal values by using equations (2) and (3).

Fig. 8 shows the measured EVM for *M*-QAM signals for the hybrid link (5 km of SMF, 2 m of FSO and 3.3 m of MMW channel) with C_n^2 of 3.07×10^{-14}, 3.23×10^{-11} and 1.61×10^{-10} $\mathrm{m}^{-2/3}$, which corresponds to weak, moderate and strong turbulence regimes, respectively. Note that, a short indoor FSO link under strong turbulence can be re-calculated to represent medium-range outdoor FSO links under weak to moderate turbulence conditions as was discussed in Section II. Therefore, for the same Rytov variance, C_n^2 of 1.61×10^{-10} $\mathrm{m}^{-2/3}$ corresponds to C_n^2 of 6.46×10^{-15} and 1.81×10^{-15} $\mathrm{m}^{-2/3}$ for FSO link spans of 500 and 1000 m, respectively. Also shown are the EVM limits of 17.5, 12.5 and 8%, which are met at P_{rMMW} of −51.8, −51 and −50.2 dBm for 4-, 16- and 64-QAM, respectively, see Fig. 8(a), with marginal power penalties for the moderate turbulence. However, under strong turbulence, see Fig. 8(c), the MMW power penalties are higher by about 4.3, 4 and 4.7 dB for 4-, 16- and 64-QAM, respectively compared to the weak turbulence at the corresponding EVM values. This is because under strong turbulence the propagating optical beams experience much higher degree of both intensity and phase fluctuations, which lead to deterioration of the signal quality as in [28], [29]. Compared with the B2B link in Fig. 7 and considering 64-QAM under weak and strong turbulence regimes, Figs. 8(a) and (c) show MMW power penalties about about 14 and 19 dB, respectively at the EVM of 8%. It is worth to mention

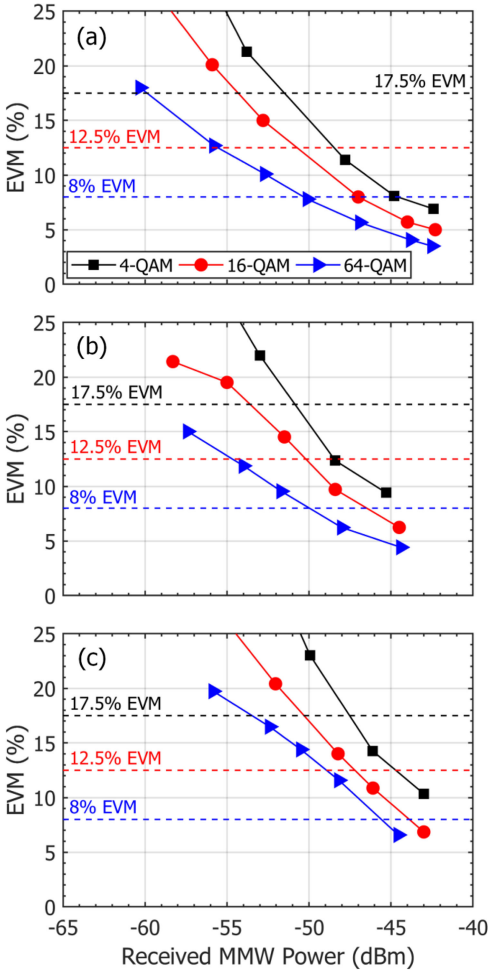

Fig. 8. EVM versus received MMW power for the 4-, 16- and 64-QAM hybrid link for: (a) weak, (b) moderate and (c) strong turbulence regimes.

that, the effect of chromatic dispersion on the 20 MHz LTE signals used in our experiment can be neglected since the SMF length is relatively short. However, for RoF links employing broader bandwidth signals, chromatic dispersion effect must be considered. For example, as demonstrated in [30], after 11.8 km SMF transmission in a SC-DSB-based RoF system operating at 24 GHz, there is 2.1% EVM degradation when the 64-QAM LTE signal bandwidth is increased from 20 to 100 MHz.

We also evaluated the BER performance of the proposed 25 GHz *M*-QAM RoF-FSO and MMW system using:

$$\mathrm{BER}_{M-\mathrm{QAM}} = \frac{2}{\log_2(M)}\left(1-\frac{1}{\sqrt{M}}\right) \times \mathrm{erfc}\left(\sqrt{\frac{3}{2(M-1)}\times\frac{1}{\mathrm{EVM}^2}}\right) \quad (7)$$

where erfc (·) is the complementary error function [26], [27].

The $\log_{10}$(BER) as a function of the received power of MMW for the hybrid transmission under weak, moderate and strong turbulence regimes are shown in Figs. 9(a), (b) and (c), respectively. Also shown is the forward error correction (FEC) limit of 10^{-3}. In general *M*-QAM signals display acceptable

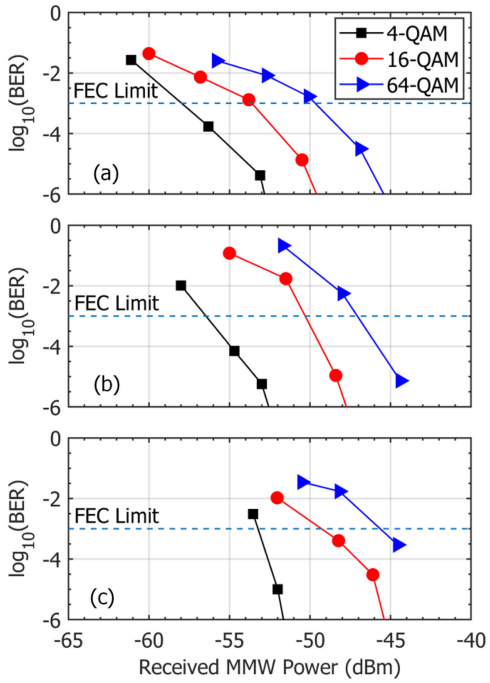

Fig. 9. BER against the received MMW power for the 4-, 16- and 64-QAM hybrid link under: (a) weak, (b) moderate and (c) strong turbulence regimes.

TABLE II
SUMMARY OF TRANSMISSION RESULTS AT P_{rMMW} OF -50 dBm. EVM: MEASURED AND BER: CALCULATED

	B2B	Seamless Converged Link		
		Weak	Moderate	Strong
M-QAM	EVM (BER)	EVM (BER)	EVM (BER)	EVM (BER)
4	4% ($<10^{-12}$)	15% (1.3×10^{-11})	15.8% (1.2×10^{-10})	23% (6.9×10^{-6})
16	2.5% ($<10^{-12}$)	11.6% (4.3×10^{-5})	12.2% (9.3×10^{-5})	17% (3.2×10^{-3})
64	2% ($<10^{-12}$)	7.7% (1.3×10^{-3})	8% (1.9×10^{-3})	14% (3.5×10^{-2})

BER performance regardless of turbulence levels. However, at P_{rMMW} of -50 dBm, which is the minimum power for the B2B link, see Fig. 7, the BER values for 64-QAM are above the FEC limit for all turbulence regimes. Table II summarizes the measured EVMs and predicted BERs for all three QAM signals for the B2B and hybrid links under weak-to-strong turbulence regimes for P_{rMMW} of -50 dBm.

Fig. 10 shows the measured constellation diagrams for 4-, 16- and 64-QAM signals for the hybrid link under weak, moderate and strong turbulence regimes, respectively. The impairments due to turbulence-induced fading compared to the B2B link, see insets of Fig. 7, are more evident for higher-orders QAM under strong turbulence. These results clearly illustrate that, signals with higher bits per symbol are more susceptible to atmospheric

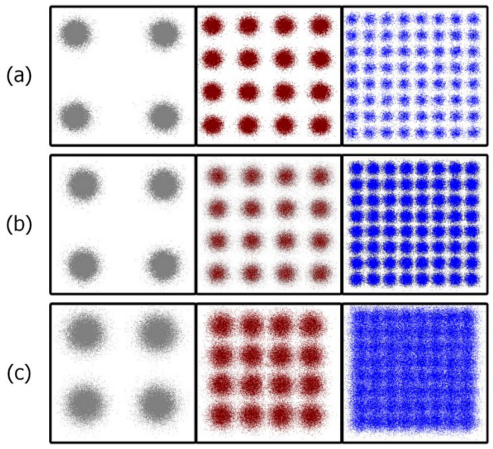

Fig. 10. The measured constellation diagrams for 4-, 16- and 64-QAM signals at the output of a hybrid channel under: (a) weak, (b) moderate and (c) strong turbulence regimes for *P*rMMW of -50 dBm.

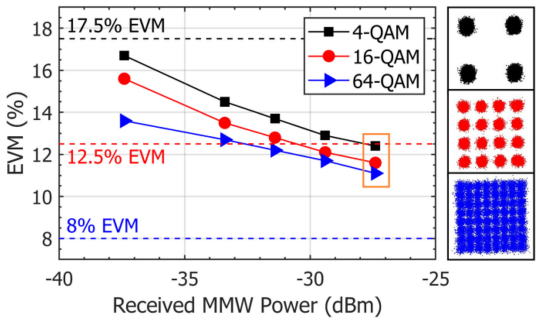

Fig. 11. Simulated EVM versus received MMW power for 4/16/64-QAM signals in hybrid link (5 km of SMF and 500 m of FSO link) with C_{n2} of $5\times10-15$ $\mathrm{m}^{-2/3}$ at 10 Gb/s. Orange box marks *P*rMMW of -27.4 dBm illustrating the constellation diagrams of 10 Gb/s 4-, 16- and 64-QAM as shown in insets.

turbulence due to the reduced spacing between symbols; i.e., Euclidean distance in constellation points.

D. Simulation for the Outdoor Link

In this section, we analyze by means of simulation the performance of the proposed hybrid 25 GHz RoF-FSO link for 4/16/64-QAM at a high bit rate of 10 Gb/s to provide more insight on the practical outdoor system.

Note that, the SMF length is kept at 5 km while the FSO link is extended up to 500 m, which is a typical range for the last mile access network applications. Note, the simulation is based on the experimental parameters given in Table I. Fig. 11 shows the simulated EVM as a function of P_{rMMW} for the hybrid link with C_n^2 of 5×10^{-15} $\mathrm{m}^{-2/3}$ (i.e., weak turbulence in an outdoor environment) for 4/16/64-QAM. Also shown are the constellation diagrams for *M*-QAM signals. The results confirm that, the proposed system is feasible for practical applications at high bit rates using 4- and 16-QAM signals with best EVM values well below the corresponding 3GPP EVM requirements. E.g., for 4-QAM at a P_{rMMW} of -27.4 dBm the EVM is 12.5%, which corresponds to error-free transmission. While for 16- and

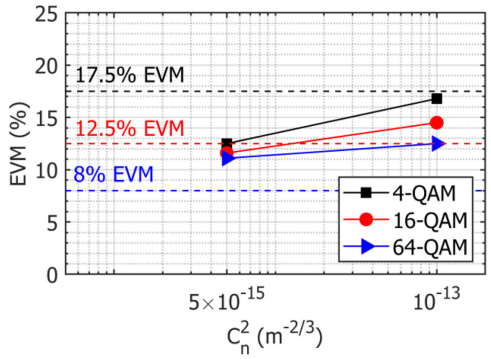

Fig. 12. Simulated EVM versus different turbulence levels.

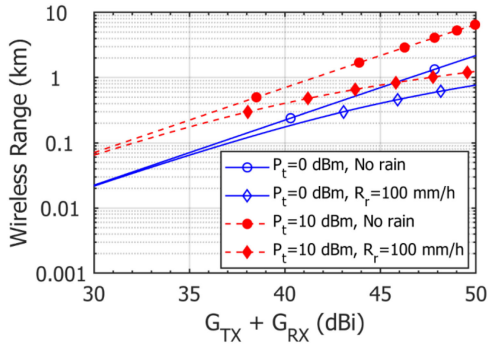

Fig. 13. Attainable wireless transmission range as a function of the combined Tx and Rx ANT gain.

64-QAM the EVM values are 11.6 and 11.1%, respectively, which correspond to the BERs of 4.3×10^{-5} (i.e., below the FEC limit) and 1.4×10^{-2} (i.e., above the FEC limit), respectively. Notice that the simulated P_{rMMW} of -27.4 dBm is about 20 dB higher than the experimental results as was discussed in previous section. This is because, the simulated results are achieved for the hybrid link operating at 10 Gb/s whereas the experiment e.g., 20 MHz LTE 64-QAM provides a speed of 75 Mb/s.

We also evaluated the transmission performance of 10 Gb/s M-QAM hybrid link for C_n^2 of 1×10^{-13} m$^{-2/3}$, see Fig. 12, where the EVM values for all M-QAM signals are above the required limits except for 4-QAM. This further confirms our experimental results.

Finally, we investigated the MMW wireless transmission range using equation (6) as a function of the total antenna gains (i.e., $G_{\mathrm{Tx}} + G_{\mathrm{Rx}}$) for P_t of 0 and 10 dBm and R_r of 0 (no rain) and 100 mm/h as depicted in Fig. 13. At 25 GHz, L_{rain} is about 12 dB/km. This is adopted from the outdoor measurement over a 4-year period in Prague, Czech Republic for R_r of 100 mm/h, which is considered as heavy rain [31]. Note that, 25 GHz horn ANTs with a gain of 20 dBi are commercially available. Therefore, as can be seen, increasing aggregate G_{Tx} and G_{Rx} from 30 dBi (i.e, ANTs used in the experiment) to 40 dBi greatly improves the transmission range regardless of R_r. For example, under heavy rain, considering P_{rMMW} of -27.4 dBm and P_t of 0 and 10 dBm, the maximum attainable wireless ranges are extended from 21 to 175 and 404 m, respectively. While in case of no rain, the links are extended to 224 and 703 m, respectively.

IV. Conclusion

We experimentally demonstrated a seamlessly converged double-sideband carrier-suppressed RoF-FSO and millimeter wave communication system at the emerging 5G frequency band of 25 GHz, which can provide high-capacity long-distance wireless transmission. Weak, moderate and strong turbulences for the FSO channel were generated and comprehensively characterized. Three 20 MHz LTE test models of 4/16/64-QAM were sucessfully transmitted over the proposed hybrid system under weak-to-strong turbulence regimes. We showed that, for strong turbulence the best EVMs of 10.5, 7 and 6.5% satisfied the required limits defined by the 3GPP standards, respectively. We achieved BER performance below the FEC limit of 10^{-3} for all test signals under all turbulence conditions. Simulation analysis was also carried out for the 10 Gb/s M-QAM hybrid link with longer FSO channel of 500 m, as part of the last mile broadband wireless access networks. Based on the link margins, we further estimated the maximum achievable wireless transmission range for different rain rates. System capacity of the proposed system can be significantly scaled by using wavelength multiplexing techniques, which is part of our future works.

References

[1] I. A. Alimi, A. L. Teixeira, and P. P. Monteiro, "Toward an efficient C-RAN optical fronthaul for the future networks: A tutorial on technologies, requirements, challenges, and solutions," *IEEE Commun. Surv. Tut.*, vol. 20, no. 1, pp. 708–769, Jan.–Mar. 2018.

[2] G. Kalfas *et al.*, "Next generation fiber-wireless fronthaul for 5G mmWave networks," *IEEE Commun. Mag.*, vol. 57, no. 3, pp. 138–144, Mar. 2019.

[3] F. Boccardi, R. Heath, A. Lozano, T. L. Marzetta, and P. Popovski, "Five disruptive technology directions for 5G," *IEEE Commun. Mag.*, vol. 52, no. 2, pp. 74–80, Feb. 2014.

[4] R. Waterhouse and D. Novack, "Realizing 5G: Microwave photonics for 5G mobile wireless systems," *IEEE Microw. Mag.*, vol. 16, no. 8, pp. 84–92, Sep. 2015.

[5] C. Lim, Y. Tian, C. Ranaweera, A. Nirmalathas, E. Wong, and K. Lee, "Evolution of radio-over-fiber technology," *J. Lightw. Technol.*, vol. 37, no. 6, pp. 1647–1656, Mar. 2019.

[6] C.-Y. Lin *et al.*, "Millimeter-wave carrier embedded dual-color laser diode for 5G MMWoF link," *J. Lightw. Technol.*, vol. 35, no. 12, pp. 2409–2420, Jun. 2017.

[7] A. J. Seeds and T. Ismail, "Broadband access using wireless over multimode fiber systems," *J. Lightw. Technol.*, vol. 28, no. 16, pp. 2430–2435, Aug. 2010.

[8] "IEEE 802.15 WPAN task group 3c (TG3c) millimeter wave alternative PHY." [Online]. Available: http://ieee802.org/15/pub/TG3c, Accessed on: Feb. 2019.

[9] "WirelessHD specification overview (Version 1.1)." Feb. 2007. [Online]. Available: http://www.wirelesshd.org/

[10] "5G spectrum GSMA public policy position," 2018. [Online]. Available: https://www.gsma.com/

[11] R. M. Borges *et al.*, "Integration of a GFDM-based 5G transceiver in a GPON using radio over fiber technology," *J. Lightw. Technol.*, vol. 36, no. 19, pp. 4468–4477, Oct. 2018.

[12] M. Sung, S. Cho, J. Kim, J. K. Lee, and J. H. Lee, "Demonstration of IFoF-based mobile fronthaul in 5G prototype with 28-GHz millimeter wave," *J. Lightw. Technol.*, vol. 36, no. 2, pp. 601–609, Jan. 2018.

[13] K. Kazaura, K. Wakamori, M. Matsumoto, T. Higashino, K. Tsukamoto, and S. Komaki, "RoFSO: A universal platform for convergence of fiber and free-space optical communication networks," *IEEE Commun. Mag.*, vol. 48, no. 2, pp. 130–137, Feb. 2010.

[14] Z. Ghassemlooy, S. Arnon, M. Uysal, Z. Xu, and J. Cheng, "Emerging optical wireless communications-advances and challenges," *IEEE J. Sel. Areas Commun.*, vol. 33, no. 9, pp. 1738–1749, Sep. 2015.
[15] J. Bohata, M. Komanec, J. Spáčil, Z. Ghassemlooy, S. Zvánovec, and R. Slavík, "24–26 GHz radio-over-fiber and free-space optics for fifth-generation systems," *Opt. Lett.*, vol. 43, no. 5, pp. 1035–1038, Mar. 2018.
[16] Z. Ghassemlooy, W. O. Popoola, and S. Rajbhandari, *Optical Wireless Communications – System and Channel Modelling With Matlab*, 2nd ed. Cham, Switzerland: CRC Press, 2019.
[17] N. A. M. Nor *et al.*, "Experimental investigation of all-optical relay-assisted 10 Gb/s FSO link over the atmospheric turbulence channel," *J. Lightw. Technol.*, vol. 35, no. 1, pp. 45–53, Jan. 2017.
[18] L. C. Andrews and R. L. Phillips, *Laser Beam Propagation Through Random Media*, vol. 1. Bellingham, WA, USA: SPIE, 2005.
[19] M. Grabner and V. Kvicera, "Measurement of the structure constant of refractivity at optical wavelengths using a scintillometer," *Radioengineering*, vol. 21, no. 1, pp. 455–458, 2012.
[20] ITU-R P.676-11, "Attenuation by atmospheric gases," 2016.
[21] ITU-R P.838-3, "Specific attenuation model for rain for use in prediction methods," 2005.
[22] M. Weiß, M. Huchard, A. Stöhr, B. Charbonnier, S. Fedderwitz, and D. S. Jäger, "60-GHz photonic millimeter-wave link for short- to medium-range wireless transmission up to 12.5 Gb/s," *J. Lightw. Technol.*, vol. 26, no. 15, pp. 2424–2429, Aug. 2008.
[23] P. T. Dat, A. Kanno, K. Inagaki, and T. Kawanishi, "High-capacity wireless Backhaul network using seamless convergence of radio-over-fiber," *J. Lightw. Technol.*, vol. 32, no. 20, pp. 3910–3923, Oct. 2014.
[24] A. Bekkali, T. Kobayashi, K. Nishimura, N. Shibagaki, K. Kashima, and Y. Sato, "Millimeter-wave-based fiber-wireless bridge system for 8K UHD video streaming and gigabit ethernet data connectivity," *J. Lightw. Technol.*, vol. 36, no. 18, pp. 3988–3998, Sep. 2018.
[25] 3GPP TS 36.104, "Base station (BS) radio transmission and reception," 2018.
[26] V. J. Urick, J. X. Qiu, and F. Bucholtz, "Wide-band QAM-over-fiber using phase modulation and interferometric demodulation," *Photon. Technol. Lett.*, vol. 16, no. 10, pp. 2374–2376, 2004.
[27] X. Chen and J. Yao, "A high spectral efficiency coherent microwave photonic link employing both amplitude and phase modulation with digital phase noise cancellation," *J. Lightw. Technol.*, vol. 33, no. 14, pp. 3091–3097, Jul. 2015.
[28] M. Hulea, Z. Ghassemlooy, S. Rajbhandari, and X. Tang, "Compensating for optical beam scattering and wandering in FSO communications," *J. Lightw. Technol.*, vol. 32, no. 7, pp. 1323–1328, Apr. 2014.
[29] L. Zunino, D. Gulich, G. Funes, and D. G. Pérez, "Turbulence-induced persistence in laser beam wandering," *Opt. Lett.*, vol. 40, no. 13, pp. 3145–3148, Jul. 2015.
[30] M. Noweir *et al.*, "Digitally linearized radio-over fiber transmitter architecture for cloud radio access network's downlink," *IEEE Trans. Microw. Theory Tech.*, vol. 66, no. 7, pp. 3564–3574, Jul. 2018.
[31] P. Thorvaldsen and I. Henne, "Outdoor transmission measurement at 26 GHz; results of a 4 years trial in Prague," in *Proc. 1st URSI Atlantic Radio Sci. Conf.*, 2015, pp. 1–9.

Authors' biographies not available at the time of publication.

Research Article | Vol. 27, No. 23 / 11 November 2019 / Optics Express 33745
Optics EXPRESS

M-QAM transmission over hybrid microwave photonic links at the K-band

DONG-NHAT NGUYEN,[1,*] JAN BOHATA,[1] JAN SPACIL,[1] DANIEL DOUSEK,[1] MATEJ KOMANEC,[1] STANISLAV ZVANOVEC,[1] ZABIH GHASSEMLOOY,[2] AND BEATRIZ ORTEGA[3]

[1] *Department of Electromagnetic Field, Faculty of Electrical Engineering, Czech Technical University in Prague, Prague 166 27, Czech Republic*
[2] *Optical Communication Research Group, Northumbria University, Newcastle upon Tyne NE1 8ST, UK*
[3] *Instituto de Telecomunicaciones y Aplicaciones Multimedia, ITEAM, Universitat Politècnica de València, Camino de Vera, Valencia 46022, Spain*
[*] *dongnhat@fel.cvut.cz*

Abstract: Two experimental configurations of a hybrid K-band (25 GHz) microwave photonic link (MPL) are investigated for seamless broadband wireless access networks. Experimental configurations consist of optical fiber, free-space optics (FSO) and radio frequency (RF) wireless channels. We analyze in detail the effects of channel impairments, namely fiber chromatic dispersion, atmospheric turbulence and multipath-induced fading on the transmission performance. In the first configuration, transmission of the 64-quadrature amplitude modulation (QAM) signal with 5, 20 and 50 MHz bandwidths over 5 km standard single-mode fiber (SSMF), 2 m turbulent FSO and 3 m RF wireless channels is investigated. We show that, for QAM with a high bandwidth, the link performance is being affected more by atmospheric turbulence. In the second configuration, the 20 MHz 4/16/64-QAM signals over a 50 km SSMF and 40 m FSO/RF wireless links are successfully transmitted with the measured error vector magnitude (EVM) values of 12, 9 and 7.9%, respectively. It is shown that, for all transmitted microwave vector signals, the bit error rate is lower than the hard-decision forward-error-correction limit of 3.8×10^{-3}. Moreover, an extended FSO link span of 500 m for 25 GHz hybrid MPL with 16-QAM at 10 Gb/s under the weak and strong turbulence regimes is evaluated via simulation analysis to mimic a practical outdoor system.

1. Introduction

The low-frequency range (< 6 GHz) in the radio frequency (RF) spectrum adopted for broadband wireless access (BWA) networks is overloaded due to the growing use of wireless technologies in recent years [1–3]. In order to increase the network capacity and efficiency as well as offer the users certain unique benefits, the next-generation BWA networks should operate at higher-carrier frequencies i.e., millimeter-wave (MMW) bands. The radio-over-fiber (RoF) or microwave photonic link (MPL) technology operating at the MMW band has recently been investigated as a viable solution for high-capacity networks (i.e., up to 24 Gb/s per lambda) [4–7]. In centralized architectures, these systems use optical fibers (OFs) as the transmission medium to transfer data from the central office to the base stations, where the MMW signal is wirelessly transmitted to the end users. However, in practical OF-based MPLs there are several drawbacks including (i) installation time; (ii) right of access to public spaces; and (iii) natural disasters [8]. Recent literature reports a number of MPL schemes with an extended fiber-reach, e.g., 4- and 16-quadrature amplitude modulated (QAM) signals at 2.5 GHz were successfully transmitted over a 25 km of standard single-mode fiber (SSMF) using a coherent receiver and advanced digital signal processing for phase noise cancellation [1]. A 6 GHz link transmitting 4- and 16-QAM was also demonstrated over a 25 km of SSMF with optimization of the chromatic dispersion

#376377 https://doi.org/10.1364/OE.27.033745
Journal © 2019 Received 27 Aug 2019; revised 22 Oct 2019; accepted 22 Oct 2019; published 4 Nov 2019

Optics EXPRESS

induced power fading [3]. Note that, RF wireless transmission was not considered in these works and therefore multipath-induced fading has not been investigated. An attractive alternative wireless transmission option in MPLs is the free-space optics (FSO) technology, which offers similar capabilities as OFs, i.e., huge bandwidth, electromagnetic immunity and wavelength division multiplexing (WDM) compatibility with significantly reduced deployment costs [8,9]. The concept of radio over FSO, denoted as RoFSO, has been introduced and standardized by International Telecommunication Union [10]. Since then, further experimental demonstrations have been reported in this field. In 2012, orthogonal frequency-division-multiplexing (OFDM)-based digital television signals were successfully transmitted over a 1 km FSO link under different outdoor weather conditions [11]. In 2016, 4 Gb/s 16-QAM-OFDM signal at 60 GHz was transmitted over 1.83 m FSO and RF wireless links and evaluated with synthesized weather conditions i.e., fog, rain and turbulence [12]. In 2018, we demonstrated 100 MHz 64-QAM transmission at different carrier frequencies of 24–26 GHz using a low-cost directly modulated laser over 2 m turbulent FSO and 3.6 m RF wireless links with the lowest measured EVM of 4.7% [13]. Very recently, the transmission of 1 Gbaud 16-QAM at 28 GHz over a 0.9 m FSO channel with dust and a 1 m RF wireless link was demonstrated with a bit error rate (BER) well below the hard-decision forward-error-correction (HD-FEC) limit of 3.8×10^{-3} [14].

In recent years only a limited number of works on RoFSO systems operating at MMW carrier frequency have been reported in the literature as outlined in Table 1. Therefore, it is timely to report on a RoFSO system utilizing the K-band (i.e., 25 GHz) QAM signals over a 40-meter-long FSO channel, which is so far the longest reported FSO transmission of such signals. Note that, the 25 GHz carrier frequency is optically generated by frequency multiplication with the optical carrier suppression (OCS) scheme using an optical modulator. This MMW band has gained increasing attention in recent years as part of the 5th generation (5G) wireless networks [15,16]. In addition, the photonic up-conversion-based technique has been investigated by both the research community and the commercial sector in the past several years [17–19]. This is because the OCS offers significant advantages such as (i) relaxed requirements on RF components; (ii) higher tolerance to chromatic dispersion; (iii) wavelength reuse for the uplink; and (iv) lower phase noise due to the fact that the two sidebands are produced by the same laser.

Table 1. Summary of recent RoFSO transmission experiments with MMW carrier frequencies from 2016–2019

Modulation format	Bit rate	Carrier frequency (frequency band)	FSO distance (m)	Year	Reference
16-QAM	4 Gb/s	60 GHz (V)	1.83	2016	[12]
64-QAM	600 Mb/s	24–26 GHz (K)	2	2018	[13]
4/16-QAM	6/12 Gb/s	25 GHz (K)	8	2018	[20]
16-QAM	4 Gb/s	28 GHz (K_a)	0.9	2019	[14]
4/16/64-QAM	40/80/120 Mb/s	60 GHz (V)	1	2019	[21]
64-QAM	18/75/300 Mb/s	25 GHz (K)	2	2019	**This work**
4/16/64-QAM	16/31/75 Mb/s	25 GHz (K)	40	2019	**This work**

In specific, we demonstrate a proof-of-concept seamless hybrid MPL scheme composed of RoF, RoFSO and RF wireless transmission for two configurations. In configuration A, we focus on the effect of atmospheric turbulence-induced fading on 64-QAM with a variable bandwidth transmitted over the proposed hybrid MPL consisting of 5 km SSMF, 2 m turbulent FSO and 3 m RF wireless channels. In configuration B, M-QAMs for $M = 4$, 16 and 64 with the bandwidth of 20 MHz are transmitted over the proposed hybrid MPL consisting of SSMF (5 or 50 km) and FSO/RF indoor wireless links (40 m each). The multipath-induced fading in RF wireless channel is examined.

Optics EXPRESS

The remainder of the paper is organized as follows. Section 2 describes the two experimental configurations and the supporting theoretical basis for turbulence characterization. Section 3 presents and discusses the corresponding experimental results. Section 4 presents the simulation analysis of the proposed hybrid MPL with a FSO link span extended up to 500 m under the weak and strong turbulence regimes for practical outdoor applications. Finally, section 5 concludes the paper.

2. Experimental Setup of Hybrid MPL

2.1. Configuration A

Figure 1 shows the schematic diagram of the experimental setup for the hybrid MPL (configuration A). The insets (i) and (ii) show the laboratory testbed and the controlled FSO channel, respectively. At the transmitter (Tx), a continuous wave optical signal emitted by the laser (ID Photonics CoBrite-DX4) was applied through a polarization controller (PC) into a single-drive Mach-Zehnder modulator (MZM 1) where it is externally modulated by a 12.5 GHz RF clock signal generated by a signal generator (R&S SMF 100A) with an output power of 18 dBm. Note that, MZM 1 was biased at the minimum transmission point and therefore its output optical spectrum showed double-sideband with OCS having a frequency spacing of 25 GHz (i.e., twice the original RF clock signal frequency), see the inset (iv) in Fig. 1. The measured optical carrier to sideband ratio (CSR) was 27 dB at a bias voltage of 3.4 V and was adopted in all modulation formats for a fair comparison. Next, the output of MZM 1 was launched via another PC into MZM 2, which is externally modulated by a 64-QAM signal with an intermediate frequency (IF) of 200 MHz and output power of 4 dBm, generated by a vector signal generator (R&S SMW 200A). Note that, this output power is chosen following a number of tests that were carried out for different power levels ranging from -10 to 8 dBm. The selected value was based on the low EVM value and low nonlinear distortion. In this work, we have considered the bandwidth of 5, 20 and 50 MHz for the 64-QAM signal.

The up-converted signal was then applied to the WDM multiplexer (MUX) serving to mimic practical high-capacity multi-wavelength networks prior to being launched into a 5 km of SSMF. By using two doublet optical collimators (Thorlabs F810APC-1550), the light was launched from the SSMF into a free-space link and injected back into the SSMF at the receiver (Rx) side. An external fan heater was used to generate turbulence by blowing hot air perpendicularly to the propagating optical beam, see inset (ii) in Fig. 1. Note, we have used an atmospheric chamber with a dimension of 2 ×0.4 ×0.4 m^3 to mimic the turbulent FSO channel. For this purpose, 20 thermal sensors were equidistantly spaced (i.e., by 10 cm) along the chamber to accurately measure the thermal profiles.

The measured thermal profiles were then used to determine the refractive index structure parameter C_n^2 [$m^{-2/3}$], which defines the strength of turbulence, given as [22]:

$$C_n^2 = \left(79 \times 10^{-6} \frac{P}{T^2}\right)^2 C_T^2, \tag{1}$$

where P is atmospheric pressure in millibar, T is the absolute temperature in Kelvin and C_T^2 is the thermal structure parameter defined as:

$$C_T^2 = (T_1 - T_2)^2 / d^{2/3}, \tag{2}$$

where T_1 and T_2 are the temperatures measured at two adjacent thermal sensors separated by the propagation distance d (i.e., 10 cm). Note that, in this work the C_n^2 value was processed off-line with more than 1400 sets of thermal profiles. This is to maintain the same temperature profile along the chamber and ensure the fair comparison for all considered 64-QAM signals.

Optics EXPRESS

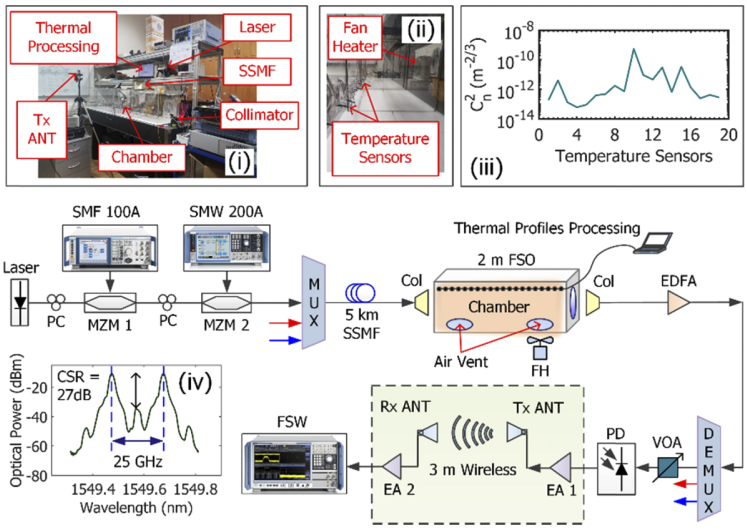

Fig. 1. Experimental configuration A. Insets: (i) Overview of the hybrid MPL setup, (ii) Turbulent FSO chamber, (iii) Recorded C_n^2 ($m^{-2/3}$) and (iv) Optical spectrum with a carrier-suppressed modulation scheme measured after MZM 1. PC: polarization controller, MZM: Mach-Zehnder modulator, MUX: multiplexer, Col: collimator, FH: fan heater, EDFA: erbium-doped fiber amplifier, DEMUX: de-multiplexer, VOA: variable optical attenuator, PD: PIN photodiode, EA: electrical amplifier and ANT: antenna.

The average C_n^2 values without and with turbulence using the laboratory FSO chamber are about 2.4×10^{-14} and 3.2×10^{-11} $m^{-2/3}$, respectively. Inset (iii) in Fig. 1 shows the recorded C_n^2 for the case of turbulence. Note, the high level of turbulence for the short-range indoor FSO link can be re-calculated based on Eq. (3) to determine the turbulence level for the longer range outdoor FSO link by retaining the same σ_R^2. Thus, C_n^2 of 3.2×10^{-11} $m^{-2/3}$ for a 2 m FSO link corresponds to the magnitudes of 1.3×10^{-15} and 3.6×10^{-16} $m^{-2/3}$ for the medium-distance FSO links of 500 and 1000 m, respectively. The measured FSO channel loss was 4 dB. Another important parameter that is commonly used to determine the turbulence strength is Rytov variance σ_R^2, given by [22]:

$$\sigma_R^2 = 1.23 C_n^2 k^{7/6} L^{11/6}, \tag{3}$$

where $k = 2\pi/\lambda$ is the optical wave number, λ is the laser wavelength and L is the FSO propagation distance (i.e., 2 m in this case). Note that, determining σ_R^2 is essential when scaling the FSO system performance from short-link indoor to long-distance outdoor environments.

The optical signal was amplified using an erbium-doped fiber amplifier (EDFA, Keopsys KPS-BT2-C-10-LN-SA,) with an output power of 3 dBm and applied to the wavelength demultiplexer (DEMUX) prior to direct detection using an InGaAs PIN photodiode (Optilab PD-40). The converted electrical signal was amplified using a low-noise electrical amplifier (EA 1, Miteq AMF-4F-260400-40-10p) with a gain and a noise figure of 27 and 2 dB, respectively. Afterward, the signal was transmitted over a 3 m RF wireless link using a pair of double-ridged waveguide horn antennas (ANT – RFSpin DRH40). The Tx and the Rx ANTs were identical with a gain of 15 dBi at the frequency of 25 GHz. Note, the ANTs were mounted on adjustable tripods in line of sight in order to maximize the signal strength at the Rx and reduce multipath-induced fading as well as to avoid the effect of the first Fresnel zone. At the Rx ANT output, the signal was further amplified using another low-noise EA 2 (Analog device HMC1131) with a gain and a noise figure of 22 and 1.7 dB, respectively. The signal was finally captured by a signal analyzer

Optics EXPRESS

(R&S FSW) for further assessment. The main system parameters adopted in the experiments are summarized in Table 2.

Table 2. Key experimental parameters

Parameter	Value (Configuration A)	Value (Configuration B)
Laser		
• Wavelength	1549.58 nm	1549.58 nm
• Output power	16 dBm	16 dBm
Data signal		
• Format	64-QAM	4/16/64-QAM
• Bandwidth	5/20/50 MHz	20 MHz
• Power	4 dBm	4 dBm
MMW carrier frequency	25 GHz	25 GHz
EDFA		
• Output power	3 dBm	7 dBm
• Noise figure	< 5 dB	< 5 dB
SSMF length (loss)	5 km (1dB)	5 and 50 km (1 and 10 dB)
FSO length (loss)	2 m (4 dB)	40 m (12 dB)
• Tx/Rx collimator aperture	24 mm	24 mm
PD		
• Responsivity	0.8 A/W @ 1550 nm	0.8 A/W @ 1550 nm
• Dark current	10 nA	10 nA
RF wireless length	3 m (40 dB)	40 m (62 dB)

2.2. Configuration B

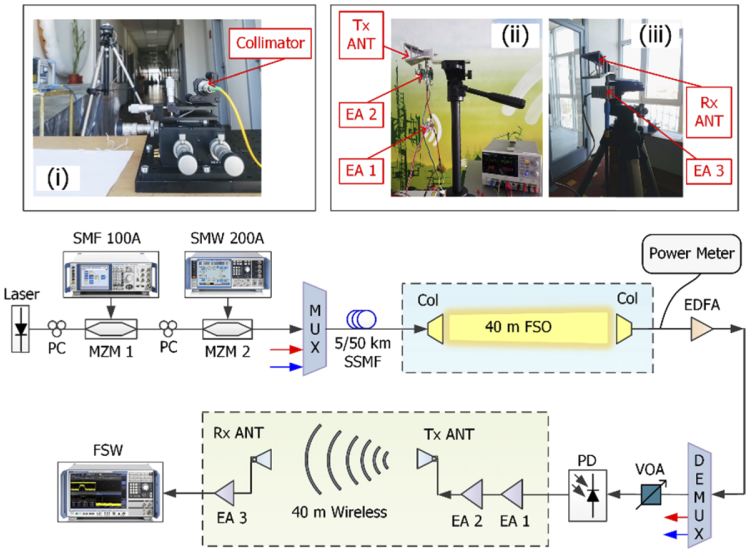

Fig. 2. Experimental configuration B. Insets: (i) FSO coupling, (ii) Tx ANT in the corridor and (iii) Rx ANT in the corridor.

Optics EXPRESS

The second set of experiments was carried out in a corridor of Faculty of Electrical Engineering, CTU in Prague with FSO and RF wireless channels extended up to 40 m as depicted in Fig. 2 (inset (i) and (ii)). Unlike configuration A, this testbed employed different modulation formats (i.e., 4/16/64-QAM) but using static signal bandwidth of 20 MHz. The SSMF link lengths were 5 and 50 km. At the output of the FSO channel, the optical power level was monitored by using a power meter connected to a 1% branch of a 1/99 coupler in order to ensure the FSO link alignment during the experiment. The measured FSO channel loss for 40 m was 12 dB. The EDFA output power was then set at 7 dBm and an additional EA 3 (Miteq AMF-4F-260400-40-10p) was used to boost the signal level. The remaining setup parameters were kept the same as in configuration A (see Table 2).

3. Experimental results and discussion

3.1. Configuration A

Figures 3(a) and (b) show the measured EVM as a function of received MMW power for the 64-QAM signal with 5, 20 and 50 MHz bandwidth following transmission over the hybrid MPL, which consists of SSMF (5 km), FSO (2 m) (without and with turbulence) and RF wireless channel (3 m). Also shown is the 8% EVM limit for 64-QAM, as defined in the third-generation partnership project (3GPP) specifications [23]. The EVM values were recorded over 90000 points and averaged over 50 sets of readings. Note that a variable optical attenuator (VOA) was used in front of the PD to adjust the level of received optical power and therefore the received MMW power.

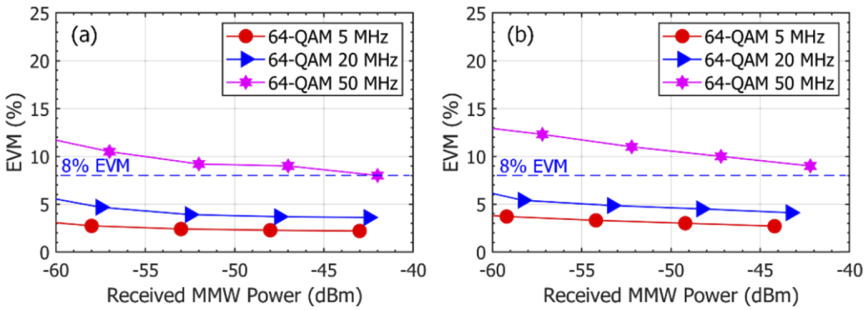

Fig. 3. EVM versus received MMW power of Configuration A with 5 km SSMF, 2 m FSO and 3 m RF wireless for 5, 20 and 50 MHz 64-QAM signals a) without and b) with atmospheric turbulence.

As can be observed, 64-QAM signals with 5 and 20 MHz bandwidth lead to EVM values well below the required limit of 8% regardless of the turbulence level. However, the signal with a 50 MHz bandwidth is more susceptible to turbulence. The impairment due to turbulence-induced fading is then clearly recognized in Fig. 3(b) with the EVMs exceed the 8% required limit at all received MMW powers. This is because of the fact that the wider QAM signal bandwidth, the higher noise power. In addition, 64-QAM signals with 5 and 20 MHz bandwidth were adopted as long-term evolution (LTE) evolved universal terrestrial radio access (E-UTRA) test model TM3.1, which provide a throughput of 18 and 75 Mb/s respectively. Lower data rate signals are less affected by the turbulence-induced intersymbol interference in comparison to 50 MHz 64-QAM signal, which was a custom digital modulation whose bit rate is up to 300 Mb/s. Table 3 summarizes the measured EVMs and calculated BER values for 64-QAM with 5, 20 and 50 MHz 64-QAM without and with turbulence for the hybrid MPL in configuration A at its maximal received MMW power. The turbulence-induced EVM penalties are 0.5, 0.5 and 1% for 5, 20 and 50 MHz, respectively, compared to non-turbulent performances. As can be seen, the EVM

Optics EXPRESS

penalties are relatively small; this is because the generated turbulence is moderate turbulence. However, for strong turbulence (i.e., C_n^2 of 2.4×10^{-10} $m^{-2/3}$ as in [13]), the EVM penalty was about 4% compared with no turbulence. We also evaluate the calculated BER of the M-QAM hybrid MPL based on the EVM as given by [1,3]:

$$\mathrm{BER}_{M-\mathrm{QAM}} = \frac{2}{\log_2(M)}\left(1-\frac{1}{\sqrt{M}}\right)\times \mathrm{erfc}\left(\sqrt{\frac{3}{2(M-1)}\times\frac{1}{\mathrm{EVM}^2}}\right), \tag{4}$$

where erfc(·) is the complementary error function. As shown in Table 3, the BER values are below the HD-FEC BER limit in all cases.

Table 3. Measured EVM and calculated BER results for hybrid MPL (Configuration A) consisting of 5 km SSMF, 2 m FSO and 3 m RF wireless channels.

	Hybrid MPL Performance			
	Without Turbulence		With Turbulence	
64-QAMSignal Bandwidth (MHz)	EVM (%)	BER	EVM (%)	BER
5	2.2	$< 1\times10^{-12}$	2.7	$< 1\times10^{-12}$
20	3.6	3.9×10^{-10}	4.1	2.9×10^{-8}
50	8.0	1.9×10^{-3}	9.0	9.0×10^{-2}

One of the most limiting factors in MPLs is the nonlinear distortion reducing dynamic range and affecting the overall system performance. The link performance was therefore further quantified in terms of 2nd and 3rd nonlinear distortions from which the spurious-free dynamic range (SFDR2 and SFDR3) values have been obtained. Note that the SFDR2 and SFDR3 measurements were carried out by introducing the fundamental signal, i.e., single carriers at frequencies of 200 and 201 MHz to MZM 2 while MZM 1 was fed by 12.5 GHz RF carrier frequency resulting in two tones test at the frequency of 25.2 GHz having 1 MHz spacing. The remaining experimental setup for SFDR measurement was maintained the same as depicted in Fig. 1 including both optical and RF channels to show real system parameters.

Figure 4 shows the measured RF output power as a function of the RF input power $P_{\mathrm{in-RF}}$ for the fundamental frequency and intermodulation distortions (IMDs) (i.e., 2nd and 3rd) components for the hybrid MPL. The overall IMDs refer to the distortions due to nonlinear characteristics of the components employed in the MPL, i.e., EAs. The fitted lines of the 2nd and 3rd order distortions cross the fundamental line at output intercept points (OIP2 and OIP3) with output

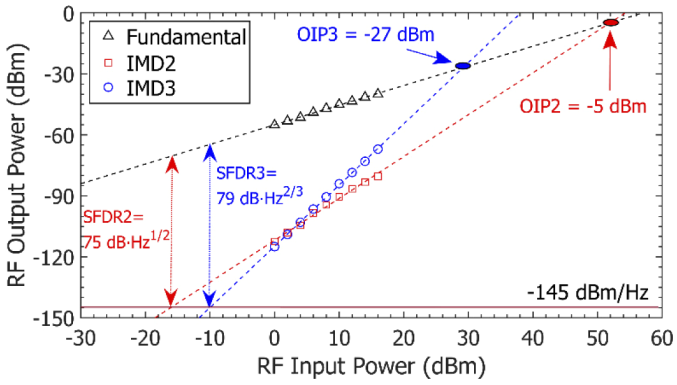

Fig. 4. The measured spurious-free dynamic range of Configuration A.

Optics EXPRESS

power values of -5 and -27 dBm, respectively. The SFDRs are limited by the system noise mainly by the amplifiers such as EAs and EDFA (i.e., amplified spontaneous emission noise). For the proposed system, the measured noise floor is about -145 dBm/Hz, which includes noise contributions from both EA1 and EA2. The resultant SFDR2 and SFDR3 are 75 dB·Hz$^{1/2}$ and 79 dB·Hz$^{2/3}$, respectively. Since we used a broadband signal, the crucial performance parameter is in particular SFDR3. The measured OIP3 and SFDR values are sufficient for the proposed hybrid MPL employing a direct detection receiver. In addition, these can be further improved by adopting a coherent detector [24] or a self-homodyne detector [25] but at the cost of increased complexity. Moreover, the phase noise of the generated signal was determined as low as -107 dBc/Hz at 10 kHz offset.

3.2. Configuration B

To investigate the overall transmission performance of the hybrid MPL for configuration B, which consists of 5 km SSMF and 40 m FSO/RF wireless channels, we first measured the EVM values as a function of the electrical signal-to-noise ratio (SNR) for M-QAM signal with 20 MHz bandwidth as shown in Fig. 5. Note that, 20 MHz 4/16/64-QAM signals used were E-UTRA test models TM3.3, 3.2 and 3.1, respectively [23]. For the SNR measurement of each QAM signal at the output of the hybrid MPL, we first adjusted the VOA and then measured the corresponding received MMW power and the noise floor level.

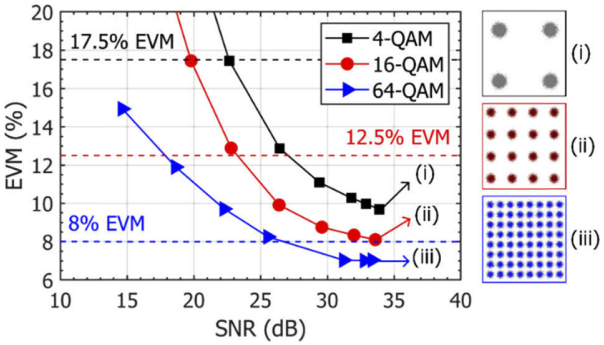

Fig. 5. EVM performance at different SNR levels for 4/16/64-QAM signals with 20 MHz bandwidth of Configuration B with 5 km SSMF, 40 m FSO and 40 m RF wireless links. Insets show corresponding constellations.

The EVM limits of 17.5, 12.5 and 8% for 4-, 16- and 64-QAM, respectively, as defined in the 3GPP specifications [23], are presented by horizontal dashed lines. As shown, at a SNR higher than 27 dB, all M-QAM signals meet the EVM requirements. The minimal SNR required to fulfill the limit is 23 dB at an EVM of 12.5% for 16-QAM. The lowest observed EVM values for 4/16/64-QAM are 9.6, 8.1 and 7%, respectively, corresponding to calculated BERs lower than 1×10^{-12}, 1.3×10^{-8} and 5.3×10^{-4}, respectively. All BER values are well below the HD-FEC limit. Also shown in the insets are the clear square-shaped constellations diagrams for M-QAM, further demonstrating high-quality signal transmission.

Figure 6 shows the EVM as a function of the received MMW power for M-QAM formats with fiber lengths of 5 and 50 km SSMF. Note that, transmission over a 50 km of SSMF (i.e., the maximal expected span for the hybrid MPL in rural areas) is possible due to the OCS modulation scheme effectively combating the fiber chromatic dispersion. As shown in Fig. 6, 4/16/64-QAM meet the EVM requirements for the received minimal MMW power of -49, -48 and -43 dBm, respectively. Moreover, the power penalty for the hybrid link with a 50 km of SSMF compared with 5 km of SSMF is lower than 1 dB for 4- and 16- QAM and 6 dB for 64-QAM. The insets in

Optics EXPRESS

Fig. 6 illustrate discernible constellation diagrams for M-QAM for the hybrid MPL with a 50 km of SSMF. Table 4 summarizes the measured EVM and calculated BER values for all three tested signals at its maximal received MMW power. The achieved BER performances for all QAM signals are below the HD-FEC limit.

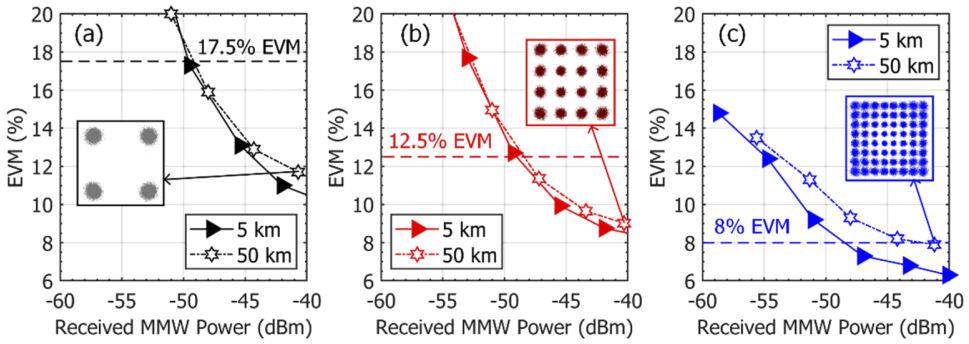

Fig. 6. EVM versus the received MMW power of Configuration B with SSMF lengths of 5 and 50 km, FSO and RF wireless lengths of 40 m: (a) 4-QAM, (b) 16-QAM and (c) 64-QAM format. Insets are the corresponding constellation diagrams.

Table 4. Measured EVM and calculated BER results for hybrid MPL (Configuration B) consisting of 50 km SSMF, 40 m FSO and 40 m RF wireless.

	Hybrid MPL Performance	
M-QAM (20 MHz)	EVM (%)	BER
4-QAM	11.7	$< 1\times10^{-12}$
16-QAM	9.0	2.5×10^{-7}
64-QAM	7.9	1.7×10^{-3}

Furthermore, we examined the effect of multipath-induced fading in the hybrid MPL with 20 MHz 64-QAM at 25 GHz by measuring the EVM as a function of the Rx ANT's angular orientation (also known as ANT misalignment) utilizing a high-precision rotation mount. The results are shown in Fig. 7. Note that, for ANT misalignment measurements, the hybrid MPL was composed of 50 km SSMF, 40 m FSO and 40 m RF wireless links. We observed EVM

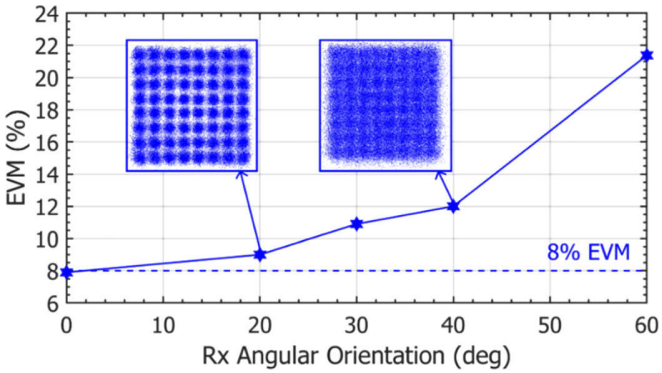

Fig. 7. EVM performance of the 64-QAM signal (Configuration B) under the variable angular orientation of Rx ANT off-axis of propagation.

Optics EXPRESS

impairment (i.e., above the limit of 8%) at the angular orientation values > 3°. This is because of fading due to reflected signals from walls along the 40 m corridor and the first Fresnel zone, which affects the signal strength. To better illustrate the impact of fading, the insets in Fig. 7 shows the measured constellation diagrams at the angular orientation values of 20° and 40°, which are distorted but still identifiable even for the EVMs significantly higher than 8% limit. However, the degradation of EVM/BER performance due to the RF wireless channel effects can be overcome by means of modulation, coding and adaptive equalization schemes [26,27]. Recently, the ANT misalignment has also been investigated in the D-band (141 GHz) RoF system, but over short RF wireless length of only 0.5 m [28], where the tolerable misalignment angle was found to be less than 1°. Note that, as reported in [28], angles higher than 1° lead to the increased BER above the HD-FEC limit.

4. Evaluation for extended outdoor link length

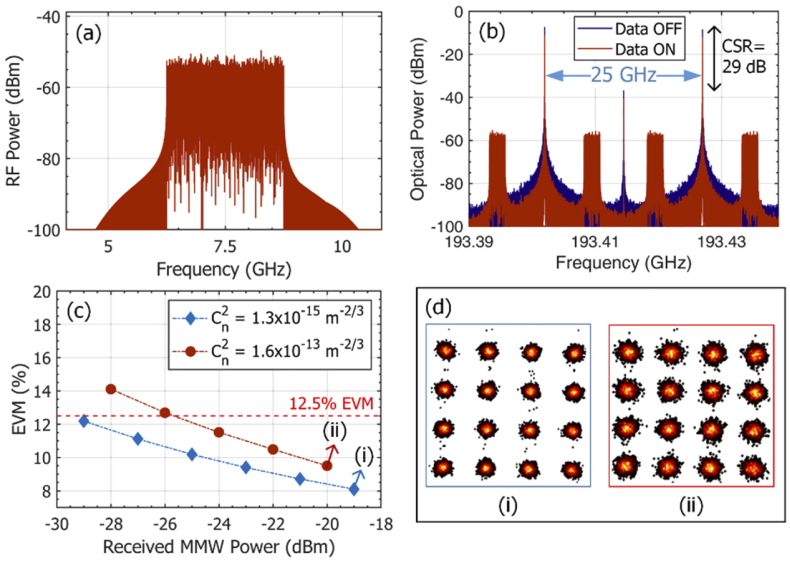

Fig. 8. Simulation results for hybrid MPL of 5 km SSMF and 500 m FSO links: (a) Electrical spectrum of transmitted 16-QAM signal, (b) Optical spectra obtained without and with 16-QAM data signal (c) EVM versus received MMW power for 10 Gb/s 16-QAM under weak and strong turbulence and (d) Corresponding constellation diagrams.

To further evaluate the proposed hybrid MPL for a practical outdoor scenario as part of the 5G network, we performed a simulation-based analysis at a bit rate of 10 Gb/s and a carrier frequency of 25 GHz using OptiSystem and MATLAB software co-simulation [29]. In detail, OptiSystem is used to accurately model the hybrid MPL as the experimental setup while MATLAB is used for signal analysis, i.e., EVM calculation. The link is composed of a 5 km of SSMF, however the FSO length is extended up to 500 m. The RF wireless link is not considered in this investigation. We have considered the weak and strong turbulence regimes in FSO channel with C_n^2 of 1.3×10^{-15} $m^{-2/3}$ and 1.6×10^{-13} $m^{-2/3}$, respectively. The simulation parameters are the same as those employed in Configuration B. A 16-QAM-based OFDM over IF of 7.5 GHz with a total signal bandwidth of 2.5 GHz was transmitted, as shown in Fig. 8(a). Figure 8(b) shows the simulated OCS spectrum with and without the 10 Gb/s 16-QAM signal. The CSR is about 29 dB demonstrating a good agreement between simulation and experimental results as can be seen in the inset (iv) in Fig. 1. Figure 8(c) illustrates the simulated EVM as a function of the received

Optics EXPRESS

MMW power for 16-QAM under the weak and strong turbulence conditions in the FSO channel. As shown, 16-QAM meets the EVM requirement of 12.5% at the received MMW power level > -25.5 dBm. For weak and strong turbulence regimes, the lowest obtained EVM values are 8.1 and 9.5%, which correspond to the BER values of 1.3×10^{-8} and 9.4×10^{-7}, respectively. It is worth mentioning that, there is a distinctive difference of > 20 dB between the experimentally measured (see Fig. 3) and simulated (see Fig. 8(c)) power levels. This is because, the simulated results are for the 10 Gb/s hybrid link requiring more power whereas the measured data is for the 300 Mb/s link (i.e., 50 MHz 64-QAM).

The effect of turbulence on the link performance can also be comprehended by means of the constellation diagrams, see Fig. 8(d), which are still distinguishable even under strong turbulence, thus confirming the feasibility of the proposed hybrid scheme for practical applications. Note that, the power penalty due to turbulence can be reduced by using a digital turbulence compensation technique which is a combination of a 12-spatial mode digital coherent receiver and a multimode pre-amplifier as recently demonstrated in [30].

5. Conclusions

We have proposed and experimentally demonstrated a hybrid microwave photonic link at the K-band having the frequency of 25 GHz with two different configurations. We demonstrated potential applications in seamless broadband wireless access networks. For the first configuration, we examined the hybrid MPL consisting of 5 km SSMF, 2 m turbulent FSO and 3 m RF wireless channels with the focus on the effect of turbulence-induced fading on the 64-QAM signals with 5, 20 and 50 MHz bandwidths. We determined the non-linear distortions by showing that the 2^{nd} and 3^{rd} order SFDRs of the hybrid MPL are 75 and 79 dB·$Hz^{2/3}$, respectively, as well as overall phase noise below -107.3 dBc/Hz at 10 kHz offset. For the second MPL configuration, we individually transmitted 20 MHz 4/16/64-QAM signals over 50 km of SSMF, 40 m FSO and 40 m RF wireless channels and compared the performance. Depending on the data rates and applications, each modulation can be adaptively configured. The result showed that the recovered signals displayed EVM values well below the required limits as defined by 3GPP specifications with no significant received MMW power penalties. The tolerable ANT misalignment angle for such an indoor corridor transmission was also investigated and found to be less than 3°. Moreover, we have provided a simulation analysis carried out for 10 Gb/s 16-QAM link with the FSO span of 500 m under weak and strong turbulence conditions in the FSO channel. The experimental and simulation results have demonstrated the feasibility of the proposed hybrid MPL for use in practical applications since the scheme reduces demands on high-frequency equipment and therefore showing high potential for the 5G wireless networks.

Funding

The Ministry of Education, Youth and Sports of Czech Republic (CZ.02.2.69/0.0/0.0/16_027/0008465); Czech Technical University in Prague (SGS17/182/OHK3/3T/13).

References

1. X. Chen and J. Yao, "A high spectral efficiency coherent microwave photonic link employing both amplitude and phase," J. Lightwave Technol. **33**(14), 3091–3097 (2015).
2. Y. Li, Q. Yang, I. A. Hemadeh, M. El-Hajjar, C.-K. Chan, and L. Hanzo, "Experimental characterization of the radio over fiber aided twin-antenna spatial modulation downlink," Opt. Express **26**(10), 12432 (2018).
3. W. Zhang, A. Wen, Y. Li, and J. Ma, "A high spectral efficiency microwave photonic link with optimization of chromatic-dispersion-induced power fading," J. Lightwave Technol. **37**(4), 1123–1132 (2019).
4. L. Zhang, M. Zhu, C. Ye, S.-H. Fan, C. Liu, X. Hu, P. Cao, Q. Chang, Y. Su, and G.-K. Chang, "Generation and transmission of multiband and multi-gigabit 60-GHz MMW signals in an RoF system with frequency quintupling technique," Opt. Express **21**(8), 9899 (2013).
5. S. E. Alavi, M. R. K. Soltanian, I. S. Amiri, M. Khalily, A. S. M. Supa'at, and H. Ahmad, "Towards 5G: A photonic based millimeter wave signal generation for applying in 5G access fronthaul," Sci. Rep. **6**(1), 19891 (2016).

Optics EXPRESS

6. H. Wen, H. Zheng, Q. Mo, A. M. Velázquez-Benítez, C. Xia, B. Huang, H. Liu, H. Yu, P. Sillard, J. E. A. Lopez, R. A. Correa, and G. Li, "Few-mode fibre-optic microwave photonic links," Light: Sci. Appl. **6**(8), e17021 (2017).
7. C. Vagionas, S. Papaioannou, G. Kalfas, N. Pleros, N. Argyris, K. Kanta, N. Iliadis, G. Giannoulis, D. Apostolopoulos, and H. Avramopoulos, "A six-channel mmWave/IFoF link with 24Gb/s capacity for 5G fronthaul networks," in *MWP 2018 – 2018 International Topical Meeting on Microwave Photonics* (IEEE, 2018), p. Tu4B.6.
8. Z. Ghassemlooy, W. O. Popoola, and S. Rajbhandari, *Optical Wireless Communications – System and Channel Modelling with Matlab*, 2nd ed. (CRC Press, 2019).
9. K. Wang, A. Nirmalathas, C. Lim, K. Alameh, and E. Skafidas, "Full-duplex gigabit indoor optical wireless communication system with CAP modulation," IEEE Photonics Technol. Lett. **28**(7), 790–793 (2016).
10. K. Kazaura, K. Wakamori, M. Matsumoto, T. Higashino, K. Tsukamoto, and S. Komaki, "RoFSO: A universal platform for convergence of fiber and free-space optical communication networks," IEEE Commun. Mag. **48**(2), 130–137 (2010).
11. C. Ben Naila, K. Wakamori, M. Matsumoto, A. Bekkali, and K. Tsukamoto, "Transmission analysis of digital TV signals over a radio-on-FSO channel," IEEE Commun. Mag. **50**(8), 137–144 (2012).
12. J. Zhang, J. Wang, Y. Xu, M. Xu, F. Lu, L. Cheng, J. Yu, and G.-K. Chang, "Fiber–wireless integrated mobile backhaul network based on a hybrid millimeter-wave and free-space-optics architecture with an adaptive diversity combining technique," Opt. Lett. **41**(9), 1909 (2016).
13. J. Bohata, M. Komanec, J. Spáčil, Z. Ghassemlooy, S. Zvánovec, and R. Slavík, "24–26 GHz radio-over-fiber and free-space optics for fifth-generation systems," Opt. Lett. **43**(5), 1035–1038 (2018).
14. M. A. Esmail, A. M. Ragheb, H. A. Fathallah, M. Altamimi, and S. A. Alshebeili, "5G-28 GHz signal transmission over hybrid all-optical FSO/RF link in dusty weather conditions," IEEE Access **7**, 24404–24410 (2019).
15. R. M. Borges, T. R. R. Marins, M. S. B. Cunha, H. R. D. Filgueiras, I. F. Da Costa, R. N. Da Silva, D. H. Spadoti, L. L. Mendes, and A. C. Sodre, "Integration of a GFDM-based 5G transceiver in a GPON using radio over fiber technology," J. Lightwave Technol. **36**(19), 4468–4477 (2018).
16. "5G spectrum GSMA public policy position," https://www.gsma.com/.
17. R. Zhang, F. Lu, M. Xu, S. Liu, P. Peng, S. Shen, J. He, H. J. Cho, and Q. Zhou, "An ultra-reliable MMW / FSO A-RoF system based on coordinated mapping and combining technique for 5G and beyond mobile fronthaul," J. Lightwave Technol. **36**(20), 4952–4959 (2018).
18. A. Pandey and S. K. Selvaraja, "Broadly tunable wideband optical single sideband generation using self-coupled silicon resonator," Opt. Express **27**(6), 8476 (2019).
19. P. T. Dat, A. Kanno, and N. Yamamoto, "Seamless convergence of fiber and wireless systems for 5G and beyond networks," J. Lightwave Technol. **37**(2), 592–605 (2019).
20. M. A. Esmail, A. Ragheb, H. Fathallah, and S. Alshebeili, "Demonstration of photonics-based switching of 5G signal over hybrid all-optical network," IEEE Photonics Technol. Lett. **30**(13), 1250–1253 (2018).
21. Y. Alfadhli, P. C. Peng, H. Cho, S. Liu, R. Zhang, Y. W. Chen, and G. K. Chang, "Real-time FPGA demonstration of hybrid bi-directional MMW and FSO fronthaul architecture," in *2019 Optical Fiber Communications Conference and Exhibition, OFC 2019 – Proceedings* (OSA, 2019), p. W2A.39.
22. L. C. Andrews and R. L. Phillips, *Laser Beam Propagation through Random Media* (SPIE, 2005), 1.
23. 3GPP TS 36.104, *Base Station (BS) Radio Transmission and Reception (2018)*, **version 16**(version 16.0.0).
24. R. Li, X. Han, X. Chen, X. Chen, and J. Yao, "A phase-modulated microwave photonic link with an extended transmission distance," IEEE Photonics Technol. Lett. **27**(24), 2563–2566 (2015).
25. P. T. Dat, A. Kanno, N. Yamamoto, and T. Kawanishi, "Full-duplex transmission of LTE-A carrier aggregation signal over a bidirectional seamless fiber-millimeter-wave system," J. Lightwave Technol. **34**(2), 691–700 (2016).
26. J. Proakis and M. Salehi, *Digital Communications*, 5th ed. (McGraw-Hill, 2008).
27. T. F. B. de Sousa and M. A. C. Fernandes, "Butterfly neural equalizer applied to optical communication systems with two-dimensional digital modulation," Opt. Express **26**(23), 30837 (2018).
28. R. Puerta, J. Yu, X. Li, Y. Xu, J. J. Vegas Olmos, and I. Tafur Monroy, "Antenna misalignment effects in 100 Gbit/s D-band wireless transmissions," Microw. Opt. Technol. Lett. **59**(6), 1431–1434 (2017).
29. "OptiSystem archives-Optiwave," https://optiwave.com/.
30. N. K. Fontaine, R. Ryf, Y. Zhang, J. C. Alvarado-Zacarias, S. Van Der Heide, M. Mazur, H. Huang, H. Chen, R. Amezcua-Correa, G. Li, M. Capuzzo, R. Kopf, A. Tate, H. Safar, C. Bolle, D. T. Neilson, E. Burrows, K. Kim, M. Bigot-Astruc, F. Achten, P. Sillard, A. Amezcua-Correa, and J. Carpenter, "Digital turbulence compensation of free space optical link with multimode optical amplifier," in *European Conference on Optical Communication, ECOC 2019*, p. PD1.1.

IEEE Photonics Journal
An IEEE Photonics Society Publication

Open Access

Impact of Thermal-Induced Turbulent Distribution Along FSO Link on Transmission of Photonically Generated mmW Signals in the Frequency Range 26–40 GHz

Volume 12, Number 1, February 2020

Luis Vallejo
Matej Komanec
Beatriz Ortega, *Member, IEEE*
Jan Bohata
Dong-Nhat Nguyen, *Member, IEEE*
Stanislav Zvanovec, *Senior Member, IEEE*
Vicenç Almenar, *Member, IEEE*

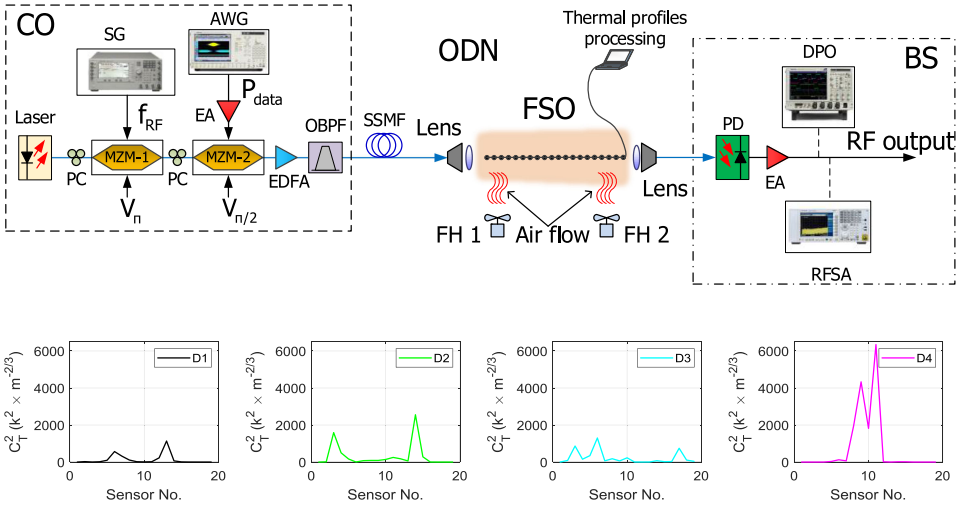

DOI: 10.1109/JPHOT.2019.2959227

Impact of Thermal-Induced Turbulent Distribution Along FSO Link on Transmission of Photonically Generated mmW Signals in the Frequency Range 26–40 GHz

Luis Vallejo [1], **Matej Komanec** [2], **Beatriz Ortega** [1], ***Member, IEEE***, **Jan Bohata** [2], **Dong-Nhat Nguyen** [2], ***Member, IEEE***, **Stanislav Zvanovec** [2], ***Senior Member, IEEE***, **and Vicenç Almenar** [1], ***Member, IEEE***

[1]Instituto de Telecomunicaciones y Aplicaciones Multimedia, Universitat Politecnica de Valencia, Camino de vera, 46022 Valencia, Spain
[2]Department of Electromagnetic Field, Faculty of Electrical Engineering, Czech Technical University in Prague, 166 27 Prague, Czech Republic

DOI:10.1109/JPHOT.2019.2959227

Manuscript received November 5, 2019; revised December 4, 2019; accepted December 7, 2019. Date of publication December 11, 2019; date of current version January 17, 2020. This work was supported in part by the Research Excellence Award Programme GVA under Grant PROMETEO 2017/103 and in part by the Spanish Ministerio de Ciencia, Innovación y Universidades, under RTI2018-101658-B-I00 FOCAL Project and MEYS Project LTC18008 within COST CA16220. Corresponding author: Luis Vallejo (e-mail: luivalc2@iteam.upv.es).

Abstract: Microwave photonics is a promising solution to transmit millimeter wave (mmW) signals for the 5th generation (5G) mobile communications as part of a centralized radio access network (C-RAN). In this paper, we experimentally evaluate the impact of turbulent free space optics links on photonically generated mmW signals in the frequency range of 26−40 GHz. We analyze the remote generation of mmW signals over hybrid links based on free-space optics (FSO) and standard single mode optical fiber (SSMF) with −39.97 dBm received electrical power and phase noise level at 100 kHz as low as −95.92 dBc Hz at 26 GHz. Different thermal distributions along the FSO link have been implemented and Gamma-Gamma model has been employed to estimate the thermally induced turbulence. The results show high electrical power decrease and fluctuation of the generated mmW signal according to the particular level of the turbulence in terms of refractive index structure parameter and thermal distribution along the FSO link. 8 Gb/s 16-quadrature amplitude modulation (QAM) data transmission at 42 GHz has been demonstrated over the hybrid link with minimal error vector magnitude (EVM) value of 5% whereas turbulent FSO link introduced up to 5 dB power penalty.

Index Terms: Access networks, free space optics, millimeter waves, microwave photonics.

1. Introduction

Mobile data traffic is expected to grow up to 77 exabytes per month by 2022 according to [1], i.e., a sevenfold increase over 2017, which leads to a compound annual growth rate of 46% from 2017

to 2022. To deal with such explosive growth, the 3rd Generation Partnership Project (3GPP) has been developing the new upcoming mobile network, known as the 5th generation (5G). However, 5G will not only be an evolution of the mobile network but represent significant progress in wireless communications since it requires massive machine-type communications, ultra-reliable and low latency communications, enhanced mobile broadband and ultra-fast data transfer [2] to support emergency services and applications such as internet of things, mobile ultra-high definition video streaming or autonomous driving [3].

5G definition includes the proposal of two main frequency bands: FR1 (below 6 GHz) and FR2 (24.25−52.60 GHz) [4]. Nowadays, the spectrum below 6 GHz is congested due to many current wireless services. However, millimeter-wave (mmW) technology, in which frequency range can exceed 100 GHz, will play a key role in 5G networks due to its enormous available bandwidth [5]. In this context, radio over fiber (RoF), basically consisting of an optical carrier modulated by a radio signal, is a promising technology for cloud radio access networks (C-RAN) [6]. In such architecture, optical distribution networks (ODN) deliver mmW signals from a central office (CO) over variable long distances to many remote base stations (BS) with low attenuation, immunity to radio frequency interference, transparency to modulation formats, high capacity, flexibility and dynamic resource allocation as its main advantages [7].

Microwave photonics, as a discipline combining microwave and photonic fields, has been recently extensively employed to generate mmW signals with low phase noise and frequency tenability [8]. The simplest method to photonically generate high radio frequency signal is to beat two heterodyne lasers separated by the desired frequency, but phase control loop or optical injection locking techniques are required for frequency and phase stabilization [9]. The literature shows various proposals to generate mmW signals by using multimode light sources, such as dual-mode lasers, mode-locked lasers, Fabry-Perot lasers or supercontinuum sources but in general, these designs need to be customized and they are therefore costly [10]. Moreover, optical fiber non-linear effects such as four-wave mixing [11], cross-gain modulation [12] or stimulated Brillouin Scattering [13] have also been proposed for mmW signal generation schemes with even more increased cost and complexity.

The use of external modulation by a $LiNbO_3$ Mach-Zehnder modulator (MZM) shows an excellent compromise among the aforementioned factors. A continuous optical wave (CW) is modulated by a radio signal, and optical frequency multiplication is achieved when two sidebands, separated by the desired frequency, beat each other at the photodetector [14]. Frequency doubling, quadrupling and up to octupling [15] have been recently demonstrated allowing to reduce the electric bandwidth requirements significantly.

The transmission of radio signals over free-space optics (FSO), so-called RoFSO [16], offers typical flexibility of wireless communications and speed of light transmission [17]. It also provides a higher level of coverage and mobility while exploiting unlicensed frequencies in the optical wireless domain [18]. Furthermore, the FSO link can be employed to transmit multiple wavelength division multiplexed (WDM) channels simultaneously. Nevertheless, FSO is highly affected by atmospheric phenomena, especially by thermal turbulence. The thermal distribution can vary significantly based on the day time and as well within the urban environment due to several sources of heating [19], [20]. High thermal differences can be experienced, e.g., up 30 °C [19], resulting in different turbulence levels in the vicinity of buildings, air conditions, highways, masts and in and over the street canyons – see illustrated temperature profile across a city in Fig. 1.

In this paper, mmW signals in the frequency range of 26−40 GHz are photonically generated by using a MZM biased at the carrier suppression point. Furthermore, 8 Gb/s signal transmission is demonstrated over 40 GHz mmW signal along the RoF/FSO link and system penalties have been measured under different thermal-induced turbulence distributions along the FSO channel. To the best authors' knowledge, this paper presents for the first time the experimental characterization of mmW signals transmission at such a frequency band under turbulence on RoF/FSO links providing an estimation of the impact of different temperature distributions.

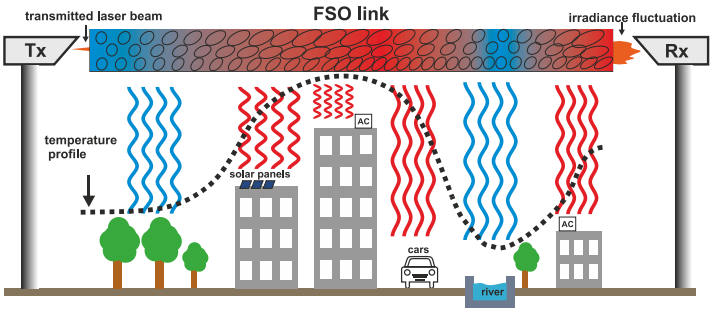

Fig. 1. Illustration of different turbulent flows influencing FSO in urban areas.

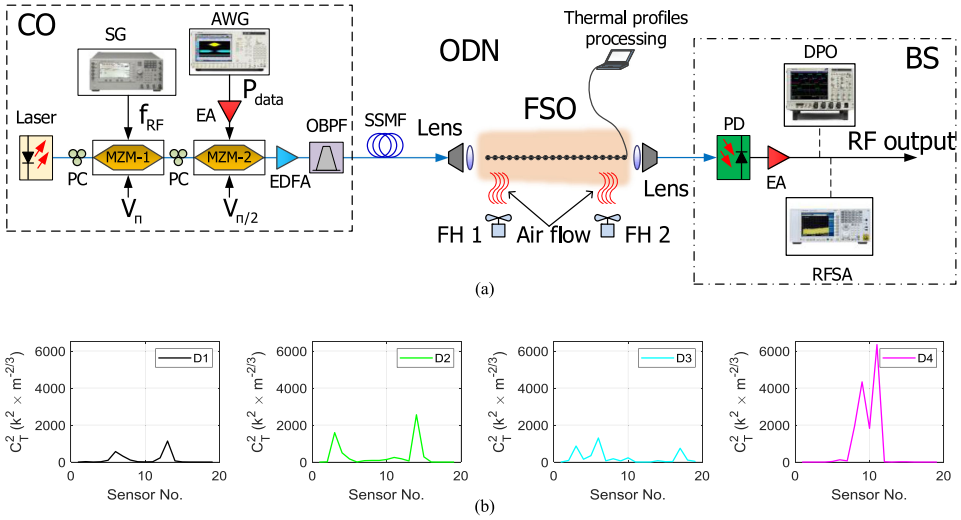

Fig. 2. (a) Experimental setup (CO: central office, ODN: optical distribution network, PC: polarization controller, MZM: Mach–Zehnder modulator, AWG: arbitrary waveform generator, EA: electrical amplifier, EDFA: erbium-doped fiber amplifier, OBPF: optical bandpass filter, SSMF: standard single mode fiber, FSO: free-space optics, FH: fan heater, PD: photodetector, RFSA: RF spectrum analyzer, DPO: digital phosphor oscilloscope), and (b) C_T^2 distributions.

2. System Description

The experimental setup of mmW signal transmission over a hybrid optical link of SSMF and FSO is shown in Fig. 2(a). A distributed feedback (DFB) laser (EXFO IQS) at a wavelength of 1550.12 nm with an output optical power of 10 dBm provides the optical carrier. A polarization controller (PC) adjusts the state of polarization to minimize MZM-1 (Photline MX-LN-40) losses. MZM-1 is biased at null transmission point (half-wave voltage, V_π), i.e., at 6.4 V, to obtain the carrier suppressed double sideband (CS-DSB) modulated signal. The optical carrier is then modulated by a radio frequency (RF), f_{RF}, which is generated by a signal generator (Agilent PSG E8267C) with an output RF power of 22 dBm.

The experimental setup employs another PC before a second modulator, MZM-2 (Avanex PowerBit F-10), which is biased at the linear point (quadrature voltage $V_{\pi/2}$), i.e., 5.8 V. The optical signal is then modulated by the data generated by an arbitrary waveform generator (AWG, Tektronix AWG7122C). Note that the data signal with 28 dBm output power is amplified by a 12 dB gain RF electrical amplifier (Minicircuits ZX60-14012L-S+).

The modulated optical signal is amplified by an erbium-doped fiber amplifier (EDFA, Amonics EDFA-23-B-FA) with 13 dBm output power and filtered out by an optical bandpass filter (OBPF,

Finisar Waveshaper 4000S) having a bandwidth of $\Delta\lambda = 1.5$ nm to reduce amplified spontaneous emission. The signal is then launched into 1.4 km long standard single mode fiber (SSMF) what is followed by a 1.2 m long FSO channel using a pair of air-spaced doublet collimators (Thorlabs F810APC-1550). The FSO link loss is 4.5 dB, which is significantly lower compared to free space propagation of radio waves in the mmW band.

Artificial turbulence is produced on the FSO channel according to four different spatial temperature distributions (D1–D4), as shown in Fig. 2(b). The distribution is expressed in terms of the temperature structure parameter C_T^2 distribution along the link, which is explained further. Turbulence is generated by two fan heaters introducing temperature gradients into the FSO channel and measured by 20 temperature sensors equidistantly located along the FSO link with 0.06 m spacing. These distributions represent inhomogeneous temperature profile when the collimated laser beam propagates in FSO link through differently heated areas, according to Fig. 1. D1 introduces almost uniform turbulence along the link, whereas in the case of D2 and D3, the fans' thermal flow was set in order to reach increased thermal gradient close to the receiver and transmitter, respectively, which can be induced e.g., by thermal flow close to the building/masts of transmitting/receiving FSO heads. Finally, D4 represents peak turbulence in the middle of the link, which can be caused e.g., by an increased airflow over the street canyons, roads or air-condition outlets as indicated in Fig. 1.

According to photonic mmW signal generation approach based on external CS-DSB modulated signals [14], the mmW signal $f_{\mathrm{mmW}} = 2f_{RF}$, is generated after beating the modulated sidebands at photodetector (PD, Finisar BPDV2020R) and subsequently, it is amplified by an RF electrical amplifier (SHF-810). The mmW signal is analyzed by an RF spectrum analyzer (RFSA) showing the RF signal potentially launched to an antenna located in the C-RAN BS infrastructure.

3. Turbulence Effect on FSO System

FSO is widely affected by atmospheric phenomena including high attenuation due to fog, rain, snow or irradiance fluctuation, known as scintillation, as a result of the optical turbulence [21]. The extent of field amplitude fluctuation in the atmospheric turbulence can be characterized by the log-amplitude variance σ_R^2, commonly referred to as Rytov parameter, which is related to the refractive index structure parameter C_n^2 for a plane wave as follows [22]:

$$\sigma_R^2 = 2.25k^{7/6} \int_0^L C_n^2(x)\,(L-x)^{5/6}dx, \tag{1}$$

where k is the wave number and L is the horizontal distance travelled by the optical field/radiation. Note that, uniform C_n^2 leads to Rytov variance given by:

$$\sigma_R^2 = 1.23k^{\frac{7}{6}}C_n^2L^{\frac{11}{6}}, \tag{2}$$

The C_n^2 parameter, which determines the strength of the turbulence, is defined as:

$$C_n^2 = \left(79 \times 10^{-6}\frac{P_a}{T^2}\right)^2 C_T^2, \tag{3}$$

where P_a is the atmospheric pressure in millibars and C_T^2 is the temperature structure parameter, which is defined as:

$$C_T^2 = (T_1 - T_2)^2/L_p^{2/3}. \tag{4}$$

T_1 and T_2 are temperatures at two points separated by distance L_p. Therefore, based on the thermal distributions along the FSO propagation path, it is possible to determine C_T^2 and consequently C_n^2. According to the Gamma-Gamma (GG) atmospheric turbulence (AT) model [23], the probability

TABLE 1
Refractive Index and Temperature Structure Parameters of Different Temperature Distributions

Turbulent scenarios	C_T^2 $(K^2\, m^{-2/3})$	C_n^2 $(m^{-2/3})$ (L=1.2 m)	C_n^2 $(m^{-2/3})$ (L=500 m)
D1	138.01	$1 \cdot 10^{-10}$	$1.6 \cdot 10^{-15}$
D2	315.59	$2.3 \cdot 10^{-10}$	$3.6 \cdot 10^{-15}$
D3	227.83	$1.5 \cdot 10^{-10}$	$2.4 \cdot 10^{-15}$
D4	775.43	$5.7 \cdot 10^{-10}$	$8.9 \cdot 10^{-15}$

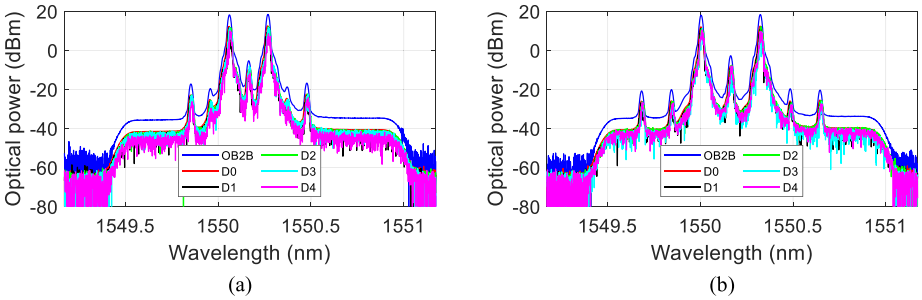

Fig. 3. Optical spectra of the carrier-suppressed RF modulated signal (Resolution bandwidth (RBW) = 0.02 nm) for different turbulence conditions at different frequencies: (a) 26 GHz and (b) 40 GHz.

of a given intensity I at the end of the link is given by:

$$P(I) = \frac{2(\alpha\beta)^{(\alpha+\beta)/2}}{\Gamma(\alpha)\,\Gamma(\beta)} I^{(\alpha+\beta)/2-1} K_{\alpha-\beta}\left(2\sqrt{\alpha\beta I}\right)$$

$$\alpha = \exp\left[\frac{0.49\sigma_R^2}{\left(1+1.11\sigma_R^{\frac{12}{5}}\right)^{\frac{5}{6}}}\right] - 1, \quad \beta = \exp\left[\frac{0.51\sigma_R^2}{\left(1+0.69\sigma_R^{\frac{12}{5}}\right)^{\frac{5}{6}}}\right] - 1 \tag{5}$$

where $1/\alpha$ and $1/\beta$ are the variances of the small and large scale eddies, respectively, $\Gamma(\cdot)$ is the Gamma function and $K_{\alpha-\beta}(\cdot)$ is the modified Bessel function of the second kind. The intensity fluctuations are characterized by the probability distribution, which is classified as: Weak turbulence ($\sigma_R^2 < 1$), Moderate turbulence ($\sigma_R^2 \approx 1$)or Strong turbulence ($\sigma_R^2 > 1$).

In our setup, turbulence is generated using two fans blowing hot air perpendicular into the FSO channel in order to create a thermal gradient along the optical propagation path. Table 1 shows the averaged C_T^2 and C_n^2 corresponding to D1–D4 temperature distributions in our experiment. Note that the spacing between adjacent sensors is $L_p = 0.06$ m, the atmospheric pressure $P_a = 1024$ mm and wavelength $\lambda = 1550.12$ nm. Direct calculation of Rytov variance ($\sigma_R^2 < 0.05$ in all cases) leads to a weak turbulence regime in our experimental setup. In order to show impact for a longer span, C_n^2 values have been recalculated via σ_R^2 to reflect 500 m FSO transmission distance.

The effect of the turbulence on the optical signal transmitted over the FSO channel is shown by the optical spectra comparison of the OB2B and the hybrid links (D0–D4) under different turbulent levels in Fig. 3(a) and (b) for 26 GHz and 40 GHz, respectively. Note that optical power measurements over FSO link employ higher sensitivity mode in the optical spectrum analyzer, leading to lower noise level. The turbulent-induced signal fluctuations in the optical domain result in reduced optical power by values up to 3 dB and 4 dB for the highest impact turbulence distributions at 26GHz and 40 GHz, respectively, with respect to D0.

Fig. 4(a) shows the RF spectra of the signal generated at 26 GHz after opto-electronic conversion and measured by the MXA analyzer (Agilent N9020A) in order to evaluate the impact of the

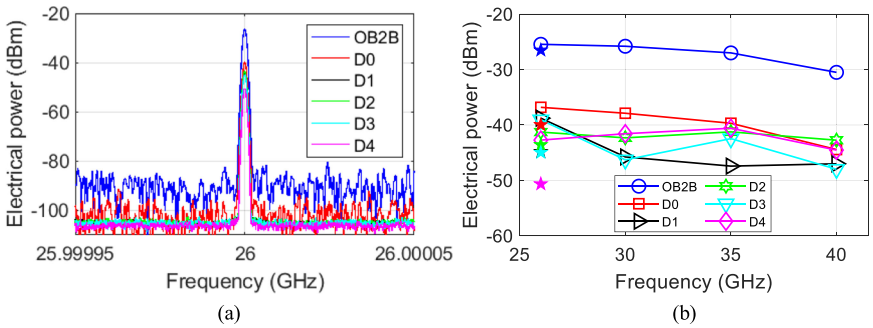

Fig. 4. Impact of turbulence on the electrical power: (a) Spectral distribution and (b) Dependence on the electrical frequency.

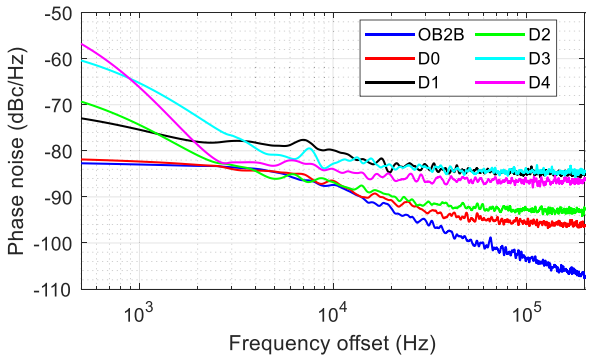

Fig. 5 Phase noise measurements at 26 GHz (RBW = 220 Hz).

turbulence along the FSO transmission in terms of RF power and also the noise floor. The measured received electrical power for OB2B is −26.5 dBm, whereas −39.97 dBm is obtained after transmission over the hybrid link without induced turbulence (D0) and up to 12 dB power decrease is measured when turbulence (D1–D4) is applied in the FSO link. Note that trace average mode is employed to reduce the noise level after FSO transmission in the RFSA. Nevertheless, no effects on the signal linewidth can be observed.

Fig. 4(b) shows the measured electrical power of the signal in the frequency range of 26 − 40 GHz mmW after photodiode by using PNA-X (Agilent N4373C). Star markers at 26 GHz show the results obtained by the high-resolution MXA analyzer where each color represents different temperature distribution according to D1–D4 profiles. As expected, the RF power decreases due to the overall system frequency response when the frequency increases, as shown in the OB2B and D0 curves over 26 − 40 GHz, with a total drop of 7.7 dB. However, this value is not constant for measurements under thermally induced turbulence due to power fluctuations. The power drop about 2 dB is measured for D2 and D4, whereas values over 8 dB are obtained for D1 and D3.

Fig. 5 depicts the phase noise measured at 26 GHz by MXA for different temperature distributions and Table 2 summarizes phase noise results at different offsets. The phase noise at 100 kHz offset is measured as −103.36 dBc/Hz for OB2B, whereas it is increased up to −95.92 dBc/Hz for D0 with a further increase under the turbulent regimes. As observed in Fig. 5, the impact of D1–D4 turbulence results in a higher phase noise level due to both power decrease and increased noise floor. Whereas scenario D2 with increased turbulence level close to the receiver shows the lowest phase noise among D1–D4 at 100 kHz, the highest phase noise is induced by scenarios D1 and D3 where the turbulence level is uniformly distributed and increased close to the transmitter, respectively.

TABLE 2
Phase Noise Measurements in dBc/Hz of 26 GHz Generated Signal at Different Offsets (RBW = 220 Hz)

		Frequency offset		
		$1\ kHz$	$10\ kHz$	$100\ kHz$
Scenario	OB2B	−82.97	−87.41	−103.36
	D0	−82.32	−86.49	−95.92
	D1	−75.42	−79.85	−84.85
	D2	−74.36	−86.80	−92.77
	D3	−65.29	−82.81	−84.34
	D4	−66.2	−83.93	−86.75

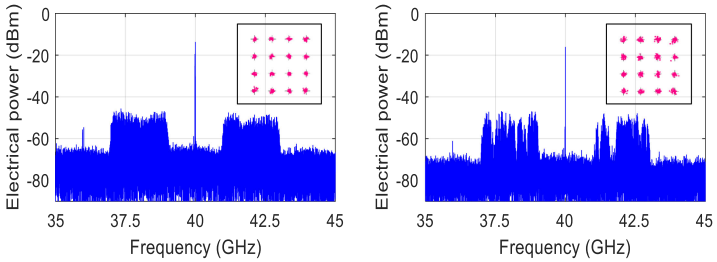

Fig. 6. Electrical spectrum of 8 Gb/s 16-QAM data signal over 40 GHz with 1 dBm at the receiver input for: (a) D0, and (b) under D3 turbulence profile. Insets show the corresponding constellation diagrams.

4. Data Transmission Experiment

In this section, an RF carrier at 20 GHz is employed to generate a 40 GHz mmW signal, which is further modulated by 16-QAM signal with 2 GHz bandwidth. Note that the modulating signal, using pseudorandom binary sequence (PRBS) length of 2^9-1, has a center frequency of 2 GHz. It results in a bitrate of 8 Gb/s throughout the hybrid ODN.

Fig. 6 shows the electrical spectra for 40 GHz mmW signals carrying 8 Gb/s data when the received optical power at PD input is 1 dBm. The RF carrier and data power is −16 dBm and −53 dBm, respectively, after transmission over the hybrid link without induced turbulence, i.e., scenario D0, which is shown in Fig. 6(a). Note that an RF electrical post-detection amplifier with 29 dB gain is employed before the signal analyzer. Fig. 6(b) shows the impact of the D3 turbulence profile on the transmitted spectrum where data signal bands undergo a time-varying fading effect due to interference between signals with different random delays at the receiver. Insets in Fig. 6(a) and (b) show the received 16-QAM constellation, whose error vector magnitudes (EVMs) are 5.1% and 6%, respectively. Note that, the EVM is measured by a digital phosphor oscilloscope (DPO) (Tektronix DPO72004C).

Finally, Fig. 7 plots the obtained EVM versus the received optical power at PD input for all tested scenarios. Since only 1.4 km SSMF and 1.2 m long FSO channel are employed, there is no significant power penalty between OB2B and D0. The EVM values of OB2B and D0 are kept below the limit of 12.5% for optical power up to −4.3 dBm at the optical receiver whereas minimum EVM of 5% is measured for a received power of 1 dBm. The largest EVM impact of turbulence has been obtained under D1 temperature distribution which represents evenly distributed turbulence along the channel. The power penalty is in this case almost 5 dB at 12.5% of EVM, compared to D0. The EVM can be kept below 12.5% for received optical power up to −2.1 dBm for D2, D3 and D4 when turbulence highly influences the areas closer to the receiver and transmitter or exhibit a peak in the center of the link, respectively. However, at least 0.3 dBm of received optical power is required

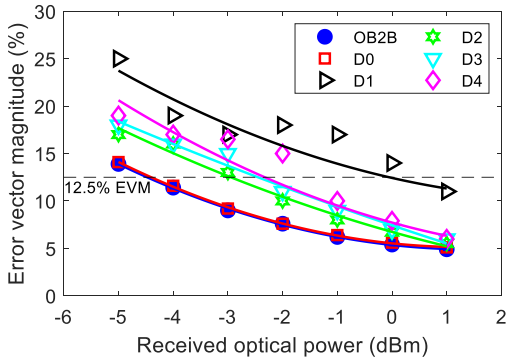

Fig. 7. Measured error vector magnitude (EVM) for different links and temperature distributions for 8 Gb/s 16-QAM signal over 40 GHz mmW signal.

for D1. Note that, despite the high phase noise level and low electrical power measurements in this scenario, the conducted measurements showed that evenly distributed turbulence in the FSO link has the highest impact on EVM performance in such system and the distribution of scintillations along the link also plays a key role in the signal transmission penalty.

5. Conclusions

In this paper, for the first time, we have experimentally demonstrated the impact of different turbulent distributions along the RoFSO link on mmW signal transmissions in the frequency range of 26−40 GHz in a hybrid FSO/SSMF network. Optical carrier suppression at MZM has been used to generate double frequency signals, i.e., the measured RF power and phase noise at 100 kHz offset at 26 GHz were −39.97 dBm and −95.92 dBc/Hz, respectively. Moreover, 8 Gb/s 16-QAM data signal transmission at 42 GHz has been demonstrated over hybrid links with an EVM as low as 5% providing enough capacity for considered transmission within 5G networks. Several turbulence distributions along the FSO link have been implemented and their impact on the signal transmission have been evaluated. We experimentally verified that the highest impact on RoFSO link transmission can be expected under turbulence evenly distributed along the link. The measured turbulence scenarios resulted in up to 5 dB power penalty in terms of received optical power for EVM level of 12.5% in comparison with the performance of the hybrid link without turbulence.

References

[1] "Cisco visual networking index: Forecast and trends, 2017-2022," Cisco, Feb. 2019. [Online]. Available: https://www.cisco.com/c/en/us/solutions/collateral/service-provider/visual-networking-index-vni/white-paper-c11-741490.pdf
[2] 3GPP, "5G; Study on scenarios and requirements," 3GPP, Sophia Antipolis Cedex, France, Tech. Rep. 38.913 V 15.0.0, 2018.
[3] R. Waterhouse and D. Novack, "Realizing 5G: Microwave photonics for 5G mobile wireless systems," *IEEE Microw. Mag.*, vol. 16, no. 8, pp. 84–92, Sep. 2015.
[4] 3GPP, "5G; NR; User Equipment (UE) radio transmission and reception; Part 2: Range 2 Standalone," 3GPP, Sophia Antipolis Cedex, France, TS 38.101-2 V 15.5.0, 2019.
[5] X. Wang *et al.*, "Millimeter wave communication: A comprehensive survey," *IEEE Commun. Surveys Tuts.*, vol. 20, no. 3, pp. 1616–1653, Jul.–Sep. 2018.
[6] A. Checko *et al.*, "Cloud RAN for mobile networks - A technology overview," *IEEE Commun. Surveys Tuts.*, vol. 17, no. 1, pp. 405–426, Jan.–Mar. 2015.
[7] C. H. Lee, *Microwave Photonic*, 2nd ed. Boca Raton, FL, USA: CRC Press, 2013.
[8] J. Yao, "Microwave photonics," *J. Lightw. Technol.*, vol. 27, no. 3, pp. 314–335, Feb. 2009.
[9] Y. Doi, S. Fukushima, T. Ohno, and K. Yoshino, "Frequency stabilization of millimeter-wave subcarrier using laser heterodyne source and optical delay line," *IEEE Photon. Technol. Lett.*, vol. 13, no. 9, pp. 1002–1004, Sep. 2001.
[10] J. Liu *et al.*, "Efficient optical millimeter-wave generation using a frequency-tripling Fabry–Pérot laser with sideband injection and synchronization," *IEEE Photon. Technol. Lett.*, vol. 23, no. 18, pp. 1325–1327, Sep. 2011.

[11] L. Xu, C. Li, S. M. G. Lo, and H. K. Tsang, "Millimeter wave generation using four wave mixing in silicon waveguide," *OECC 2010 Tech. Dig.*, Jul. 2010, pp. 860–861.
[12] Y.-K. Seo, C.-S. Choi, and W.-Y. Choi, "All-optical signal up-conversion for radio-on-fiber applications using cross-gain modulation in semiconductor optical amplifiers," *IEEE Photon. Technol. Lett.*, vol. 14, no. 10, pp. 1448–1450, Oct. 2002.
[13] T. Kanesa *et al.*, "Dual pump brillouin laser for RoF millimeterwave carrier generation with tunable resolution," in *Proc. IEEE Region 10 Conf.*, Nov. 2015, pp. 1–6.
[14] G. Qi, J. Yao, J. Seregelyi, S. Paquet, and C. Belisle, "Generation and distribution of a wide-band continuously tunable millimeter-wave signal with an optical external modulation technique," *IEEE Trans. Microw. Theory Techn.*, vol. 53, no. 10, pp. 3090–3097, Oct. 2005.
[15] H. Zhang, C. Lin, S. Xie, K. Zhang, X. Wu, and Z. Dong, "A novel radio-over-fiber system based on carrier suppressed frequency eightfold millimeter wave generation," *IEEE Photon. J.*, vol. 9, no. 5, pp. 1–6, Oct. 2017, Art no. 7203506.
[16] J. Bohata, M. Komanec, J. Spáčil, Z. Ghassemlooy, S. Zvánovec, and R. Slavík, "24-26 GHz radio over fiber and free space optics for 5G systems," *Opt. Lett.*, vol. 43, no. 5, pp. 1035–1038, Mar. 2018.
[17] J. Bohata, S. Zvanovec, P. Pesek, T. Korinek, M. Mansour Abadi, and Z. Ghassemlooy, "Experimental verification of long-term evolution radio transmissions over dual-polarization combined fiber and free-space optics optical infrastructures," *Appl. Opt.*, vol. 55, no. 8, pp. 2109–2116, Mar. 2016.
[18] J. Bohata, M. Komanec, J. Spáčil, S. Zvánovec, Z. Ghassemlooy and R. Slavík, "Hybrid RoF-RoFSO system using directly modulated laser for 24–26 GHz 5G networks," in *Proc. 11th Int. Symp. Commun. Syst. Netw. Digit. Signal Process.*, 2018, pp. 1–5.
[19] J. Libich and S. Zvanovec, "Influences of turbulences in near vicinity of buildings on free-space optical links," *IET Microw. Antennas Propag.*, vol. 5, no. 9, pp. 1039–1044, 2011.
[20] K. Niachou, I. Livada, and M. Santamouris, "Experimental study of temperature and airflow distribution inside an urban street canyon during hot summer weather conditions—Part I: Air and surface temperatures," *Build. Environ.*, vol. 43, no. 8, pp. 1383–1392, Aug. 2008.
[21] S. Bloom, E. Korevaar, J. Schuster, and H. Willebrand, "Understanding the performance of free-space optics [Invited]," *J. Opt. Netw.*, vol. 2, no. 6, pp. 178–200, May 2003.
[22] L. C. Andrews and R. L. Phillips, *Laser Beam Propagation Through Random Media*, 2nd ed. Bellingham, WA, USA: SPIE Press, 2005.
[23] M. A. Khalighi and M. Uysal, "Survey on free space optical communication: a communication theory perspective," *IEEE Commun. Surveys Tuts.*, vol. 16, no. 4, pp. 2231–2258, Oct.–Dec. 2014.

Optical Fiber Delay Lines in Microwave Photonics: Sensitivity to Temperature and Means to Reduce it

Meng Ding, Zitong Feng, David Marpaung, Xi Zhang, Matěj Komanec, Dmytro Suslov, Daniel Dousek, Stanislav Zvánovec, Eric R. Numkam Fokoua, Thomas D. Bradley, Francesco Poletti, David J. Richardson, *Fellow, IEEE, Fellow, OSA*, and Radan Slavík, *Senior Member, IEEE, Fellow, OSA*

***Abstract*—One of the key functionalities in microwave photonics is to be able to define controllable time delays during the signal processing. Optical fibers are often used to achieve this functionality, especially when a long delay or a widely-tunable delay is needed. However, the stability of this delay in the presence of environmental changes (e.g., temperature) has not, to the best of our knowledge, been reviewed yet. Here, we firstly discuss the impact of temperature-induced variations on the signal propagation time in optical fibers and its implications in microwave photonics. We compare the impact of the thermal sensitivity of various delay lines for applications in which the signal is transported from point A to point B, as well as for applications in which the propagation time through a fiber or the fiber dispersion is used to create a fixed or tunable delay. In the second part of the article we show the impact of fiber thermal sensitivity on a narrow-band microwave photonics filter made of standard single mode fiber (SSMF) and a hollow core fiber (HCF), which has significantly lower thermal sensitivity of propagation time to temperature. The central frequency of the band-pass filter changes almost 16 times more in the filter made of SSMF as compared to that of HCF, dictating very tight (0.05 °C) temperature stabilization for SSMF-based filters. On the basis of our thermal sensitivity analysis we conclude that HCFs are very promising for environmentally stable microwave photonics applications.**

***Index Terms*—Fabry–Perot, microwave filters, microwave photonics, optical fiber applications.**

Manuscript received October 7, 2020; revised December 14, 2020 and January 12, 2021; accepted January 13, 2021. Date of publication January 18, 2021; date of current version April 16, 2021. This work was supported in part by EPSRC Project "Airguide Photonics" under Grant EP/P030181/1; in part by the Czech Technical University in Prague under Grant SGS SGS17/182/OHK3/3T/13; in part by EU ERC project "LightPipe" under Grant 682724; and in part by the MEYS INTER-COST Project LTC18008 under Grant COST16220 EUIMWP. The work of Meng Ding was supported by CSC scholarship. The work of Radan Slavk and Eric R. Numkam Fokoua was supported by RAEng Fellowship. *(Corresponding author: Zitong Feng.)*

Meng Ding, Zitong Feng, Xi Zhang, Eric R. Numkam Fokoua, Thomas D. Bradley, Francesco Poletti, David J. Richardson, and Radan Slavík are with the Optoelectronic Research Centre, University of Southampton, SO17 1BJ, U.K. (e-mail: m.ding@soton.ac.uk; zitong.feng@soton.ac.uk; xi.zhang@soton.ac.uk; eric.numkam-fokoua@soton.ac.uk; t.bradley@soton.ac.uk; frap@orc.soton.ac.uk; djr@orc.soton.ac.uk; r.slavik@soton.ac.uk).

David Marpaung is with Nonlinear Nanophotonics Group, University of Twente 7522 NB Enschede, the Netherlands (e-mail: david.marpaung@utwente.nl).

Matěj Komanec, Dmytro Suslov, Daniel Dousek, and Stanislav Zvánovec are with the Faculty of Electrical Engineering, Czech Technical University in Prague, 16627 Prague, Czech Republic (e-mail: komanmat@fel.cvut.cz; suslodmy@fel.cvut.cz; dousedan@fel.cvut.cz; xzvanove@fel.cvut.cz).

Color versions of one or more figures in this article are available at https://doi.org/10.1109/JLT.2021.3052609.

Digital Object Identifier 10.1109/JLT.2021.3052609

I. Introduction

MICROWAVE photonics uses optical devices and techniques for advanced processing and transport of radio frequency (RF) signals. Although integrated microwave photonics is compelling due to advantages such as small size and compactness, optical fibers still play a key role due to their ultralow loss (particularly relevant for long distances). One of the key microwave photonics requirements is to be able to set a a controllable delay of the signal being processed [1]. Defining a fixed delay is straightforwardly realized with minimum loss or signal distortion via signal propagation through a length of an integrated optics waveguide or an optical fiber. Some microwave photonics applications, however, require a tunable delay line, which is more challenging to implement. Quasi-tunable delay lines have been implemented, e.g., using a set of fiber lengths and switches with a fixed wavelength laser, Fig. 1(a) [1], while a continuously tunable delay line can be achieved, e.g., with a dispersive fiber and a tunable laser source, Fig. 1(b) [2].

Delay lines in microwave photonics are often used to construct filters in finite input response (FIR) configurations [2], whose schematic is shown in Fig. 2(a). By combining several (at least two) replicas of the original signal (delayed with respect to each other using delay lines) with adjusted amplitudes and phases, a filtering functionality is achieved. Indeed, infinite impulse response (IIR) configurations [2] that use output signal (after an appropriate delay) fed back into the input are also used, Fig. 2(b). When combined with gain, such feedback structures can also be made to oscillate, forming an optoelectronic oscillator (OEO) [3]. Fig. 2(c) shows a schematic of a simple OEO. As its noise properties are directly related to the magnitude of the delay introduced in the feedback loop [3], a long delay (e.g., created in km-length fibers) is often used.

For stable operation of microwave photonics filters and other related devices such as OEOs, the delay introduced by a delay line should be stable with temperature. Even when using optical fibers for transport of the microwave signal (such as clock distribution [4], 5G networks [5], or radio astronomy [6]), changes in the RF signal phase due to temperature are of importance. However, the topic of this thermal stability has not, to the best of our knowledge, been comprehensively discussed in the literature in the field of microwave photonics yet.

In this paper, we first carry out a comprehensive comparison of fiber-based microwave photonics delay lines in terms of their

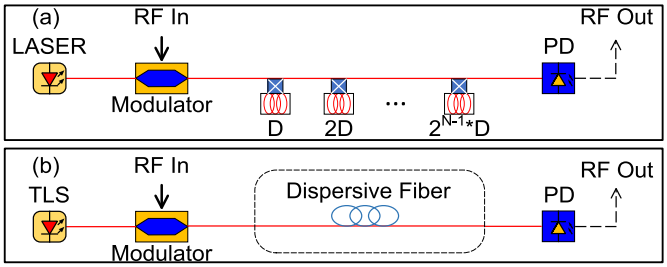

Fig. 1. Principle of tunable delay lines based on (a) switched fiber lengths with a fixed laser wavelength, and (b) a dispersive delay line with tunable laser source. D: delay; PD: photodetector; TLS, tunable laser source.

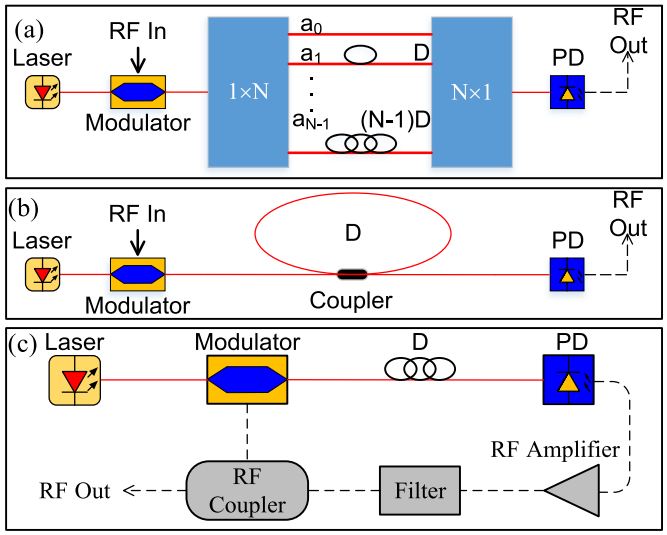

Fig. 2. Schematic of a FIR (a) and IIR (b) microwave photonics filters [2] and a simple OEO (c).

thermal stability. We introduce the key effects that influence the thermal stability and quantify their contribution, allowing for comprehension of the topic as well as enabling microwave photonics engineers to design their systems taking the thermal stability into account. For example, using a dispersion compensating fiber instead of a standard optical fiber in the dispersive tunable delay line, up to 6 times lower sensitivity to temperature can be obtained.In the second part, we demonstrate our thermal sensitivity analysis on an IIR microwave photonics filter based on an all-fiber Fabry-Perot etalon made of standard fiber as well as novel hollow core optical fiber (the microwave photonics filter based on hollow core fibre (HCF) is demonstrated for the first time here). Thanks to the significantly better thermal stability of the HCF as compared to standard single mode fiber (SSMF), the developed HCF based microwave filter has a more than ten times better central frequency stability. We show this is of key importance in ultra-narrow pass-band filters (180 kHz in our filter, measured up to a central frequency of 40 GHz) and how this scales with the operational frequency.

II. Fibers' Thermal Sensitivity

There are several key configurations (Section III) used to generate delays in microwave photonics using optical fibers. Before analyzing their thermal sensitivities, we need to know the relevant thermal sensitivity properties of the optical fibers used and in particular of their propagation time and chromatic dispersion.

A. Fiber Delay

The propagation time τ of a microwave photonics signal propagating through a length L of an optical fiber or a waveguide is given by:

$$\tau_{delay}=\frac{n_g L}{c}, \tag{1}$$

where n_g in the group refractive index of the propagating medium and c is the speed of light in vacuum. When temperature T changes, two effects contribute to the time delay change: the fiber elongation with temperature (thermal expansion) and the change of propagation speed with temperature [7]. The change of time delay due to the temperature change per unit length is characterized by the thermal coefficient of delay (TCD). For an SSMF, which is made of fused silica, the TCD is about 40 ps/km/K to which the change of propagation speed with temperature contributes about 95% [7]. The thermal expansion contribution is very small thanks to the extremely low thermal expansion coefficient ($S_L = 5 \times 10^{-7}$ /K [8]) of silica glass, contributing about 2 ps/km/K [7]. For applications where the TCD of SSMF is too high, fibers with a specialty coating were developed [9] known as phase stable optical fiber (PSOF), reducing the TCD down to 3.7 ps/km/K.

Another approach is to use HCF in which light propagates through a central hole, eliminating the contribution of thermal induced propagation speed change, reducing the TCD to 2 ps/km/K, limited by the thermally-induced fiber elongation. This advantage has already been demonstrated in microwave photonics, resulting in the demonstration of an OEO with 16 times smaller sensitivity of the oscillating frequency to temperature as compared to an OEO made with SSMFs [10]. By careful design, HCFs can even be achieved with a TCD close to 0 ps/km/K [11] and an OEO with >100 times better thermal stability than SSMF has been reported using such a design [12]. Besides lower TCD, HCFs have other advantages over SSMFs relevant for microwave photonics, e.g., low nonlinearity in combination with low chromatic dispersion [13]. The key limitation to using HCF in microwave photonics applications had been up to recently transmission loss, which used to be significantly higher compared to SSMF. However, with the development of the latest generation of hollow core fibers: nested antiresonant nodeless fibers (NANFs) [14]–[17], attenuation levels of 0.28 dB/km have recently been achieved [17] and one can expect it to become even lower in the near future. NANF is therefore expected to be an ideal candidate for delay lines designed for microwave photonic and should open new device opportunities. However, to date, the use of NANF has not been demonstrated in any microwave photonics application to the best of our knowledge.

B. Chromatic Dispersion

The chromatic dispersion of an optical fiber is given by the sum of material and waveguide dispersions [18]. For weakly-guiding fibers like SSMFs or typical dispersion compensation

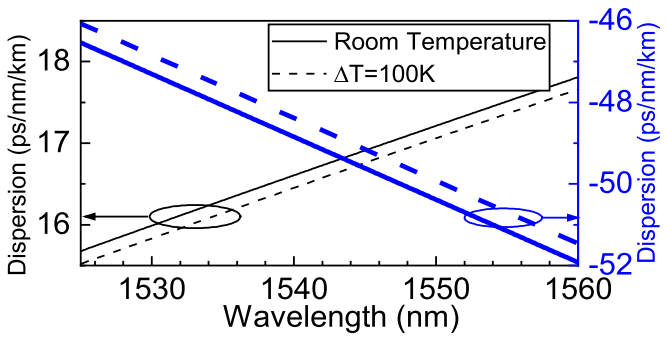

Fig. 3. Chromatic dispersion of SSMF (thin black) and DCF (thick blue, at room temperature calculated with Eq. (2) and data from [20], [21]. Chromatic disperiosn at temperature 100 K higher for SSMF was calculated with Eq. (3) and data from [20] (thin black dashed) and DCF calculated from the second term of Eq. (3) and data from [21] (thick blue dashed).

fibers (DCFs), the chromatic dispersion can be approximated by the three term Sellmeier equation [18], [19]:

$$D(\lambda) = \frac{S_0}{4}\left(\lambda - \frac{{\lambda_0}^4}{\lambda^3}\right), \tag{2}$$

where λ_0 is the zero dispersion wavelength and S_0 is the dispersion slope at the zerodispersion wavelength. The chromatic dispersion of SSMF and a typical DCF at C band obtained using Eq. (2) and fiber data from [20] and [21] are both plotted in Fig. 3. The temperature sensitivity of chromatic dispersion can be obtained by differentiating Eq. (2) with respect to temperature T:

$$\frac{dD}{dT} = \frac{D}{S_0}\cdot\frac{dS_0}{dT} - \frac{S_0\lambda_0^3}{\lambda^3}\cdot\frac{d\lambda_0}{dT}. \tag{3}$$

We then used Eq. (3) to calculate the chromatic dispersion of SSMF with a temperature increase of 100 K by using data from [20] (fiber Type A1 in [20]) and show it in Fig. 3. As concerns DCF, only the parameters relevant to the zero dispersion wavelength have been published so far (e.g., in [21]), which allows us to calculate the second term in Eq. (3), but not the first one. To allow us to illustrate the DCF's thermal sensitivity, we made an assumption that the first term in Eq. (3) (proportional to the change of S_0) is negligible as compared to the second one (proportional to the change of λ_0). We consider it a reasonable assumption, as for SSMF, the first term in Eq. (3) typically contributes to only 5–9% of the overall thermal sensitivity in the C-band [21]. Although it may have a larger contribution for the DCF, it is unlikely to be a dominant term.

In Fig. 3 we see that over a limited bandwidth (e.g., C-band in Fig. 3) the dispersion curve is mainly red-shifted when the temperature is increased. Although this observation has been done with DCF characteristics that are approximate (as discussed earlier), it is in line with [21] and [22], where for all studied fiber types (including SSMF and DCF), the dispersion thermal sensitivity was considered to be:

$$\frac{dD(\lambda)}{dT} \cong S(\lambda)\cdot\frac{d\lambda_0}{dT}. \tag{4}$$

TABLE I
SUMMARY OF DISCUSSED PROPERTIES OF OPITCLA FIBERS

	Silica-core fibers				Hollow-core	
	SSMF	PSOF	DCF	PCF	PBGF	NANF
TCD, ps/km/K	40 [7]	3.7 [9]			2.2 [10]	1.7 [13]
Loss, dB/km	0.2	0.4 [27]			1.7 [28]	0.28 [17]
Disp., ps/nm/km	17		-30 to -300	-700 [26]	0-100	2 - 6
Disp. thermal sensitivity, fs/nm/km/K	-1.5 [20]		0.9 to 4 [21]	1600 [26]		

*SSMF: Standard single-mode fiber, PSOF: Phase-stable optical fiber, DCF: Dispersion-compensating fiber; PCF: Photonic crystal fiber, PBGF: Photonic bandgap fiber, NANF: Nested antiresonant nodeless fiber. All of these data are given in the C band.

where D(λ) is the chromatic dispersion of interest and S(λ) is the dispersion slope at that wavelength. As $d\lambda_0/dT$ is almost constant for any fiber type ($d\lambda_0/dT$ = (0.02–0.03) nm/K [20]–[24]), $dD(\lambda)/dT$ depends predominantly on the dispersion slope S(λ), as follows from Eq. (4).

For SSMF, chromatic dispersion and its thermal sensitivity are 17 ps/nm/km (at 1550 nm) and −1.5 fs/nm/km/K. For DCF, the chromatic dispersion ranges from −30 to −300 ps/nm/km [25] and $dD(\lambda)/dT$ is between 0.9 and 4 fs/nm/km/K [21] for λ∼1550 nm. Photonic crystal fiber (PCF) generally provides larger dispersion, e.g., −700 ps/nm/km [26], but also has a larger dispersion slope S(λ) (as compared to DCF), making its dD/dT relatively large, e.g., data from [26] leads to $dD/dT \sim$ 1.6 ps/nm/km/K.

The key properties of optical fibers relevant for microwave photonics delay lines and their thermal behavior are summarized in Table I.

III. Optical Microwave Photonics Delay Lines and Their Thermal Sensitivity

Here, we divide the key configurations to generate delay in microwave photonics into three main categories that we discuss in the following text: (i) Fiber delay, (ii) Delay via fiber chromatic dispersion, and (iii) Delay with chirped fiber Bragg gratings (CFBG).

In the literature, there are two main concepts used to characterize the thermal properties of optical fibers. The first one normalizes time delay changes to the fiber length as characterized by the TCD (used, e.g., [9]) and is appropriate for applications in which fiber is used to transport a signal from point A to point B (e.g., to synchronize telescopes in radio astronomy [6]). Fiber properties relevant to these applications are summarized in Table I. The other uses normalization to unit delay (1 s). For delay lines that serve to delay a signal, normalization to delay is more appropriate:

$$S_\tau = \frac{1}{\tau}\frac{d\tau}{dT}. \tag{5}$$

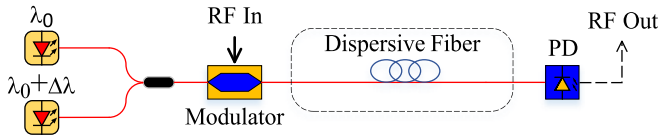

Fig. 4. Schematic of a two-tap tunable filter using a dispersive fiber structure with two lasers.

To distinguish between the normalization to length and delay, we use the relative unit (ppm/K) for the normalization to delay (as opposed to the ps/km/K we use for normalization to the length). In the previous section (Section II), we have already compared delay lines in terms of TCD. Here, we will discuss comparison in terms of S_τ.

A. Fiber Delay

The thermal sensitivity normalized to unit delay S_τ can be obtained from Eqs. (1) and (5) as:

$$S_\tau = \frac{1}{n_g}\frac{dn_g}{dT} + \frac{1}{L}\frac{dL}{dT} = S_n + S_L. \tag{6}$$

The first term describes the sensitivity of fiber group index to temperature, the second the thermally-induced expansion.

The thermal sensitivities S_τ of SSMF delay lines can be caculated from the TCD published in [9] to be around 8 ppm/K. A PSOF-based delay line was reported to have S_τ of 1.4 ppm/K [29]. HCF-based delay lines have been measured to have S_τ of 0.6 ppm/K using PBGF [10] and values as low as -0.08 ppm/K have been achieved when operating the PBGF close to its zero thermal sensitivity wavelength [12]. NANF has been demonstrated to achieve 0.5 ppm/K [13].

B. Delay Via Fiber Chromatic Dispersion

Fig. 1(b) shows a simple schematic of a tunable dispersive fiber delay line, it's temperature sensitivity is essentially similar to that of a simple fiber delay line, Fig. 1(a) analyzed in the previous section. However, the dispersive tunable delay line is often used in FIR filters in which signals generated by several lasers emitting at different wavelengths propagate through the same fiber and it is only the difference in their propagation times that is of importance. Fig. 4 shows a simple schematic of such a filter using two lasers with a wavelength separation of $\Delta\lambda$. Signals from both lasers are modulated by an RF signal and then the RF modulated signals at two wavelengths share the same fiber, where they experience different time delays due to the chromatic dispersion. The difference in the time delay experienced by the two lasers τ can be expressed as:

$$\tau_{disp} = LD\Delta\lambda. \tag{7}$$

Here, D indicates the fiber's chromatic dispersion. Since we are interested how the delay (tuned to the desired value) changes with temperature, we consider fixed wavelength separation here, leading to:

$$S_\tau = \frac{1}{D}\frac{dD}{dT} + \frac{1}{L}\frac{dL}{dT} = S_D + S_L. \tag{8}$$

The first term is the normalized thermally induced change of dispersion and dD/dT is exactly the thermal sensitivity of dispersion as discussed in Section II-B. Its value for all the considered fiber types (SSMF: -88 ppm/K at 1550 nm; DCF: -20 to -80 ppm/K, and PCF: -2800 ppm/K) is significantly higher than the second term that represents thermally-induced elongation (0.5 ppm/K).

For SSMF, a tunable delay of up to 4.2 ns was demonstrated using 46 km of fiber within 5.4 nm range [2], while DCF with its significantly larger dispersion than SSMF (up to -300 ps/nm/km [25]), allowed a delay of up to 4 ns in only 1 km of fiber to be achieved with 40 nm wavelength tuning range[30]. PCFs were demonstrated to offer dispersion values of up to -700 ps/nm/km, enabling 60 ps tuning using just 10 m of fiber [31].

The length of the fiber is limited by its loss and there are other practical considerations such as cost, volume and weight. We add to this list also thermal sensitivity, which, as we mentioned earlier, is lowest with DCF, followed by SSMF, with the worst performance obtained with PCF.

C. Delay Via Chirped Fiber Bragg Gratings

Dispersive fiber from the previous sub-section can be substituted with a CFBG, which can have a large chromatic dispersion when operated in reflection, [32], [33]. The time delay difference between two lasers separated by $\Delta\lambda$ approximates as:

$$\begin{aligned}\tau_{chirp} &\approx \left(\frac{L}{c}\cdot\frac{1}{\Delta\Lambda_{chirp}} + \frac{LD\Delta\lambda}{n_{eff}\Delta\Lambda_{chirp}}\right)\Delta\lambda \\ &= D_{chirp}\cdot\left(1+\frac{cD\Delta\lambda}{n_{eff}}\right)\cdot\Delta\lambda\end{aligned} \tag{9}$$

where $\Delta\Lambda_{chirp}$ and L are the period change and the length of the CFBG respectively, and $D_{chirp} = L/(c\cdot\Delta\Lambda_{chirp})$ is the CFBG chromatic dispersion that does not take into account the fiber chromatic dispersion. n_{eff} is the average effective refractive index of a CFBG. Since L and $\Delta\Lambda_{chirp}$ change at the same rate with temperature (for consistency with the previous analysis, we consider a uniform temperature change along the CFBG), D_{chirp} does not change with temperature. Consequently, the only parameters that change with temperature are fiber chromatic dispersion and refractive index:

$$\frac{d\tau_{chirp}}{dT} = \frac{cD_{chirp}D(\Delta\lambda)^2}{n_{eff}}\left(\frac{1}{D}\frac{dD}{dT} - \frac{1}{n_{eff}}\frac{dn_{eff}}{dT}\right). \tag{10}$$

Considering a CFBG with a $D_{chirp} = 250$ ps/nm inscribed in SSMF as an example and $\Delta\lambda = 20$ nm, $d\tau_{chirp}/dT = -4\times 10^{-5}$ ps/K, equating to a thermal sensitivity S_τ of 0.008 ppm/K, which is almost negligible.

However, real CFBGs exhibits ripples in the group delay [34], [35] due to fabrication imperfections. These ripples are essentially time delay deviations from the ideal CFBG response. Consequently, the time delay changes significantly with temperature. The amplitude of the group delay ripples is typically independent of the CFBG parameters and is around 10 ps [34] (but this can be reduced to 1 ps by careful apodization [36]). As temperature changes, the delay of both signals (separated by $\Delta\lambda$) can change by up to ± 10 ps for a typical CFBG and ± 1 ps

TABLE II
OPTICAL DELAY-LINES SUMMARY

	Name		Maximum time delay*		S_τ (ppm/K)
Fiber delay lines	Solid-core fiber	SSMF	100 µs	L = 56 km [1]	~8
		PSOF	1 µs	L = 0.5 km [32]	1~2.2
	HCFs	PBGF	33 µs 3 µs	L = 11 km [37] L=1 km [12]	0.6 0
		NANF	1 µs	L = 1.7 km [17]	0.5
Dispersive fiber delay lines	SSMF		10 ns	D = 17 ps/nm/km	-88
	DCF		1 ns	D = -300 ps/nm/km [25]	-18~-80
	PCF		10 ps	D = -700 ps/nm/km [30]	-2800
	CFBG		1 ns	D_{chirp} = 2500 ps/nm [38]	Delay variations of ±10 ps

*Maximum delay limited by maximum fiber length L or chromatic dispersion (D or D_{chirp}).

for the lowest-reported ripple CFBG, generating up to 20 ps and 2 ps peak-to-peak delay variations in τ_{chirp} respectively. As this variation does not change linearly with temperature (depends on the ripple period, grating chirp, etc.) we cannot define its sensitivity S_τ and can only give the peak-to-peak variations.

D. Summary

We have discussed various microwave photonics fiber delay lines. Table II summarizes the results. Although we do not cover all the microwave photonics delay line implementations, their thermal sensitivities can generally be calculated from the parameters and configurations described above.

For delay generated by signal propagation in an optical fiber, HCFs are the least sensitive to temperature variations. For delays generated via chromatic dispersion, a DCF based delay line is several times less thermally sensitive than a SSMF based delay line. PCF is by far the most temperature sensitive. When using a CFBG, particular attention should be paid to the group delay ripples, which determine the delay variations with temperature and even for extremely low levels of group delay ripple (1 ps) can produce a significant sensitivity to temperature. The key parameters of the delay lines just discussed in terms of S_τ are summarized in Table II.

IV. NOVEL HOLLOW CORE FIBER MICROWAVE FILTER AND ITS TEMPERATURE SENSITIVITY

In this section, we show an example of a microwave photonics filter in which the thermal stability of the fiber used is important. We fabricate the same filter using SSMF as well as HCF and compare their performance, showing that the SSMF-based filter embodiment would only operate reliably with high-precision temperature stabilization, increasing its cost, size, and power consumption.

A. Set-up

The core of our filter consists of an alignment-free all-fiber Fabry-Perot (FP) etalon made of 5-m of NANF, which has been reported in detail in [13]) or a 3.6-m long FC/PC-connectorized SSMF with mirrors directly-deposited on the FC/PC connector end-facets [40]. Due to the refractive index (n) difference (~1 for HCF and ~1.45 for SSMF), the optical length (nL) of the two FP

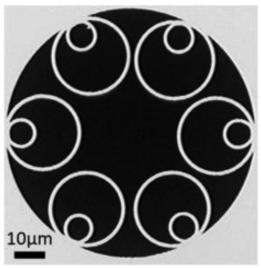

Fig. 5. The cross-sectional electron microscope (SEM) image of the NANF used in our FP etalon.

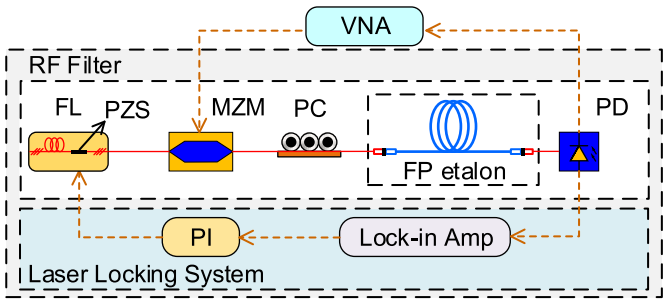

Fig. 6. Experimental set-up.FL: fiber laser; PZS: piezo-stretcher; MZM: Mach-Zehnder modulator; PC: Polarization controller; PD: photodiode; VNA: Vector network analyzer; PI: proportional-integral controller.

etalons is nominally identical, allowing for a fair comparison. The cross-sectional electron microscope (SEM) image of the HCF we used (NANF design, with similar parameters to that used in [16]), is shown in Fig. 5.

The schematic of our microwave photonics filter (we refer to it later simply as a 'filter') is shown in Fig. 6. A signal from a continuous-wave fiber laser (Rock from NP Photonics) with an output power of 16 dBm passes through a 40-GHz bandwidth Mach-Zehnder modulator (MZM), which generates two sidebands at the frequency of the RF input signal. After passing through a polarization controller (PC), the signal is injected into the FP. The laser central frequency is set (we explain later how we set this) to be resonant with the FP, i.e., to have minimum transmission loss. Both sidebands experience the same transmission loss – i.e., both are transmitted (when

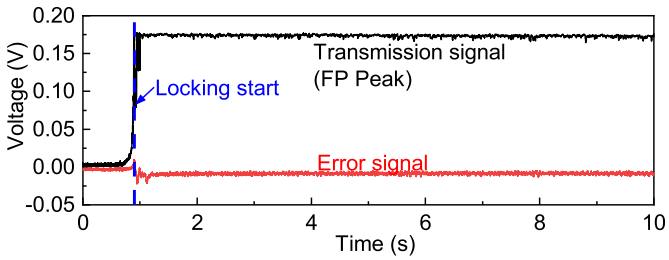

Fig. 7. Transmission signal and error signal before and after the laser wavelength has been locked to a transmission peak of the FP etalon.

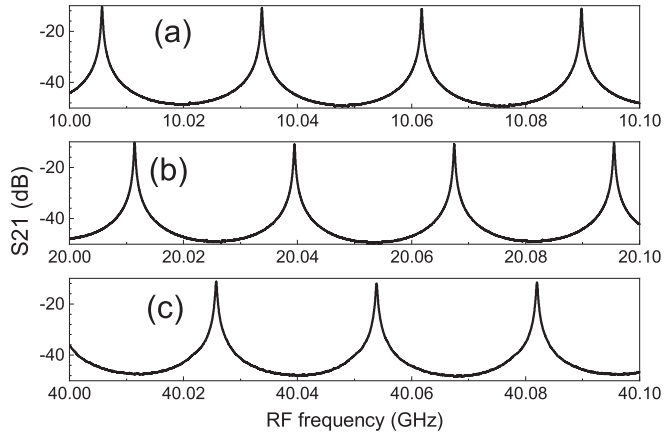

Fig. 8. Amplitude transfer characteristics of the HCF-based filter at 10 GHz (a), 20 GHz (b), and 40 GHz (c) over spans of 100 MHz.

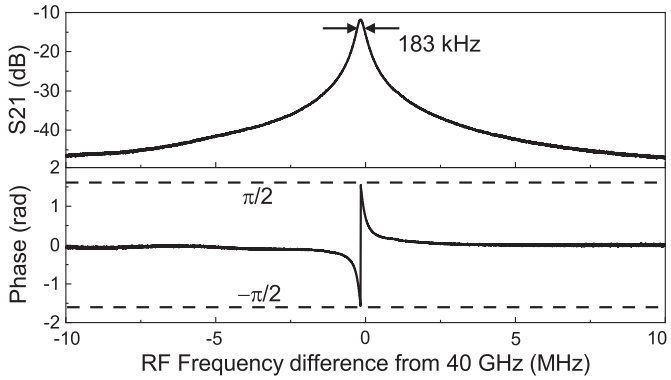

Fig. 9. Detailed amplitude and phase responses of the hollow core fiber based filter around 40 GHz RF frequency.

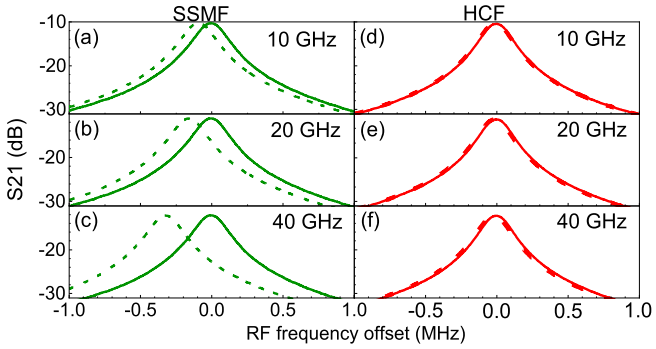

Fig. 10. Transmission characteristics measured at 25 °C (solid) and 26 °C (dashed) for SSMF-based filter (a–c, red) and HCF-based filter (d–f, green) measured at 10 GHz (a, d), 20 GHz (b, e), and 40 GHz (c, f).

the RF signal frequency is a multiple of the FP spectral period) or both are equally attenuated. Thus, the FP output signal is amplitude-modulated with a modulation depth dependent on the RF signal frequency. The output signal from the FP is photodetected and then divided into two parts. One of them is the output RF signal and is received by a vector network analyzer (VNA) to measure the amplitude and phase response of the FP. The other one is used for the laser wavelength locking to a transmission peak of the FP etalon via a feedback loop consisting of a lock-in amplifier, proportional-integral (PI) controller, and a piezo-stretcher that controls the wavelength of the Rock fiber laser. Fig. 7 shows the transmission signal and error signal before and after turning on the locking loop.

B. Filter Transmission Characteristics

For the sake of space, we show here only the filtering characteristics for the HCF-based filter, as the filter characteristics for SSMF-based filter were very similar.

The filter has a periodic transfer function with period of 28.1 MHz (given by the FP length of 5 m), shown in Fig. 8 at RF frequencies close to 10 GHz, 20 GHz and 40 GHz.

Details of the amplitude S21 response together with the phase response are shown in Fig. 9. The 3 dB passband width is 183 kHz and the phase response has the expected π jump at the transmission peak.

C. Filter Temperature Sensitivity

We placed the two FP etalons (based on HCF and SSMF, respectively) into the same thermal chamber. Firstly, we stabilized the temperature and measured the filters' characteristics at frequencies of 10 GHz, 20 GHz and 40 GHz. Subsequently, we increased the temperature by 1 °C and repeated the measurement, as shown in Fig. 10. The filter transmission peaks shifted in frequency. This shift was about 16 times larger for the SSMF-based filter than for HCF-based filter. As expected, the shift also depends linearly on the central frequency: i.e., the shift at 40 GHz is 4 times larger than at 10 GHz).

To extract temperature sensitivity data with good accuracy and to confirm the shift in filter transmission characteristics is linear with temperature, we kept increasing the temperature in 1 K steps and measured the position of the transmission peaks. The filters transmission peak shifts (at 40 GHz, where the change is the largest) are shown in Fig. 11. For SSMF-based filter, the transmission characteristics shift at a rate of 334 kHz/K while for the HCF-based filter the rate is only 21 kHz/K – a value almost 16 times lower as would be expected.

We also measured the filters characteristics when subject to our air-conditioned lab environment (temperature variations of about 1 K due to the air-conditioning turning on and off). Within about an hour, the frequency variations for the SSMF based filter

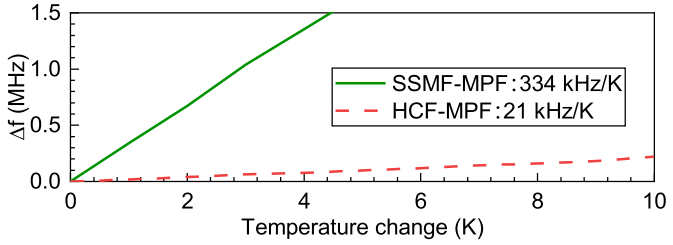

Fig. 11. Filter characteristics frequency shift at 40 GHz over 10 K temperature change for HCF-based filter (dashed, red) and SSMF-based filter (solid, green). FS: Frequency Shift of RF signal.

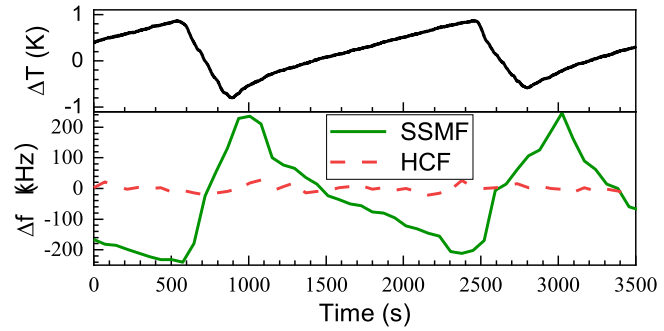

Fig. 12. Temperature variations ΔT in the laboratory and measured transmission peak frequency variations Δf for HCF (solid, green) and SSMF based (dashed, red) filters when subject to laboratory environment over 1 hour.

were up to 480 kHz (at 40 GHz), while for the HCF-based filter, they were less than 30 kHz, see Fig. 12.

D. Discussion

The results presented in Fig. 12 show that the SSMF-based bandpass filter operating at 40 GHz changes its central frequency (by up to 480 kHz) by more than is its bandwidth (3-dB bandwidth of 183 kHz), even in a temperature-controlled laboratory environment. On the other hand, an HCF-based filter allows for accurate operation without any further environmental stabilization.

To ensure that the central filter frequency does not change by more than 10% of its 3-dB bandwidth, the SSMF based filter (temperature shift of 334 kHz/K, Fig. 11) requires temperature stabilization better than 0.05 °C, which is rather impractical. On the other hand, the HCF based filter (21 kHz/K, Fig. 11) requires temperature stabilization of just 0.9 °C, easily achievable with simple temperature control. These requirements could be relaxed if the filter is operated at a lower frequency (e.g., at 10 GHz, four times larger temperature variations are acceptable), or with a larger bandwidth. However, if a lower bandwidth is targeted (e.g., in our recent work, we presented a FP fiber etalon with 10 times narrower transmission peaks [41] than presented here), the temperature stabilization needs to be improved, rendering a filter made of SSMF unstable and needing impractical mK-level temperature stabilization.

From the temperature-induced shifts given earlier (334 kHz/K and 21 kHz/K, Fig. 11), the thermal sensitivity of the used fibers (NANF hollow core fiber and SSMF) can be calculated by:

$$S_\tau = -\frac{df_{peak}/dT}{f_{peak}}. \tag{11}$$

Here, f_{peak} indicates the measured central frequency of the filter. From our data and Eq. (11) we calculated a thermal sensitivity of 8.4 ppm/K (SSMF) and 0.5 ppm/K (NANF), which agrees well with the previously-published data summarized in Table II.

V. Conclusion

In this paper, we reviewed different configurations of optical fiber-based delay lines for microwave photonics in terms of their thermal sensitivity. The thermal sensitivity of point-to-point delay lines is best characterized by the Thermal Coefficient of Delay (TCD), which is normalized to the delay line length. Key parameters of delay lines using different optical fibers are summarized in Table I, suggesting hollow core fiber (HCF) performs the best, having a TCD of as little as 2 ps/km/K.

For comparison of delay lines used primarily to create a delay, we normalize their thermal sensitivity to unit delay. There are two main configurations of such fiber-based photonic delay lines: based on propagation through a length of a fiber or propagation through a dispersive fiber or a chirped fiber Bragg grating (CFBG). The key results are summarized in Table II. For simple propagation through a length of a fiber, HCF performs the best (thermal sensitivity of 0.5 ppm/K), For the dispersive delay line, devices based on dispersion compensating fiber (DCF) have the smallest thermal sensitivity ($-18\sim-80$ ppm/K). The thermal stability of a CBGF is limited by its group delay ripple, which even when strongly reduced by tight CFBG apodization is typically still at the 1-ps level.

To demonstrate the importance of the fiber thermal sensitivity in microwave photonics, we built two narrow-band IIR filters based on all-fiber Fabry-Perot etalons. The first one was made of a standard single mode fiber (SSMF), while the other one was made of low-thermally-sensitive HCF. Compared to SSMF-based filters, the HCF-based filter changes its central frequency almost 16 times less with temperature. As a result, the HCF-based filter is stable under laboratory conditions, and in real world applications would require only simple temperature control, while a SSMF-based filter would require impractically accurate/tight temperature control levels of 0.05 °C.

The experiments we have presented represent the first demonstration of the latest generation of HCF (which was recently demonstrated to enable a loss as low as 0.28 dB/km) in microwave photonics. Besides the low thermal sensitivity and a loss approaching that of SSMF, HCFs also exhibit a high nonlinear threshold, making them a very promising technology for the realization of delay lines in microwave photonics.

Acknowledgment

The data in this paper is accessible through the University of Southampton research repository (https://doi.org/10.5258/SOTON/D1708).

REFERENCES

[1] J. F. Diehl, J. M. Singley, C. E. Sunderman, and V. J. Urick, "Microwave photonic delay line signal processing," *Appl. Opt.*, vol. 54, no. 31, 2015, Art. no. F35.

[2] J. Capmany, B. Ortega, and D. Pastor, "A tutorial on microwave photonic filters," *J. Lightw. Technol.*, vol. 24, no. 1, pp. 201–229, 2006.

[3] X. S. Yao and L. Maleki, "Optoelectronic microwave oscillator," *J. Opt. Soc. Amer. B*, vol. 13, no. 8, Aug. 1996, Art. no. 1725.

[4] S. Wang *et al.*, "2 GHz clock quantum key distribution over 260 km of standard telecom fiber," *Opt. Lett.*, vol. 37, no. 6, Mar. 2012, Art. no. 1008.

[5] L. Gavrilovska, V. Rakovic, and V. Atanasovski, "Visions towards 5G: Technical requirements and potential enablers," *Wireless Pers. Commun.*, vol. 87, no. 3, pp. 731–757, 2016.

[6] M. Burla *et al.*, "System integration and radiation pattern measurements of a phased array antenna employing an integrated photonic beamformer for radio astronomy applications," *Appl. Opt.*, vol. 51, no. 7, pp. 789–802, 2012.

[7] A. H. Hartog, A. J. Conduit, and D. N. Payne, "Variation of pulse delay with stress and temperature in jacketed and unjacketed optical fibres," *Opt. Quantum Electron.*, vol. 11, no. 3, pp. 265–273, 1979.

[8] N. Lagakos, J. A. Bucaro, and J. Jarzynski, "Temperature-induced optical phase shifts in fibers," *Appl. Opt.*, vol. 20, no. 13, 1981, Art. no. 2305.

[9] M. Bousonville *et al.*, "New phase stable optical fiber," in *Proc. Beam Instrum. Work.*, 2012, pp. 101–103.

[10] U. S. Mutugala *et al.*, "Optoelectronic oscillator incorporating hollow-core photonic bandgap fiber," *Opt. Lett.*, vol. 42, no. 13, 2017, Art. no. 2647.

[11] E. N. Fokoua, M. N. Petrovich, T. Bradley, F. Poletti, D. J. Richardson, and R. Slavík, "How to make the propagation time through an optical fiber fully insensitive to temperature variations," *Optica*, vol. 4, no. 6, pp. 659–668, Jun. 2017.

[12] U. S. Mutugala *et al.*, "Hollow-core fibres for temperature-insensitive fibre optics and its demonstration in an optoelectronic oscillator," *Sci. Rep.*, vol. 8, no. 1, pp. 1–6, 2018.

[13] M. Ding *et al.*, "Long-Length and thermally stable high-finesse Fabry–Perot interferometers made of hollow core optical fiber," *J. Lightw. Technol.*, vol. 38, no. 8, pp. 2423–2427, 2020.

[14] F. Poletti, "Nested antiresonant nodeless hollow core fiber," *Opt. Exp.*, vol. 22, no. 20, 2014, Art. no. 23807.

[15] T. D. Bradley *et al.*, "Record low-loss 1.3dB/km data transmitting antiresonant hollow core fibre," in *Proc. Eur. Conf. Opt. Commun.*, 2018, pp. 1–3.

[16] T. D. Bradley *et al.*, "Antiresonant hollow core fibre with 0.65 dB/km attenuation in the C and l telecommunication bands," in *Proc. Eur. Conf. Opt. Commun.*, 2019, Art. no. PDP3.1.

[17] G. T. Jasion *et al.*, "Hollow core NANF with 0.28 dB/km attenuation in the C and l bands," in *Proc. Opt. Fiber Commun. Conf. Exhib.*, 2020, pp. 4–6.

[18] P. S. Andre, A. N. Pinto, and J. L. Pinto, "Effect of temperature on the single mode fibers chromatic dispersion," in *Proc. 2003 SBMO/IEEE MTT-S Int. Microw. Optoelectron. Conf.*, 2004, pp. 231–234.

[19] P. S. André and A. N. Pinto, "Chromatic dispersion fluctuations in optical fibers due to temperature and its effects in high-speed optical communication systems," *Opt. Commun.*, vol. 246, nos. 4–6, pp. 303–311, 2005.

[20] M. J. Hamp, J. Wright, M. Hubbard, and B. Brimacombe, "Investigation into the temperature dependence of chromatic dispersion in optical fiber," *IEEE Photon. Technol. Lett.*, vol. 14, no. 11, pp. 1524–1526, Nov. 2002.

[21] T. Kato, Y. Koyano, and M. Nishimura, "Temperature dependence of chromatic dispersion in various types of optical fiber," *Opt. Lett.*, vol. 25, no. 16, Aug. 2000, Art. no. 1156.

[22] J. Rathje and M. Andersen, "Temperature induced change in the dispersion spectrum of dispersion compensating fibers," in *Proc. OFC 2003 Opt. Fiber Commun. Conf.*, 2003, pp. 712–713.

[23] W. H. Hatton and M. Nishimura, "Temperature dependence of chromatic dispersion in single mode fibers," *J. Lightw. Technol.*, vol. 4, no. 10, pp. 1552–1555, 1986.

[24] K. S. Kim and M. E. Lines, "Temperature dependence of chromatic dispersion in dispersion-shifted fibers: Experiment and analysis," *J. Appl. Phys.*, vol. 73, no. 5, pp. 2069–2074, Mar. 1993.

[25] L. Grüner-Nielsen *et al.*, "Dispersion-compensating fibers," *J. Lightw. Technol.*, vol. 23, no. 11. pp. 3566–3579, Nov. 2005.

[26] Y. Jiang, X. Chen, B. Howley, M. Y. Chen, and R. T. Chen, "Effects of temperature fluctuation on highly dispersive photonic crystal fibers," *Appl. Phys. Lett.*, vol. 88, no. 1, 2006, Art. no. 011108.

[27] Linden Photonics, Inc. "STFOC optical cable Non-kink crush proof," datasheet, 2020. [Online]. Available: http://www.lindenphotonics.com/documents/Linden - STFOC.pdf

[28] P. J. Roberts *et al.*, "Ultimate low loss of hollow-core photonic crystal fibres," *Opt. Exp.*, vol. 13, no. 1, pp. 236–244, 2005.

[29] J. J. Liu, X. P. Ma, G. X. Pei, N. Gan, and J. S. Yang, "Phase-stabilized RF transmission system based on LLRF controller and optical delay line," *Nucl. Sci. Tech.*, vol. 30, no. 12, pp. 1–8, 2019.

[30] X. Zhu, F. Chen, H. Peng, and Z. Chen, "Novel programmable microwave photonic filter with arbitrary filtering shape and linear phase," *Opt. Exp.*, vol. 25, no. 8, 2017, Art. no. 9232.

[31] Y. Jiang *et al.*, "Dispersion-enhanced photonic crystal fiber array for a true time-delay structured X-band phased array antenna," *IEEE Photon. Technol. Lett.*, vol. 17, no. 1, pp. 187–189, Jan. 2005.

[32] B. Ortega, J. L. Cruz, J. Capmany, M. V. Andrés, and D. Pastor, "Variable delay line for phased-array antenna based on a chirped fiber grating," *IEEE Trans. Microw. Theory Tech.*, vol. 48, no. 8, pp. 1352–1360, Aug 2000.

[33] Y. Liu, J. Yang, and J. Yao, "Continuous true-time-delay beamforming for phased array antenna using a tunable chirped fiber grating delay line," *IEEE Photon. Technol. Lett.*, vol. 14, no. 8, pp. 1172–1174, Aug. 2002.

[34] B. Zhou, X. Zheng, X. Yu, H. Zhang, Y. Guo, and B. Zhou, "Impact of group delay ripples of chirped fiber grating on optical beamforming networks," *Opt. Exp.*, vol. 16, no. 4, 2008, Art. no. 2398.

[35] M. Sumetsky, B. Eggleton, and C. de Sterke, "Theory of group delay ripple generated by chirped fiber gratings," *Opt. Exp.*, vol. 10, no. 7, pp. 332–340, 2002.

[36] N. K. Srivastava, R. Parihar, and S. K. Raghuwanshi, "Efficient photonic beamforming system incorporating a unique featured tunable chirped fiber bragg grating for application extended to the ku-band," *IEEE Trans. Microw. Theory Tech.*, vol. 68, no. 5, pp. 1851–1857, May 2020.

[37] D. Kwon and J. Kim, "All-fiber interferometer-based repetition-rate stabilization of mode-locked lasers to 10^−14-level frequency instability and 1-fs-level jitter over 1 s," *Opt. Lett.*, vol. 42, no. 24, Dec. 2017, Art. no. 5186.

[38] Y. Chen *et al.*, "Multi-kilometer long, longitudinally uniform hollow core photonic bandgap fibers for broadband low latency data transmission," *J. Lightw. Technol.*, vol. 34, no. 1, pp. 104–113, Jan. 2016.

[39] J. Zhang and J. Yao, "Broadband microwave signal processing based on photonic dispersive delay lines," *IEEE Trans. Microw. Theory Tech.*, vol. 65, no. 5, pp. 1891–1903, May 2017.

[40] M. Ding, D. J. Richardson, and R. Slavik, "Long length fibre Fabry–Perot interferometers and their applications in fibre characterization and temperature sensing," in *Proc. Conf. Lasers Electro-Opt. Europe Eur. Quantum Electron. Conf., CLEO/Europe-EQEC 2019*, 2019, Art. no. Ch_p_9.

[41] M. Ding, E. R. N. Fokoua, T. D. Bradley, F. Poletti, D. J. Richardson, and R. Slavik, "Hollow core fiber Fabry–Perot interferometers with finesse over 3000," in *Proc. Conf. Lasers Electro-Opt.*, 2020, Art. no. 2F2P.

applied optics

Experimental demonstration of a microwave photonic link using an optically phased antenna array for a millimeter wave band

J. Bohata,[1,*] M. Komanec,[1] J. Spáčil,[1] P. Hazdra,[1] T. Lonský,[1,2] Z. Hradecký,[1,2] and S. Zvánovec[1]

[1]Department of Electromagnetic Field, Czech Technical University in Prague, Technicka 2, Prague 6, 166 27, Czech Republic
[2]RFspin s.r.o., Na Beránce 2, Prague 6, 160 00, Czech Republic
*Corresponding author: bohatja2@fel.cvut.cz

Received 6 November 2020; revised 14 December 2020; accepted 23 December 2020; posted 4 January 2021 (Doc. ID 414069); published 28 January 2021

We present a hybrid radiofrequency and microwave photonic link at 25 GHz using the chromatic dispersion of an optical fiber to steer the beam of a three-element planar dipole-based phased antenna array (PAA). Our team has designed and developed an in-house built PAA, experimentally verified its parameters, and successfully demonstrated optically controlled beam steering as measured in an anechoic chamber. Moreover, a detailed analysis of the optically based beam steering in the proposed microwave photonics system has been carried out, with data transmission achieving an error vector magnitude as low as 5.6% for the frequency of 25 GHz and 20 MHz bandwidth.

https://doi.org/10.1364/AO.414069

1. INTRODUCTION

The ever-increasing demands on transmission capacity, notably in mobile networks, have led to the logical step of exploiting higher-frequency bands providing sufficient bandwidth for high data rate transmissions. This validates the usage of fifth-generation mobile networks (5G) whose planned frequency bands involve frequencies significantly exceeding previous mobile network generations by reaching frequencies up to 86 GHz [1]. However, the transmission of high frequencies, i.e., millimeter wave (mmW), has significant path and penetration losses. One practical solution to compensate for the higher losses is to deploy a large-scale phased antenna array (PAA) to achieve high PAA gain in a high-frequency system due to the smaller wavelength [2]. An example of this is a base station operating at 30 GHz with a 200 m transmit range and needing 60 dBm effective isotropic radiated power (EIRP) for a reasonable signal-to-noise ratio (SNR) at the receiver. This is almost impossible to achieve using a single-element transmitter. However, if, for example, a 100 element PAA transmitter is used, only 20 dBm output power is required from each element of the phased array, which is reasonable with today's low-cost fully integrated solutions [3].

The widespread application of optical fibers for 5G networks [4] contributes to the deeper convergence of mmW and optical systems [5], especially in the 5G fronthaul network where optical fibers serve as a medium connecting the baseband unit (BBU), commonly located in a central office (CO), to a remote radio head (RRH) found in a cell site. Such centralized mobile network architecture, called a cloud radio access network, consists of several BBUs jointly controlled in a CO and connected to the RRHs in a particular cell over a fronthaul network, providing higher energy and cost efficiency [5]. The connectivity over the optical fiber will also be crucial for high-density antenna deployment within the cell-less architecture being considered for 6G [6]. The difference between optical and radio mmW systems can be bridged via microwave photonics technology by combining the advantages of high radiofrequency (RF) systems and optical networks [7]. Microwave photonics research involves radio over fiber (RoF) which, in principle, allows the modulation of a light wave by the RF signal, then transmits it via an optical fiber where the photodetector recovers the original RF signal [8]. Thus, analog RoF systems can be used as an effective solution for fronthaul networks [9]. In [10], the use of analog RoF has been demonstrated, leading to scalable 5G fronthaul with centralized architecture. An 800 MHz bandwidth has been successfully transmitted over 10 km 7 core multi-core optical fiber and over 9 m mmW wireless transmission at 25.5 GHz. The mmW frequency transmission of up to 96 GHz, while aggregating four 400 MHz bandwidths, has been presented in [11] to show a seamless solution for the RAN in 5G and beyond networks. An intermediate frequency (IF) over fiber has been used for 360° coverage in V-Band massive multiple-input multiple-output (MIMO) small cells at a target frequency of 60 GHz [12]. The beamforming capability, controlled in the

electrical domain, was 90° for each PAA out of four. An overall evolution of the RoF technology with faced challenges related especially to the high-frequency fronthaul network in 5G is described in detail in [13].

Along with the use of microwave photonics in RF networks, the optical system enables beamforming by employing variable true-time delay (TTD) modules to introduce a phase difference in particular PAA elements [14]. For instance, an ultra-fast (<50 ps) mmW photonic beamforming system using a tunable delay component and two-element Vivaldi PAA, with up to 30° steering angle at 35 GHz, has been described in [15]. An optical TTD was also used for a PAA radar allowing beam steering at 10 GHz [16]. The TTD was, in this case, realized by a combination of optical sources at different wavelengths, wavelength division multiplexers (WDMs), and fiber-optic delay lines, with optical 2 × 2 switches activating variable fiber-optic paths to introduce phase difference between particular branches. A steering angle of 28.7° was achieved with a maximal radiation angle error from the main beam direction of less than 2.1°. Variable delay lines were used as TTD in [17] to perform optical beamforming with a two-element PAA transmitting 1 Gb/s on–off keying data on the 19 GHz RF carrier, with steering angles ±26.4° over 20 cm free space distance. A 38 GHz mmW beam-steered fiber-optic and wireless system based on an arrayed waveguide grating (AWG) feedback loop was proposed and experimentally tested over a 26 cm long wireless antenna channel in [18] while achieving up to an 8 Gb/s bit rate. The setup consisted of a two-element PAA and receiving antenna placed on an optical rail offsetting the receiving antenna position at a range of ±20 cm. The same authors later published an enhanced optical beamformer at 38 GHz based on a bidirectional optical delay network, which included an integrated AWG. The AWG was fully controlled by the wavelength of the incoming optical signal to achieve beamforming [19]. The performance was verified through 28 cm long free space distance while using up to 4 Gb/s data signal with 4-quadrature amplitude modulation (4-QAM). However, the presented two-element PAA cannot allow sufficient scanning angle range for antenna beam steering in such a high-frequency mmW system. Moreover, the systems used a photonically doubled frequency technique to set the desired mmW frequency, which needs to use two Mach–Zehnder modulators (MZMs) in setup. The first MZM is used for the optical carrier suppression and the second is used for the data modulation with intermediate frequency, therefore representing a more complex approach. Other photonic phase-control circuits using TTDs are listed, e.g., in [3].

Another approach for optical TTD for an mmW frequency band is the usage of the chromatic dispersion phenomenon with a multi-wavelength optical signal, allowing phase delays to be optically set up for different wavelengths. In [20], a multiple-wavelength tunable laser was used to feed 5 km of standard single-mode fiber (SMF), a four-element patch PAA at 2 GHz, and a two-element patch PAA at 20 GHz. In this configuration, an up to ±30° radiation angle with single-tone RF signal has been obtained for both 2 and 20 GHz frequencies. The same authors researched two-dimensional beam steering using an mmW RoF link at 37 GHz [21] with the 2 × 3 patch PAA used with a combined chromatic dispersion-induced phase difference in one dimension and an RF phase shifter in the other dimension. The chromatic dispersion-induced delay was realized in a 1 km long SMF obtaining a π -shift at 37 GHz by tuning the signal wavelength by 0.8 nm and measuring the received continuous wave (CW) signal over a 1.5 m long wireless distance. A centralized beamforming control for base stations using PAA based on different signal propagation delays in the optical fiber due to the chromatic dispersion theoretically is presented in [22]. The transmission over 10 km of standard SMF at 1550 nm and a four-element PAA in the proposed system was tested at frequencies of 3.5, 5, and 29.5 GHz with seven basic beamforming directions to be used in a 5G cellular network. The chromatic dispersion effect has also been exploited in [23], where the RoF system handled phase difference from a CW signal between two phase antenna subarrays forming a 4 × 2 array, which was further steered at 60 GHz by additional variable delay lines. The photodetectors were, in this case, integrated directly onto a PAA substrate and the authors demonstrated 0 and 30° radiation angle in both the E and H planes over 45 cm of the free space by using arrayed patch antennas.

In this paper we present, for the first time to our knowledge, an experimental validation of data transmission in the 24–28 GHz band using optical beam steering via chromatic dispersion in a hybrid RF/optical system. For this purpose, we have proposed a microwave photonic link (MPL) in a given band with an in-house built application-tailored three-element PAA based on planar dipoles to provide enough beam steering scalability. We demonstrate PAA beam steering performance and confirm the usability of our approach within a microwave photonic network by evaluating data transmission quality over a 1.5 m long wireless distance. The paper is structured as follows: Section 2 describes the experimental setup, Section 3 presents the results and discussion, and finally, the conclusion is provided in Section 4.

2. EXPERIMENTAL SETUP

The principle of beamforming with a PAA using an optical TTD is illustrated in the example of a linear three-element PAA in Fig. 1. The equal distance between antenna elements is denoted as Λ, i.e., $\Lambda = 6$ mm, and the requested steered angle is Θ. The time delay difference between two adjacent elements, which is required for the beam steering with angle Θ, can be obtained as [3]

$$\Delta t = \frac{\Lambda \sin(\theta)}{c}, \tag{1}$$

where c is the speed of the light in the air. Based on Eq. (1), the introduced time delays necessary to point the wavefront to angle θ in the three-element PAA are 0, $(\Lambda \sin\theta)/c$, and $2(\Lambda \sin\theta)/c$, respectively, for particular PAA branches. For a steering angle of $\Theta = 25°$ at 25 GHz, the delays correspond to $\Delta t_1 = 0$, $\Delta t_2 = 8.45$ ps, and $\Delta t_3 = 16.9$ ps, which stands for the 80° difference in phase. Note that we consider the middle element as a reference and then add and subtract the requested phase difference from the middle element, i.e., 80°.

To change the phase difference among PAA elements, a tunable laser source is used. The wavelength tuning range $\Delta\lambda$ to obtain the 180° phase shift of the RF signal is given by the

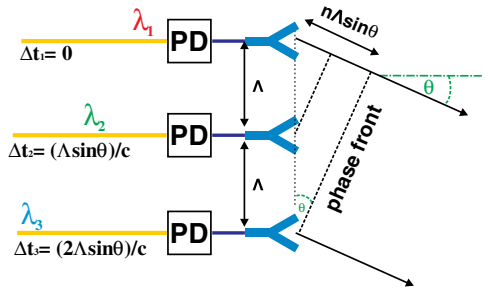

Fig. 1. Beamforming principle based on the optical TTD for a PAA with three elements.

Table 1. Optical Beamforming Parameters at 25 GHz

λ (nm)	D (ps/nm km)	Calculated Δλ (nm/°)	Measured Δλ (nm/°) at λ (nm)
1534.5	16.019	0.000679	0.000675 at 1534.695
1550.0	17.205	0.000633	0.000629 at 1550.031
1571.0	18.763	0.000580	0.000575 at 1571.178

following equation [20]:

$$\Delta\lambda = \frac{1}{2L\,D\,f_{\mathrm{RF}}}, \tag{2}$$

where L is the length of the SMF used, D is the chromatic dispersion coefficient, and f_{RF} is the RF carrier frequency. Measured coefficients D, for particular wavelengths, and the SMF, which is a standard G.652 type, are given in Table 1. Also shown are the calculated and measured wavelength tuning ranges $\Delta\lambda$ for the $\pi/180$ phase shift at $f_{\mathrm{RF}} = 25$ GHz and $L = 10.2$ km. Note that the wavelengths have been chosen according to the coarse wavelength division multiplexer (CWDM) grid.

For example, for $\Delta\lambda$ to achieve an 80° phase difference at 25 GHz in the outer branches from the middle reference element, with a wavelength of 1550 nm, 0.054 and 0.048 nm shifts for optical wavelengths 1534 and 1571 nm, respectively, are needed. Similarly, the wavelength offsets are halved if a 40° steering angle is requested and so on. Further, based on Eq. (2), if a shorter optical fiber is deployed, e.g., 5 km, then a twice-as-wide tuning wavelength range has to be chosen to achieve the same RF phase shift at a given frequency. Note that the slight difference between the calculated and measured values of $\Delta\lambda$ in Table 1 is caused by the small difference between wavelengths at which the D parameters were measured and wavelengths used in the experiment. Moreover, there is also some uncertainty due to the presence of the electrical amplifiers (EAs) and 10 cm long coaxial cables with a mini-SMP connector because the phase difference is measured by a vector network analyzer behind photodiodes (PD), excluding EAs and the coaxial cables. The combination of all aforementioned uncertainty and bigger wavelength difference between lasers causes a squint effect, which results in non-identical phase difference between PAA branches over the considered frequency range. However, based on measurements, the adverse effect of squinting appears in the proposed system for bandwidths wider than 500 MHz. Note that the phase-change variation in PAA elements with up to ±10° difference has almost a negligible impact on the main lobe shape. The complete experimental demonstration of beamforming carried out in MPL has been realized according to the scheme in Fig. 2.

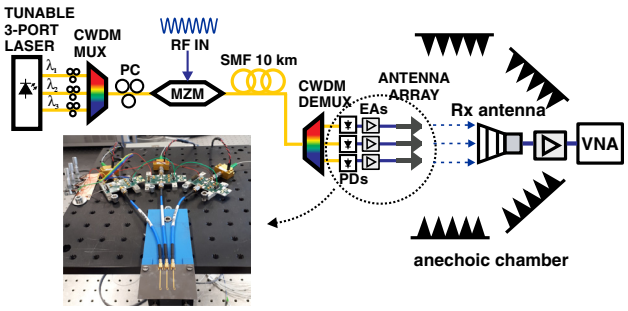

Fig. 2. Experimental setup of an RoF link for mmW transmission and optical-controlled beamforming.

A tunable 3-port laser source (CoBrite DX4) is used to adaptively control the phase difference between particular link outputs feeding the PAA due to the effect of chromatic dispersion in the optical fiber. Each of the three ports of the laser source (providing signals at 1534.695, 1550.031, and 1571.178 nm, all with optical power 16 dBm) is connected via polarization controllers (PCs) to the CWDM to combine the signals into a single SMF. After multiplexing, the signals pass through another PC adjusting the polarization state to the MZM (Optilab IML-1550-50-PM), which serves as an electrical-to-optical convertor. The MZM is biased in a quadrature operation point corresponding to a bias voltage of 0.8 V. Note that the MZM allows the modulation of all three optical carriers by an identical RF signal. A 10 km long SMF is employed to emulate the distance coverage of the radio signal in a real network. The SMF allows chromatic dispersion-induced time delay between particular optical carriers by introducing a phase delay for the RF signals. This particular SMF length also avoids the chromatic-dispersion-induced RF power fading. Please note that the chromatic dispersion can indeed induce power fading for certain frequencies in the intensity-modulated analog radio over fiber transmission with direct detection based on the chromatic dispersion coefficient at the particular optical wavelength and the length of the fiber according to the Eq. (3) in [21]. At the output of the SMF, the CWDM divides particular carriers, according to their wavelength, into three optical branches which are terminated by PDs (Optilab PD40). The PDs transform the optical signals back to the RF domain. To reach sufficient RF power for radiating the signal from the PAA to free space, three identical RF electronic amplifiers (EAs, Analog Devices HMC1131) are deployed with an average gain of 21 dB over the 24–35 GHz band. Finally, the PAA is connected to the EAs via 10 cm long coaxial cables with mini-SMP connectors. Note that to reduce unwanted reflections in our experiment, the PAA, with EAs, PDs, and the WDM demultiplexer, has been placed on a rotating board and characterized within an anechoic chamber situated at the Czech Technical University in Prague, Faculty of Electrical Engineering. The PAA-transmitted CW signal is received after a 3 m long wireless propagation in the chamber

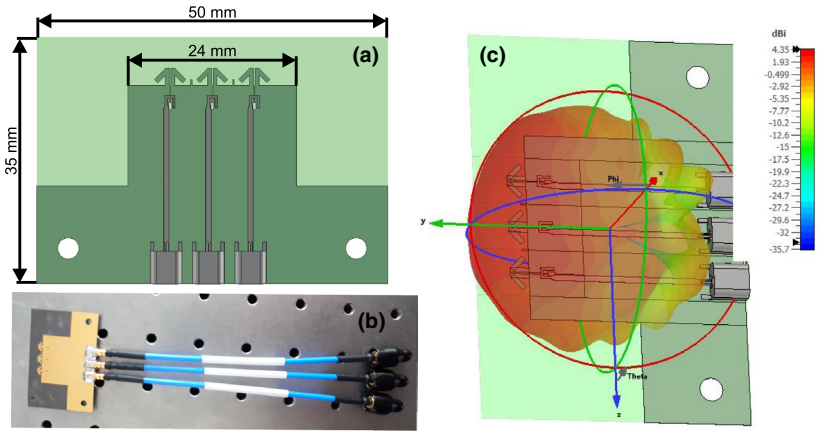

Fig. 3. PAA structure: (a) model from CST Studio Suite, (b) manufactured antenna with attached coaxial cables, and (c) simulated 3D embedded radiation pattern from the PAA.

by a double-ridged horn antenna (RFspin DRH40 with 15 dBi gain at 25 GHz), amplified by low-noise EA (Miteq AMF-4F-260400-40-10p) and delivered to the receiver. To obtain the radiation pattern of the PAA, a vector network analyzer (VNA, Rohde & Schwarz ZVA40) is used, whereas for data transmission, a combination of the signal generators (Rohde & Schwarz SMW200A, SMF100A), RF mixer, and spectral analyzer (Rohde & Schwarz FSW) is leveraged. The system operates in a transmitting mode. However the proposed system could also be used in receiving mode. In that case, the system needs to be capable to match the phase of the incoming signal to the antenna as has been shown, e.g., in [24], where the authors used one CW laser and electro-optical modulators and variable fiber lengths for each of the PAA branch for a microwave radar receiver. In our setup, conversely, the same fiber length as for the transmitter would be fixed with one common MZM modulator and one tunable laser for each particular PAA branch. Then, the signals would be separated behind the WDM demultiplexer based on their wavelength, detected by photodiodes and combined in the electrical domain. Note that in order to achieve more optically phased PAA elements, a DWDM scheme can also be applicable.

A three-element PAA based on planar dipole antennas [25] was designed in CST Studio Suite for the frequency range of 24 to 28 GHz. The PAA, shown in detail with structure dimensions in Fig. 3(a), was then manufactured [Fig. 3(b)].The simulated 3D embedded radiation pattern of the PAA, middle element excited while the others are open-circuit, is then shown in Fig. 3(c). Note that the element spacing is 6 mm and the substrate used is Isola Astra MT77 with a thickness of 0.254 mm. The particular antenna element in the array, having itself a gain of about 5 dBi in the 23.5 to 39.5 GHz band, is connected to the RF signal source via coaxial cable with a mini-SMP connector to maintain a small footprint. The efficiency of the PAA at the considered bandwidth of 24–28 GHz, falling to the 5G FR2 frequency area [1], is about 65% and the entire PAA gain is 9 dBi.

3. RESULTS AND DISCUSSION

At first, the proposed hybrid system is tested in terms of S_{21} frequency response at a target bandwidth between 24 and 28 GHz. Results from measurements, using VNA (Rohde & Schwarz ZVA67), are depicted in Fig. 4(a). In the designed bandwidth, the S_{21} curve is flat, i.e., the difference over the whole bandwidth is less than 1 dB for all three signals. Moreover, impedance matching in terms of S_{11} is better than −10 dB for the given bandwidth. Also, the simulated radiation patterns of the PAA with side-steering is shown in Fig. 4(b) for the frequency range from 24 to 28 GHz.

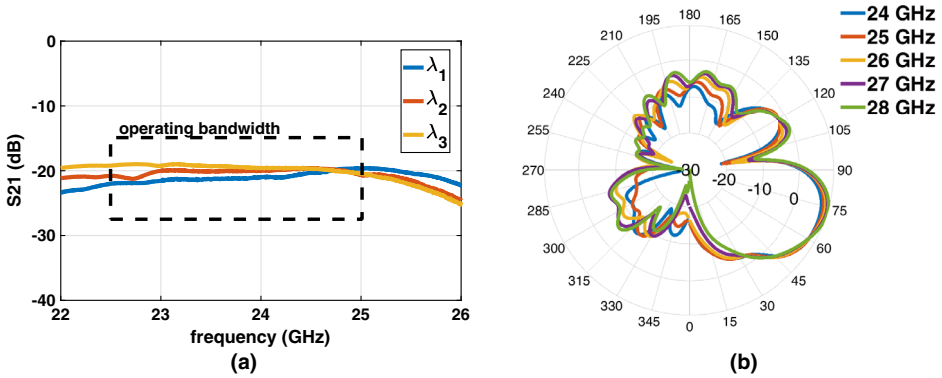

Fig. 4. (a) Signal transmission for three branches at wavelengths $\lambda_1 = 1534.695$ nm, $\lambda_2 = 1550.031$ nm, and $\lambda_3 = 1571.178$ nm at the frequency range of 22 to 30 GHz, and (b) simulated radiation pattern of the PAA for frequency range 24–28 GHz.

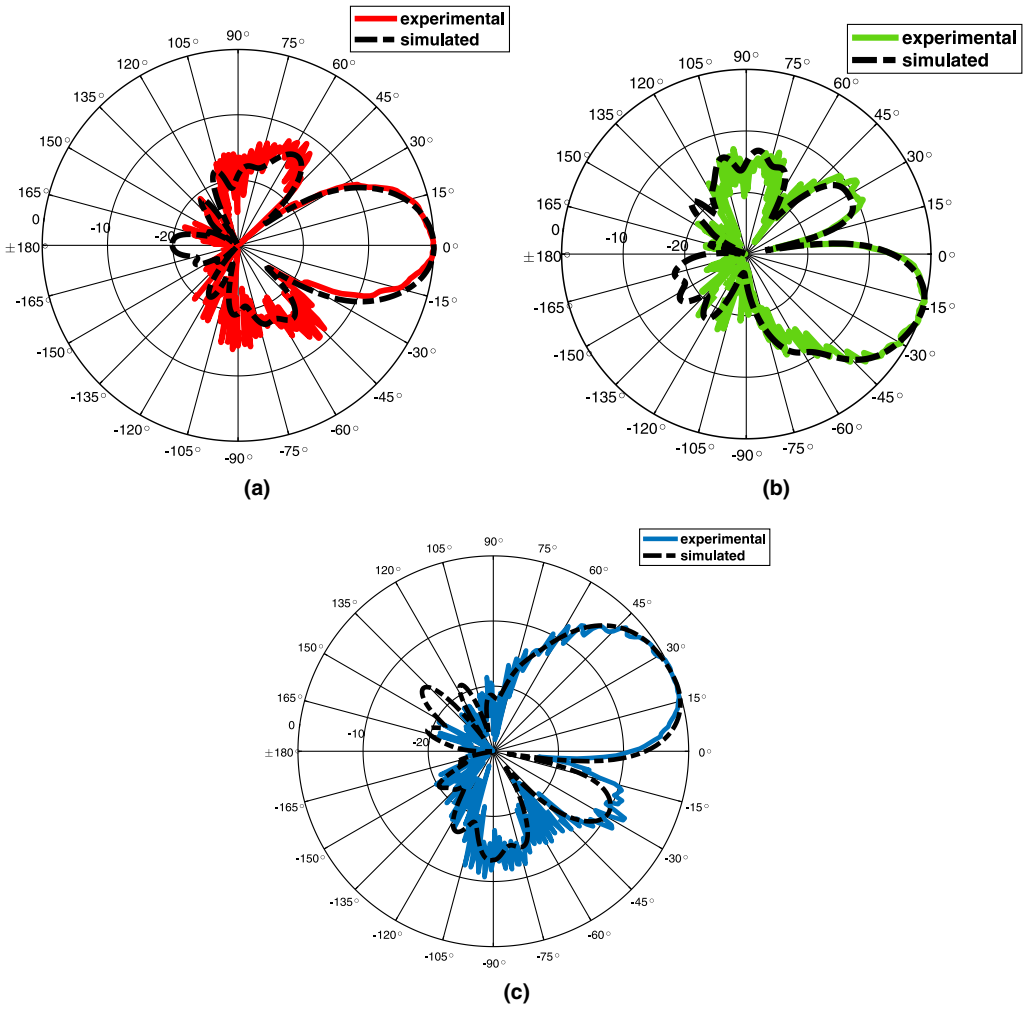

Fig. 5. Measured and simulated radiation patterns at 26 GHz for steering angles (a) 0°, (b) −25°, and (c) 25°.

In the next step, the whole setup, including an MPL, was tested in an anechoic chamber over the 3 m long wireless distance to obtain radiation patterns for specific steering angles. The transmitting side (tunable lasers, PCs, CWDM, MZM, and optical fiber) was located outside of the anechoic chamber while the CWDM, PDs, EAs, and PAA were placed inside. The PAA was attached to a rotating board, whereas the receiving antenna was fixed and the signal was measured by VNA for an azimuth range of ± 180°. The radiation pattern was measured for a CW signal at frequencies of 24, 26, and 28 GHz to verify the functionality and system design in the proposed bandwidth. Selected results for the frequency of 26 GHz with steering angles of 0°, −25°, and 25° are shown in Figs. 5(a)–5(c), respectively. For the sake of comparison, black dashed lines denote simulated results obtained by CST Studio Suite. Meanwhile Fig. 5(a) shows the radiation pattern with no phase difference among the PAA elements, while Figs. 5(b) and 5(c) depict the radiation pattern of the system with an introduced phase difference of ± 80° from the middle element to steer the wavefront in the desired angle, i.e., ± 25°. Note that these measurements have been carried out for a single-tone signal without any modulation (i.e., data).

We can observe remarkable agreement between simulated and measured results. The minimal main-to-side lobe ratio is 10 dB in this case. More importantly, it has been experimentally demonstrated that the usage of the chromatic dispersion phenomenon is capable of carrying out TTD beamforming in a hybrid mmW/optical link at the 26 GHz band with a three-element PAA.

Later, a data signal was added to analyze our hybrid system performance for practical use within the given bandwidth. For these purposes, we transmitted the signal from the PAA over a distance of 1.5 m of free space. For signal generation, a baseband generator (R&S SMW200A) was used with predefined cellular network test models according to the long-term evolution (LTE), and test model TM 3.1 using 64-QAM was adopted. This model is, in general, proposed to test transmitted signal quality and output power dynamics [26]. The baseband was up-converted to the desired frequency using a mixer and signal generator (R&S SMF100A) serving as a local oscillator with a frequency of 25 GHz. The signal was subsequently amplified using an EA (Analog Devices HMC1131) which led to the MZM RF input, so all three optical carriers carried the same RF signal. At the receiver side, a spectral analyzer (R&S FSW) was

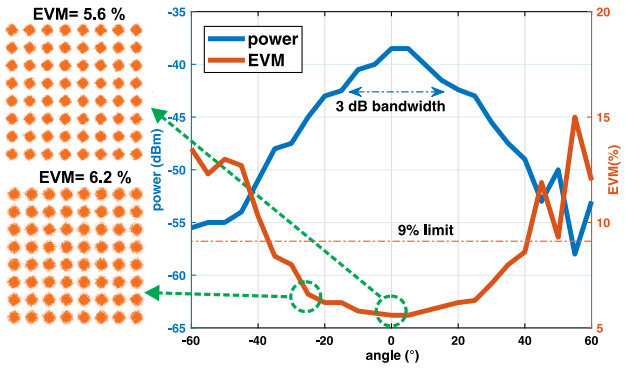

Fig. 6. EVM and received power versus PAA azimuth angle at 25 GHz for 64-QAM signal with 20 MHz bandwidth for steering angle 0°. Constellation diagrams are shown at azimuth 0° and −25°.

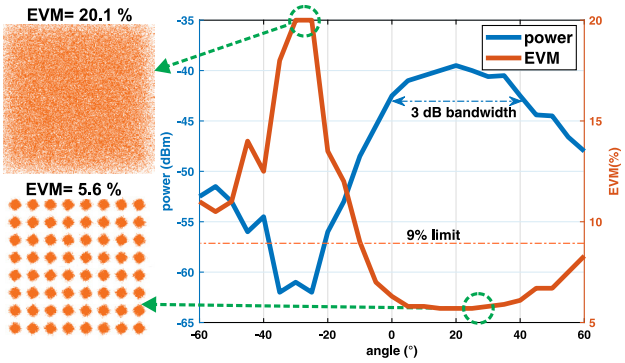

Fig. 7. EVM and received power versus PAA azimuth angle at 25 GHz for 64-QAM with 20 MHz bandwidth for steering angle 25°. Constellation diagrams are shown at azimuth −25° and 25°.

used for the demodulation and data evaluation. Note that this measurement was performed outside the anechoic chamber.

In the first series of tests, with regard to the previous experiment, we set the steering angle to 0° and 25° by tuning the laser to the above-mentioned wavelengths and then measuring received power and error vector magnitude (EVM) with the dependence on the PAA azimuth in the range of ± 60°. Test model 3.1 was used with 64-QAM and 20 MHz bandwidth, resulting in a data throughput of 75 Mb/s. Figure 6 shows the result for a 0° steering angle, while Fig. 7 depicts results for 25°. EVM performance, in terms of constellation diagrams for 64-QAM, is shown in the azimuths of −25, 0, and 25°.

For the error-free transmission, the EVM limit for 64-QAM is given as 9% [26]. One can observe the EVM below the given limit for a wide range of the azimuth, i.e., approximately 80°. However, the received power curve, considering a 3 dB decrease, is much sharper in the direction of the steering angle with an azimuth range of approximately 25° and 40° in the cases of direct steering and steering to the side, respectively, representing an effective directing of the beam to achieve maximum power in the selected direction. For both steering angles, the minimum EVM is as low as 5.6% and maximum power is −38.5 and −40.0 dBm for the direct steering and steering to the side, respectively. Also evident in the results displayed in Fig. 7 is a side lobe which is shifted by 80° and has a signal power magnitude 15 dB lower than the main lobe. The constellation diagrams of the received 64-QAM in the direction of maximum power, i.e., 0° and 25°, respectively, are also shown, as well as −25° for the sake of comparison. Clear constellations for the intended steering angle and high EVM in the opposite direction in the case of Fig. 7 can be seen. On the other hand, Fig. 6 shows the results with direct steering and the EVM for ±25° azimuth is still below the given EVM limit but with significantly decreased received power, i.e., lower than 5 dB. In other words, for direct beam pointing, we still see excellent EVM performance even for the azimuth range ±25°, but EVM performance for the steering to the side at an angle of 25° is unacceptable with a received signal power drop of more than 20 dB. It is worth mentioning that the power characteristic of the side lobes differs from those in the radiation pattern shown in Fig. 5. This is because the radiation patterns were obtained in anechoic chamber with a CW signal source, whereas for the broadband measurement of the whole system, the testbed was located in a laboratory with other equipment around. These different measurement conditions result in small differences in observed radiation patterns (especially in side lobes). Next, an analysis of bandwidth dependence, i.e., from 1.4 to 20 MHz, for both selected steering angles has been carried out to show the performance for the wideband signal at the carrier frequency of 25 GHz. The EVM results are shown in Fig. 8(a). As expected, the lowest EVM, i.e., 5.1%, is achieved for the narrowest signal with a bandwidth

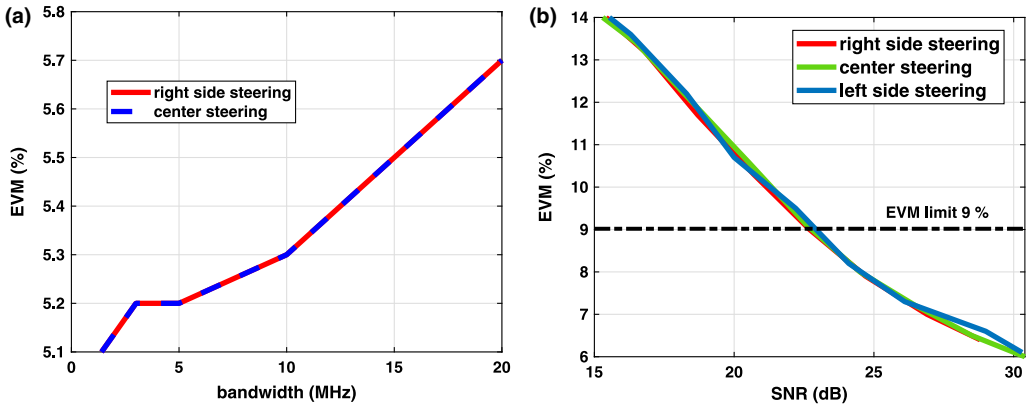

Fig. 8. (a) EVM 64-QAM performance of the received signal for variable signal bandwidth, and (b) EVM 64-QAM performance for variable SNR with 20 MHz bandwidth.

of 1.4 MHz. However, even for the maximal bandwidth of 20 MHz, the EVM is only 0.6% higher, which is still well below the EVM limit for 64-QAM. Moreover, both steering angles show identical performance, proving there is no difference in the performance for the broadband signal in different directions when steering for bandwidth up to 20 MHz. Finally, the whole system performance has been tested in terms of EVM for the variable SNR at the receiver, which has been changed by the placing and tuning of the variable optical attenuator (VOA) in the optical path before the WDM demultiplexer. Note that the attenuator (Oz optics DA-100-SC-1300/1550-9/125-S-40) has itself an insertion loss of 1.5 dB, resulting in a 3 dB loss in the RF domain. Additional losses have been set from 0 to 9 dB, which emulates either decreased optical power at the optical domain due to, for example, lower laser power or increased losses in the RF channel since the maximum 9 dB optical loss is translated to an 18 dB RF power decrease. The SNR has been then obtained by measurement of the difference between signal power and noise adjacent to the signal bandwidth on the spectral analyzer while the optical loss in VOA was increased. The noise floor of the system was −146 dBm/Hz. This measurement was repeated for three steered directions, i.e., −25°, 0°, and 25°, and the results are depicted in Fig. 8(b).

It can be seen that there is, again, negligible difference in EVM performance between signals steered in different directions. Furthermore, system EVM performance is below the error-free transmission limit for SNR higher than 23 dB. Due to the 10 km of optical fiber span providing enough of both signal reach and small wavelength tuning range, the wavelength changing is in the order of tens of thousands of nanometers per one degree of electrical phase at 25 GHz. In practical terms, the wavelength variation can then be realized, for example, by changing the TEC temperature in the distributed feedback laser, as shown in [27].

4. CONCLUSION

A hybrid transmission system, including an MPL and a three-element antenna, operating at an mmW frequency band between 24 and 28 GHz and which is capable of realizing beam steering in the optical domain by using the chromatic dispersion approach, has been experimentally demonstrated. The system, using designed and developed three-element planar dipoles PAA, evinced perfect agreement between simulated and experimental results in terms of radiation patterns at selected bandwidth. It has also been shown that a PAA with only three elements can effectively steer the beam which, consequently, significantly decreases demand for radiating power to provide sufficient SNR in all cell directions. We have experimentally verified the proposed hybrid system with data transmission over a 1.5 m long wireless channel. Moreover, the optically controlled steering has been tested with real data transmission at the frequency of 25 GHz, achieving an EVM as low as 5.6% with a 64-QAM modulation scheme and 20 MHz bandwidth. Experimental measurements with data transmission also confirmed theoretical assumptions about the potential usage of such an approach to be deployed in future cellular mmW frequency fronthaul networks.

Funding. European Cooperation in Science and Technology (CA 16220); Ministerstvo Průmyslu a Obchodu (FV30427); Grant Agency of CTU Prague (SGS20/166/OHK3/3T/13).

Disclosures. The authors declare no conflicts of interest.

REFERENCES

1. A. Tikhomirov, E. Omelyanchuk, and A. Semenova, "Recommended 5G frequency bands evaluation," in *Systems of Signals Generating and Processing in the Field of on Board Communications* (2018), pp. 1–5.
2. Y. R. Li, B. Gao, X. Zhang, and K. Huang, "Beam management in millimeter-wave communications for 5G and beyond," IEEE Access **8**, 13282–13293 (2020).
3. Z. Cao, Q. Ma, A. B. Smolders, Y. Jiao, M. J. Wale, C. W. Oh, H. Wu, and A. M. J. Koonen, "Advanced integration techniques on broadband millimeter-wave beam steering for 5G wireless networks and beyond," IEEE J. Quantum Electron. **52**, 1–20 (2016).
4. B. Imanilov, M. Sauer, and A. Kobyakov, "Optical fiber in wireless networks: from radio-over-fiber DAS to 5G RAN," in *IEEE Photonics Conference (IPC)* (2019), pp. 1–2.
5. T. R. Raddo, S. Rommel, B. Cimoli, and I. T. Monroy, "The optical fiber and mm wave wireless convergence for 5G fronthaul networks," in *IEEE 2nd 5G World Forum (5GWF)* (2019), pp. 607–612.
6. L. U. Khan, I. Yaqoob, M. Imran, Z. Han, and C. S. Hong, "6G wireless systems: a vision, architectural elements, and future directions," IEEE Access **8**, 147029 (2020).
7. D. Marpaung, J. Yao, and J. Campany, "Integrated microwave photonics," Nat. Photonics **13**, 80–90 (2019).
8. J. Bohata, M. Komanec, J. Spacil, R. Slavik, and S. Zvanovec, "Transmitters for combined radio over a fiber and outdoor millimeter-wave system at 25 GHz," IEEE Photon. J. **12**, 1–14 (2020).
9. D. Novak, R. B. Waterhouse, A. Nirmalathas, C. Lim, P. A. Gamage, T. R. Clark, M. L. Dennis, and J. A. Nanzer, "Radio-over-fiber technologies for emerging wireless systems," IEEE J. Quantum Electron. **52**, 1–11 (2016).
10. S. Rommel, D. Dodane, E. Grivas, B. Cimoli, J. Bourderionnet, G. Feugnet, A. Morales, E. Pikasis, C. Roeloffzen, P. van Dijk, M. Katsikis, K. Ntontin, D. Kritharidis, I. Spaleniak, P. Mitchell, M. Dubov, J. B. Carvalho, and I. T. Monroy, "Towards a scaleable 5G fronthaul: analog radio-over-fiber and space division multiplexing," J. Lightwave Technol. **38**, 5412–5422 (2020).
11. P. T. Dat, A. Kanno, N. Yamamoto, and T. Kawanishi, "Seamless convergence of fiber and wireless systems for 5G and beyond networks," J. Lightwave Technol. **37**, 592–605 (2019).
12. E. Ruggeri, A. Tsakyridis, C. Vagionas, G. Kalfas, R. M. Oldenbeuving, P. W. L. Van Dijk, C. G. H. Roeloffzen, Y. Leiba, N. Pleros, and A. Miliou, "A 5G fiber wireless 4 Gb/s WDM fronthaul for flexible 360 coverage in V-band massive MIMO small cells," J. Lightwave Technol. (to be published).
13. C. Lim, Y. Tian, C. Ranaweera, T. A. Nirmalathas, E. Wong, and K. Lee, "Evolution of radio-over-fiber technology," J. Lightwave Technol. **37**, 1647–1656 (2019).
14. V. J. Urick, Jr., J. D. McKinney, and K. J. Williams, *Fundamentals of Microwave Photonics* (Wiley, 2015).
15. R. Bonjour, M. Singleton, S. A. Gebrewold, Y. Salamin, F. C. Abrecht, B. Baeuerle, A. Josten, P. Leuchtmann, C. Hafner, and J. Leuthold, "Ultra-fast millimeter wave beam steering," IEEE J. Quantum Electron. **52**, 1–8 (2016).
16. B. Jung, D. Kim, I. Jeon, S. Shin, and H. Kim, "Optical true time-delay beamformer based on microwave photonics for phased array radar," in *3rd International Asia-Pacific Conference on Synthetic Aperture Radar (APSAR)* (2011), pp. 1–4.
17. Z. Cao, F. Li, H. P. A. van den Boom, E. Tangdiongga, and A. M. J. Koonen, "Optical true-time-delay microwave beam-steering with 1 Gb/s wireless transmission for in-building networks," in *39th European Conference and Exhibition on Optical Communication (ECOC 2013)*, (2013), pp. 1–3.
18. Z. Cao, X. Zhao, F. M. Soares, N. Tessema, and A. M. J. Koonen, "38-GHz millimeter wave beam steered fiber wireless systems for 5G

indoor coverage: architectures, devices, and links," IEEE J. Quantum Electron. **53**, 1–9 (2017).
19. X. Zhang, M. Zhao, Y. Jiao, Z. Cao, and A. M. J. Koonen, "Integrated wavelength-tuned optical mm-wave beamformer with doubled delay resolution," J. Lightwave Technol. **38**, 2353–2359 (2020).
20. S. Akiba, M. Oishi, Y. Nishikawa, J. Hirokawa, and M. Ando, "Photonic approach to beam steering of phased array antenna," in *International Symposium on Electromagnetic Theory* (2013), pp. 448–451.
21. M. Oishi, Y. Nishikawa, S. Akiba, J. Hirokawa, and M. Ando, "2-dimensional beam steering by 2×3 photonic antenna using millimeter-wave radio over fiber," in *IEEE International Topical Meeting on Microwave Photonics (MWP)* (2013), pp. 130–133.
22. H. Huang, C. Zhang, C. Chen, T. Wu, H. Huang, and K. Qiu, "Optical true time delay pools based centralized beamforming control for wireless base stations phased-array antennas," J. Lightwave Technol. **36**, 3693–3699 (2018).
23. T. Hirasawa, K. Furuya, M. Oishi, S. Akiba, J. Hirokawa, and M. Ando, "Integrated photonic array-antennas in RoF system for MMW-RF antenna beam steering," in *International Topical Meeting on Microwave Photonics (MWP)* (2015), pp. 1–4.
24. Z. G. Tegegne, C. Decroze, P. Di Bin, T. Fromenteze, and C. Aupetit-Berthelemot, "Single channel microwave photonics digital beamforming radar imaging system," J. Lightwave Technol. **36**, 675–681 (2018).
25. J. Bohata, T. Lonsky, J. Spacil, P. Hazdra, Z. Hradecky, M. Komanec, S. Zvanovec, L. Vallejo, and B. Ortega, "Antenna phased array beamforming at 26 GHz using optical true time-delay," in *12th IEEE/IET International Symposium on Communication Systems, Networks and Digital Signal Processing (CSNDSP)* (2020).
26. The 3rd Generation Partnership Project (3GPP), "LTE, Evolved Universal Terrestrial Radio access (E-UTRA)," https://www.etsi.org/deliver/etsi_ts/136100_136199/136141/08.03.00_60/ts_136141v080300p.pdf.
27. V. Polo, P. Borotau, A. Lerin, and J. Prat, "DFB laser reallocation by thermal wavelength control for statistical udWDM in PONs," in *The European Conference on Optical Communication (ECOC)* (2014), pp. 1–3.

Optical Switching Based on Arsenic-Selenide and Lead-Silicate Fibers

Matej Komanec, Tomas Nemecek, Dmytro Suslov, Redwan Ahmad and Tomas Martan
Faculty of Electrical Engineering
Czech Technical University in Prague
Prague, Czech Republic 166 27
Email: komanmat@fel.cvut.cz

***Abstract*—The paper reports our progress on soft-glass fibers for optical switching purposes based on four-wave mixing. Specific development of connectorized nonlinear modules for switching application is presented. For the arsenic-selenide fiber we present a novel solid joint technology, with connection losses of only 0.25 dB, which is the lowest value presented up-to-date. We have carried out conversion efficiency simulations, conversion efficiency of -16.1 dB was obtained with arsenic-selenide fiber of length reduced to 5 m. Finally experimental tests are included employing our developed optical switch testbed. Measurement results with a 26 m and a 4.5 m long arsenic-selenide nonlinear modules are presented.**

I. Introduction

Increasing data traffic such as 3D multi-media data streams, full-HD videos and real-time data transfers imposes demands for all-optical network solutions, represented by optical burst or packet switching. With the rise of new modulation formats in optical communication such as dual-polarization quadrature phase-shift keying (DP-QPSK) [1] and m-ary quadrature amplitude modulation (m-QAM) [1], [2] or orthogonal-frequency division multiplexing (OFDM) [3], optical networks require modulation format transparent, polarization insensitive switching processes with switching speeds in orders of Tbit/s. Several solutions to optical switching have been proposed, e.g. based on optical gating [4] , optical flip-flops [5] or silicon nanowires [6].

Optical switching based on wavelength conversion offers a viable solution for future optical packet switched networks. The major advantage of wavelength conversion based on four-wave mixing (FWM) stands in modulation format and data bitrate insensitivity. Highly-nonlinear fibers (HNLFs) have been exploited for wavelength conversion [7]. Specialty non-silica and microstructured fibers, e.g. chalcogenide fibers [8], bismuth fibers [9] and microstructured fibers thereof [10], [11], provide extremely high nonlinearities (γ>1000 $\mathrm{W^{-1}km^{-1}}$), promising enhanced conversion efficiencies while simultaneously decreasing component length, which can result in neglection of dispersive effects. A major drawback of the fibers stands in high coupling losses when connected to a conventional silica fiber. Free-space optic approaches were proposed for coupling into arsenic-selenide fibers with only 37% coupling efficiency [12], but these are not suitable for real network applications. Solid joints for arsenic-selenide fibers were presented [13] with 2.45 dB loss per joint achieved by butt-coupling to silica fiber via 5 mm of high NA fiber and index matching oil to improve coupling. Furthermore in [13] arsenic-selenide single-mode fibers were measured and provided attenuation of ≈1 dB/m.

This paper presents our results from the development of nonlinear modules for optical switching based on four-wave mixing (FWM). Dispersion properties were studied with the emphasis on zero-dispersion wavelength (ZDWL) and dispersion flatness in the vicinity of 1550 nm. Novel solid joint technologies have been developed for arsenic-selenide fibers to enable efficient broadband wavelength conversion. Wavelength conversion efficiencies were measured for selected nonlinear modules, considering limiting effects and module insertion loss.

The paper first discusses selected soft-glass nonlinear fibers. Afterwards dispersion simulations are presented. Next technological aspects of nonlinear module preparation are covered. Optical switch experimental setup and conversion efficiency results are described and discussed. The paper concludes with a summary of achieved results, current work and future possibilities.

II. Studied fibers

Two fibers of different glass materials are considered: lead-silicate glass optical fibers in either suspended-core microstructured optical fiber (SC-MOF) or hexagonal-structure microstructured optical fiber (HS-MOF) design (see Fig. 1) and a single-mode chalcogenide arsenic-selenide fiber. The lead-silicate glass exhibits refractive index of 1.89 at 1550 nm and nonlinearity 1000 $\mathrm{W^{-1}km^{-1}}$, where SC-MOF has a 1 μm core with 100 nm thick bridges and the HS-MOF has a core diameter of 2.8 μm. Chalcogenide As_2Se_3 single-mode fiber with single-mode cut-off at approximately ∼1300 nm, γ of approximately 1300 $\mathrm{W^{-1}km^{-1}}$ and refractive index of 2.80 at 1550 nm has been employed in our measurements.

Attenuation of lead-silicate fibers is 3 dB/m, which is a limiting factor for further nonlinear application, therefore the maximum length of one meter is considered. Arsenic-selenide fiber attenuation is around 0.6 dB/m.

978-1-5090-2526-8/16/$31.00 ©2016 IEEE

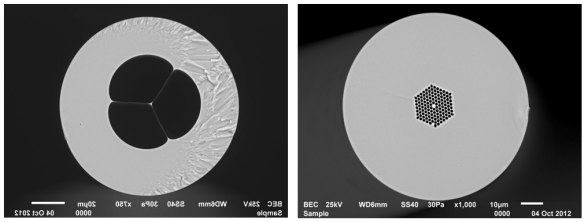

Fig. 1. Lead-silicate fiber: SC-MOF (left) and HS-MOF (right).

III. Simulations

For the purposes of optical switching we have considered degenerate FWM, where we need the pump to operate above ZDWL and meanwhile to have the dispersion curve flat in maximum bandwidth. For simulations we have employed the COMSOL simulation software. Figure 2 depicts the dispersion curve for lead-silicate SC-MOF, which has the first ZDWL at 1113 nm. Important is the flat band around 1550 nm which is suitable for broadband FWM process.

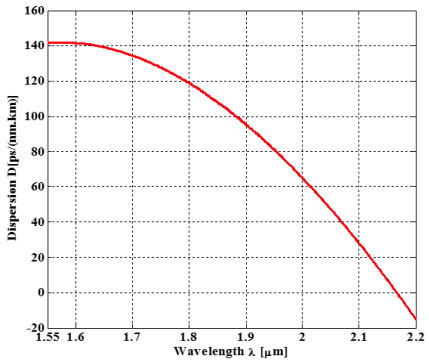

Fig. 2. Lead-silicate SC-MOF dispersion profile.

Figure 3 depicts the dispersion curve for our hexagonal-structure lead-silicate fiber, where ZDWL was design tailored for 1550 nm.

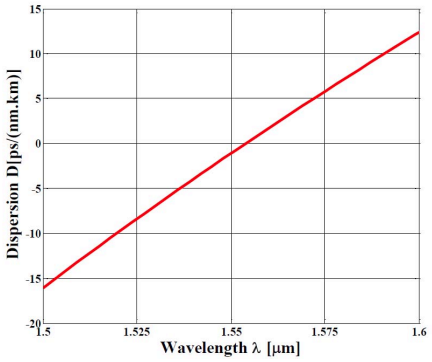

Fig. 3. Lead-silicate HS-MOF dispersion profile.

Dependence of conversion efficiencies for different As_2Se_3 fiber lengths are presented in Fig. 4. We observe that with employment of 3 m to 6 m long As_2Se_3 fiber segment, maximized switching efficiencies are obtained. Considering that for switching wavelength band depends on dispersion slope, i.e. pump and signal walk-off, it is suitable to utilize As_2Se_3 fiber segment of the shortest length, thus eliminating the effects of dispersion. Conversion efficiency increases to -16.1 dB which can be obtained for a 5 m long As_2Se_3 fiber.

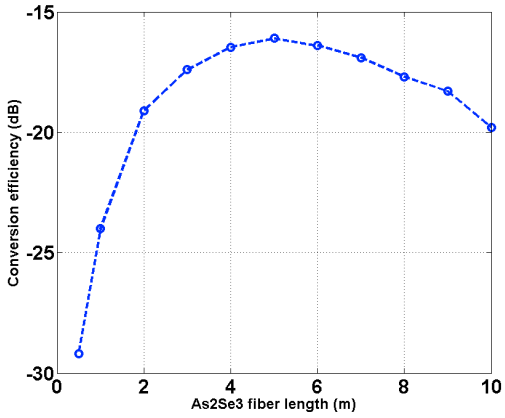

Fig. 4. Simulated switched data conversion efficiency in As_2Se_3 fiber with respect to fiber length.

IV. Module Preparation

For the laboratory work with soft-glass fibers a specialized working station had to be built in SQS Fiber optics. The working station is depicted in Fig. 5.

Fig. 5. Working station for soft-glass fiber modules polishing (right), a specialist in protective suit (right).

Tests with direct fiber connectorization have been performed, the main technological challenge introduce cracks appearing after the glue treatment in the connector ferrule. This effect is attributed to the glass fragility, where conventional silica fibers can resist much stronger pressure force. Figure 6 depicts cracks at the fiber facet observed in case of the arsenic-selenide fiber.

Employing a different technique we have prepared two arsenic-selenide fiber modules, each of them including 4.5 m of the chalcogenide fiber. The modules were designed for a different operational wavelengths, one for 1550 nm and one for 2000 nm. As reflections may be detrimental in many

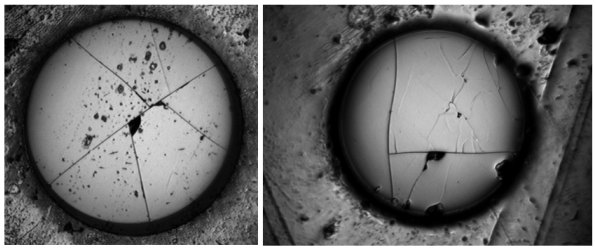

Fig. 6. Cracks in arsenic-selenide fiber facet after glue treatment.

optical setups, we have eliminated this factor by depositing anti-reflex coatings (ARCs). A novel solid joint technology allowed connection losses of only 0.25 dB, which is the lowest value presented up-to-date. This was achieved by a mode-field diameter (MFD) matching fiber with an ARC deposited to compensate for the refractive index difference. The MFD-matching fiber was then spliced to a conventional SMF-28e.

Following the assembly procedure we have measured the loss spectral characteristic of both developed modules - see Fig. 7. We experienced slight interferometric pattern, which is attributed to remaining reflections in the module. This is probably not caused by the ARC quality but rather by small air-gap or improper mode-field diameter (MFD) matching.

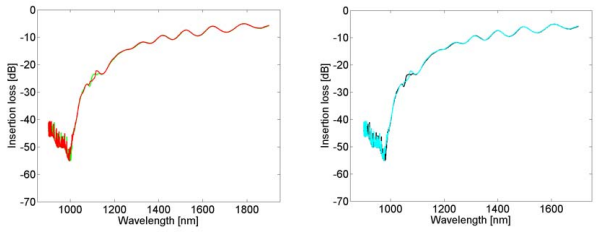

Fig. 7. Spectral characteristic of 1550 nm (left) and 2000 nm (right) arsenic-selenide 4.5m-long fiber modules, both measured in the region 900-1700 nm (limited by OSA spectral range).

V. Experimental Results

Our arsenic-selenide modules were measured in cooperation with ORC University of Southampton and the measured chromatic dispersion at 1550 nm was D = -560 ps/nm.km, which is in direct correlation with already published results for similar fiber types [14]

For switching experiment a 1x2 switch testbed was employed (depicted in Fig. 8). Data payload and label were multiplexed (MUX) forming the data signal, which was afterwards propagated through a 50 km segment. Label was then separated and the routing signal was realized by an opto-electronic controller (OEC) with an embedded FPGA (field-programmable gateway array). Afterwards the buffered input data was multiplexed with the routing signal in an athermal arrayed-waveguide grating (AWG). The coupled routing signals and input data propagated through the nonlinear module and the switched data appeared at a new wavelength defined by the FWM process.

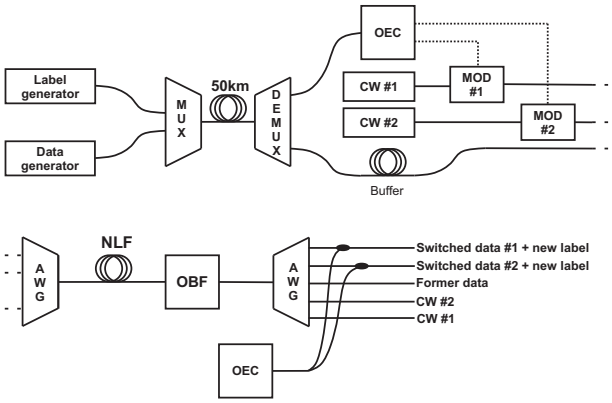

Fig. 8. Scheme of the proposed optical switch setup, MOD - Mach-Zehnder modulator, MUX/DEMUX - multi/demultiplexer, PRBS - pseudo-random bit sequence, OEC - opto-electronic controller, NLF - fiber with enhanced nonlinearity, AWG - arrayed-waveguide grating, OBF - optical bandpass filter.

Results from switching experiment with a 26 m long As_2Se_3 nolinear module are illustrated in Fig. 9. Conversion efficiencies were under -38 dB, where the major detrimental effect was implied by the component IL of 16.0 dB.

Further tests were carried out then on the 4.5 m As_2Se_3 long nonlinear module with IL of only 4.9 dB we observed conversion efficiency of almost -30 dB, with pump power up to 20 dBm, where we encountered the stimulated Brillouin scattaring limit at 18 dBm of CW power. We verified that reflections were suppressed by 30 dB with respect to input signal, thus they are not a source of limitation.

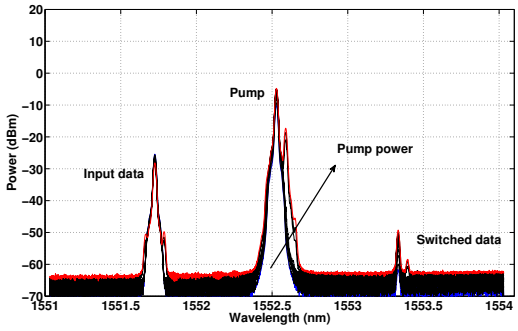

Fig. 9. Four-wave mixing in 26 m As_2Se_3 fiber, pump power from 6 dBm (blue) to 16 dBm (red).

VI. Conclusion

We have presented simulations, solid-joint technology development and experimental tests with soft-glass fibers for optical switching. The main aim was the development of nonlinear modules for efficient FWM based optical switching. Technology of solid-joint chalcogenide fiber was mastered with minimized ILs of the whole module.

An optical switching testbed was utilized for experimental tests. Results showed FWM efficiency of -30 dB for arsenic-selenide nonlinear modules, which was in contrast to simulation predictions. It is clear that though arsenic-selenide provides extreme nonlinearity, due to the dispersion value (-550

ps/nm.km) at 1550 nm conventional core/cladding structure is not suitable for FWM switching, therefore a chalcogenide MOF design will be pursued in our future work.

Lead-silicate MOFs are promising candidates, with tailored dispersion curves, thez are currently being tested and results will be presented at the conference. Technology of solid-joint connections for lead-silicate SC-MOF and HS-MOF are also currently being worked on.

In comparison to other switching techniques the discussed approach based on FWM offers the possibility of preserving not only amplitude but also phase information of the input signal, thus enabling switching of m-PSK and m-QAM signals. On the other hand compared to eg optical gating [4] precise wavelength allocation is required, so the channel efficiency is limited.

ACKNOWLEDGMENT

This work was supported by the TA CR grant TA04010220 and CTU grant SGS14/190/OHK3/3T/13.

Authors would like to thank ORC University of Southampton (especially Dr. Radan Slavik), Institute of Photonics and Electronics and SQS Fiber optics for close cooperation.

REFERENCES

[1] E. Tipsuwannakul, J. Li, M. Karlsson, and P. Andrekson, "Performance Comparisons of DP-16QAM and Duobinary-Shaped DP-QPSK for Optical Systems With 4.1 Bit/s/Hz Spectral Efficiency," *Lightwave Technology, Journal of*, vol. 30, no. 14, pp. 2307–2314, 2012.

[2] M. Nakazawa, S. Okamoto, T. Omiya, K. Kasai, and M. Yoshida, "256-QAM (64 Gb/s) Coherent Optical Transmission Over 160 km With an Optical Bandwidth of 5.4 GHz," *Photonics Technology Letters, IEEE*, vol. 22, no. 3, pp. 185–187, 2010.

[3] E. Pincemin, M. Song, J. Karaki, O. Zia-Chahabi, T. Guillossou, D. Grot, G. Thouenon, C. Betoule, R. Clavier, A. Poudoulec, M. V. der Keur, Y. Jaouen, R. L. Bidan, T. L. Gall, P. Gravey, M. Morvan, B. Dumas-Feris, M. L. Moulinard, and G. Froc, "Multi-band OFDM transmission at 100 Gbps with sub-band optical switching," *Journal of Lightwave Technology*, vol. 32, no. 12, pp. 2202–2219, June 2014.

[4] N. Calabretta, W. Wang, T. Ditewig, O. Raz, F. Agis, S. de Waardt, and H. Dorren, "Scalable Optical Packet Switches for Multiple Data Formats and Data Rates Packets," *Photonics Technology Letters, IEEE*, vol. 22, no. 7, pp. 483–485, 2010.

[5] K. Huybrechts, G. Morthier, and R. Baets, "Fast all-optical flip-flop based on a single distributed feedback laser diode," *Opt. Express*, vol. 16, no. 15, pp. 11 405–11 410, Jul 2008.

[6] H. Hu, H. Ji, M. Pu, M. Galili, K. Yvind, and L. K. Oxenlowe, "160-gb/s silicon all-optical packet switch for buffer-less optical burst switching," *Journal of Lightwave Technology*, vol. 33, no. 4, pp. 843–848, Feb 2015.

[7] T. Nakanishi, M. Hirano, T. Okuno, and M. Onishi, "Silica-Based Highly Nonlinear Fiber with γ =30/W/km and Its FWM-Based Conversion Efficiency," in *Optical Fiber Communication Conference and Exposition and The National Fiber Optic Engineers Conference*. Optical Society of America, 2006, p. OTuH7.

[8] J. S. Sanghera, L. B. Shaw, P. Pureza, V. Q. Nguyen, D. Gibson, L. Busse, I. D. Aggarwal, C. M. Florea, and F. H. Kung, "Nonlinear Properties of Chalcogenide Glass Fibers," *International Journal of Applied Glass Science*, vol. 1, no. 3, pp. 296–308, 2010.

[9] Y.-M. Chang, J. Lee, and J. H. Lee, "Bismuth Nonlinear Optical Fiber for Photonic Ultrawideband Radio-Signal Processing," *Selected Topics in Quantum Electronics, IEEE Journal of*, vol. 18, no. 2, pp. 891–898, 2012.

[10] X. Feng, F. Poletti, A. Camerlingo, F. Parmigiani, P. Petropoulos, P. Horak, G. M. Ponzo, M. Petrovich, J. Shi, W. H. Loh, and D. J. Richardson, "Dispersion controlled highly nonlinear fibers for all-optical processing at telecoms wavelengths," *Optical Fiber Technology*, vol. 16, no. 6, pp. 378 – 391, 2010.

[11] S. D. Le, D. M. Nguyen, M. Thual, L. Bramerie, M. C. e Silva, K. Lenglé, M. Gay, T. Chartier, L. Brilland, D. Méchin, P. Toupin, and J. Troles, "Efficient four-wave mixing in an ultra-highly nonlinear suspended-core chalcogenide As38Se62 fiber," *Opt. Express*, vol. 19, no. 26, pp. B653–B660, Dec 2011.

[12] J. Sanghera, L. B. Shaw, P. Pureza, V. Q. Nguyen, D. Gibson, I. D. Aggarwal, C. M. Florea, and F. Kung, "Progress of chalcogenide glass fibers," in *Optical Fiber Communication Conference and Exposition and The National Fiber Optic Engineers Conference*. Optical Society of America, 2007, p. OWA2.

[13] V. G. Ta'eed, L. Fu, M. Pelusi, M. Rochette, I. C. Littler, D. J. Moss, and B. J. Eggleton, "Error free all optical wavelength conversion in highly nonlinear as-se chalcogenide glass fiber," *Opt. Express*, vol. 14, no. 22, pp. 10 371–10 376, Oct 2006. [Online]. Available: http://www.opticsexpress.org/abstract.cfm?URI=oe-14-22-10371

[14] M. Lamont, L. B. Fu, M. Rochette, D. J. Moss, and B. J. Eggleton, "2r optical regenerator in as2se3 chalcogenide fiber characterized by frog analysis," in *2006 Conference on Lasers and Electro-Optics and 2006 Quantum Electronics and Laser Science Conference*, May 2006, pp. 1–2.

Development and characterization of highly-nonlinear multicomponent glass photonic crystal fibers for mid-infrared applications

Nemecek, Tomas, Komanec, Matej, Suslov, Dmytro, Peterka, Pavel, Pysz, Dariusz, et al.

Tomas Nemecek, Matej Komanec, Dmytro Suslov, Pavel Peterka, Dariusz Pysz, Ryszard Buczynski, Bryan Nelsen, Stanislav Zvanovec, "Development and characterization of highly-nonlinear multicomponent glass photonic crystal fibers for mid-infrared applications," Proc. SPIE 10232, Micro-structured and Specialty Optical Fibres V, 1023204 (16 May 2017); doi: 10.1117/12.2265722

SPIE.

Event: SPIE Optics + Optoelectronics, 2017, Prague, Czech Republic

Development and characterization of highly nonlinear multicomponent glass photonic crystal fibers for mid-infrared applications

Tomas Nemecek[a], Matej Komanec[a], Dmytro Suslov[a], Pavel Peterka[b], Dariusz Pysz[c], Ryszard Buczynski[d], Bryan Nelsen[e] and Stanislav Zvanovec[a]

[a]*Czech Technical University in Prague, Faculty of Electrical Engineering, Technicka 2, Prague, Czech Republic*

[b]*Institute of Photonics and Electronics, Czech Academy of Sciences, Chaberská 57, Prague, Czech Republic*
[c]*Institute of Electronic Materials Technology, Wolczynska Str 133, Warsaw, Poland*
[d]*University of Warsaw, Krakowskie Przedmieście 26/28, Warsaw, Poland*
[e]*Westsächsische Hochschule Zwickau, Dr.-Friedrichs-Ring 2a, Zwickau, Germany*

ABSTRACT

We present a detailed chromatic dispersion characterization of heavy-metal oxide (HMO) glass photonic crystal fibers (PCFs) suitable for mid-infrared applications. Based on previous work with hexagonal and suspended-core fibers the focus was placed on determination of the chromatic dispersion curve to reach precise correlation between simulation model and real fiber based on both a post-draw model correction and broadband chromatic dispersion measurement. The paper covers the fiber design, discusses fiber manufacturing, presents measurements of fiber chromatic dispersion, provides the simulation model correction and finally proposes further applications. Selected fiber designs from simulation model were fabricated by the stack-and-draw technique. The dispersion measurement setup was based on an unbalanced Mach-Zehnder interferometer. The influence of optical elements on the measurement results and broadband coupling is discussed. We have proved that the critical factor represents the accuracy of the refractive index equation of the HMO glass and real fiber structure. By improved technique we reached the zero-dispersion wavelength with a reasonable precision of less than 30 nm.

Keywords: Chromatic dispersion, Mach-Zehnder interferometer, Photonic crystal fibers, Suspended-core, Heavy-metal oxide glass, Nonlinearity

1. INTRODUCTION

Multicomponent and non-silica glasses have drawn attention for several decades due to their inherently high nonlinearity and transparency within the mid-infrared (MIR) region [1-3]. With the onset of photonic crystal fibers (PCFs), dispersion tailoring [3] and a further increase of fiber nonlinearity by core size reduction became viable [3]. Progress in drawing techniques has enabled fabrication of suspended-core microstructured optical fibers (SC-MOFs) of non-silica and multicomponent glass materials, thus opened new research and application possibilities [4-6]. SC-MOFs generally have three or six large cladding air-holes surrounding a small solid-core, which makes them suitable for nonlinear purposes since with the core size in the range of several micrometers the effective mode-field area is considerably reduced.

Heavy-metal oxide (HMO) SC-MOFs were presented in [1, 4], chalcogenide SC-MOFs were later discussed in [5, 6] and bismuth SC-MOFs were also evaluated in [7]. SC-MOFs can be further utilized for sensing purposes of gasses [8] and liquids [9] and other detection applications such as fluorescence [10].

Theoretical studies and numerical models form a basis for every fiber preparation, and examine a specific application far before a preform is manufactured. When it comes to supercontinuum generation (SCG), precise allocation of the zero-dispersion wavelength (ZDWL) is essential. It has been presented in numerous example cases that modelled dispersion curve, more specifically the position of ZDWL does not precisely match the real-drawn fiber parameters [11].

In this paper, we present at first the design of two SC-MOFs based on two heavy-metal oxide (HMO) glass compositions, having the main difference in SiO_2 content. The primary focus was to design SC-MOFs with ZDWL at distinct wavelengths to enable verification of the proposed simulation model and measurement technique covering the wavelength range from 900 to 2400 nm. The fibers are drawn according to the pre-calculated simulation model by the stack-and-draw technique. Afterward chromatic dispersion profiles of developed fibers are precisely characterized by a

Micro-structured and Specialty Optical Fibres V, edited by Kyriacos Kalli, Jiri Kanka, Alexis Mendez, Pavel Peterka, Proc. of SPIE Vol. 10232, 1023204 · © 2017 SPIE
CCC code: 0277-786X/17/$18 · doi: 10.1117/12.2265722

free-space optic (FSO) interferometric method. The basic configuration for such methods can be found in [12, 13], where in [12] a tunable filter or a monochromator in front of the Mach-Zehnder interferometer (MZI) was applied, whereas in [13] the tunable filter was located at the MZI output. However in our configuration, we tried to avoid the above-mentioned components and rather to exploit the spectral domain similar to our prior work with a fiber-based interferometer [14]. This principle eliminates filtering at the detector. Moreover, this method has the advantage of being able to measure very short pieces of fiber samples (approx. several centimeters long) while maintaining very high measurement accuracy. Given the measured chromatic dispersion profile results, scanning-electron microscope (SEM) photographs of developed HMO SC-MOFs were acquired and the simulation model was corrected, which provided a significant increase in measurement/simulation matching, especially regarding the ZDWL location.

2. FIBER DESIGN AND FABRICATION PROCESS

We have designed a high-content silica HMO SC-MOF, which was accompanied by an already presented HMO SC-MOF design [4] and a HMO hexagonal structure PCF [15], both serving as reference fibers to provide a step-wise process of precise measurement verification. Such newly designed fiber (PBG-01) is therefore with an unknown transparency, unknown chromatic dispersion profile and nonlinear refractive index. Reference HMO fibers have been already studied (either theoretically, experimentally or using both approached) and were typically made of PBG-08 glass, which is composed of PbO 39.17 %, Bi_2O_3 27.26 %, Ga_2O_3 14.26 %, SiO_2 14.06 % and CdO 5.26 %. PBG-08 glass provides transparency up to 4500 nm and nonlinear refractive index $n_2 = 4.3 \times 10^{-19}$ m^2/W [4] at 1240 nm. The newly designed glass composition (PBG-01) contains significantly higher amount of SiO_2 of over 60 %, the composition is SiO_2 60.7 %, PbO 28.0 %, K_2O 4.0 %, Na_2O 4.0 %, Al_2O_3 3.0 % and As_2O_3 0.3 %.

Prior to the fiber structure design/draw, bulk glass samples were analyzed at five wavelengths in the range from 400 nm to 1600 nm and subsequently fitted by the Sellmeier equation. Refractive index dependence on wavelength is plotted in Fig. 1 altogether with the Sellmeier equations of each glass.

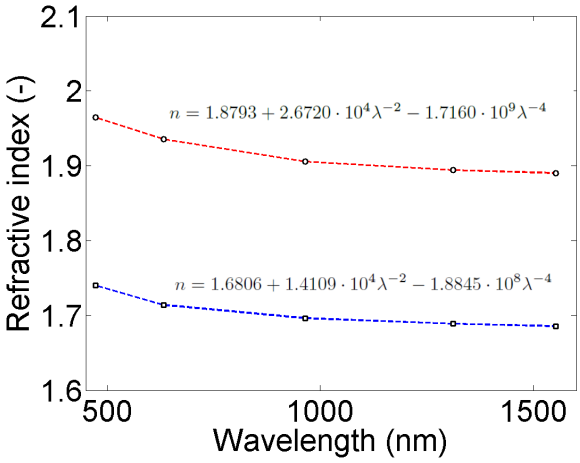

Figure 1. Refractive index profile of HMO glasses with Sellmeier equations, PBG-08 (red), PBG-01 (blue).

Based on the bulk glass refractive index profiles, SC-MOF model was prepared. We have utilized COMSOL Multiphysics 5.0 software featuring the full vector finite element method (FEM) with circularly perfectly matched layer (PML) to investigate the optical properties of the proposed SC-MOFs. For precise simulations of analyzed SC-MOFs, we have modelled the SC-MOF in an ideal case, where all three cladding air-holes are exactly similar, and there is no inhomogeneity in the SC-MOF structure. The pre-draw simulation model structure is depicted in Fig. 2.

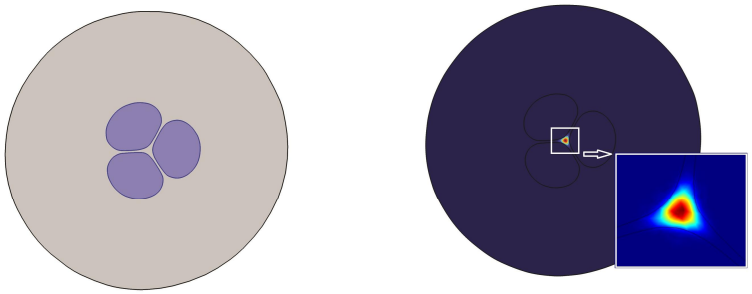

a) b)

Figure 2. Pre-draw simulation model of HMO SC-MOF with 1 μm core diameter a) structure of the fiber, b) mode distribution

The designed SC-MOF has been fabricated using the conventional stack and draw technique. The structure of fiber is shown in Fig. 3a). Core diameter is approximately 1.22 μm, while the supporting struts are 290 nm thin. Obtained thin and relatively long supporting struts ensure a high degree of isolation of the core area, which results in a negligible modal confinement loss for the fundamental mode. Nevertheless, the core diameter slightly differs from the designed 1 μm core diameter, which could cause a shift in the ZDWL value.

3. MEASUREMENT SETUP FOR FIBER CHARACTERIZATION

For the purpose of chromatic dispersion analysis an unbalanced Mach-Zehnder interferometer was employed. The unbalanced MZI provides several advantages in comparison to other setups for chromatic dispersion measurement; one can measure the relative value of the group refractive index N instead of an absolute value. To measure in relative values is enabled by the post-processing calculation where the derivation eliminates the influence of all constants such as precise lengths and all elements out of the MZI. Another advantage is that only a short fiber piece of several centimeters can be tested. Last but not least broadband dispersion profile is obtained.

The measurement setup is depicted in Fig. 3. A supercontinuum source (NKT, SuperK Extreme EXR-15) was used as a light source with a wide and relatively flat spectrum. The supercontinuum source was followed by a lens, collimating source light in the axis of MZI. In one of the MZI arms, the studied FUT is placed, while the second arm contains a pair of mirrors with the possibility of varying the arm-length, thus influencing the delay of light propagation. To couple signal efficiently into the PCFs (i.e. with insertion loss (IL) < 4.0 dB), it can be used a Nikon objective with 40x magnification or alternatively molded aspheric lenses with effective focal length 4.5mm with thickness 2 mm, and RI around 1.776 with respect to wavelength. These lenses and filters however cause dispersion shift in the FUT arm of MZI resulting, in some cases, in a significant ZDWL error. To achieve optical power balance in both MZI arms, absorptive neutral density filters with thickness 0.6 mm from doped glass material based on N-BK7 substrate, i.e. having a refractive index (RI) 1.50 at 1550 nm, were used. The combined signal from both arms is via a focal lens collimated into the optical spectrum analyzer (OSA, Yokogawa 600-1700 nm). At the OSA detector, an interference pattern from the MZI creates a beat signal at certain wavelengths.

Relative group refractive index N is then calculated using:

$$N_{FUT}^{relative} = \frac{2\Delta l - OPD_{lens1} - OPD_{lens2}}{l_{FUT}} + 1 \quad , \tag{1}$$

Where Δl is the optical path difference, OPD_{lens1} and OPD_{lens2} are optical signal time delays introduced by included lenses, objective or filters, l_{FUT} is the FUT length. Equation (1) is commonly approximated by the Sellmeier equation and further derived, which gives the chromatic dispersion as:

$$D = \frac{1}{c}\frac{dN_{FUT}^{relative}}{d}, \tag{2}$$

Where c is the speed of light and λ stands for the wavelength.

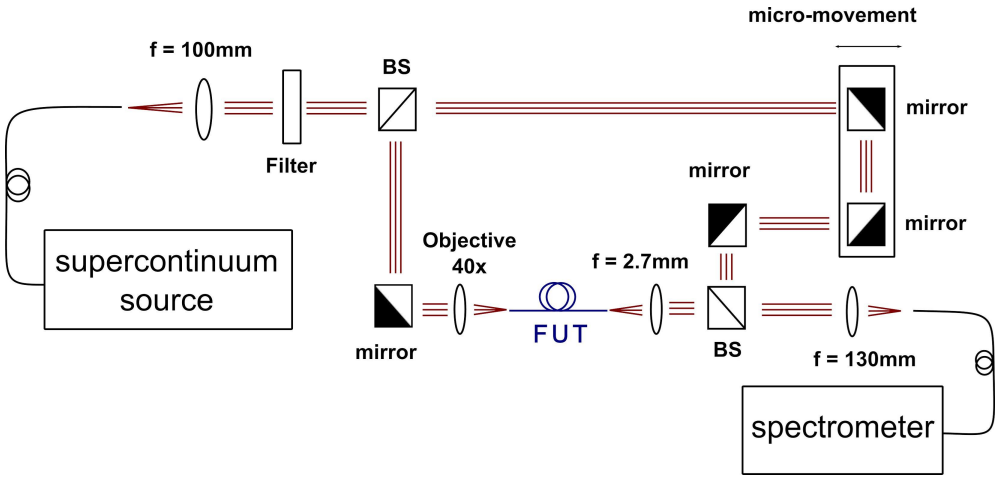

Figure 3. Chromatic dispersion measurement configuration based on an unbalanced Mach-Zehnder interferometer; BS – beam splitter, FUT – fiber under test

4. CALIBRATION PROCEDURES

Our setup was calibrated using a hexagonal PCF with a known ZDWL at 1060 nm, where we obtained a perfect match (Δn < 5 nm). Following a broadband spectral calibration, we evaluated a commercial endlessly single-mode PCF (Thorlabs, ESM-12B). Our goal was to analyze on this particular fiber the effect of additional optical elements, FUT length (with regard to inaccurate length FUT measurement) and correlation of measurement and simulation model. The advantage of calibrating with ESM-12B is that the fiber is made of pure silica material where the Sellmeier coefficients are extremely precisely determined (down to 5th decimal).

We have tested a 28cm-long ESM fiber. The accuracy of FUT length measurement is approximately ± 1 mm. Thickness of lenses and filters was taken from datasheets (providing accuracy better than 0.2 mm) to mathematically suppress their dispersion influence on the measurement. In Fig. 4, a comparison of measurement and simulation outputs is depicted. After mathematical suppression of the influence of lenses and filters the accuracy of measured ZDWL increased from 15 nm to 5 nm. This measurement and simulation results are also matching datasheet dispersion curves (depicted in the Fig. 4 inset). Further we were investigated the effect of parameter uncertainties on the ZDWL position. The FUT length measurement accuracy influence on the dispersion curve is shown in Fig. 5, where we observe no effect on the ZDWL position, only the dispersion slope varies. The effect of additional optical elements such as lenses or filters exhibits in a several nanometer influence on the ZDWL position, whereas the dispersion slope is unaffected. Thus FUT length determination is not crucial for ZDWL measurements, on the other hand, all optical elements must be well described to allow the possibility of mathematical suppression of their influence on the final result.

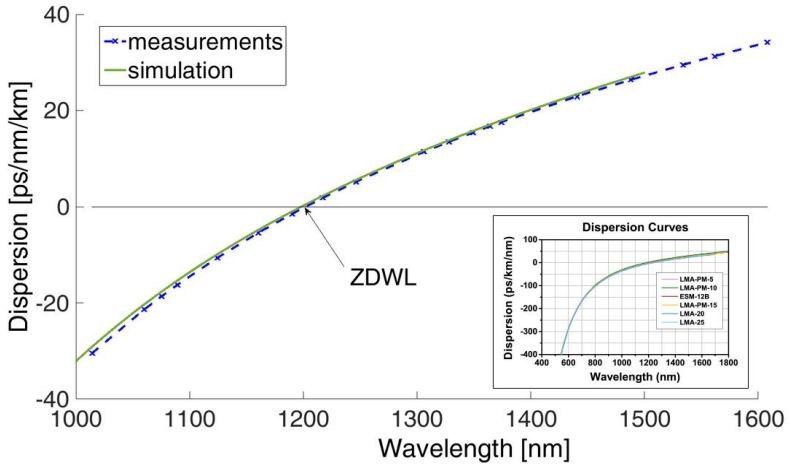

Figure 4. Comparison of measurement and simulation outputs for ESM-12B fiber by Thorlabs; inset shows the curve from manufacturer´s datasheet.

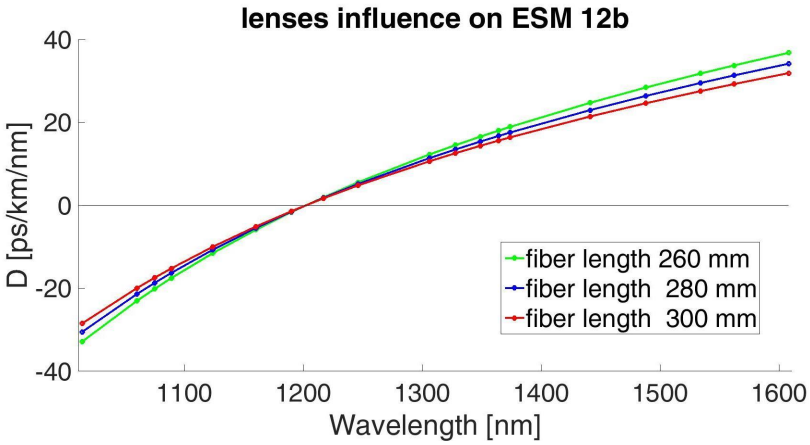

Figure 5. Influence on the ESM-12B dispersion curve profile depending on FUT length (inaccurate length estimation).

5. RESULTS

First tests were performed on a previously studied HMO PCF [15, 16], where the simulation model varied more than 50 nm regarding the ZDWL location from the measurement result. This PCF has a hexagonal symmetric structure with a 3 µm core diameter and is made of PBG-08 glass. We have verified previous measurement results in our configuration by obtaining the ZDWL at 1412 nm, which is in perfect coherence (1409 nm in [16]). Contrary to previous work [15] we have not compared the measurement result to the pre-draw model, but utilized a real fiber model, based on a SEM photograph of the fiber cleave. By employing this technique, ZDWL of 1443 nm was calculated, providing only a 31 nm mismatch from the measured data. This outcome underlines the fact, that ideal fiber design is strongly affected during fiber drawing, which may not be obvious from the fiber cleave (SEM photograph) but has significant impact on the ZDWL location. Comparison of dispersion profile of measured and calculated based on real fiber is presented in Fig. 6.

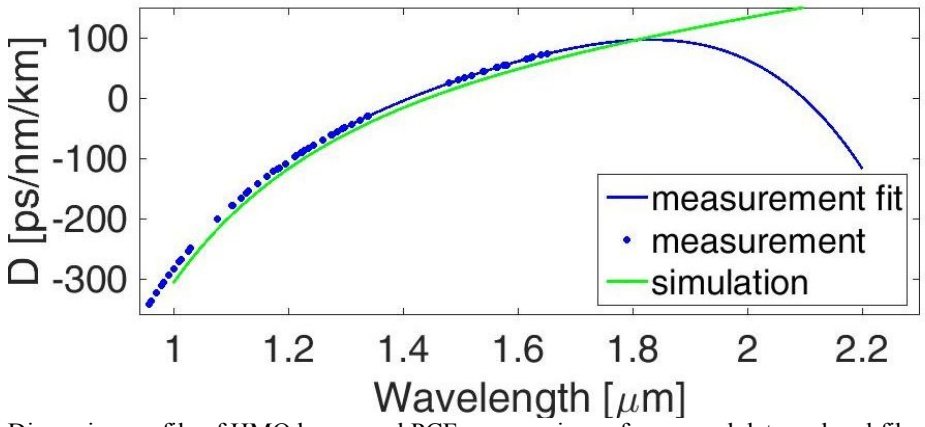

Figure 6. Dispersion profile of HMO hexagonal PCF - comparison of measured data and real fiber simulation.

To move towards 1 µm core diameters, we have chosen a silica SC-MOF with 4µm core diameter. We again used a SEM image of manufactured fiber to estimate the real fiber design dimensions for simulation purposes. This prevented any potentially large discrepancies in measured and simulated ZDWL and dispersion curve. We have proved a perfect measurement to simulation match, thanks to the precise equation for the refractive index of silica. Broad-band coupling is extremely challenging for SC-MOFs and to equalize optical power in both MZI arms, attenuators had to be added. One attenuator (filter NENIR30, Thorlabs) caused a ZWDL shift of 30 nm, two of them caused a total shift of 60 nm. This shift was compensated as depicted in Fig. 7.

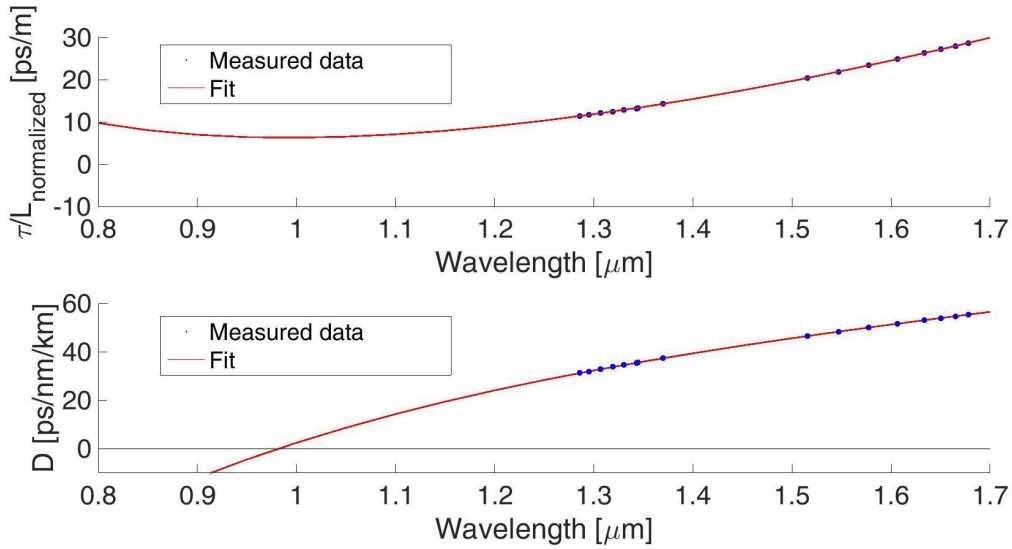

Figure 7. Results of dispersion measurement of SC-PCF with 4um core with ZDWL at 965 nm after correction of the filter shift, measured group delay (up) and calculated chromatic dispersion (down).

For HMO SC-MOF we have performed simulations of real fiber structure. Results are depicted in Fig. 8, where both the previously studied (PBG-08 glass) and the newly proposed PBG-01 glass SC-MOFs are depicted. We observed a significant difference in the ZDWLs of both HMO SC-MOFs.

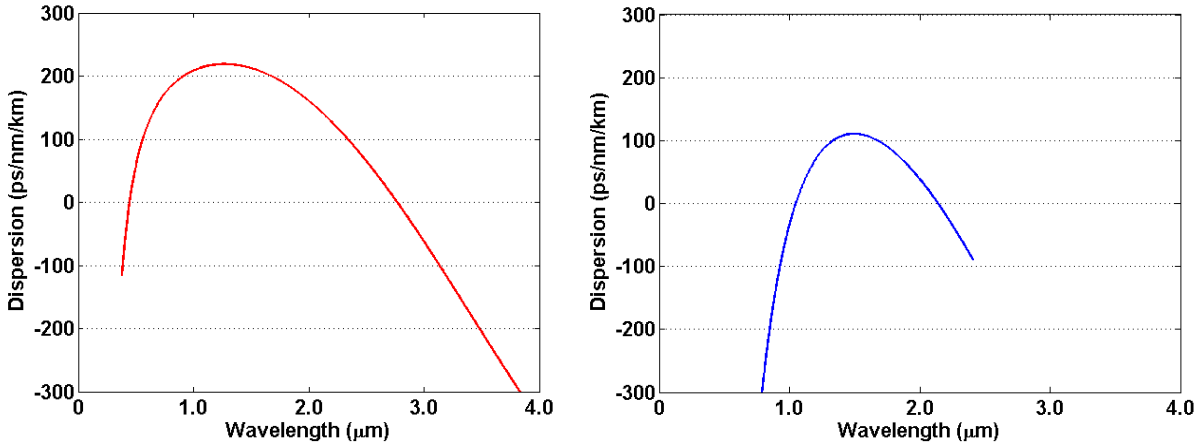

Figure 8. Real-fiber simulations for HMO SC-MOFs, PBG-08 (left), PBG-01 (right).

6. CONCLUSION

We have presented a detailed characterization of photonic crystal fibers from the point of chromatic dispersion, which is essential mainly for nonlinear applications such as supercontinuum generation. We have considered multicomponent glass fibers, based on lead-silicates, where two glass compositions were evaluated. Hexagonal-structured and suspended-core fiber designs were studied and fiber chromatic dispersion was analyzed in simulation environment and by experimental verification.

The chromatic dispersion measurement was based on the Mach-Zehnder interferometer, where we focused on precise ZWDL estimation. Our measurement configuration was calibrated on several fibers with well-known dispersion and of silica material, which has a very precisely defined refractive index, thus simulation models can be extremely accurate. We have found a perfect match in our calibration measurements and calculated dispersion profiles. Optical elements and FUT length effects were studied and compensated if necessary. Achieved resolution of ZDWL was up to 10 nm. Mathematical compensation of known optical elements further increased measurement accuracy from 15 nm to 5 nm.

For HMO fibers we have verified our MZI-based method on an already studied HMO hexagonal PCF, where we demonstrated further increase in ZDWL precision in a corrected model simulation. The measurement result was matching the previously obtained value by our colleagues. Based on the corrected model, we can be very confident considering the refractive index equation for the PBG-08 glass. Thus when utilizing an SEM captured SC-MOF profile and the PBG-08 refractive index equation we obtained the dispersion curve of our designed PBG-08 SC-MOF. For PBG-01 SC-MOF the refractive index equation is not verified yet, so we expect bigger simulation/measurement difference. Nevertheless PBG-01 SC-MOF already shows very promising locations of both 1st and 2nd ZDWL.

Our corrected simulation model can serve for improved design of SC-MOFs with a better ZDWL matching between calculated and real fiber. Furthermore once the simulation model corresponds to real situation, generated supercontinuum can be predicted with higher accuracy. Both designed and drawn SC-MOFs may be well applied for supercontinuum generation, where PBG-08 SC-MOF provides a significantly higher nonlinearity and PBG-01 SC-MOF on the other hand is expected to have ZDWL in the vicinity of 1060 nm and 2100 nm. The limiting factor for PBG-01 supercontinuum will be the material transparency, which needs to be characterized.

ACKNOWLEDGMENTS

This joint work This work has been supported by the European Commission through the COST Action MP1401 “Advanced fibre laser and coherent source as tools for society, manufacturing and lifescience”, by the Ministry of Education, Youth and Sports of the Czech Republic, grant COST LD15803 and CTU project SGS14/190/OHK3/3T/13.

REFERENCES

[1] Feng, X., *et al*., "Dispersion controlled highly nonlinear fibers for all-optical processing at telecoms wavelengths," Optical Fiber Technology 16(6), 378-391 (2010). Special Fiber Structures and their Applications.
[2] T. Hasegawa, *et al*., "High nonlinearity bismuth fibers and their applications," 2006 Optical Fiber Communication Conference and the National Fiber Optic Engineers Conference, Anaheim, CA, 2006, pp. 3
[3] M. D. Pelusi et al., "Applications of Highly-Nonlinear Chalcogenide Glass Devices Tailored for High-Speed All-Optical Signal Processing," in IEEE Journal of Selected Topics in Quantum Electronics, vol. 14, no. 3, pp. 529-539 (2008)
[4] M. Klimczak, *et al.,* “Mid-infrared supercontinuum generation in soft-glass suspended core photonic crystal fiber,” Opt Quant Electron 46: 563 (2014)
[5] Renversez, G., *et al.*., “Nonlinear effects above 2 um in chalcogenide suspended core microstructured optical fibers: Modeling and experiments," in Photonics Conference (PHO), 2011 IEEE, 61-62 (2011)
[6] Troles, J., *et al*., “Chalcogenide suspended-core fibers: Manufacturing and non-linear properties at 1.55 um," in [Transparent Optical Networks (ICTON), 2011 13th International Conference, 1-4 (2011)
[7] Ryasnyanskiy, A., *et al*., “Nonlinear frequency conversion in bismuth-doped tellurite suspended core fiber," Optics Communications 284(1617), 3977-3979 (2011)
[8] O. Frazao, *et al*., “Suspended-core fibers for sensing applications," Photonic Sensors 2(1617), 118-126 (2012)
[9] T. Nemecek, *et al*., “Suspended-core microstructured fiber for refractometric detection of liquids," Appl. Opt. 54, 8899-8903 (2015)
[10] S. C. Warren-Smith, *et al.*, "Exposed-core microstructured optical fibers for real-time fluorescence sensing," Opt. Express 17, 18533-18542 (2009)
[11] A. Hartung, *et al.*, "Pulse-preserving broadband visible supercontinuum generation in all-normal dispersion tapered suspended-core optical fibers," Opt. Express 19, 12275-12283 (2011)
[12] M. J. Saunders and W. B. Gardner, “Precision interferometric measurement of dispersion in short single-mode fibers,“ in Tech Dig. NBS Symp. on Opt. Fib. Meas. (Boulder, CO), pp. 123126, (1984)
[13] H. T. Shang, “Chromatic dispersion measurement by white-light interferometry on metrelength single-mode optical fibers,“ Electron. Lett., Vol. 17, pp. 603605 (1981)
[14] P. Peterka, *et al*., "Measurement of chromatic dispersion of microstructure optical fibers using interferometric method", Optica Applicata, vol. 38, no. 2, pp. 295-303 (2008).
[15] R. Buczynski, *et al.,* “Two Octaves Supercontinuum Generation in Lead-Bismuth Glass Based Photonic Crystal Fiber,“ Materials 7(6), 4658-4668, (2014)
[16] G. Stepniewski, *et al.*, "Temperature sensitivity of chromatic dispersion in nonlinear silica and heavy metal oxide glass photonic crystal fibers," Opt. Mater. Express 6, 2689-2703 (2016)

Long-term stability of hollow core to standard optical fiber interconnection

Dousek, Daniel, Komanec, Matěj, Zhong, Ailing, Suslov, Dmytro, Zvánovec, Stanislav, et al.

Daniel Dousek, Matěj Komanec, Ailing Zhong, Dmytro Suslov, Stanislav Zvánovec, Petr Veselý, Yong Chen, Thomas D. Bradley, Eric R. Numkam Fokoua, Francesco Poletti, David J. Richardson, Radan Slavík, "Long-term stability of hollow core to standard optical fiber interconnection," Proc. SPIE 11773, Micro-structured and Specialty Optical Fibres VII, 117731B (18 April 2021); doi: 10.1117/12.2592377

SPIE.

Event: SPIE Optics + Optoelectronics, 2021, Online Only

Long-term stability of hollow core to standard optical fiber interconnection

Daniel Dousek[a], Matěj Komanec[a], Ailing Zhong[a], Dmytro Suslov[a], Stanislav Zvánovec[a], Petr Veselý[b], Yong Chen[c], Thomas D. Bradley[c], Eric R. Numkam Fokoua[c], Francesco Poletti[c], David J. Richardson[c], and Radan Slavík[c]

[a]Department of Electromagnetic Field, Czech Technical University in Prague, Technická 1902/2, 166 27 Prague 6, Czech Republic
[b]Department of Electrotechnology, Czech Technical University in Prague, Technická 1902/2, 166 27 Prague 6, Czech Republic
[c]Optoelectronics Research Centre, University of Southampton, Southampton, SO17 1BJ, UK

ABSTRACT

In this paper, we present results of long-term stability tests of a low-loss (<0.55 dB) hollow core fiber (HCF) to standard optical fiber interconnection prepared by modified gluing-based fiber-array technology. We measured insertion loss of three interconnected HCF samples over a period of 100 days at room temperature, observing a variation in insertion loss of less than 0.02 dB. Subsequently, we placed the HCF samples in a climatic chamber and heated to +85°C in four cycles. Maximum insertion loss variation of 0.10 dB was observed for HCF samples with angled 8° interconnections and only 0.02 dB for a HCF sample with a flat interconnection.

Keywords: Hollow core fiber, Long-term stability, Heating cycles, Coupling loss, Interconnection

1. INTRODUCTION

Hollow-core fibers (HCFs) are an advanced type of optical fibers where light is guided and confined in a low index air/vacuum core surrounded by a microstructured cladding. HCFs provide low nonlinearity,[1] low latency,[2] and allow for mid-infrared propagation.[3] HCFs are also predicted to achieve lower attenuation than that of standard single-mode fibers (SSMFs) in the very near future. The latest achievement boasts HCF attenuation as low as 0.28 dB/km[4] for a nested antiresonant nodeless fiber (NANF) at 1550 nm as compared to the state-of-the art attenuation of 0.14 dB/km for SSMF.[5] Note, for wavelengths below 800 nm HCFs are already matching the attenuation of standard optical fibers.[6]

For effective and widespread inclusion of HCFs into SSMF-based systems we need to have a reliable and permanent interconnection. The key parameters of such interconnection are insertion loss (IL), return loss (RL) and ideally strictly fundamental mode excitation, i.e. low higher-order mode (HOM) cross-coupling. Achieving good values across these parameters simultaneously has proven to be challenging due to the 4% Fresnel back-reflection at the silica-air interface and, the mode-field shape and size mismatch between SSMF and HCF.

Recently, we presented a HCF-SSMF interconnection technique that is based on a standard fiber array technology.[7] The main advantage of this technology is that the interconnection is glued, which unlike popular fusion splicing, does not require any heating to high temperatures. This in turn allows for an optical coating such as anti-reflective (AR) coating to be applied at the HCF-SSMF boundary. AR coatings reduce the relatively high (4 %) back-reflection at the air-glass interface to negligible values, which also means lower insertion (transmission) loss at the interface by 0.16 dB. Fiber array technology is proven to be long-term resilient and to withstand -40 to +85°C thermal changes required in, e.g., telecommunication application. Adapting this technique for HCFs however, requires careful dosing of the glue, since the glue must not seep into the air-hole structure, but at the same time has to provide hermetic seal around the central hole to avoid insertion loss degradation over time.[8]

Further author information:
Daniel Dousek: E-mail: dousedan@fel.cvut.cz

Micro-structured and Specialty Optical Fibres VII, edited by Kyriacos Kalli, Alexis Mendez, Pavel Peterka,
Proc. of SPIE Vol. 11773, 117731B · © 2021 SPIE · CCC code: 0277-786X/21/$21 · doi: 10.1117/12.2592377

To fully assess the long-term and temperature stability of our HCF-SSMF interconnection, we prepared three HCF-SSMF interconnected samples (two with an angled 8° interconnection and one with a flat interconnection) and observed them under room temperature for over a 100-day period and then in a climatic chamber with temperature ranging from +20 to +85°C. These HCF samples were based on a 19-cell photonic-bandgap fiber (PBGF).[9] In this paper we show results of aforementioned tests and how they affected the HCF samples.

2. SAMPLE PREPARATION AND MEASUREMENT CONFIGURATION

First, we spliced SSMF to a graded-index multimode (GRIN) fiber to match the PBGF mode field diameter[9] and glued it into the first fiber array, forming a mode-field adapter (MFA). We then polished the fiber array to a specific length of the GRIN fiber, to provide best matching to the mode-field diameter (MFD) of particular PBGF. The MFD of our 19-cell PBGF was measured to be 20.1 µm at 1550 nm. We have selected a commercially available GRIN fiber - OM1, where OM1-based MFA provides MFD of 19.1μm at the 1/4 pitch length (260 µm). To reduce unwanted back-reflections we deposited a simple two-layer AR coating on polished MFAs, thus reducing RL below -30 dB in the 1550 nm band. The AR coating has the added benefit of reducing IL of the interconnection, as the Fresnel loss is mitigated (lowering the transmission loss by 0.16 dB).

Subsequently, we pre-polished the second fiber array with an empty fiber slot. This is because the PBGF cannot be polished without damaging the air-hole microstructure or getting the debris inside it. We then cleaved the PBGF, inserted it into the fiber array, and aligned its end-face with the fiber array end-face, and glued them together at the back side of the fiber array. We paid particular attention to avoid any glue seeping into the PBGF microstructure.

Finally, we aligned both SSMF and PBGF fiber arrays using 5D micromovement stages (3D stage Thorlabs NanoMax with APY002 pitch and yaw extension platform). After alignment (minimizing the transmission IL), we glued them together to form the permanent interconnection (See Fig. 1). This method has been described in detail in our previous paper.[7] Besides transmitted optical power, we simultaneously observed also the transmission spectrum, which enables monitoring of HOM excitation.[10,11] To avoid glue getting in between the PBGF and MFA fiber arrays, delicate application of limited amount of the glue was necessary, followed by its quick curing. This gluing process is carried out for only one side of the PBGF, with the other end always re-aligned before each measurement. Although it would be more practical to glue both ends and monitor the transmitted power, such measurement would involve two interconnections. Our approach ensures properties of a single interconnection point are studied, removing any ambiguity.

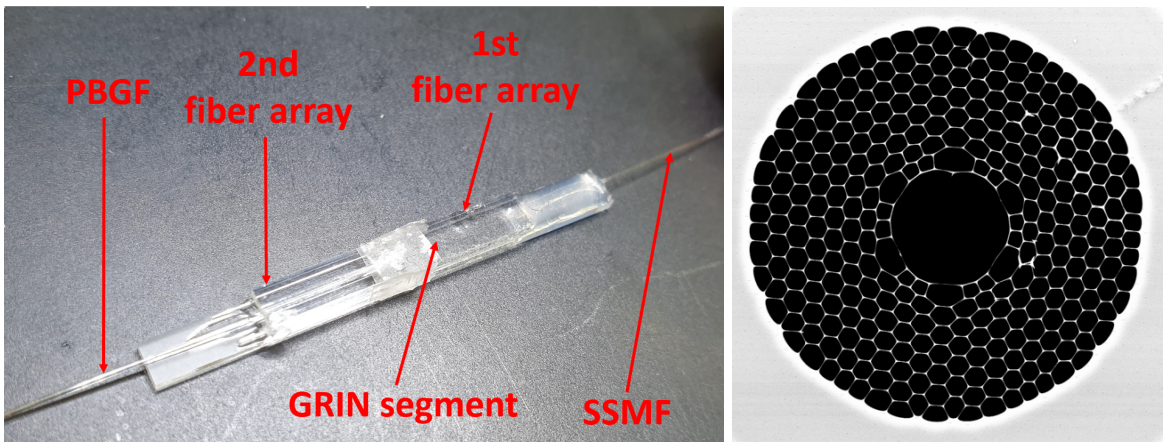

Figure 1. Finalized interconnection, a) Glued interconnection photograph, b) PBGF microstructure SEM image.

Two of our samples were based on an angled interconnection (RL below -50 dB) and one on a flat interconnection (RL below -30 dB). All samples had a simple two-layer AR coating with minimum reflection at 1550 nm. The prepared samples are listed in Table 1.

Sample	PBGF length (m)	MFA type	IL (dB)	RL (dB)
1	18	Flat	0.37	≤-30 dB
2	13	8°	0.50	≤-50 dB
3	13	8°	0.53	≤-50 dB

Table 1. List of prepared PBGF interconnected samples.

As we can see, the angled interconnections offer slightly higher IL but provide better RL. We expected the angled interconnections to have lower resilience to heat exposure, as they require larger amount of glue due to the large gap required to interconnect flat fibre array with HCF to the angled fibre array with MFA.

We have measured all samples at once during the heat cycling, ensuring all samples experience the same environmental changes. We used an Erbium-doped fiber amplifier (EDFA) as a broadband light source, which was subsequently filtered by a 1545-1555 nm optical band-pass filter (OBF). The filtered signal was then divided using a 1x3 power splitter with its outputs connected to the inputs of our samples (input SSMF). The outputs of all samples (cleaved PBGF ends) were then coupled back into SSMF using identical MFAs using 5D stages which were placed outside of the thermal chamber. This precise alignment was necessary to ensure we do not introduce any error in the measured signal apart from the heating effects on the interconnections located in the thermal chamber. The signal was finally analyzed using a power meter (PM, Thorlabs S154C) with an optical spectrum analyzer (OSA, Yokogawa AQ6035B) to verify HOM cross-coupling.

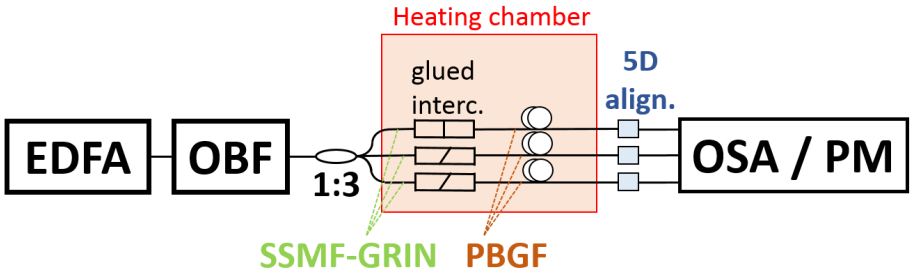

Figure 2. Measurement setup, EDFA - Erbium-doped fiber amplifier, OBF - optical bandpass filter, SSMF - standard single-mode fiber, GRIN - graded-index multimode fiber, PBGF - photonic-bandgap fiber, OSA - optical spectrum analyzer, PM - power meter.

3. LONG-TERM AND TEMPERATURE CYCLING RESULTS

To analyze long-term stability we first kept all 3 samples at room conditions, with temperature of 24°C and stable relative humidity below 40% for 100 days. During this time we repeatedly measured the IL, always by freshly cleaving the free end of PBGF and aligning it for minimum IL and sealing it after measurement to prevent water absorption. We observed maximum IL variation of 0.02 dB. The majority of these fluctuations occurred in the first week of measurements, which is likely due to some relaxation/post-cure processes within the glue. We concluded that all our interconnections are long-term stable at room conditions.

The results of subsequent heat cycling are presented in Figures 3-5 for each sample. We have carried out 4 heat cycles consisting of temperature increase in 5°C steps and a dwell time of approximately 10 minutes at each temperature step. A day long relaxing period at room temperature was between subsequent heating cycles.

Sample 1 (flat MFA interconnection) shows very distinctive properties of the first cycle. We assume that this is related to the final relaxation of the glued interconnection, as following three cycles can be considered consistent. IL fluctuation is below 0.02 dB which is close to our measurement accuracy of 0.01 dB and we thus consider Sample 1 to be temperature stable.

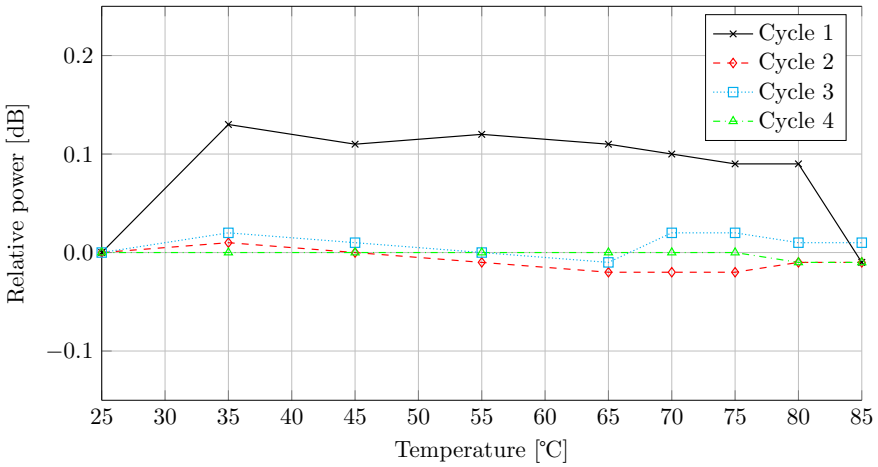

Figure 3. Relative power dependence on temperature of Sample 1 (18 m PBGF) - with flat mode-field adapters, positive values represent IL improvement (gain).

Sample 2 does not show the distinctive first cycle as does Sample 1, so the glue was cured sufficiently during the interconnection preparation. However, we observed significant IL variations over increasing temperature of up to 0.1 dB. We attribute this behavior to the angled MFA, where the interconnection includes on one side a bigger gap (between the distant side of the angled fiber array and the flat fiber array including PBGF). Furthermore, for Sample 2 the angled MFA based interconnection was developed as a proof of concept, thus the interconnection technology was not as proven as for the flat interconnections.

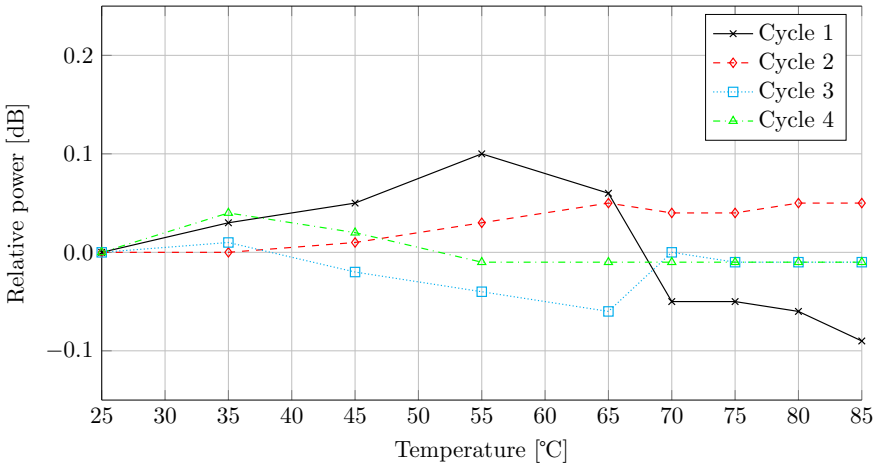

Figure 4. Relative power dependence on temperature of Sample 2 (13 m PBGF)- with angled mode-field adapters, positive values represent IL improvement (gain).

Sample 3 was glued after gaining experience with first angled MFA-based interconnection (Sample 2), where results are presented in Figure 4 with only IL improvement over the whole temperature range. The IL variations have a monotone trend across all four cycles. We expect that this insertion loss improvement with increasing temperature is caused by slight misalignment caused during the gluing process which is then corrected by heating the sample and by strain release on the PBGF which is fixed in the fiber array.

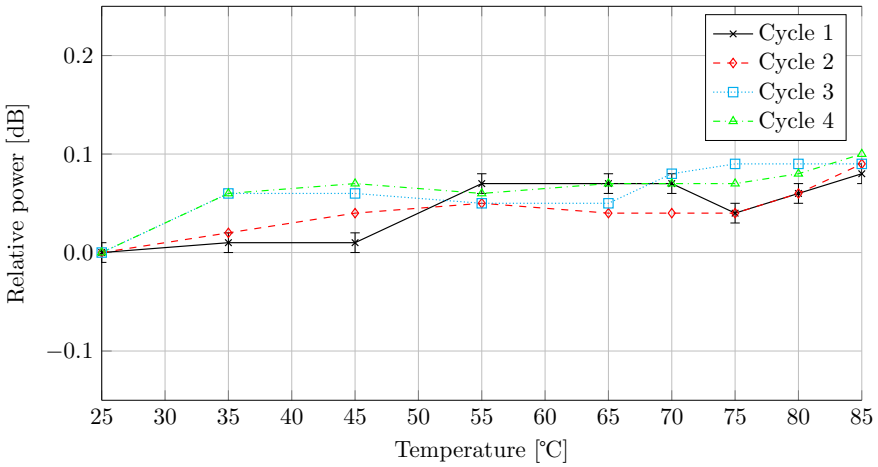

Figure 5. Relative power dependence on temperature of Sample 3 (13 m PBGF)- with angled mode-field adapters, positive values represent IL improvement (gain).

4. CONCLUSION

We showed long-term performance evaluation of our HCF interconnection technology on 3 samples based on a 19-cell PBGF, one with flat and two with angled interconnections. At room conditions, all interconnections have been stable over 100 days period (IL fluctuation below 0.02 dB). Once heated to +85°C, the flat MFA based interconnection proved stable with IL fluctuation identical to room conditions. For angled MFA based interconnections, our first developed sample (Sample 2) showed larger IL fluctuations (below 0.1 dB) with rising temperatures. Our second developed angled MFA interconnection (Sample 3) was then more consistent, showing only IL improvement once heated. This improvement can be explained by strain release in the glued interconnection as it is heated, compensating a slight angle misalignment produced during gluing of the interconnection. The angled MFA based interconnections are in our view worth of additional exploration. It is important to note that each sample returned to the initial measured IL after each heating cycle.

Our fiber-array based gluing interconnection approach is easily transferable to any HCF design, any wavelength desired and thanks to optical coating deposition, may be used in applications where low-level of back-reflection is required, e.g., gas cells, gas lasers, interferometry, and communications.

ACKNOWLEDGMENTS

This work was supported by the Department of Electromagnetic Field, Faculty of Electrical Engineering, CTU in Prague, by CTU project SGS17/182/OHK3/3T/13 and by EPSRC project “Airguide Photonics”, under grant EP/P030181/1

REFERENCES

[1] Liu, Z., Karanov, B., Galdino, L., Hayes, J. R., Lavery, D., Clark, K., Shi, K., Elson, D. J., Thomsen, B. C., Petrovich, M. N., Richardson, D. J., Poletti, F., Slavík, R., and Bayvel, P., “Nonlinearity-free coherent transmission in hollow-core antiresonant fiber,” *Journal of Lightwave Technology* **37**, 909–916 (Feb 2019).

[2] Kuschnerov, M., Mangan, B. J., Gong, K., Sleiffer, V. A. J. M., Herrmann, M., Nicholson, J. W., Fini, J. M., Meng, L., Windeler, R. S., Monberg, E. M., DeSantolo, A., Mukasa, K., Mikhailov, V., Feiste, U., Zhang, W., and Yu, R., “Transmission of commercial low latency interfaces over hollow-core fiber,” *Journal of Lightwave Technology* **34**, 314–320 (Jan 2016).

[3] Klimczak, M., Dobrakowski, D., Ghosh, A. N., Stępniewski, G., Pysz, D., Huss, G., Sylvestre, T., and Buczyński, R., “Nested capillary anti-resonant silica fiber with mid-infrared transmission and low bending sensitivity at 4000 nm,” *Opt. Lett.* **44**, 4395–4398 (Sep 2019).

[4] Jasion, G. T., Bradley, T. D., Harrington, K., Sakr, H., Chen, Y., Fokoua, E. N., Davidson, I. A., Taranta, A., Hayes, J. R., Richardson, D. J., and Poletti, F., "Hollow Core NANF with 0.28 dB/km Attenuation in the C and L Bands," *Optical Fiber Communication Conference Postdeadline Papers 2020*, Th4B.4, Optical Society of America (2020).

[5] Tamura, Y., Sakuma, H., Morita, K., Suzuki, M., Yamamoto, Y., Shimada, K., Honma, Y., Sohma, K., Fujii, T., and Hasegawa, T., "The First 0.14-dB/km Loss Optical Fiber and its Impact on Submarine Transmission," *J. Lightwave Technol.* **36**, 44–49 (Jan 2018).

[6] Sakr, H., Chen, Y., Jasion, G. T., Bradley, T. D., Hayes, J. R., Mulvad, H. C. H., Davidson, I. A., Numkam Fokoua, E., and Poletti, F., "Hollow core optical fibres with comparable attenuation to silica fibres between 600 and 1100 nm," *Nature Communications* **11**, 6030 (Nov 2020).

[7] Komanec, M., Suslov, D., Zvánovec, S., Chen, Y., Bradley, T., Sandoghchi, S. R., Numkam Fokoua, E. R., Jasion, G. T., Petrovich, M. N., Poletti, F., Richardson, D. J., and Slavík, R., "Low-loss and low-back-reflection hollow-core to standard fiber interconnection," *IEEE Photonics Technology Letters* **31**, 723–726 (May 2019).

[8] Rikimi, S., Bradley, T., Gouveia, M., Horley, R., Harker, A., Bawn, S., Poletti, F., Petrovich, M., Richardson, D., and Wheeler, N., "Long-term behaviour of water vapour absorption in hollow core fibres," *Sixth Workshop on Specialty Optical Fibers* (11 2019).

[9] Chen, Y., Liu, Z., Sandoghchi, S. R., Jasion, G. T., Bradley, T. D., Numkam Fokoua, E., Hayes, J. R., Wheeler, N. V., Gray, D. R., Mangan, B. J., Slavík, R., Poletti, F., Petrovich, M. N., and Richardson, D. J., "Multi-kilometer long, longitudinally uniform hollow core photonic bandgap fibers for broadband low latency data transmission," *Journal of Lightwave Technology* **34**, 104–113 (Jan 2016).

[10] Gray, D. R., Li, Z., Poletti, F., Slavík, R., Wheeler, N. V., Baddela, N. K., Petrovich, M. N., Obeysekara, A., and Richardson, D. J., "Complementary analysis of modal content and properties in a 19-cell hollow core photonic band gap fiber using time-of-flight and S2 techniques," in [*2012 38th European Conference and Exhibition on Optical Communications*], 1–4 (Sep. 2012).

[11] Nicholson, J. W., Yablon, A. D., Fini, J. M., and Mermelstein, M. D., "Measuring the modal content of large-mode-area fibers," *IEEE Journal of Selected Topics in Quantum Electronics* **15**(1), 61–70 (2009).

Highly-efficient and low return-loss coupling of standard and antiresonant hollow-core fibers

Dmytro Suslov[1], Matej Komanec[1], Stanislav Zvánovec[1], Tom Bradley[2], Francesco Poletti[2], David J. Richardson[2] and Radan Slavík[2]

[1]*Department of Electromagnetic Field, Czech Technical University in Prague, Technicka 1902/2, 166 27 Prague 6, Czech Republic*

[2]*Optoelectronics Research Centre, University of Southampton, Southampton, SO17 1BJ, UK*
suslodmy@fel.cvut.cz

Abstract: We show results on adopting our new technique, developed for connecting solid-core fibers with hollow-core photonic bandgap fibers, to connect solid-core with antiresonant hollow core fibers. We achieved insertion loss below 0.5 dB per connection.

OCIS codes: 060.2340, 060.4005.

1. Introduction

Hollow-core fibers (HCFs) present many benefits over traditional glass-core fibers due to the light propagating in air, which leads e.g. to low nonlinearity, low latency, low thermal sensitivity and potentially to low loss [1]. Due to these properties HCFs have been identified as a possible candidate for the next generation of telecommunication fibers [2]. However, for a wider adoption of HCF it is necessary to efficiently integrate them with the existing fiber systems for example to interconnect HCFs with standard single-mode fibers (e.g. SMF-28) with low loss and low back-reflection.

In our recent work [3] we demonstrated such an interconnection between a 19-cell hollow-core photonic bandgap fiber (PBGF) and SMF-28. To reduce the interconnection loss down to 0.3 dB per interconnection, we used graded-index multimode fiber mode-field adapter (GRIN MFA) to convert the SMF-28 mode into the HCF fundamental mode. To suppress the back-reflection due to the glass-air interface (due to light propagation from the glass-core of SMF-28 to the air-core of HCF or vice-versa), we deposited an antireflective coating on GRIN MFA surface. Permanent interconnection was established via gluing (as fusion-splicing would destroy the coating), which is a well-established technique from the interconnection of planar lightwave circuits to optical fibers.

Recently, various geometries of antiresonant fibers (rather than PBGF) have emerged as the best candidates to achieve low-loss HCF, including nested antiresonant nodless fibers (NANF) [4] (with minimum published loss of 1.3 dB/km at 1450 nm [5]) and conjoined-tube negative-curvature fiber with minimum loss of 2 dB/km at 1512 nm [6]. Here, we report on our initial work on adapting our interconnection technique to interconnect SMF-28 with NANFs.

2. The experiment

Firstly, we measured the mode-field diameter (MFD) of NANF and PBGF using the setup shown in Fig. 1 (a) to evaluate the difference between these two fibers. To measure the MFD light escaping from the fiber under test (FUT) was collimated with Lens 1 and captured with a camera. To put FUT into the Lens 1 focus and to precisely evaluate the magnification of Lens 1 (necessary to accurately measure the MFD), Laser 2 with Lens 2 illuminated the surface of FUT with the back-reflection of FUT's structure captured on the camera.

Using this method we measured $\mathrm{MFD}_{\mathrm{PBGF}} = 20.9\,\mu\mathrm{m}$ and $\mathrm{MFD}_{\mathrm{NANF}} = 24.3\,\mu\mathrm{m}$ at 1550 nm. The slightly larger MFD of NANF means that GRIN MFA with larger MFD (or GRIN with different refractive index profile to obtain larger MFD) will be needed for matching its mode and thus obtaining low insertion loss of the interconnection. We used GRIN MFAs with core diameter of $62.5\,\mu\mathrm{m}$ with quarter-pitch length (fully-collimated output) at $265\,\mu\mathrm{m}$. For PBGF the optimal GRIN MFA length was determined as $295\,\mu\mathrm{m}$, therefore a shorter GRIN MFA (in the interval of 265-290 μm) will provide a greater MFD and thus possibly adequate MFD matching in case of NANF. To verify this prediction, we interconnected the PBGF and NANF with SMF-28 using a set of GRIN MFAs (with different length) that we had available from our previous work in which PBGF interconnection was investigated [3] and measured the insertion loss.

The used setup is shown in Fig. 1 (b). An amplified spontaneous emission (ASE) from an erbium doped fiber amplifier (EDFA) filtered with an optical bandpass filter (OBPF 1545 - 1555 nm) was used as a broadband source.

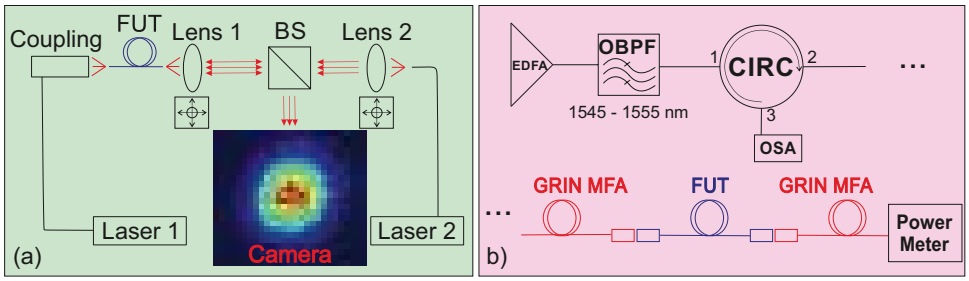

Fig. 1. Setup for MFD measurement (a) and setup for IL measurement of NANF and PBGF (b).

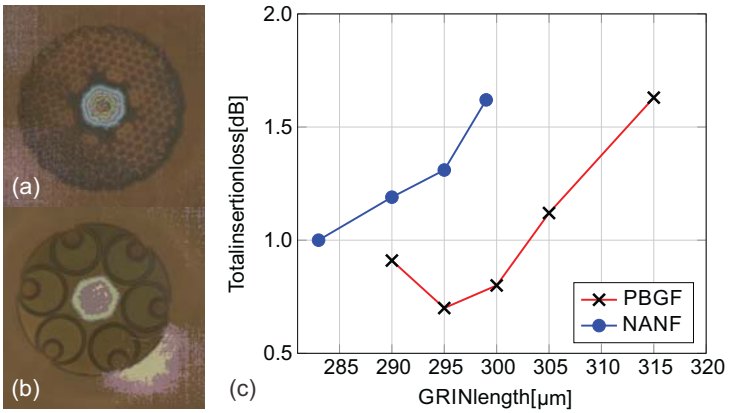

Fig. 2. The images of MFD measurement of NANF (a) and PBGF (b) overlaid with the image of the core area of FUT. Results of the measured IL of NANF and PBGF using pairs of GRIN MFAs (c).

After passing through circulator (CIRC) light was launched into the FUT using antireflection coated GRIN MFA. Another GRIN MFA (of the same length) was used to out-couple the light from FUT.

The results are shown in Fig. 2 (c). For PBGF, we achieved optimum GRIN MFA length of 295 μm (with single-interface GRIN-PBGF loss of 0.3 dB). For NANF, the optimum GRIN MFA length is shorter (as predicted by MFD analysis), being $< 283\,\mu$m. Unfortunately, GRIN MFAs shorter than 283 μm were not available at the time to find the minimum obtainable interconnection loss of NANF. However, our results in case of NANF-SMF of $<$ 1 dB (single interface loss of $<$ 0.5 dB) are very encouraging (giving very low interconnection loss, sufficient for most applications). The trending in Fig. 2 (c) suggests that lower IL is achievable provided we use even shorter GRIN MFA. The return-loss was measured to be below -35 dB, which is a similar result we achieved with PBGF.

References

1. D.J. Richardson, N.V. Wheeler, Y. Chen, J.R. Hayes, S.R. Sandoghchi, G.T. Jasion, T.D. Bradley, E.N. Fokoua, Z. Liu, R. Slavík, P.E. Horak, M.N. Petrovich, and F. Poletti. Hollow Core Fibres and their Applications. In *Optical Fiber Communication Conference*, page Tu3H.1. Optical Society of America, 2017.
2. F. Poletti, N.V. Wheeler, M.N. Petrovich, N. Baddela, E. Numkam Fokoua, J.R. Hayes, D.R. Gray, Z. Li, R. Slavík, and D.J. Richardson. Towards high-capacity fibre-optic communications at the speed of light in vacuum. *Nature Photonics*, 7(4):279–284, 2013.
3. M. Komanec, D. Suslov, S. Zvánovec, Y. Chen, T. Bradley, S. R. Sandoghchi, E. R. N. Fokoua, G. T. Jasion, M. N. Petrovich, F. Poletti, D. J. Richardson, and R. Slavík. Low-Loss and Low-Back-Reflection Hollow-Core to Standard Fiber Interconnection. *IEEE Photonics Technology Letters*, pages 1–1, 2019.
4. F. Poletti. Nested antiresonant nodeless hollow core fiber. *Opt. Express*, 22(20):23807–23828, Oct 2014.
5. T. D. Bradley, J. R. Hayes, Y. Chen, G. T. Jasion, S. R. Sandoghchi, R. Slavík, E. N. Fokoua, S. Bawn, H. Sakr, I. A. Davidson, A. Taranta, J. P. Thomas, M. N. Petrovich, D. J. Richardson, and F. Poletti. Record Low-Loss 1.3dB/km Data Transmitting Antiresonant Hollow Core Fibre. In *2018 European Conference on Optical Communication (ECOC)*, pages 1–3, Sep. 2018.
6. S.-F. Gao, Y.-Y. Wang, W. Ding, D.-L. Jiang, S. Gu, X. Zhang, and P. Wang. Hollow-core conjoined-tube negative-curvature fibre with ultralow loss. *Nature Communications*, 9(1), 2018.

Angled interconnection between standard single-mode fiber and nested nodeless antiresonant fibers

Dmytro Suslov[1], Daniel Dousek[1], Stanislav Zvánovec[1], Eric R. Numkam Fokoua[2], Francesco Poletti[2], David J. Richardson[2], Matěj Komanec[1], and Radan Slavík[2]

[1]*Department of Electromagnetic Field, Czech Technical University in Prague, Technicka 1902/2, 166 27 Prague 6, Czech Republic*

[2]*Optoelectronics Research Centre, University of Southampton, Southampton, SO17 1BJ, UK*
suslodmy@fel.cvut.cz

Abstract: We present angled interconnection between standard single-mode fiber and nested nodeless antiresonant fibers achieving an insertion loss of 0.45 dB and return loss below -60 dB over a wide (1450-1650 nm) spectral range.

1. Introduction

Hollow-core fibers show great promise for many fields including telecommunications, high power laser beam delivery, and optical sensing. Recently, hollow-core fibers of nested anti-resonant nodeless geometry (NANF) have reached an attenuation of only 0.28 dB/km [1], which is approaching that of standard single-mode fibers (SSMFs), as well as transmission over a broad spectral range with low chromatic dispersion and non-linearity.

To enable seamless integration with existing fiber systems and components it is necessary to interconnect the NANF with SSMF. This poses three main challenges. Firstly, the mode field diameter (MFD) of NANF is more than twice as large as that of SSMF. Secondly, there is a strong back-reflection (about 3.5%) due to the guided light passing through the glass-air interface. Finally, parasitic coupling into NANF higher order modes (HOMs) needs to be controlled, as these modes could otherwise cause multi-path interference.

Here we show how NANF can be interconnected to SSMF with a return loss below -60 dB over a broad wavelength range, an insertion loss as low as 0.45 dB and with minimal HOM excitation. We achieve this by modification of our previously-published method of low insertion loss permanent interconnection [2], in which we introduce to include angled mode-field adapters (MFAs). This result compares favourably to the state-of-the-art in low return loss hollow core to standard fiber interconnection [3], where significantly a higher insertion loss of 1-2 dB with a return loss of $<$-50 dB was achieved.

2. Measurement setup and results

The MFAs used in our study were based on a 265 µm long OM2 type graded-index (GRIN) fiber, which we measured to provide the best adaptation of mode field from SSMF (SMF-28, MFD = 10.5 µm) to our NANF (MFD = 24 µm, with a design identical to [4]). We first spliced the GRIN MFA to the SSMF and angle-polished their other end under angles of 2, 4, 6, 8 and 10°.

The return loss of the MFAs was measured using a 10-nm bandwidth unpolarized light source (generated with a band-pass filtered EDFA) and a 2x2 coupler, Fig. 1a). The results are shown in Fig. 1b), where we see the expected trend of return loss reduction with increasing angle. Beyond 8°, our measurement is most probably limited by parasitic reflections or reflection at the SSMF-MFA spliced interface. Nevertheless, we achieved the target return loss of over -60 dB for angles of 8°and 10°.

We have then prepared a SSMF-MFA-NANF-MFA-SSMF component (Fig. 1a), green box). An 8-m long NANF sample was interfaced with two identical MFAs that were spliced to SSMFs. The two MFAs were aligned with the NANF using 5D-micropositioning stages while observing the output power and transmission spectrum. The measured insertion loss of the entire SSMF-MFA-NANF-MFA-SMF component over a 5 nm spectral band using 10° MFAs is shown in Fig. 2a). For comparison, we also show the loss obtained with flat MFAs. To obtain single interconnect SSMF-NANF (SSMF-MFA-NANF) loss, we divided the total SSMF-MFA-NANF-MFA-SMF system loss by two. The measured SSMF-NANF loss was 0.45 dB when using 10° MFAs, which is only slightly higher than that obtained with flat MFAs (0.3 dB). There might be several reasons for this slight degradation, e.g., the ellipticity of the MFA output beam due to the 10° angle or the fact that angled MFA cannot be put as close to

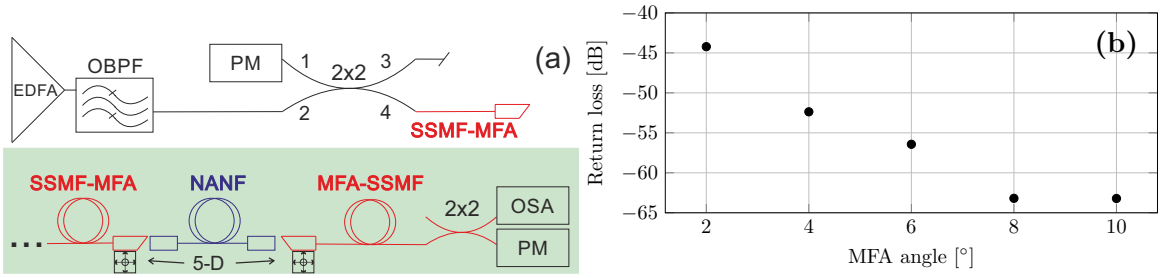

Fig. 1. (a) Setup for return loss and insertion loss measurement and (b) measured return loss of MFAs with various angles.

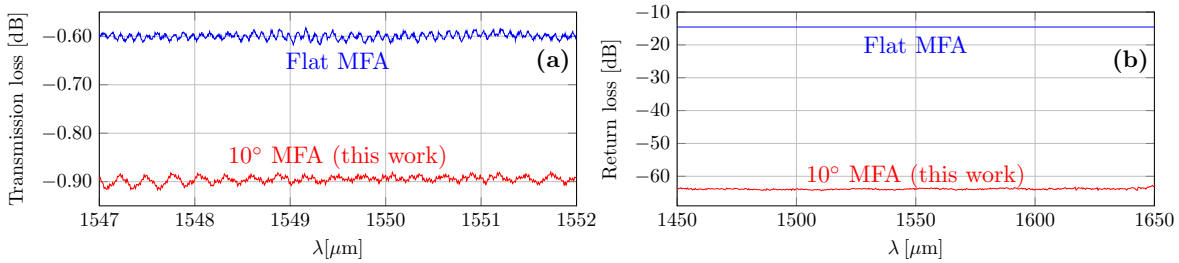

Fig. 2. (a) Measured transmission loss of SSMF-NANF-SSMF (two SSMF-NANF interconnections) over 5 nm bandwidth when using 10° MFAs and 0° MFAs. (b) Measured return loss of 10° MFA over 200 nm bandwidth and expected return loss for 0° MFA (for comparison).

NANF as the flat MFA (due to the angle, which means one side of the MFA is closer to the NANF than the other one). We plan to investigate this further.

The spectral transmission traces in Fig. 2a) showed small oscillations caused by the multi-path interference between the fundamental NANF mode and excited HOMs [2]. However, their amplitude is very small (<0.03 dB peak-to-peak), which should be acceptable for most applications.

Finally, we measured the return loss of the entire SSMF-MFA-NANF-MFA SSMF component. To enable broadband measurement we used a supercontinuum light source. Results for the 10° MFA over the 1450-1650 nm spectral range together with the 3.5% reflection expected from a single flat MFA (shown for comparison) are shown in Fig. 2b). This measurement confirms broadband back-reflection suppression by >60 dB over the entire spectral range.

3. Discussion

The achieved performance can be further improved by applying an anti-reflective coating on the angled MFA surface, which should further reduce the IL by 0.16 dB. Currently, this portion of signal is lost due to the Fresnel back-reflection: it is not coupled back into the fiber due to the MFA angle-polish, but is nevertheless lost.

The presented interconnect can also be glued to form a permanent connection, as already demonstrated on an interconnect with a flat MFA [2]. Our preliminary work on angled-MFA interconnect gluing shows that the difficulties due to the angle (the gap between NANF and angled MFA being smaller on one side than the other side) can be addressed by a slight modification of the gluing procedure.

References

1. G. T. Jasion, et al. Hollow Core NANF with 0.28 dB/km Attenuation in the C and L Bands. In *OFC Postdeadline Papers 2020*, page Th4B.4. Optical Society of America, 2020.
2. M. Komanec, et al. Low-Loss and Low-Back-Reflection Hollow-Core to Standard Fiber Interconnection. *IEEE Photonics Technology Letters*, pages 1–1, 2019.
3. G. A. Miller and G. A. Cranch. Reduction of intensity noise in hollow core optical fiber using angle-cleaved splices. *IEEE Photonics Technology Letters*, 28(4):414–417, Feb 2016.
4. T. D. Bradley, et al. Record Low-Loss 1.3dB/km Data Transmitting Antiresonant Hollow Core Fibre. In *44th European Conference on Optical Communication (ECOC 2018)*, pages 1–3, Sep. 2018.